A Powder Diffraction Study
of Problems in
PLATINUM GROUP METAL
EXTRACTION

□□□
□□□

A Powder Diffraction Study
of Problems in
PLATINUM GROUP METAL
EXTRACTION

IAN WILLIAM SANDS SMITH
B.Sc.(Hons.)
University of Natal, South Africa

Submitted in fulfilment of the
requirements for the degree of
Doctor of Philosophy in the Department
of Chemistry and Applied Chemistry,
University of Natal.

DURBAN
1994

To Stuart

ABSTRACT

The base metal and platinum group metal extractive processes for two South African refineries were examined using x-ray powder diffraction.

Base metal refinery matte contained nickel sulphide (Ni_3S_2), copper sulphide (Cu_2S), nickel-copper alloy (Ni-Cu), iron oxide (Fe_3O_4) - nickel iron oxide ($NiFe_2O_4$) and nickel oxide (NiO). Nickel iron oxide and cobalt sulphide (Co_3S_4) were found in matte aeration cavities. Matte fast cooling caused alloy zoning.

Alloy stoichiometry and weight percentages of matte constituents were calculated. Magnetic separation of the alloy phase was unfeasible due to high bulk and poor separation from Ni_3S_2. Sulphuric acid matte leaching produced residues containing copper sulphide ($Cu_{1.8}S$) and nickel sulphides (Ni_3S_4, NiS). Potassium cyanide residue leaching produced NiS-rich residues, while thiourea / hydrochloric acid leaching produced residues almost free of copper sulphide.

PGM concentrates were examined. Base metals occurred as: copper sulphate pentahydrate; copper sulphate hydroxide hydrate ($Cu_4SO_4(OH)_6 \cdot H_2O$); copper sulphide (CuS); copper platinum (Cu_3Pt); nickel oxide (NiO); nickel iron oxide ($NiFe_2O_4$). Lead occurred as lead sulphate and silicon as quartz and enstatite ($(Mg,Fe,Al)SiO_3$). Heating the concentrate to 260°C with sulphuric acid converted copper sulphide to copper sulphate. PGMs were mostly metallic. Overdrying concentrates caused pgm sintering. Drying with sulphuric acid reduced sintering.

PGM oxidative leach solubility was examined. Platinum sulphide (Pt,Pd)S caused low platinum and palladium solubility. (Ru,Rh,Ir,Pt)AsS caused low rhodium and ruthenium solubility. Platinum-rhodium ($Rh_{0.57}Pt_{0.43}$), ruthenium-osmium ($\sim Ru_{16}Os$), iridosmine (Os,Ir,Ru) also caused low pgm solubility. Silver chloride remained in residues. Concentrate overdrying produced insoluble sintered platinum, palladium monoxide, and ruthenium dioxide.

In minor concentrates sintered platinum, rhodium selenide ($RhSe_{2+x}$), ruthenium dioxide and possibly palladium monoxide lowered pgm solubility.
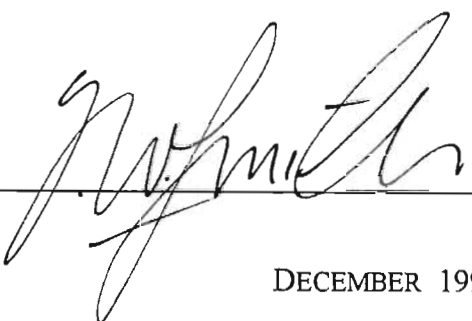
Precipitates and salts were examined. Iron precipitated as iron oxide hydroxide (β-FeOOH); gold as metallic gold; lead as lead chloride. Common salts were: sodium chloride; sodium iron hydroxide sulphate hydrate ($Na_2Fe(SO_4)_2(OH)\cdot 3H_2O$); ammonium chloride; sodium carbonate monohydrate.

PGM-lead fusion was examined. Fusion produced the insoluble alloy $Pb(Pd,Pt)_3$. Ruthenium dioxide reacted with lead carbonate forming lead ruthenium oxide ($Pb_2Ru_2O_{6.5}$). Nitric acid insoluble residues also contained lead sulphate and iron oxide (Fe_3O_4).

This study demonstrated that solution problems can be understood by identifying the crystalline insoluble phases in intractable residues.
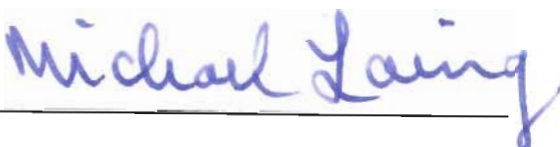
DECLARATION

I, IAN WILLIAM SANDS SMITH, declare that the work embodied in this thesis is my own original work, except as otherwise acknowledged in the text and has not been submitted for degree purposes at any other University.

DECEMBER 1994

I, Professor MICHAEL LAING, certify that the above statement is correct.

PROJECT SUPERVISOR

Acknowledgements

CONTENTS

□□□
CHAPTER 1

INTRODUCTION
□□□

1.1 OVERVIEW

This project was initiated by the South African base metal and platinum group metal refinery BARPLATS, which was being run largely on the basis of overseas research done by the Sherritt Gordon Group. Interest was shown in using x-ray powder diffraction to analyse more completely the nickel-copper concentrate they were processing. In addition, the idea of magnetically separating this concentrate had been proposed and a feasibility study was required. Also requiring analysis were some leach residues and leaching processes. Unfortunately due to economic and geological factors the mine supplying nickel-copper concentrate to BARPLATS was forced to close. This led to the take-over and closure of the base metal refinery shortly after the commencement of this project.

WESTERN PLATINUM REFINERY was then approached and showed an interest in a project aimed at solving some of the problems occurring in the platinum group metal extraction process at their refinery, focusing mainly on pgm solubility in the oxidative leach. To this end, process samples (some with elemental analyses) were to be provided for examination. As the study developed, clear links between base metal refinery operations and platinum group metal refinery operations emerged. The initial part of the project performed for BARPLATS, which focused on base metal refining, thus greatly assisted in explaining observations that otherwise would have remained a mystery.

1.2 PREVIOUS INVESTIGATIONS

Although much work has been done investigating base metal operations using x-ray powder diffraction [1], every refinery seems to have quite different ratios of base metal phases present in concentrate and residue samples. As these ratios play a major role in determining leaching characteristics, accurate analyses of the concentrates remain an important part of optimizing leach processes.

Relatively little has been done in the area of platinum group metal extraction. The low crystallinity of refinery samples imposes severe limits on the x-ray powder diffraction method. These difficulties are only overcome by comparing the analyses of numerous samples and persistently searching for inoganic and mineral phases that make chemical sense and explain observed facts.

Prior to this present study, a limited investigation of the phases occurring in the extractive process had been performed for WESTERN PLATINUM REFINERY. Although several samples were analysed, only one pgm phase was assigned. The report ended with the comment, *'There appears to be scope for much more detailed work on the nature and composition of the platinum [group metal] phases present.'*

As many extraction problems remained unresolved, a more thorough investigation remained a priority. The aim of this second study has thus been to determine the *'nature and composition'* of phases causing problems in platinum group metal extraction.

□□□
CHAPTER 2

X-RAY POWDER DIFFRACTION ANALYSIS
□□□

2.1 INTRODUCTION

The analytical method of x-ray powder diffraction makes use of the interference patterns produced when x-rays are scattered by the regular arrays of atoms present in crystalline powders. The atomic and structural uniqueness of every known compound has the important analytical implication that a unique x-ray diffraction pattern exists for all known pure substances possessing some degree of crystallinity. Knowing these patterns allows a qualitative analysis of phases in mixtures to be performed simply by comparing the observed pattern from the mixture with the patterns of known standard compounds. Two important subjects involved in the use of the powder diffraction method are :

Elementary crystallographic principles, and

The nature and generation of x-rays.

2.2 ELEMENTARY CRYSTALLOGRAPHIC PRINCIPLES [1]

The packing of ions, atoms or molecules into ordered three-dimensional arrays usually bounded by well-defined flat planes is known as crystallization, and the solids produced are known as crystals. The huge variety of crystals of various morphologies formed by this process necessitates some kind of classification.

2.2.1 THE CLASSIFICATION OF CRYSTALS ACCORDING TO EXTERNAL CHARACTERISTICS

For morphologically similar crystals of a given crystalline material it is noted that the flat planes bounding the crystal are orientated and inclined such that the angles between related intersecting planes are always the same. The first classification system is based on the axes required to describe these planes and their angles of intersection. Only seven categories, known as the **seven crystal systems**, are needed to classify every known crystal. **Table 2.2.1-1** lists these systems where a, b and c denote the lengths of each axis as related to the others, and α, β and γ denote the angles between the b/c, a/c, and a/b axes respectively. The equalities listed are the *minimum* required for the symmetry of the system. For example, it is possible for a crystal of triclinic symmetry to have a=b=c and $\alpha=\beta=\gamma=90°$ purely by chance.

Table 2.2.1-1   The Seven Crystal Systems

Crystal System	Axes	Angles of Itercepts		Abbreviation
Cubic	a=b=c	$\alpha=\beta=\gamma=90°$		Cub.
Tetragonal	a=b≠c	$\alpha=\beta=\gamma=90°$		Tet.
Hexagonal	a=b≠c	$\alpha=\beta=90°$	$\gamma=120°$	Hex.
Rhombohedral	a=b=c	$\alpha=\beta=90°$	$\gamma=120°$	Rhom.
(or Trigonal)		(or	$\alpha=\beta=\gamma\neq90°$)	
Orthorhombic	a≠b≠c	$\alpha=\beta=\gamma=90°$		Ortho.
Monoclinic	a≠b≠c	$\alpha=\gamma=90°$	$\beta\neq90°$	Mono.
Triclinic	a≠b≠c	$\alpha\neq\beta\neq\gamma\neq90°$		Tri.

A second more accurate way of classifying crystals based on their external idealized form has been devised using the elements of symmetry : reflection and rotation. Defining certain minimum symmetries, expressed by n-fold rotation axes, n-fold rotation/inversion axes and reflection (or mirror) planes, 32 classes, known as the **32 point groups** have been established, each of which relates to one of the seven crystal systems. The 32 point groups are however rarely used in qualitative x-ray powder diffraction analysis.

2.2.2 THE CLASSIFICATION OF CRYSTALS ACCORDING TO INTERNAL CHARACTERISTICS

Another approach in the classification of crystals involves a consideration of their internal rather than external order. Here, the emphasis is on the repetitive atomic arrangement within the crystal.

An array of points can be mathermatically defined such that each point has an identical spacial enviroment. Such an array is termed a **lattice**. In three dimensions it has been shown that there are only 14 unique arrays. These are known as the **14 Bravais lattices**. Each of these lattices is defined by a simple space-filling subunit known as the **unit cell**, which when translated in three-dimensional space, parallel to its axes produces the entire lattice structure.

The ordering of the atoms, ions or molecules in crystals corresponds to such arrays, although it is not required that an atom, ion or molecule be situated exactly on each lattice point.

Externally all unit cells are related symmetrically to the seven crystal systems discussed earlier. Seven additional unit cells are however required to fully describe the hidden internal structure of crystals. These are known as **non-primitive unit cells** and differ from **primitive unit cells** in that they contain more than one lattice point *per* cell. A primitive unit cell thus has lattice points positioned at each cell corner, while a non-primitive unit cell can have an additional lattice point positioned at the cell centre (body-centred), or on two opposite faces (end-centred), or on each face (face-centred). **Table 2.2.2-1** relates the seven crystal systems to the unit cells of the 14 Bravais lattices. See also **Figure 2.2.2-1**.

Table 2.2.2-1 Unit cells of the 14 Bravais lattices

Crystal System	Unit cell type	Symbol
Triclinic	Primitive	P
Monoclinic	Primitive	P
	End-centred	C
Orthorhombic	Primitive	P
	End-centred	C
	Body-centred	I
	Face-centred	F
Hexagonal	Primitive	P
Rhomohedral	Primitive	P
Tetragonal	Primitive	P
	Body-centred	I
Cubic	Primitive	P
	Body-centred	I
	Face-centred	F

The increased complexity introduced by considering the internal ordering of the contents of the unit cell in terms of two additional elements of symmetry (screw rotation axes and glide reflection planes) is reflected in an internal symmetry which now requires **230 space groups** to classify each possible case uniquely. These space groups define all the possible ways identical entities may be arranged in the 14 Bravais lattices. Fortunately, these space groups are hardly ever used in qualitative x-ray powder diffraction analysis.

2.2.3 DESCRIBING CRYSTALLOGRAPHIC PLANES

Having classified the three dimensional structure of crystals it becomes important to have some way of describing imaginary planes on which the atoms of crystals may lie. In order to express the differring orientations and distances between families of parallel planes, a reference system based on the unit cell is used. If a unit cell having edge lengths of a, b and c is intersected by a family of planes that are parallel and a set distance apart, then the number of divisions such a family produces along each unit cell axis length is used to identify the family of planes. A bracketed three digit number, known as the **Miller index**, is used to represent such a family. For example, the Miller index **(234)** is
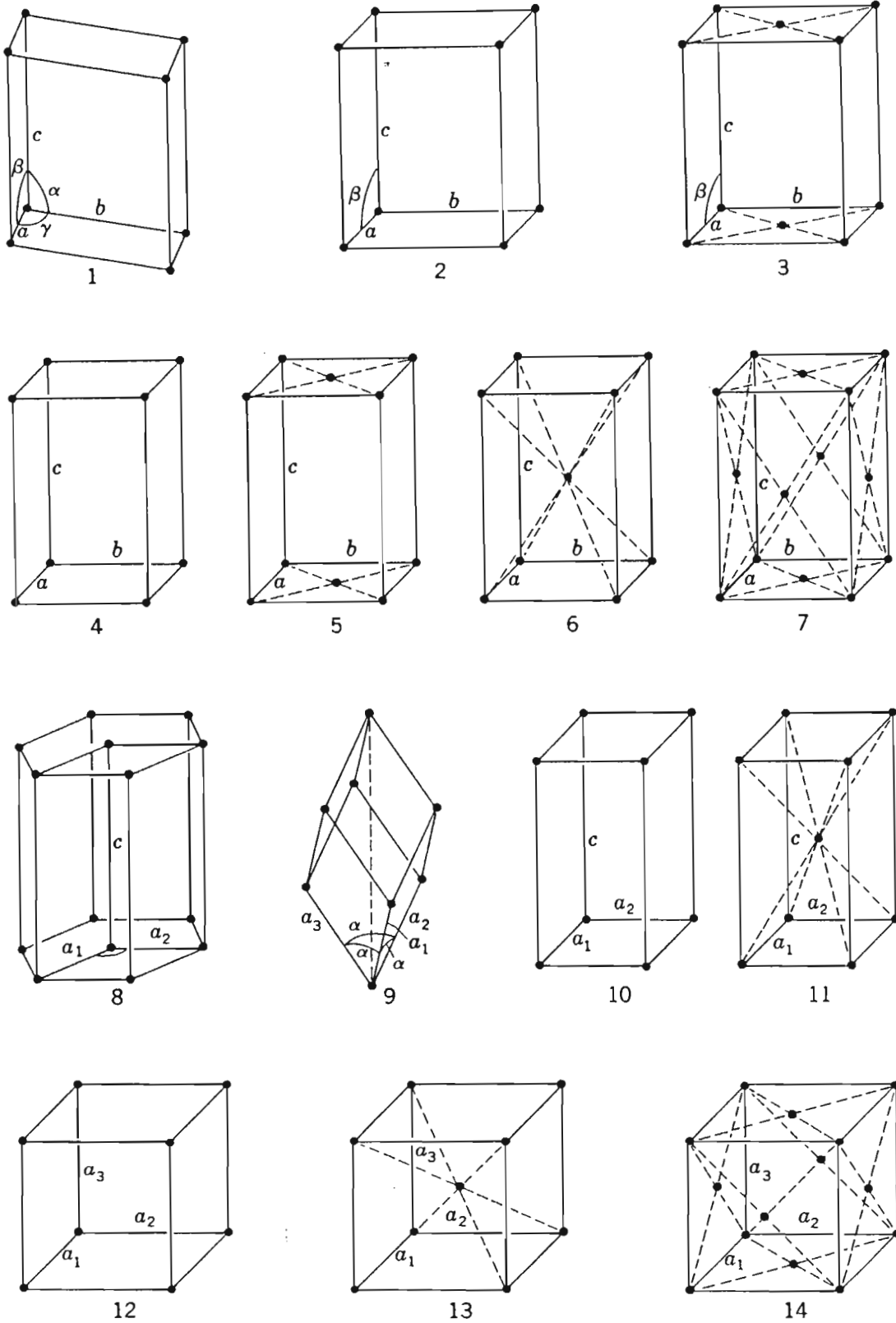
Figure 2.2.2-1 Unit Cells of the 14 Bravais Lattices [1]

1 Triclinic P	**2** Monoclinic P	**3** Monoclinic C	**4** Orthorhombic P
5 Orthorhombic C	**6** Orthorhombic I	**7** Orthorhombic F	**8** Hexagonal P
9 Rhombohedral P	**10** Tetragonal P	**11** Tetragonal I	**12** Cubic P
13 Cubic I	**14** Cubic F		

taken to mean a family of parallel equidistant planes that, on passing through the crystals unit cell, produces **2** divisions along the **a** axis, **3** divisions along the **b** axis and **4** divisions along the **c** axis (note that the order of the numbers in the Miller index follows the order **abc**) **(Figure 2.2.3-1(a))**. A zero digit indicates that the family of planes is orientated parallel to the axis indicated by the zero. For example, **(101)** planes produce one division along the **a** axis and one division along the **c** axis and are orientated parallel to the **b** axis **(Figure 2.2.3-1(b))**. In practice, Miller indices are important because they are used to calculate unit cell dimensions. They are also used for labelling diffraction peaks.

2.3 *THE NATURE AND GENERATION OF X-RAYS* [2]

2.3.1 INTRODUCTION

X-rays form the band of electromagnetic radiation falling in the wavelength range 0.1 - 100Å ($1Å = 10^{-10}$m). They are produced whenever matter is bombarded with high energy electrons. X-rays used for diffraction analysis commonly have wavelengths of about 0.5 - 2.3Å and are generated in evacuated tubes containing an anode, known as the **target**, and a cathode. A high potential difference (35 - 90kV) is applied between these electrodes so as to accelerate a stream of electrons, produced by a heated tungsten wire, towards the anodic target.

2.3.2 CHARACTERISTIC X-RAY RADIATION

If an electron from one of the inner shells of the atoms making up the anodic target is ejected by one of the high speed electrons, an unstable cation having an inner shell vacancy is produced. A series of electronic transitions followed by electon capture now occur which ultimately returns the unstable cation to a ground state atom. Each transition is accompanied by the emission of an x-ray photon of energy equivalent to the difference between the binding energies associated with the shells involved. The energies of such photons are high (short wavelength), of very specific wavelengths, and form what is known as **characteristic radiation**. The three most important electronic

Figure 2.2.3-1(a) Family of planes having Miller indices **(234)**

Figure 2.2.3-1(b) Family of planes having the Miller indices **(101)**
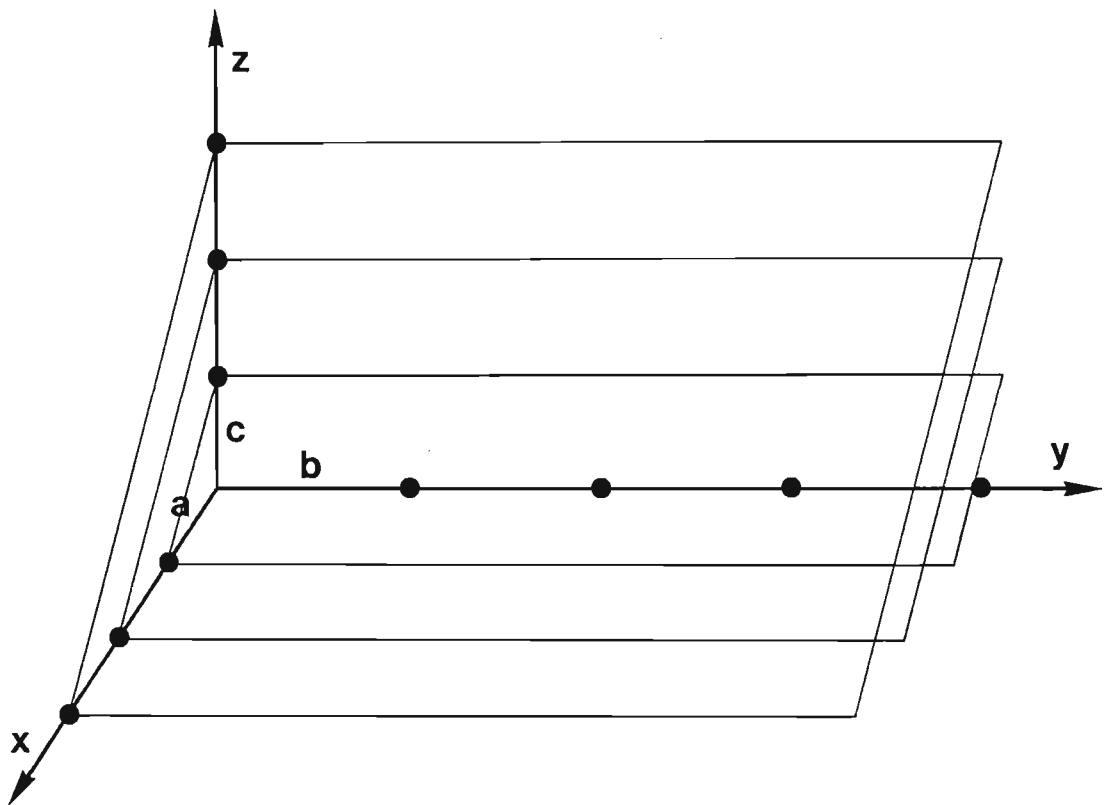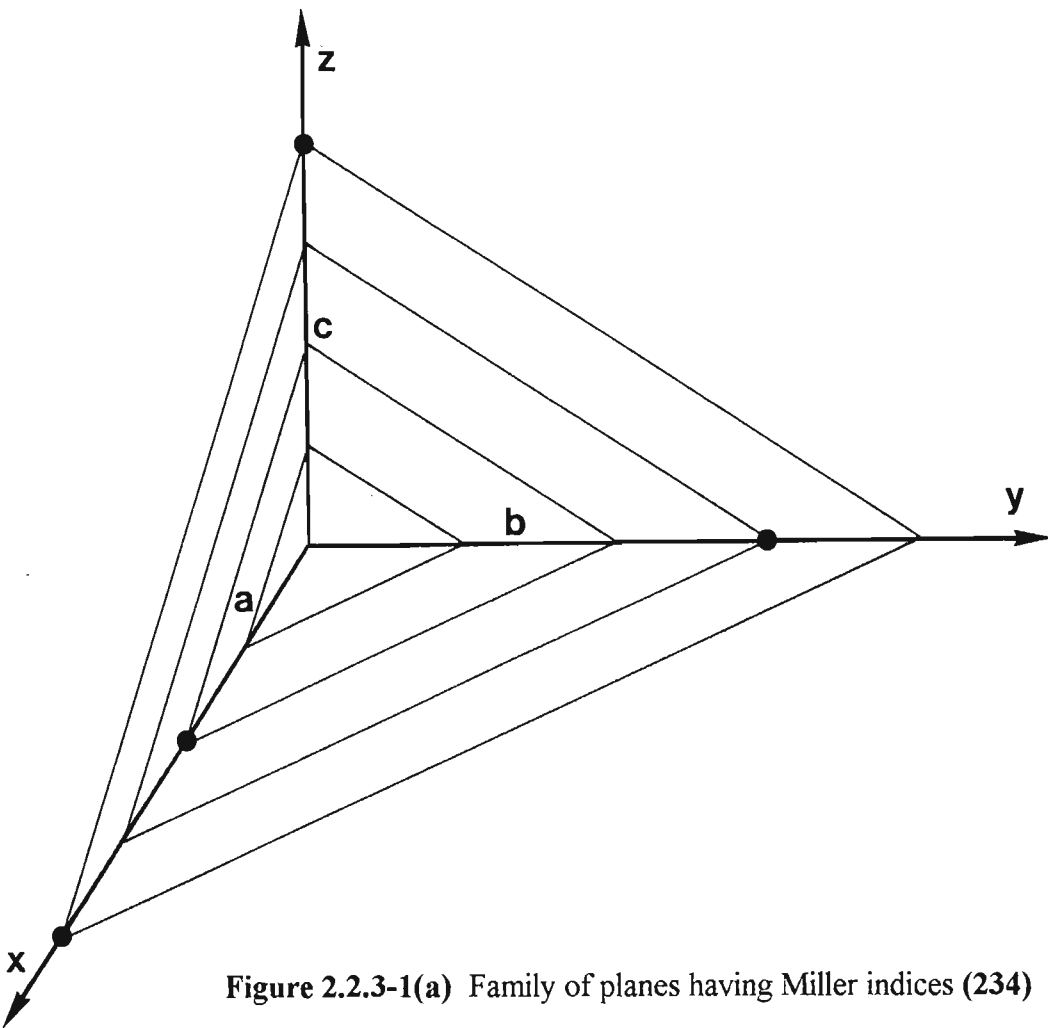
shells involved in x-ray emission have the principal quantum numbers 1, 2 and 3. These are usually referred to as the K, L and M shells respectively (see below).

NUCLEUS

	K shell	L shell	M shell
	$n = 1$	$n = 2$	$n = 3$
	s orbital	s and p orbitals	s, p and d orbitals
	1 level (K)	3 levels ($L_{I,II,III}$)	5 levels ($M_{I,II,III,IV,V}$)

Only a limited number of transitions are allowed under the quantum-mechanical selection rules and so the x-ray emission spectrum for the target is relatively simple. Each transition is given a three symbol label indicating the shell of the vacancy (K, L, M etc.), the shell of the outer electron filling it relative to the first shell (α, β, γ etc.) and a numerical subscript denoting the intensity of the transition radiation (1 > 2 > 3 etc.). Some important transitions are :

$K\alpha_1$	$L_{III} \rightarrow K$	$L\alpha_1$	$M_V \rightarrow L_{III}$
$K\alpha_2$	$L_{II} \rightarrow K$	$L\alpha_2$	$M_{IV} \rightarrow L_{III}$
$K\beta_1$	$M_{II} \rightarrow K$	$L\beta_1$	$M_{IV} \rightarrow L_{II}$

2.3.3 CONTINUOUS X-RAYS

Continuous x-ray radiation originates quite differently but is not used in powder diffraction analysis, being polychromatic and of relatively low intensity. It is however of value for the study of single crystals by the Laue method.

2.4 THE DIFFRACTOMETER [3]

A diffactometer is an instrument which allows a sample to be irradiated with a monochromatised x-ray beam while recording reflected beams using a detector. For *powder* diffractometers the sample is finely powdered, producing crystallites orientated in every possible direction. On irradiation with monochromatic x-rays, the regular arrays of atoms in each crystalline phase diffract the incident beam into many reflected beams which are reflected out in all directions. The intensities of these beams are not equal, the

differences being determined by the arrangement of the atoms in the unit cell. For constructive interference to occur for a set of planes of interplanar spacing d, and Miller indices **(hkl)**, the following simple condition, known as the **Bragg equation**, has to be met :

$$n\lambda = 2d\sin\theta$$

where   n = order of reflection (1 in almost all cases) (unitless)

            λ = wavelength of the incident monochromatic x-ray (Å)

            d = interplanar or d-spacing of the diffracting planes in the crystal (Å)

            θ = angle of incidence (and reflection) between the crystallographic planes

               and x-ray beam (degrees)

Using this condition the direction (angle) of each intense reflected beam can be related to the interplanar spacings, d, and unit cell dimensions a, b, c, α, β and γ of a crystal. As the crystals of each compound have numerous crystallographic planes separated by different interplanar distances and orientated in various directions, each compound generates a unique set of constructivly reinforced reflections that can be detected by rotating a detector around the irradiated powder sample.

X-ray powder diffractometers are expensive and complex instruments being made up of many sub-components. Typical components of a diffraction system are listed below.

1. Stabilized high-voltage AC power supply

2. DC power supply

3. Water supply

4. High intensity x-ray tube

5. Multi-sample chamber that can be evacuated

6. Goniometer for measuring diffraction angles

7. Detector for diffracted beams

8. A scaler, amplifier, analyser and recorder for the detected signals

9. A dedicated computer system for control of the goniometer and storage and analysis of the measured data.

The following section describes the powder diffractometer system used to collect the data used in this project.

2.5 DESCRIPTION OF THE DIFFRACTOMETER SYSTEM

2.5.1 OVERVIEW

A Philips PW 1710 APD (automated powder diffractometer) direct recording powder diffraction system was used (**Figure 2.5-1**).

2.5.2 THE POWER SUPPLY

The PW 1710 APD system was powered by a PW 1730 high-performance generator.

2.5.3 THE X-RAY TUBE

A Philips PW 2256/20 (Version A - with a PW 1316 tube shield) cobalt tube was used. This had a **cobalt** anodic target set to earth and gave a broad focus beam with a focal spot measured at the anode of $2 \times 12mm$ (focal area $24mm^2$). The maximum output power rating for the tube was 2700watt at constant potential with a specific loading of $112watt/mm^2$. This tube was operating at 40kV, well within the maximum allowable of 60kV. The current used was 30mA. This target produced x-ray emission spectra with the following characteristics :

CONTINUOUS SPECTRUM

The continuous spectrum (white radiation) had a short wavelength limit, λ_o, of 0.3100Å. The wavelength of maximum intensity, λ_{max}, was 0.4649Å.

CHARACTERISTIC SPECTRUM

Cobalt targets have a critical excitation potential of 7.71kV above which they emit radiation of the following wavelengths :
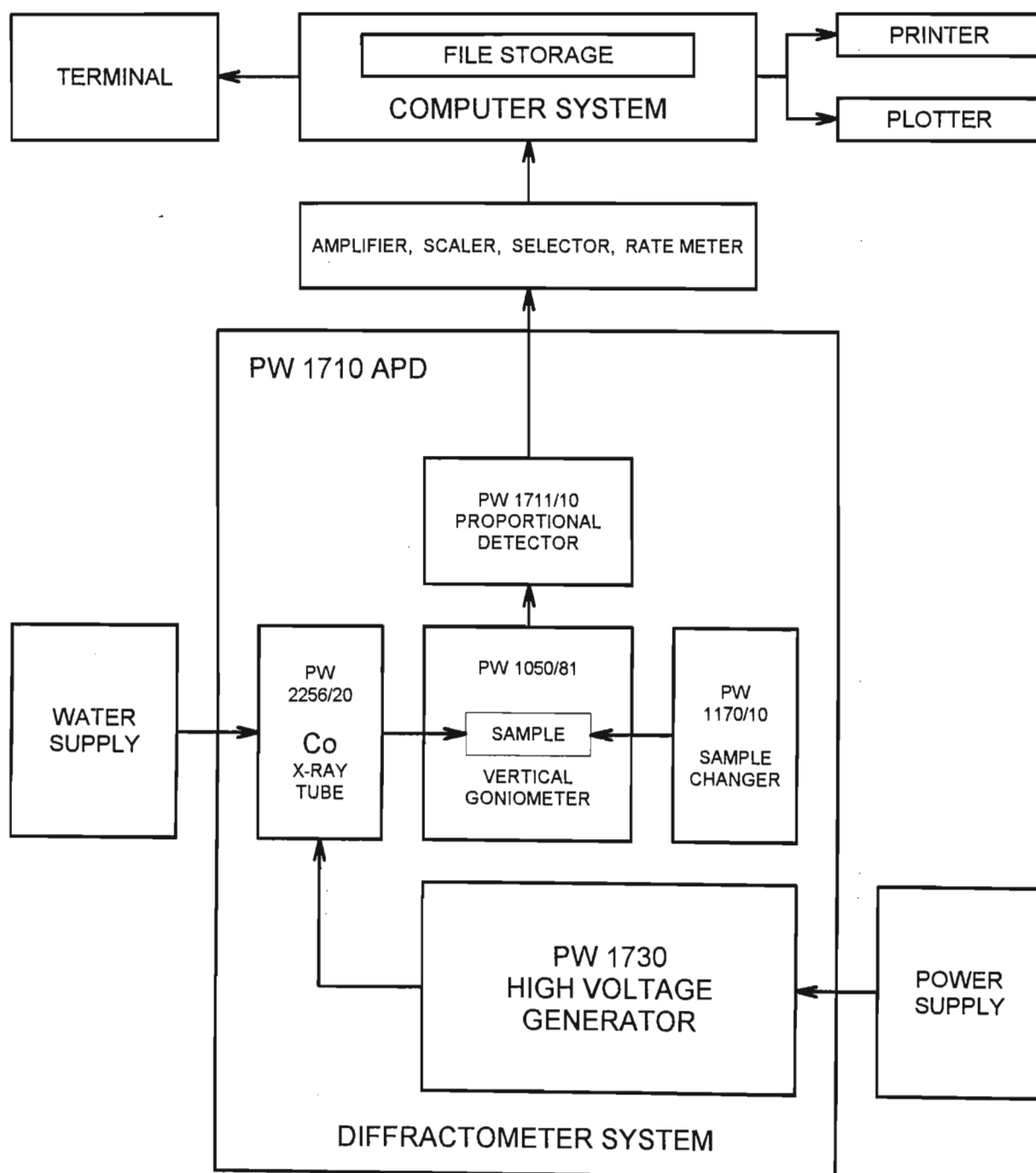
Figure 2.5-1 Schematic diagram of the Powder Diffraction System

$$K\alpha_1 \qquad \lambda = 1.78892\text{Å}$$
$$K\alpha_2 \qquad \lambda = 1.79278\text{Å} \qquad\qquad (K\alpha_{1,2} \text{ or } K\alpha : \lambda = 1.79026\text{Å})$$
$$K\beta_1 \qquad \lambda = 1.62079\text{Å}$$

The wavelength used by the computer system to convert the diffraction angle 2θ, measured in degrees, into d-spacings, measured in Ångstroms, was 1.78894Å. The equation for converting diffraction angles (2θ) into d-spacings (d) is thus (§ 2.4) :

$$d\ (\text{Å}) = 0.89447\ /\ \sin\ (2\theta\ /\ 2) \qquad\qquad \mathbf{2\theta \rightarrow d}$$

while that for converting d-spacings (d) into diffraction angles (2θ) is :

$$2\theta\ (\text{degrees}) = 2 \times \arcsin(1.78894\ /\ (2 \times d)) \qquad\qquad \mathbf{d \rightarrow 2\theta}$$

The anode was cooled by a continuous flow of water (about 3.5 l/min).

The $CoK\beta_1$ radiation was removed by a graphite monochromator positioned in the diffracted beam.

A cobalt tube was chosen because :

1) The longer $K\alpha$ wavelength allows larger d-spacings to be measured.

2) The $K\alpha$ radiation does not cause iron to fluoresce.

3) The longer wavelength is scattered better by softer materials.

2.5.4 THE GONIOMETER

A vertical Philips PW 1050/81 goniometer was used. This had a 50Hz synchronous motor drive and was fitted with an automatic Philips PW 1386/55 theta-compensating divergence slit which ensured a fixed area of sample was irradiated by the x-ray beam at all diffraction angles (2θ), thereby enhancing the intensities of diffracted beams at high diffraction angles, which are normally weak. This also resulted in low background at low diffraction angles and good peak to background ratios.

It is important to note that as an **automatic divergence slit** (ADS) was used in the data collection, the relative intensities of diffracted peaks will differ considerably from those that would be measured using a fixed divergence slit (FDS). An ADS gives higher intensities at high angles and lower intensities at low angles relative to those measured with a FDS. Thus the relative intensities observed with this system often differed considerably from those in the standard Powder Diffraction File (§ 2.7.2)..

The conversion equation (which assumes that intensity varies linearly with the divergence of the x-ray beam) is given below [4] :

$$I_F = (0.20268 \times D \times I_A) / (\sin (11.16 + ((79 \times \theta) / 90)) - 0.19355)$$

where I_F = intensity using a fixed divergence slit

   D = fixed slit divergence in degrees (*eg.* ½°, 1°, 2°, 4°)

   I_A = intensity using an automatic divergence slit

   $\theta = 2\theta / 2$

This equation can be used when comparing observed data with data of a standard file pattern measured using a fixed divergence slit. The value of D is however usually not quoted, and so has to be derived by comparison.

The goniometer was regularly aligned using quartz powder as a standard, the scan being run from 5 - 30°. Quartz (α-SiO_2, low) gives peaks at the following d-spacings in this range:

1) 4.26 Å   Relative intensity 35
2) 3.343 Å   Relative intensity 100

2.5.5 THE DETECTOR

A Philips PW 1711/10 proportional detector equipped with a sealed xenon detector chamber was used. This detector had an entry window of beryllium 300μm thick. The counting gas was a mixture of xenon (97%) and carbon dioxide (3%). A 60 × charge preamplifier gave an overall counting efficiency for cobalt radiation of 88%.

The pulse-height descriminator window was set at 35 - 70% so as to prevent sample fluorescence and background tube radiation of low wavelength from increasing the counts of the recorded pulses.

2.5.6 SCAN SETTINGS

Scans were run from $2\theta = 5.010$ to $120.010°$ (d = 20.465 to 1.033Å) using step sizes of 6.66s / degree (2θ) and 5.00s / degree (2θ). Peak positions were taken as the peak maxima. The minimum peak significance was set to 0.75.

2.6 SAMPLE PREPARATION

The only real criteria for a sample to be analysable with XPD is that it should be in powder form (if not metallic) and have some degree of crystallinity. A few important considerations on sample handling and preparation as performed are given below.

2.6.1 SAMPLE LABELLING

Every sample was labelled chronologically as received with a simple unique source and number code.

2.6.2 SAMPLE EXAMINATION AND COMPONENT SEPARATIONS

Each sample was mixed well and divided into two parts, one being retained as representing the sample as received. The other part was examined physically and chemically.

In several cases, physical examination allowed the removal of crystals which had formed in the sample on drying, and the separation of large alloy crystals or granules. Strongly magnetic particles usually indicated the iron oxide Fe_3O_4. The diffraction pattern of the non-magnetic fraction was far simpler to interpret, as most of the iron oxide peaks were now removed.

Sometimes salts not completely removed by residue washing at the plant produced peaks which severely interfered with peaks due to other phases. In such cases, simple washing and mild drying gave satisfactory results. Drying of residues at the plant sometimes gave samples containing soluble salts detectable at the 1 to 2% level.

Some samples could be separated into fractions of different sizes by sorting, or settling techniques in water or organic solvents. (With inert powders such as pgm residues flotation methods can also be used.) In most cases these fractions produced dissimilar scans. On occasions large silvery alloy granules were detected and removed from the sample and scanned separately. Some were examined under a scanning electron microscope possessing a microprobe analyser, to identify the elements present.

Thermal decomposition of components of a sample sometimes yielded valuable clues as to the exact identity of the phases present. Thermal decomposition products are generally easy to identify using XPD.

Leaching with various reagents is a favoured method of component separation in XPD analysis. For most pgm residues however this method could not be used as residue components were quite inert and generally insoluble in everything. Concentrated (fuming) acids were sometimes used to chemically attack certain alloy phases. Flux dissolution methods were also used in rare cases.

Drying at higher than normal temperatures (~250°C) was found to improve the quality and resolution of peaks corresponding to alloys because the process of sintering partially melted fine alloy particles, resulting in crystal growth.

2.6.3 SAMPLE AND SLIDE PREPARATION

When samples were not fine homogeneous powders, they were powdered with a clean acetone-washed agate pestle and mortar. The method used for powdering is important. Crushing granules so as to fracture them was preferred over grinding, as shearing forces sometimes led to crystalline disorder [5]. PGM residues are generally extremely fine black powders and so crushing is not important unless the sample has been dried as a cake and broken up. In some cases sample powdering was observed to greatly affect the intensities of peaks, especially those of the iron oxide Fe_3O_4. The powdered sample was mounted in a clean flat-bed aluminium slide by pressing a portion of powder into the rectangular cavity. Glue was smeared on the base plate to secure the compressed powder cake. Surface irregularities were avoided by pressing with a microscope slide. (Smoothing is not recommended, as some crystalline particles can be plate-like, and smoothing therefore causes preferred orientation. This leads to some basal reflections having exaggerated intensities.) The thickness of mounted samples was 1.0mm in all cases.

Normally internal standards such as silicon dioxide are used to calibrate measured d-spacings. As most pgm residues contain silicon oxide, calibration was automatically achieved.

2.7 SOLUTIONS FROM RESULTS

2.7.1 INTRODUCTION

After the sample had been scanned, and the diffractometer system had stored the scan data in a computer file, hard copies were produced as a data listing and a plot of the diffractogram. The relative intensity values were invaluable in making qualitative

comparisons. The horizontal axis could be plotted as d-spacings or diffraction angles, calibrated in Ångstoms or degrees respectively. Diffraction angles in degrees were more practical as the peaks were better spaced across the axis. This made comparisons a lot easier.

The data listing contained such information as peak diffraction angles (2θ), peak counts and background counts, d-spacings, and relative integrated intensities.

2.7.2 SEARCH MANUALS AND POWDER DIFFRACTION FILES

In principle, once the diffraction data for a sample has been collected, the process of data analysis can begin. Data analysis can be approached in several different ways. The most common method is to use search manuals [6] to match observed peaks to reference data. Such manuals constitute various indices, some of which are based on compound type (*eg.* oxide, sulphide), while others are based on the d-spacings of the three or four most intense peaks given by the pure compound.

Every index entry gives eight or ten d-spacings corresponding to the eight or ten most intense peaks given by the compound. All other information is obtainable from a powder diffraction card, the number of which is referenced with the entry. These cards are contained in bound volumes and give such data as peak d-spacings, intensities and the Miller indices of the plane(s) of origin; crystallographic data such as the space group, lattice parameters, interaxial angles, calculated density and number of formula units per unit cell; and other information such as colour, and melting point. The data source is usually given.

Once a family of peaks has been identified, a second family of peaks from the remaining lower intensity peaks is searched for (allowing for overlap), and so on until all peaks have been assigned. In scans from mixtures containing several components, it is easy for incorrect families of peaks to be chosen. This makes the analysis of mixtures difficult.

In such cases several attempts at component separation are made, until solutions are derived from additional scans that satisfy the samples elemental analysis, make chemical sense, and explain observations.

Another approach involves matching peaks with one of the unit cell types (*eg.* cubic, tetragonal etc.) and calculating the unit cell dimensions. Indices are available that are categorised according to unit cell type and parameters.

All the above methods were used where appropriate.

2.7.3 COMPUTER METHODS

Computer search programs and diffraction data libraries are available, but solutions yielded by such programs can be totally incorrect and misleading. The specific needs of a particular user might not be met by commercially available programs due to inherent inflexibilities, although the situation is improving.

The programming of an analysis program specific to the needs of a project, with a selected compound library, sample scan filing capabilities and numerous graphical manipulation techniques (such as superimposing, shifting and matching) is often more fruitful.

In this study, all fits were initially made by hand, comparing observed d-spacings and intensities with those in the Powder Diffraction File. The peaks of low intensity for each phase were then fitted using an analysis program created specifically for this project. This approach was found to be remarkably efficient because of the limited number of phases invoved.

□□□
CHAPTER 3

PLATINUM GROUP METAL MINING IN SOUTH AFRICA
□□□

3.1 INTRODUTION

This chapter provides an overview of platinum group metal mining in the South African context. Informational sources are given under REFERENCES AND NOTES (CHAPTER 3).

3.2 THE REEF

The pgms are mined almost solely from a 2 billion year old igneous assemblage occurring in the central Transvaal known as the Bushveld Igneous Complex. This is the largest known magmatic ore deposit (460km from the extreme western to eastern outcrops, and 250km from the extreme northern to southern outcrops) containing the worlds greatest reserve of the pgms, chromium and vanadium, and large amounts of nickel, copper and iron. The richest sections of the complex are chromitite seams with high associated levels of sulphide minerals. The two most important chromitite seams are known as the Merensky Suite and the UG-2 Reef (Upper Ground 2) which occur at depths of between 1100 and 1400m below ground (the Merensky Suite is actually *two* close chromitite seams). Rock temperatures at these levels range from 43 - 49°C. The UG-2 reef is found between 15 and 370m below the Merensky Suite and contains 50% of the pgm resources of the complex. The pgm ratios of the two seams are markedly different :

	PGM RATIOS				
	Pt	**Pd**	**Rh**	**Ru**	**Ir**
Merensky Suite	100	42	5	14	2
UG-2 Reef	100	46	19	29	5

The chromitite seams are predominantly chromite ($FeCr_2O_4$). Just above these seams occur the highest levels of sulphide minerals which are mainly chalcopyrite ($CuFeS_2$), pyrrhotite (FeS), pentlandite ($(Fe,Ni,Co)_9S_8$) and pyrite (FeS_2). Minor sulphides are bornite (Cu_5FeS_4), millerite (NiS) and galena (PbS). The highest concentration of the pgms occurs in these sulphide bands, either as solid solution or as tiny particles (pgm levels are close to zero outside these bands). The main pgm minerals are braggite ($(Pt,Pd,Ni)S$), cooperite ($(Pt,Pd)S$), laurite ($(Ru,Os,Ir)S_2$), vysotskite (PdS) and platinum-iron alloy ($Pt-Fe$). The mined ore contains 6-8 ppm (g/tonne) pgm + Au. The UG-2 reef has just over one, to one and a half times higher pgm levels than the Merensky Suite but lower levels of nickel and copper. The nickel to copper ratio is also considerably higher.

3.3 ORE MINING

The Merensky Suite has a high degree of width and dip uniformity and is relatively free from geological disturbances. Standard mining techniques are thus used. 95% of the reef is extracted, 5% of the reef body being left in place as mine support pillars.

3.4 ORE ENRICHMENT

Mined ore is enriched physically by flotation, after crushing and milling. The sulphide minerals respond well to normal sulphide flotation methods. The flotation concentrate constitutes 4 - 5% of the mined ore. Pyrometallurgical enrichment involves smelting and converting the extracted sulphide minerals.

3.5 RECOVERIES

95% of the available reef is extracted by mining. 4 - 5% of this ore is extracted by flotation representing a recovery of 85% of the original ore nickel, copper and pgm content. Over 95% of the metal content of the flotation concentrate is recovered during smelting and converting. The base metal refinery extracts about 98% of the nickel and copper from converter concentrate and 96% of the pgms are recovered in the pgm

concentrate. The platinum group metal refinery recovers 98% of the pgms from base metal refinery pgm concentrate. Thus about 25% of the pgm content of the original mined ore is lost.

3.6 PLATINUM GROUP METAL USE

Uses of the pgms are many and varied. The table below lists these in order of current importance together with the general demand for each metal in each sector.

Table 3.6-1 Uses of the Platinum Group Metals

Use					
Automobile exhaust catalysts	v a r i a b l e				
Petroleum reforming, refining and isomerization	Pt	Rh	Pd	Ir	Ru
Electrical equipment	Pd	Pt	Rh	Ir	Ru
Industrial chemical synthesis (HNO_3, catalysts)	Pd	Pt	Rh	Ru	Ir
Ceramics and Glass (incl. glass fibre production)	Pt	Rh	Pd	Ir	Ru
Jewellery	Pt	Pd	Rh	Ir	Ru

□□□
CHAPTER 4

THE BASE METAL REFINERY
□□□

4.1 INTRODUCTION

The base metal refinery plays an important (although often overlooked) role in platinum group metal extraction, forming the link between the mine and the platinum group metal refinery (**Figure 4.1-1**). As will be demonstrated in the next chapter, many of the most serious extraction problems faced by the platinum group metal refinery have their origins in base metal refinery processes. This chapter presents the results of an examination of these processes using the analytical method of x-ray powder diffraction.

4.2 OVERVIEW OF MINE OPERATIONS [1, 2, 3, 4, 4a]

The base metal refinery (BMR) depends entirely on the ore concentrate produced and supplied by the mine. The purpose of this section is thus to give an overview explaining the various operations leading to the production of this concentrate, known as **matte**.

The concentrate produced at the mine differs greatly from the mined ore, being the result of various physical and chemical ore enrichment processes. These are aimed at the separation of the valuable components from the rock matrix, and the conversion of these components into metal-rich species or to the impure metals themselves. When nickel-copper sulphide ores are involved the final three pyrometallurgical extractive processes taking place at the mine are **roasting**, **smelting** and **converting**. It is important to
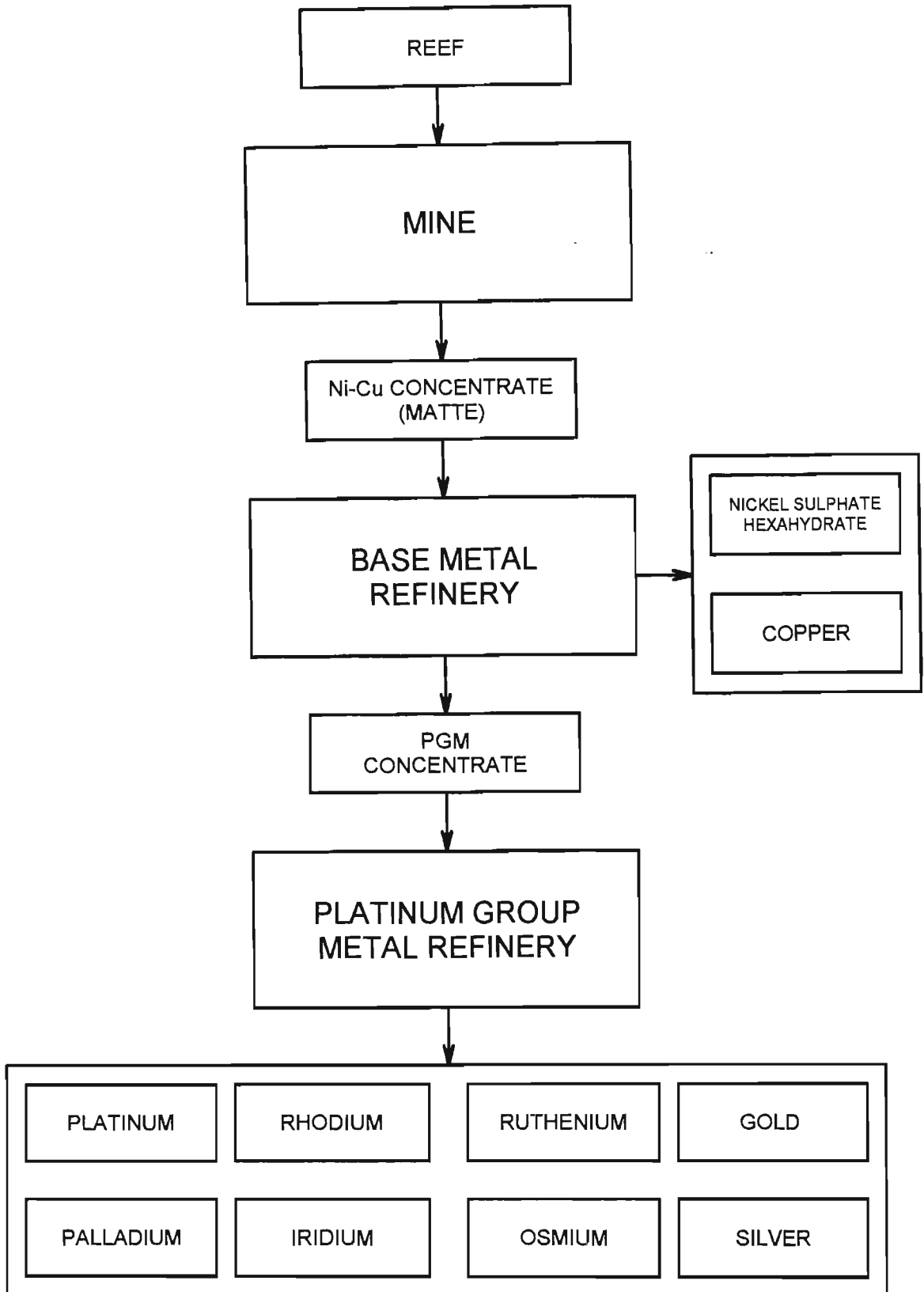
Figure 4.1-1

consider these three processes in some detail because the species finally encountered in matte derive from them.

4.2.1 ROASTING

The main aim of roasting concentrated ore is to remove as much sulphur as possible and to selectively convert about half the iron sulphide present to iron oxide. At the typical roasting temperature of 760°C all the base metal (nickel, copper and iron) sulphides are unstable with respect to their oxides in the presence of oxygen. Iron however has a far greater affinity for oxygen than nickel or copper. The following exothermic reactions can therefore take place :

$$4 \, FeS + 7 \, O_2 \longrightarrow 2 \, Fe_2O_3 + 4 \, SO_2 \qquad \textbf{hematite} \text{ formation}$$

$$3 \, FeS + 5 \, O_2 \longrightarrow Fe_3O_4 + 3 \, SO_2 \qquad \textbf{magnetite} \text{ formation}$$

$$2 \, FeS + 3 \, O_2 \longrightarrow 2 \, FeO + 2 \, SO_2 \qquad \textbf{wustite} \text{ formation}$$
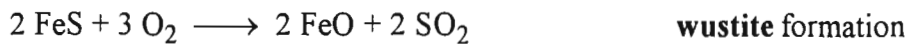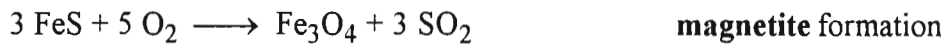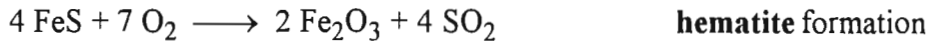
These are simplified reactions as iron sulphide (FeS) is actually the mineral pyrrhotite, better formulated Fe_7S_8, and all reactions proceed through the unstable and quickly decomposed sulphate $Fe_2(SO_4)_3$ ($T_{dec.} = 710$°C). The oxide species of iron produced are critically dependant on the gaseous composition inside the roaster and on the temperature, higher roasting temperatures favouring magnetite followed by wustite formation. The three main parameters defining the conditions of the roast are :

1) temperature

2) time of heating

3) p_{O_2}/p_{SO_2} ratio of the roast atmosphere

The oxidation of copper and nickel sulphides is much less favourable as the oxides have much higher free energies of formation, and so reactions terminate once the metal-rich sulphides have been formed.

For example :

$$2 \, CuS + O_2 \longrightarrow Cu_2S + SO_2 \qquad \text{termination reaction}$$

$$2 \, Cu_2S + 3 \, O_2 \longrightarrow 2 \, Cu_2O + 2 \, SO_2 \qquad \text{energetically unfavourable}$$
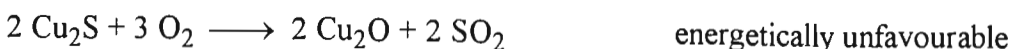
A second consequence of roasting is that some elements can be partially or entirely removed from the charge because their oxides are volatile. Examples are :

arsenic $\qquad 2\,As_2S_3 + 9\,O_2 \longrightarrow 2\,As_2O_3 + 6\,SO_2$

$\qquad\qquad\quad 4\,AsS + 7\,O_2 \longrightarrow 2\,As_2O_3 + 4\,SO_2$

antimony $\qquad 2\,Sb_2S_3 + 9\,O_2 \longrightarrow 2\,Sb_2O_3 + 6\,SO_2$

zinc $\qquad\quad 2\,ZnS + 3\,O_2 \longrightarrow 2\,ZnO + 2\,SO_2$
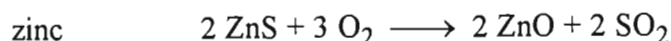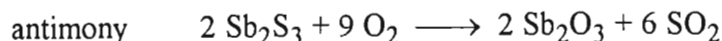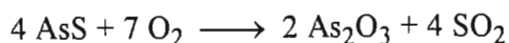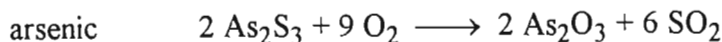
Other oxides are not volatilized, as is the case for bismuth :

bismuth $\qquad 2\,Bi_2S_3 + 9\,O_2 \longrightarrow 2\,Bi_2O_3 + 6\,SO_2$
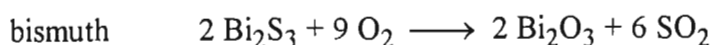
The roasted concentrate is known as **calcine**.

4.2.2 SMELTING

The purpose of smelting is to collect the iron oxides formed during roasting and other undesired species into a slag. The charge is melted in an electric arc smelter or flash smelted at temperatures from 1230°C to 1500°C (according to calcine constituents). These high temperatures are necessary for the melting of the nickel sulphides. A silica flux (SiO_2) is added, this acting as an acidic collector of the basic iron oxides. The percentage of each iron oxide present depends on the conditions of the roast. The hematite (Fe_2O_3) present passes very quickly into the slag; the magnetite (Fe_3O_4) less so. On liquification the melt separates over time into two immiscible liquid layers. The upper layer constitutes the **slag**, which is mainly iron silicate (fayalite : Fe_2SiO_4 or $2FeO{\cdot}SiO_2$) formed by the following acid-base reaction :

$\qquad SiO_2 + 2\,FeO \longrightarrow Fe_2SiO_4 \qquad\qquad$ **fayalite** formation

Silica reacts with all basic and amphoteric oxides present in a similar way, although it should be noted that magnetite (Fe_3O_4) needs to be reduced to wustite (FeO) before removal into the slag layer can occur :

$\qquad 3\,Fe_3O_4 + FeS \longrightarrow 10\,FeO + SO_2$

$\qquad 2\,FeO + SiO_2 \longrightarrow Fe_2SiO_4$
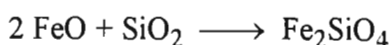
The lower layer constitutes the **smelter matte** and is a highly concentrated mixture of base metal sulphides. The remaining iron sulphide is important as any copper or nickel

oxides that might have formed and passed into the slag are reconverted to sulphides by double decomposition reactions and enter back into the molten matte layer :

$$Cu_2O + FeS \longrightarrow Cu_2S + FeO$$

$$9\,NiO + 7\,FeS \longrightarrow 3\,Ni_3S_2 + 7\,FeO + SO_2$$
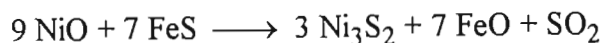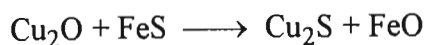
Control of the separation process allows almost all major impurities to separate into the slag layer and all the nickel, copper and platinum group metals to be collected into the smelter matte.

4.2.3 CONVERTING

The purpose of converting is to further reduce the sulphur level by the formation of a metallic alloy phase. This is accomplished by blowing air or oxygen through the liquid matte.

NICKEL : A complete conversion to the impure metal is not possible for nickel as the mutual reduction or roast reaction between nickel sulphide and the nickel oxide formed has a positive free energy change at 1200°C :

$$Ni_3S_2 + 4\,NiO \longrightarrow 7\,Ni + 2\,SO_2 \qquad \text{roast reaction}$$

The overall conversion reaction,

$$Ni_3S_2 + 2\,O_2 \longrightarrow 3\,Ni + 2\,SO_2$$
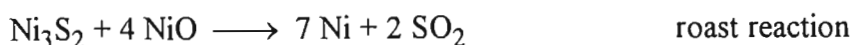
although unfavourable, can be achieved using high converter temperatures and ensuring intimate contact between the matte and oxygen.

COPPER : The copper sulphide proves much easier to convert as the roast reaction between copper sulphide and the copper oxide formed has a negative free energy change at 1200°C, and CuO (unlike NiO) is soluble in the molten sulphide phase :

$$Cu_2S + 2\,CuO \longrightarrow 6\,Cu + SO_2 \qquad \text{roast reaction}$$
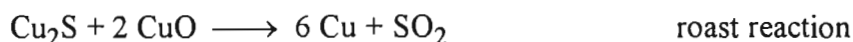
The overall conversion reaction is also exothermic (*ie.* it has a negative enthalpy) :

$$Cu_2S + O_2 \longrightarrow 2\,Cu + SO_2$$
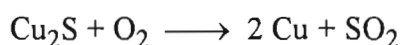
The result of the above reactions for nickel and copper is that a fair amount of metallic nickel-copper alloy is formed as a solution (the metals are mutually soluble).

IRON : The presence of iron sulphide (as pyrrhotite) at this stage is essential for two reasons :

1) Iron sulphide aids in the autogenous conversion of the fraction of the sulphide phase which converts into the metallic alloy phase by the heat that is produced on oxidation of iron sulphide to iron oxide :

$$2\,FeS + 3\,O_2 \longrightarrow 2\,FeO + 2\,SO_2 \qquad\qquad \text{highly exothermic}$$
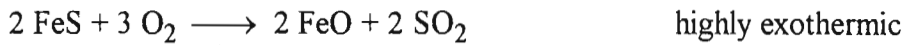
2) Iron sulphide also prevents copper and nickel (a small amount of which might have been converted to oxides) from passing into the slag during conversion (see § 4.2.2).

Most of the iron oxide that forms is removed by reaction with the residual silica present, although if the temperature is not kept high Fe_3O_4 can be deposited beneath the molten matte layer.

PLATINUM GROUP METALS : The pgms, including gold, are not oxidised as their free energies of oxidation are all positive, and usually collect in the alloy phase. Platinum can however partially remain in the sulphide phase.

4.2.4 POST CONVERSION

After the conversion stage, which is usually carried out at temperatures around 1200°C, the liquid matte is cooled. This can be done rapidly or slowly. Slow cooling in the temperature range 925°C to 370°C over about a week causes an almost complete separation of matte constituents by crystallization of the three main phases present in the order :

1) copper sulphide   - crystallization begins around 921°C

2) nickel-copper alloy   - crystallization begins around 699°C

3) nickel sulphide   - crystallization begins around 575°C

Below about 371°C no further separation occurs.

The **post-converter matte** (known as 'white metal' if iron free), once solidified, is crushed into small chunks (of about 2cm diameter) and supplied to the base metal refinery where the extractive process continues following hydrometallurgical techniques.

4.3 BASE METAL REFINERY OPERATIONS [5]

In this section a relatively detailed description is given of the various extractive processes taking place in a base metal refinery.   To some extent these are specific to the process used at BARPLATS REFINERIES, although many refineries (especially in South Africa) follow the same general scheme.

The BMR at BARPLATS REFINERIES received its post-converter matte from the CROCODILE RIVER MINE.   This mine concentrated and converted ore provided solely by the LEFKOCHRYSOS UG-2 reef.   The matte was **slow cooled** in the post conversion step.

4.3.1 THE GRINDING CIRCUIT

In the BMR the matte chunks were ground in a ball mill under highly controlled conditions.   The slurry from the grinding circuit was stored in a surge tank which continuously fed the nickel circuit.   **(Figure 4.3-1)**

4.3.2 THE NICKEL CIRCUIT

The nickel circuit involved leaching the ground matte (in an 80% slurry) for nickel with sulphuric acid.   This first stage leach (FSL) extracted 60-70% of the approximately 50% nickel content of the matte.   In addition 30-50% of any iron present in the matte was also extracted.   Five tanks (in a cascade) were operated at atmospheric pressure.   Steam and oxygen were fed into the first two or three tanks to achieve temperatures in the range 85-95°C and oxidising conditions.   (The potential and pH of the final tanks was important as in the event of copper and pgm dissolution, these had to be reprecipitated by reducing the potential without reprecipitating iron.   This was done by starving the final tanks of oxygen and ensuring their pH was around 4.)   The first stage leach discharge slurry was pumped into a thickener tank.   Part of the underflow of this tank was recycled into the first tank and part was repulped with water in an agitated surge tank which fed the copper circuit.   The thickener overflow solution was filtered and sent to crystallization vessels.   The filter cake was routed into the last FSL tank.
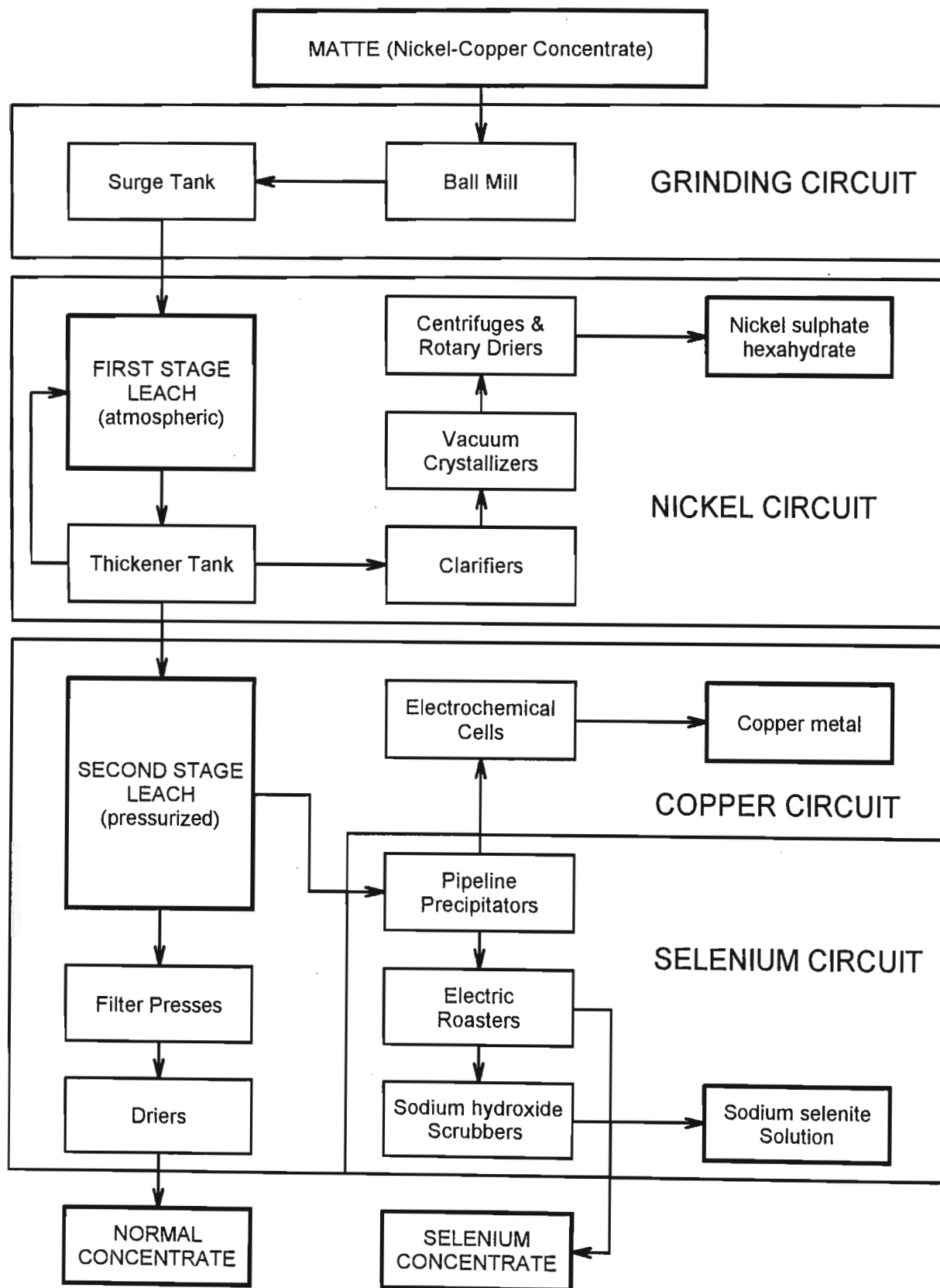
Figure 4.3-1 Simplified flowchart of the BASE METAL REFINERY

Nickel sulphate hexahydrate, $NiSO_4 \cdot 6H_2O$, was crystallized from the FSL clarifier filtrate by vacuum crystallization. The pregnant solution contained about 100g/l Ni. The stainless steel vacuum crystallizers were steam heated shell and tube exchangers operated at 50°C. The crystals in the crystallizer slurry (50% by weight) were separated by centrifuges, washed, removed and dried in a rotary drier. The filtrate was recycled. **(Figure 4.3-1)**

4.3.3 THE COPPER CIRCUIT

The copper circuit involved leaching the thickened FSL pulp for copper using sulphuric acid. The leaching conditions were much more severe than those of the FSL, the aim being to dissolve everything except the precious metals. Two autoclaves were operated at elevated pressures. Once again steam was used for heating, and oxygen sparged in to create the desired oxygen partial pressure. Heating was controlled to achieve initial temperatures of 120-125°C. At this stage the exothermic oxidation of sulphur raised the temperature to the final operating range of 150-160°C. Sulphuric acid was added in two stages. 70% of that required was added on charging and the final 30% once the final operating temperature range had been reached. After several hours the autoclave contents were discharged and filtered. The filtrate typically contained 100g{Ni + Cu}/l and 20g/l free acid. The filter cake was washed, dried, blended and weighed. This residue formed the **'NORMAL CONCENTRATE'** for the platinum metal refinery.

The filtrate was pumped into a recirculation tank which fed the electrowinning section of the copper circuit. Various additives were added to this tank to aid in the subsequent plating process. The electrochemical cells were piped in parallel. Each had 43 stainless steel sheet cathodes and 44 lead-antimony anodes. The electrolyte was pumped into the cells and the current density adjusted to achieve a copper concentration of 20g/l in the spent electrolyte. (It was important to maintain an electrolyte temperature of 55°C. This was controlled by heating or cooling the feed.) The spent electrolyte was returned to the leaching vessels of both the nickel and copper circuits. Once the steel cathodes

had formed a sufficient copper deposit, they were removed and the deposits stripped. (**Figure 4.3-1**)

4.3.4 THE SELENIUM CIRCUIT

The so called selenium circuit at BARPLATS primarily involved the removal of selenium from the filtrate of the copper circuit by precipitation with sulphur dioxide. This was necessary as high levels of the heavy chalcogens (selenium and tellurium) in the filtrate contaminate the copper deposit formed in the copper electrowinning section, in which this filtrate is the electrolyte. The selenium circuit was fed by a surge tank containing the filtered pressure leach solution. A steam heat exchanger heated this solution to 90°C as it passed into the precipitator (a pipeline reactor). Aqueous sulphur dioxide was injected into the reactor and the precipitate filtered out. In addition to the heavy chalcogens, almost all of the pgms which might have dissolved in the copper circuit, were precipitated. The filter cake was washed, collected and roasted in air at 700°C in an electric roaster. The selenium present was volatilized and scrubbed from the vent gasses with a 20% sodium hydroxide solution. The relevant reactions are :

$$Se + O_2 \longrightarrow SeO_2$$

$$SeO_2 + H_2O \longrightarrow H_2SeO_3$$

$$H_2SeO_3 + 2\,NaOH \longrightarrow Na_2SeO_3 + 2\,H_2O$$
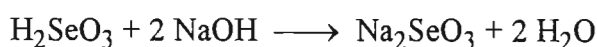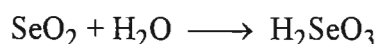
This roast residue was termed the '**SELENIUM CONCENTRATE**' for the platinum metal refinery. This residual concentrate was sometimes blended with the '**NORMAL CONCENTRATE**' from the copper circuit (see § 4.3.3) for input to the PGM refinery. (**Figure 4.3-1**)

4.4 THE ANALYSIS OF NICKEL-COPPER CONCENTRATE

In general, the post-converter matte provided by the smelter is essentially a mixture of metal-rich sulphides and alloy. Three samples of ground matte from the grinding circuit were provided by the BARPLATS BMR for intensive analysis. These represented three different consignments from the mine. Matte chunks prior to grinding have a metallic

brassy appearance and are weakly magnetic. The density of unground chunks was found to range from **6.2** to **6.3g/cm³**. This value cannot be more accurately determined as numerous gas cavities occur throughout the solid due to aeration in the conversion step. Partial elemental analyses for the three ground matte samples are given in **Table 4.4-1**.

Table 4.4-1   Partial elemental analyses for mattes A, B and C †

Element	Matte A	Matte B	Matte C
Ni	52.9	50.7	51.7
Cu	24.6	26.5	25.8
Pt	1.12	1.10	1.05
Pd	0.51	0.47	0.42
Ru	0.273	0.249	0.266
Rh	0.175	0.165	0.145
Ir	0.0570	0.0605	0.0562
Au	0.009	0.008	0.007

† all values in weight % (Data supplied by BARPLATS.)

The remaining 20% of the weight is made up of sulphur (~18%), iron (~1%), chromium (~0.1%) and small amounts of cobalt, selenium, arsenic, silicon and osmium. The average grade of the three samples is 20389g/tonne pgms, which is high. The samples were all finely ground, having come from the ball mill.

X-ray powder diffraction (XPD) scans over the 2θ angle range 5-120° were recorded for all three samples, these being performed using the system and methods detailed in CHAPTER 2, **X-RAY POWDER DIFFRACTION ANALYSIS.**

All three samples yielded similar scans and showed relatively high levels of crystallinity as indicated by the number of counts recorded for the most intense peak (symbol : I_1). The average count value of I_1 was 1018. Analysis of the data listings and spectra enabled several phases to be identified. Most of the high intensity lines were assignable to the

nickel sulphide Ni_3S_2 known mineralogically as **heazlewoodite**.   **Table 4.4-2** compares the reference data for this compound with that observed in the samples.

Table 4.4-2   Comparison of Ni_3S_2 reference data with that observed of Ni_3S_2 found in matte samples

Reference data [6]		Matte A (obs.)		Matte B (obs.)		Matte C (obs.)		
d(Å)	(I/I$_1$)	d(Å)	(I/I$_1$)	d(Å)	(I/I$_1$)	d(Å)	(I/I$_1$)	
4.11	(50)	4.157	(36)	4.161	(37)	4.163	(39)	
2.89	(90)	2.911	(100)	2.911	(95)	2.911	(100)	
2.38	(40)	2.405	(43)	2.404	(46)	2.402	(45)	
2.36	(10)	2.371	(13)	2.373	(15)	2.374	(16)	
2.03	(50)	2.059	(57)	2.059	(59)	2.058	(57)	
1.826	(100)	1.846	(84)	1.846	(89)	1.846	(86)	
1.816	(100)	1.831	(71)	1.832	(76)	1.831	(78)	
1.673	(10)	1.690	(24)	1.690	(27)	1.690	(27)	
1.660	(80)	1.674	(92)	1.674	(100)	1.674	(93)]	split
		1.672	(60)	1.673	(68)	1.672	(69)]	peak
1.371	(5)	1.366	(9)	1.367	(8)	1.366	(9)	
1.357	(10)	1.360	(7)	1.360	(10)	1.360	(8)	
1.294	(20)	1.299	(20)	1.299	(19)	1.300	(17)	
1.222	(20)	1.229	(19)	1.229	(21)	1.232	(19)	
1.188	(5)	1.191	(2)	1.192	(2)	1.192	(2)	
1.171	(5)	1.178	(6)	1.178	(7)	1.178	(8)	
1.135	(10)	1.139	(15)	1.140	(19)	1.139	(17)]	split
		1.139	(10)	-	-	1.137	(10)]	peak
1.124	(10)	1.129	(18)	1.130	(23)	1.130	(21)	
1.099	(20)	1.101	(28)	1.101	(33)	1.101	(35)]	split
		1.101	(17)	-	-	1.101	(21)]	peak
1.089	(5)	1.094	(17)	1.094	(23)	1.094	(20)	
1.083	(30)	1.089	(36)	1.089	(41)	1.089	(37)]	split
		1.087	(33)	1.087	(35)	1.087	(35)]	peak

The following should be noted :

1) In some cases observed peaks at low d-spacings are split.   These peaks are known as '$\alpha_1\alpha_2$ **doublets**' and arise from $CoK\alpha_1$ ($\lambda = 1.78892$Å) and $CoK\alpha_2$ ($\lambda = 1.79278$Å) wavelengths giving one peak at a low 2θ value (higher $d_{obs.}$ value) of higher intensity, and one peak at a high 2θ value (lower $d_{obs.}$ value) of lower intensity respectively.   Line splitting is mainly observed at higher diffraction angles and indicates good crystallinity.

2) As the goniometer uses an **automatic divergence slit** and reference data is usually measured with fixed divergence slits, the observed scan when compared to reference data will have lower intensities at lower diffraction angles and higher intensities at higher angles. (See § 2.5.4.)

3) At large d-spacings the difference between $d_{reference}$ and $d_{observed}$ can be quite high (± 0.050Å) but is generally lower at smaller d-spacings (± 0.005Å) (*ie.* large d-spacings are less accurate than small d-spacings when measured experimentally).   These large differences need to be taken into account when assigning lines to reference data.

Table 4.4-3   Diffraction angles, 2θ [†] : Ni_3S_2

Reference data [6]		Observed data (average)	
2θ	(I/I_1)	2θ	(I/I_1)
25.1	(50)	24.8	(38)
36.1	(90)	35.8	(100)
44.2	(40)	43.7	(46)
44.5	(10)	44.3	(15)
52.3	(50)	51.5	(59)
58.7	(100)	58.0	(88)
59.0	(100)	58.5	(77)
64.6	(10)	63.9	(27)
65.2	(80)	64.6	(97)]
		64.7	(67)]
81.4	(5)	81.8	(9)
82.5	(10)	82.2	(8)
87.5	(20)	87.0	(19)
94.1	(20)	93.3	(20)
97.7	(5)	97.3	(2)
99.6	(5)	98.8	(7)
104.0	(10)	103.4	(17)]
		103.6	(10)]
105.5	(10)	104.7	(21)
109.0	(20)	108.6	(33)]
		108.7	(19)]
110.4	(5)	109.7	(20)
111.4	(30)	110.4	(39)]
		110.7	(35)]

† Applicable for radiation of wavelength $\lambda = 1.78894$Å $(CoK\alpha_1)$

Table 4.4-3 gives the reference and average observed diffraction angles for Ni_3S_2 peaks. The I/I_1 data for the observed data has been adjusted so as to give the most intense line a maximum intensity of 100. This allows reasonable intensity comparisons to be made. Figure 4.4-1(a) and (b) shows the scan for matte A with the Ni_3S_2 peaks indicated and the reduced or line spectrum for matte A compared to that of reference Ni_3S_2. The matching lines are indicated in the strip above the sample pattern.

The second phase identified from the low intensity lines in the matte samples was the copper sulphide Cu_2S known mineralogically as chalcocite.

Table 4.4-4 Comparison of Cu_2S reference data with that observed of Cu_2S found in matte samples

Reference data [7]		Matte A (obs.)		Matte B (obs.)		Matte C (obs.)	
d(Å)	(I/I_1)	d(Å)	(I/I_1)	d(Å)	(I/I_1)	d(Å)	(I/I_1)
3.73	(20)	3.805	(2)	3.802	(2)	3.810	(2)
3.59	(16)	3.664	(1)	3.652	(1)	3.662	(1)
3.31	(25)	3.352	(2)	3.330	(3)	3.326	(2)
3.18	(40)	3.231	(3)	3.212	(4)	3.231	(3)
3.05	(20)	3.098	(1)	3.101	(2)	3.097	(2)
2.942	(45)	2.998	(3)	2.997	(3)	2.996	(4)
2.718	(55)	2.761	(6)	2.764	(7)	2.762	(7)
2.659	(25)	2.701	(1)	-	-	2.701	(4)
2.609	(16)	-	-	-	-	2.648	(1)
2.524	(40)	2.560	(5)	2.559	(4)	2.557	(4)
2.469	(45)	2.502	(4)	2.495	(4)	2.504	(5)
2.396	(85)	2.432	(10)	2.429	(13)	2.431	(11)
2.325	(40)	2.353	(8)	2.351	(7)	2.351	(8)
2.237	(25)	-	-	2.270	(3)	2.263	(3)
2.207	(30)	2.233	(3)	2.234	(5)	2.232	(3)
1.977	(100)	1.992	(15)	1.997	(17)	1.998	(15)
1.876	(90)	1.893	(14)	1.893	(15)	1.893	(14)
1.704	(35)	1.718	(5)	1.714	(7)	1.717	(6)
1.526	(25)	1.535	(2)	1.534	(2)	1.536	(2)
1.361	(10)	1.377	(2)	1.378	(3)	1.377	(3)

Table 4.4-4 compares the reference data for this compound with that observed in the samples. As the reference data for Cu_2S contains 38 peaks, only those lines

Slow cooled matte [A]   Card number : BP-006
(from the grinding circuit)

Nickel sulphide
Ni_3S_2 (Heazlewoodite)
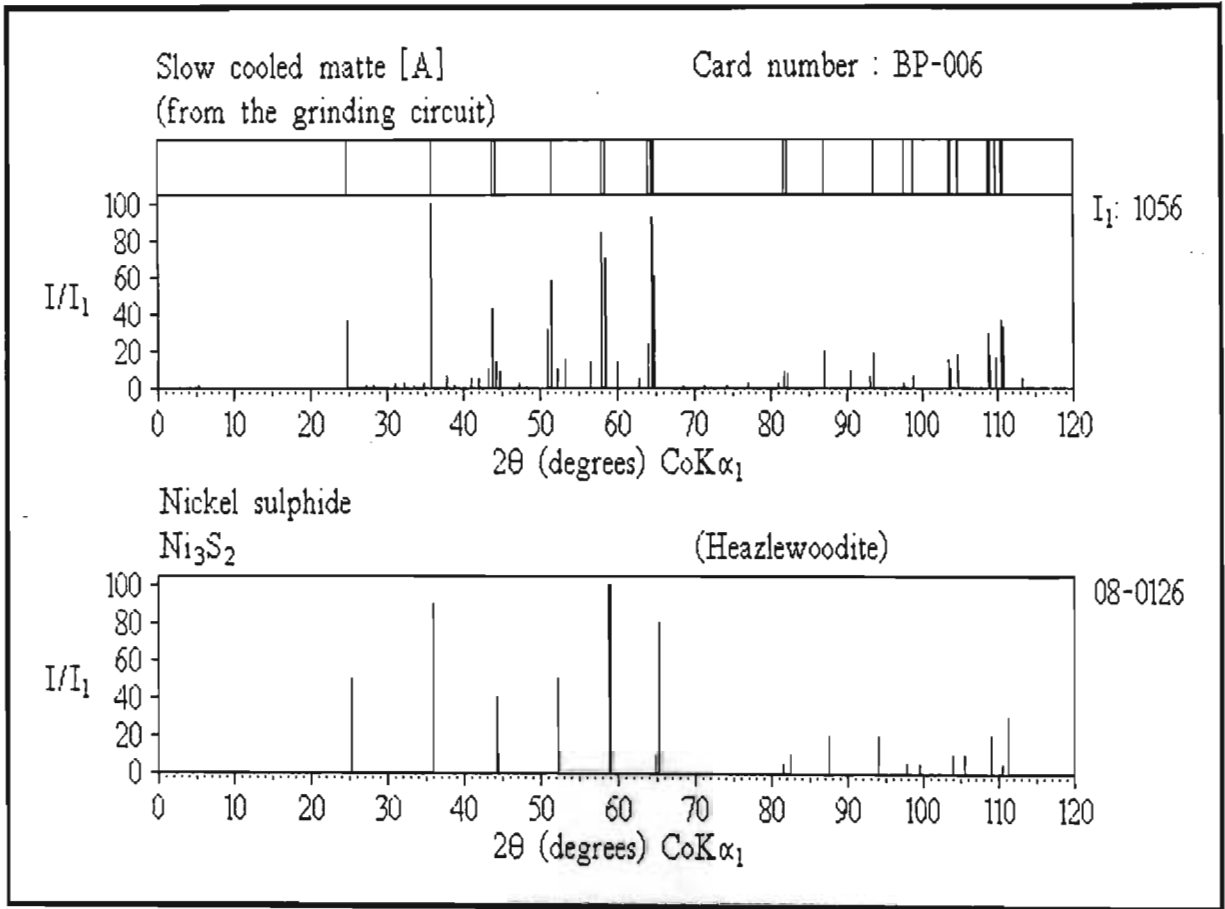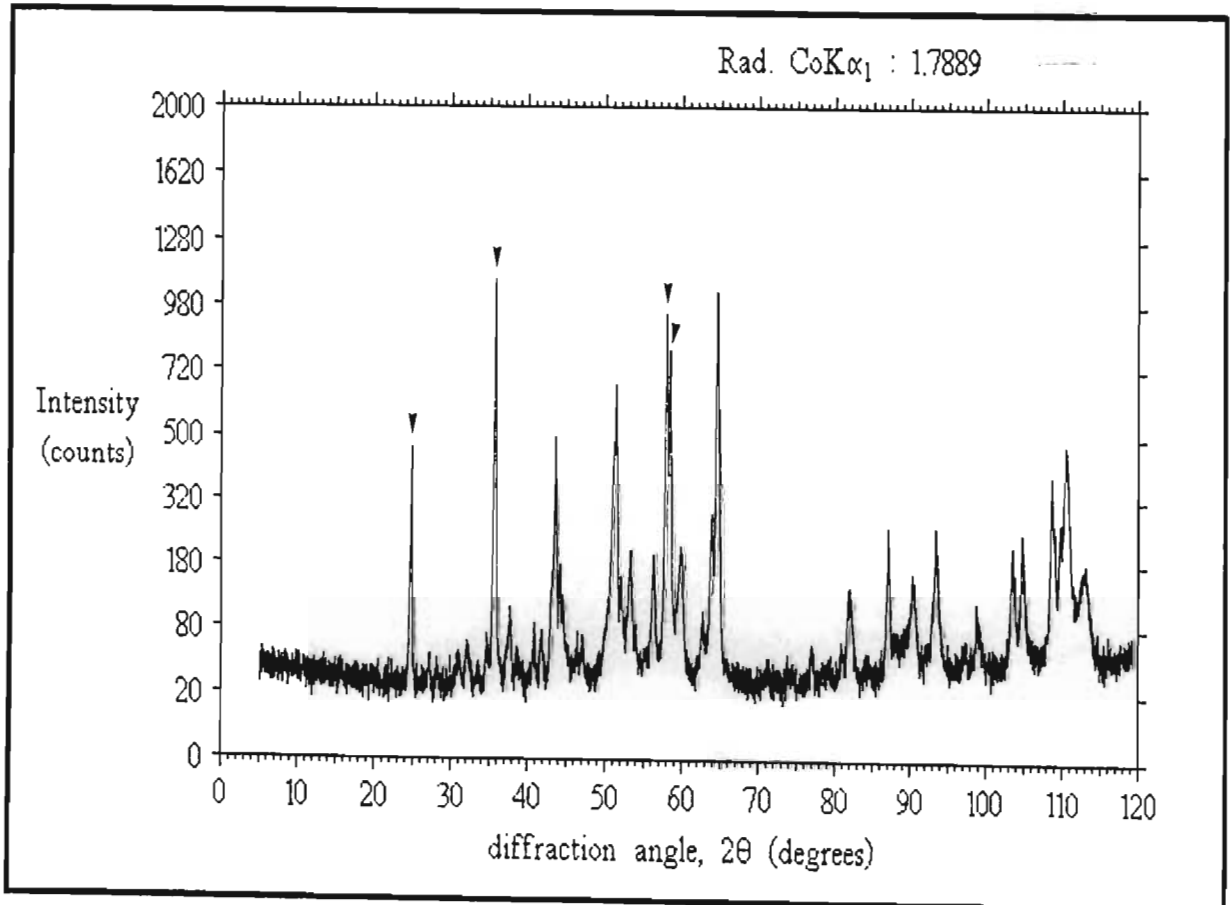
Figure 4.4-1(a)

Figure 4.4-1(b)

corresponding to peaks found in the sample scans have been listed. Note especially the large differences in the d-spacings for planes with d-spacings less than about 2.5Å.

Table 4.4-5 gives the reference and average observed diffraction angles for Cu_2S peaks.

Figure 4.4-2(a) and **(b)** shows the scan for matte B with the main Cu_2S peaks indicated, and the reduced spectrum for matte B compared to that of reference Cu_2S.

Table 4.4-5 Diffraction angles, 2θ [†] : Cu_2S

Reference data [(7)]		Observed data (average)	
2θ	(I/I_1)	2θ	(I/I_1)
25.1	(50)	24.8	(38)
27.8	(20)	27.2	(12)
28.9	(16)	28.3	(6)
31.4	(25)	31.1	(12)
32.7	(40)	32.2	(19)
34.1	(20)	33.6	(12)
35.4	(45)	34.7	(19)
38.4	(55)	37.8	(44)
39.3	(25)	38.7	(12)
40.1	(16)	39.5	(6)
41.5	(40)	40.9	(25)
42.5	(45)	41.9	(25)
43.8	(85)	43.2	(69)
45.2	(40)	44.7	(50)
47.1	(25)	46.5	(19)
47.8	(30)	47.2	(25)
53.8	(100)	53.3	(100)
57.0	(90)	56.4	(88)
63.3	(35)	62.8	(38)
71.8	(25)	71.3	(12)
82.2	(10)	81.0	(19)

† Applicable for radiation of wavelength $\lambda = 1.78894$Å $(CoK\alpha_1)$

Remaining lines could be assigned to the nickel-copper alloy phase, **Ni-Cu**. As these two metals form solid solutions in any ratio no card data exists for this alloy. The peaks

Slow cooled matte [B] Card number : BP-007
(from the grinding circuit)

I_1: 936

Copper sulphide
Cu_2S (Chalcocite, low)

23-0961

Figure 4.4-2(a)

Rad. $CoK\alpha_1$: 1.7889
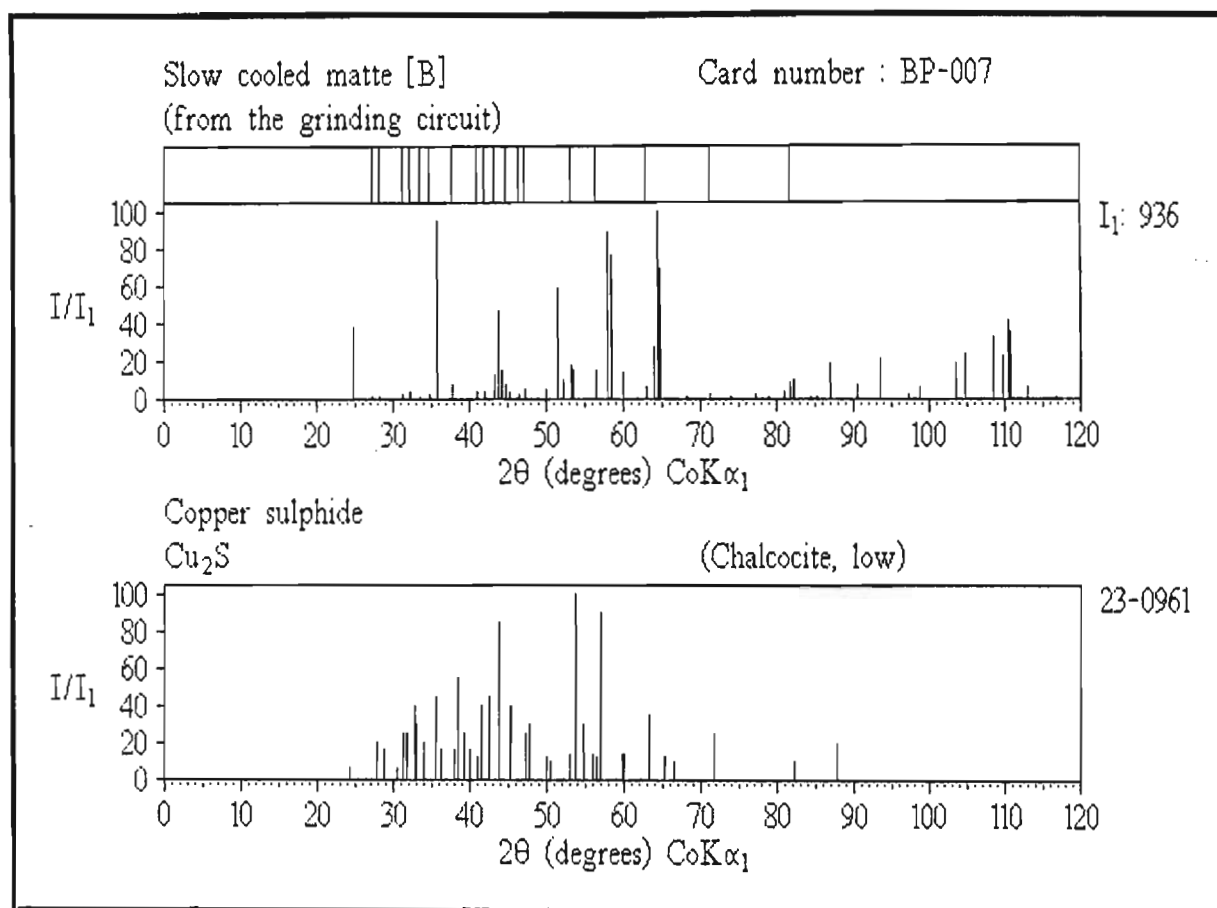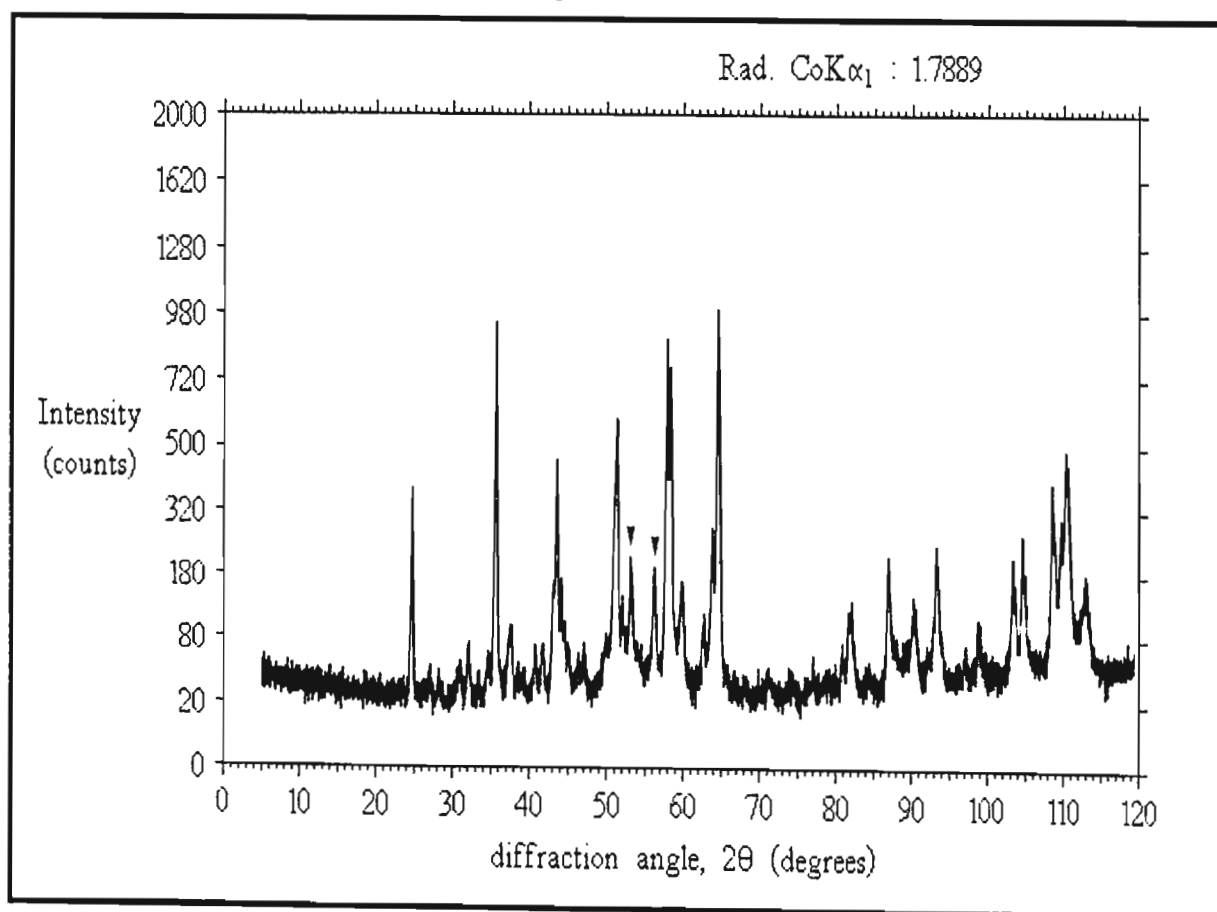
Figure 4.4-2(b)

however fall between those of pure nickel and those of pure copper for which reference data is available.

Table 4.4-6 compares this reference data with that observed for the alloy phase in the matte samples.

Table 4.4-6 Comparison of Ni and Cu reference data with that observed of the Ni-Cu alloy found in matte samples

Reference data [8] d(Å) (I/I$_1$)	Matte A (obs.) d(Å) (I/I$_1$)	Matte B (obs.) d(Å) (I/I$_1$)	Matte C (obs.) d(Å) (I/I$_1$)
2.034- (100) [†] 2.088 (100)	2.0741 (31)	2.0587 (58)	2.0577 (57)
1.762- (42) [†] 1.808 (46)	1.7871 (14)	1.7911 (13)	1.7883 (10)
1.246- (21) [†] 1.278 (20)	1.2601 (9)	1.2596 (7)	1.2593 (5)
1.0624- (20) [†] 1.0900 (17)	1.0714 (5)	1.0720 (7)	1.0707 (4)

† Data for nickel is given first, followed by that for copper.

It should be noted that the first alloy peak (the reflection from the **(111)** planes) has overlapped in mattes B and C with one of the nickel sulphide peaks (the reflection from the **(202)** Ni$_3$S$_2$ planes).

Table 4.4-7 gives the reference and average observed diffraction angles for the alloy.

Figure 4.4-3(a) and **(b)** shows the scan for matte C with the Ni-Cu alloy peaks indicated and the reduced spectrum for matte C compared to that of reference copper and nickel.

Slow cooled matte [C]   Card number : BP-008
(from the grinding circuit)
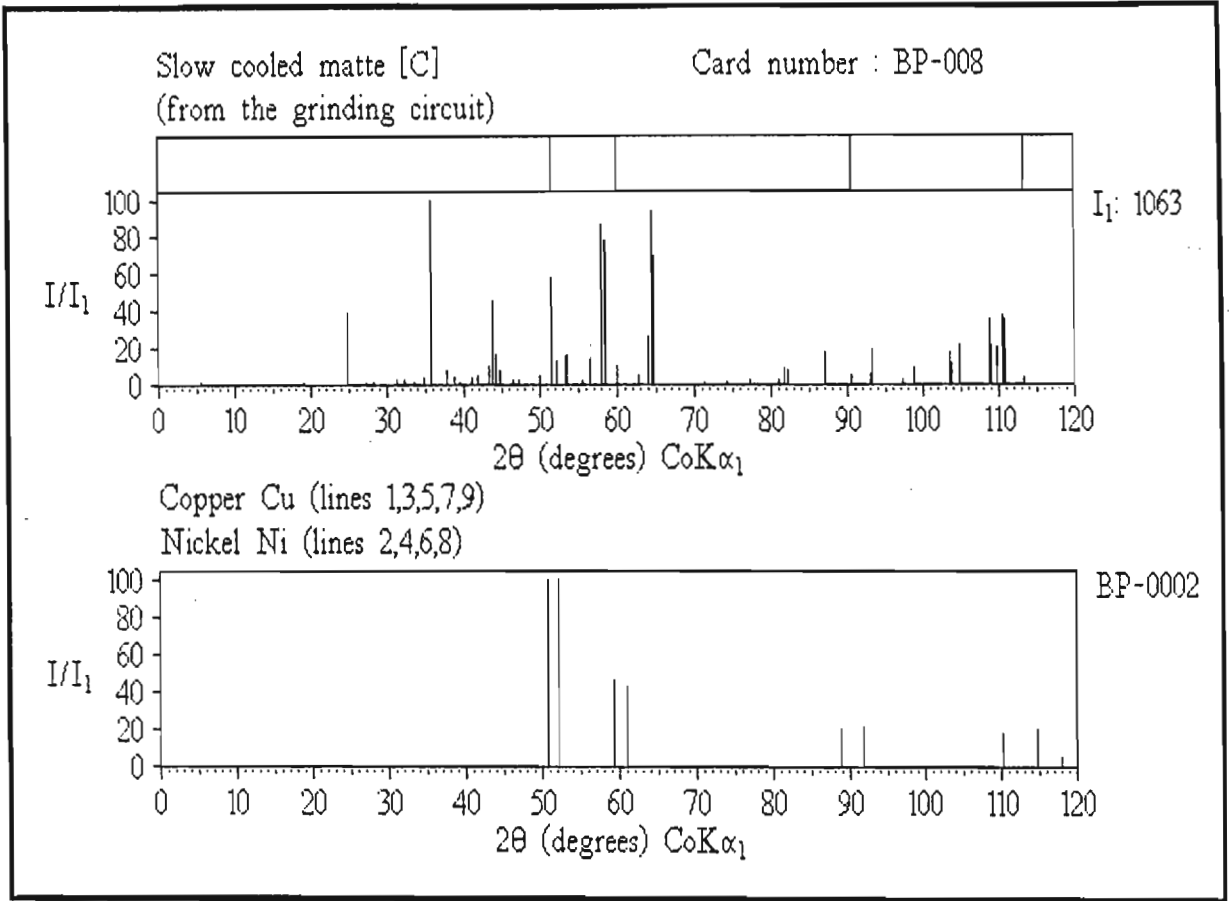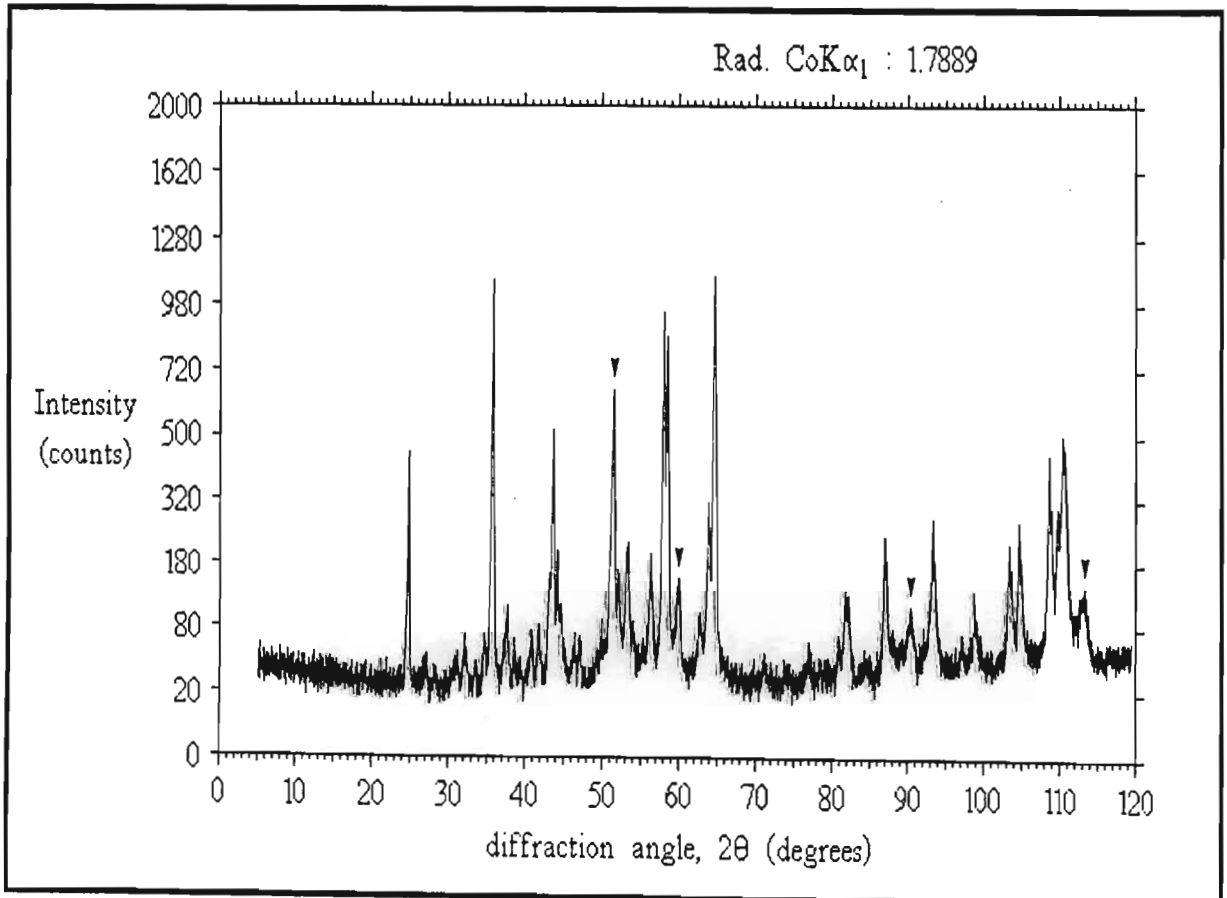
Figure 4.4-3(a)

Figure 4.4-3(b)

Table 4.4-7 Diffraction angles, 2θ [†] : Ni-Cu alloy

Reference data [8]		Observed data for mattes A, B & C					
2θ	(I/I_1)	2θ	(I/I_1)	2θ	(I/I_1)	2θ	(I/I_1)
50.7- 52.2	(100) [‡] (100)	51.1	(100)	51.5	*(100)*	51.5	*(100)*
59.3- 61.0	(46) [‡] (42)	60.1	(45)	59.9	*(41)*	60.0	*(48)*
88.8- 91.8	(20) [‡] (21)	90.4	(29)	90.5	*(22)*	90.5	*(24)*
110.3- 114.7	(17) [‡] (20)	113.2	(16)	113.1	*(22)*	113.3	*(19)*

[†] Applicable for radiation of wavelength $\lambda = 1.78894\text{Å}$ (CoKα_1)

[‡] Copper data given first

In **Table 4.4-7**, estimated intensity data is given in italics.

Other matte samples (without elemental analyses) with a high iron content were also provided by the BARPLATS BMR.   Scans of these samples showed numerous additional peaks of high intensity which in some cases corresponded closely to the iron oxide Fe_3O_4 known mineralogically as **magnetite**, and in other cases to the nickel iron oxide $NiFe_2O_4$ known mineralogically as **trevorite**.   **Table 4.4-8** compares the reference data for these two compounds with that observed in two selected samples (mattes D and E).

Observed data shown in italics overlaps with other phases such as nickel sulphide, copper sulphide and the alloy phase.

Table 4.4-9 gives the reference diffraction angles for Fe_3O_4 and $NiFe_2O_4$ corresponding to those found in mattes D and E.   Data in italics indicates overlap with other phases.

Table 4.4-8 Comparison of Fe_3O_4 and $NiFe_2O_4$ reference data with corresponding peaks observed in matte

Fe_3O_4 Reference data [9] d(Å)	(I/I_1)	Matte D (obs.) d(Å)	(I/I_1)	Matte E (obs.) d(Å)	(I/I_1)	$NiFe_2O_4$ Reference data [9a] d(Å)	(I/I_1)
4.852	(8)	4.916	(4)	4.803	(10)	4.82	(20)
2.967	(30)	2.983	(29)	2.942	(21)	2.948	(30)
2.532	(100)	2.544	(87)] split	2.516	(100)	2.513	(100)
		2.531	(51)] peak				
2.4243	(8)	*2.436*	*(40)*	*2.409*	*(34)*	2.408	(8)
2.0993	(20)	2.106	(69)	2.089	(84)	2.085	(25)
		2.105	(51)	2.083	(70)		
1.7146	(10)	1.714	(11)	1.704	(10)	1.7025	(8)
1.6158	(30)	1.615	(32)	1.607	(34)	1.6051	(30)
1.4845	(40)	1.483	(78)	1.477	(51)] split	1.4760	(40)
				1.477	(48)] peak		
1.4192	(2)	1.415	(2)	1.411	(2)	1.4100	(2)
1.3277	(4)	1.325	(5)	1.319	(4)	1.3187	(6)
1.2807	(10)	1.277	(11)	1.276	(12)	1.2706	(10)
1.2659	(4)	*1.264*	*(23)*	*1.261*	*(18)*	1.2573	(4)
1.2119	(2)	1.212	(15)	1.208	(9)] split	1.2036	(6)
				1.204	(8)] peak		
1.1221	(4)	1.118	(5)	1.117	(4)] split	1.1145	(6)
				1.114	(3)] peak		
1.0930	(12)	*1.089*	*(64)*	*1.087*	*(57)*] split	1.0857	(16)
				1.086	*(34)*] peak		
1.0496	(6)	1.048	(18)	1.046	(11)] split	1.0424	(6)
		1.048	(20)	1.043	(9)] peak		

From **Table 4.4-9** it can be seen that some peaks have intensities substantially higher than expected (shown in boldface type). In order to determine whether this was an effect of using an automatic divergence slit, a geological sample of Fe_3O_4 was run and compared to the reference data.

Table 4.4-10 compares the reference data for Fe_3O_4 with that collected from the geological sample showing that the increase in the intensity of these peaks is due to another crystalline phase.

Table 4.4-9 Diffraction angles, 2θ [†] : Fe_3O_4 and $NiFe_2O_4$

Fe_3O_4 Reference data [9]		Matte D (obs.)		Matte E (obs.)		$NiFe_2O_4$ Reference data [9a]	
2θ	(I/I_1)	2θ	(I/I_1)	2θ	(I/I_1)	2θ	(I/I_1)
21.2	(8)	21.0	(5)	21.5	(10)	21.4	(20)
35.1	(30)	34.9	(33)	35.4	(21)	35.3	(30)
41.4	(100)	41.2	(100)] split	41.6	(100)	41.7	(100)
		41.4	(59)] peak				
43.3	(8)	*43.1*	*(46)*	*43.6*	*(34)*	43.6	(8)
50.4	(20)	**50.3**	**(79)**	**50.7**	**(84)**	50.8	(25)
		50.3	**(59)**	**50.8**	**(70)**		
62.9	(10)	62.9	(13)	63.3	(10)	63.4	(8)
67.2	(30)	67.3	(37)	67.6	(34)	67.7	(30)
74.1	(40)	**74.2**	**(90)**	**74.5**	**(51)**] split	74.6	(40)
				74.6	**(48)**] peak		
78.1	(2)	78.4	(2)	78.7	(2)	78.7	(2)
84.7	(4)	84.9	(6)	85.4	(4)	85.4	(6)
88.6	(10)	88.9	(13)	89.0	(12)	89.5	(10)
89.9	(4)	*90.1*	*(26)*	*90.4*	*(18)*	90.7	(4)
95.1	(2)	**95.2**	**(17)**	**95.6**	**(9)**] split	96.0	(6)
				95.9	**(8)**] peak		
105.7	(4)	106.3	(6)	106.4	(4)] split	106.8	(6)
				106.8	(3)] peak		
109.8	(12)	*110.5*	*(74)*	*110.8*	*(57)*] split	110.9	(16)
				110.9	*(34)*] peak		
116.9	(6)	**117.2**	**(21)**	**117.6**	**(11)**] split	118.2	(6)
		117.2	**(23)**	**118.1**	**(9)**] peak		

† Applicable for radiation of wavelength $\lambda = 1.78894\text{Å}$ ($CoK\alpha_1$)

The phase responsible for the increase in the intensity of these lines was determined as being nickel oxide **NiO**, known mineralogically as **bunsenite**.

Table 4.4-11 lists the reference data for this compound and compares it with peaks in mattes D and E.

Figure 4.4-4(a) and **(b)** shows the scan for matte D compared with that from a geological sample of Fe_3O_4 for comparison.   Note peaks of higher than expected

intensity. As nickel replaces iron in the Fe_3O_4 lattice forming $NiFe_2O_4$ the peaks shift slightly to higher diffraction angles.

Table 4.4-10 Comparison of Fe_3O_4 reference data and data measured for a geological sample of Fe_3O_4

Fe_3O_4 Reference data [9]			Fe_3O_4 Measured data			Mattes D and E Measured data	
d(Å)	(I/I_1)	2θ †	d(Å)	(I/I_1)	2θ †	(I/I_1)	(I/I_1)
4.852	(8)	21.2	4.815	(9)	21.4		
2.967	(30)	35.1	2.963	(28)	35.1		
2.532	(100)	41.4	2.531	(100)	41.4		
2.4243	(8)	43.3	2.413	(6)	43.5		
2.0993	(20)	50.4	2.093	(26)	50.6	(79)	(84)
1.7146	(10)	62.9	1.715	(15)	62.9		
1.6158	(30)	67.2	1.616	(33)	67.2		
1.4845	(40)	74.1	1.483	(42)	74.2	(90)	(51)
1.4192	(2)	78.1	1.418	(1)	78.2		
1.3277	(4)	84.7	1.327	(5)	84.7		
1.2807	(10)	88.6	1.279	(12)	88.7		
1.2659	(4)	89.9	1.265	(4)	90.0		
1.2119	(2)	95.1	1.212	(7)	95.2	(17)	(9)
1.1221	(4)	105.7	1.122	(11)	105.8		
1.0930	(12)	109.8	1.093	(23)	109.9		
1.0496	(6)	116.9	1.049	(17)	116.9	(21)	(11)

† Applicable for radiation of wavelength $\lambda = 1.78894$Å $(CoK\alpha_1)$

Table 4.4-11 Comparison of NiO reference data with peaks observed in matte scans

NiO Reference data [10]			Matte D Measured data			Matte E Measured data		
d(Å)	(I/I_1)	2θ †	d(Å)	(I/I_1)	2θ †	d(Å)	(I/I_1)	2θ †
2.410	(91)	43.6	2.395	(54)	43.9	2.409	(40)	43.6
2.088	(100)	50.7	2.106	(100)	50.3	2.089	(100)	50.7
1.476	(57)	74.6	1.483	(-)	74.2	1.477	(61)	74.5
1.259	(16)	90.5	1.259	(38)	90.6	1.255	(27)	91.0
1.206	(13)	95.8	1.209	(23)	95.5	1.208	(11)	95.6
1.0441	(8)	117.9	1.048	(29)	117.2	1.046	(13)	117.6

† Applicable for radiation of wavelength $\lambda = 1.78894$Å $(CoK\alpha_1)$

4.5 COMMENT ON MATTE PHASES

The table below lists the phases detected in BARPLATS base metal refinery matte :

Table 4.5-1   Matte phases (detectable by XPD)

Phase	Formula	Mineral name	JCPDS Card number
Nickel sulphide	Ni_3S_2	heazlewoodite	08-0126
Copper sulphide	Cu_2S	chalcocite (low)	23-0961
Nickel-copper alloy	Ni-Cu	-	04-0850, 04-0836
Iron oxide	Fe_3O_4	magnetite	19-0629
Nickel iron oxide	$NiFe_2O_4$	trevorite	10-0325
Nickel oxide	NiO	bunsenite	04-0835

4.5.1 THE NICKEL SULPHIDE PHASE

On the Ni-S phase diagram [11] Ni_3S_2 falls on the 26.7 wt% sulphur line. This phase can however show a metal excess or metal deficiency according to the non-ideal formula $Ni_{3\pm x}S_2$ [12], small amounts of iron and cobalt making up the deficiencies. The density is **5.82g/cm^3** [13]. Structurally Ni_3S_2 is strictly hexagonal or rhombohedral, but can be regarded as **pseudocubic** with a body centred arrangement of sulphur atoms (a_0 = 4.08Å, α = 89°25'), with nickel atoms being positioned at tetrahedral sites [14]. The phase is pseudometallic and paramagnetic due to complex Ni-Ni bonding [15].

The only real difference between the measured XPD pattern and the reference XPD pattern measured from a geological specimen is a more definite separation of the **(113)** and **(211)** lines (these occur at 1.83Å and 1.82Å in geological specimens (0.01Å difference); 1.85Å and 1.83Å were the measured values, 0.02Å difference). This is characteristic of Ni_3S_2 of synthetic origin [16].

4.5.2 THE COPPER SULPHIDE PHASE

On the Cu-S phase diagram [17] Cu_2S falls on the 20.1 wt% sulphur line. The density is 5.5 - 5.8g/cm^3 [18]. Cu_2S is crystallographically a superstucture based on a **hexagonal** system of close packed sulphur atoms [19]. These planes are layered with copper atoms triangularily coordinated in two different positions; one between sulphur atoms in the layer and the other between sulphur atoms of two different layers [20]. The phase is a semiconductor and diamagnetic [21].

The XPD analysis confirmed that the copper sulphide phase of matte is Cu_2S rather than the sulphur-richer $Cu_{31}S_{16}$ (djurleite) phase which is almost structurally identical.

4.5.3 THE NICKEL COPPER ALLOY PHASE

As nickel and copper are mutually soluble at all concentrations [22] forming no alloys of definite stoichiometry but rather solid solutions, diffraction peaks occur at spacings intermediate between those of nickel and copper. The exact position of these peaks is important and is dealt with later in § 4.7.2. Structurally the alloy is **cubic** [23]. The density of the alloy is usually about **8.9g/cm^3** [24].

In most cases the maximum intensity **(111)** line overlaps with the **(202)** Ni_3S_2 line in matte XPD patterns.

4.5.4 THE IRON OXIDE - NICKEL IRON OXIDE PHASE

Iron oxide Fe_3O_4 has a **cubic** structure (a_0 = 8.397Å) very similar to that of nickel iron oxide $NiFe_2O_4$ which is also **cubic** (a_0 = 8.339Å) [25]. Fe_3O_4 can be formulated as $Fe^{3+}(Fe^{2+}Fe^{3+})O_4$ where Fe^{2+} and half the Fe^{3+} ions occupy octahedral sites and half the Fe^{3+} ions occupy tetrahedral sites in an inverse spinel framework. Ni^{2+} ions can replace Fe^{2+} ions in this structure leading to the formation of nickel iron oxide $Fe^{3+}(Ni^{2+}Fe^{3+})O_4$. This phase can then form a continuous range of solid solutions with Fe_3O_4 [26].

Possible reactions leading to the formation of the phases are :

(i) $2 FeS + 3 O_2 \longrightarrow 2 FeO + 2 SO_2$ iron sulphide oxidation

(ii) $3 FeS + 5 O_2 \longrightarrow Fe_3O_4 + 3 SO_2$ iron sulphide oxidation

(iii) $6 FeO + O_2 \longrightarrow 2 Fe_3O_4$ iron oxide oxidation

(iv) $2 Ni_3S_2 + 7 O_2 \longrightarrow 6 NiO + 4 SO_2$ nickel sulphide oxidation

(v) $4 FeO + 2 NiO + O_2 \longrightarrow 2 NiFe_2O_4$ iron oxide / nickel oxide reaction

(vi) $4 Fe_3O_4 + 6 NiO + O_2 \longrightarrow 6 NiFe_2O_4$ iron oxide / nickel oxide reaction

(vii) $Fe_3O_4 + NiFe_2O_4 \longrightarrow$ solid solution   mutually soluble

Note that all the above reactions require oxygen.   An XPD analysis of matte showing high levels of Fe_3O_4 / $NiFe_2O_4$ generally indicates too much oxygen has been used during the conversion step at the mine.

The two phases have densities of **5.20g/cm³** and **5.37g/cm³** repectively.

4.5.5 THE NICKEL OXIDE PHASE

The NiO structure is also **cubic** ($a_0 = 4.177$Å) and usually contains both Ni^{2+} and Ni^{3+} ions [27].   NiO plays an important role in the formation of $NiFe_2O_4$ [28] (see § 4.5.4). The density of this phase is **6.81g/cm³** [29].

4.6 MICROSCOPIC EXAMINATION OF MATTE PHASES

Many metallic and non-metallic phases are optically anisotropic in that their optical properties vary with crystallographic direction [30].   Use can be made of this property by illuminating a cut and polished surface of a crystalline solid with plane polarized light.   If the surface is isotropic, the **reflected** light remains polarized and on rotation of a second polarizer, known as the analyser, (through which the reflected light is beamed) can be completely extinguished.   Reflection from an anisotropic surface produces a component perpendicular to the plane of polarization of the incident light.   This component cannot be completely extinguished and so rotation of the analyser, when examining

heterogeneous crystalline surfaces, produces regions of differing light intensity. Cubic crystals are optically isotropic simply because light can travel in all crystallographic directions with the same velocity [31]. All other non-cubic crystals are optically anisotropic. In hexagonal crystals for example, a light ray travelling through the crystal is split into two rays of different velocities, polarized at right angles to each other [32]. The changed velocities of light produce different colours in the reflected beam as light of, for example, long wavelength (these would be red-band rays) which are now plane polarized will be removed from the original incident plane polarized light and so be extinguished by the analyser. The reflected light seen in this case would be blue-green.

The constituents of matte can be differentiated under plane polarized light as they are crystallographically different (see § 4.5). The Ni-Cu alloy is **cubic** and therefore optically isotropic and so will not change the plane of polarization. Reflected light is thus expected to remain white. Ni_3S_2 is **pseudocubic**, and so will show only a slight effect. Cu_2S however has a structure based on the **hexagonal** system which is optically anisotropic and so will show the greatest effect, as hexagonal crystals split light considerably (for example, hexagonal 'Iceland spar' calcite - $CaCO_3$). On rotation of the analyser the colour of reflected light from this phase should change the most, possibly to blue or green.

A small sample of solid matte (matte F) was thus cut to give a thin section, and after polishing and mounting, examined using a polarized-light microscope fitted with a sodium lamp (λ = 589.3 nm). It should be noted that although a tungsten lamp gives higher intensity light it does not give as good a contrast (the wavelength is unsuitable). Two of the photomicrographs obtained are shown in **Figures 4.6-1(a)** and **4.6-1(b)**.

The Ni-Cu alloy, containing the pgms, shows up as white cubic crystals or as anhedral masses. The copper sulphide phase shows up as larger blue-green dentritic crystals. The pale yellow-green backround is a matrix of crystalline nickel sulphide. This
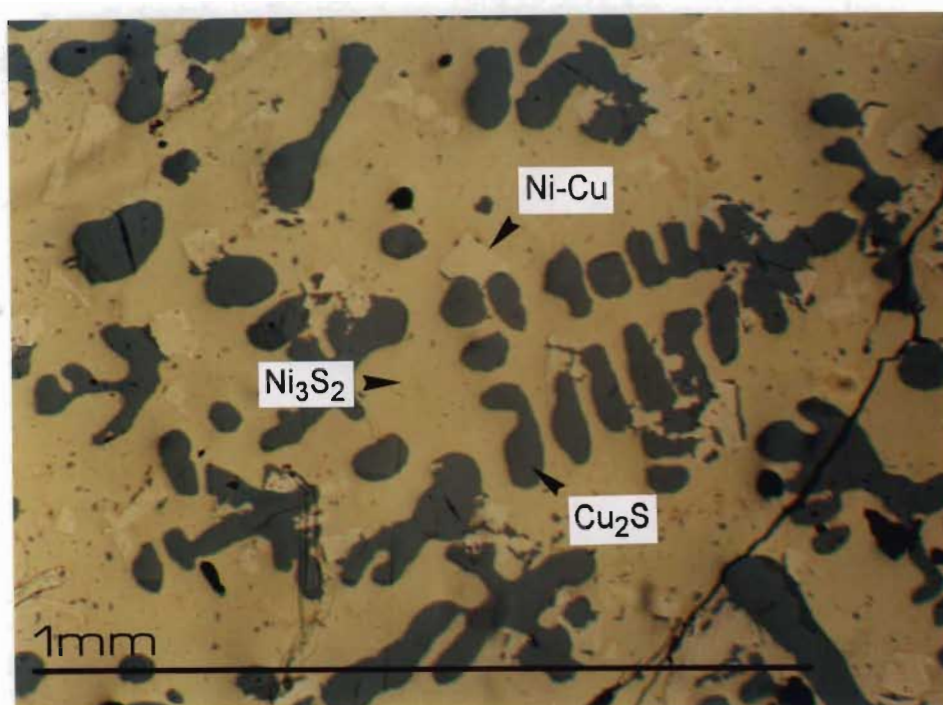
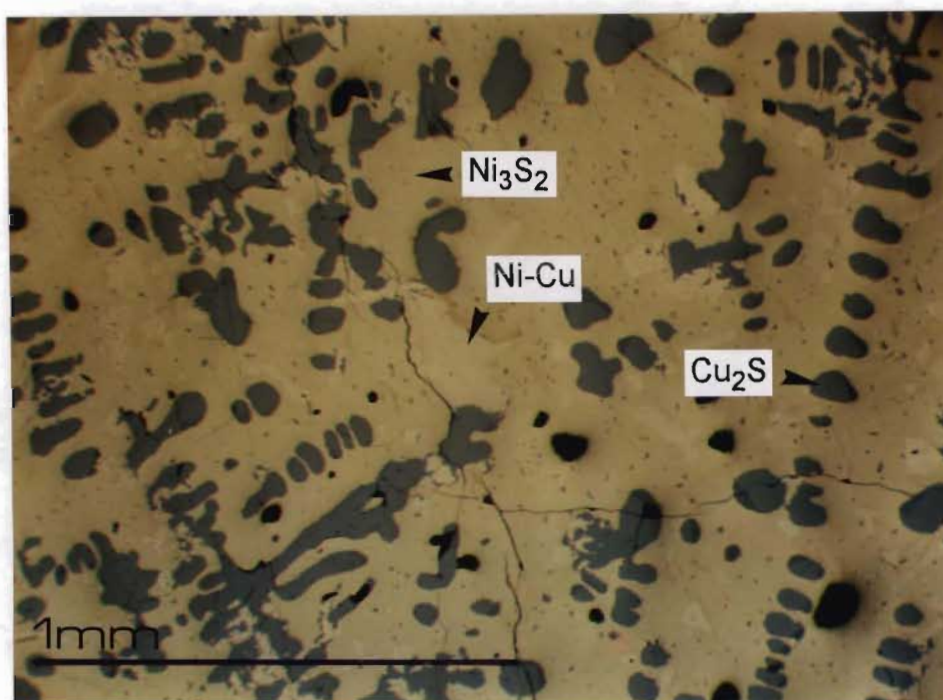**Figure 4.6-1(a)** Photomicrograph of a slow cooled matte section (λ = 589nm)

Figure 4.6-1(b) Photomicrograph of a slow cooled matte section (λ = 589nm)

particular sample had no iron oxide phase present (the black dots are voids). Thus the XPD analysis was fully confirmed.

An interesting feature of matte crystallization is that an organic system exists which crystallizes in a very similar manner. When a molten mixture of 88 wt% camphor ($C_{10}H_{16}O$: mp 180°C) and 12 wt% anthracene ($C_{14}H_{10}$: mp 218°C) solidifies, dentritic crystals of camphor form, associated with a eutectic of camphor and anthracene, in an anthracene matrix [33]. The similarity demonstrates that the crystallization of a liquid mixture of Cu_2S, Cu-Ni and Ni_3S_2 can probably be explained using a constitutional supercooling model. **Table 4.6-1** compares these two systems.

Table 4.6-1   Comparison of matte crystallization with that of a similar organic system

Inorganic system	Organic system	Manner of crystallization
Cu_2S	Camphor	Dentritic
Cu-Ni	Camphor-anthracene eutectic	Associated with dentrites
Ni_3S_2	Anthracene	Matrix

Figure 4.6-2(a) shows crystals from the matte system and **Figure 4.6-2(b)** crystals from the camphor + anthracene system.

4.7 THE MAGNETIC SEPARATION OF MATTE

Research by the South African minerals research group, MINTEK, has shown that 97% of the pgms present in ore concentrate can be collected into a magnetic alloy fraction with a mass of 10% of the matte by the process of slow cooling [34]. This study was however done on ore concentrate from the Merensky reef. Further work done using ore concentrate from the UG-2 reef and mixed ore concentrate showed that in order to
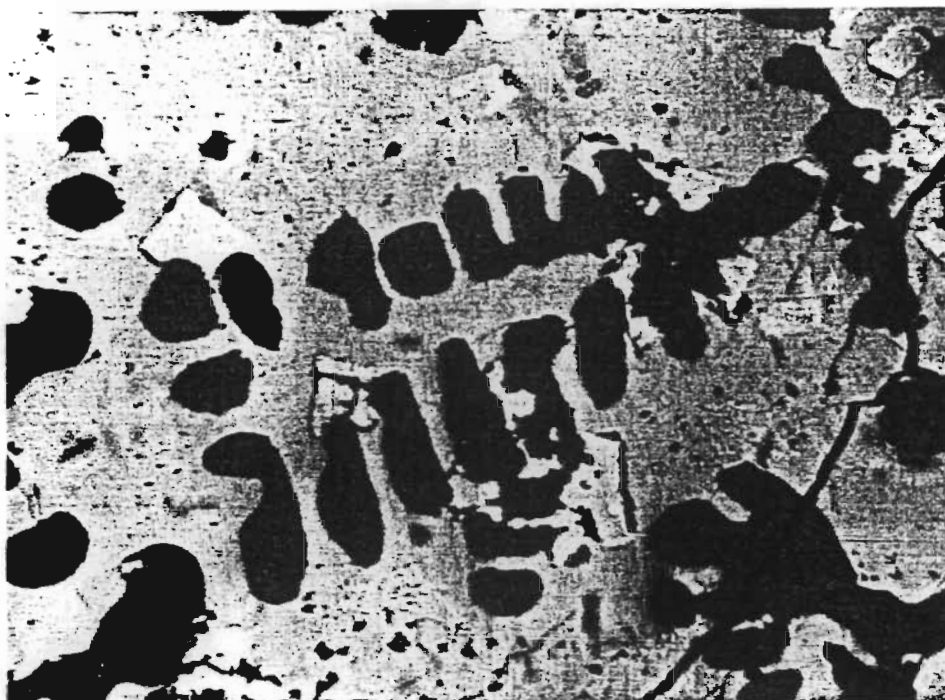
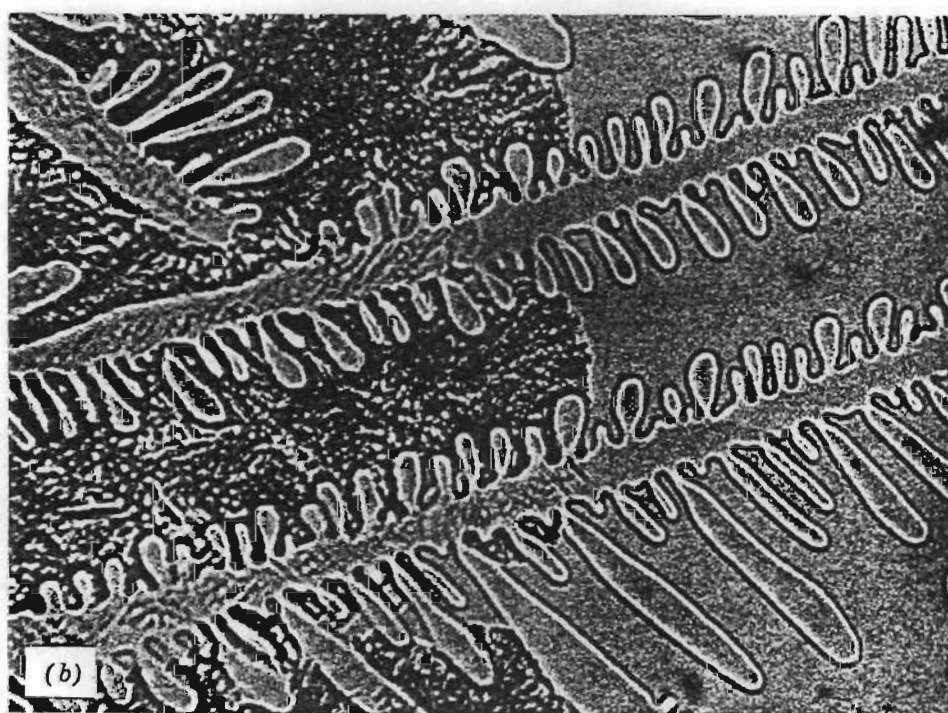**Figure 4.6-2(a)** Crystals from the matte system

Figure 4.6-2(b) Crystals from the camphor + anthracene system

achieve reasonable pgm recoveries a greater fraction of magnetic material had to be produced [35].

As the BARPLATS base metal refinery showed an interest in the feasibility of magnetically separating the slow cooled matte they were using, a study in this area was felt necessary. For this purpose various magnetic and non-magnetic fractions of matte were provided. The study had the following aims :

    (a) To determine the percentage alloy present in the matte

    (b) To determine whether pgms were being collected by the alloy phase

    (c) To determine the success of the magnetic separation process

4.7.1 THE SLOW COOLING OF MATTE

The slow cooling process takes place at the mine during the post conversion stage (see § 4.2.4). As this step is vital in ensuring satisfactory pgm collection, it becomes important to have some way of finding out whether the mine has in fact *slow* cooled the matte. Under non-equilibrium conditions of cooling non-homogeneous solid solutions are formed [36]. In the case of the nickel-copper alloy this means that instead of homogeneous cubic crystals forming, the crystals will be zoned. As the melting point of nickel is 1555°C and that of copper is 1083°C, fast cooling will initially produce small nuclei of nickel-rich alloy. As there is no time for the solution around these nuclei to equilibrate, the matrix solution becomes richer in copper, until finally the remaining copper-rich alloy solution of low melting point crystallizes out around each nucleus.

The XPD scan of a matte sample exhibiting the effects of fast cooling is shown in **Figure 4.7.1-1**. Each alloy line has broadened and partially split . The low angle side of each split peak is due to copper-rich zones (approaching pure copper) while the high angle side is due to nickel-rich zones within the alloy crystals (see **Figure 4.7.1-2**). Thus an XPD analysis can be used to confirm whether slow cooling has taken place.
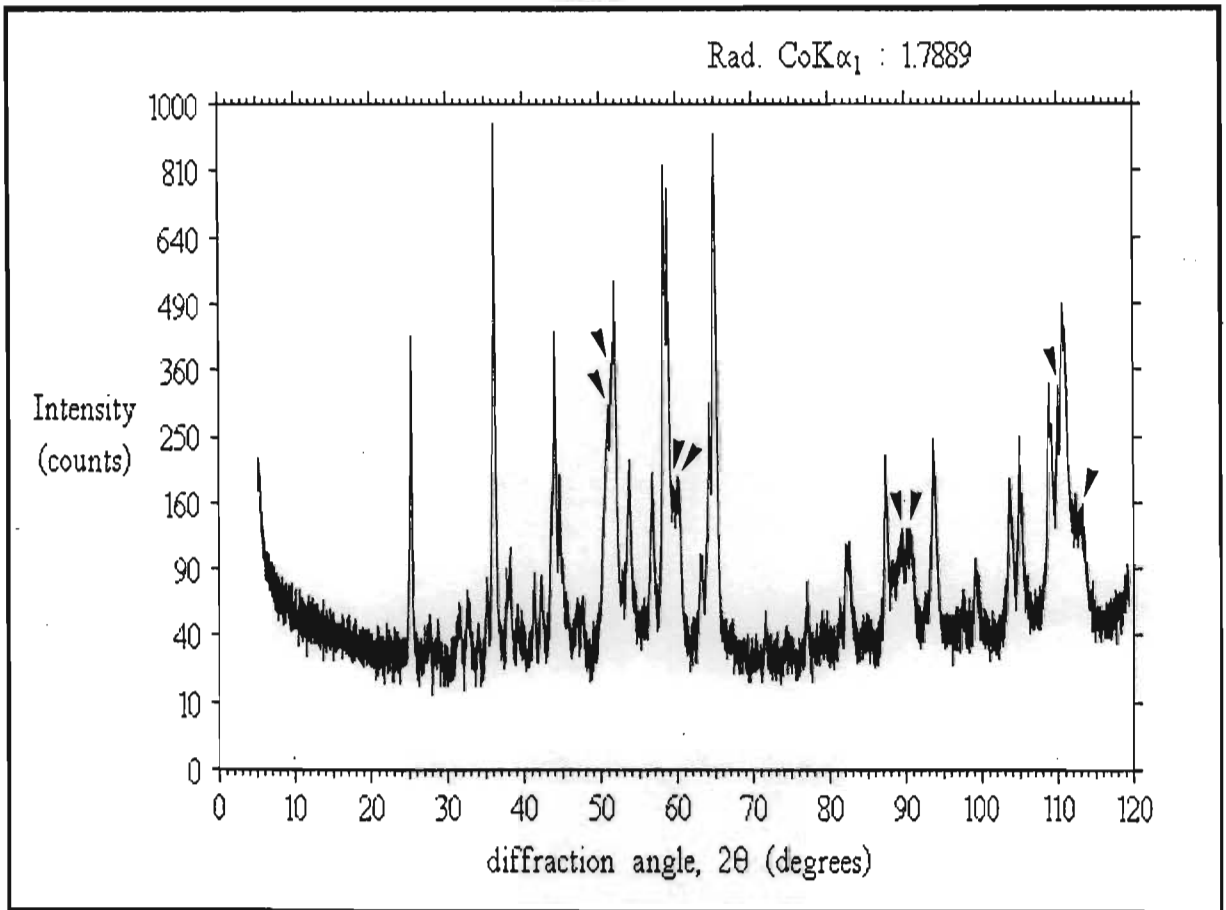
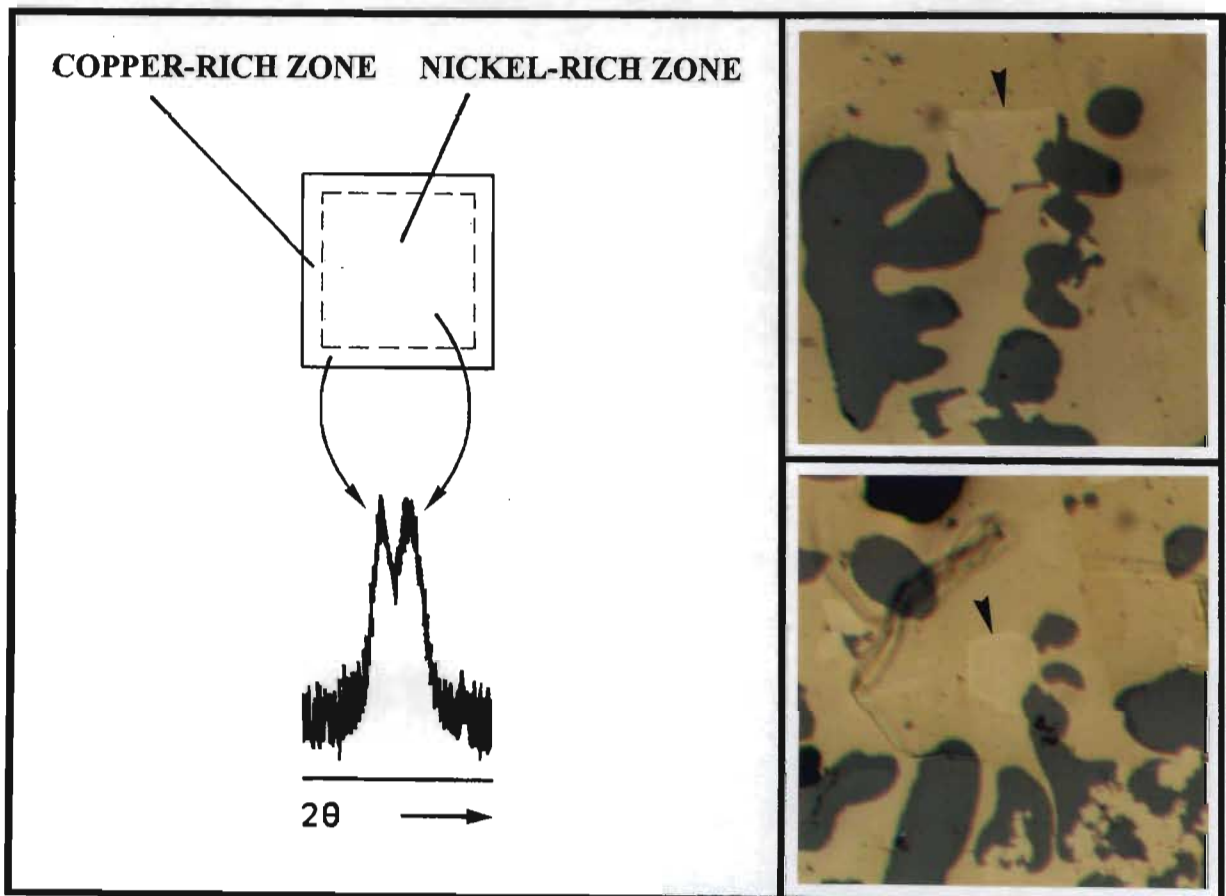**Figure 4.7.1-1** XPD scan of fast cooled matte showing alloy peak splitting

Figure 4.7.1-2 Origin of split alloy peaks

4.7.2 DETERMINATION OF THE STOICHIOMETRY OF THE MATTE ALLOY

In order to determine the percentage of alloy present in matte, it is first necessary to determine its stoichiometry. This is possible if the unit cell dimensions are known. The alloy phase gives four diffraction peaks over the 2θ range $5°$ - $120°$, these being reflections off the **(111)**, **(200)**, **(220)** and **(311)** planes. **Table 4.7.2-1** gives the observed data for these peaks for mattes A, B and C.

Table 4.7.2-1 Observed alloy data for mattes A, B and C

Peak	(hkl)	Matte A d(Å)	Matte B d(Å)	Matte C d(Å)
1	**(111)**	2.0741	2.0587	2.0577
2	**(200)**	1.7871	1.7911	1.7883
3	**(220)**	1.2601	1.2596	1.2593
4	**(311)**	1.0714	1.0720	1.0707

As the nickel-copper alloy is **cubic** the Bragg equation for determining the unit cell dimensions, in the absence of systematic errors, is [37] :

$$\sin^2\theta = (\lambda^2 / 4a_o^2)(h^2 + k^2 + l^2)$$

where λ is the wavelength of the radiation used (for the x-ray system used, $\lambda = 1.78894\text{Å}$); a_o is the edge length of the cubic cell; h, k, and l are the Miller indices of the diffraction planes (Table 4.7.2-1), and θ is the angle of reflection calculated from the relation below [38] :

$$n\lambda = 2d\sin\theta$$

where, for single order reflections $n = 1$, and d is the d-spacing of the peak in Ångstroms (given in Table 4.7.2-1).

Accurate determination of unit cell dimensions using the Bragg equation requires virtually all systematic errors to be eliminated. This is seldom achieved in practice. Significant errors are introduced by small axial divergences and rotational axis

malalignments, both of which shift peak positions slightly. Cohen has shown that when such systematic errors are present, the introduction of a second term involving a 'drift' constant, D, into the above Bragg equation for cubic systems enables the accurate calculation of a_0 (See **Appendix 1 : Cohen's least-squares method**).

Using Cohen's method on the data given in Table 4.7.2-1 the following alloy unit cell dimensions were obtained :

$$\text{Matte A} \; : \; a_0 = 3.5419\text{Å}$$

$$\text{Matte B} \; : \; a_0 = 3.5426\text{Å}$$

$$\text{Matte C} \; : \; a_0 = 3.5378\text{Å}$$

$$\textbf{Average} \; : \; \textbf{a}_0 = \underline{\textbf{3.5408Å}}$$

The stoichiometry of the alloy can now be determined by using Végard's law which states that for solid solutions the lattice parameter is a linear function of the atomic concentrations of the dissolved atoms [39]. This law is approximately true for most solid solutions, and for nickel-copper alloys has the form :

$$\text{at\% nickel} = [(a_0, \text{alloy} - a_0, \text{copper}) / (a_0, \text{nickel} - a_0, \text{copper})] \times 100$$

where for nickel $\quad a_0 = 3.5236\text{Å}$ (25°C) (Literature value)

for copper $\quad a_0 = 3.6147\text{Å}$ (25°C) (Literature value)

for the alloy $\quad a_0 = 3.5408\text{Å}$ (25°C) (Calculated average)

Thus the atomic concentration of nickel in the alloy is 81.12 at% on average (79.87 wt% Ni), and the alloy can be formulated as ranging from $Ni_{3.978}Cu$ to $Ni_{5.414}Cu$.

Average stoichiometry : $Ni_{4.297}Cu$ (based on average a_0 value)

4.7.3 DETERMINATION OF THE WEIGHT PERCENTAGE OF MATTE ALLOY

Having determined the stoichiometry of the alloy, the weight percentage present in the matte can be estimated by considering the matte as a three component system and solving as a set of three linear equations. In the case of matte A the equations would be :

$$Ni_3S_2 \qquad Ni_{3.978}Cu \quad Cu_2S$$

$$0.733\,x \;+\; 0.786\,y \;+\; 0.000\,z \;=\; 52.9 \qquad : \text{total nickel content (Table 4.4-1)}$$

$$0.000\,x \;+\; 0.214\,y \;+\; 0.799\,z \;=\; 24.6 \qquad : \text{total copper content (Table 4.4-1)}$$

$$0.267\,x \;+\; 0.000\,y \;+\; 0.201\,z \;=\; 18.0 \qquad : \text{total sulphur content (estimate)}$$

where x, y and z are the weight percentages of Ni_3S_2, $Ni_{3.978}Cu$ and Cu_2S present in matte A. Solution of the above equations, and similar equations for mattes B an C gave the results shown in **Table 4.7.3-1**.

Table 4.7.3-1   Weight percent composition of mattes A, B and C

Matte	Ni_3S_2	Ni-Cu	Cu_2S
A	48.7	21.9	24.9
B	46.8	21.0	27.3
C	46.4	21.2	27.9

What these results show is that the alloy phase makes up about **21.0 - 21.9%** of the weight of the matte. This might not seem likely based on the photomicrographs, except that it must be remembered that the alloy has a much higher density than the other two phases. The Ni_3S_2 : Cu_2S : Ni-Cu volume ratio is **3.4 : 2.0 : 1.0**.

Based on the values in Table 4.7.3-1 an average calculated density for the three mattes (using the densities given in § 4.5) would be about **6.25g/cm³**. This agrees well with the measured density of 6.2 - 6.3g/cm³ and indicates the weight percentages are correct.

4.7.4 DETERMINING THE SUCCESS OF A MAGNETIC SEPARATION

The success of a magnetic separation depends on several factors. Three of these are :

(1) Having an alloy phase into which most of the pgms have been collected

(2) Having a low bulk of alloy present in the matte

(3) Having an alloy with good magnetic properties

An observation to be covered later (§ 4.8) will indicate that the alloy phase is rich in the pgms, thus satisfying condition (1). From § 4.7.3 however it seems that there is quite a high bulk of alloy present in the matte (about 21 wt%). Thus condition (2) is only partially met.

An interesting feature of the nickel-copper alloy is that when the weight percentage of nickel rises above 68% (*ie.* $Ni_{2.30}Cu$), it undergoes a magnetic transformation in which numerous electron spins become locked into cooperative parallel orientations over large domains, rendering the material ferromagnetic rather than paramagnetic [40]. As the weight percentage of nickel in the alloy has been determined as being about 79.9% (see § 4.7.2) the alloy will be ferromagnetic, and a separation of phases should be easy. This was not the case, as the alloy crystals were tiny and dispersed throughout the matte (See § 4.8 and **Appendix 2 : Isolation of the alloy phase**).

Figures 4.7.4-1(a) and **4.7.4-2(a)** show the reduced patterns of a magnetically separated matte (matte [1]) compared to the alloy lines. The scans of these two fractions are shown in **Figures 4.7.4-1(b)** and **4.7.4-2(b)**. As can be seen, both fractions contain paramagnetic Ni_3S_2 and the intensities of the alloy peaks are not very different.

Figures 4.7.4-3(a), 4.7.4-4(a), 4.7.4-3(b) and 4.7.4-4(b) show a slightly better alloy separation (matte [2]).

From the analysis of various samples, the following observations were made :

1) In all cases the paramagnetic nickel sulphide phase (Ni_3S_2) occurs in both fractions.

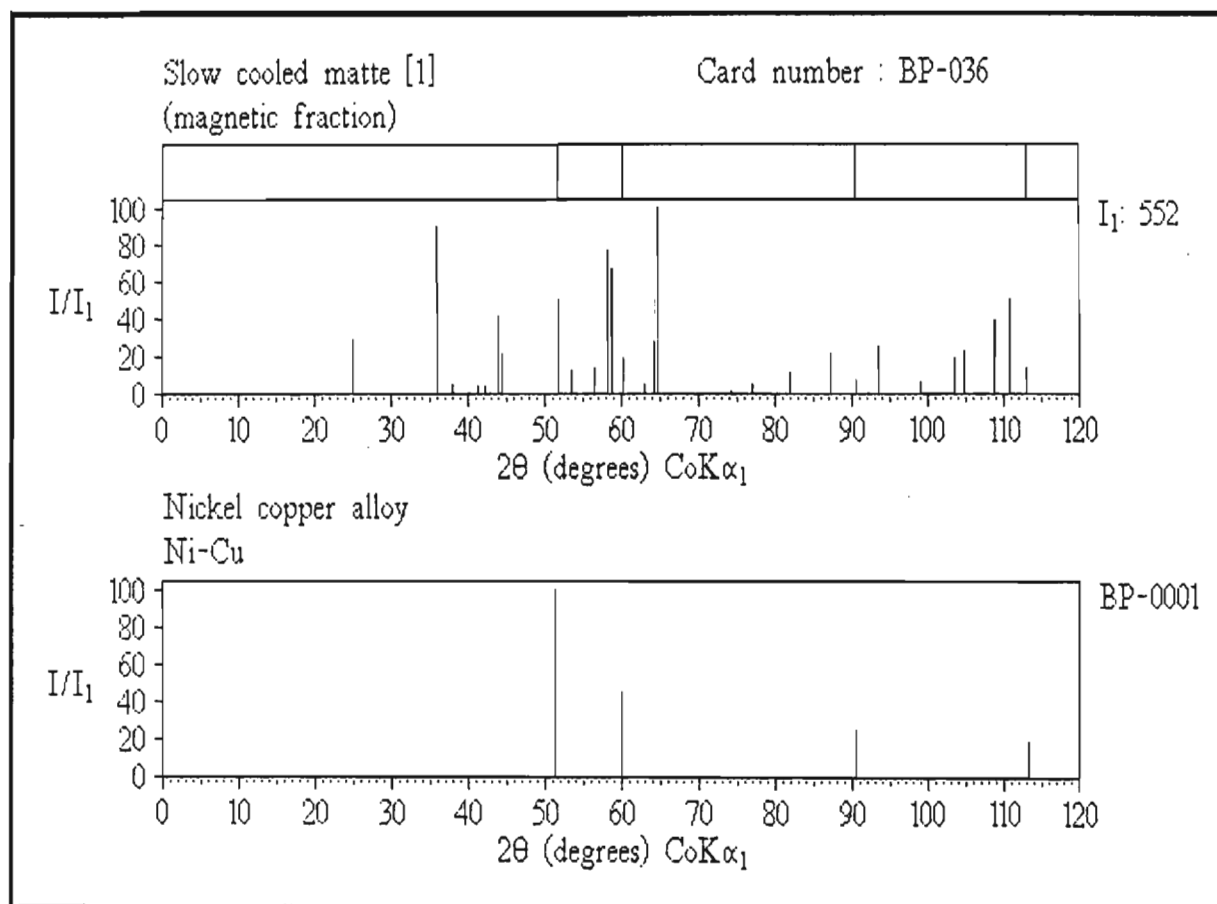2) The diamagnetic copper sulphide phase (Cu_2S) occurs mainly in the non-magnetic fraction.
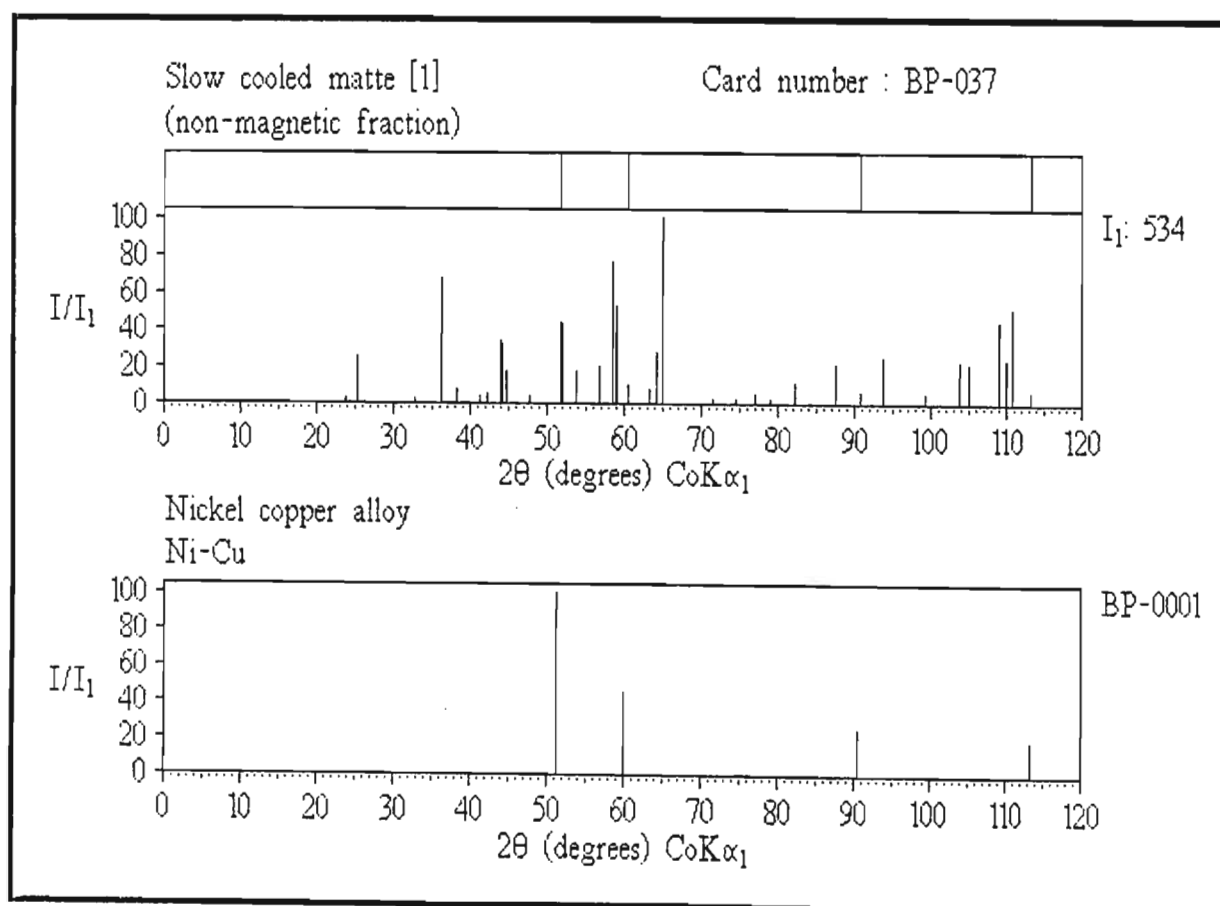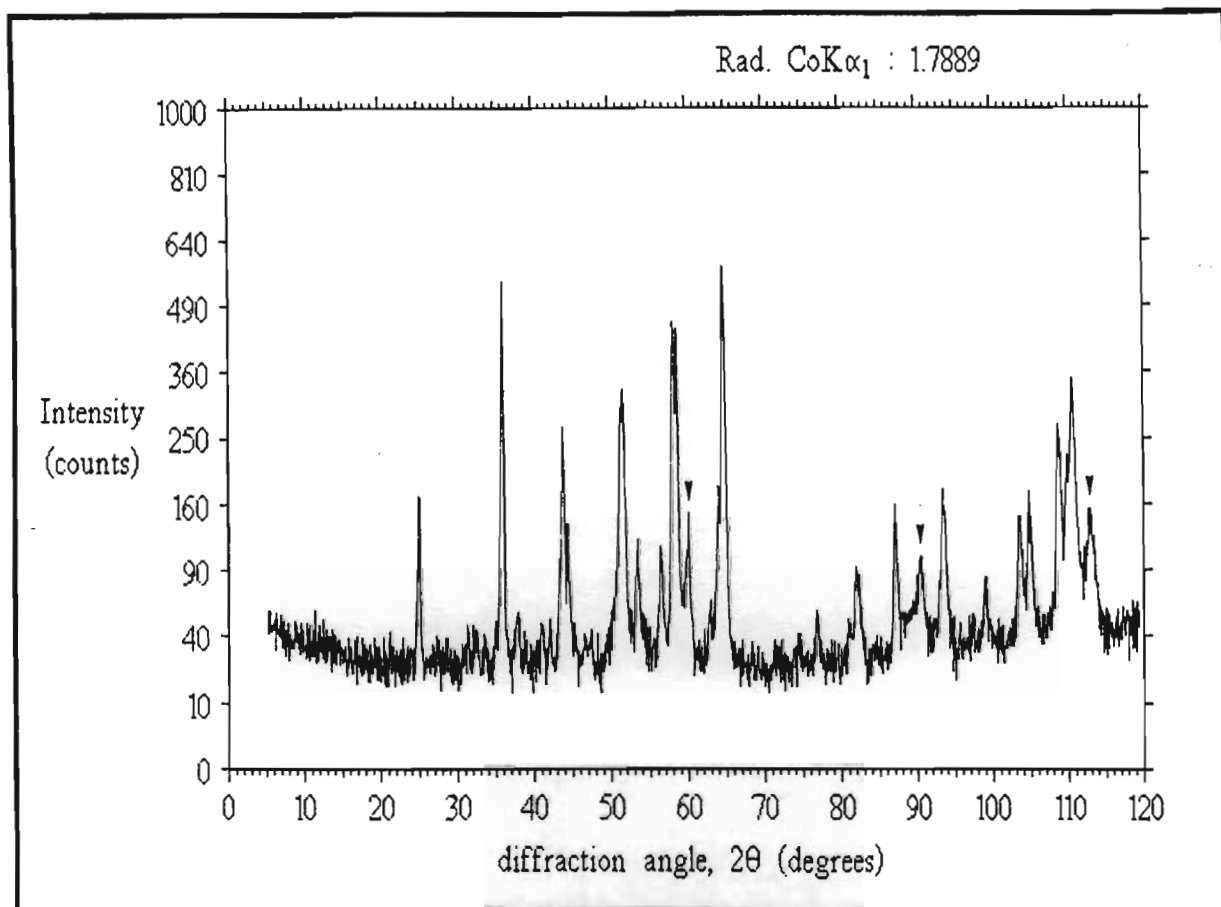
Figure 4.7.4-1(a)

Figure 4.7.4-2(a)

Rad. CoKα_1 : 1.7889

Figure 4.7.4-1(b) XPD scan of the magnetic fraction of matte [1]
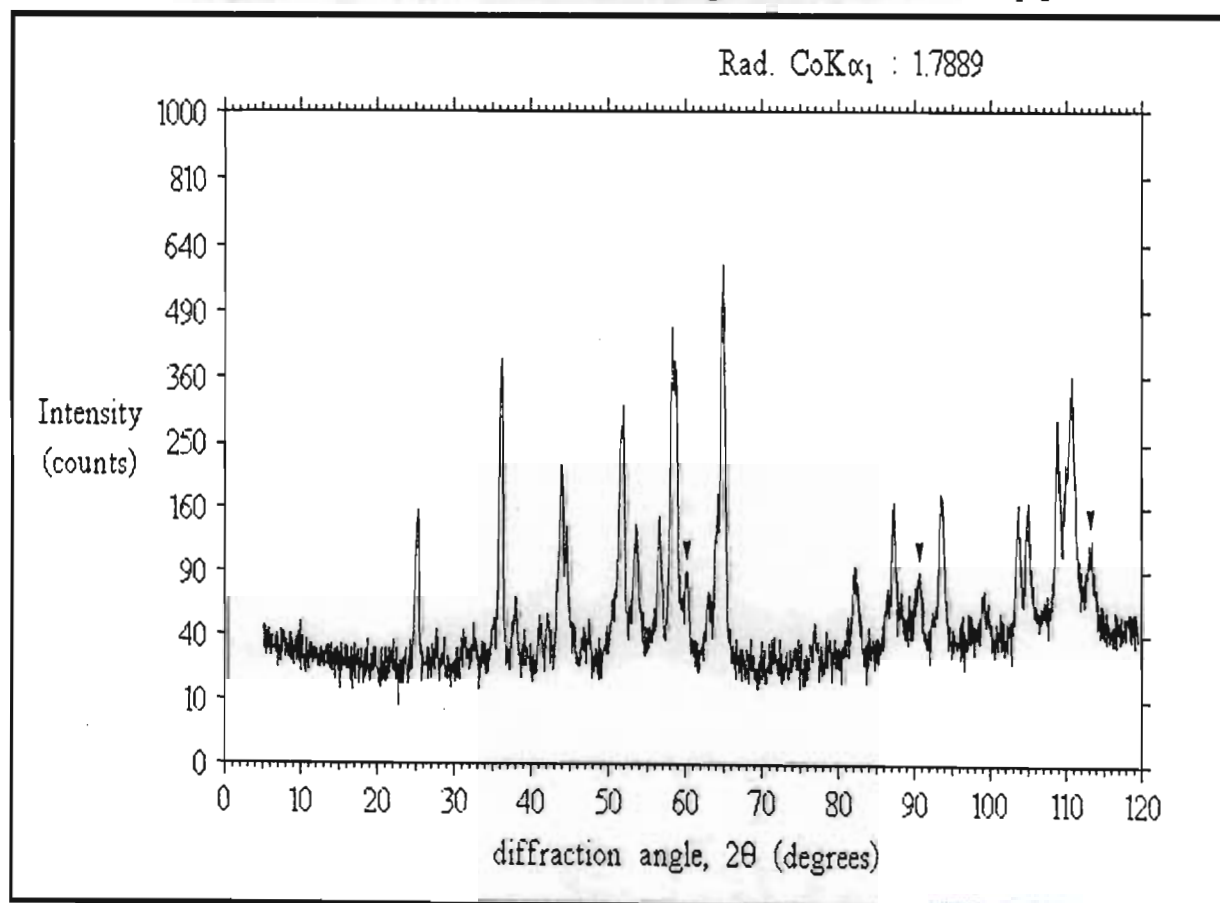
Rad. CoKα_1 : 1.7889

Figure 4.7.4-2(b) XPD scan of the non-magnetic fraction of matte [1]

Figure 4.7.4-3(a)

Figure 4.7.4-4(a)

Figure 4.7.4-3(b) XPD scan of the magnetic fraction of matte [2]

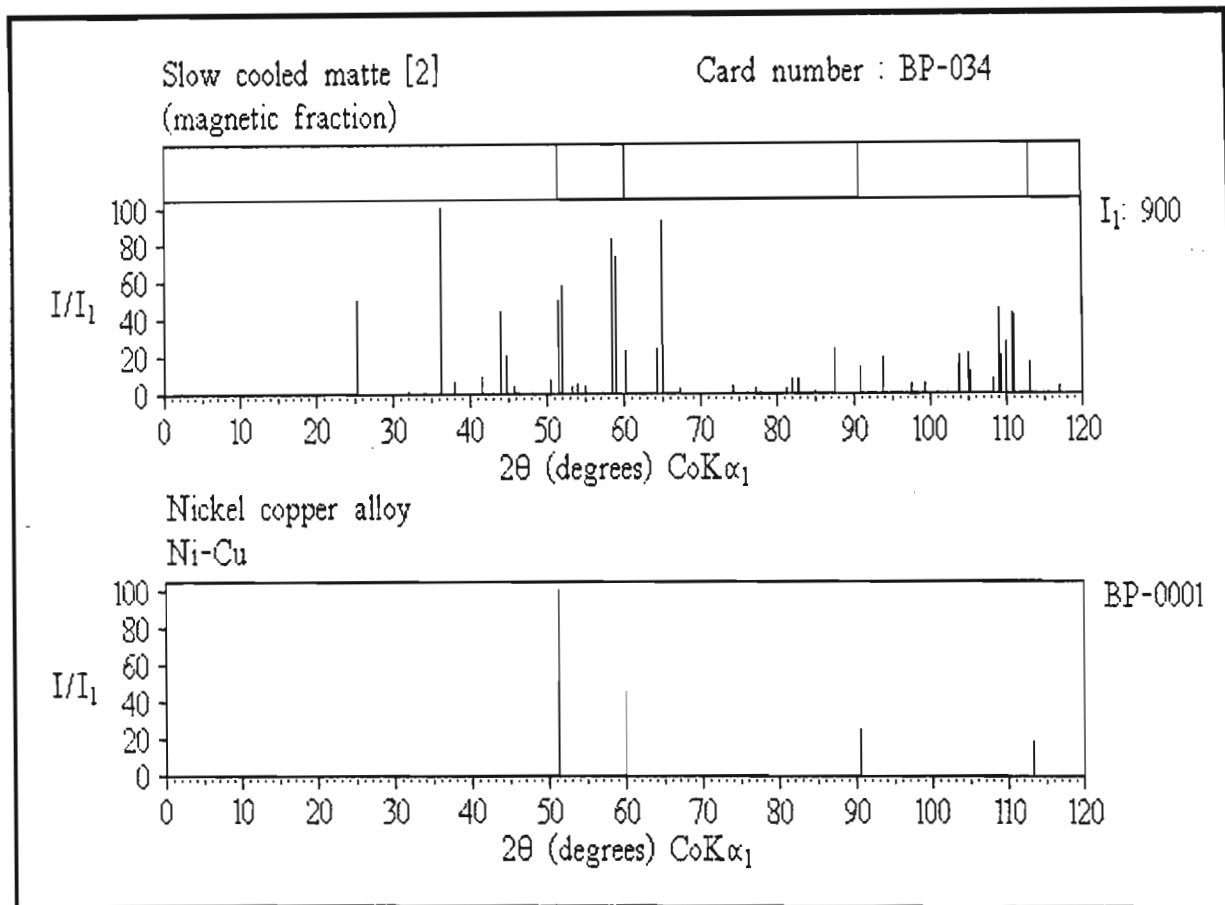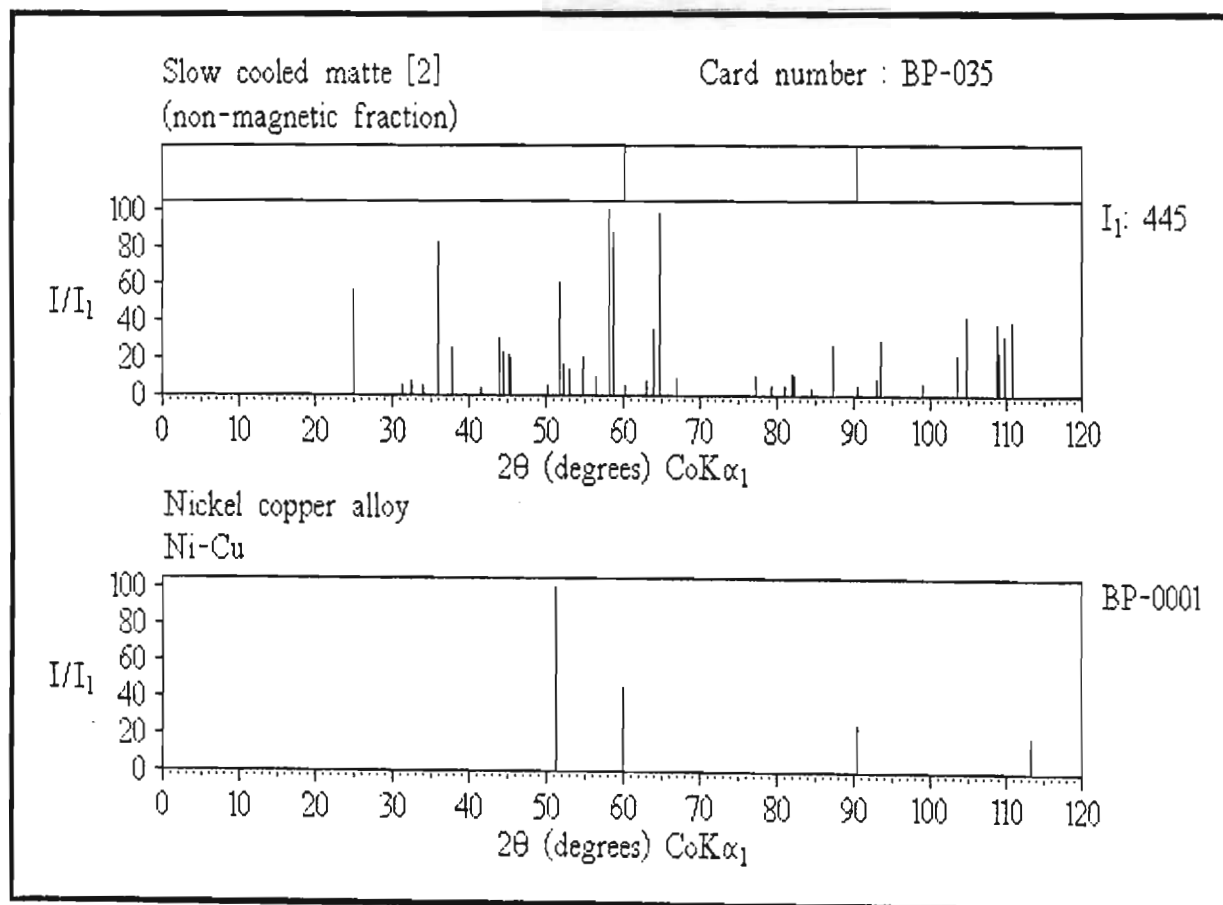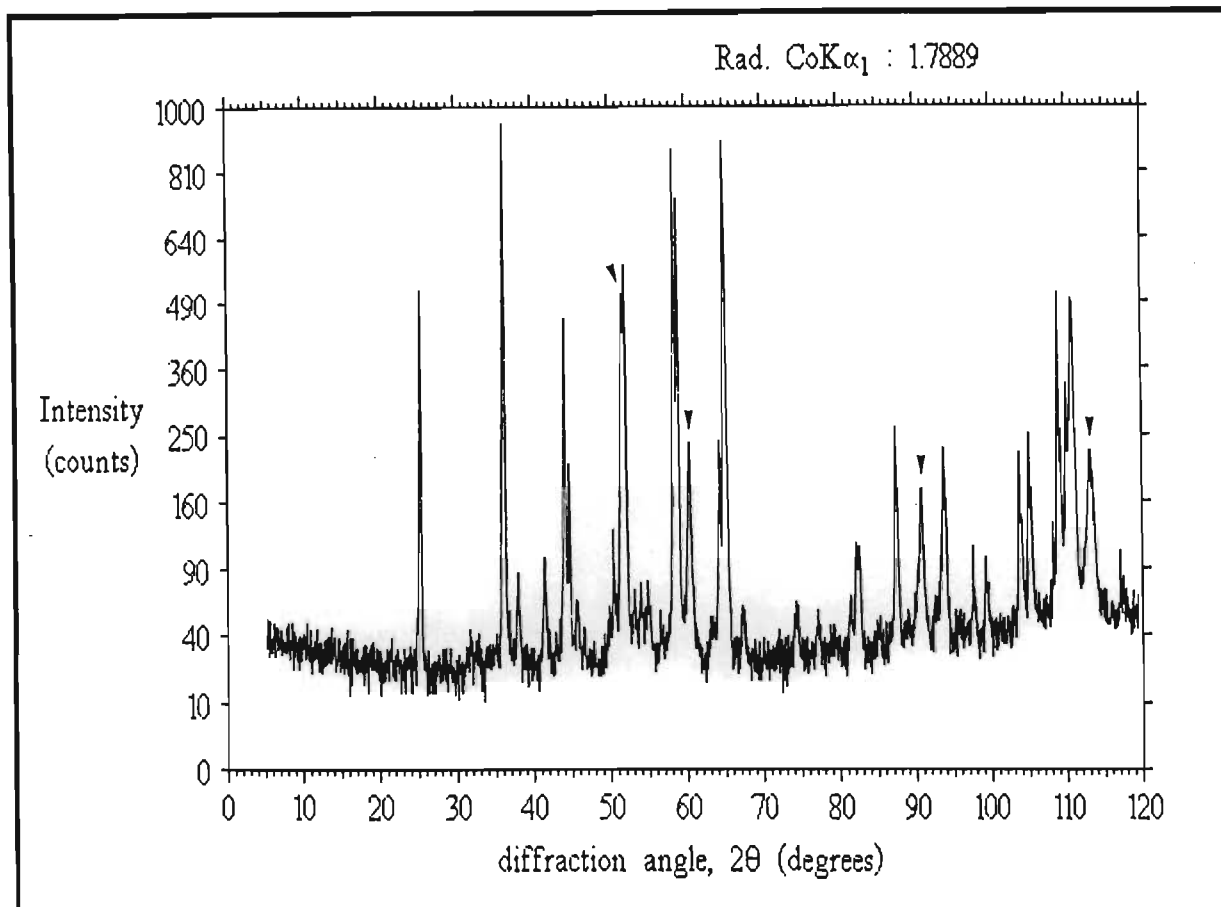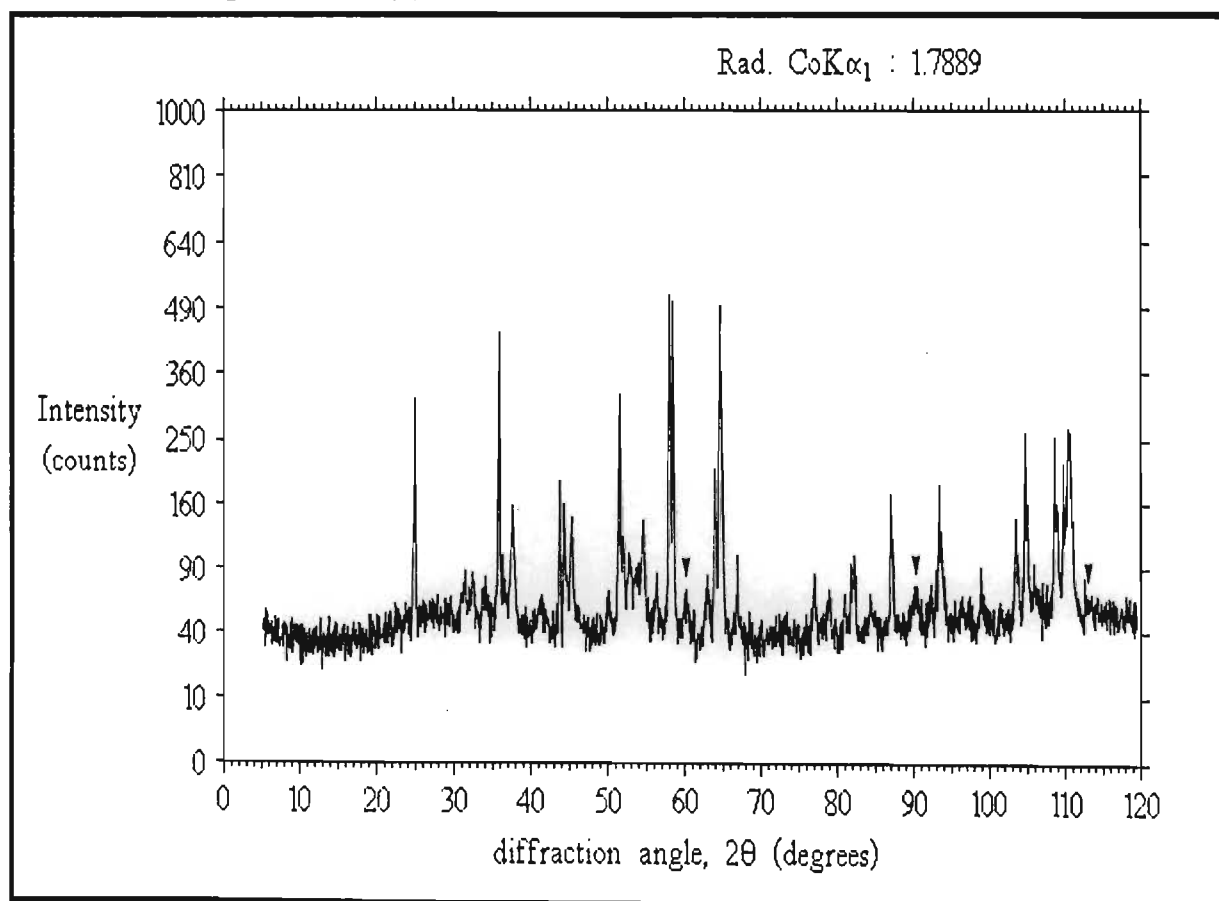**Figure 4.7.4-4(b)** XPD scan of the non-magnetic fraction of matte [2]

3)   The magnetic fraction always has a higher crystallinity than the non-magnetic fraction (as measured by the most intense scan peak).

4)   No differences in the d-spacings of the alloy lines were observed between the two fractions (this confirms slow cooling).

Thus a magnetic separation of the matte being provided to the BARPLATS base metal refinery was shown not to be feasible.

4.8   ANALYSIS OF FIRST STAGE LEACH RESIDUE

After passing through the grinding circuit (**Figure 4.3-1**) the nickel-copper concentrate or matte is leached for nickel with sulphuric acid at atmospheric pressure in what is known as the **first stage leach**.   A sample of first stage leach residue from the underflow of the thickener tank (representing the feed of the second stage leach tanks) was provided by the base metal refinery for analysis.

This residue showed substantially lower crystallinity than the matte samples (maximum count, $I_1 = 471$).   Many of the high intensity lines were identified as those of the nickel sulphide Ni_3S_4 known mineralogically as **polydymite**.   **Table 4.8-1** compares the reference data for this compound with that observed for the sample.   Boldface indicates overlap with another phase.

From Table 4.8-1 it can be seen that there is a good correlation between reference and observed d-spacings, but not for the intensity values.   This is probably due to the age of reference data (the original pattern was recorded on film in 1953 and the intensities estimated visually).

Figure 4.8-1(a) and **(b)** shows the reduced pattern of first stage leach residue compared with that of Ni_3S_4.   Two good diagnostic lines are indicated in the sample peak scan.

Table 4.8-1 Comparison of Ni$_3$S$_4$ reference data with that observed of Ni$_3$S$_4$ found in the first stage leach residue

Ni$_3$S$_4$ Reference data [41]			Observed data First stage leach residue		
d(Å)	(I/I$_1$)	2θ †	d(Å)	(I/I$_1$)	2θ †
5.50	(20)	18.7	5.402	(7)	19.1
3.34	(40)	31.1	**3.318**	**(23)**	**31.3**
2.85	(90)	36.6	2.841	(86)	36.7
2.36	(90)	44.5	2.360	(50)	44.5
1.941	(30)	54.9	**1.954**	**(-)**	**54.5**
1.820	(90)	58.9	**1.819**	**(41)**	**58.9**
1.674	(100)	64.6	**1.671**	**(100)**	**64.7**
1.600	(10)	68.0	**1.599**	**(11)**	**68.0**
1.499	(10)	73.3	1.499	(4)	73.3
1.444	(50)	76.6	1.443	(10)	76.6
1.369	(60)	81.6	1.366	(10)	81.8
1.269	(30)	89.6	1.278	(6)	88.9
1.232	(80)	93.1	1.234	(16)	92.9
1.185	(70)	98.0	1.185	(10)	98.1
1.117	(10)	106.4	1.113	(7)	106.9
1.095	(70)	109.5	1.096	(17)	109.5
1.055	(60)	116.0	1.055	(7)	116.0

† Applicable to radiation of wavelength $\lambda = 1.78894$Å (CoKα_1)

The remaining high intensity lines had to be due to a copper sulphide. Altogether 13 crystallographically different copper sulphides have been identified [42]. **Table 4.8-2** lists the reference data for each.

The similarity of the data in Table 4.8-2 makes the assignment of lines difficult. The sulphides giving the best match with the observed data were Cu$_9$S$_5$, Cu$_{1.8}$S, and Cu$_7$S$_4$. The sulphide Cu$_7$S$_4$ can also transform to Cu$_{1.8}$S on grinding [43]. The best intensity and d-spacing fit was obtained with the sulphide Cu$_{1.8}$S (known mineralogically as **digenite**) although slight shifts were noted.
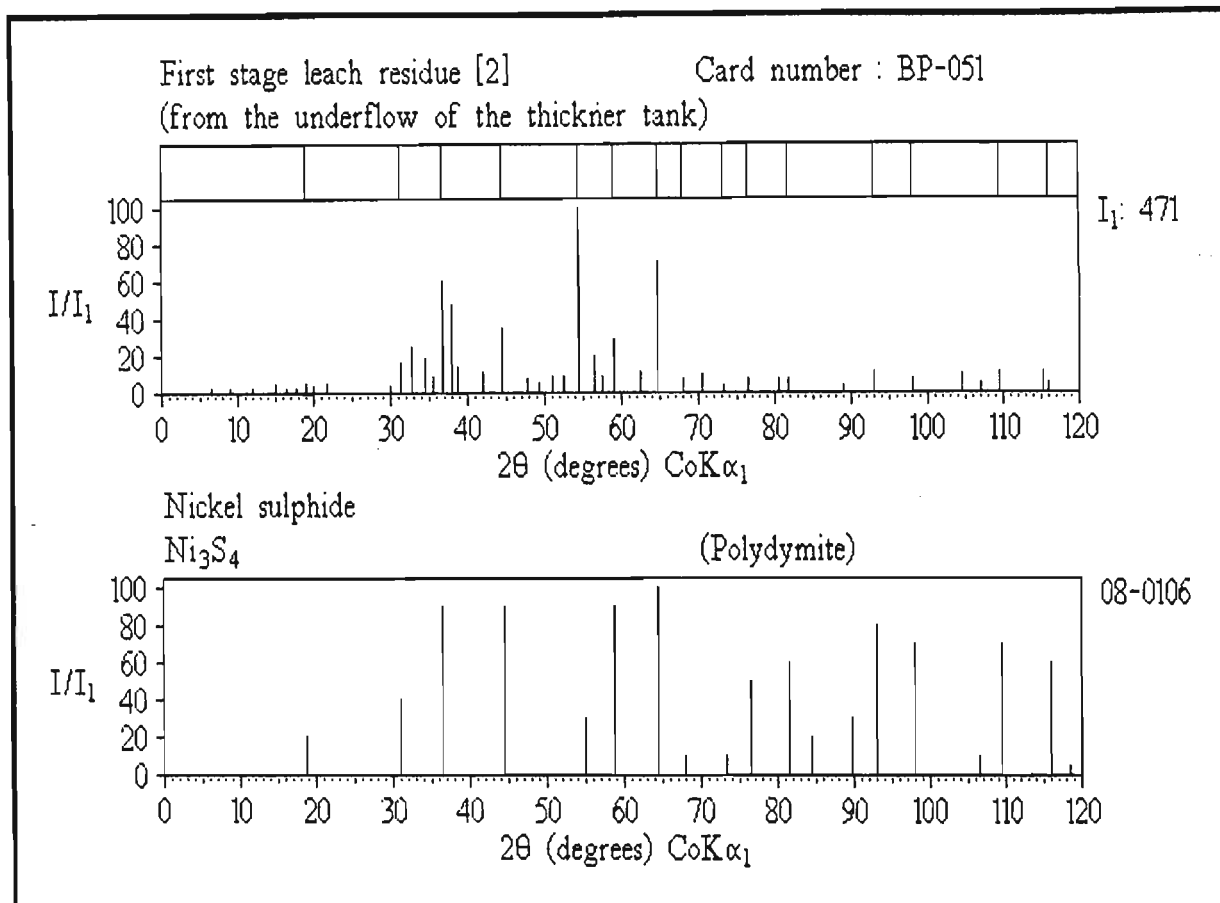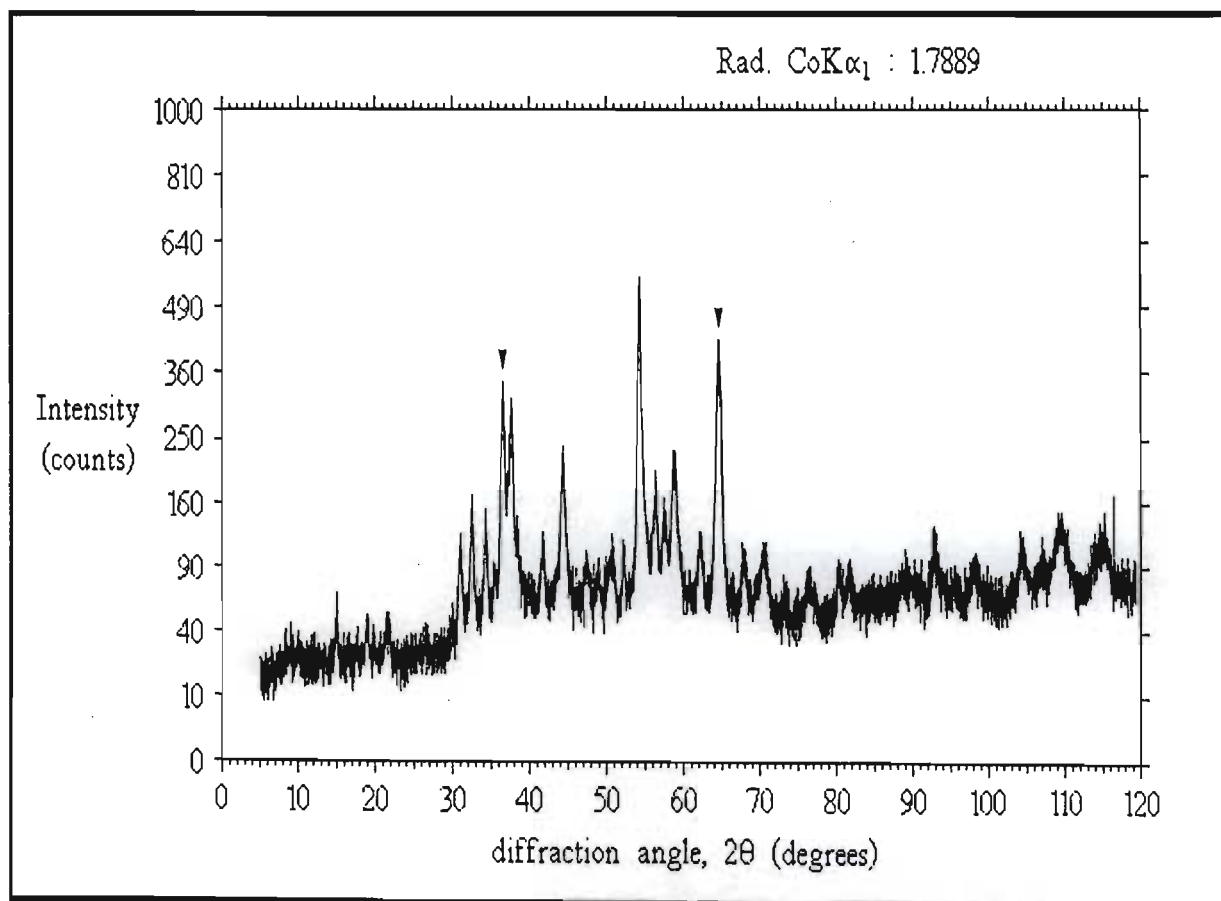
First stage leach residue [2]   Card number : BP-051
(from the underflow of the thickner tank)

I/I₁

100
80
60
40
20
0

0   10   20   30   40   50   60   70   80   90   100 110 120
2θ (degrees) CoKα₁

I₁: 471

Nickel sulphide
Ni₃S₄   (Polydymite)

I/I₁

100
80
60
40
20
0

0   10   20   30   40   50   60   70   80   90   100 110 120
2θ (degrees) CoKα₁

08-0106

Figure 4.8-1(a)

Rad. CoKα₁ : 1.7889

Intensity
(counts)

1000
810
640
490
360
250
160
90
40
10
0

0   10   20   30   40   50   60   70   80   90   100 110 120
diffraction angle, 2θ (degrees)

Figure 4.8-1(b)

Table 4.8-2   XPD reference data for Copper sulphides [42]

Formula	Peak 1 †	Peak 2	Peak 3	Peak 4	Card No.
Cu_2S	2.403_X	3.051_X	1.9750_8	1.7046_4	**24-0057**
Cu_2S	1.9805_X	1.8759_X	2.401_9	1.7063_5	**26-1116**
Cu_2S	1.977_X	1.876_9	2.396_9	2.718_6	**23-0961**
$Cu_{1.96}S$	2.74_X	2.302_8	1.994_4	1.883_4	**17-0449**
$Cu_{1.96}S$	2.016_X	2.852_6	1.720_6	3.30_3	**12-0174**
$Cu_{1.93}S$	1.870_X	1.959_X	2.389_9	1.966_4	**23-0959**
$Cu_{1.91}S$	1.938_X	2.374_9	1.861_9	2.864_4	**23-0958**
$Cu_{7.2}S_4$	1.9693_X	2.785_7	3.216_4	1.6794_1	**24-0061**
Cu_9S_5	1.9594_X	2.954_3	3.200_3	3.042_2	**26-0476**
$Cu_{1.8}S$	1.967_X	2.779_5	3.21_4	1.678_2	**23-0962**
Cu_7S_4	1.956_X	2.77_7	3.20_6	2.16_4	**22-0250**
CuS	2.813_X	1.896_8	3.048_7	2.724_6	**06-0464**
CuS_2	2.89_X	2.04_8	1.73_8	2.57_7	**19-0381**

† X denotes most intense line(s); subscript numbers denote intensities relative to 10

Table 4.8-3 compares the reference data for this compound with that observed for the relatively low intensity copper sulphide peaks.   Many lines overlapped those of other phases (shown in boldface).   **Figure 4.8-2** shows the reduced spectra of first stage leach residue compared to that of $Cu_{1.8}S$.

Table 4.8-3   Comparison of $Cu_{1.8}S$ reference data with that observed of $Cu_{1.8}S$ found in first stage leach residue

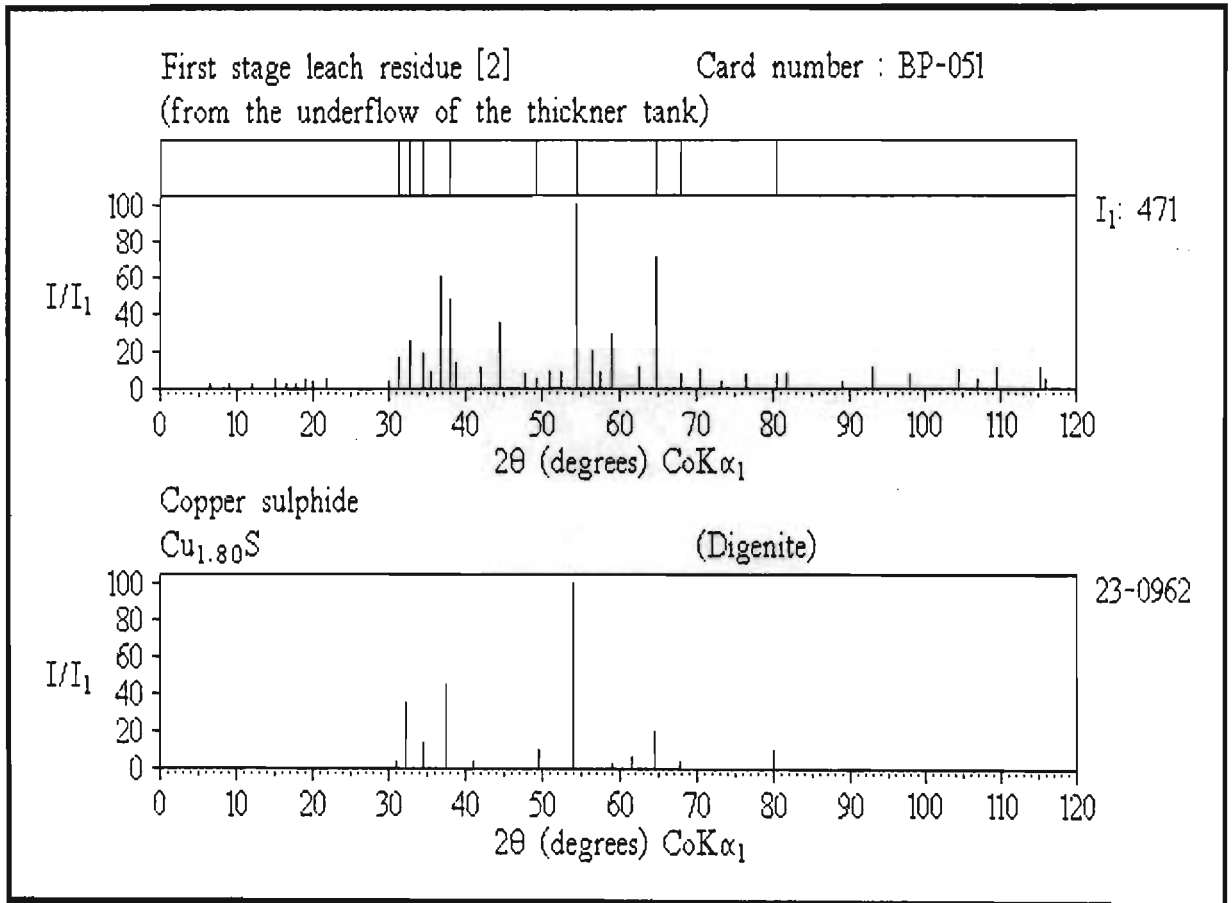| $Cu_{1.8}S$ Reference data [44]			Observed data First stage leach residue		
d(Å)	(I/I₁)	2θ	d(Å)	(I/I₁)	2θ
3.35	(4)	31.0	**3.318**	**(16)**	**31.3**
3.21	(35)	32.4	3.174	(25)	32.7
3.01	(14)	34.6	3.021	(19)	34.4
2.779	(45)	37.6	2.752	(48)	37.9
2.141	(10)	49.4	2.150	(4)	49.2
1.967	(100)	54.1	**1.954**	**(100)**	**54.5**
1.814	(2)	59.1	**1.819**	**(29)**	**58.9**
1.678	(20)	64.4	**1.671**	**(70)**	**64.7**
1.607	(4)	67.6	**1.599**	**(8)**	**68.0**
1.392	(10)	80.0	1.385	(8)	80.4

Figure 4.8-2

The choice of $Cu_{1.8}S$ is supported by the observation that the shift of the maximum intensity peak is that predicted on averaging the reference d-spacing with the reference d-spacing of an overlapping nickel sulphide peak :

Ni_3S_4 1.941 Å   peak intensity = 30

$Cu_{1.8}S$ 1.967 Å   peak intensity = 100

Average :   1.954 Å

Observed :   1.954 Å   overlapped peak

After the assignment of Ni_3S_4 and $Cu_{1.8}S$ peaks only a few very low intensity peaks remained which seemed to indicate the nickel sulphide NiS.   A cyanide leach was therefore carried out to remove most of the Ni_3S_4 and $Cu_{1.8}S$ from the sample.

2.00g of FSLR were placed in a solution of 5.20g KCN in 50.0ml water.   The suspension was heated with stirring at 95°C for 30 minutes, cooled and filtered.   The residue was dried at 100°C for 45 minutes.   The residue mass was 0.16g (8% of the original sample mass).   XPD analysis of this residue indicated that it was predominantely the nickel sulphide NiS. $Cu_{1.8}S$ had been completely removed, although a little Ni_3S_4 remained.

Thus the nickel sulphide **NiS** was confirmed as also being present in first stage leach residues.

Table 4.8-4 compares the reference data for NiS with that observed for the cyanide leach residue

Figure 4.8-3(a) and **(b)** shows the reduced and peak spectra for the cyanide leach residue.

Table 4.8-4   Comparison of NiS reference data with that observed of the NiS in the FSLR cyanide leach residue

NiS Reference data [45]			Observed data Cyanide FSLR leach residue		
d(Å)	(I/I$_1$)	2θ †	d(Å)	(I/I$_1$)	2θ †
4.807	(60)	21.4	4.755	(24)	21.7
2.946	(40)	35.4	2.934	(40)	35.5
2.777	(100)	37.6	2.763	(100)	37.8
2.513	(65)	41.7	2.506	(58)	41.8
2.228	(55)	47.3	2.220	(45)	47.5
1.8631	(95)	57.4	1.858	(96)	57.6
1.8178	(45)	59.0	1.814	(52)	59.1
1.7372	(40)	62.0	1.734	(39)	62.1
1.6340	(18)	66.4	1.633	(12)	66.4
1.6037	(35)	67.8	1.601	(35)	67.9
1.5470	(25)	70.6	1.546	(30)	70.7
1.3884	(8)	80.2	1.387	(10)	80.3
1.3343	(4)	84.2	1.329	(5)	84.6
1.3008	(10)	86.9	1.299	(14)	87.0
1.2560	(8)	90.8	1.254	(16)	91.0
1.2023	(6)	96.1	1.199	(6)	96.5
1.1783	(4)	98.8	1.182	(8)	98.4
1.1447	(6)	102.8	1.143	(8)	103.0
1.1133	(16)	106.9	1.113	(32)	106.9
1.0846	(8)	111.1	1.084	(4)	111.2

† Applicable to radiation of wavelength λ = 1.78894Å (CoKα_1)

A leach performed on FSLR using thiourea and hydrochloric acid (method provided by BARPLATS) was found to remove $Cu_{1.8}S$ almost completely, leaving a residue containing Ni_3S_4 and NiS.   2.00g of FSLR were placed in a solution of 11.00g thiourea in 50.0ml 1M HCl.   The suspension was stirred for 180 minutes at room temperature (22°C), and filtered.   The residue was dried at 100°C for 45 minutes and weighed 0.81g (40.5% of the original sample mass).   It should be noted that this leach can only give an estimate of $Cu_{1.8}S$ present in the sample as the residual Ni_3S_4 can be structurally contaminated with copper [46].

During this leach a silvery-grey highly magnetic metallic powder separated and floated on the meniscus.   An EDAX analysis showed the powder to be about 50% Ni, 13% Cu,
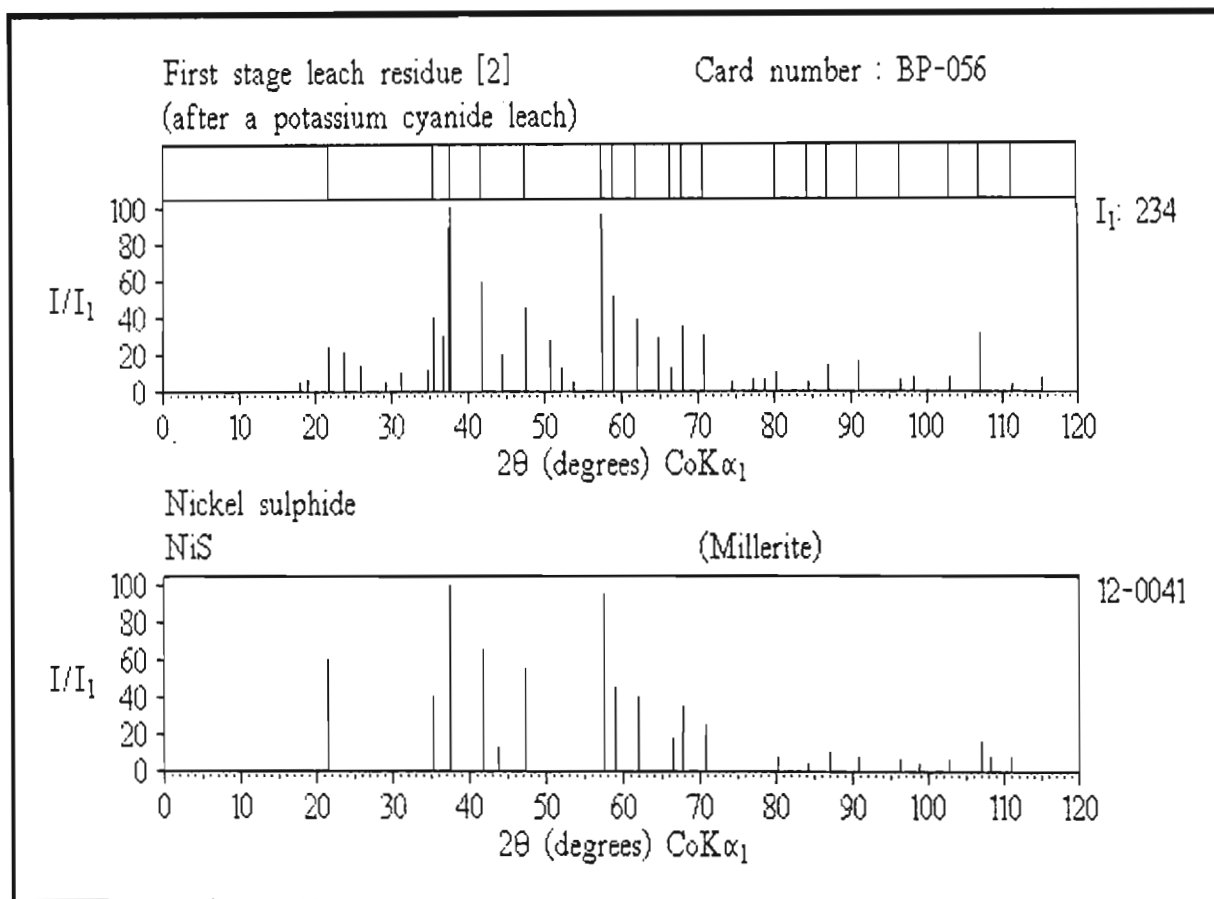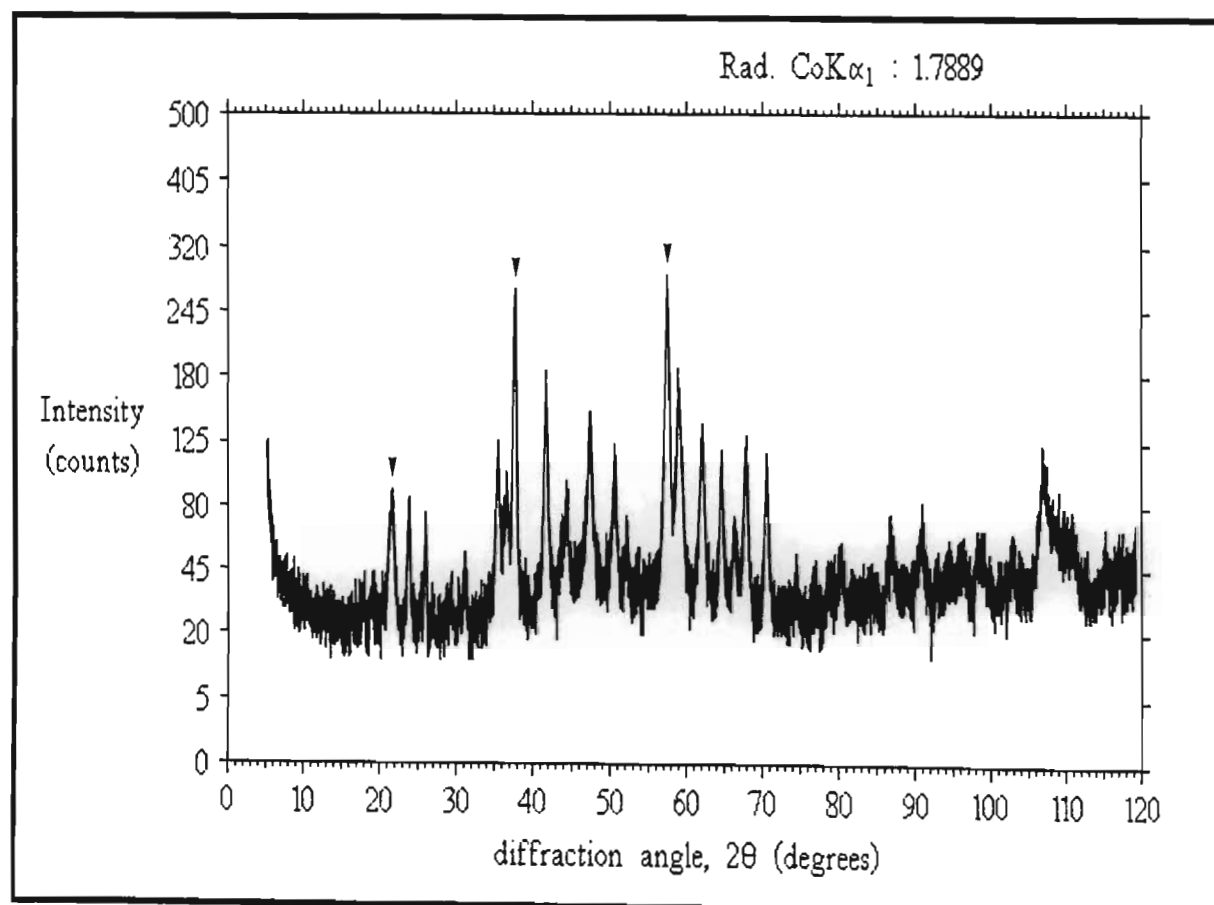
Figure 4.8-3(a)

Figure 4.8-3(b)

13% Fe, 21% Pt, 2% Rh and 1% Pd. Not enough was formed to analyse using XPD. The high platinum, nickel and copper content suggests it might be residual matte alloy. The presence of iron was unusual although both nickel and platinum are known to form alloys with iron [47]. This powder was later confirmed as residual alloy (See **Appendix 2 : Isolation of the alloy phase.**). The high pgm content should be noted. **Figure 4.8-4(a), (b)** and **(c)** show the presence of Ni_3S_4 and NiS in this leach residue.

4.9 FIRST STAGE LEACH RESIDUE PHASES
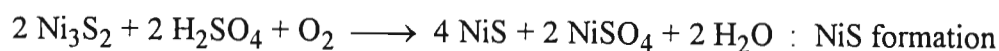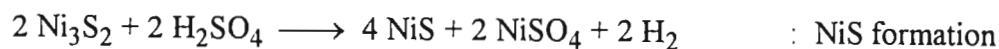
The table below lists the phases detected in the first stage leach residue :

Table 4.9-1   First stage leach residue phases (detectable by XPD)

Phase	Formula	Mineral name	JCPDS Card Number
Nickel sulphide	Ni_3S_4	polydymite	08-0106
Copper sulphide	$Cu_{1.8}S$	digenite	23-0962
Nickel sulphide	NiS	millerite	12-0041
Nickel-copper alloy	$Ni_{4.3}Cu$	-	-

4.9.1 THE NICKEL SULPHIDE PHASES

The identification of the nickel sulphides Ni_3S_4 and NiS showed that the following reactions were taking place in the first stage leach [48] :
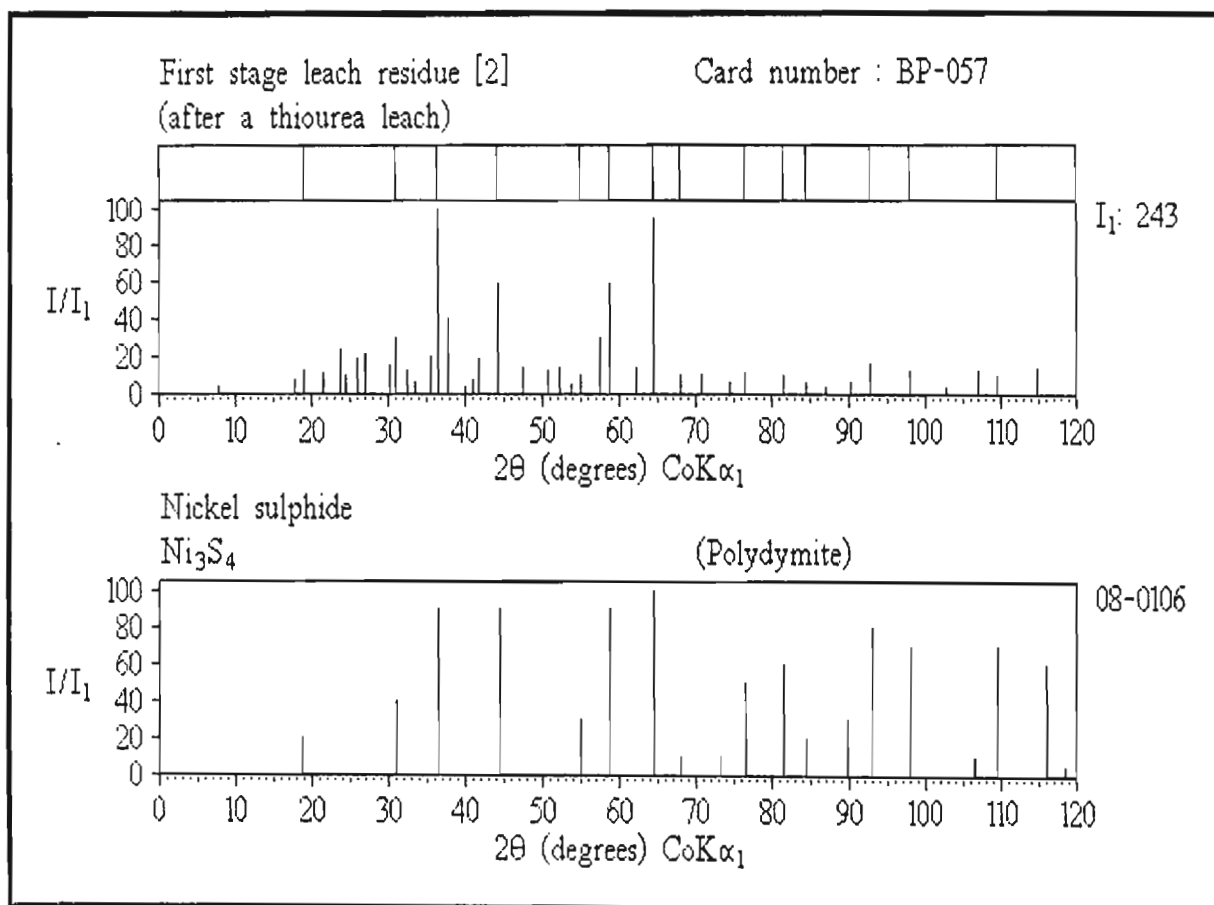
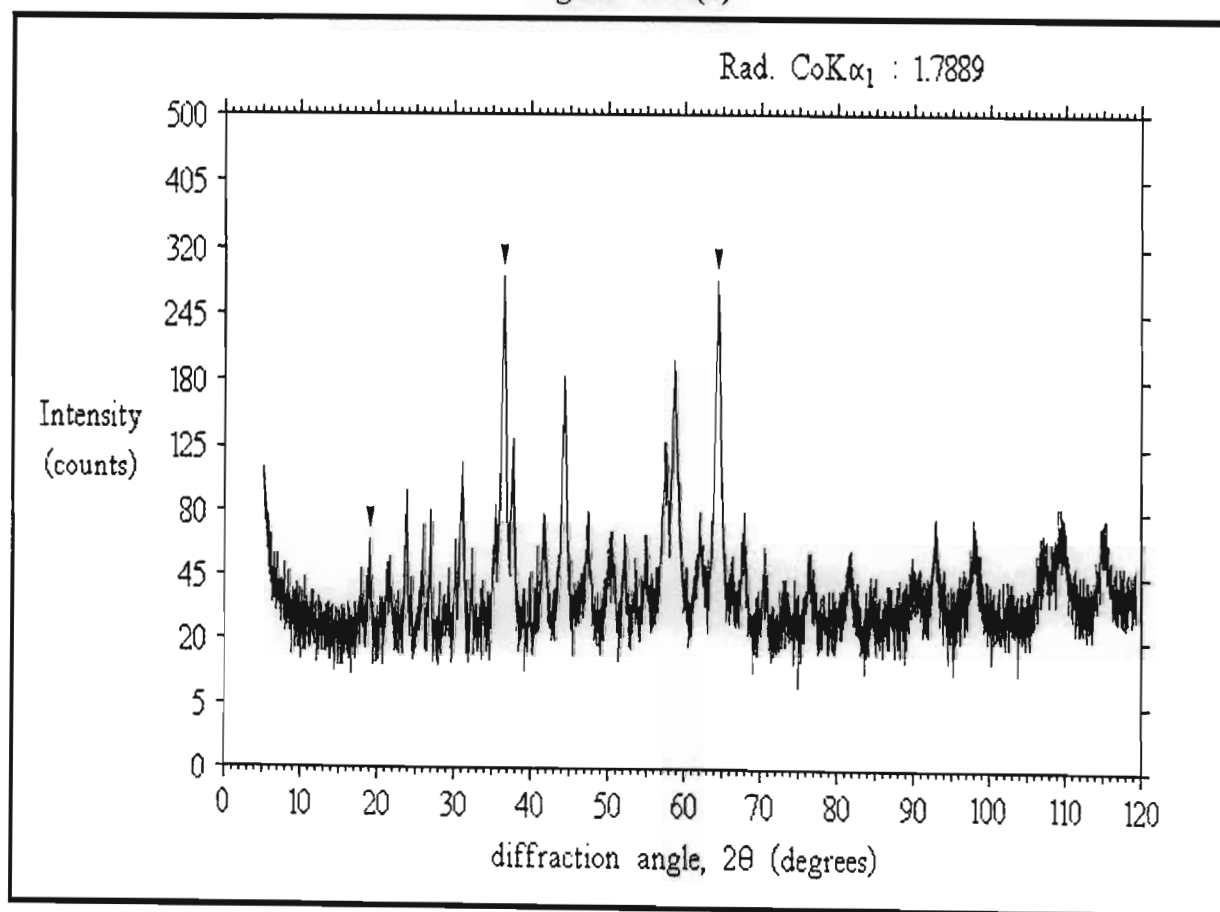$$2\,Ni_3S_2 + 2\,H_2SO_4 \longrightarrow 4\,NiS + 2\,NiSO_4 + 2\,H_2 \qquad : NiS\ formation$$

$$2\,Ni_3S_2 + 2\,H_2SO_4 + O_2 \longrightarrow 4\,NiS + 2\,NiSO_4 + 2\,H_2O : NiS\ formation$$

$$8\,NiS + 2\,H_2SO_4 + O_2 \longrightarrow 2\,Ni_3S_4 + 2\,NiSO_4 + 2\,H_2O : Ni_3S_4\ formation$$

First stage leach residue [2]   Card number : BP-057
(after a thiourea leach)

Nickel sulphide
Ni_3S_4 (Polydymite)

08-0106

Figure 4.8-4(a)

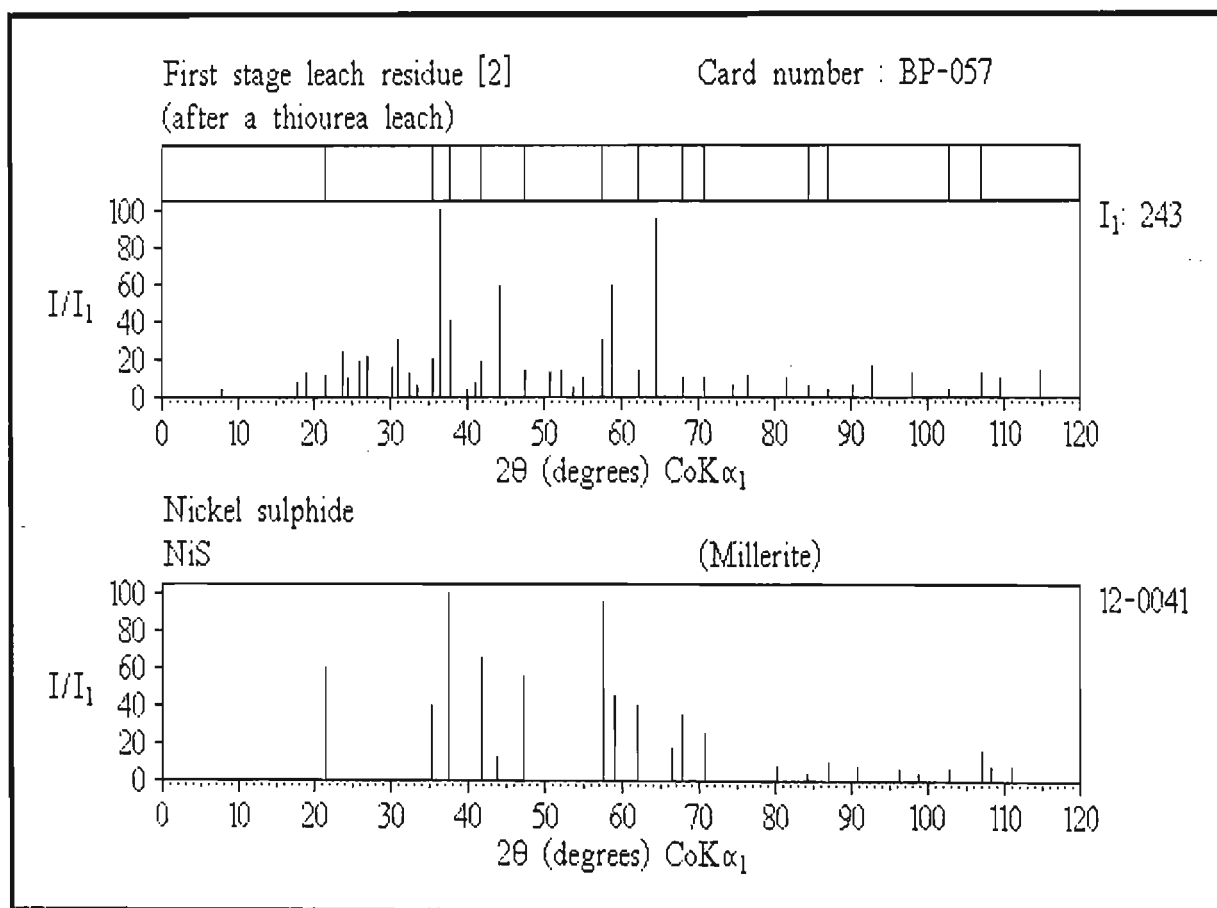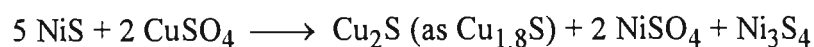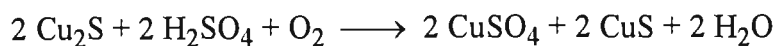Rad. $CoK\alpha_1$: 1.7889
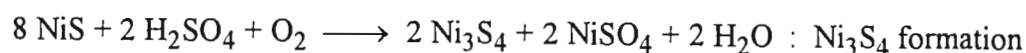
Figure 4.8-4(b)

Figure 4.8-4(c)

4.9.2 THE COPPER SULPHIDE PHASE

The identification of the copper sulphide $Cu_{1.8}S$ suggested that the following reactions were taking place in the first stage leach [49] :

$$2\ Cu_2S + 2\ H_2SO_4 + O_2 \longrightarrow 2\ CuSO_4 + 2\ CuS + 2\ H_2O$$
$$5\ NiS + 2\ CuSO_4 \longrightarrow Cu_2S\ (as\ Cu_{1.8}S) + 2\ NiSO_4 + Ni_3S_4$$

The first reaction was proposed by a researcher at another refinery. Almost no CuS was observed in the first stage leach residue however. This suggested the reaction occurring was rather [50] :

$$10\ Cu_2S + 2\ H_2SO_4 + O_2 \longrightarrow 2\ Cu_9S_5 + 2\ CuSO_4 + 2\ H_2O$$
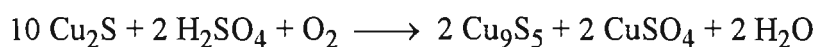
Residual copper phases from the pressure leach present in pgm concentrates are dealt with in the next chapter.

□□□
CHAPTER 5

THE PLATINUM GROUP METAL REFINERY
□□□

5.1 INTRODUCTION

The platinum group metal refinery in essence has to perform three functions. These are :

1) Extraction of the pgms from the base metal refinery concentrates into hydrochloric acid.

2) Separation of the pgms by precipitation, solvent extraction and other methods.

3) Purification of the separated species prior to reduction to the metals.

This chapter focuses on the first of these operations. In many ways it is the most challenging of the three, having to contend with a feedstock of highly variable composition containing over 30 elements.

Numerous process samples, provided by WESTERN PLATINUM REFINERY and BARPLATS REFINERY, have thus been investigated with the aim of gaining a better understanding of problems being encountered in the extraction of the pgms into hydrochloric acid. It should be appreciated that this has taken the form of a qualitative speciation study, and in many instances the exact details of certain processes are not given under the constraints of the confidentiality that exists in this industry.

5.2 OVERVIEW OF PGM REFINERY OPERATIONS (1)

Whereas the base metal refinery depends entirely on the ore concentrate provided by the mine, known as matte, the platinum group metal refinery depends entirely on the pgm concentrates provided by the base metal refinery. The purpose of this section is to give a broad overview of the various operations taking place at the pgm refinery.

5.2.1 PGM CONCENTRATES

The base metal refinery produces and supplies two different concentrates to the pgm refinery. The origin of each was described in § 4.3.3 and § 4.3.4, and appears in **Figure 4.3-1**. Normal concentrates are essentially the insoluble residue from the copper circuit, while the minor so called "selenium concentrates" derive from the selenium circuit. These minor concentrates may be treated and supplied separately, blended into a mixed concentrate, or re-introduced to the BMR circuit. The percentage of precious metals present in normal concentrates is highly variable, ranging anywhere from 40 to 66%. The pgm grade relative to the total precious metal content (pgms + Au + Ag) is usually between 49.5 and 56.3%. Normally very little osmium is present (0.6 - 2.7% relative to the total pgm content). This is a feature of Merensky and UG-2 pgm concentrates, although the UG-2 reef tends to yield concentrates with slightly higher levels of osmium.

5.2.2 CONCENTRATE PRE-TREATMENT

Before undergoing the oxidative leach to extract the pgms, it is usually of benefit to subject concentrates to a number of pre-treatment steps aimed at the removal of unwanted impurities and further enrichment of the feedstock. Typical pre-treatment steps are :

1) An acid leach to remove iron and nickel

2) A sulphidising process to increase pgm solubility

3) A polysulphide leach to remove most of the metalloids

4) A roast to upgrade the residue

5.2.3 THE HCl/Cl₂ OXIDATIVE LEACH

After pre-treatment, the concentrate is leached using 6M hydrochloric acid and chlorine gas at elevated temperatures. Oxidation leads to the dissolution of almost all the platinum, palladium, rhodium and iridium, which pass into solution as the chloro- species $[PtCl_6]^{2-}$, $[PdCl_4]^{2-}$, $[RhCl_6]^{3-}$, and $[IrCl_6]^{2-}$. Gold dissolves similarily forming tetrachloroaurate(III), $[AuCl_4]^-$. A fair amount of ruthenium and osmium also dissolve (forming $[RuCl_6]^{2-}$, $[OsCl_6]^{2-}$).

5.2.4 REMOVAL OF HYDROUS OXIDES

The pH of the filtrate is adjusted to initiate hydrolysis reactions that precipitate most of the antimony, bismuth, tellurium, silver and lead as their hydrous oxides. These are filtered off.

5.2.5 GOLD EXTRACTION

The pH of the solution is further adjusted, and a reductant added to reduce $[AuCl_4]^-$ to metallic gold. The reduction leads initially to a fine colloidal suspension, which can be made to agglomerate by boiling, into gold sponge, known as 'brown gold'. The impure sponge is filtered off and purified.

One purification method involves redissolving the sponge in aqua-regia (HCl/HNO₃) or HCl/Cl₂ at 60°C thereby forming soluble $[AuCl_4]^-$ once more. This solution is diluted and sodium sulphate added. In this way silver is removed as the chloride and lead as the sulphate. A second reduction yields a sponge with very low levels of silver, palladium and copper. Leaching this sponge with nitric acid removes these impurities almost entirely and after ignition at 900°C, pure gold of 99.9% purity is obtained.

5.2.6 RUTHENIUM EXTRACTION

Ruthenium is next extracted by adding sodium chlorate to the filtrate and boiling. In this way $[RuCl_6]^{2-}$ is oxidized to ruthenium tetroxide gas, RuO_4. (A small amount of OsO_4 also forms.) The gaseous oxide is distilled out and collected into carbon tetrachloride (CCl_4), from which it is extracted back into hydrochloric acid. Thermal reduction follows, to ensure that all soluble ruthenium is present as $[RuCl_6]^{3-}$ which is solvent extracted using triethylphosphate in an organic solvent. After purification of the solvent by washing, ruthenium can be extracted back into hydrochloric acid and precipitated as the ammonium salt, $(NH_4)_3[RuCl_6]$, by boiling with ammonium chloride. Ignition of this salt at 1000°C under hydrogen produces pure ruthenium powder.

5.2.7 PLATINUM EXTRACTION

After the oxidation step to remove ruthenium, all the platinum is present as $[PtCl_6]^{2-}$. Platinum can now be precipitated as the ammonium salt, $(NH_4)_2[PtCl_6]$, by adjusting the pH to 5 and adding ammonium chloride as a saturated solution. The salt is filtered off and after washing and drying, ignited in air at 1000°C to give impure Pt sponge.

This sponge can be purified by redissolving in HCl (using Cl_2 as the oxidant) and adjusting the pH by adding aqueous ammonia. Hydrolysis leads to the precipitation of most impurities (Ru, Ir, Rh and Fe) as the hydrous oxides. Controlled reduction of Pt^{IV} to Pt^0 yields the pure metal which can be melted and cast into ingots.
(Numerous other methods exist.)

5.2.8 PALLADIUM EXTRACTION

The platinum-free filtrate is now adjusted to pH 5-6 by the addition of aqueous ammonia and the temperature reduced to 60°C. Slow addition of hydrochloric acid to this solution results in the precipitation of the impure neutral complex $Pd(NH_3)_2Cl_2$ (almost entirely the *trans-* isomer, formed as a result of the *trans effect*).

The precipitate is purified by redissolving in aqueous ammonia of pH 10 at 80°C. At this high pH, all the base metals precipitate as their hydroxides and can be filtered off. Pure $Pd(NH_3)_2Cl_2$ is reprecipitated by the addition of hydrochloric acid and filtered off, washed and dried. Ignition under hydrogen at 1000°C produces palladium sponge of 99.99% purity.

Very successful solvent extraction methods are currently replacing this method.

5.2.9 IRIDIUM EXTRACTION

The filtrate now contains iridium and rhodium which are separated by the addition of ammonium chloride solution and refluxing for 1 hour. On cooling the solution, the impure salt $(NH_4)_2[IrCl_6]$ precipitates. After pufication by precipitation methods, ignition of this salt in hydrogen at 1000°C yields pure iridium sponge.

5.2.10 RHODIUM EXTRACTION

The filtrate from the iridium extraction step still contains numerous impurities such as copper, nickel, iron, lead and silver. After these have been removed, the solution contains rhodium present as the hexachloro- anion $[RhCl_6]^{3-}$. By adding a small amount of ammonium chloride and boiling down to a slurry to remove most of the acid, followed by the addition of further ammonium chloride and cooling to room temperature, the salt $(NH_4)_3[RhCl_6]$ can be precipitated.

Purification of this salt involves redissolving in aqueous ammonia of pH 10 at room temperature. After several hours, the slurry is boiled. Lowering the pH to 5 by the addition of hydrochloric acid at 90°C and then cooling causes the complex salt $[Rh(NH_3)_5Cl]Cl_2$ to precipitate. This is further purified by leaching and after washing and drying is ignited at 1000°C under hydrogen to produce pure rhodium powder.

5.2.11 RESOLUBILISATION

Using a number of different processes, most of the highly inert insolubles from the oxidative leach can be converted to pgm species which are acid soluble.

5.2.12 LEAD FUSION

During the separation process, numerous waste residues, dust, and precipitates containing low but significant levels of the pgms are produced. A large bulk of precipitate containing ruthenium, palladium and some platinum is produced in the purification of ammonium hexachloroplatinate(IV) for example. All such residues, together with metals precipitated with zinc or magnesium from dilute waste solutions are dried and mixed with lead carbonate and smelted in an arc furnace. The carbonate is decomposed and reduced to molten lead which acts as a collector of the pgms. Other elements form an oxide slag. After cooling, the lead ingots are dissolved in nitric acid. Metallic lead dissolves as soluble lead nitrate leaving behind an extremely fine pgm sludge that can be returned to the oxidative leach step.

5.3 CONCENTRATE PROBLEMS

5.3.1 COMPOSITION OF CONCENTRATES

The pgm concentrations of concentrates can vary widely, although the order of abundance is generally constant (see below).

> Normal concentrates : Pt > Pd > Ru > Rh > Ir > Os
>
> Minor concentrates : Ru > Rh > Pt > Pd > Ir > Os

An elemental analysis of a South African normal concentrate reveals the presence of over 30 elements. This gives an indication of the difficulty in analysing concentrates by XPD, because these elements can be present as binary or ternary alloys, oxides, and a whole series of complex mixed chalcogenides.

5.3.2 SINTERING OF THE PGM RESIDUE IN NORMAL CONCENTRATES

The nickel-copper alloy containing the bulk of the pgms dissolves easily during the first and second stage leaches in the base metal refinery. This leaves a fine residue of metallic pgms of low crystallinity. If the concentrate is dried too harshly at the base metal refinery, sintering between the fine pgm particles can occur. This effect is accompanied by an observable rise in the crystallinity of the sample (indicated by an increase in the counts registered for the maximum intensity peak, given the symbol I_1). Sintering is undesirable as it leads to a concentrate which dissolves much more slowly and erratically in the oxidative HCl/Cl_2 leach. As will be shown later, this can lead to a drop in the solubilities of some pgms.

A series of concentrate drying experiments were conducted in which it was found that sintering of the pgms can be substantially reduced by moistening the concentrate with sulphuric acid (20g/l) prior to drying.

Five concentrates were dried at the temperatures 160°C and 260°C, in each case with and without moistening with sulphuric acid, and also at 110°C without sulphuric acid. XPD scans of each were then run and the counts for the strongest pgm residue peak at a d-spacing of about 2.25Å measured (this peak originates from the **(111)** planes of the cubic pgms Pt, Pd, Rh and Ir). The results are listed in **Table 5.3.2-1**.

The sintering of the pgm residue for concentrate [3] under normal drying conditions is shown in **Figures 5.3.2-1(a)** and **(b)**, **5.3.2-2 (a)** and **(b)** and **5.3.2-3 (a)** and **(b)** (the **(111)** pgm residue peak occurs at about $2\theta = 47°$). The copper sulphide CuS, which was present in this concentrate and is not affected by normal drying, has been used as a reference peak in these figures (arrowed).
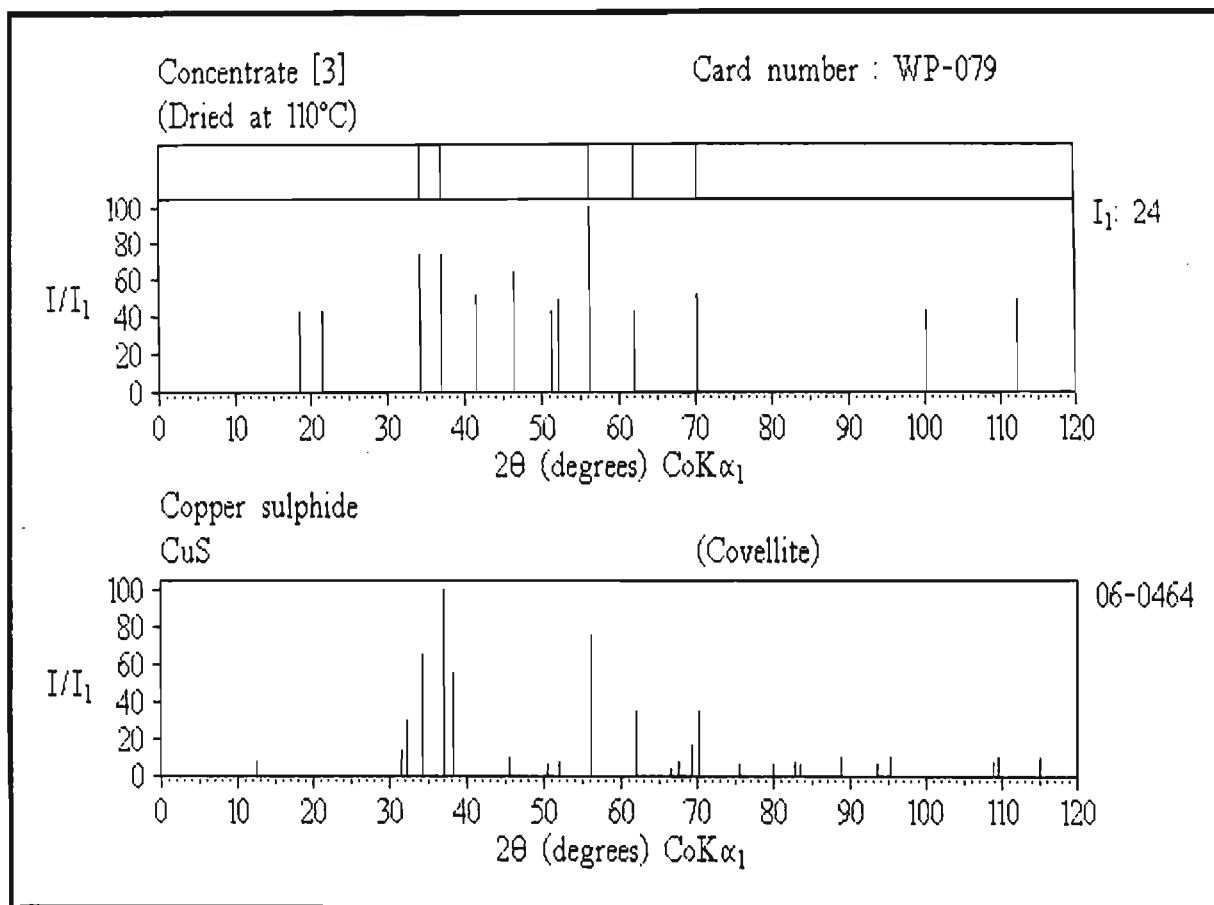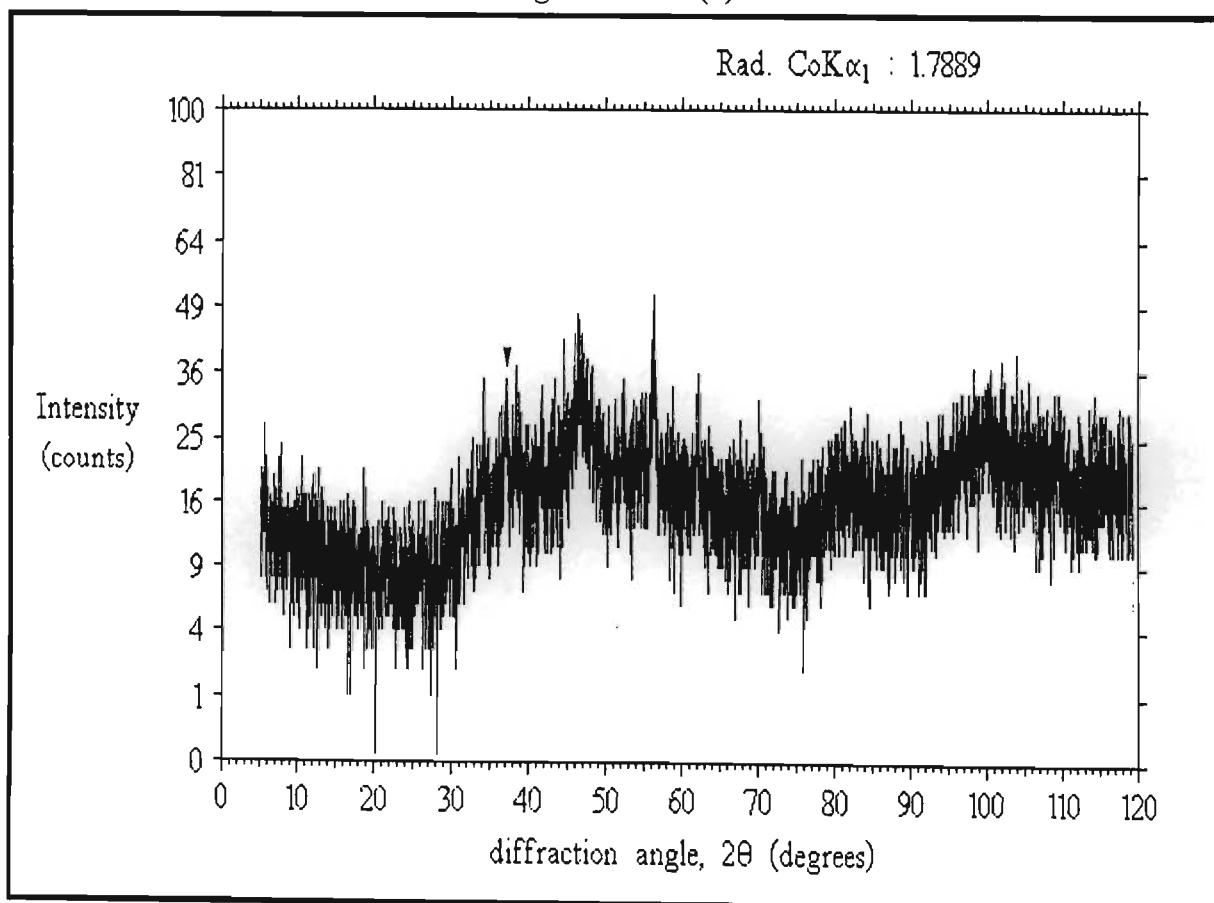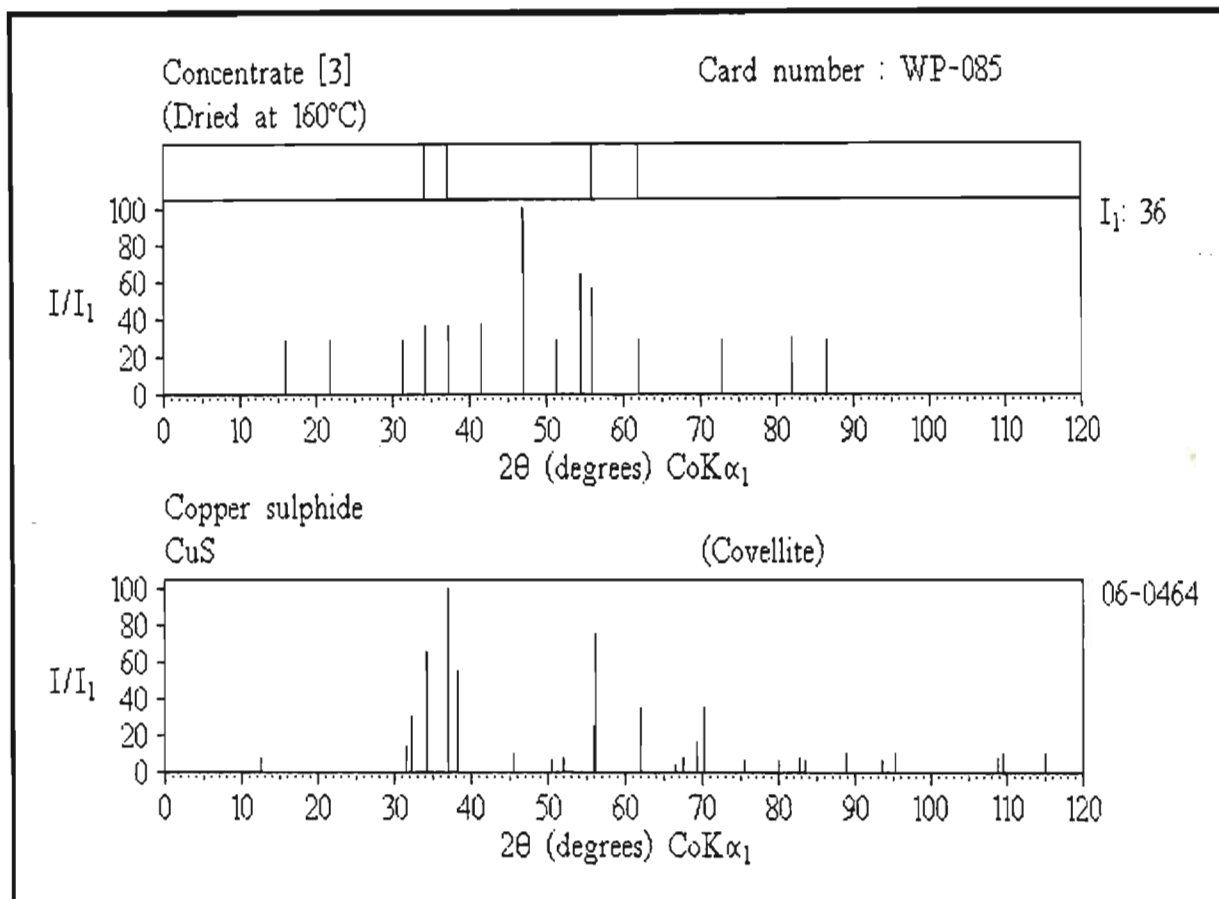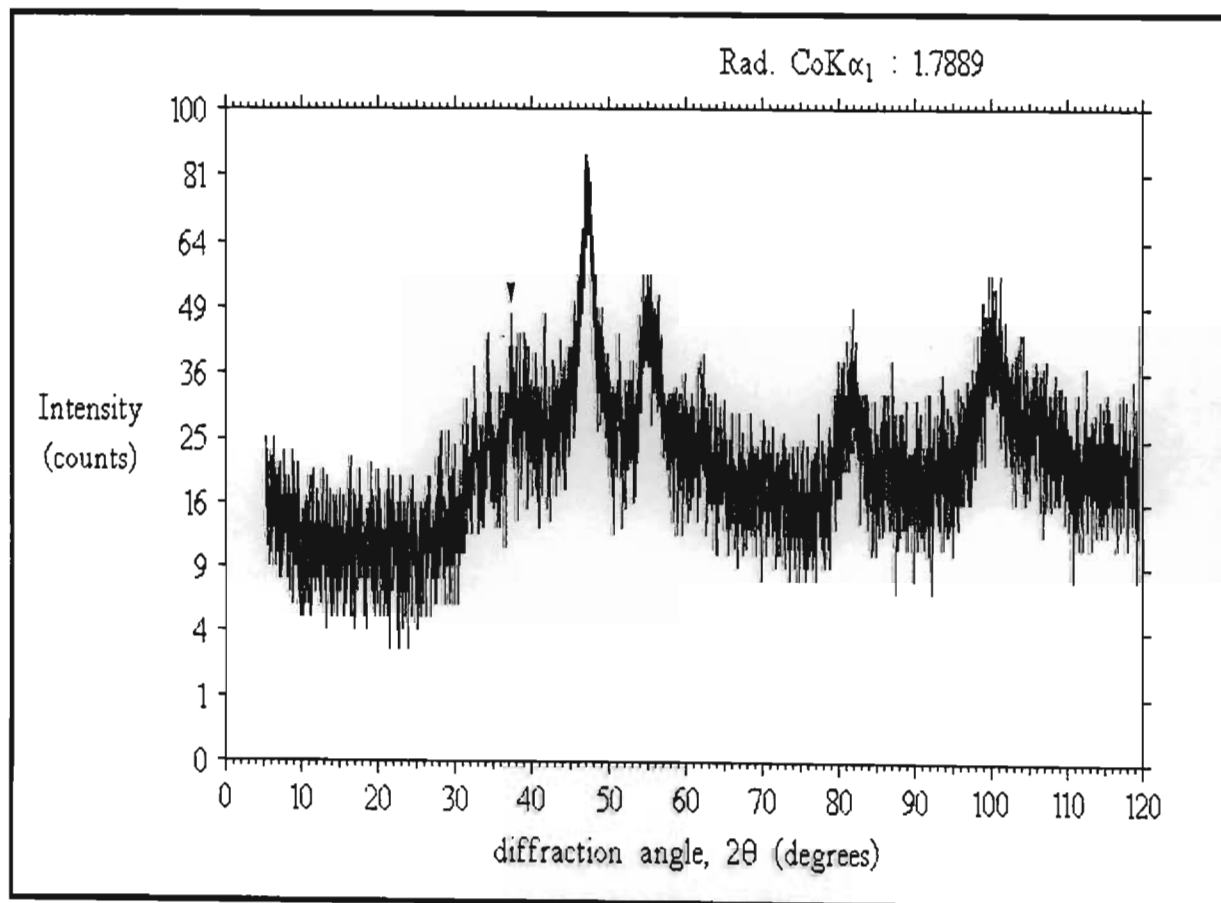
Figure 5.3.2-1(a)

Figure 5.3.2-1(b)

Figure 5.3.2-2(a)

Figure 5.3.2-2(b)

Concentrate [3]
(Dried at 260°C)

Card number : WP-097

I_1: 121

Copper sulphide
CuS   (Covellite)
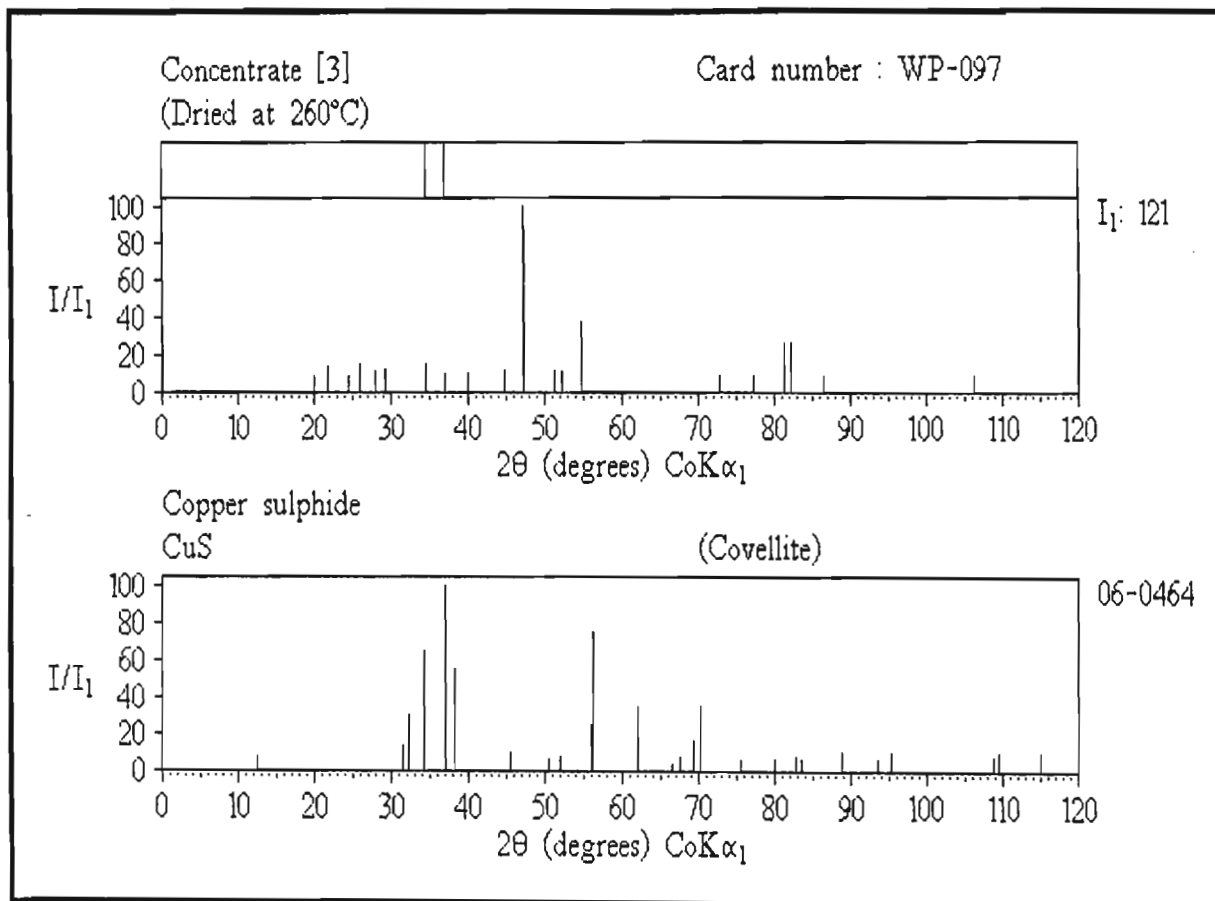
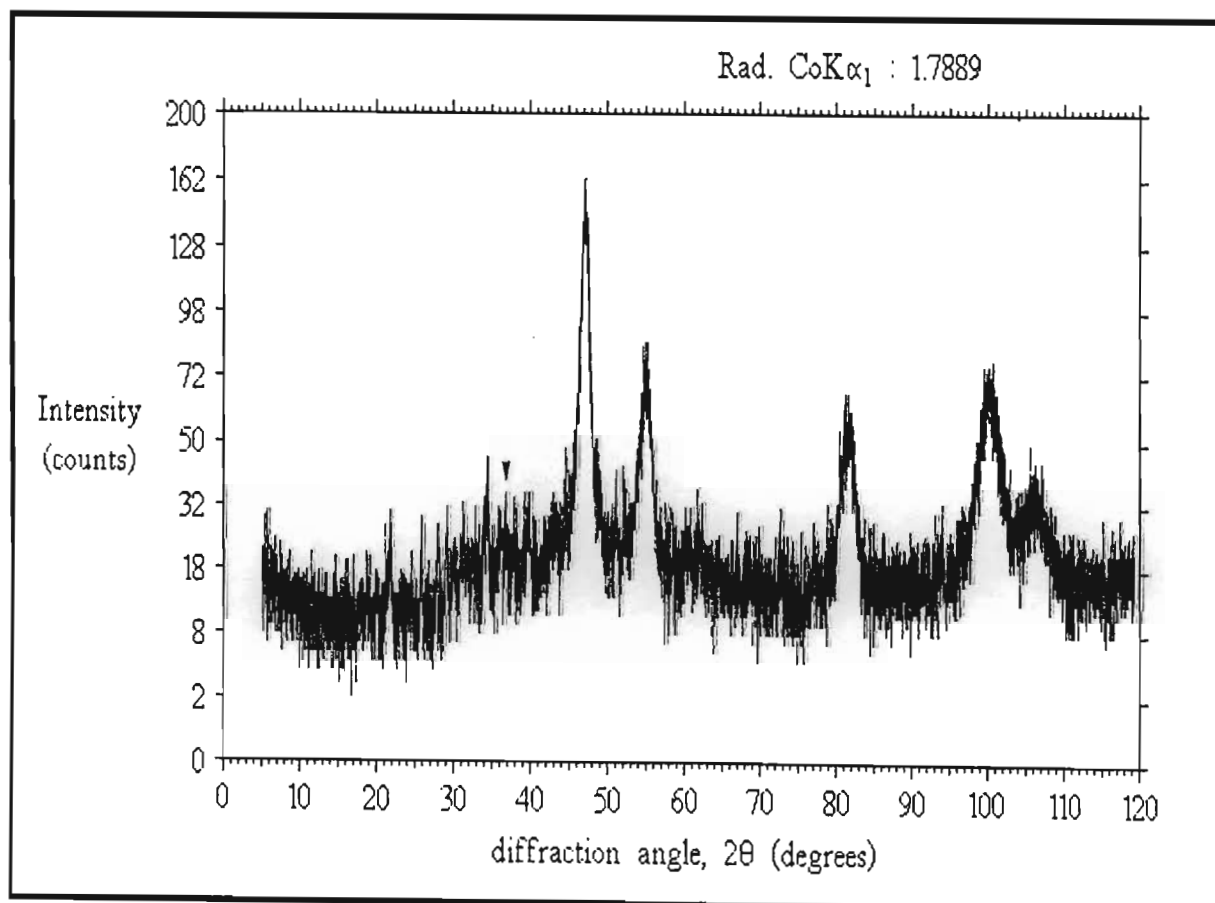06-0464

Figure 5.3.2-3(a)

Rad. CoKα₁ : 1.7889

Figure 5.3.2-3(b)

Table 5.3.2-1 Reduction of pgm sintering using H_2SO_4

Drying temperature	Counts measured for the (111) pgm residue peak				
	[2]	[3]	[4]	[5]	[6]
110°C	44	15	15	- †	25
160°C	66	36	30	10	46
160°C (+ H_2SO_4)	38	18	10	- †	19
260°C	225	121	56	20	72
260°C (+ H_2SO_4)	108	67	27	17	40

† Very low intensity - counts above background counts could not be measured

Table 5.3.2-1 shows that in each case the sintering effect is reduced by the addition of sulphuric acid. Two scans from concentrate [6] dried at 260°C with and without sulphuric acid are shown in **Figure 5.3.2-4(a)** and **(b)** and **Figure 5.3.2-5(a)** and **(b)**. Notice the measured values of I_1 corresponding to the **(111)** peak.

The detrimental effects of overdrying concentrates are dealt with in later sections.

5.4 BASE METAL PROBLEMS

The three most important base metals occurring in pgm extraction are iron, nickel and copper. Together they account for about 7% of the mass of normal concentrates and 4% of minor concentrates. If they are not carefully removed from the process, they can pose serious impurity problems. This removal is however critically reliant on a knowledge of what compounds are involved. The following three sections examine the various iron, nickel and copper compounds identifed in process samples supplied by the refinery.
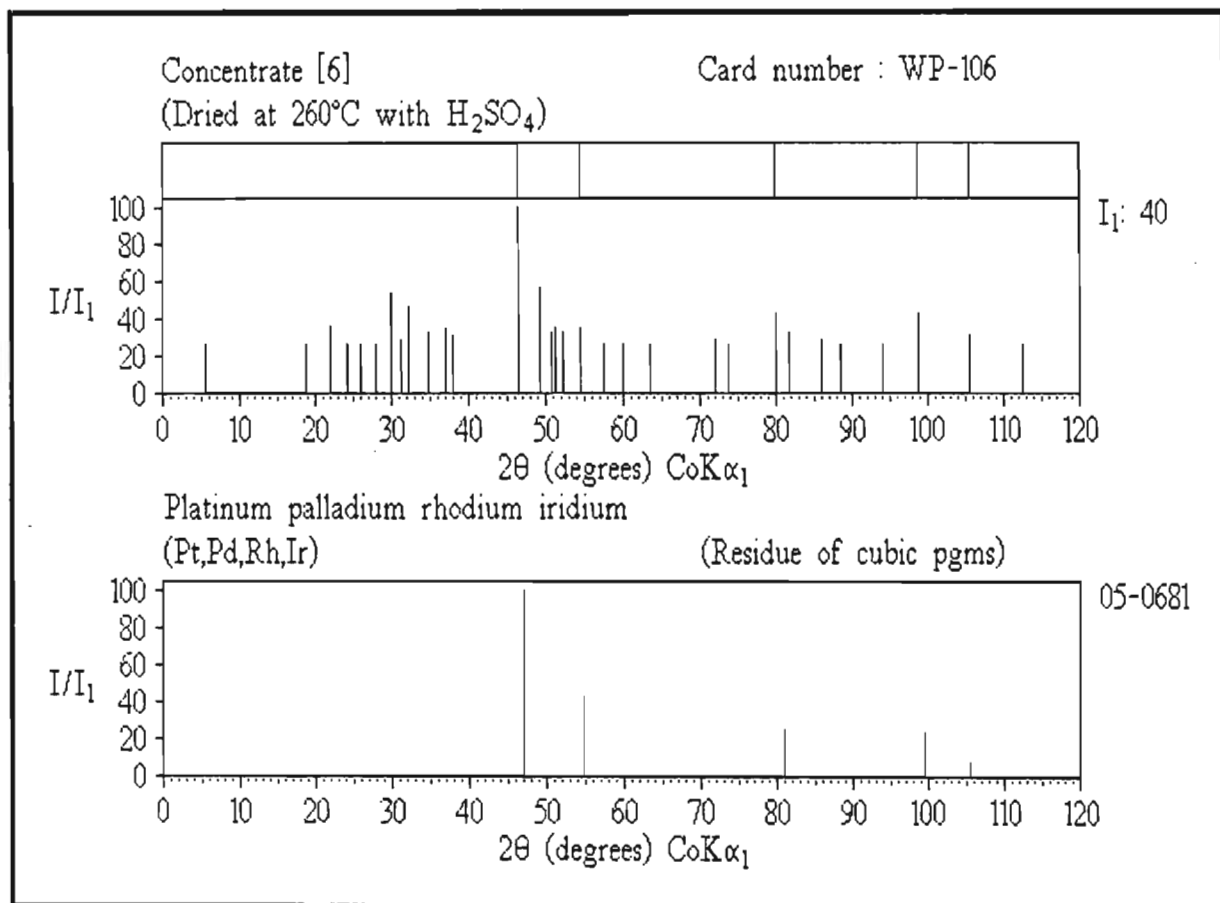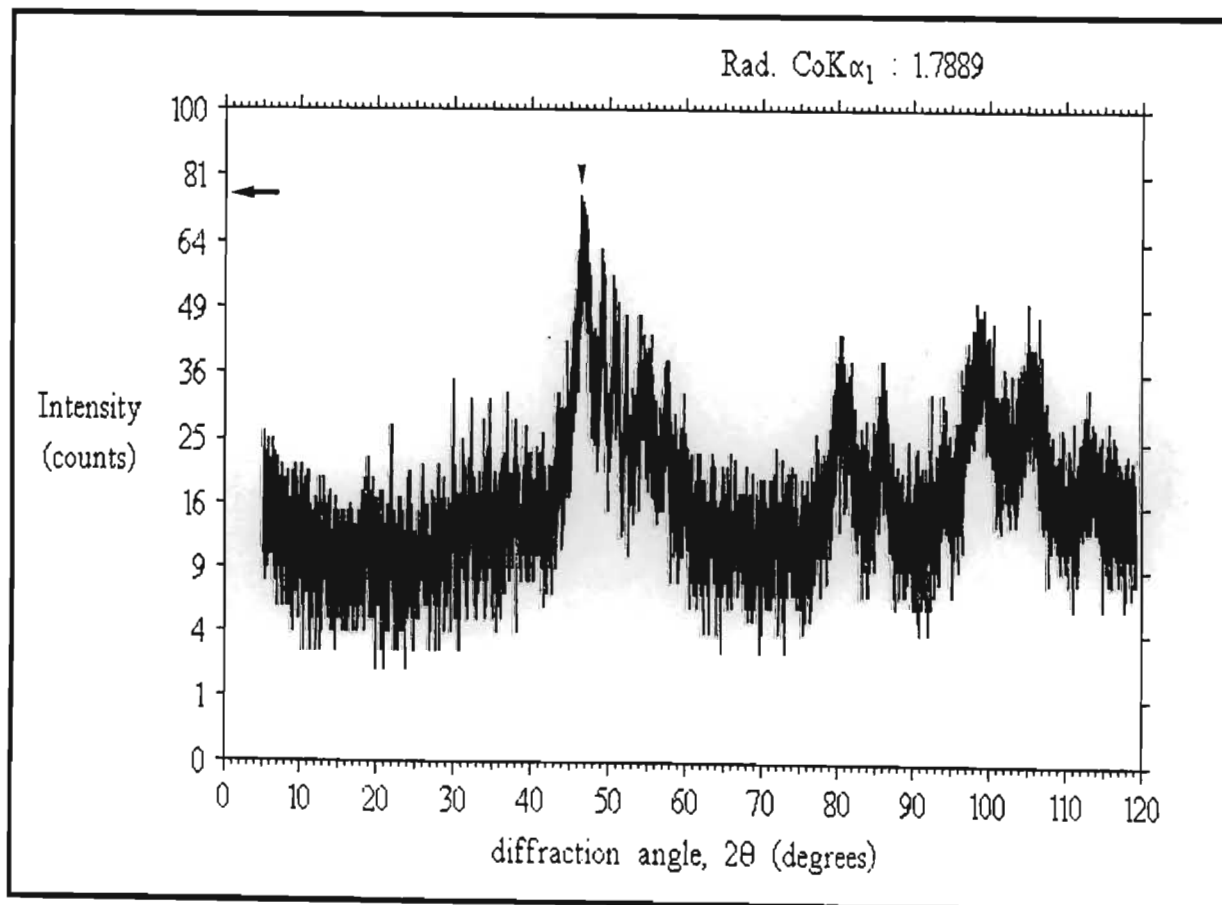
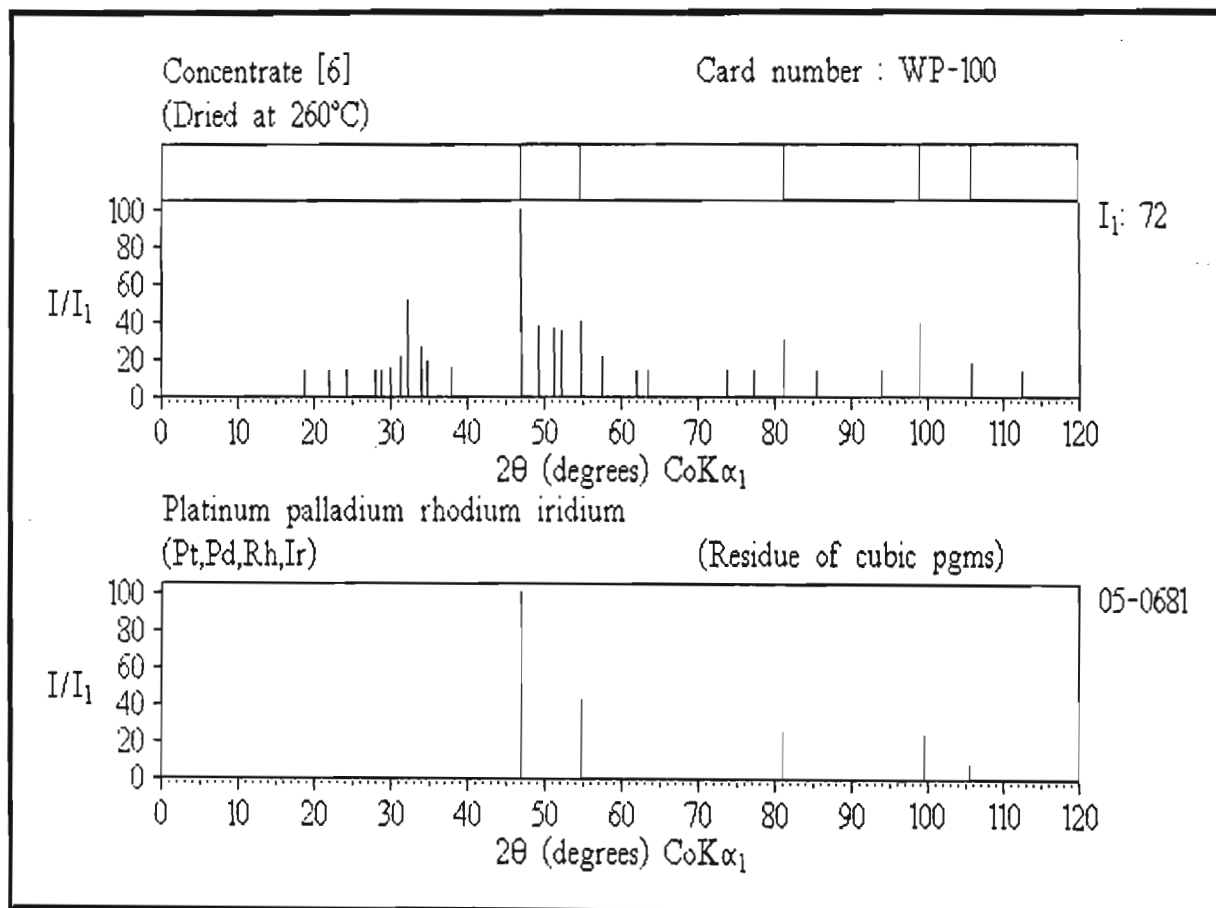**Figure 5.3.2-4(a)**

Figure 5.3.2-4(b)

Concentrate [6]   Card number : WP-100
(Dried at 260°C)

I/I_1

100
80
60
40
20
0

I_1: 72

0   10   20   30   40   50   60   70   80   90   100   110   120
2θ (degrees) CoKα₁

Platinum palladium rhodium iridium
(Pt,Pd,Rh,Ir)   (Residue of cubic pgms)

I/I_1

100
80
60
40
20
0

05-0681

0   10   20   30   40   50   60   70   80   90   100   110   120
2θ (degrees) CoKα₁

Figure 5.3.2-5(a)

Rad. CoKα₁ : 1.7889

200

162

128

98

72

Intensity
(counts)

50

32

18

8

2

0

0   10   20   30   40   50   60   70   80   90   100   110   120
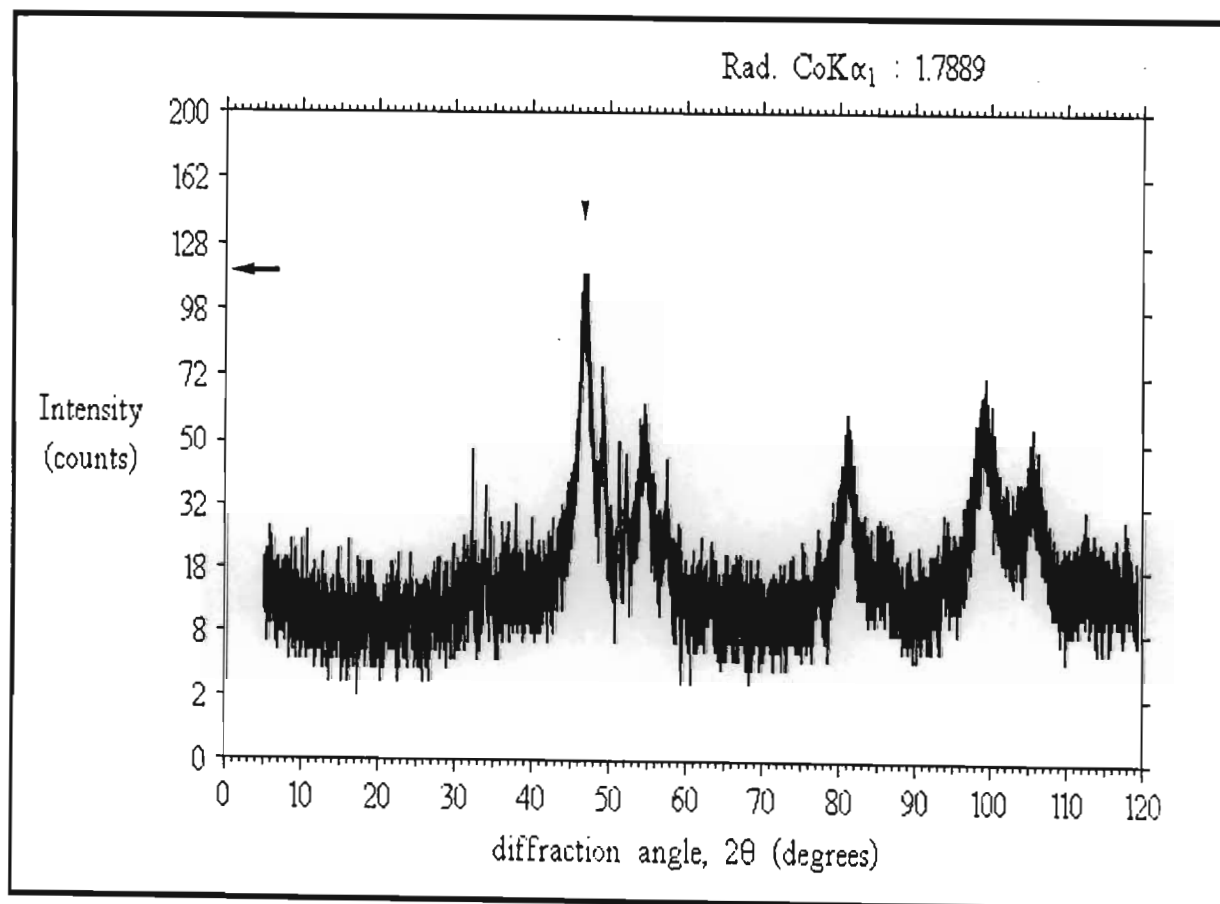diffraction angle, 2θ (degrees)

Figure 5.3.2-5(b)

5.4.1 THE IRON PROBLEM

In the previous chapter (§ 4.4), it was established that the main iron compound occurring in the base metal refinery was the oxide Fe_3O_4. It was also mentioned that reactions with nickel oxide, NiO, can result in the formation of nickel iron oxide, $NiFe_2O_4$, by replacement of Fe^{2+} with Ni^{2+} in the inverse spinel structure - $M^{3+}(M^{2+}M^{3+})O_4$. Furthermore both these oxides are mutually soluble and crystallographically almost identical. This oxide solid solution solubilizes with difficulty, even in the second stage pressure leach. Consequently these oxides would be expected in pgm refinery samples. Chemically their dissolution is not favoured by the highly oxidative (HCl/Cl_2) leach used for pgm dissolution. Therefore the presence of these oxides in oxidative leach residues would be expected. It was however observed that in all cases the diffraction peaks corresponded very closely to the oxide **$NiFe_2O_4$** rather than Fe_3O_4, as **Table 5.4.1-1** shows (values in boldface indicates overlap with another phase).

Table 5.4.1-1   Comparison of $NiFe_2O_4$ reference data with peaks observed for two HCl/Cl_2 leach residues

$NiFe_2O_4$ Reference data [2]			HCl/Cl_2 residue 1 [WP-001] Observed data			HCl/Cl_2 residue 2 [BP-027] Observed data		
d(Å)	(I/I₁)	2θ †	d(Å)	(I/I₁)	2θ †	d(Å)	(I/I₁)	2θ †
4.82	(20)	21.4	-	-	-	4.813	(8)	21.4
2.948	(30)	35.3	2.944	(45)	35.3	2.950	(12)	35.3
2.513	(100)	41.7	2.514	(100)	41.7	2.515	(100)	41.7
2.408	(8)	43.6	**2.413**	**(-)**	**43.5**	-	-	-
2.085	(25)	50.8	**2.092**	**(-)**	**50.6**	2.086	(12)	50.8
1.6051	(30)	67.7	1.601	(50)	67.9	1.605	(30)	67.7
1.4760	(40)	74.6	**1.476**	**(-)**	**74.6**	1.475	(39)	74.6
1.2706	(10)	89.5	1.274	(20)	89.2	1.272	(11)	89.3
1.2573	(4)	90.7	**1.257**	**(-)**	**90.8**	1.256	(20)	90.9
1.2036	(6)	96.0	**1.208**	**(-)**	**95.5**	1.200	(22)	96.4
1.0857	(16)	110.9	1.082	(25)	111.6	1.086	(11)	110.9
1.0424	(6)	118.2	**1.044**	**(-)**	**117.9**	1.043	(14)	118.1

† All 2θ data in this and all following tables is applicable for radiation of wavelength
$\lambda = 1.78894Å$ (CoKα₁)

(Scans for samples WP-001 and BP-027 appear in § 5.4.2.)

An XPD analysis showing traces of $NiFe_2O_4$ in oxidative leach residues immediately indicates that the pre-treatment leach to remove iron has only partially succeeded and should be revised.

In most cases iron in solution is precipitated as hydrated oxide by appropriate control of pH. Hydrated oxides are normally of such low crystallinity that they are not identifiable using XPD. In one sample however (originating from a solution where the iron had been precipitated from solution by pH control and prolonged boiling) a hydrated oxide of iron was detected and identified as being **β-FeOOH**. **Table 5.4.1-2** compares the reference data for this compound with that observed for this sample.

Table 5.4.1-2 Comparison of β-FeOOH reference data with peaks observed for an iron-rich precipitate

β-FeOOH Reference data [3]			pH 3 Cake [2] (WP-025-A) Observed data		
d(Å)	(I/I$_1$)	2θ	d(Å)	(I/I$_1$)	2θ
7.40	(100)	13.9	7.262	(38)	14.1
5.25	(40)	19.6	5.215	(33)	19.8
3.311	(100)	31.3	3.321	(89)	31.2
2.616	(40)	40.0	2.618	(36)	40.0
2.543	(80)	41.2	2.528	(100)	41.4
2.285	(40)	46.1	2.278	(56)	46.2
1.944	(60)	54.8	1.942	(42)	54.9
1.746	(40)	61.6	1.748	(35)	61.5
1.635	(100)	66.3	1.636	(75)	66.3
1.515	(40)	72.4	1.507	(44)	72.8
1.497	(20)	73.4	1.501	(35)	73.2
1.438	(80)	76.9	1.441	(50)	76.8
1.374	(40)	81.2	1.378	(31)	81.0

Figure 5.4.1-1(a) shows the reduced pattern for the sample matched with that for the reference compound. The peaks as observed are shown in the sample scan (**Figure 5.4.1-1(b)**). Only three good diagnostic lines have been arrowed. Note the low crystallinity of the sample, and that no other lines due to other phases are observed.
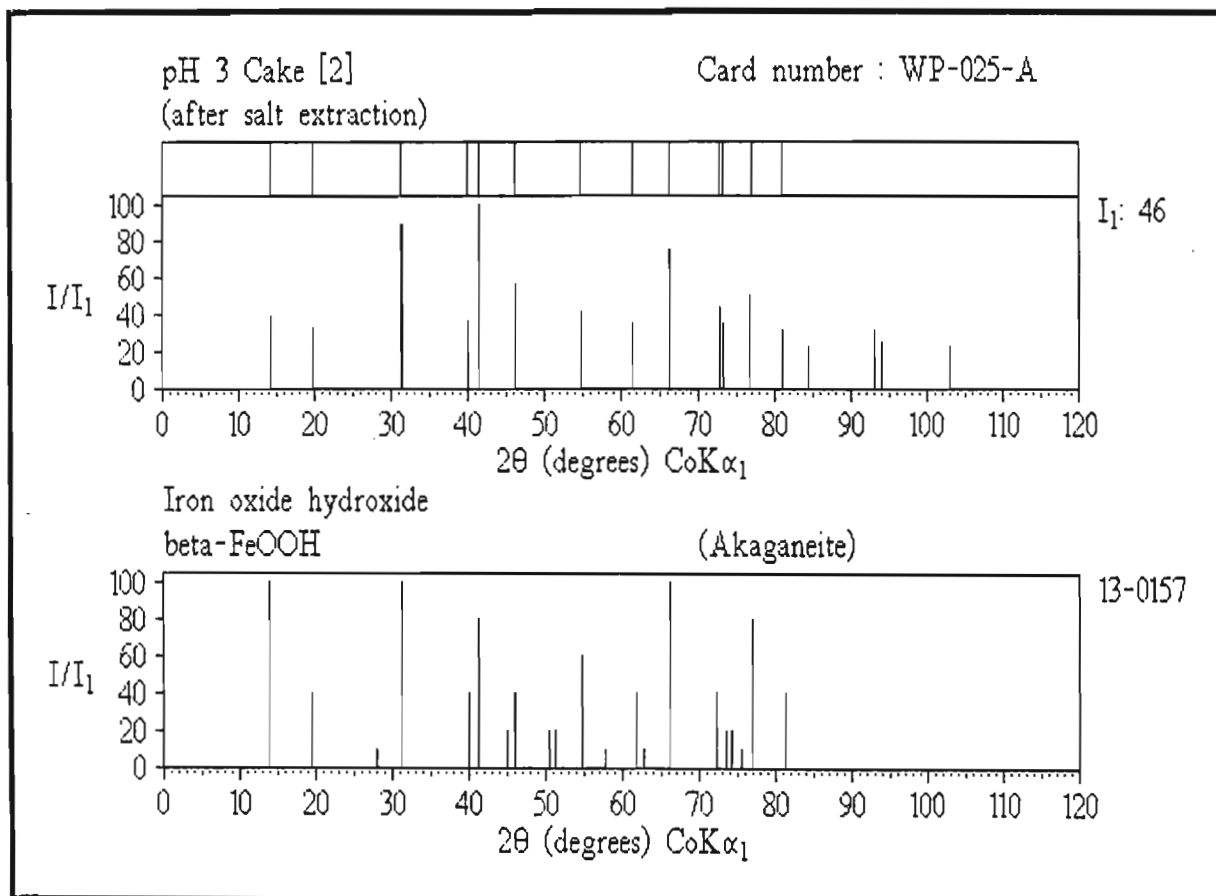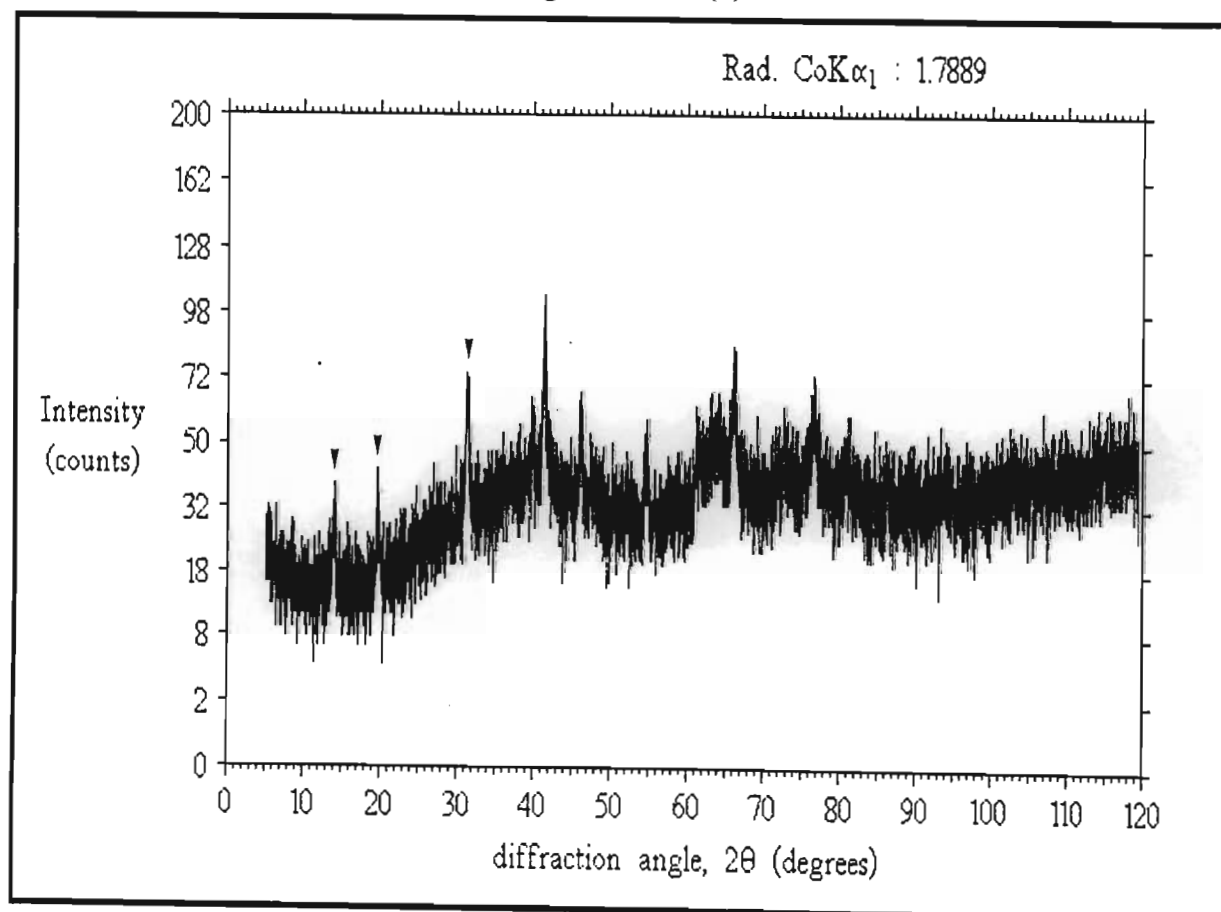
pH 3 Cake [2]   Card number : WP-025-A
(after salt extraction)

I/I₁ ... 2θ (degrees) CoKα₁   I₁: 46

Iron oxide hydroxide
beta-FeOOH   (Akaganeite)   13-0157

I/I₁ ... 2θ (degrees) CoKα₁

Figure 5.4.1-1(a)

Rad. CoKα₁ : 1.7889

Intensity (counts) ... diffraction angle, 2θ (degrees)

Figure 5.4.1-1(b)

Iron oxide hydroxide (the beta- form) can be synthetically prepared by the hydrolysis of $FeCl_3$ in solution at 60-100°C and usually takes 6 hours at these temperatures to crystallize [4, 4a]. Before crystallizing, FeOOH forms in solution as a gel with a high active surface area [5] with strong absorptive properties and is thus capable of taking down ions of other elements on precipitation. The elemental analysis (**Table 5.4.1-3**) of this sample is thus of interest as it indicates those elements favoured to co-precipitate on hydrolysis in hydrochloric acid at pH 3 (pH increased with NaOH). Tellurium appears to be very well removed from solution under these conditions.

Table 5.4.1-3   Partial elemental analysis for a precipitate of the hydrous iron oxide β-FeOOH

Element	Weight %
Iron	27.74
Tellurium	5.17
Copper	3.21
Iridium	2.97
Rhodium	1.31
Aluminium	1.23
Bismuth	1.09

Elements occurring in trace amounts (in order) : As, Pb, Sb, Se, Pt, Ni, Pd, Sn, Ru, Ag, Au
The rest of the weight of this sample was due to salt (NaCl).

One of the concentrate pre-treatment steps involves a polysulphide leach aimed at removing metalloids. Scans of residue samples showed a line of relatively high intensity at about 10Å ($2\theta = 10°$) (**Figure 5.4.1-2(a) and (b)**). This seemed to indicate sodium iron hydroxide sulphate hydrate, $Na_2Fe(SO_4)_2(OH)\cdot3H_2O$. Tiny nucleated lemon yellow crystals were isolated from one of the samples and the scan produced a good match with the reduced spectrum of the reference compound (**Figure 5.4.1-3(a) and (b)**). The comparison of reference and observed data is given in **Table 5.4.1-4** (comparison for $2\theta = 5 - 52°$). Quite high d-shifts were observed (salt of synthetic origin).
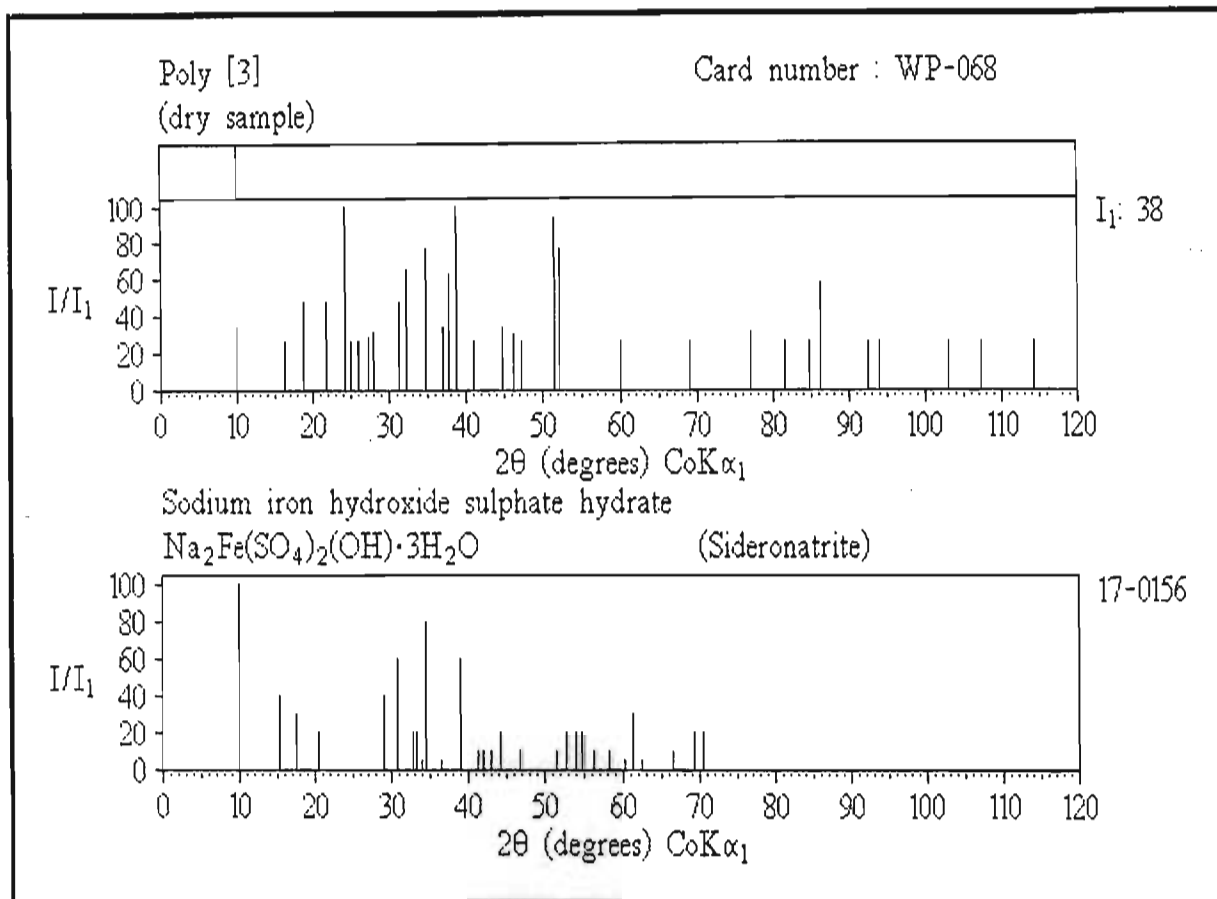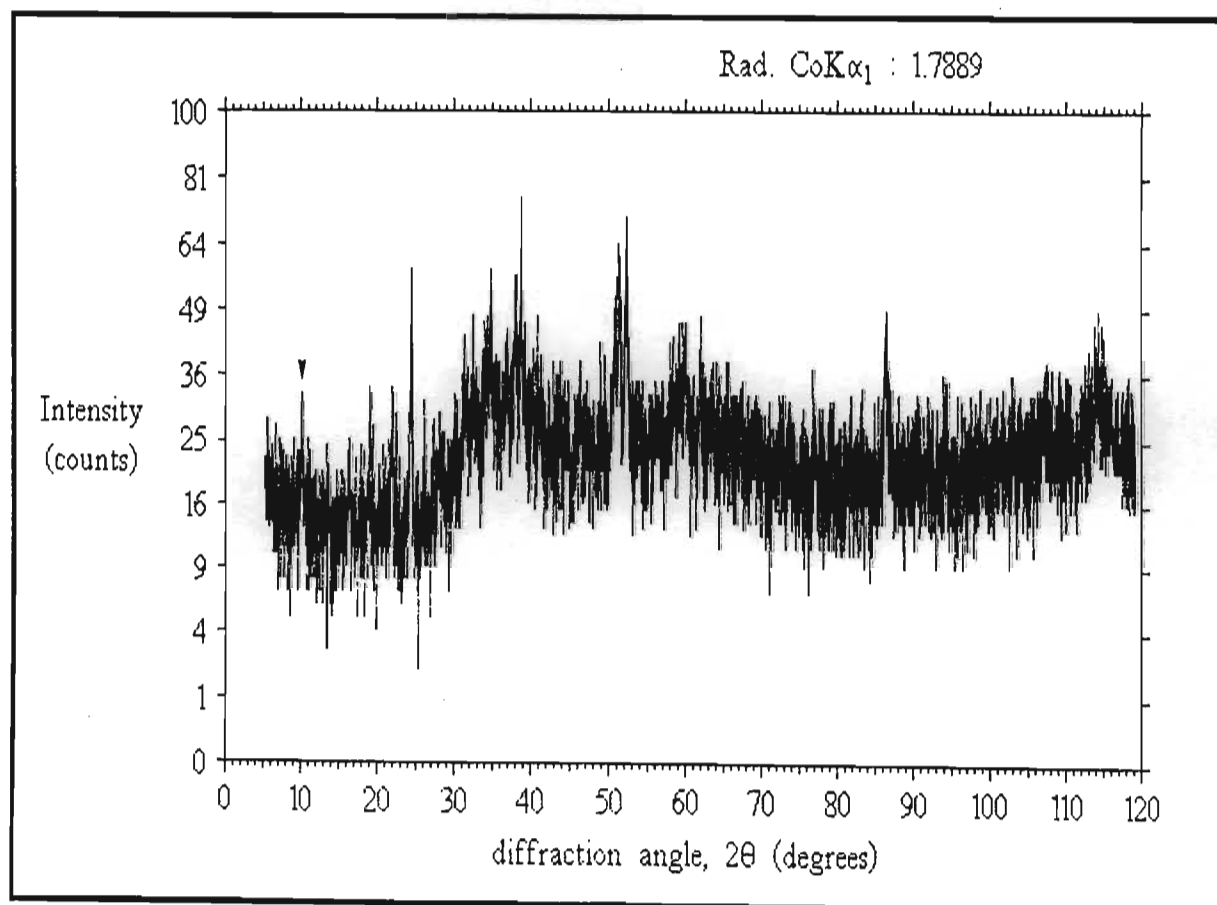
Poly [3]
(dry sample)

Card number : WP-068

I₁: 38

I/I_1

2θ (degrees) CoKα₁

Sodium iron hydroxide sulphate hydrate
$Na_2Fe(SO_4)_2(OH) \cdot 3H_2O$ (Sideronatrite)

17-0156

I/I_1

2θ (degrees) CoKα₁

Figure 5.4.1-2(a)

Rad. CoKα₁ : 1.7889

Intensity
(counts)

diffraction angle, 2θ (degrees)

Figure 5.4.1-2(b)

Lemon yellow crystals
(formed on Poly [3])

Card number : WP-068-A

I_1: 228

I/I$_1$

2θ (degrees) CoKα$_1$

Sodium iron hydroxide sulphate hydrate

$Na_2Fe(SO_4)_2(OH)\cdot 3H_2O$ (Sideronatrite)

17-0156

I/I$_1$

2θ (degrees) CoKα$_1$

Figure 5.4.1-3(a)

Rad. CoKα$_1$: 1.7889

Intensity
(counts)

diffraction angle, 2θ (degrees)

Figure 5.4.1-3(b)

Table 5.4.1-4 Comparison of $Na_2Fe(SO_4)_2(OH)\cdot 3H_2O$ reference data with peaks observed for yellow iron rich crystals

$Na_2Fe(SO_4)_2(OH)\cdot 3H_2O$ Reference data [6]			Yellow crystals in concentrates [WP-068-A] Observed data			Deviation
d(Å)	(I/I₁)	2θ	d(Å)	(I/I₁)	2θ	Δd(Å)
10.2	(100)	10.1	10.263	(100)	10.0	+ 0.063
6.78	(40)	15.2	6.873	(8)	15.0	+ 0.093
5.86	(30)	17.6	5.951	(4)	17.3	+ 0.091
5.00	(20)	20.6	5.065	(5)	20.3	+ 0.065
3.58	(40)	28.9	3.646	(15)	28.4	+ 0.066
3.38	(60)	30.7	3.430	(38)	30.2	+ 0.050
3.18	(20)	32.7	3.228	(8)	32.2	+ 0.048
3.01	(80)	34.6	3.045	(87)	34.2	+ 0.035
2.86	(5)	36.5	2.902	(5)	35.9	+ 0.042
2.68	(60)	39.0	2.725	(28)	38.3	+ 0.045
2.537	(10)	41.3	2.574	(11)	40.7	+ 0.037
2.437	(10)	43.1	2.474	(6)	42.4	+ 0.037
2.375	(20)	44.2	2.413	(11)	43.5	+ 0.038
2.251	(10)	46.8	2.288	(12)	46.0	+ 0.037
2.062	(10)	51.4	2.096	(11)	50.5	+ 0.034

Although it seems quite an unusual compound, identification was important because this salt is reported to be soluble in cold water but unstable in warm water, in which it hyrolyses, precipitating hydrated iron oxide [7] . The salt was thus synthesized according to a published method [8]. A scan of the product matched that of the salt showing a successful synthesis. The product was indeed observed to hydrolyse in hot water forming a dense brown precipitate of hydrated iron oxide (of α-FeOOH rather than β-FeOOH - hydrolysis was rapid).

The only traces of the iron oxide Fe_3O_4 that were found were in samples from the lead fusion process. After dissolving the lead ingots in nitric acid, an insoluble residue is left behind. A scan of one of these residues gave a few peaks indicative of Fe_3O_4. The sample was magnetically separated and another scan performed on the magnetic fraction.

All the Fe_3O_4 peaks were enhanced in the second scan thus confirming the assignment. A few of the lines overlapped those of another phase (**Table 5.4.1-5**).

As the lead fusion of waste residues and precipitates occurs at high temperatures this oxide is probably formed by the thermal decomposition of β-FeOOH (for example) mentioned earlier, via the reactions :

$$2\ FeOOH \longrightarrow Fe_2O_3 + H_2O$$

$$6\ Fe_2O_3 \longrightarrow 4\ Fe_3O_4 + O_2$$
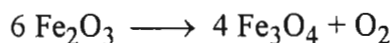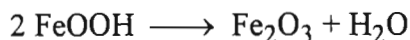
The second of these reactions only occurs at 1400°C which is quite high. Another route for the formation of Fe_3O_4 might be through the mixed metal oxide $PbFe_{12}O_{19}$ which, when leached with nitric acid, would give a precipitate of Fe_3O_4 [9]. The Fe_3O_4 found in the nitric acid insolubles was observed to have an unusually low crystallinity (**Figure 5.4.1-4(a)** and **(b)**).

Table 5.4.1-5   Comparison of Fe_3O_4 reference data with peaks observed of nitric acid insolubles (magnetics)

Fe_3O_4 Reference data [10]			Nitric acid insolubles (magnetics) [WP-005-A] Observed data		
d(Å)	(I/I$_1$)	2θ	d(Å)	(I/I$_1$)	2θ
2.967	(30)	35.1	2.968	(-)	35.1
2.532	(100)	41.4	2.520	(100)	41.6
2.0993	(20)	50.4	2.096	(59)	50.5
1.6158	(30)	67.2	1.612	(34)	67.4
1.4845	(40)	74.1	1.483	(-)	74.2
1.2807	(10)	88.6	1.280	(-)	88.7
1.0930	(12)	109.8	1.091	(24)	110.2
1.0496	(6)	116.9	1.049	(-)	117.0

Iron-pgm alloys are generally not encountered in pgm extraction (with one exception - see § 5.5.4), although in one experiment carried out by BARPLATS platinum refinery a misunderstanding lead to the formation of an iron-platinum alloy.
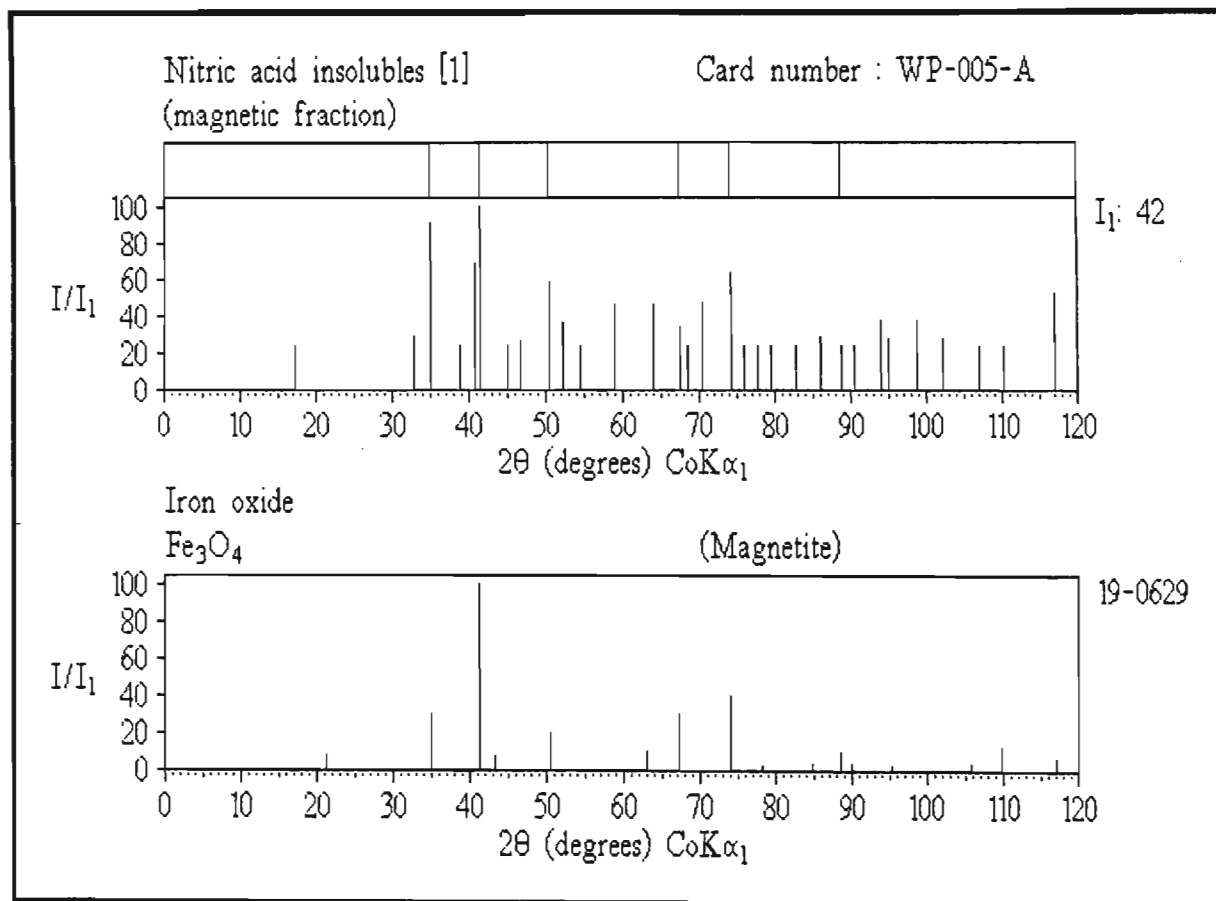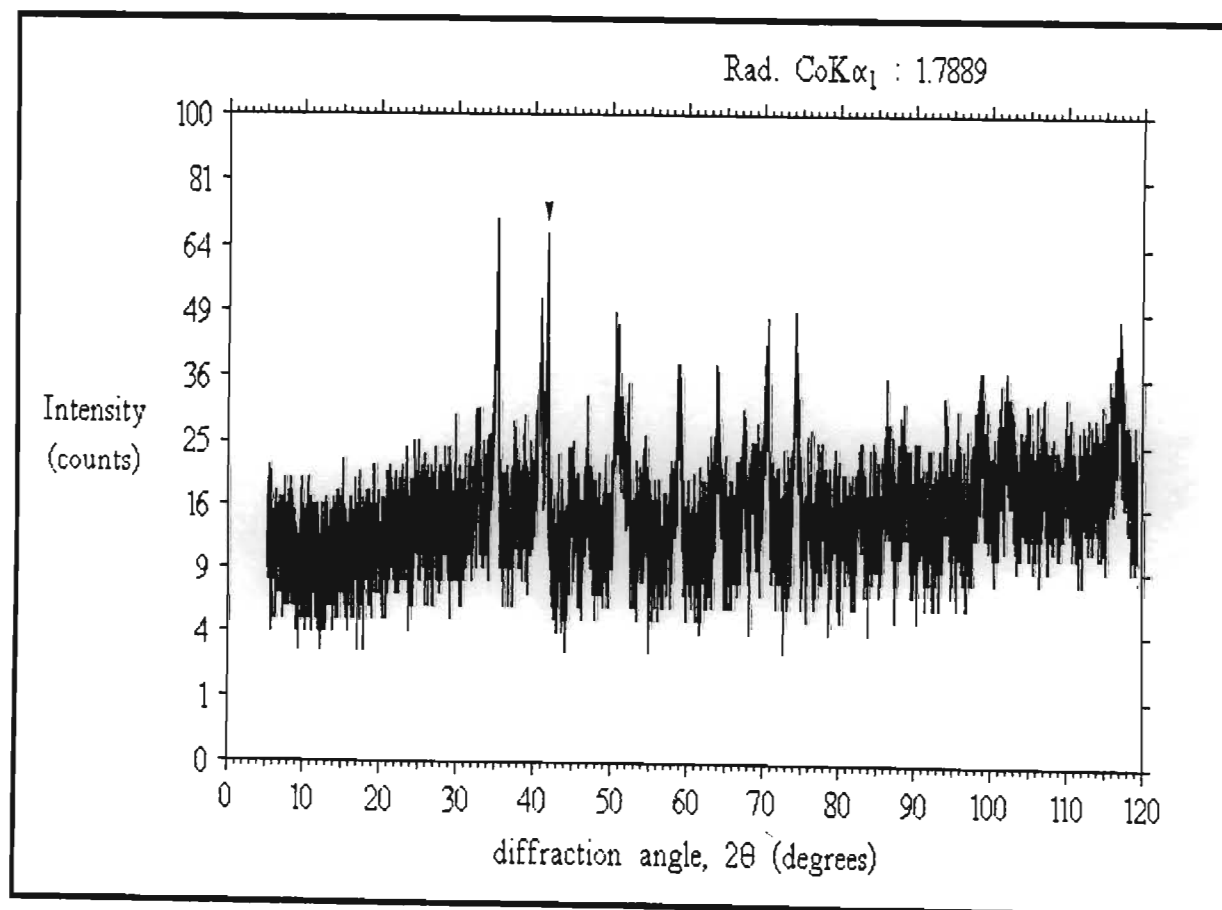
Nitric acid insolubles [1]   Card number : WP-005-A
(magnetic fraction)

I/I_1

I_1: 42

2θ (degrees) $CoK\alpha_1$

Iron oxide
Fe_3O_4 (Magnetite)

19-0629

I/I_1

2θ (degrees) $CoK\alpha_1$

Figure 5.4.1-4(a)

Rad. $CoK\alpha_1$: 1.7889

Intensity
(counts)

diffraction angle, 2θ (degrees)

Figure 5.4.1-4(b)

An insoluble pgm residue was resistant to a HCl/Cl$_2$ leach. It was felt that this might be due to sulphides. The sample was thus reduced in hydrogen at 800°C in order to convert the pgms to metals which, it was hoped, would render it soluble. Analysis showed that the reduction had produced the alloy **PtFe** (**Figure 5.4.1-5 (a) and (b)**). Evidently the insolubles in the original sample had been residual iron oxide, Fe$_3$O$_4$, and highly sintered platinum, which had reacted via the reaction :

$$Fe_3O_4 + 3\,Pt + 4\,H_2 \xrightarrow{\ \ (800°C)\ \ } 3\,PtFe + 4\,H_2O$$
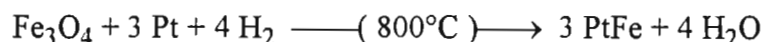
Table 5.4.1-6 compares the reference and observed data for this alloy. A few of the peaks (boldface) showed significant shifts and differences in intensity. This could be due to fast cooling the alloy or non-ideal stoichiometry. It should be noted that the reference data was collected for a geological sample having the composition $(Pt_{1.03}Ir_{0.01})(Fe_{0.69}Cu_{0.24}Ni_{0.02}Sb_{0.01})$ [10].

Table 5.4.1-6 Comparison of FePt reference data with peaks observed for a hydrogen reduced HCl/Cl$_2$ residue

| PtFe Reference data [11]			H$_2$ Reduced residue [BP-023] Observed data		
d(Å)	(I/I$_1$)	2θ	d(Å)	(I/I$_1$)	2θ
3.69	(30)	28.1	3.640	(13)	28.5
2.714	(30)	38.5	2.735	(17)	38.2
2.195	(100)	48.1	2.184	(100	48.3
1.918	(40)	55.6	1.930	(24)	55.2
1.857	(30)	57.6	**1.818**	**(13)**	**59.0**
1.707	(30)	63.2	1.706	(11)	63.2
1.534	(30)	71.3	**1.512**	**(8)**	**72.5**
1.361	(30)	82.2	1.366	(10)	81.8
1.338	(50)	83.9	1.323	(20)	85.1
1.280	(40)	88.7	1.278	(6)	88.8
1.243	(20)	92.0	**1.222**	**(8)**	**94.1**
1.218	(30)	94.5	**1.212**	**(5)**	**95.1**
1.156	(90)	101.4	1.158	(29)	101.2
1.127	(60)	105.1	**1.122**	**(1)**	**105.7**
1.098	(60)	109.1	1.091	(13)	110.2
1.068	(5)	113.8	-	-	-
1.042	(50)	118.3	**1.035**	**(2)**	**119.6**
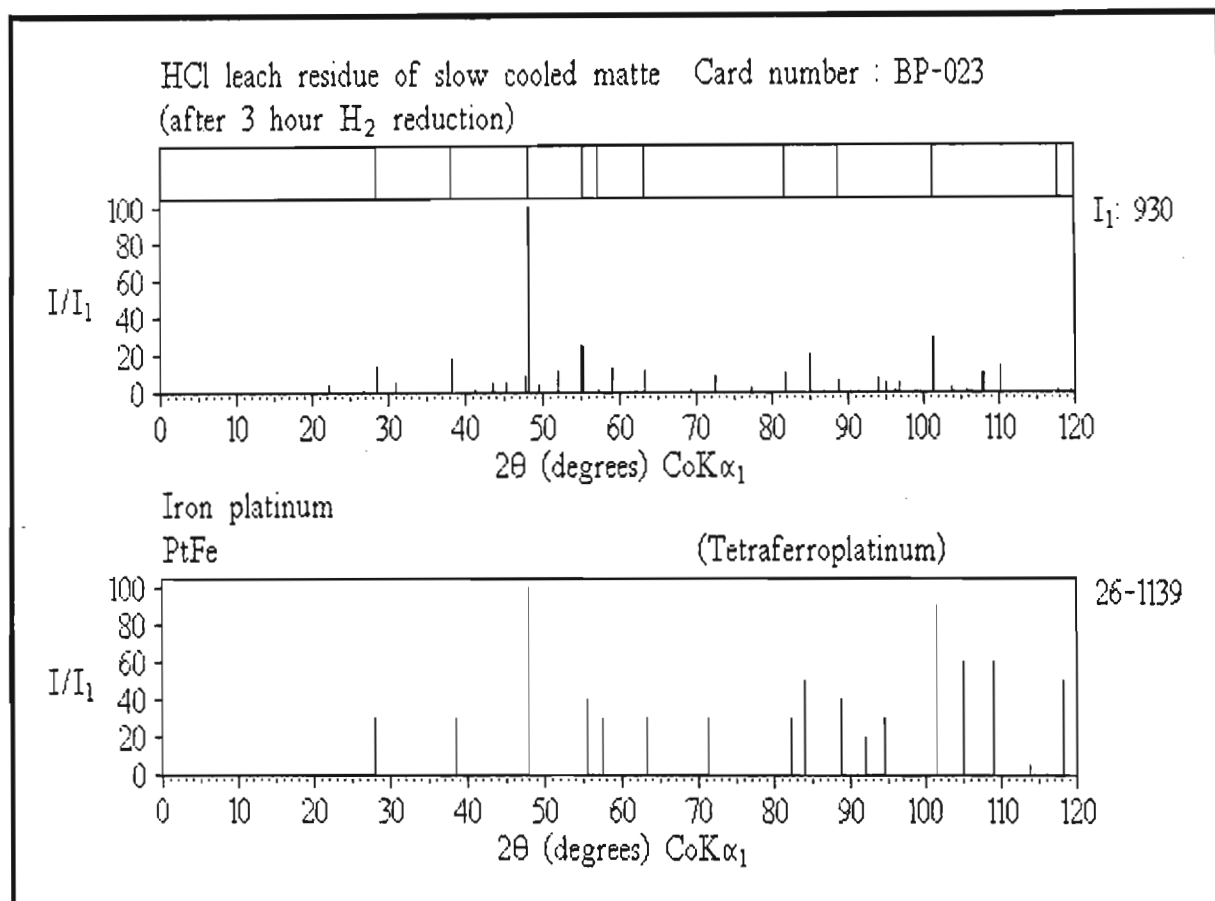
Figure 5.4.1-5(a)
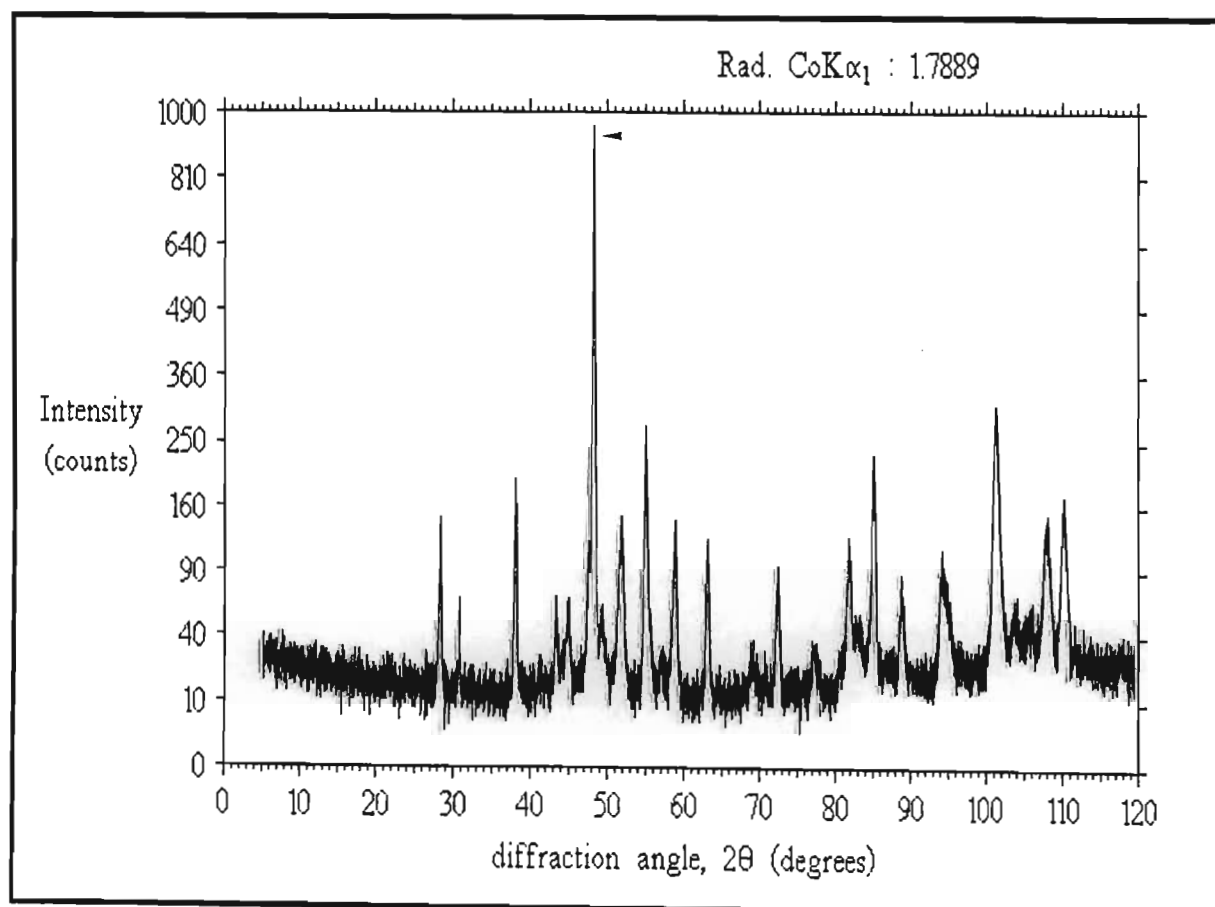
Figure 5.4.1-5(b)

Only one further compound containing iron was identified. This was a magnesium-iron silicate, **(Mg,Fe)SiO$_3$**, of geological origin. Being totally inert this compound poses no process problems (see § 5.5.9).

Table 5.4.1-7 lists the iron compounds identified in the process samples examined, their occurrence and suggested methods of removal.

Table 5.4.1-7   IRON compounds occurring in pgm extraction

Compound	Occurrence and removal
NiFe$_2$O$_4$	Concentrates and some HCl/Cl$_2$ residues *acid leach eg. HCl*
β-FeOOH	Hydrated oxide precipitates *pH control*
Na$_2$Fe(SO$_4$)$_2$(OH)·3H$_2$O	Pre-treated concentrates (polysulphide leach residues) *cold water wash*
Fe$_3$O$_4$	Nitric acid insolubles of lead ingots *magnetic separation*
PtFe alloy	Hydrogen reduced HCl/Cl$_2$ residues of Pt and Fe$_3$O$_4$ *re-leach with HCl/Cl$_2$*
(Fe,Rh)$_{1.8}$Ir$_{0.2}$ alloy [†]	Pre-treated concentrates (rare in large amounts) *partially HCl/Cl$_2$ soluble; insoluble traces remain*
(Mg,Fe)SiO$_3$ [‡]	HCl/Cl$_2$ residues (rare) *HCl/Cl$_2$ insoluble : inert*

† Covered in § 5.5.4   ‡ Covered in § 5.5.9

5.4.2 THE NICKEL PROBLEM

Nickel is far less of a problem in pgm extraction. The main nickel compound encountered is the oxide $NiFe_2O_4$ (§ 5.4.1). **Figure 5.4.2-1** shows the reduced pattern of an aqua-regia leach residue of second stage leach residue matched with the $NiFe_2O_4$ reference pattern. This phase is always of high crystallinity giving sharp intense lines. In this particular sample it survived the oxidative leach, along with highly inert quartz, SiO_2 (**Figure 5.4.2-2**). This phase is formed during the conversion stage of mine operations (§ 4.2.3). Aeration of smelter matte results in numerous tiny oxygen-filled cavities, some of which are trapped in the solid on cooling during post conversion. Each of these cavities is lined with a grey crust. A XPD scan of this aeration crust showed that it was predominantly $NiFe_2O_4$ (**Figure 5.4.2-3(a)** and **(b)**). (Another interesting phase identified was the cobalt sulphide Co_3S_4 - **Figure 5.4.2-3(c)**. This was the only cobalt compound identified in all the analyses peformed.) The aeration cavities occurring in a matte chunk are indicated in **Figure 5.4.2-3(d)**.

The only other nickel compound found in any of the samples was nickel oxide, **NiO**. **Table 5.4.2-1** compares the reference data with that observed for a leach residue sample (boldface type indicates overlap with another phase).

Table 5.4.2-1 Comparison of NiO reference data with peaks observed for a HCl/Cl$_2$ leach residue

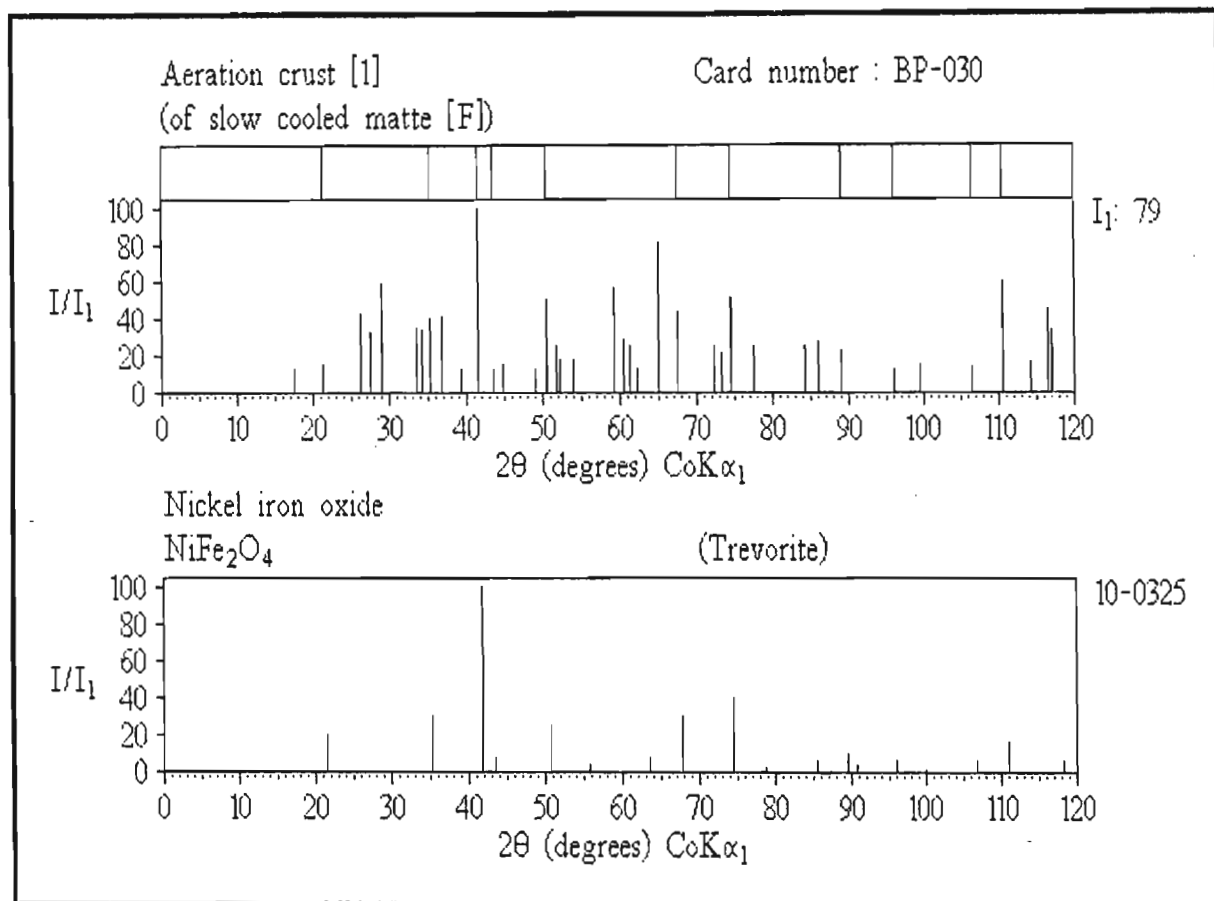| NiO Reference data [12]			HCl/Cl$_2$ residue [1] [WP-001] Observed data		
d(Å)	(I/I$_1$)	2θ	d(Å)	(I/I$_1$)	2θ
2.410	(91)	43.6	2.413	(75)	43.5
2.088	(100)	50.7	2.092	(100)	50.6
1.476	(57)	74.6	**1.476**	**(-)**	**74.6**
1.259	(16)	90.5	1.257	(14)	90.8
1.206	(13)	95.8	1.208	(11)	95.5
1.0441	(8)	117.9	**1.046**	**(-)**	**117.5**
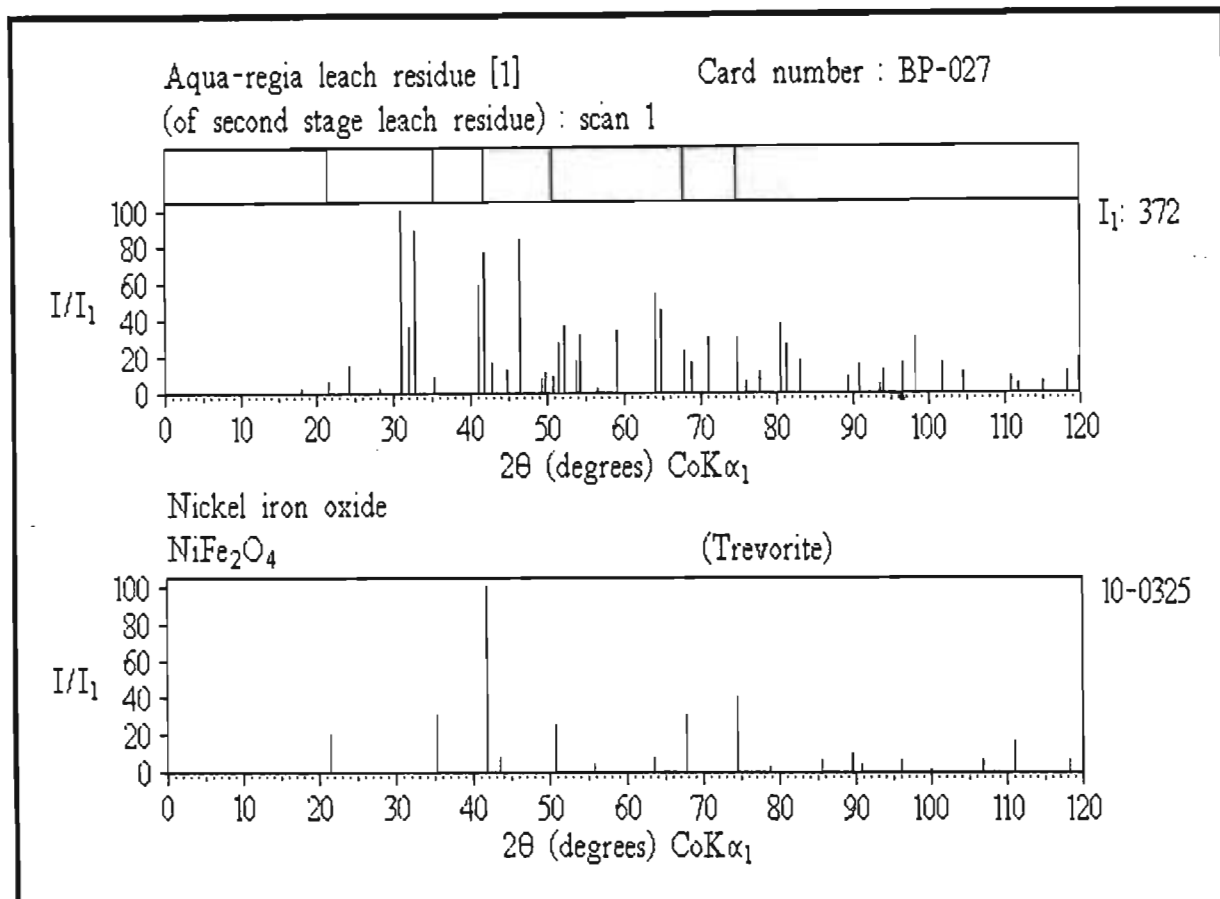
Figure 5.4.2-1
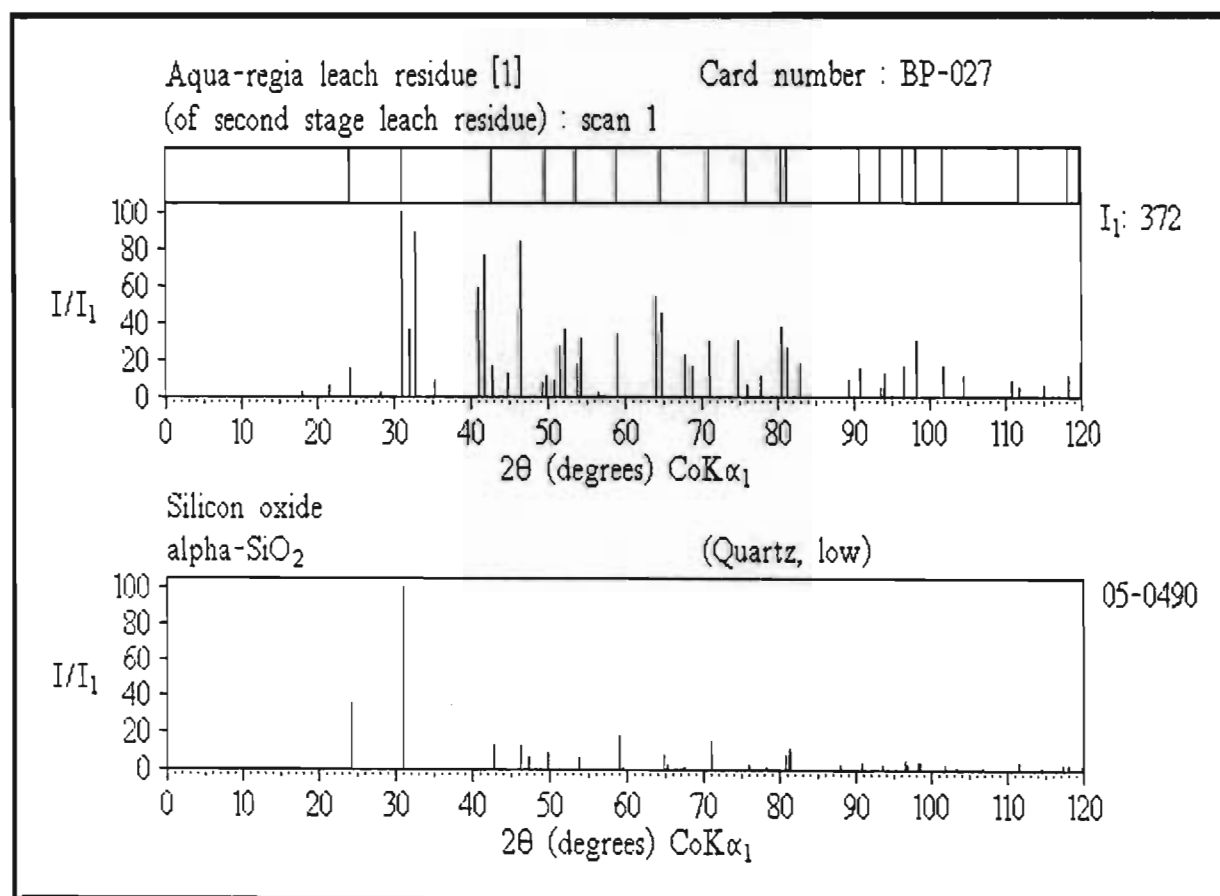
Figure 5.4.2-2
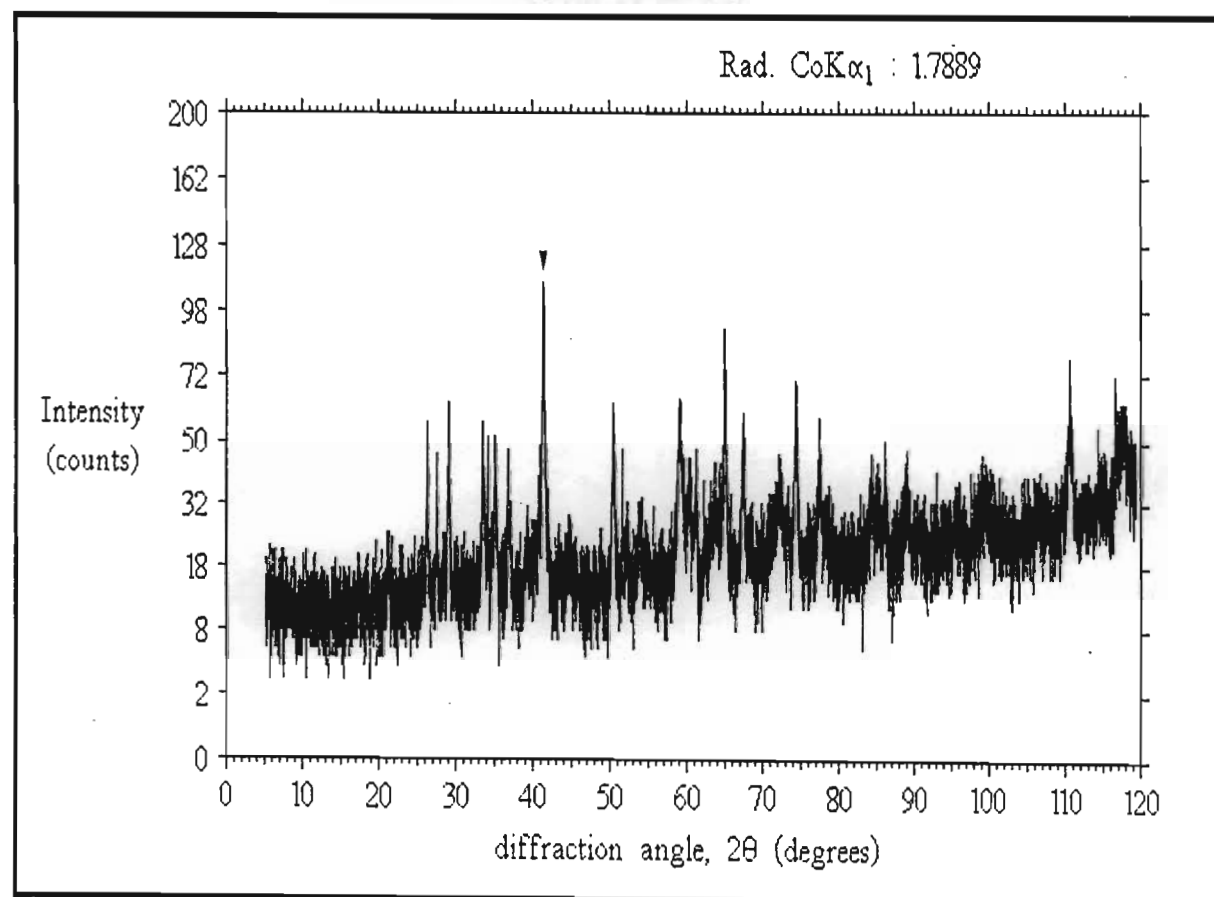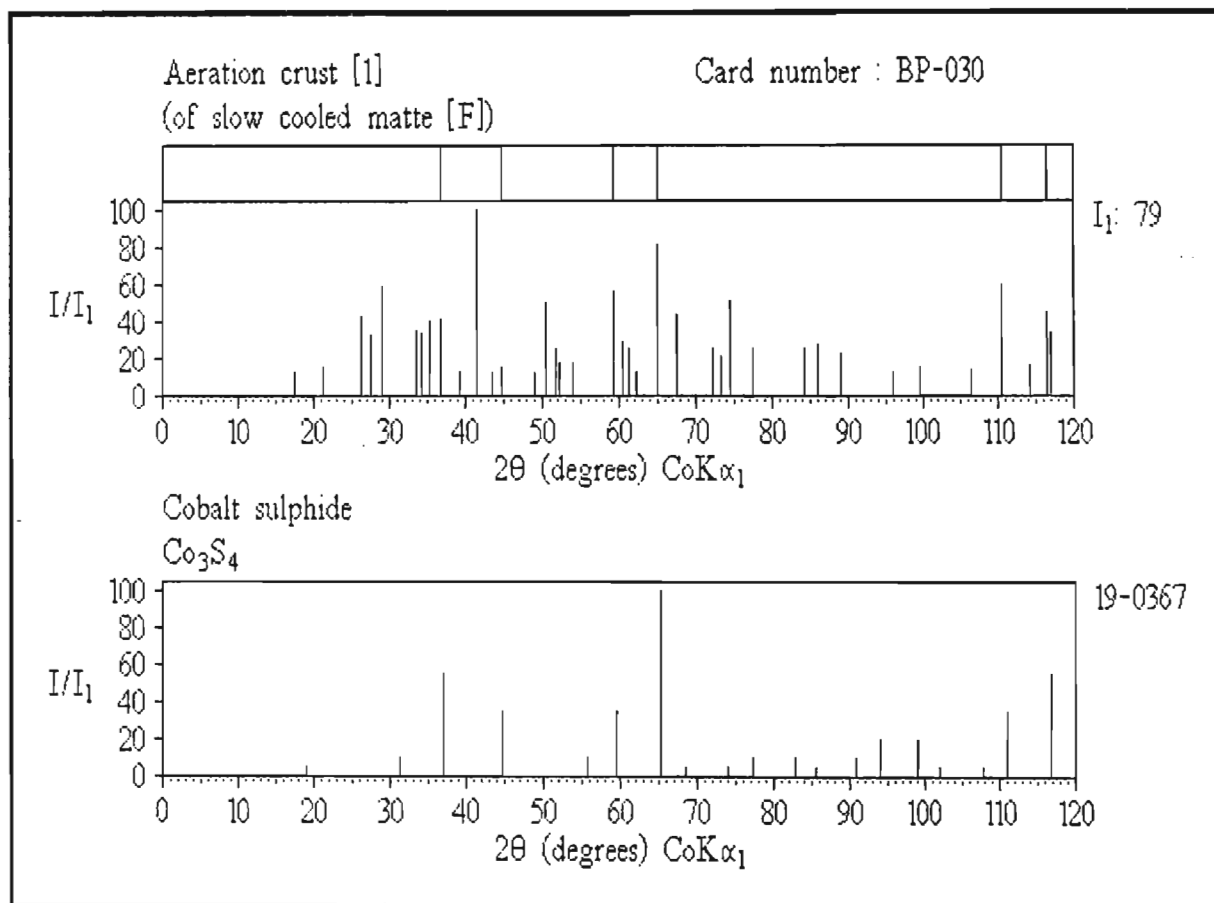
Figure 5.4.2-3(a)

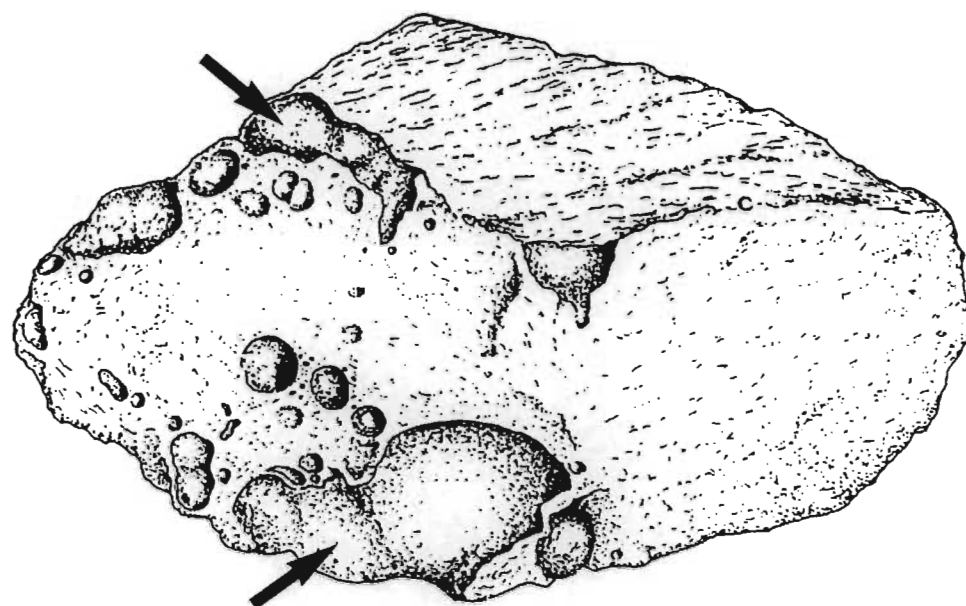**Figure 5.4.2-3(b)**

Figure 5.4.2-3(c)

Figure 5.4.2-3(d)

The reduced and peak patterns for this sample are shown in **Figure 5.4.2-4(a)** and **(b)**. Those for another sample showing small amounts of NiO are shown **Figure 5.4.2-5(a)** and **(b)**. Two good diagnostic peaks are indicated.

The high crystallinity observed of this compound in samples indicates it has probably not resulted from the leaching of iron from $NiFe_2O_4$ *ie.*

$$NiFe_2O_4 \equiv [NiO \cdot Fe_2O_3] + 6\ HCl \xrightarrow{\ \times\ } 2\ FeCl_3 + NiO + 3\ H_2O$$

but rather exists associated with $NiFe_2O_4$.

Table 5.4.2-2 lists the nickel compounds identified in the process samples examined, their occurrence and suggested methods of removal.

Table 5.4.2-2 NICKEL compounds occurring in pgm extraction

Compound	Occurrence and removal
$NiFe_2O_4$	Normal concentrates and some HCl/Cl_2 residues *acid leach eg. HCl*
NiO	Normal concentrates and some HCl/Cl_2 residues *acid leach eg. HCl*
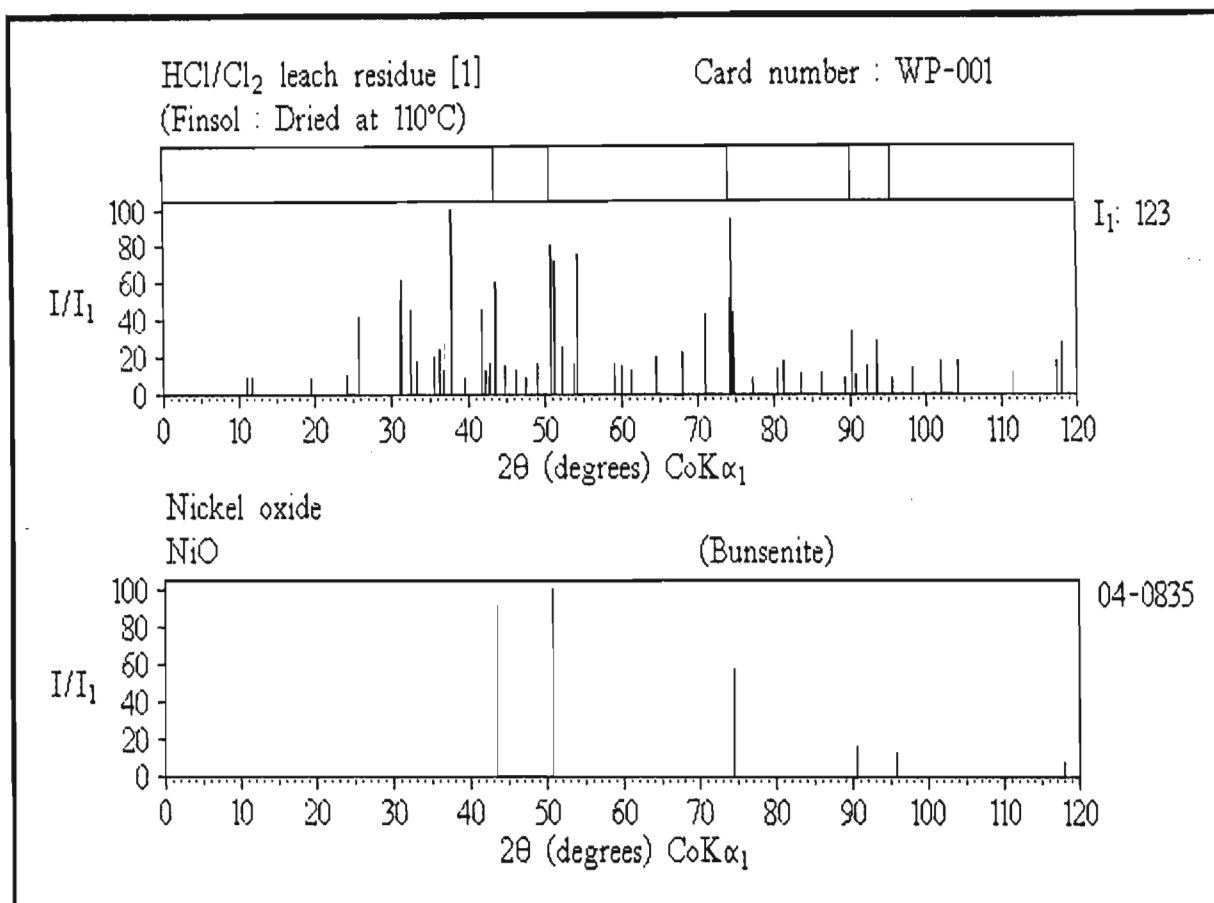
Figure 5.4.2-4(a)

Figure 5.4.2-4(b)

HCl/Cl₂ leach residue [2]
(Finsol : Dried at 110°C)

Card number : WP-002

I_1: 303

I/I₁

2θ (degrees) CoKα₁

Nickel oxide
NiO

(Bunsenite)

04-0835

I/I₁

2θ (degrees) CoKα₁

Figure 5.4.2-5(a)

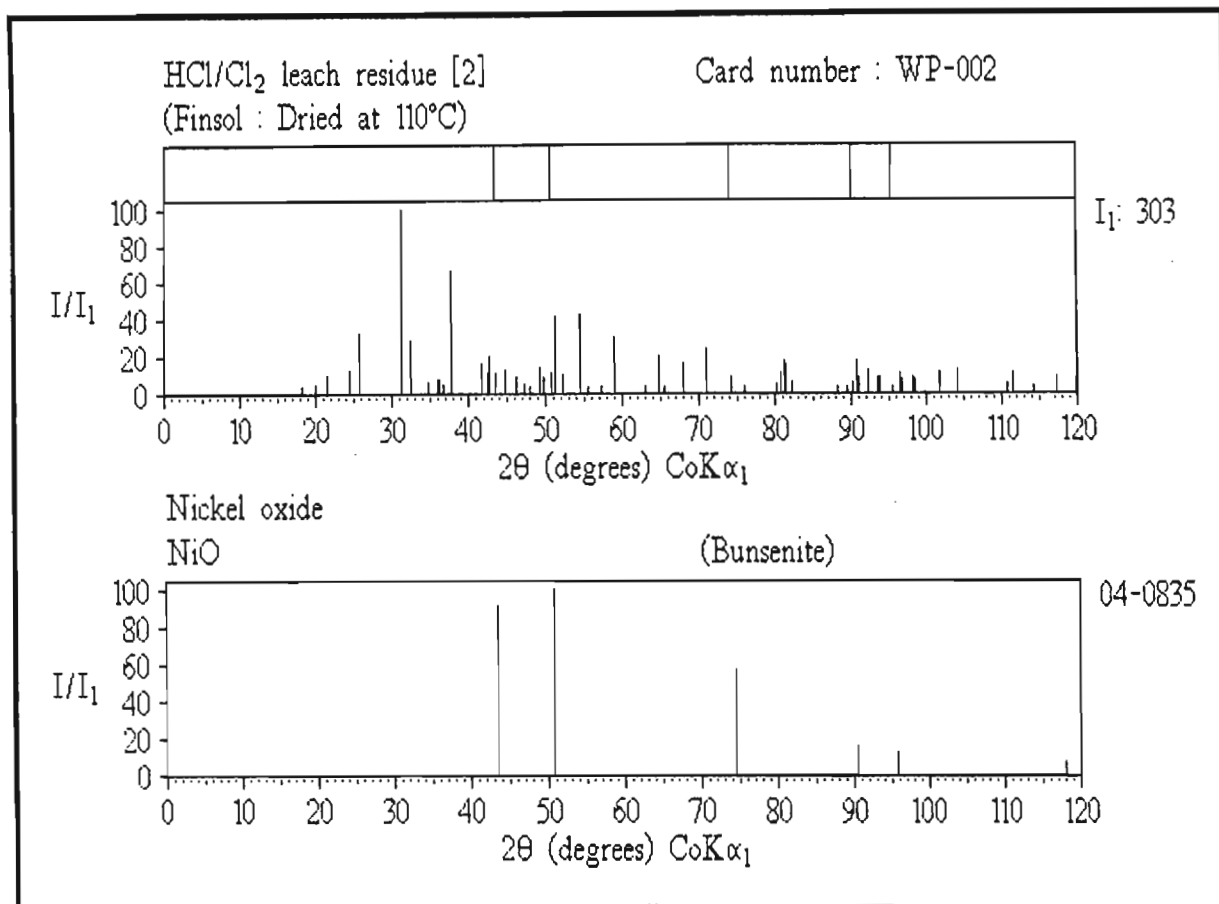Rad. CoKα₁ : 1.7889
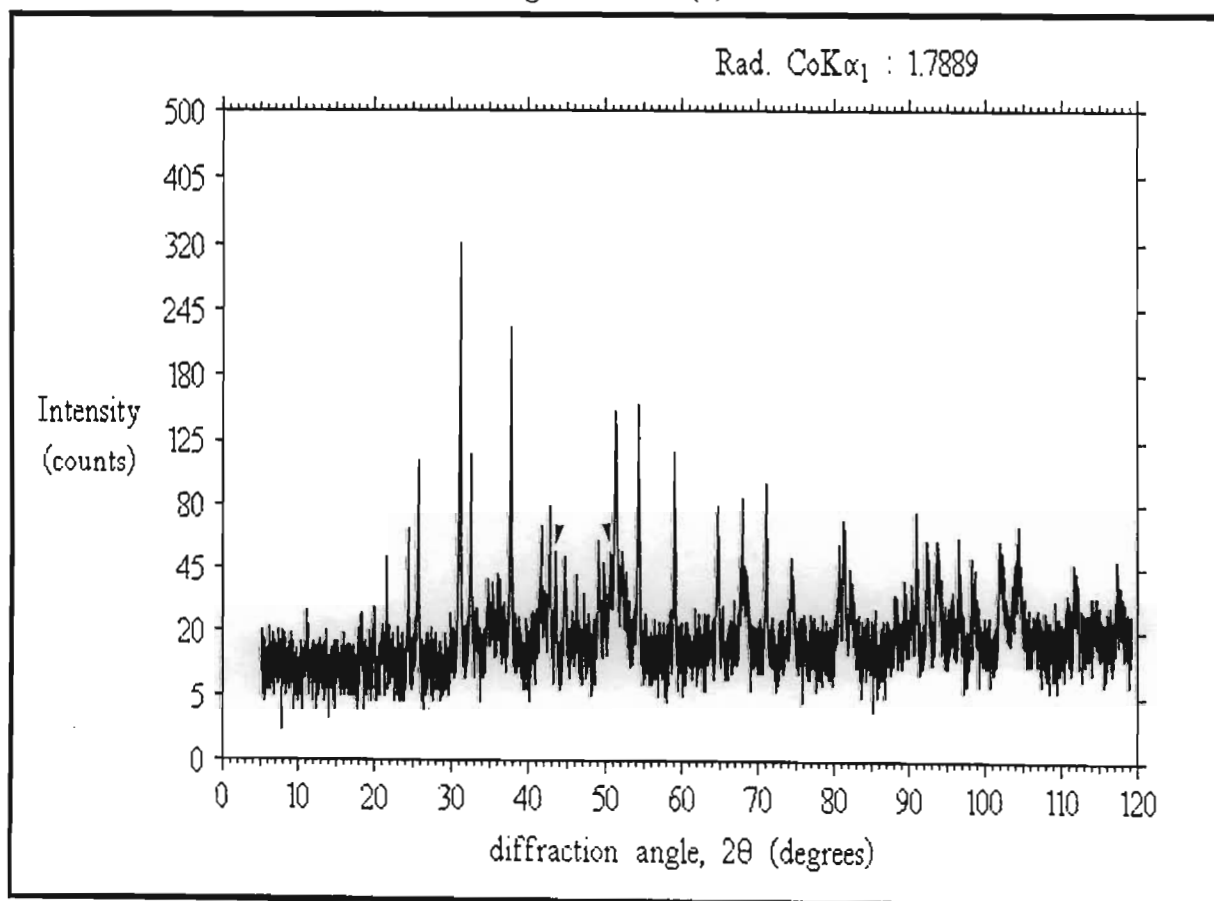
Intensity
(counts)

diffraction angle, 2θ (degrees)
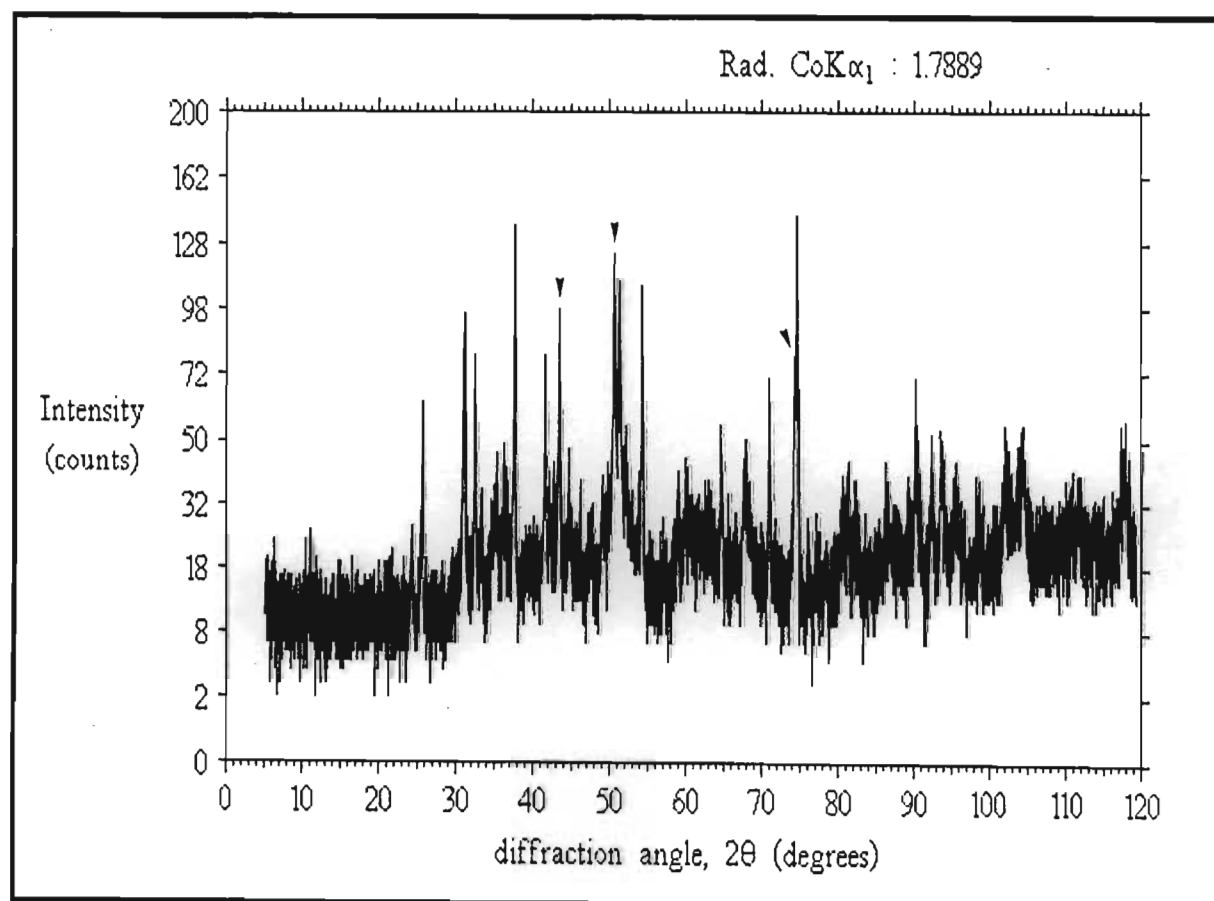
Figure 5.4.2-5(b)

5.4.3 THE COPPER PROBLEM

Copper is the most common and serious base metal impurity occurring in platinum group metal refinery operations. Normal concentrates received from the base metal refinery can be over 9% copper, while for minor concentrates the problem is less pronounced (the copper content rarely going above 4%). One of the aims of the project was to identify the copper species involved in the process, with a view to reducing the unacceptably high levels of copper being encountered throughout operations.

From the analysis of several concentrates, it became clear that much of the problem was due to the presence of very high levels of copper sulphate pentahydrate, $CuSO_4 \cdot 5H_2O$. **Figures 5.4.3-1(a)** and **(b)**, and **5.4.3-2(a)** and **(b)** show the scans of two typical normal concentrates showing copper sulphate peaks together with their reduced patterns. As is normal for hydrated salts, the peaks are observed in the low angle region. **Table 5.4.3-1** compares $CuSO_4 \cdot 5H_2O$ reference data with that observed in these two samples.

Table 5.4.3-1 Comparison of $CuSO_4 \cdot 5H_2O$ reference data with peaks observed for two normal concentrates

$CuSO_4 \cdot 5H_2O$ Reference data [13]			Concentrate [9] (WP-126) Observed data			Concentrate [13] (WP-130) Observed data		
d(Å)	(I/I_1)	2θ	d(Å)	(I/I_1)	2θ	d(Å)	(I/I_1)	2θ
5.48	(55)	18.8				5.477	(54)	18.8
5.21	(10)	19.8				5.213	(49)	19.8
4.73	(100)	21.8	4.706	(100)	21.9	4.739	(65)	21.8
4.28	(15)	24.1				4.277	(49)	24.1
3.99	(60)	25.9	3.988	(100)	25.9	3.996	(86)	25.9
3.71	(85)	27.9	3.704	(100)	27.9	3.706	(100)	27.9
3.54	(20)	29.3				3.551	(49)	29.2
3.45	(15)	30.1				3.474	(49)	29.8
3.30	(60)	31.5	3.306	(100)	31.4	3.304	(57)	31.4
3.05	(30)	34.1	3.038	(100)	34.2	3.004	(49)	34.6
2.749	(50)	38.0				3.752	(59)	27.6
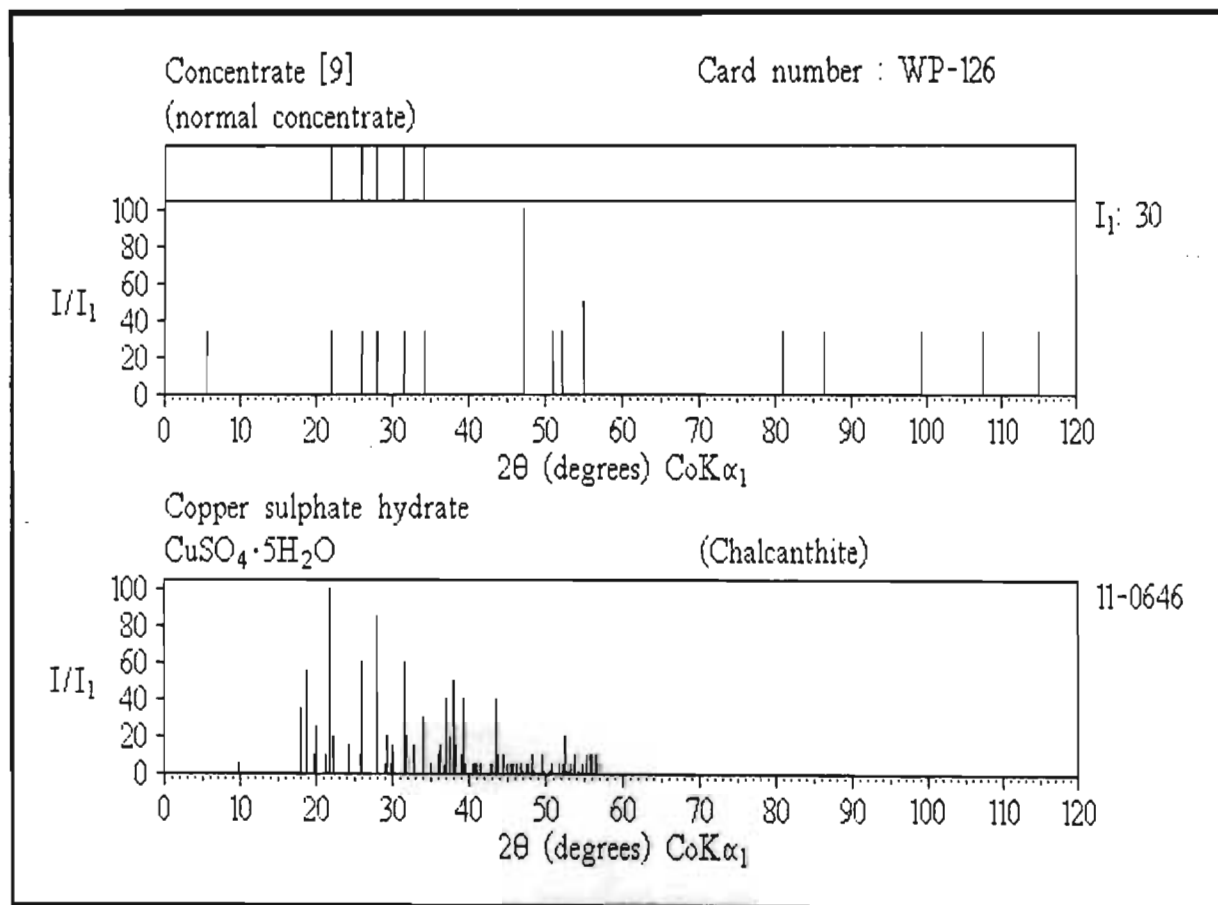
Figure 5.4.3-1(a)

Figure 5.4.3-1(b)

Concentrate [13] Card number : WP-130
(normal concentrate)

I_1: 58

I/I_1

2θ (degrees) CoKα_1

Copper sulphate hydrate
CuSO$_4$·5H$_2$O (Chalcanthite)

11-0646

I/I_1

2θ (degrees) CoKα_1

Figure 5.4.3-2(a)

Rad. CoKα_1 : 1.7889

Intensity
(counts)

diffraction angle, 2θ (degrees)
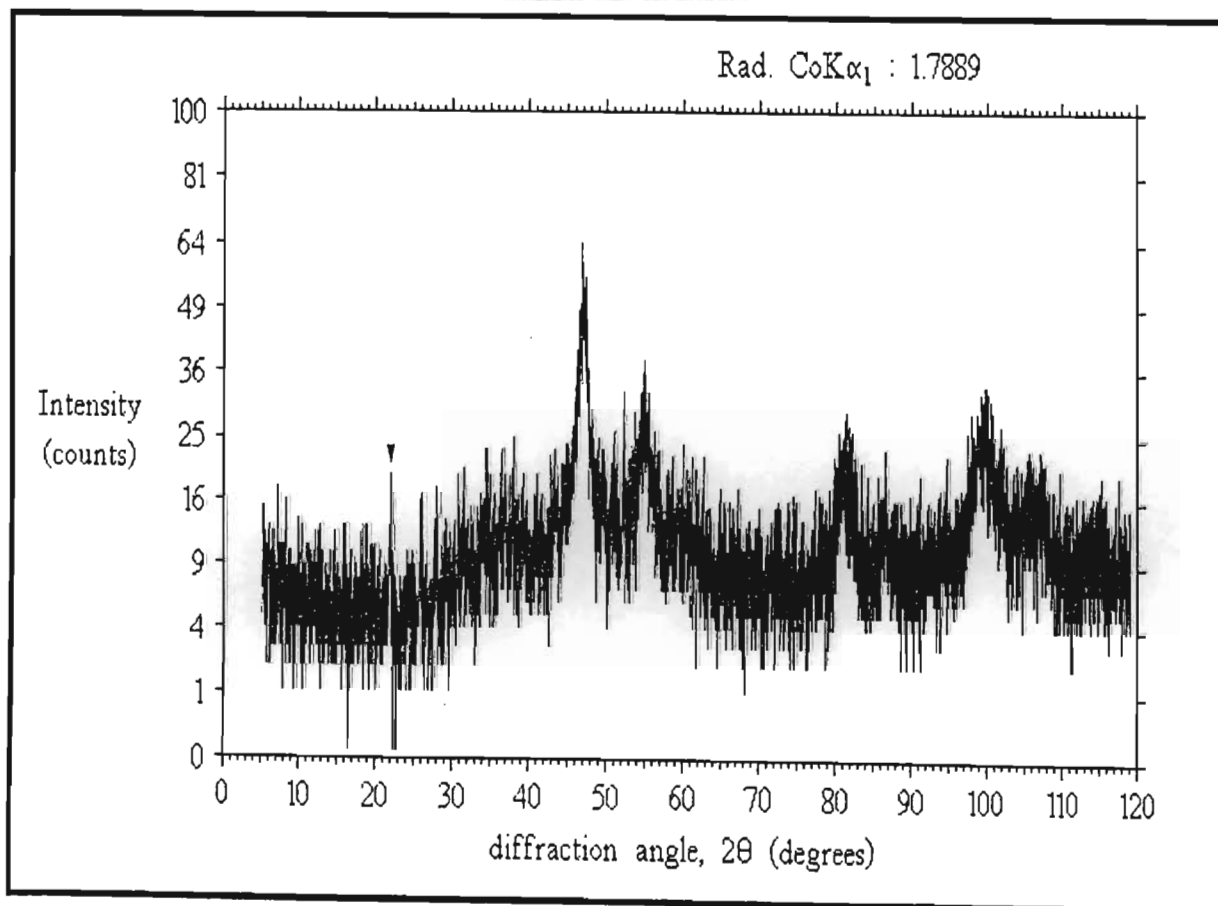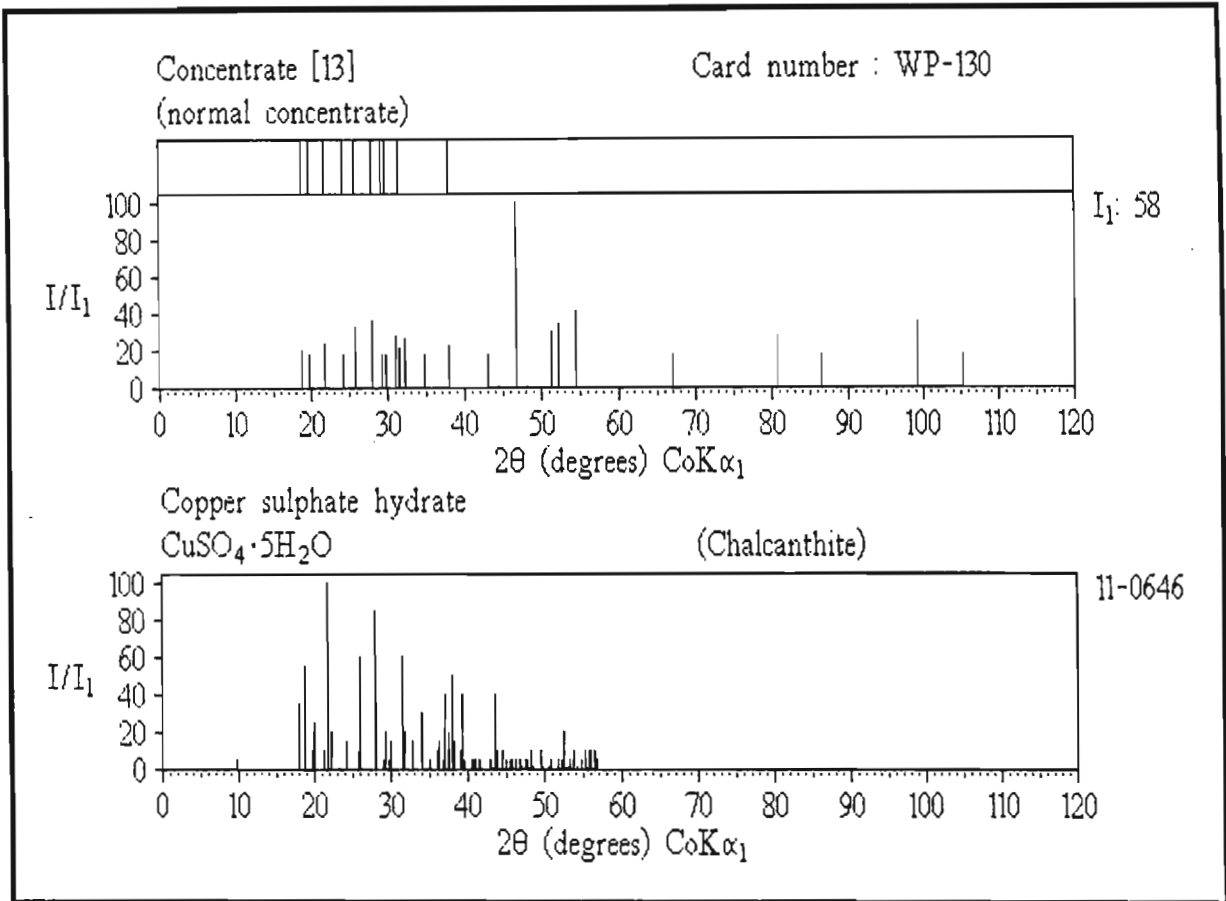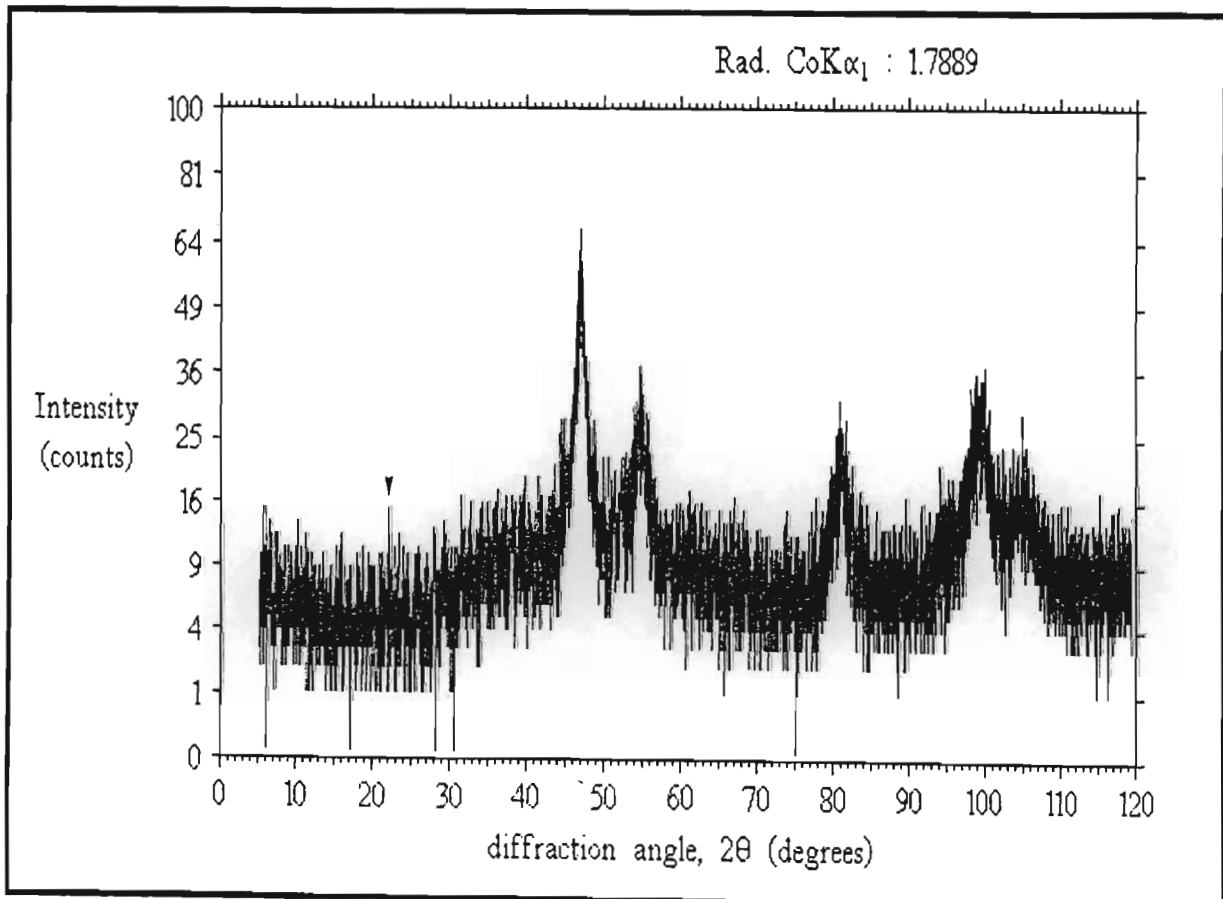
Figure 5.4.3-2(b)

The presence of this salt is due to incomplete washing of the pgm residue after the second stage pressure leach of the copper circuit. Much of the copper in concentrates can thus easily be removed by simply washing with water as a first pre-treatment step or improving the washing process at the base metal refinery. Washing at the base metal refinery can sometimes be so incomplete that dry concentrates contain masses of clear blue crystals easily identifiable as copper sulphate crystals (**Figure 5.4.3-3(a)** and **(b)**). Not only are large quantities of copper introduced into the process by this impurity, but also high levels of the sulphate anion.

Another related salt of copper found in some concentrates was copper sulphate hydroxide hydrate, $Cu_4SO_4(OH)_6 \cdot H_2O$. **Table 5.4.3-2** compares the reference and observed data for this phase.

Table 5.4.3-2 Comparison of $Cu_4SO_4(OH)_6 \cdot H_2O$ reference data with peaks observed for a normal concentrate

$Cu_4SO_4(OH)_6 \cdot H_2O$ Reference data [14]			Concentrate [2] (WP-078) Observed data		
d(Å)	(I/I$_1$)	2θ	d(Å)	(I/I$_1$)	2θ
6.94	(100)	14.8	6.939	(100)	14.8
3.47	(30)	29.9	3.472	(90)	29.9
3.33	(6)	31.2	3.338	(18)	31.1
2.882	(2)	38.7	*2.893*	*(39)*	*36.0* †
2.792	(2)	40.0	*2.820*	*(18)*	*37.0* †
2.422	(25)	43.3	2.429	(33)	43.2
2.018	(12)	52.6	2.031	(24)	52.3

† Assignment of these lines doubtful (sample had a very low crystallinity).

Figure 5.4.3-4(a) and **(b)** show the reduced and peak spectra for this sample. The salt $Cu_4SO_4(OH)_6 \cdot H_2O$ can also be formulated as $3Cu(OH)_2 \cdot CuSO_4 \cdot H_2O$ which shows it is a basic copper sulphate probably formed on inaccurate pH adjustment of the copper leach solution at the base metal refinery, via the reaction :
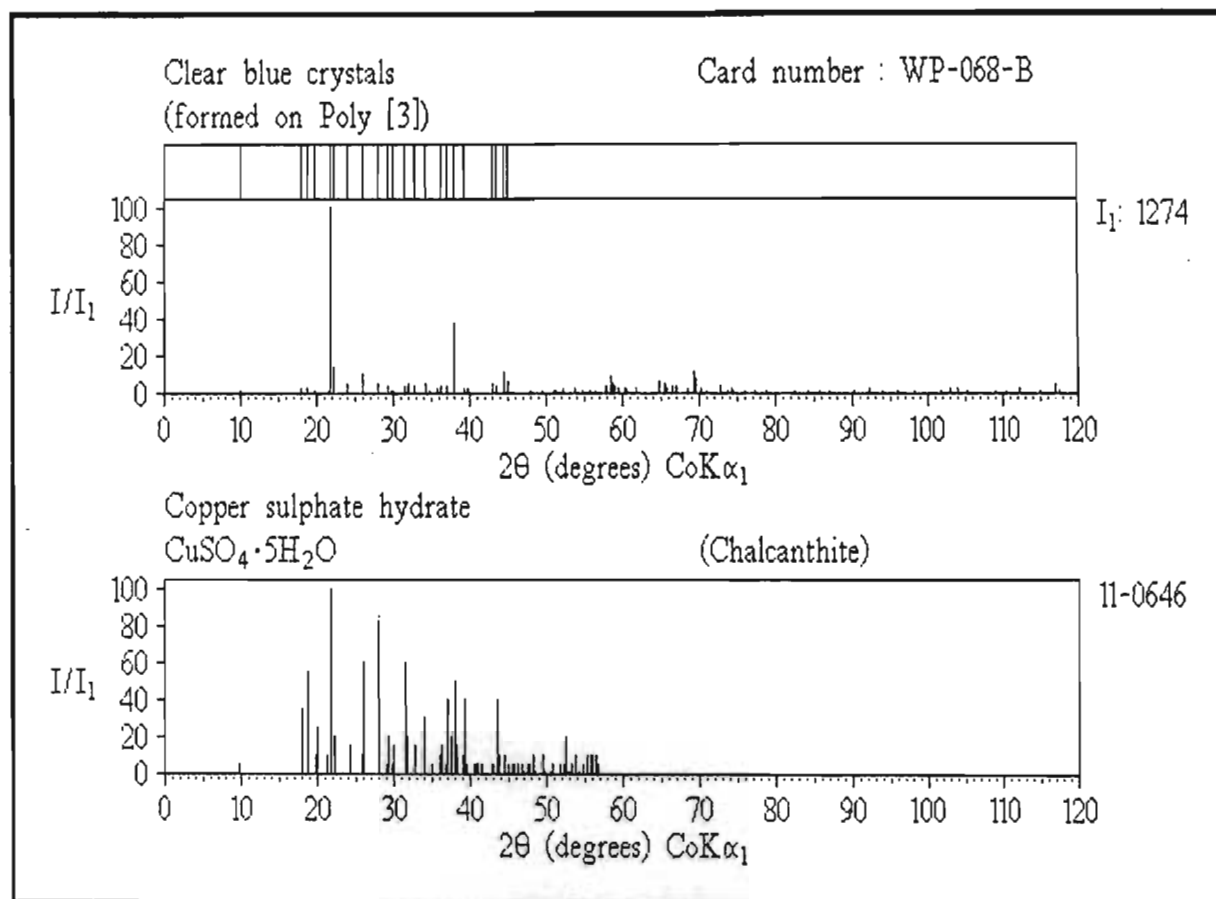
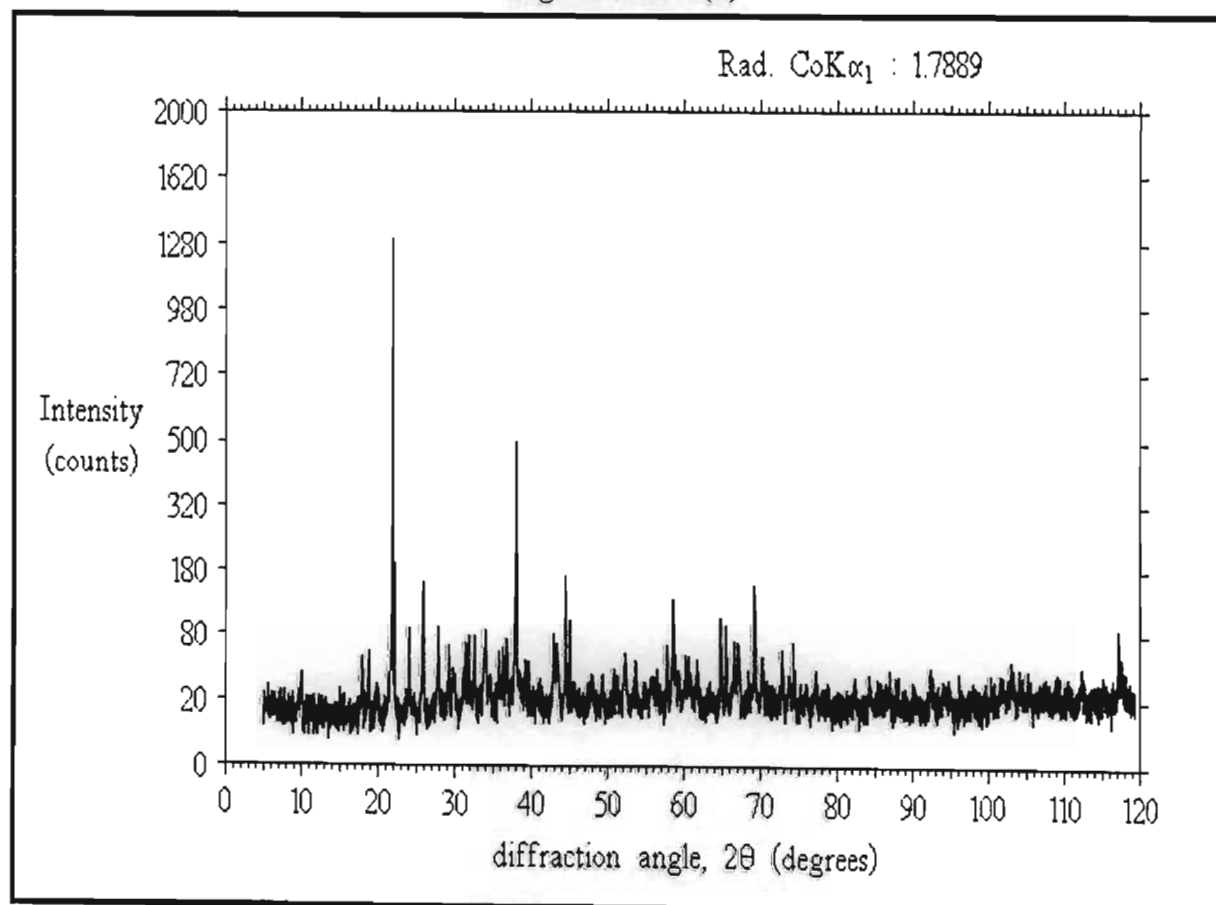$$4\ Cu^{2+} + SO_4^{2-} + 6\ OH^- + H_2O \longrightarrow 3Cu(OH)_2 \cdot CuSO_4 \cdot H_2O$$
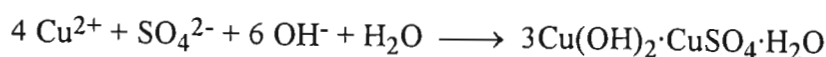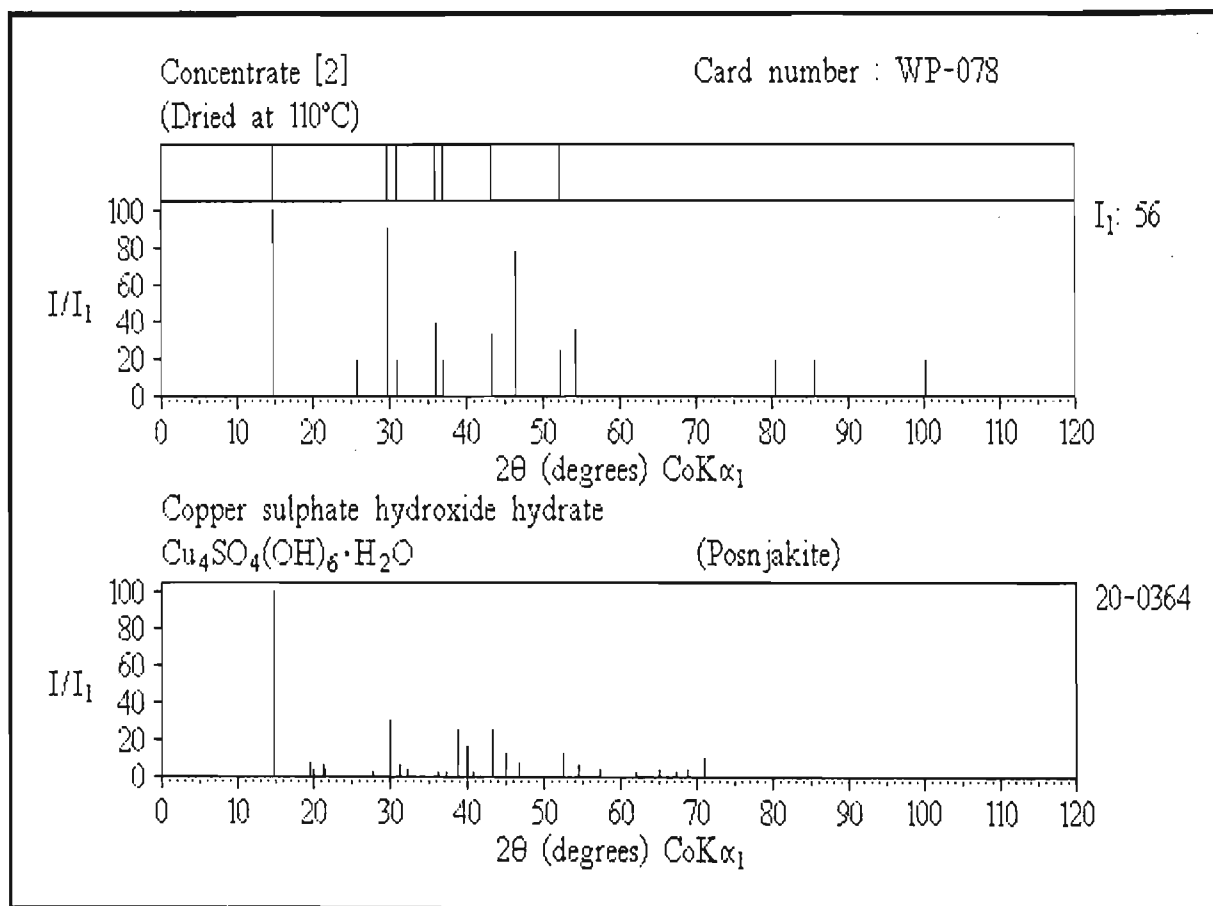
Figure 5.4.3-3(a)
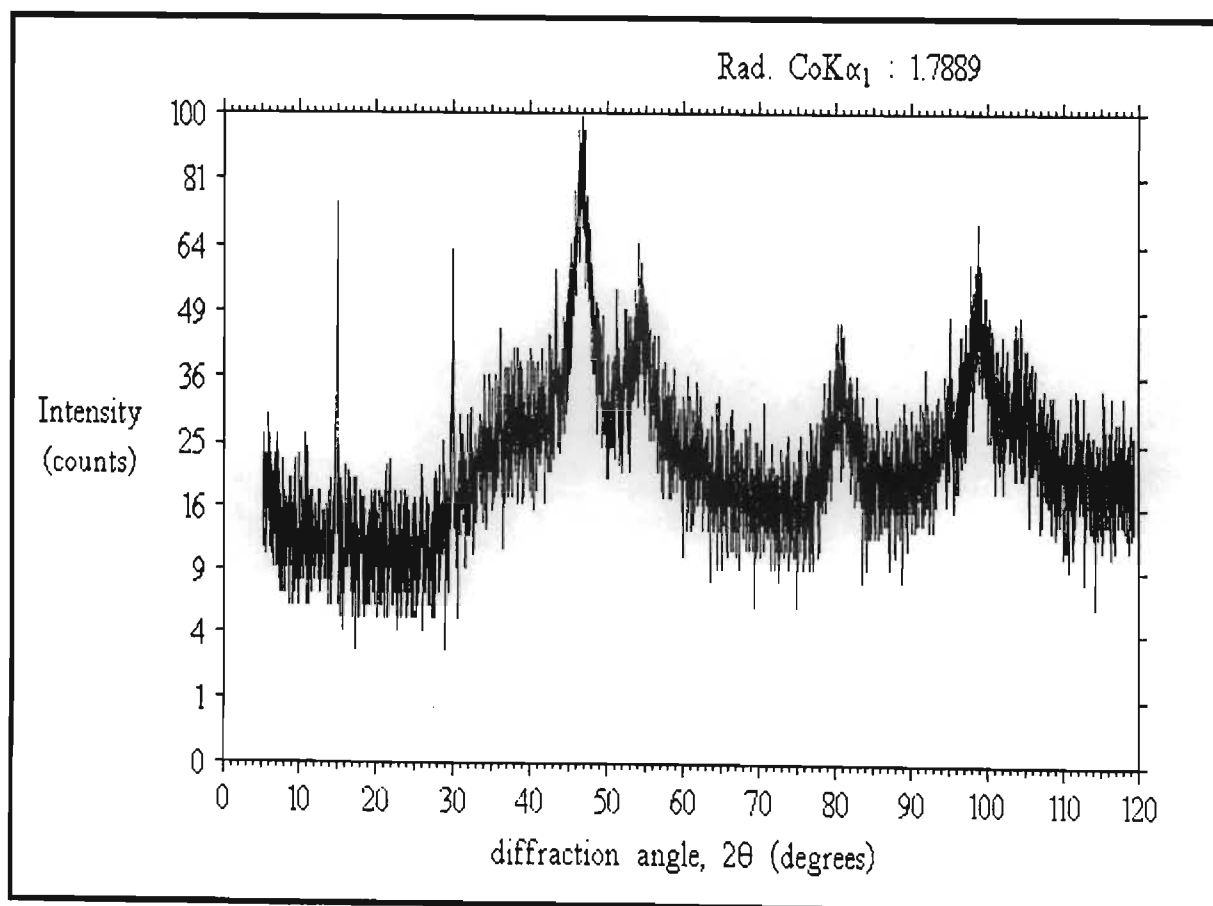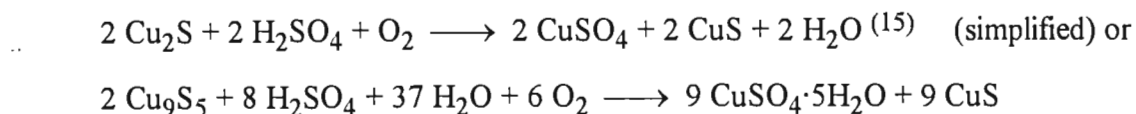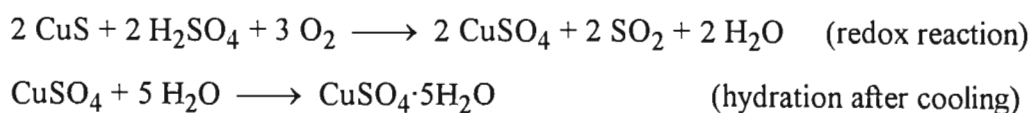

Figure 5.4.3-3(b)

Figure 5.4.3-4(a)

Figure 5.4.3-4(b)

A copper phase detected in concentrates posing a much more serious problem was the copper sulphide, **CuS** (known mineralogically as covellite). This is not water-soluble and dissolves with considerable difficulty in sulphuric acid. It originates from the acid dissolution of the copper sulphide, $Cu_{1.80}S$ or Cu_9S_5, formed in the nickel circuit and present in first stage leach residues. The formation reaction is :

$$2\,Cu_2S + 2\,H_2SO_4 + O_2 \longrightarrow 2\,CuSO_4 + 2\,CuS + 2\,H_2O \quad {}^{(15)} \quad \text{(simplified) or}$$

$$2\,Cu_9S_5 + 8\,H_2SO_4 + 37\,H_2O + 6\,O_2 \longrightarrow 9\,CuSO_4{\cdot}5H_2O + 9\,CuS$$

The scan of a residue of a sample of first stage leach residue leached for three hours with 5% (v/v) sulphuric acid at 95°C gave evidence of the above reaction. **Figure 5.4.3-5(a)** and **(b)** shows the appearence of CuS peaks (arrowed) as the $Cu_{1.80}S$ phase is leached.

The dissolution of this phase by sulphuric acid alone is not possible unless the leach is carried out at elevated temperatures and pressures - hence the pressure leach of the copper circuit. High levels of covellite were observed only occasionally, and immediately indicated an incomplete second stage leach at the base metal refinery.

Drying concentrates with sulphuric acid has been shown to reduce pgm sintering relative to drying without sulphuric acid (§ 5.3.2). A second observed benefit of drying with H_2SO_4 is that if insoluble CuS is present in the concentrate it can be converted to soluble $CuSO_4{\cdot}5H_2O$. If the concentrate is moistened with 20g/l H_2SO_4 and heated to 160°C, no reaction occurs. At 260°C however, complete conversion to the sulphate takes place. The reactions probably occurring are :

$$2\,CuS + 2\,H_2SO_4 + 3\,O_2 \longrightarrow 2\,CuSO_4 + 2\,SO_2 + 2\,H_2O \quad \text{(redox reaction)}$$

$$CuSO_4 + 5\,H_2O \longrightarrow CuSO_4{\cdot}5H_2O \qquad \text{(hydration after cooling)}$$

Two scans showing the reaction occurring only at 260°C in the presence of H_2SO_4 are shown in **Figures 5.4.3-6(a)** and **(b)**, and **5.4.3-7(a)** and **(b)**. **Figure 5.4.3-8** shows the complete absence of CuS. **Table 5.4.3-3** compares the reference data for CuS with data observed for a concentrate dried in two different ways. Note that before decomposition, the crystallinity of CuS improves when dried with H_2SO_4.
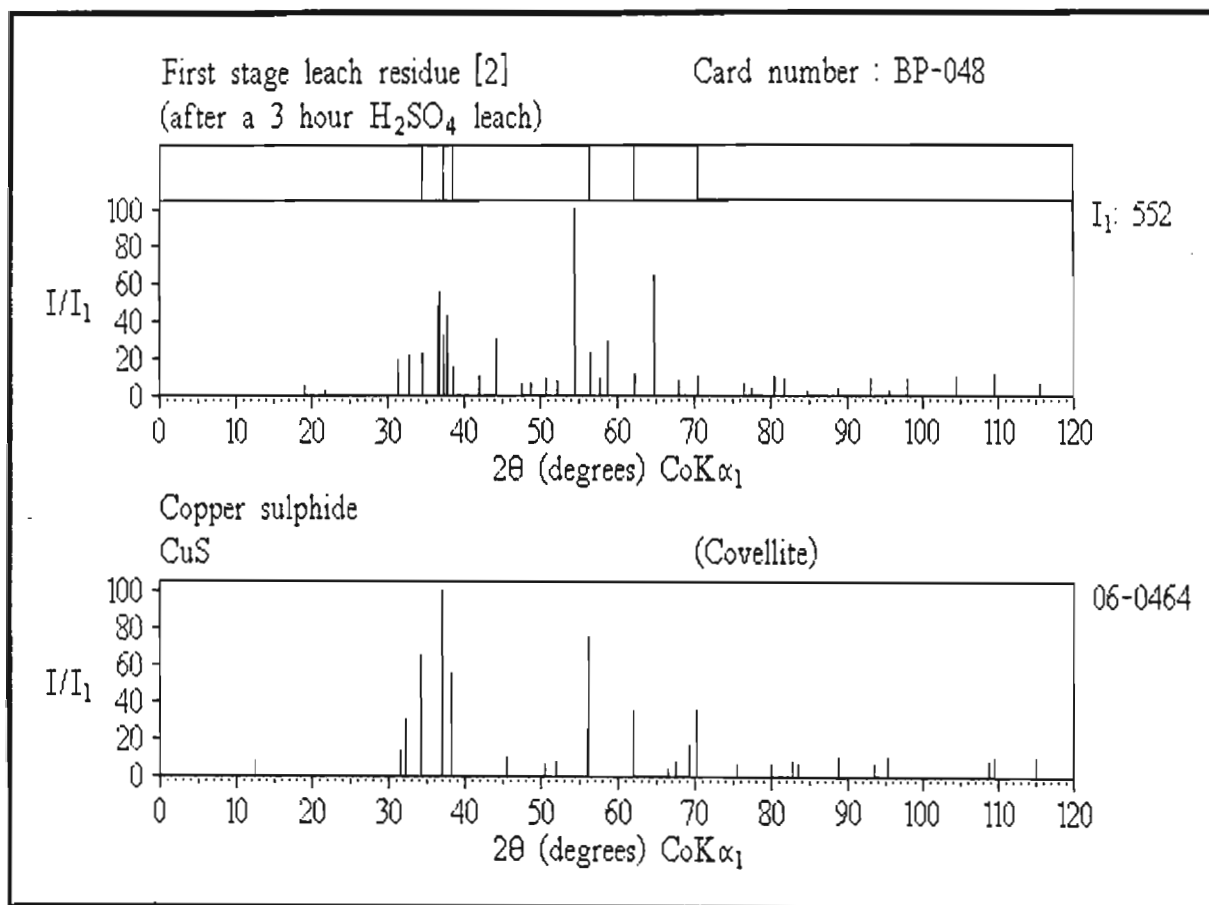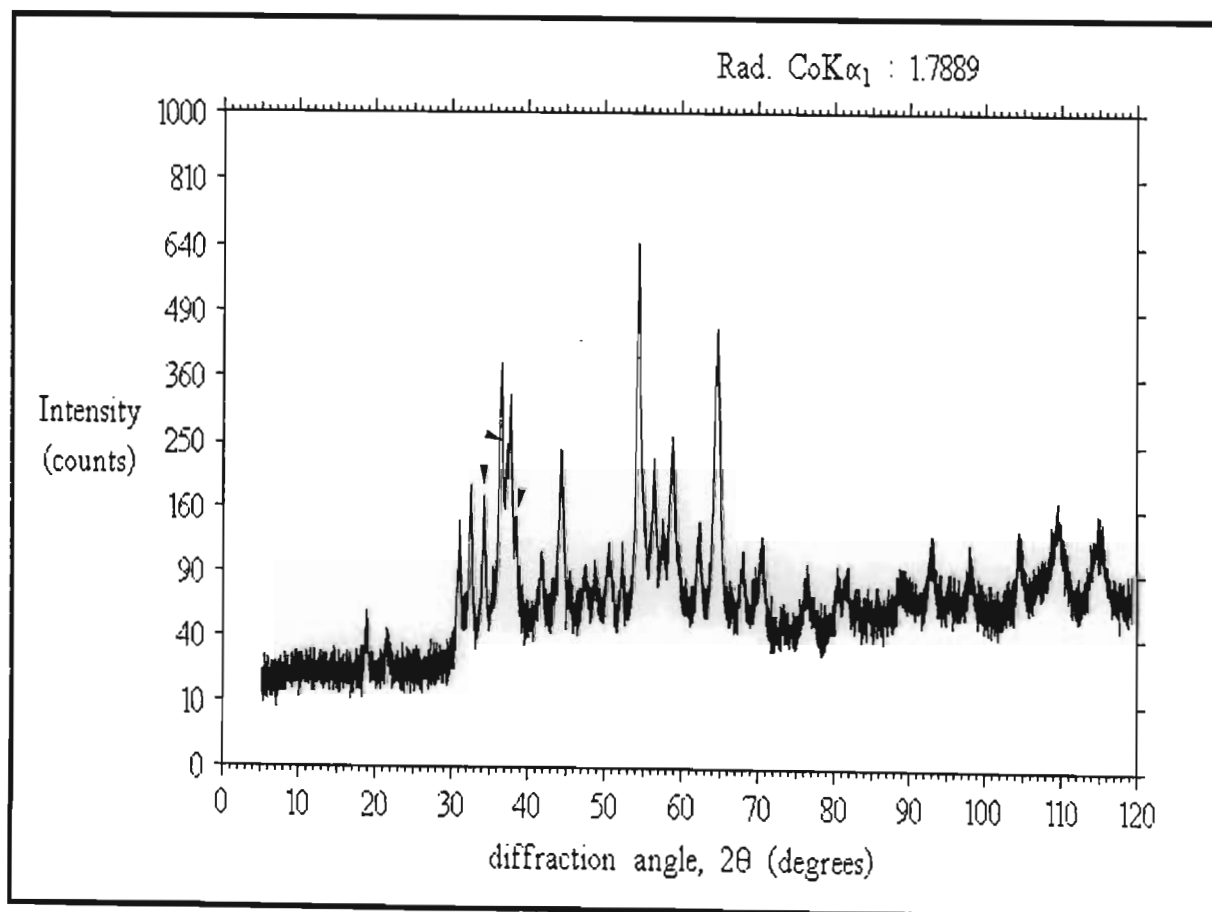
First stage leach residue [2]   Card number : BP-048
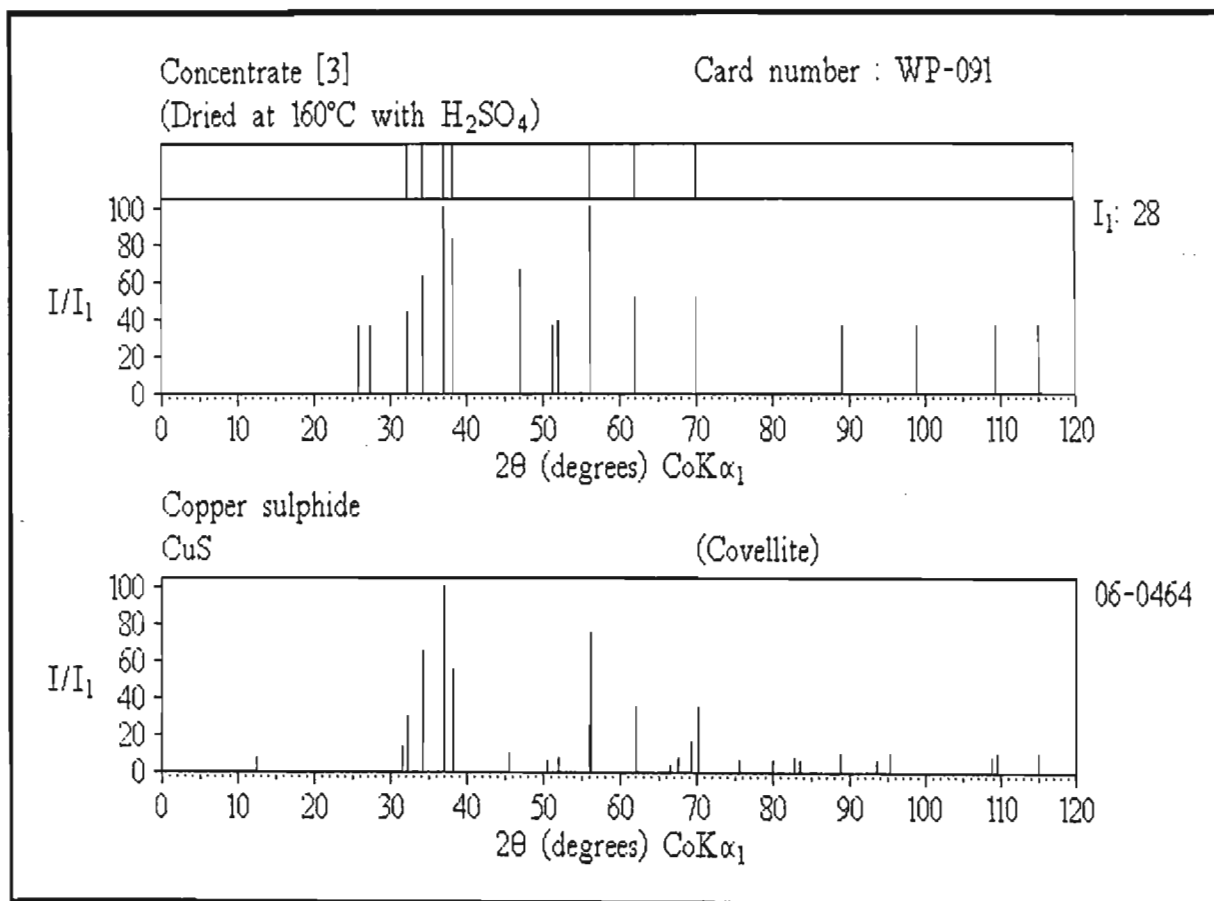(after a 3 hour H_2SO_4 leach)

I_1: 552

I/I_1

2θ (degrees) $CoK\alpha_1$

Copper sulphide
CuS   (Covellite)

06-0464

I/I_1

2θ (degrees) $CoK\alpha_1$

Figure 5.4.3-5(a)

Rad. $CoK\alpha_1$: 1.7889

Intensity
(counts)

diffraction angle, 2θ (degrees)

Figure 5.4.3-5(b)

Concentrate [3]   Card number : WP-091
(Dried at 160°C with H_2SO_4)

I_1: 28

I/I_1

2θ (degrees) CoKα_1

Copper sulphide
CuS   (Covellite)

06-0464

I/I_1

2θ (degrees) CoKα_1

Figure 5.4.3-6(a)

Rad. CoKα_1 : 1.7889
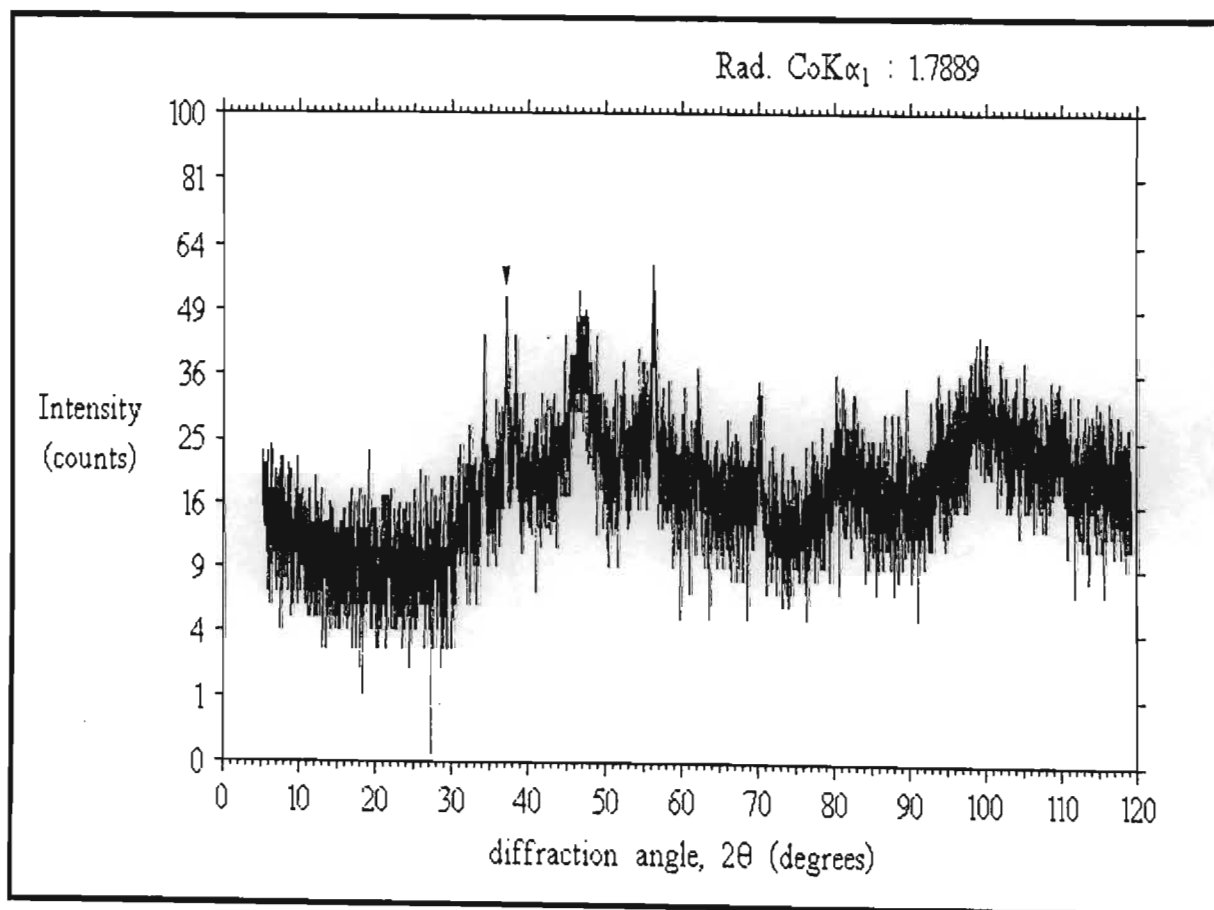
Intensity
(counts)

diffraction angle, 2θ (degrees)

Figure 5.4.3-6(b)

Figure 5.4.3-7(a)

Figure 5.4.3-7(b)

Concentrate [3]
(Dried at 260°C with H_2SO_4)

Card number : WP-103

I_1: 67

I/I_1

2θ (degrees) $CoK\alpha_1$

Copper sulphide
CuS   (Covellite)
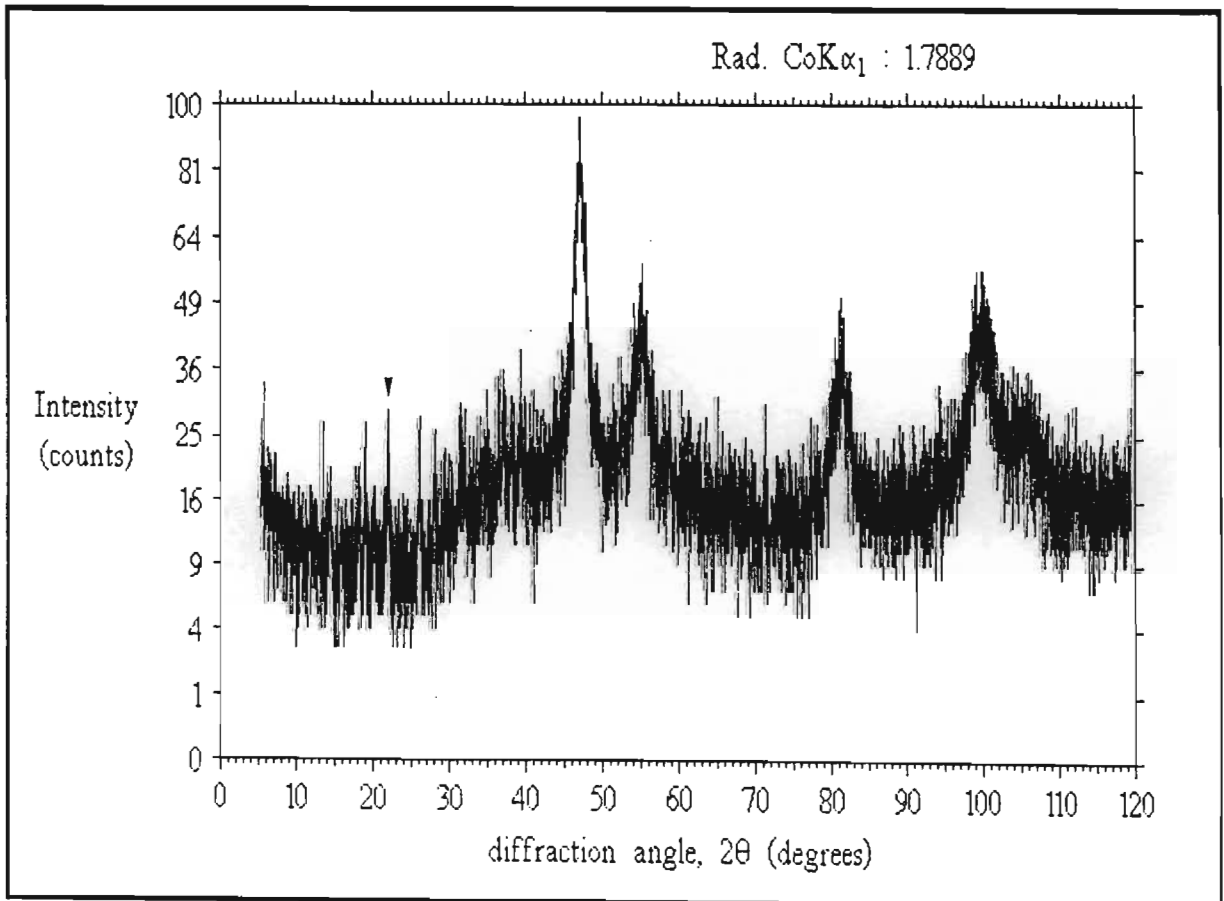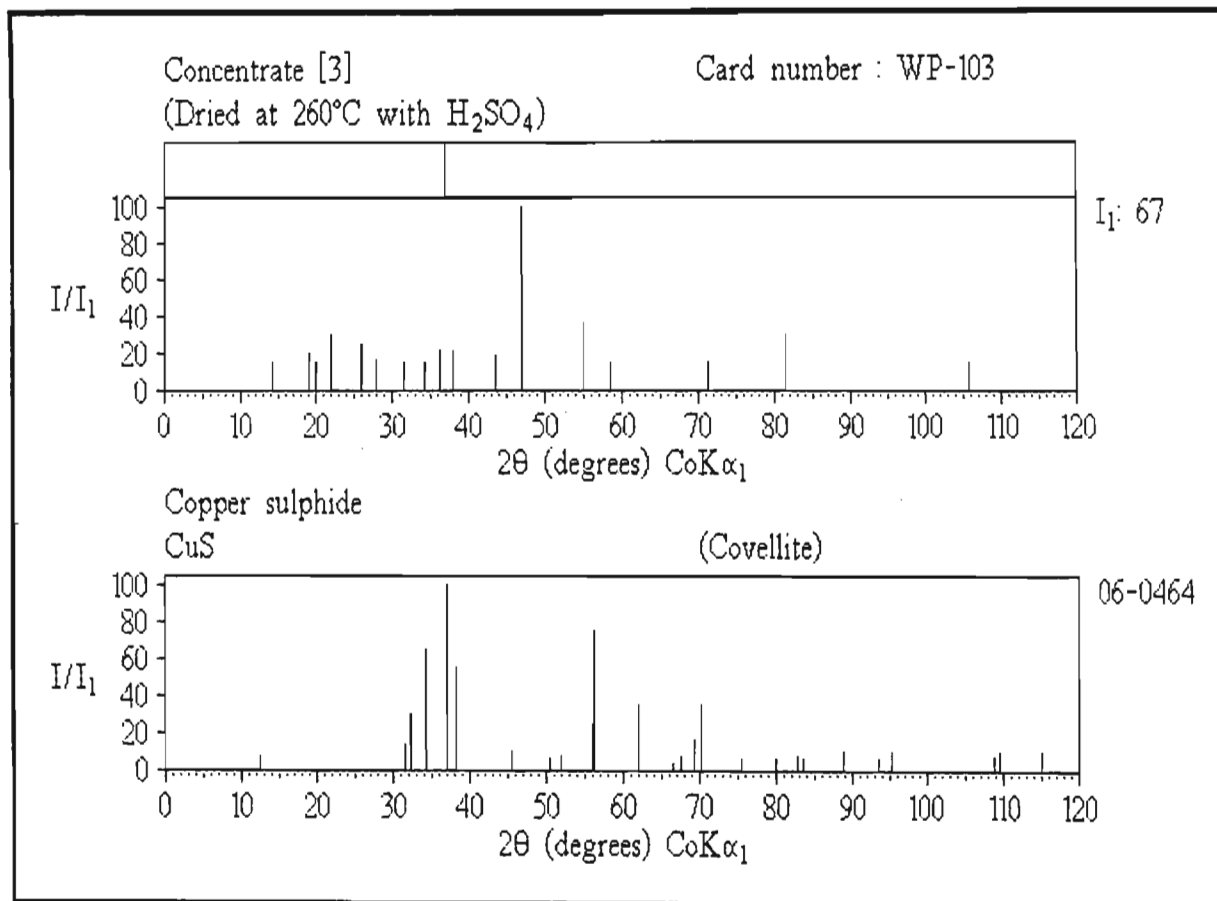
06-0464

I/I_1

2θ (degrees) $CoK\alpha_1$

Figure 5.4.3-8

Table 5.4.3-3 Comparison of CuS reference data with peaks observed for a normal concentrate

CuS Reference data [16]			Concentrate [3] † (WP-079) Observed data			Concentrate [3] ‡ (WP-091) Observed data		
d(Å)	(I/I$_1$)	2θ	d(Å)	(I/I$_1$)	2θ	d(Å)	(I/I$_1$)	2θ
3.220	(30)	32.3				3.223	(44)	32.2
3.048	(65)	34.1	3.048	(73)	34.1	3.045	(63)	34.2
2.813	(100)	37.1	2.813	(73)	37.1	2.812	(100)	37.1
2.724	(55)	38.3				2.728	(82)	38.3
1.896	(75)	56.3	1.897	(100)	56.3	1.896	(100)	56.3
1.735	(35)	62.1	1.735	(43)	62.1	1.735	(51)	62.1
1.556	(35)	70.2	1.556	(51)	70.2	1.557	(51)	70.1
1.280	(10)	88.7				1.277	(36)	89.0
1.0946	(10)	109.6				1.096	(36)	109.4
1.0607	(10)	115.0				1.060	(36)	115.1

† Dried at 160°C
‡ Dried at 160°C with H_2SO_4 (at 260°C, all these lines disappear)

Another rather interesting copper phase identified in a few samples was the copper-platinum alloy, Cu_3Pt. Figures 5.4.3-9(a) and (b), 5.4.3-10(a) and (b), and 5.4.3-11(a) and (b) show the scans and reduced spectra of three normal concentrate samples from different stages of the pre-treatment process (Note: the first sample has been selectively leached). Table 5.4.3-4 compares the observed data for these three samples with that of the reference compound.

Table 5.4.3-4 Comparison of Cu_3Pt reference data with peaks observed for three normal concentrates

Cu_3Pt Reference data [17]			Concentrate [1] Observed data			Concentrate [2] Observed data			Concentrate [3] Observed data		
d(Å)	(I/I$_1$)	2θ	d(Å)	(I/I$_1$)	2θ	d(Å)	(I/I$_1$)	2θ	d(Å)	(I/I$_1$)	2θ
2.14	(100)	49.4	2.150	(100)	49.2	2.129	(100)	49.7	2.149	(100)	49.2
1.85	(40)	57.8	1.861	(28)	57.5	1.845	(43)	58.0	1.858	(63)	57.6
1.31	(20)	86.1	1.318	(26)	85.5	1.303	(24)	86.7	1.309	(58)	86.2
1.12	(20)	106.0	1.125	(22)	105.3	1.113	(24)	107.0	1.121	(36)	105.8
1.07	(10)	113.4	1.077	(11)	112.3	-	-	-	1.068	(27)	113.8
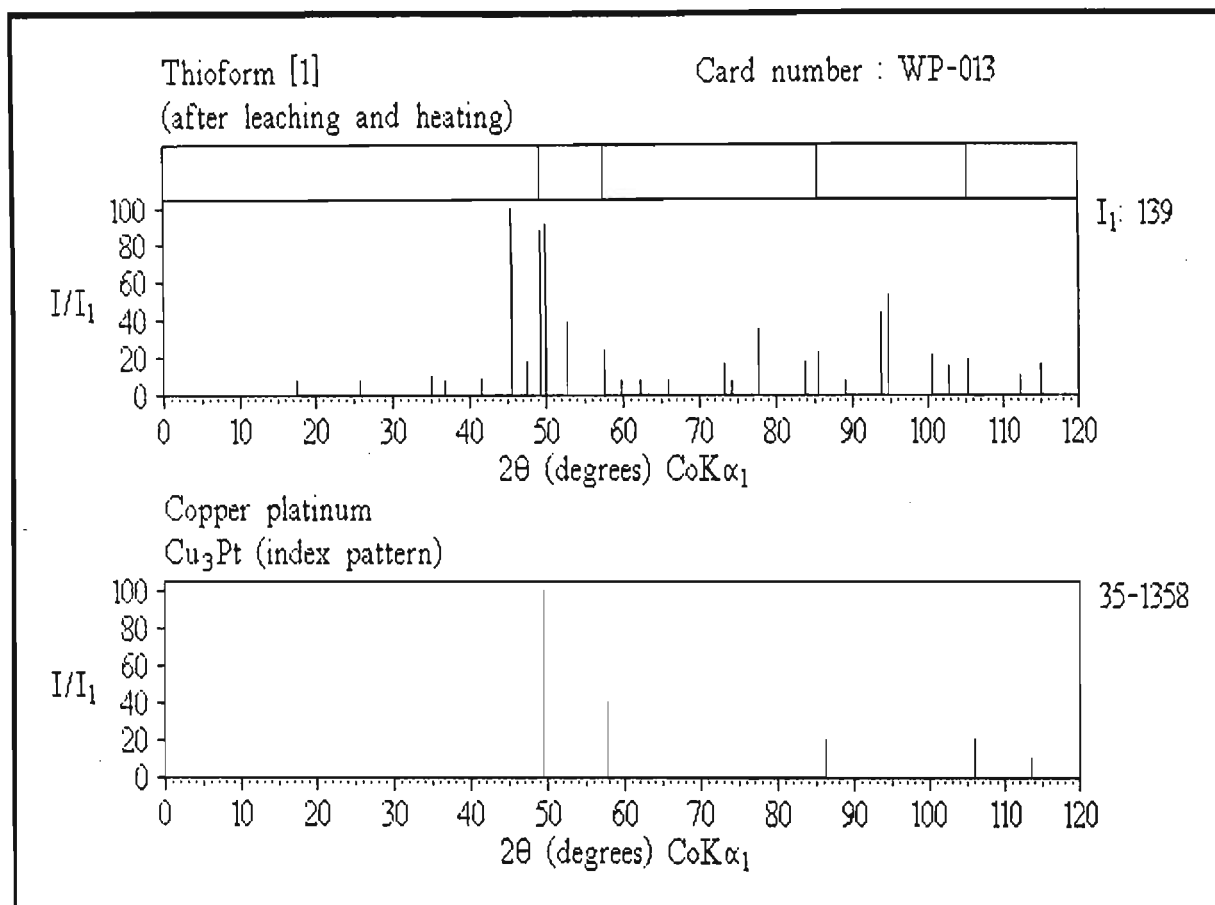
Figure 5.4.3-9(a)

Figure 5.4.3-9(b)

WPR [1]   Card number : WP-073

Copper platinum
Cu$_3$Pt (index pattern)

Figure 5.4.3-10(a)

Rad. CoKα_1 : 1.7889

Figure 5.4.3-10(b)

Concentrate [6]
(Dried at 110°C)

Card number : WP-082

I_1: 40

2θ (degrees) CoKα₁

Copper platinum
Cu₃Pt (index pattern)

35-1358

2θ (degrees) CoKα₁

Figure 5.4.3-11(a)

Rad. CoKα₁ : 1.7889

Intensity
(counts)

diffraction angle, 2θ (degrees)
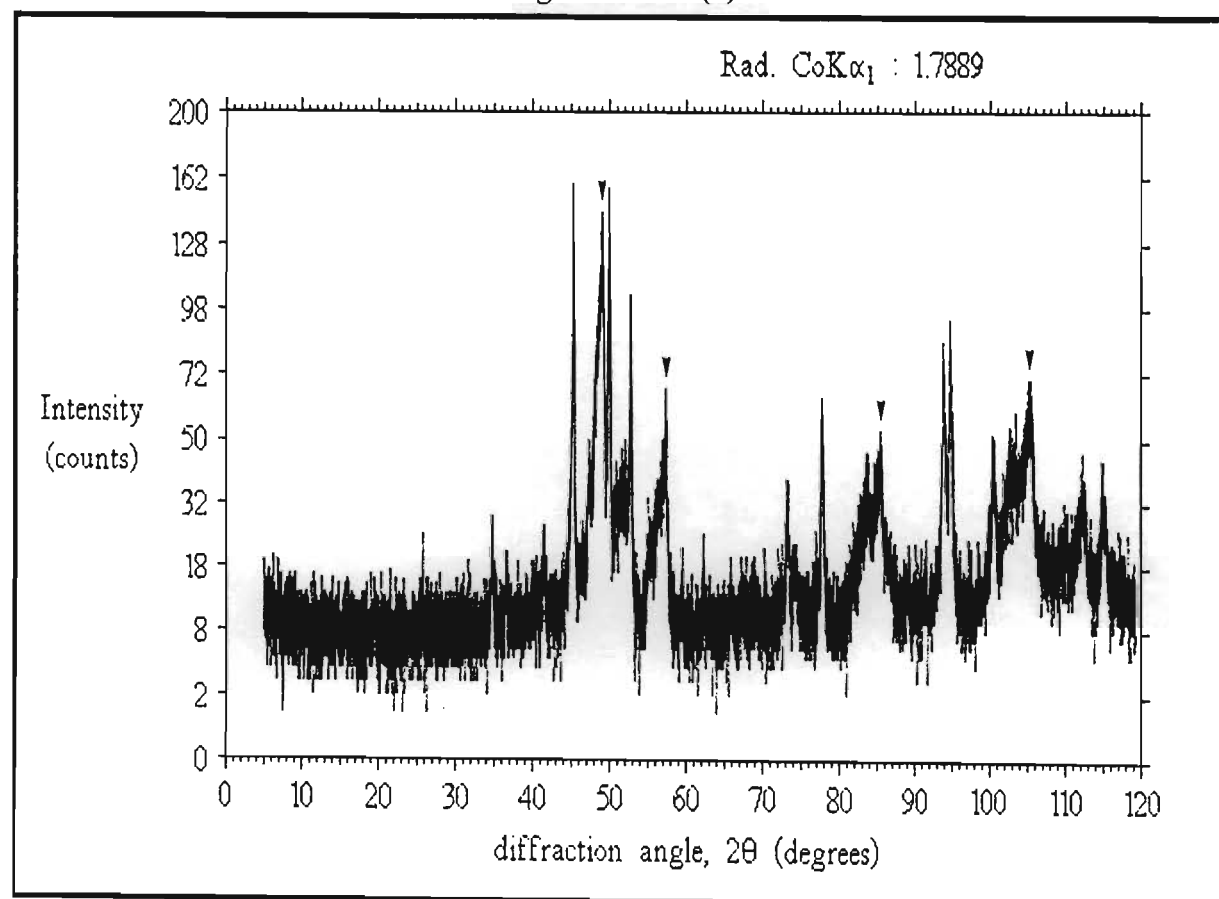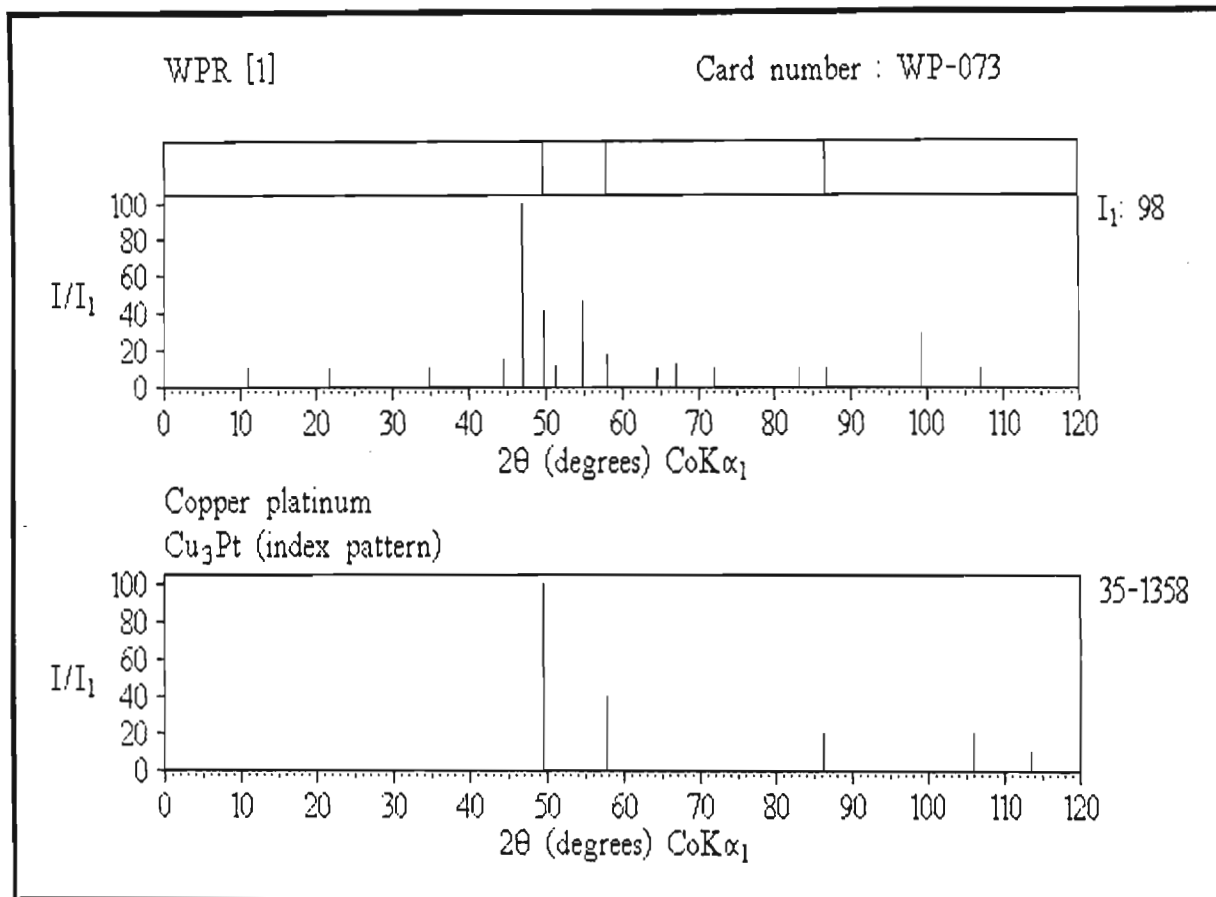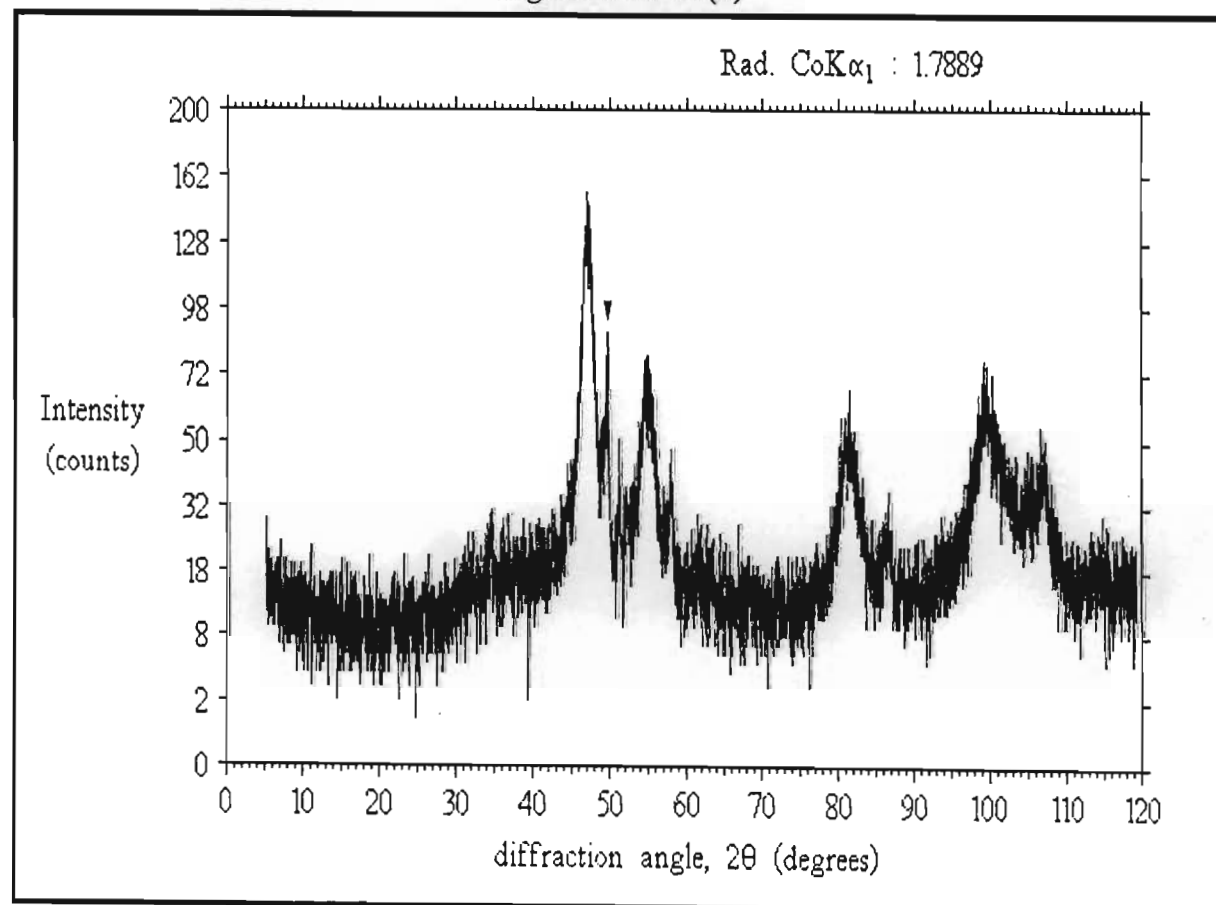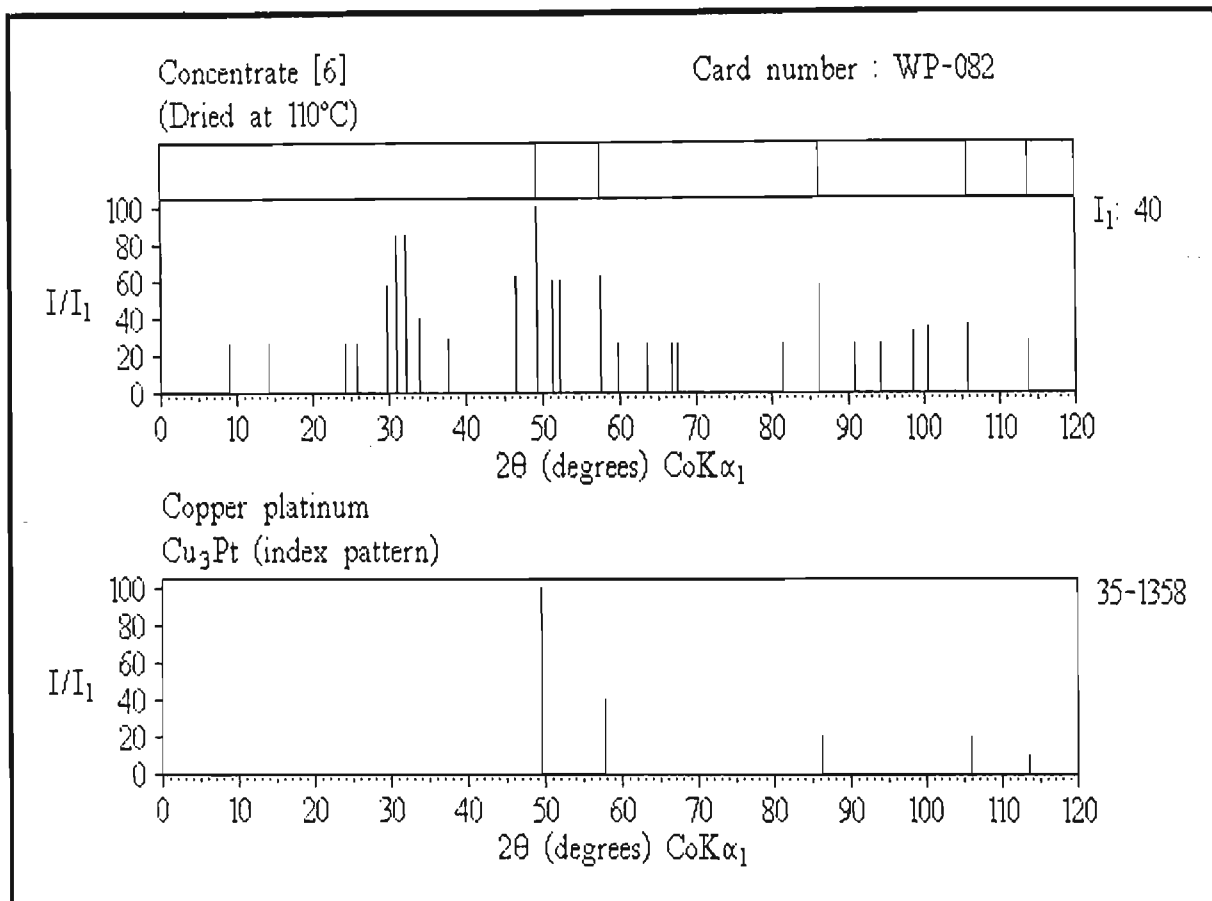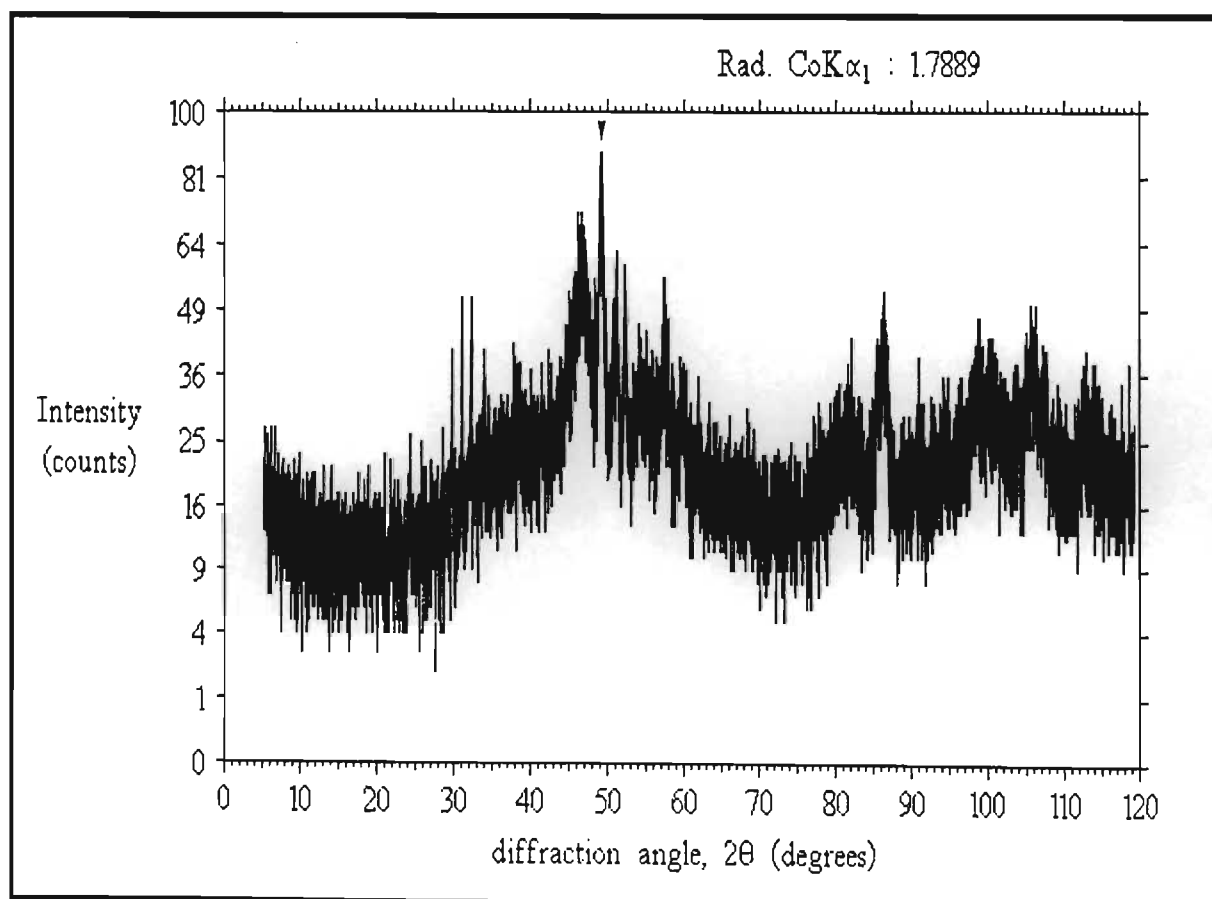
Figure 5.4.3-11(b)

In Table 5.4.3-4, Concentrate [1] is from the pre-treatment process and has been selectively leached and dried. Concentrate [2] is also from the pre-treatment process. Concentrate [3] is as received from the BMR.

(Sample numbers : [1] WP-013   [2] WP-073   [3] WP-082)

Several observations on the data and scans can be made. Firstly, the peaks are unusually asymmetric, flaring towards higher d-spacings (lower 2θ values). This is due to disorder in the alloy and indicates relatively fast cooling. Such disorder has been observed for similar alloys (eg. Cu_3Au, Cu_3Pd and Ni_3Fe) [18] which all pack face-centred cubic. The ideally ordered alloy has platinum atoms at the corners of the cubic cell and copper atoms at the centre of each face.

Secondly, the variability in the position of the lines points to variable stoichiometry. Although a similar palladium alloy of identical formula exists, the pattern differs in having stronger peak intensities and additional lines. **Table 5.4.3-5** compares the XPD reference data for these two compounds. Clearly, it should be concluded that the alloy contains very little, if any palladium, and that shifts are due to variable stoichiometry (*ie.* $Cu_{3\pm x}Pt$) rather than the inclusion of palladium.

Table 5.4.3-5   Comparison of Cu₃Pt and Cu₃Pd reference data

Cu₃Pt Reference data [17]			Cu₃Pd Reference data [19]			
d(Å)	(I/I₁)	2θ	d(Å)	(I/I₁)	2θ	
2.14	(100)	49.4	2.13	(100)	49.7	
1.85	(40)	57.8	1.86	(90)	57.5	
			1.83	(80)	58.5	not observed
1.31	(20)	86.1	1.31	(90)	86.1	
			1.30	(90)	87.0	not observed
1.12	(20)	106.0	1.12	(100)	106.0	
1.07	(10)	113.4	1.07	(90)	113.4	

The copper-platinum alloy is probably formed around the nickel-copper alloy crystals in fast cooled mattes. Fast cooling produces nickel-copper alloy crystals having nickel-rich cores and copper-rich faces (§ 4.7.1). Platinum, because of its size and factors to be covered later, is the pgm which is taken up by the nickel-copper alloy with the greatest difficulty. Movement from the molten sulphide phase is slow. The combination of fast cooling and the slow inclusion into the alloy would favour the formation of a copper-platinum alloy around each crystal. **Figure 5.4.3-12** illustrates the idea.

Ni$_3$S$_2$ matrix + Pt sulphide
Cu$_3$Pt alloy layer
Copper-rich zone
Nickel-rich zone
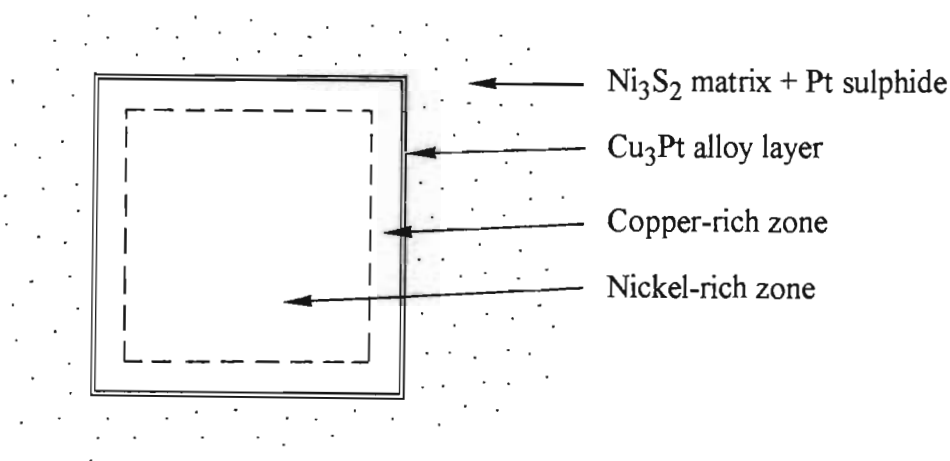
Figure 5.4.3-12 Possible origin of the Cu$_3$Pt alloy

Table 5.4.3-6 lists the copper compounds encountered in pgm extraction, their occurence and suggested methods of removal.

Table 5.4.3-6 COPPER compounds occurring in pgm extraction

Compound	Occurrence and removal
CuSO$_4$·5H$_2$O	Normal concentrates (common) *water wash*
Cu$_4$SO$_4$(OH)$_6$·H$_2$O	Normal concentrates (rare) *water (or dilute acid) wash*
CuS	Normal concentrates (occasionally observed) *moisten concentrate with H$_2$SO$_4$ (20 g/l) and heat to 260°C (wash with water after cooling)*
Cu$_3$Pt alloy	Normal / pre-treated concentrates (occasionally observed) *HCl/Cl$_2$ soluble*

5.5 OXIDATIVE LEACH PROBLEMS

5.5.1 INTRODUCTION

After pre-treatment, the concentrate is oxidatively leached using 6M hydrochloric acid and chlorine gas at elevated temperatures. The aim is to solubilise 100% of each precious metal. This is seldom achieved in practice. **Table 5.5.1-1** gives typical solubility ranges for the pgms encountered in the refinery under study.

Table 5.5.1-1 PGM solubility in the oxidative HCl/Cl_2 leach

Element	NORMAL CONCENTRATES Typical solubility range [†]	MINOR CONCENTRATES Typical solubility range [†]
Platinum	95.6 - 99.9 %	85.1 - 89.4 %
Palladium	96.7 - 99.9 %	66.9 - 90.1 %
Rhodium	80.1 - 99.2 %	2.0 - 90.1 %
Iridium	84.6 - 97.7 %	8.5 - 24.8 %
Ruthenium	76.7 - 98.9 %	0.6 - 88.8 %

[†] Minimum - maximum solubilities measured over a five month period

The above table shows that in some cases pgm solubility is unbelievably low, especially in the case of minor concentrates. In order to explain the solubility problems illustrated above, concentrates and residues showing low and high pgm solubility were examined by XPD and the analyses compared.

5.5.2 LOW RUTHENIUM SOLUBILITY

On dissolution of the nickel-copper alloy, a pgm residue is produced that gives broad diffraction peaks at the d-spacings given and assigned in **Table 5.5.2-1**. Platinum, palladium, rhodium and iridium all exhibit face-centred cubic packing. Their diffraction peaks are thus very similar. When occurring together, the averaging effect of the combined peaks of differing intensity results in broad peaks at d-spacings very similar to

those of palladium, with a maximum peak at about 2.25Å. Ruthenium and osmium however both pack according to the hexagonal system and so the maximum intensity peak occurs at a different d-spacing (about 2.07Å or 51.3°).

Table 5.5.2-1   Typical normal concentrate diffraction peaks

Observed diffraction peaks				Assignment
d(Å)	(I/I$_1$)	2θ	(hkl)	
2.252	(100)	46.9	(111)	[platinum + palladium + rhodium + iridium]
1.947	(46)	54.6	(200)	[platinum + palladium + rhodium + iridium]
1.380	(34)	80.8	(220)	[platinum + palladium + rhodium + iridium]
1.179	(39)	98.7	(311)	[platinum + palladium + rhodium + iridium]
1.128	(12)	104.9	(222)	[platinum + palladium + rhodium + iridium]
2.066	(0 - 100)	51.3	(101)	[ruthenium + osmium]

Figures 5.5.2-1 and **5.5.2-2** show two diffraction scans of typical concentrates, with the [ruthenium + osmium] **(101)** peak arrowed. Examination of the scans from numerous normal concentrates revealed that this peak is usually of high intensity and in some cases dominates all others (although the levels of ruthenium never exceeds that of platinum). This indicates that relative to the cubic pgms, the [ruthenium + osmium] metallic phase has a higher degree of crystallinity.

In almost every case residual highly crystalline metallic ruthenium was found to be responsible for low ruthenium solubility in normal concentrates. **Table 5.5.2-2** compares XPD reference data for ruthenium metal with observed data. All observed peaks are shifted to lower diffraction angles.

Examination of the peak scans and reduced patterns of two HCl/Cl$_2$ leach residues (**Figures 5.5.2-3(a)** and **(b)**, and **5.5.2-4(a)** and **(b)**) shows that in both cases peaks are shifted to lower diffraction angles.
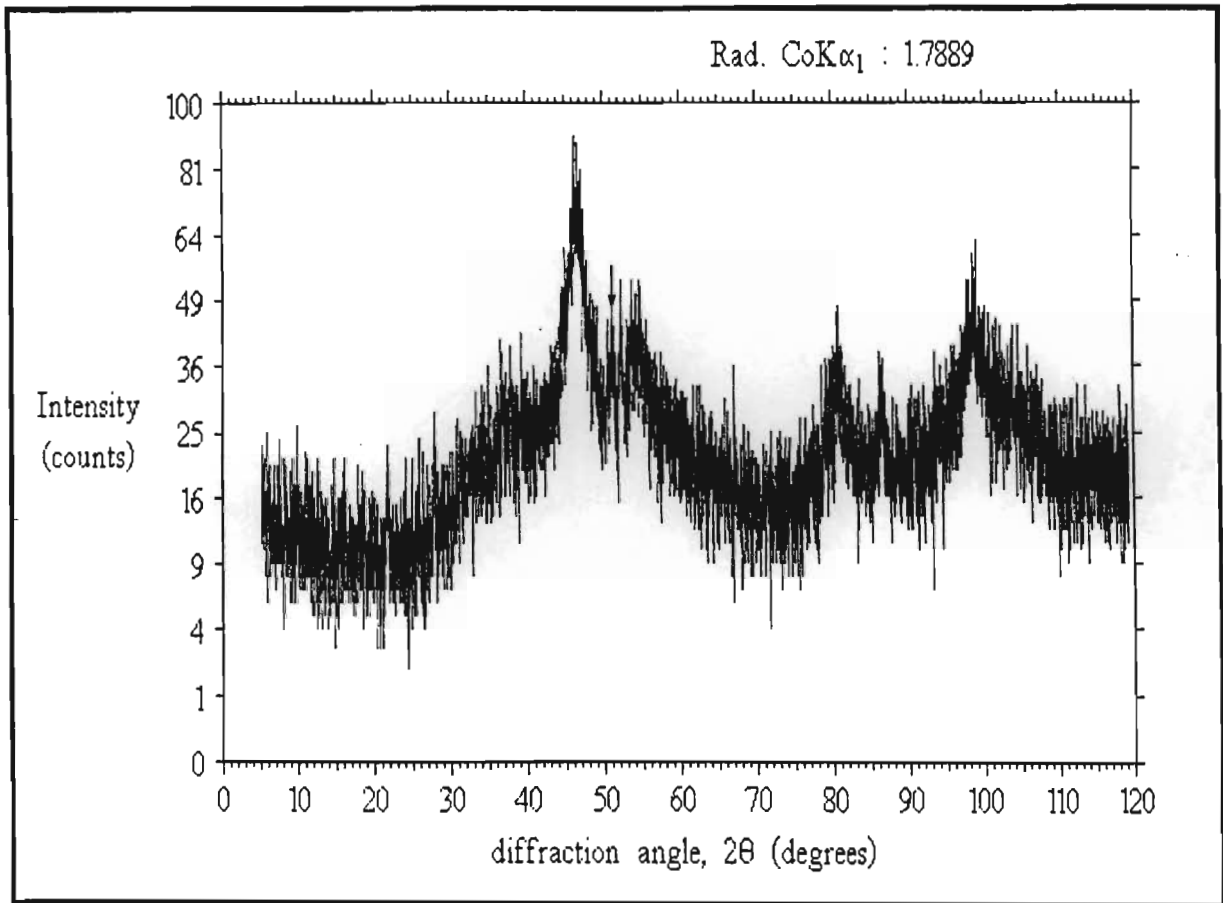
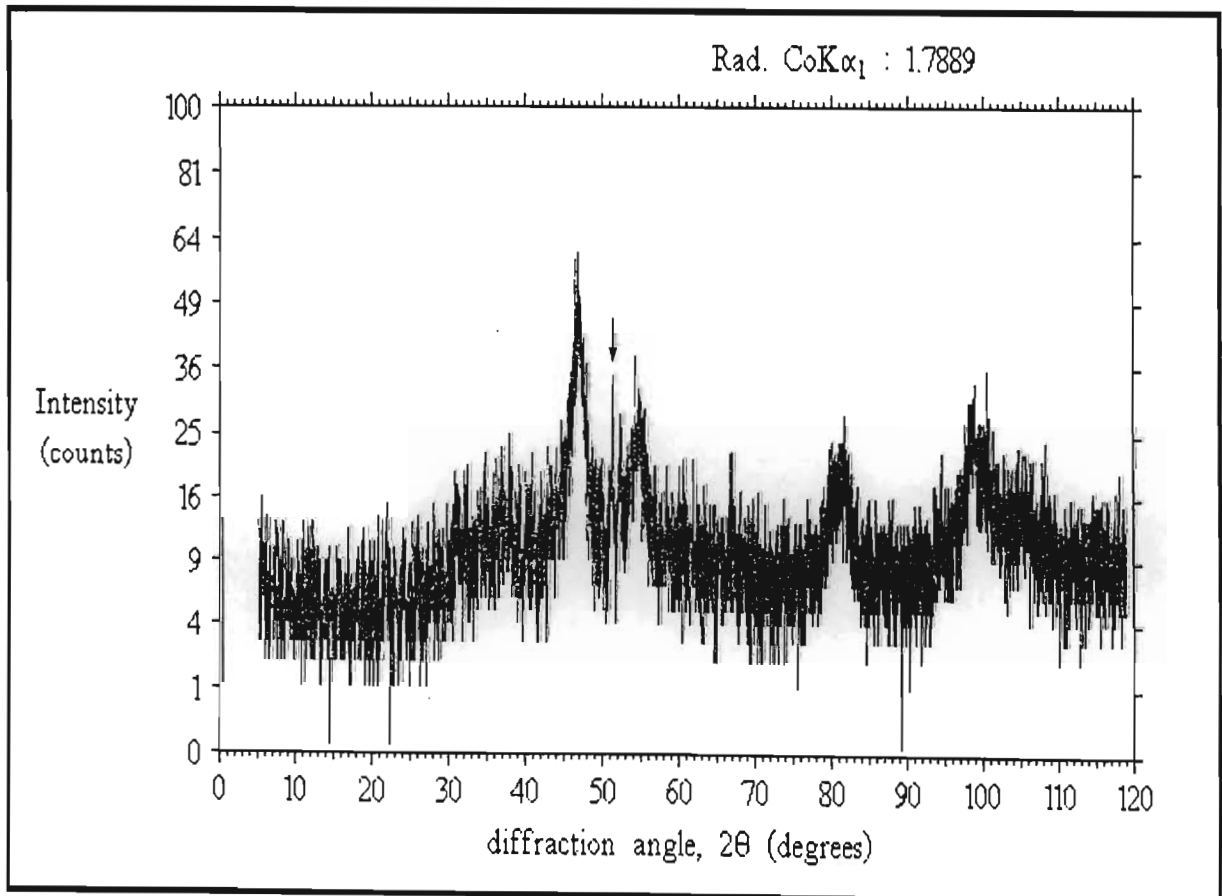**Figure 5.5.2-1** XPD scan of a normal concentrate showing the [Ru+Os] **(101)** peak

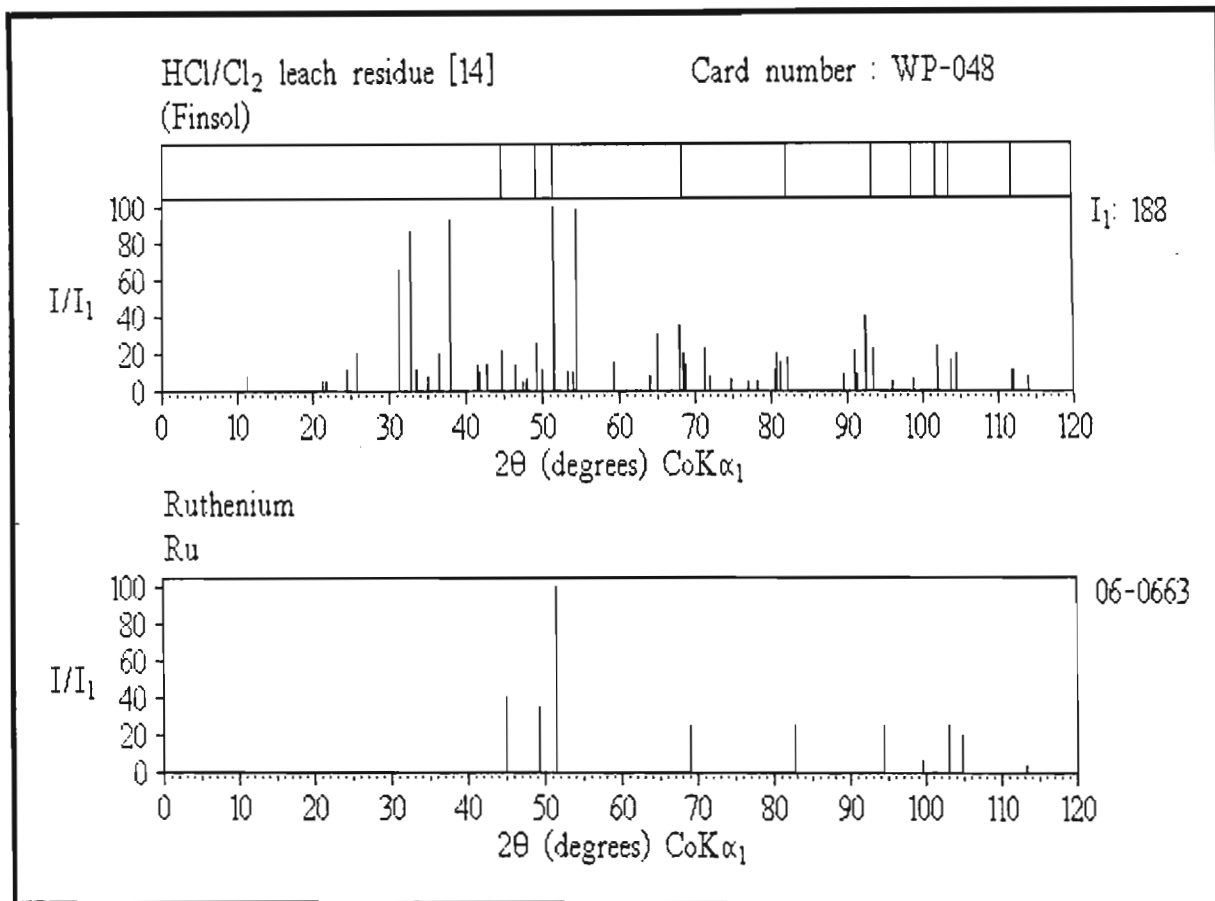**Figure 5.5.2-2** XPD scan of a normal concentrate showing the [Ru+Os] **(101)** peak
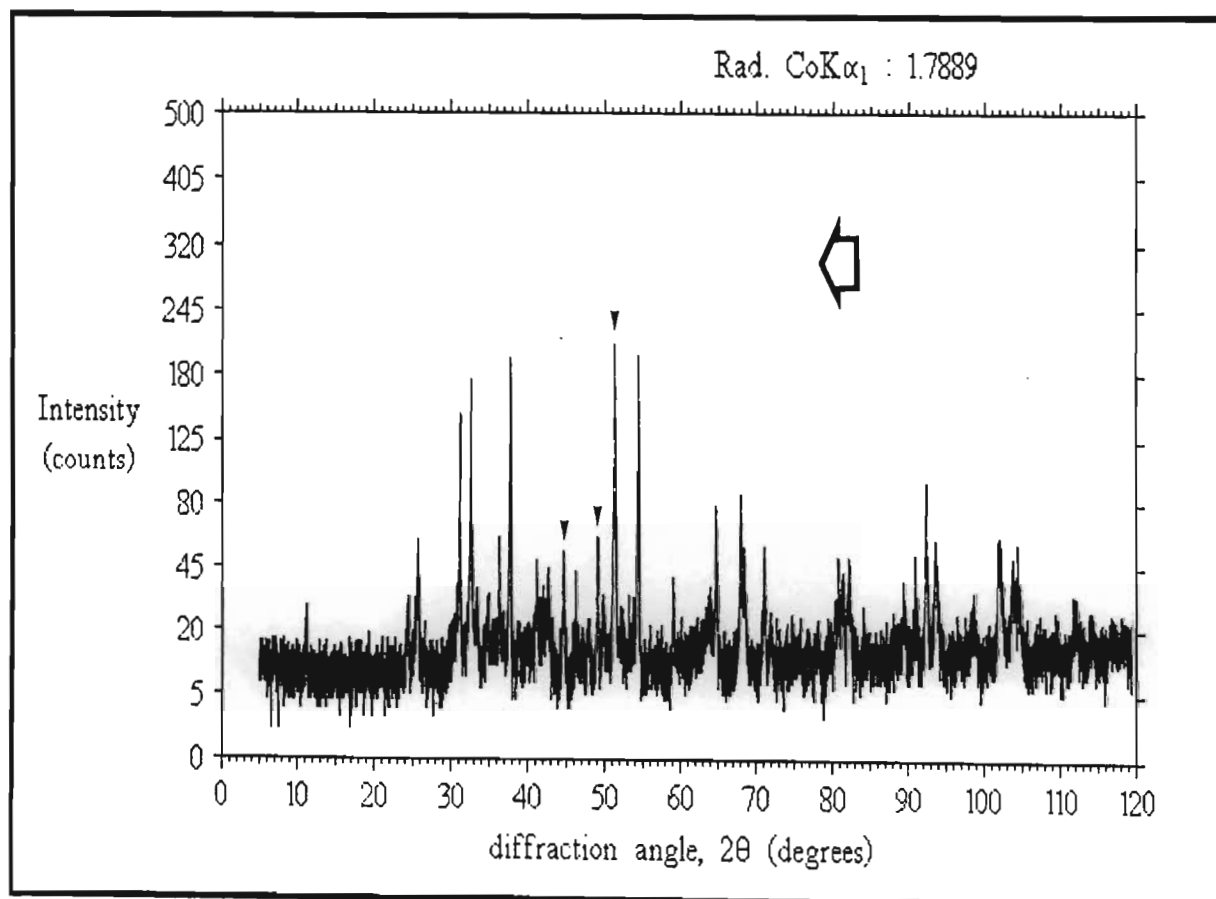
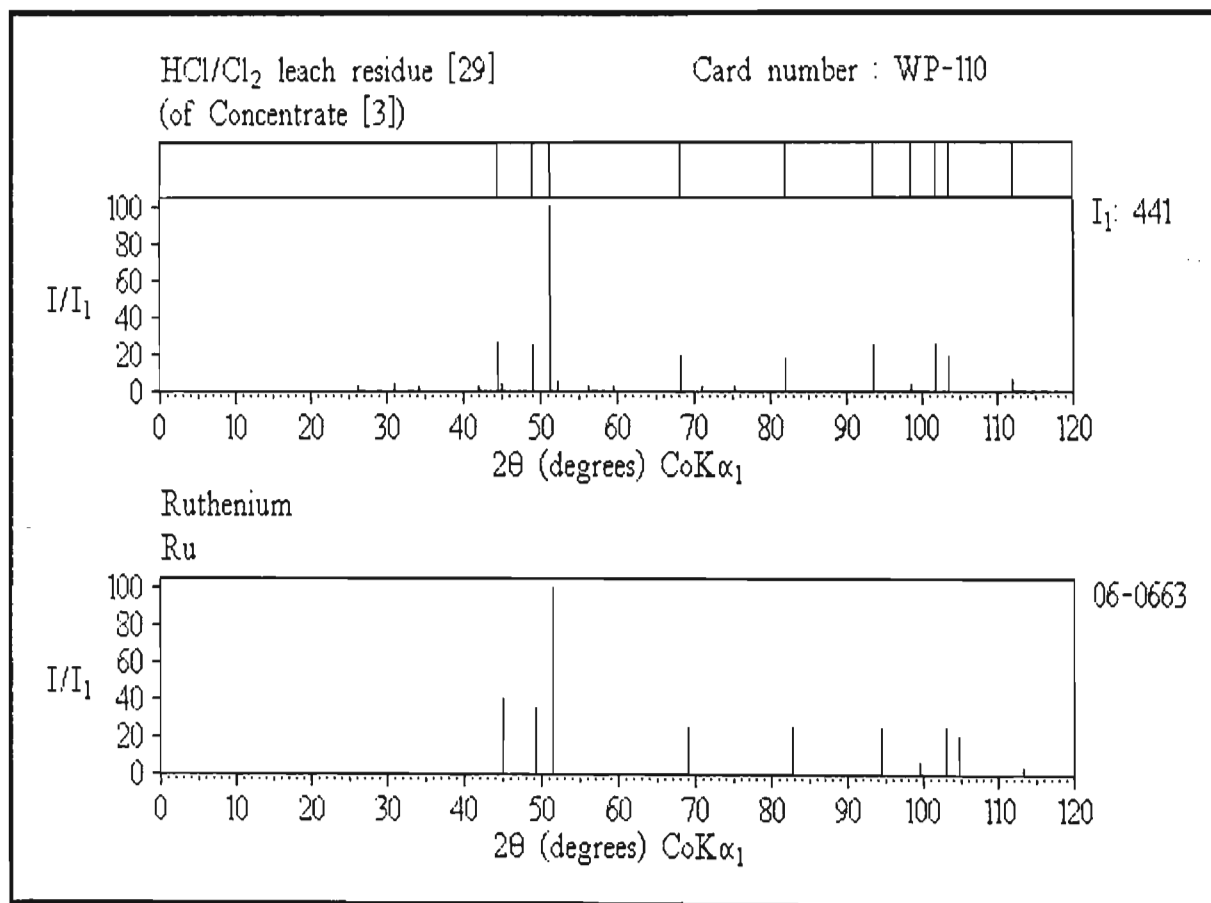**Figure 5.5.2-3(a)**
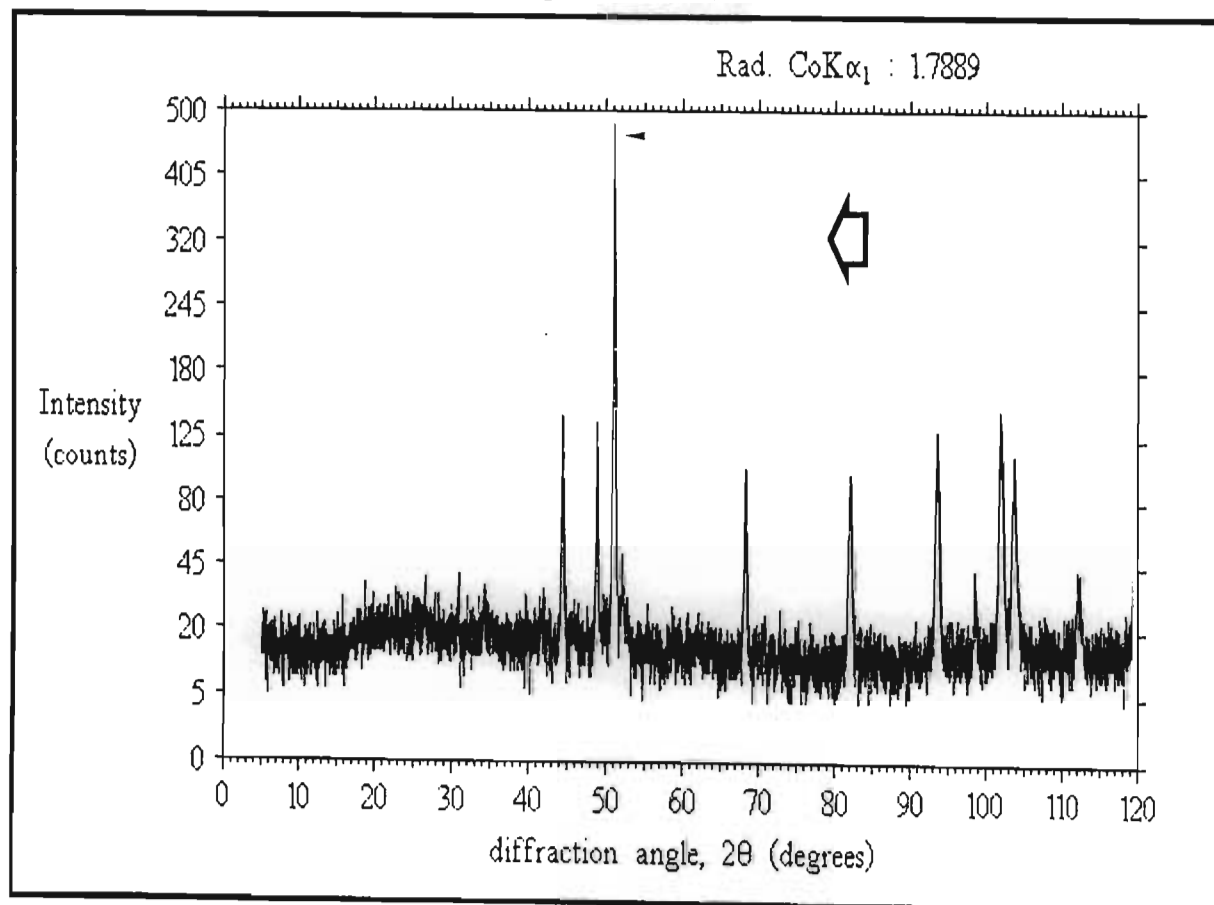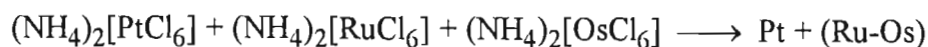

Figure 5.5.2-3(b)

Figure 5.5.2-4(a)

Figure 5.5.2-4(b)

**Table 5.5.2-2   Comparison of Ru reference data with peaks
observed for a normal concentrate HCl/Cl$_2$ residue**

Ru Reference data [20]			HCl/Cl$_2$ reidue [14] (WP-048) Observed data			Deviation	
d(Å)	(I/I$_1$)	2θ	d(Å)	(I/I$_1$)	2θ	Δd(Å)	Δ2θ(°)
2.343	(40)	44.9	2.346	(21)	44.8	+ 0.003	- 0.1
2.142	(35)	49.4	2.145	(25)	49.3	+ 0.003	- 0.1
2.056	(100)	51.6	2.061	(100)	51.4	+ 0.005	- 0.2
1.5808	(25)	68.9	1.588	(20)	68.6	+ 0.007	- 0.3
1.3530	(25)	82.8	1.360	(17)	82.3	+ 0.007	- 0.5
1.2189	(25)	94.4	1.227	(23)	93.6	+ 0.008	- 0.8
1.1715	(6)	99.6	1.178	(6)	98.7	+ 0.007	- 0.9
1.1434	(25)	102.9	1.152	(23)	101.9	+ 0.009	- 1.0
1.1299	(20)	104.7	1.137	(17)	103.7	+ 0.007	- 1.0
1.0705	(4)	113.3	1.081	(11)	111.7	+ 0.010	- 1.6

Figure 5.5.2-5 shows that the peaks of the second residue show an almost exact fit with osmium rather than ruthenium (note the high crystallinity of this sample).   An elemental analysis, performed using a scanning electron microscope, indicated a ruthenium-osmium alloy of approximately 11wt% osmium. (~Ru$_{16}$Os).   These elements are mutually soluble at all compositions [21], and so an alloy is not unexpected.   Very slow scans (1° per minute), run on another diffractometer (CoKα radiation), showed no line splitting (except when peak intensities were very low, when splitting results from poor crystallinity).   Instead a single sharp **(101)** peak was obseved at 2.067Å for one sample, almost midway between the d-spacings of the (101) lines of ruthenium (2.056Å) and of osmium (2.076Å).   **(Figure 5.5.2-6)**

It was thus concluded that this insoluble phase was a highly crystalline ruthenium-osmium alloy, generally with low levels of osmium.   Such an alloy would be highly inert.   Small amounts could be generated during ignitions of impure ammonium hexachloroplatinate(IV) to platinum sponge, which are carried out at high temperatures.
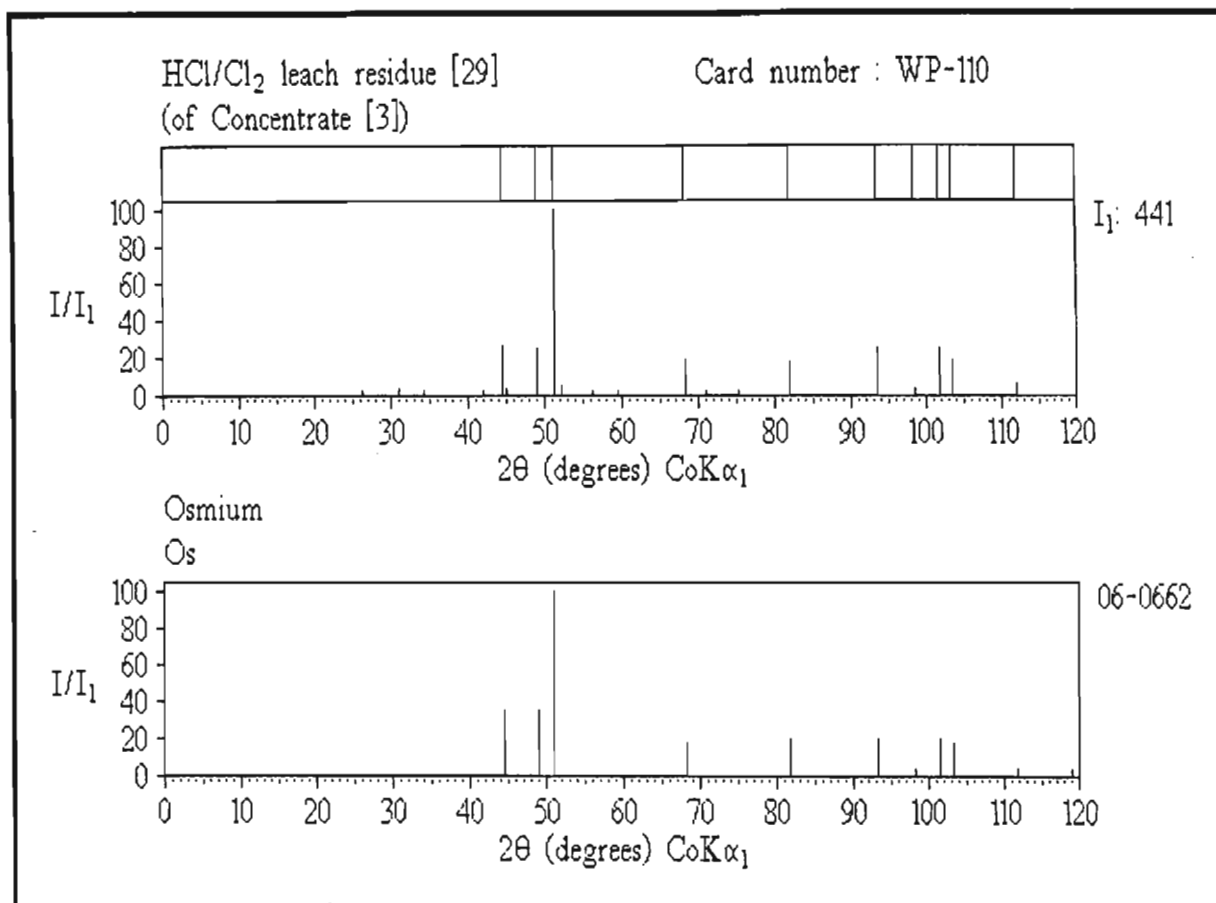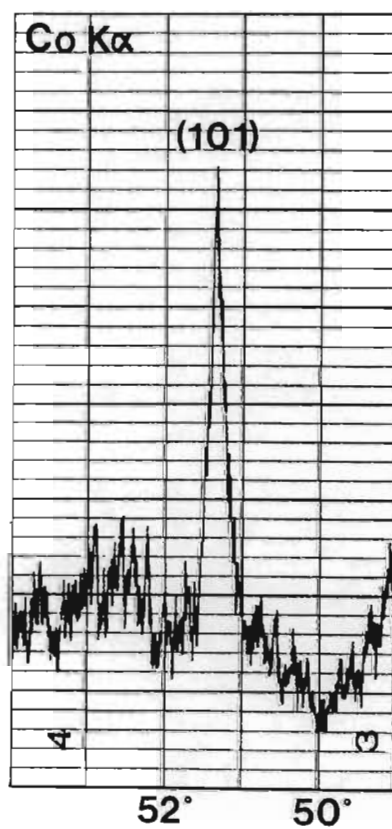
$$(NH_4)_2[PtCl_6] + (NH_4)_2[RuCl_6] + (NH_4)_2[OsCl_6] \longrightarrow Pt + (Ru\text{-}Os)$$

Figure 5.5.2-5

Figure 5.5.2-6 Expanded scan of the Ru-Os alloy **(101)** peak

Traces of ruthenium and osmium can be coprecipitated with $(NH_4)_2[PtCl_6]$ [22]. On redissolution of platinum, an insoluble residue of Ru-Os alloy remains and on recycling would appear in oxidative leach residues.

A second ruthenium phase causing low solubility was ruthenium oxide, RuO_2. Generally this phase is rarely observed in normal concentrates. When encountered, it indicates that overdrying at the base metal refinery has resulted in the reaction :

$$Ru + O_2 \longrightarrow RuO_2$$
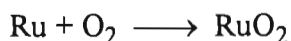
This reaction is rapid when the metal is finely divided (as in concentrates) [23], and favoured by the extreme stability of the oxide, which has a distorted rutile-type structure [24] similar to titanium dioxide, TiO_2. The product is however actually oxygen-deficient, *ie.* RuO_{2-x} [25].

A correctly dried normal concentrate was found to give 15 to 50 counts for the maximum peak. Overdrying leads to sintering and this is reflected in an increase in the number of counts recorded for the maximum peak. One overdried normal concentrate, giving 282 counts for the maximum peak, is shown in **Figure 5.5.2-7(a)** and **(b)**. As indicated, most of the metallic ruthenium has been oxidized. This oxide is not attacked in the oxidative leach, and substantial quantities are detectable in the residue. Such a residue is shown in **Figure 5.5.2-8(a)** and **(b)** with the RuO_2 peaks indicated.

Table 5.5.2-3 compares ruthenium oxide reference data with the oxide phase found in an overdried normal concentrate and its leach residue (values in boldface indicates overlap with another phase).
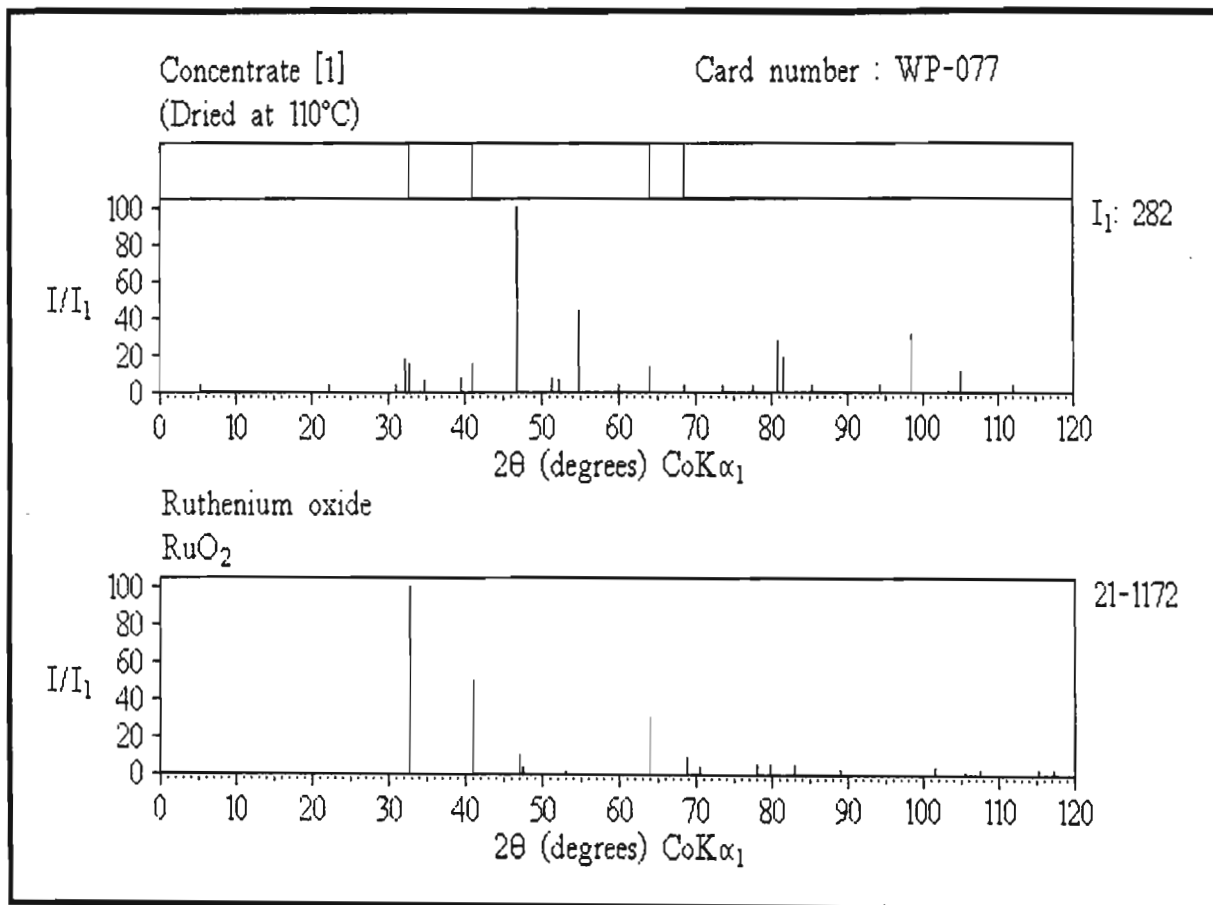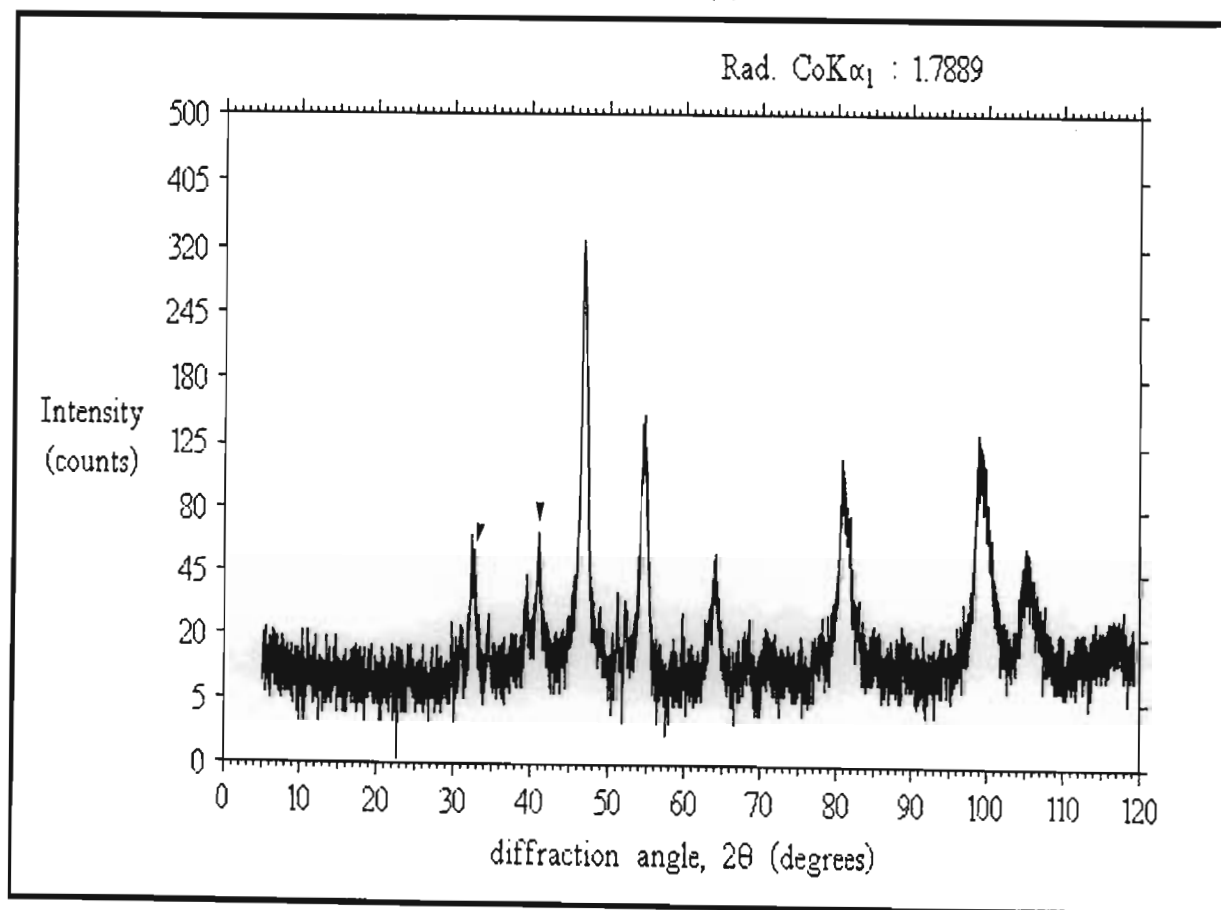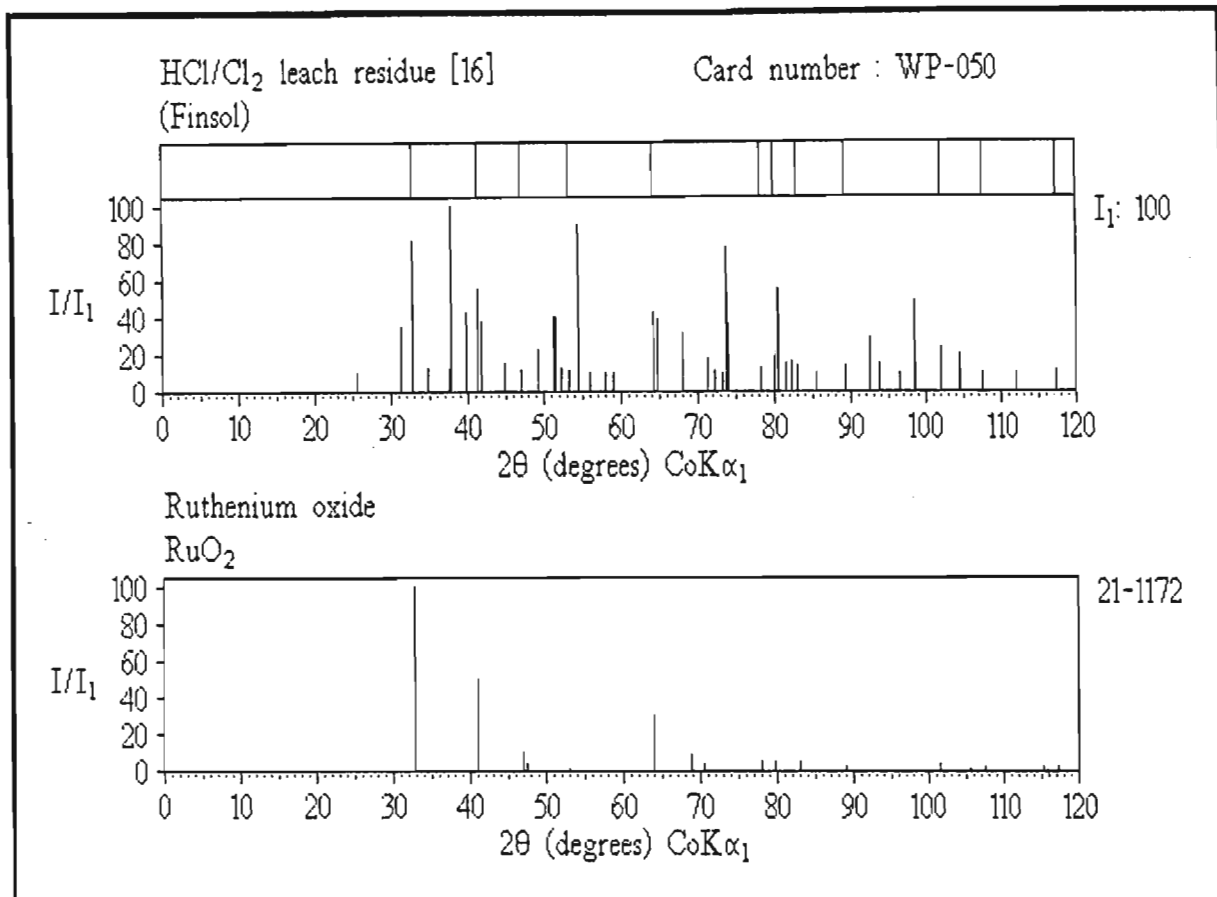
Figure 5.5.2-7(a)
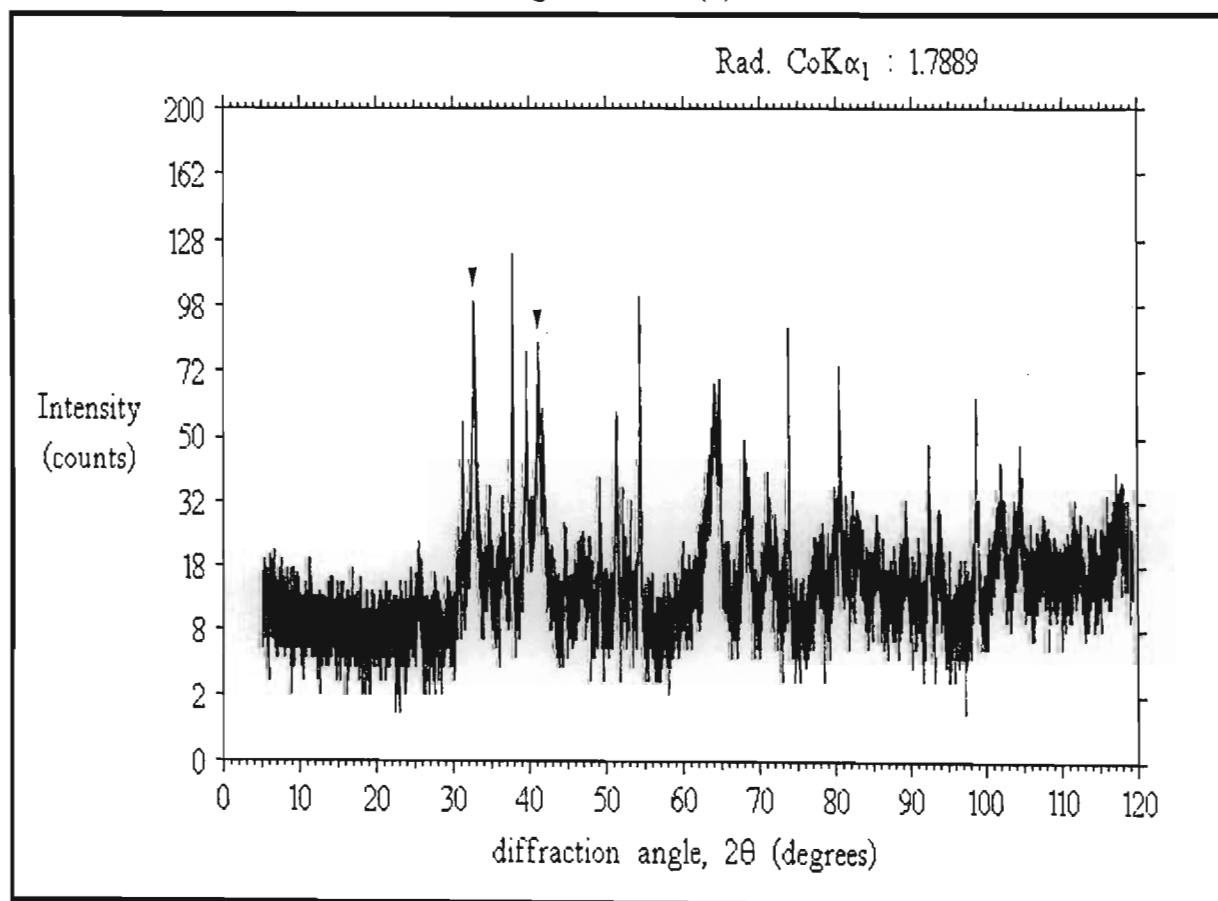

Figure 5.5.2-7(b)

Figure 5.5.2-8(a)

Figure 5.5.2-8(b)

Table 5.5.2-3 **Comparison of RuO₂ reference data with peaks observed for a normal concentrate and leach residue**

RuO₂ Reference data [26]			N-CONCENTRATE (WP-077) Observed data			HCl/Cl₂ RESIDUE (WP-107) Observed data		
d(Å)	(I/I₁)	2θ	d(Å)	(I/I₁)	2θ	d(Å)	(I/I₁)	2θ
3.17	(100)	32.8	3.178	(100)	32.7	3.149	(74)	33.0
2.550	(50)	41.1	2.557	(100)	41.0	2.539	(100)	41.2
2.243	(10)	47.0	**2.250**	**(-)**	**46.9**	2.236	(32)	47.1
1.685	(30)	64.1	1.688	(87)	64.0	1.683	(85)	64.2
1.586	(9)	68.7	1.588	(27)	68.5	1.588	(27)	68.6
1.552	(4)	70.4				1.543	(14)	70.9
1.4200	(5)	78.1				1.418	(16)	78.2
1.3943	(5)	79.8				1.394	(21)	79.9
1.3491	(5)	83.1				1.351	(24)	83.0
1.2770	(2)	88.9				1.276	(11)	89.0
1.1559	(4)	101.4				1.159	(21)	101.0
1.1097	(3)	107.4				1.108	(12)	107.6
1.0585	(2)	115.4				1.048	(17)	117.1

Ruthenium oxide was found to be a constant problem in minor concentrates. This is expected, because, after the pgms are precipitated from the copper pressure leach solution using sulphur dioxide gas, the filter cake is roasted at about 700°C in air to volatilize selenium (§ 4.3.4). Ruthenium, being in an even finer state of division than in normal concentrates, oxidises almost completely. Consequently, oxidative leach ruthenium solubility for minor concentrates can be as low as 0.6%.

Figure 5.5.2-9(a) and **(b)** shows RuO₂ as detected in a minor concentrate.

Figure 5.5.2-10(a) and **(b)** shows RuO₂ as detected in the leach residue of this concentrate.

Table 5.5.2-4 compares RuO₂ reference data with the oxide data observed for a minor concentrate and residue. Note that many more RuO₂ peaks are observed in minor concentrates due to the high level of ruthenium present (about 20%).
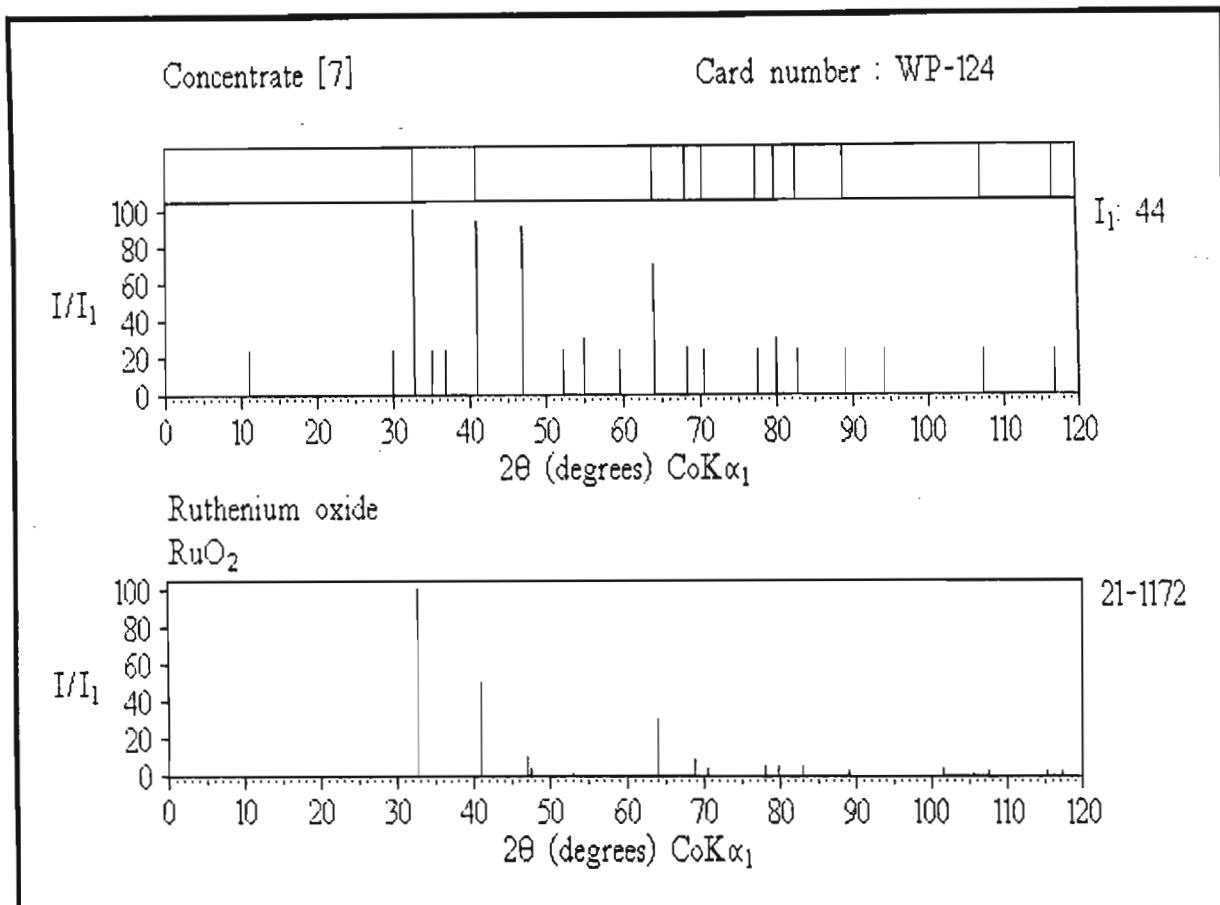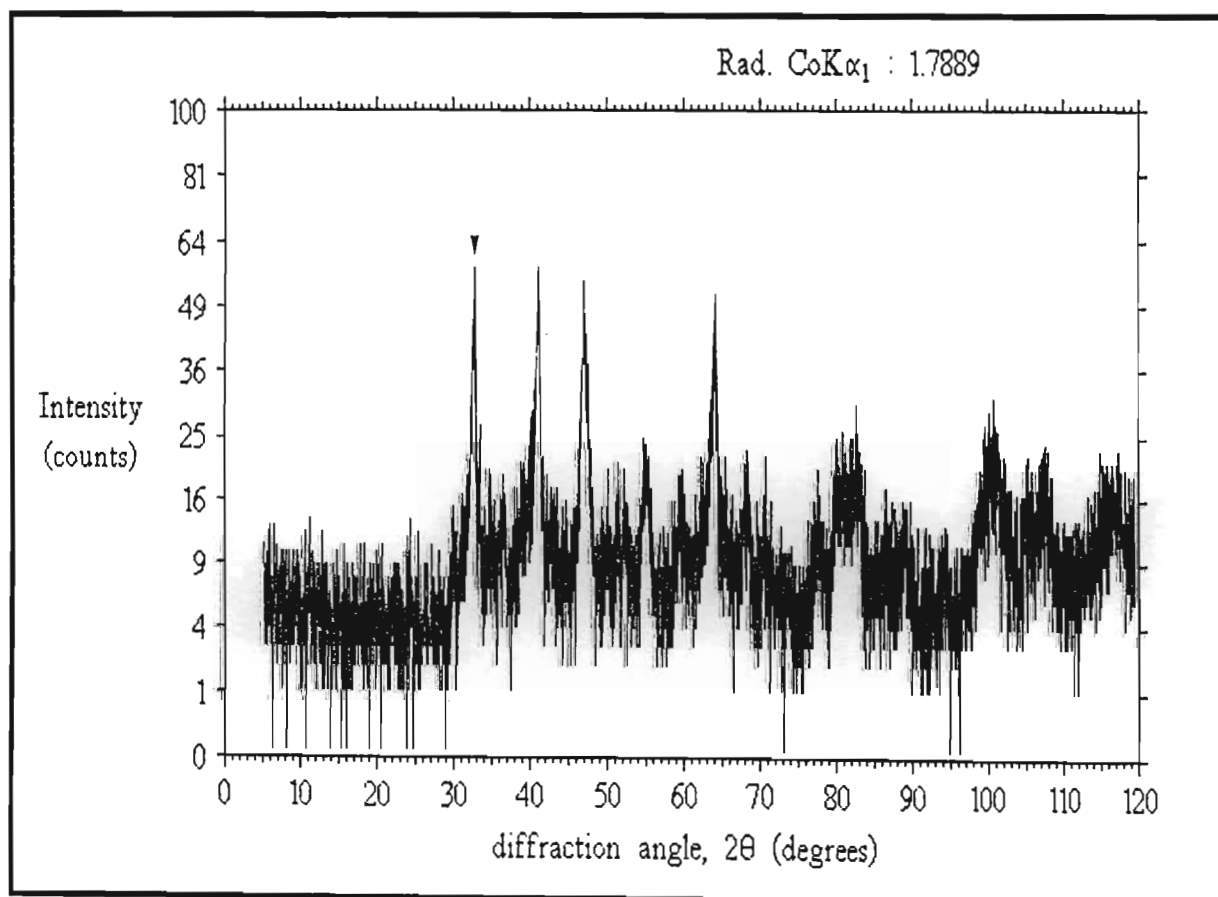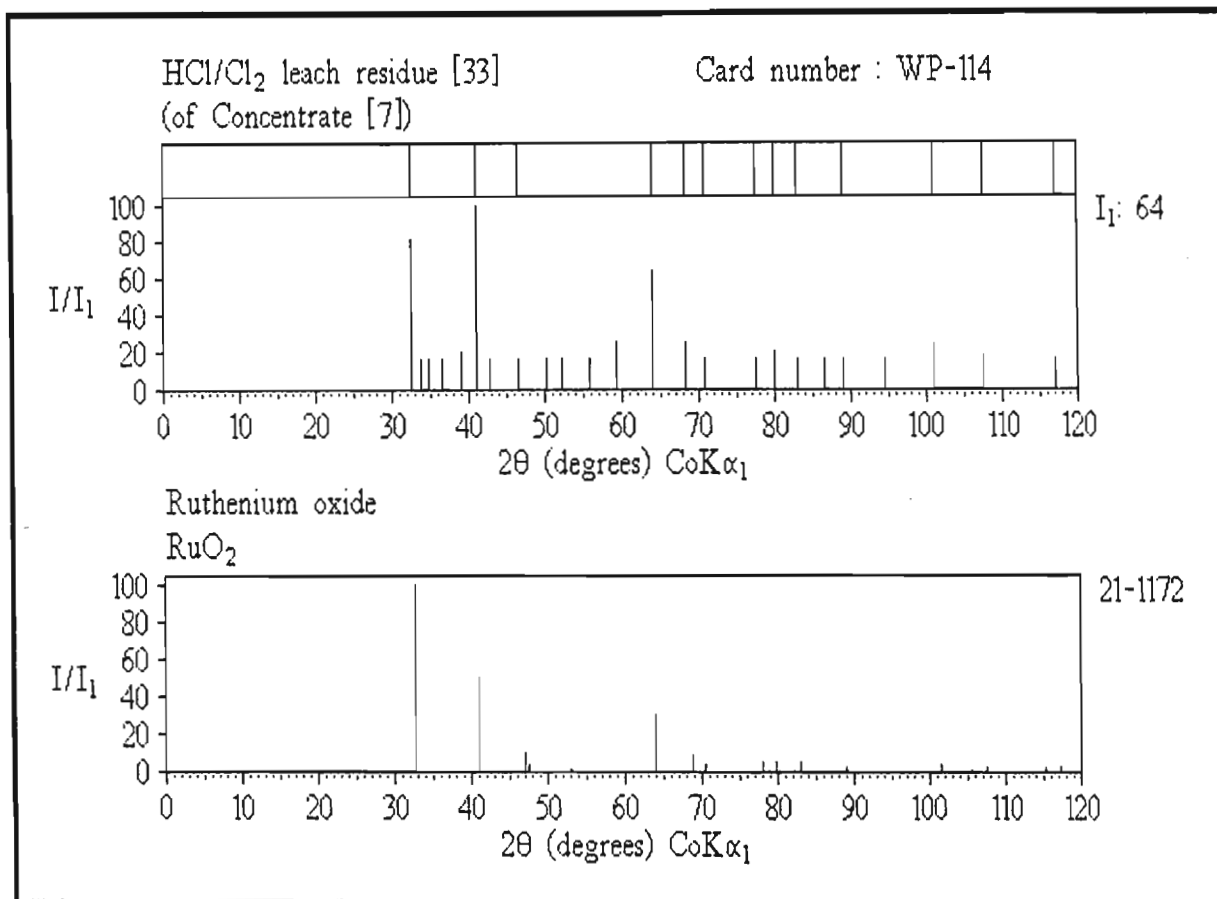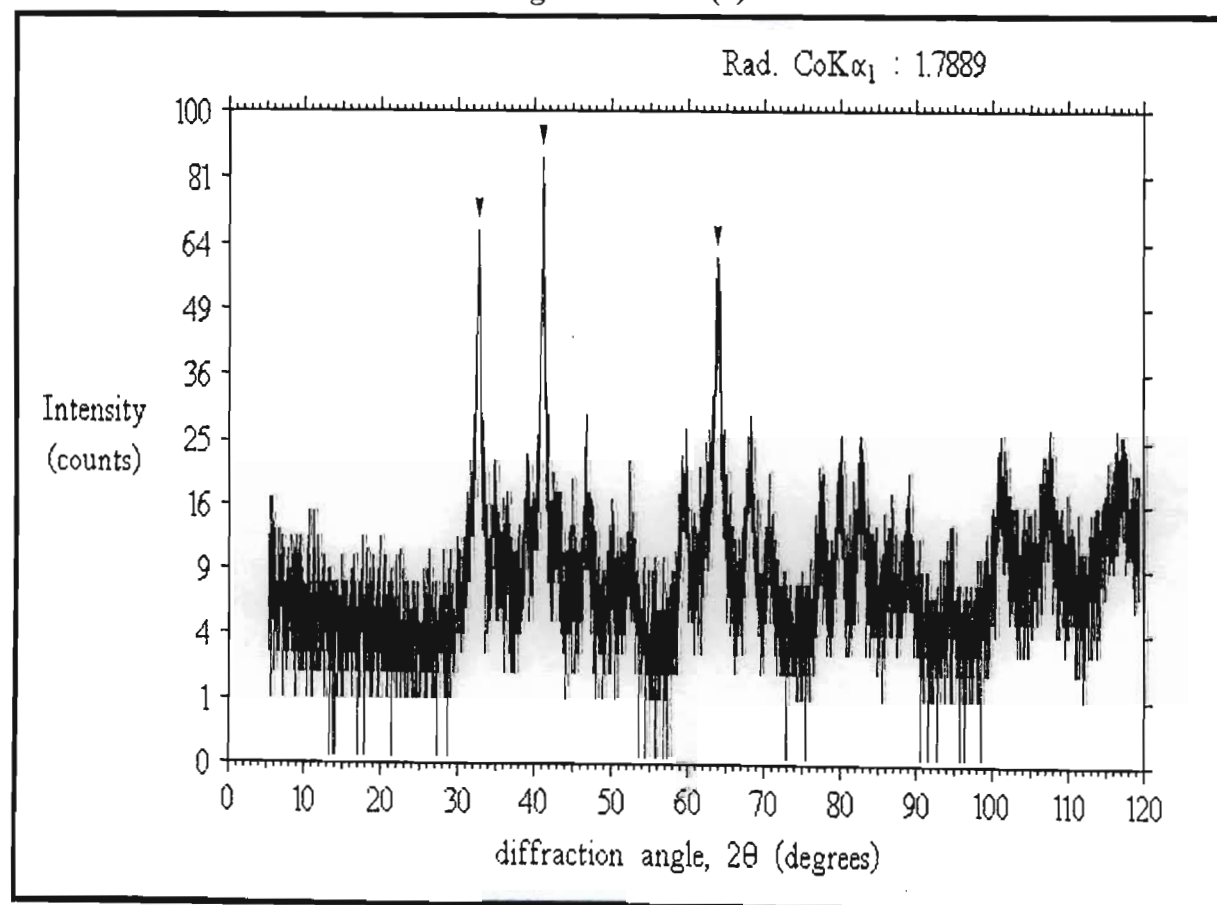
Figure 5.5.2-9(a)

Figure 5.5.2-9(b)

Figure 5.5.2-10(a)

Figure 5.5.2-10(b)

Table 5.5.2-4 Comparison of RuO$_2$ reference data with peaks observed for a minor concentrate and leach residue

RuO$_2$ Reference data [26]			M-CONCENTRATE [WP-124] Observed data			HCl/Cl$_2$ RESIDUE [WP-114] Observed data		
d(Å)	(I/I$_1$)	2θ	d(Å)	(I/I$_1$)	2θ	d(Å)	(I/I$_1$)	2θ
3.17	(100)	32.8	3.175	(100)	32.7	3.186	(81)	32.6
2.550	(50)	41.1	2.551	(94)	41.1	2.553	(100)	41.0
2.243	(10)	47.0	**2.246**	**(-)**	**46.9**	2.261	(16)	46.6
1.685	(30)	64.1	1.688	(69)	64.0	1.688	(64)	64.0
1.586	(9)	68.7	1.594	(25)	68.3	1.597	(25)	68.1
1.552	(4)	70.4	1.551	(24)	70.4	1.547	(16)	70.6
1.4200	(5)	78.1	1.429	(24)	77.5	1.429	(16)	77.5
1.3943	(5)	79.8	**1.393**	**(-)**	**79.9**	1.391	(20)	80.1
1.3491	(5)	83.1	1.353	(24)	82.8	1.350	(16)	83.0
1.2770	(2)	88.9	1.276	(24)	89.0	1.277	(16)	88.9
1.1559	(4)	101.4	-	-	-	1.160	(24)	100.9
1.1097	(3)	107.4	1.111	(24)	107.3	1.109	(17)	107.5
1.0585	(2)	115.4	1.050	(24)	116.8	1.049	(16)	117.0

Both Tables 5.5.2-3 and 5.5.2-4 show that the observed intensities for the oxide phase are much higher than would be expected. This indicates that the oxide phase is not pure RuO$_2$, but possibly contains iridium or even rhodium. In **Table 5.5.2-5** the XPD reference data for the oxides RhO$_2$, RuO$_2$, IrO$_2$ and OsO$_2$ are compared. The d-spacings are clearly very similar, stronger intensities being observed for RhO$_2$, IrO$_2$ and OsO$_2$.

When these oxides are formed together, peaks unique to each oxide are not necessarily observed in the XPD scan. Proof of this is shown in **Figure 5.5.2-11(a)** and **(b)** which is the scan of an electrode used for chlorine production, manufactured by the thermal decomposition of a mixture of ruthenium and iridium salts on a titanium surface. The combined oxides are observed as one set of unsplit peaks (Cp. **Figure 5.5.2-10(a), (b)**). In **Figure 5.5.2-12(a)** and **(b)** the reduced scan of the residue of another minor concentrate is compared with the reference patterns of IrO$_2$ and RhO$_2$. IrO$_2$ is very inert, stable to 1100°C, and formed by heating iridium in air [30]. RhO$_2$ is not too stable

(the more stable oxide being Rh_2O_3) but can form the more stable mixed metal oxide $Ru_{0.6}Rh_{0.4}O_2$ [31]. OsO_2 dissolves in hydrochloric acid forming $[OsCl_6]^{2-}$ [32] and so poses no solubility problems.

Table 5.5.2-5   Comparison of XPD reference data for the dioxides of rhodium, ruthenium, iridium and osmium

RhO$_2$ Reference data [27]			RuO$_2$ Reference data [26]			IrO$_2$ Reference data [28]			OsO$_2$ Reference data [29]		
d(Å)	(I/I$_1$)	2θ	d(Å)	(I/I$_1$)	2θ	d(Å)	(I/I$_1$)	2θ	d(Å)	(I/I$_1$)	2θ
3.18	(100)	32.7	3.17	(100)	32.8	3.178	(100)	32.7	3.18	(100)	32.7
2.546	(90)	41.1	2.550	(50)	41.1	2.582	(90)	40.5	2.600	(100)	40.2
2.245	(25)	47.0	2.243	(10)	47.0	2.2488	(25)	46.9	2.249	(80)	46.9
2.215	(6)	47.6	2.217	(4)	47.6	-	-	-	-	-	-
2.008	(2)	52.9	2.005	(1)	53.0	2.0119	(1)	52.8	-	-	-
1.683	(80)	64.2	1.685	(30)	64.1	1.6960	(55)	63.7	1.701	(40)	63.5
1.587	(18)	68.6	1.586	(9)	68.7	1.5903	(12)	68.5	1.592	(100)	68.4
1.545	(10)	70.8	1.552	(4)	70.4	1.5771	(6)	69.1	1.590	(80)	68.5
1.419	(18)	78.2	1.4200	(5)	78.1	1.4227	(12)	77.9	1.423	(80)	77.9
1.390	(20)	80.1	1.3943	(5)	79.8	1.4133	(14)	78.5	-	-	-
1.347	(25)	83.2	1.3491	(5)	83.1	1.3542	(14)	82.7	1.357	(60)	82.5
1.273	(10)	89.3	1.2770	(2)	88.9	1.2914	(8)	87.7	1.300	(80)	87.0
1.155	(16)	101.5	1.1559	(4)	101.4	1.1604	(10)	100.9	1.162	(60)	100.7
1.122	(4)	105.7	1.1230	(1)	105.6	1.1247	(4)	105.4	1.125	(60)	105.3
1.107	(12)	107.8	1.1097	(3)	107.4	1.1199	(6)	106.0	-	-	-
1.058	(6)	115.4	1.0585	(2)	115.4	1.0602	(4)	115.1	-	-	-
1.045	(14)	117.7	1.0481	(3)	117.2	1.0563	(10)	115.7	-	-	-

Table 5.5.2-6 shows that the solubilities of ruthenium and iridium are clearly linked and can be understood in terms of an insoluble ruthenium-osmium alloy, and an insoluble ruthenium-iridium oxide phase (in most cases).
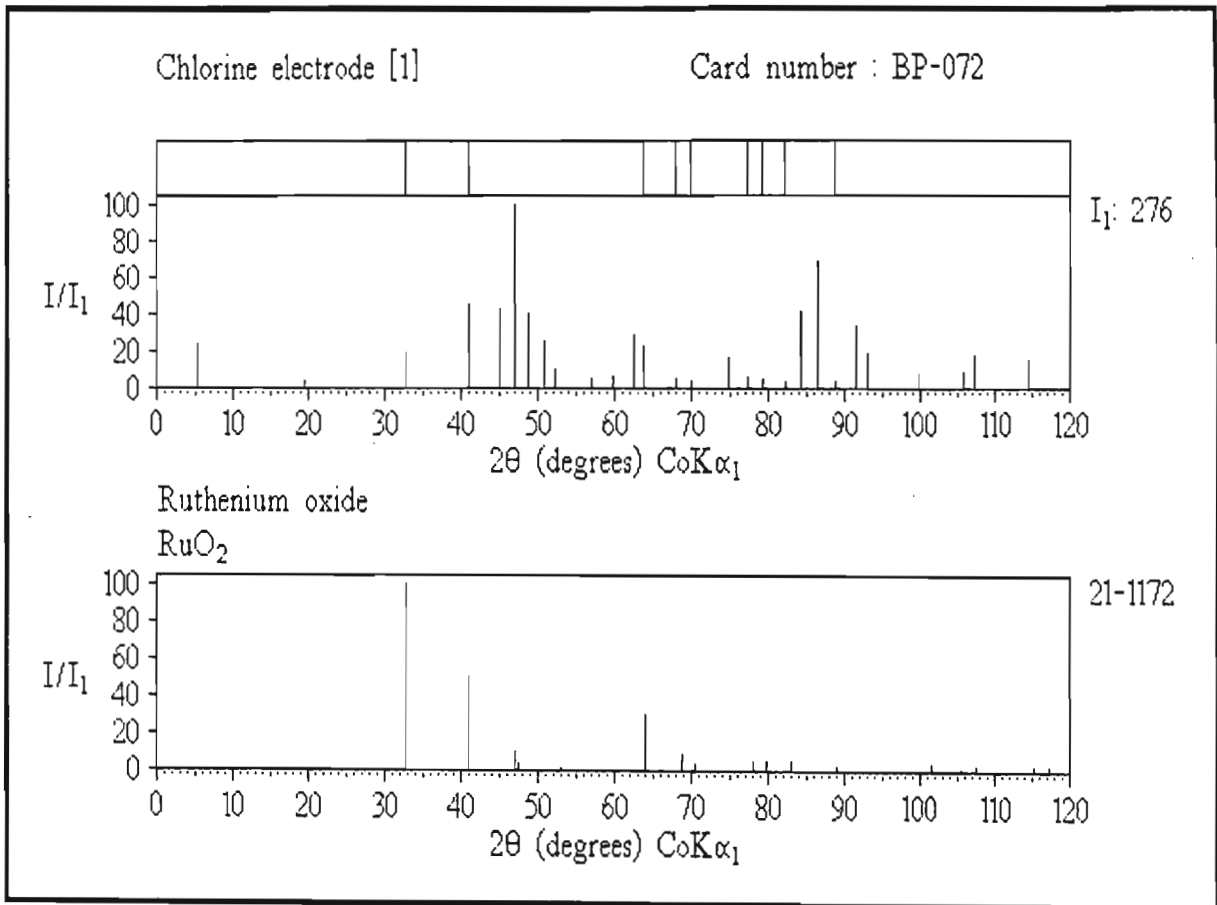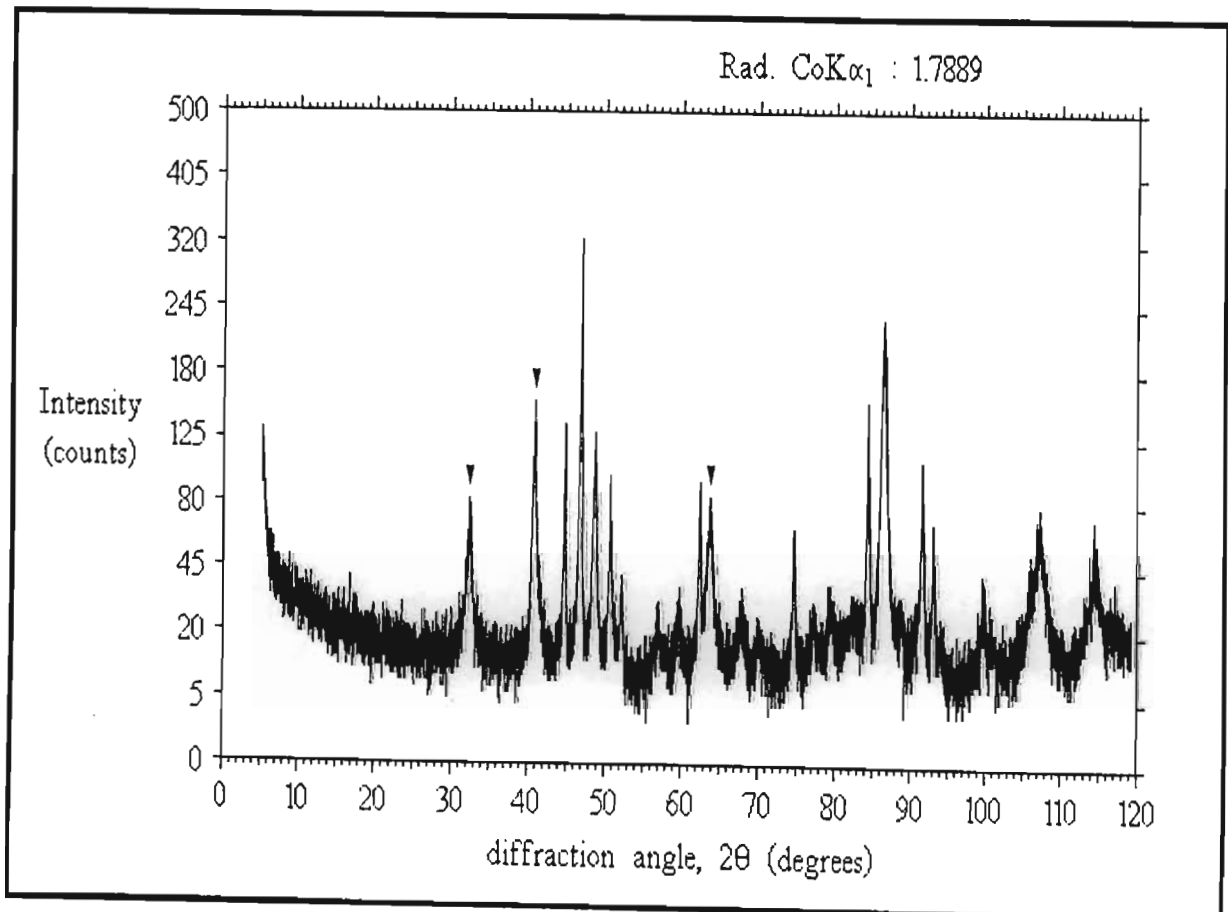
Chlorine electrode [1]   Card number : BP-072

Ruthenium oxide
RuO_2

Figure 5.5.2-11(a)
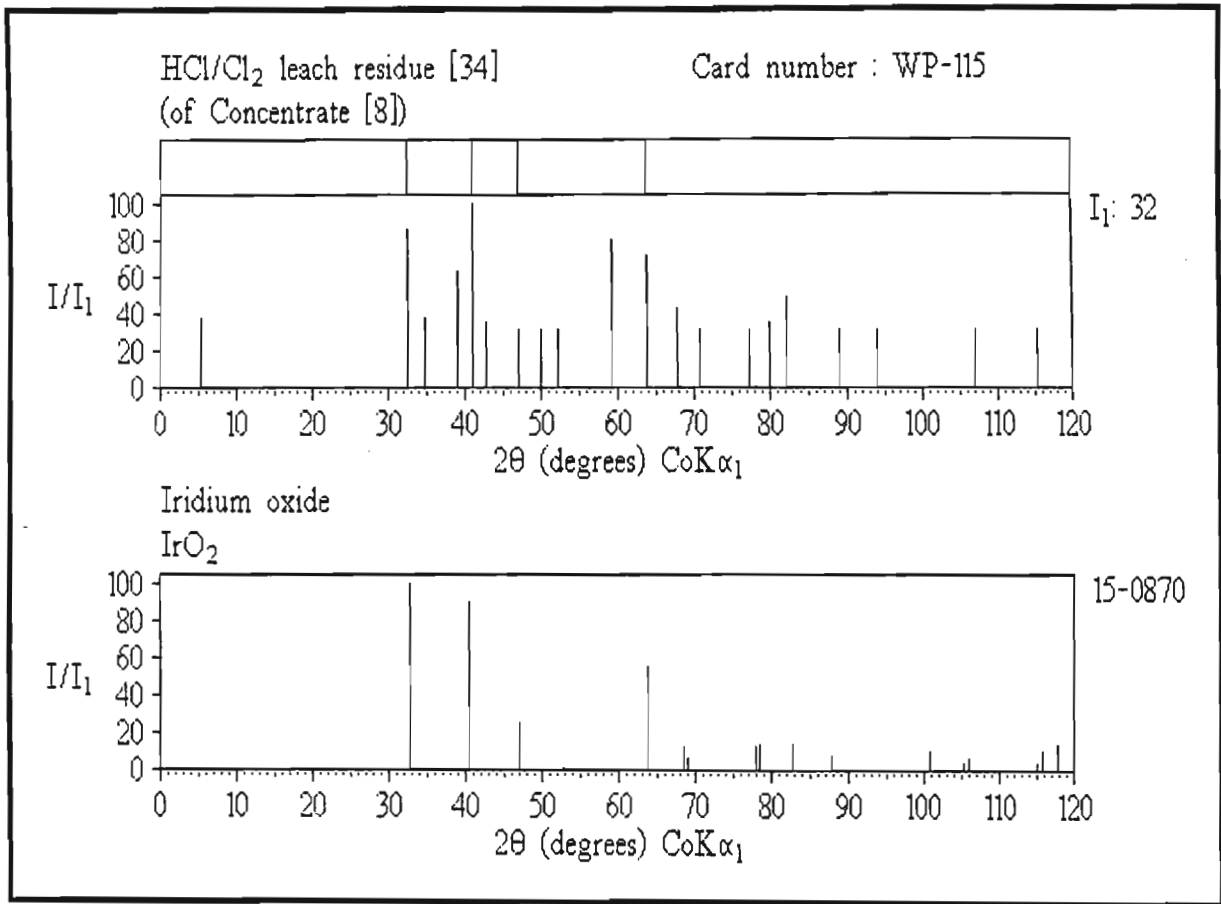
Rad. $CoK\alpha_1$: 1.7889

Figure 5.5.2-11(b)
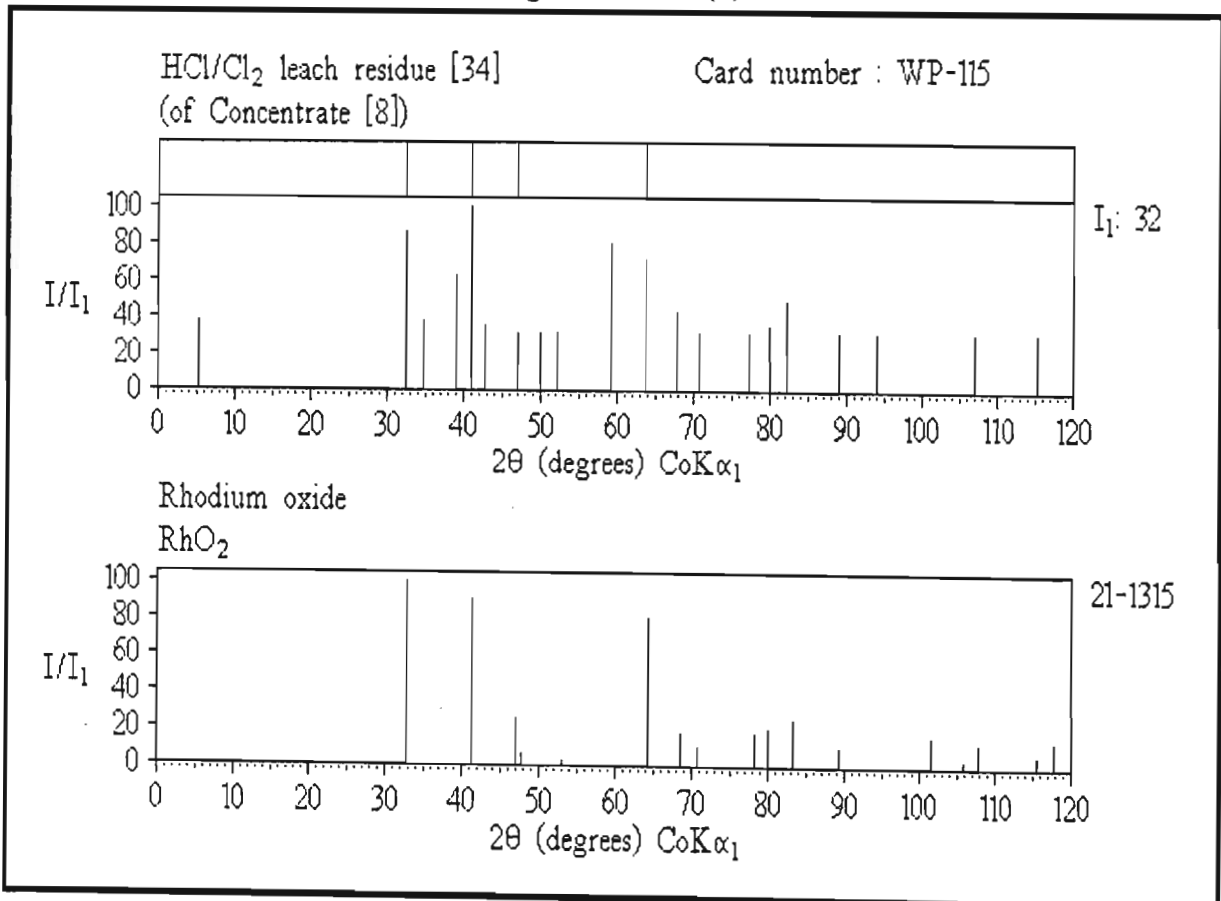
Figure 5.5.2-12(a)

Figure 5.5.2-12(b)

Table 5.5.2-6   Comparison of Ru and Ir solubility with counts
observed for the (101) Ru and RuO_2 lines

Normal Concentrate	Solubility in the HCl/Cl_2 leach Ru	Ir	Ru (101) line [†] counts	RuO_2 (101) line [‡] counts
1	93.5	91.7	49	10
2	90.6	90.0	56	12
3	89.7	89.1	74	10
4	89.4	88.8	83	14

† Observed at about 2.07Å (51.2°)
‡ Observed at about 2.54Å (41.2°)

Figures 5.5.2-13(a) and **(b)** show that both these phases were also being encountered in the concentrate being processed at BARPLATS REFINERY.

5.5.3 LOW OSMIUM SOLUBILITY

The solubility of osmium in the oxidative leach is never determined due to the very low percentage present in concentrates (about 0.6%).   The metal is not of major economic importance, its demand usually being confined to aqueous and stabilized non-aqueous solutions of OsO_4 used in organic oxidations and as stain in microscopy.
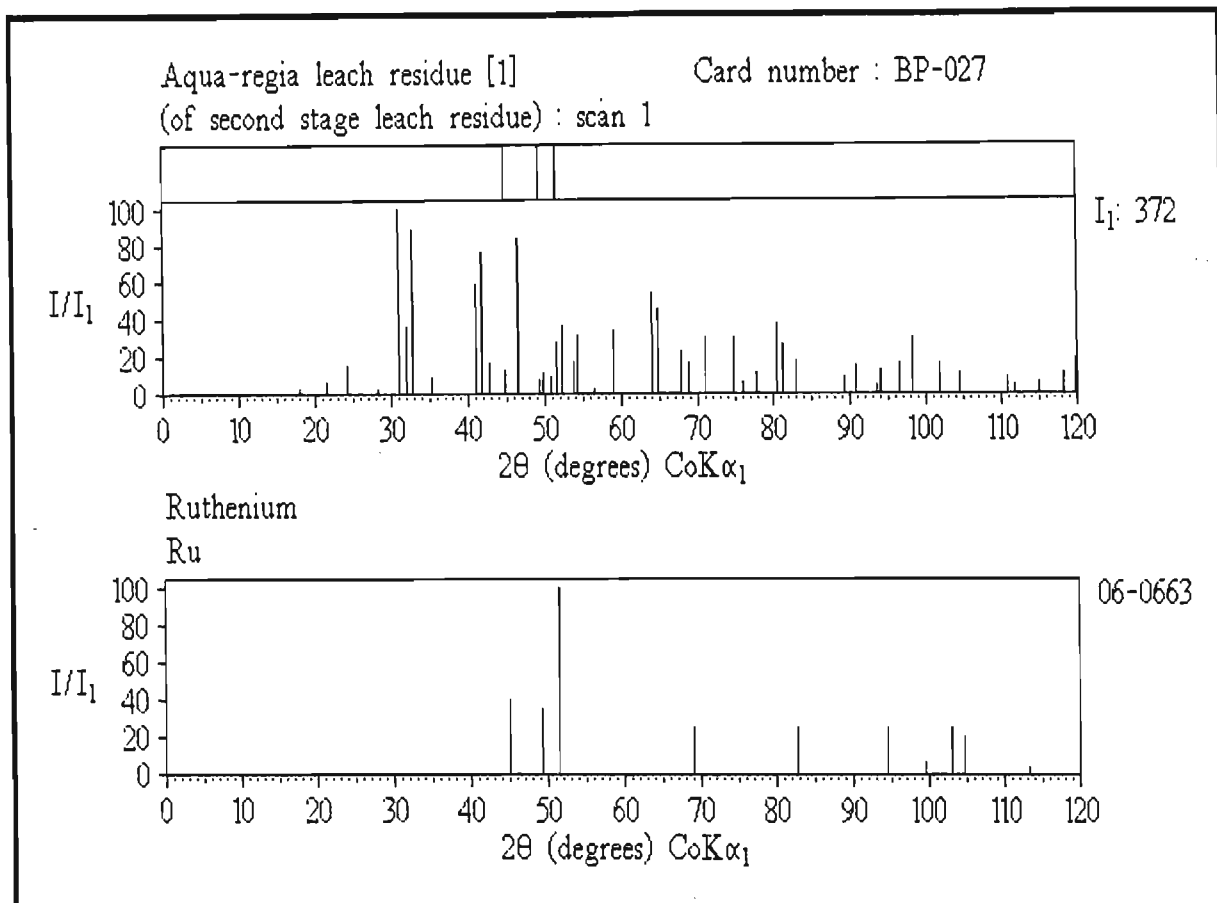
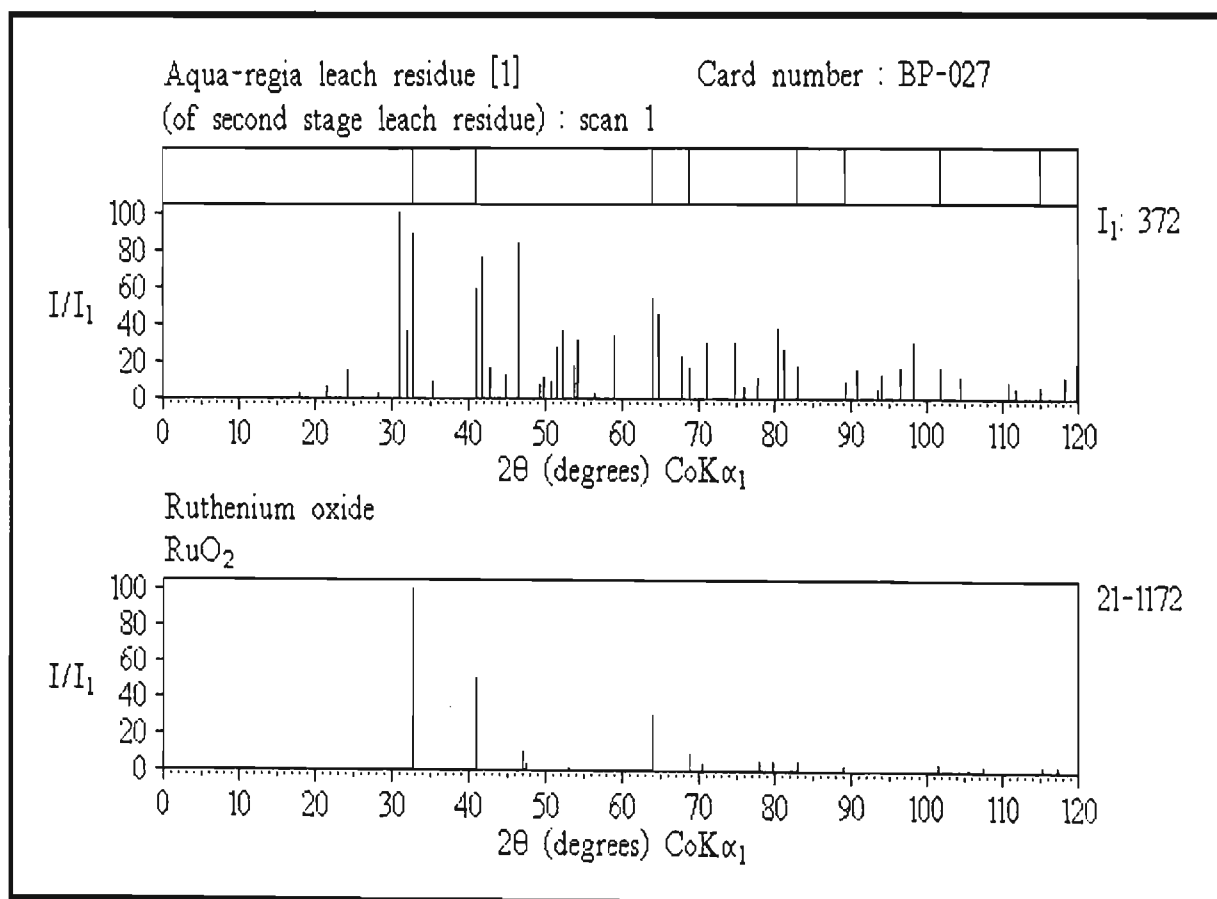(See § 5.5.2 and § 5.5.5.)

Figure 5.5.2-13(a)

Figure 5.5.2-13(b)

5.5.4 LOW RHODIUM SOLUBILITY

The oxidative leach solubility of rhodium is worst for minor concentrates where the solubility can be as low as 2%. Over a five month period, the average rhodium solubility of 9 consignments was 22.4%. In addition, rhodium solubility was highly erratic, ranging from 2 to 90%. Two minor concentrates, with rhodium solubilities of 19.0% and 27.5%, and their oxidative leach residues were examined with the aim of explaining this behaviour.

Although the XPD scans indicated very low sample crystallinity, it was possible to establish the presence of the rhodium selenide, **RhSe$_{2+x}$** (X ~ 0.01), as the main rhodium phase present in minor concentrate samples. **Table 5.5.4-1** compares the reference data for this compound with peaks observed in the concentrate scans (boldface values indicates overlap with another phase). Whenever sample crystallinity drops, peak intensities tend to become high and very similar. Some expected lines can also be lost in the background noise.

Table 5.5.4-1   Comparison of RhSe$_{2+x}$ reference data with peaks observed for two minor concetrates

RhSe$_{2+x}$ Reference data [33]			Concentrate [7] (WP-124) Observed data			Concentrate [8] (WP-125) Observed data		
d(Å)	(I/I$_1$)	2θ	d(Å)	(I/I$_1$)	2θ	d(Å)	(I/I$_1$)	2θ
3.45	(20)	30.1	3.462	(96)	29.9	-	-	-
2.99	(45)	34.8	2.984	(96)	34.9	2.992	(52)	34.8
2.68	(65)	39.0	-	-	-	2.688	(100)	38.9
2.44	(60)	43.0	-	-	-	2.444	(52)	42.9
1.808	(100)	59.3	1.800	(96)	59.6	1.810	(74)	59.2
1.603	(50)	67.8	1.594	(100)	68.3	1.601	(52)	67.9
1.281	(15)	88.6	1.276	(96)	89.0	1.278	(52)	88.8
1.227	(20)	93.6	1.221	(96)	94.2	1.222	(52)	94.1
1.156	(50)	101.4	-	-	-	1.156	(52)	101.4
1.116	(30)	106.5	**1.111**	**(-)**	**107.3**	**1.114**	**(-)**	**106.9**

Figure 5.5.4-1(a) and **(b)** show a typical minor concentrate XPD scan with its reduced pattern compared to that of reference $RhSe_{2+x}$. Note the low crystallinity of the sample. This assignment made chemical sense as both samples had relatively high levels of selenium present (**Table 5.5.4-2**). The first concentrate however had insufficient selenium to completely combine with all the rhodium present. Thus less $RhSe_{2+x}$ was expected even though the amount of insoluble rhodium was higher.

Table 5.5.4-2   Rh / Se composition of minor concentrates

Element	Concentrate [7] (WP-124)			Concentrate [8] (WP-125)		
	wt %	at%	at. ratio	wt%	at%	at. ratio
Rh	9.569	62.48	1.00	8.138	33.64	1.00
Se	4.409	37.52	0.60	12.32	66.36	1.97
Rh insoluble	7.748	57.42	1.00	5.902	26.88	1.00
Se	4.409	42.58	0.74	12.32	73.12	2.72

Scans of the oxidative leach residues showed that virtually none of the rhodium selenide present in the concentrates had dissolved (**Figure 5.5.4-2 (a)** and **(b)**). As expected, far more $RhSe_{2+x}$ was evident in the second residue, even though the solubility was better (**Table 5.5.4-3**).

Table 5.5.4-3   Evidence of the $RhSe_{2+x}$ phase being present

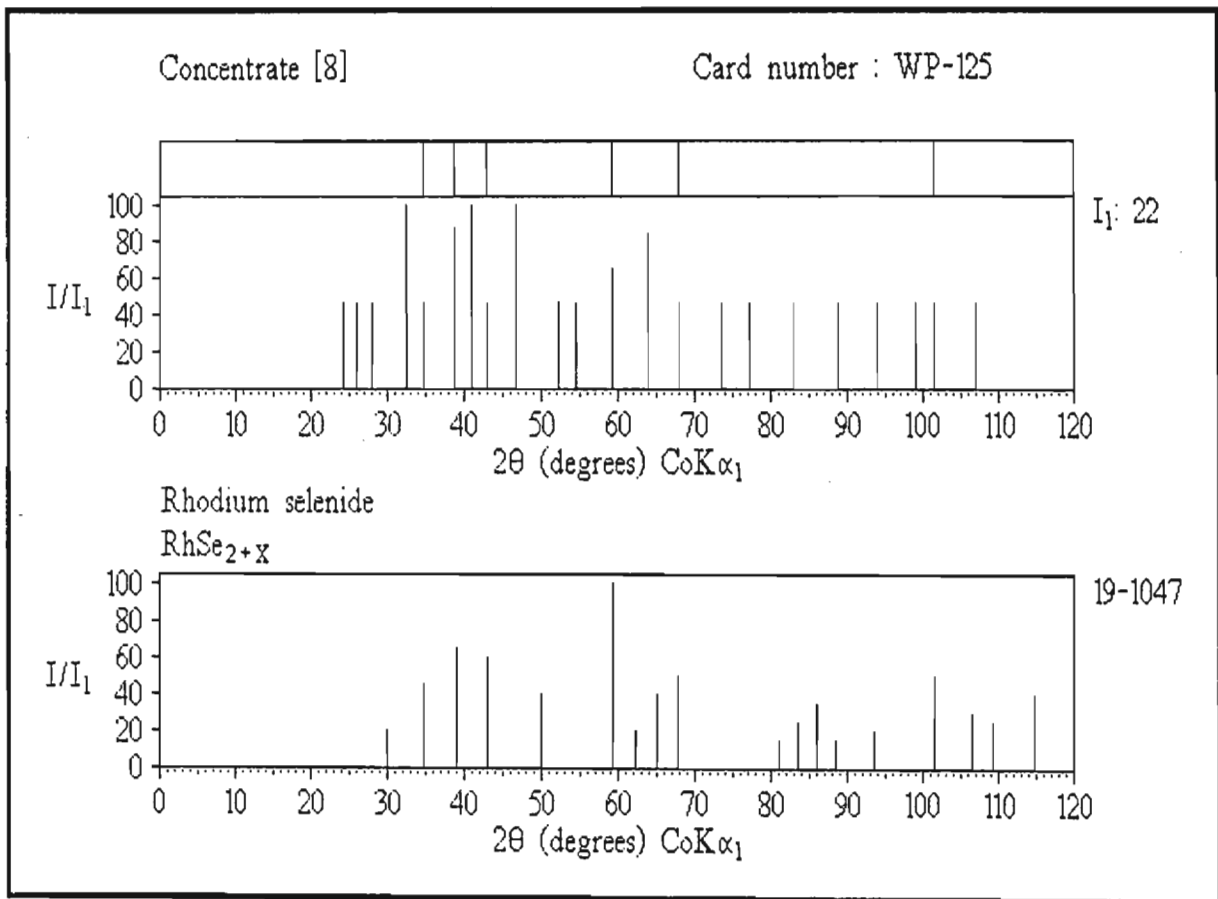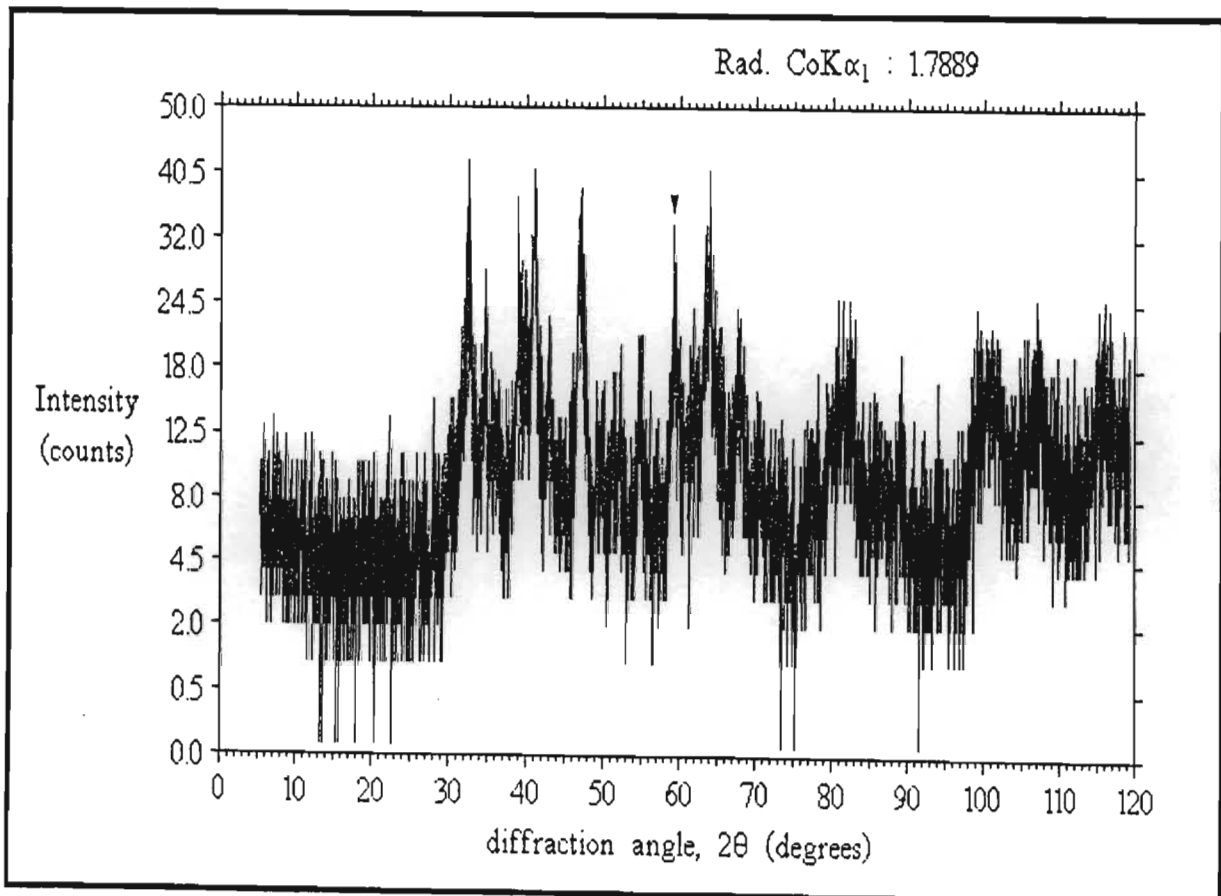|	Concentrate [7] (WP-124)	Concentrate [8] (WP-125)
Rh solubility	19.03 %	27.48 %
$RhSe_{2+x}$ expected (based on solubility)	high	low
$RhSe_{2+x}$ expected (based on analysis)	low	high
Maximum wt% $RhSe_{2+x}$ possible (based on analysis)	7.27	15.01
XPD SCAN Counts for maximum line (~1.81Å)		
concentrate	10	14
concentrate residue	16	26

Figure 5.5.4-1(a)

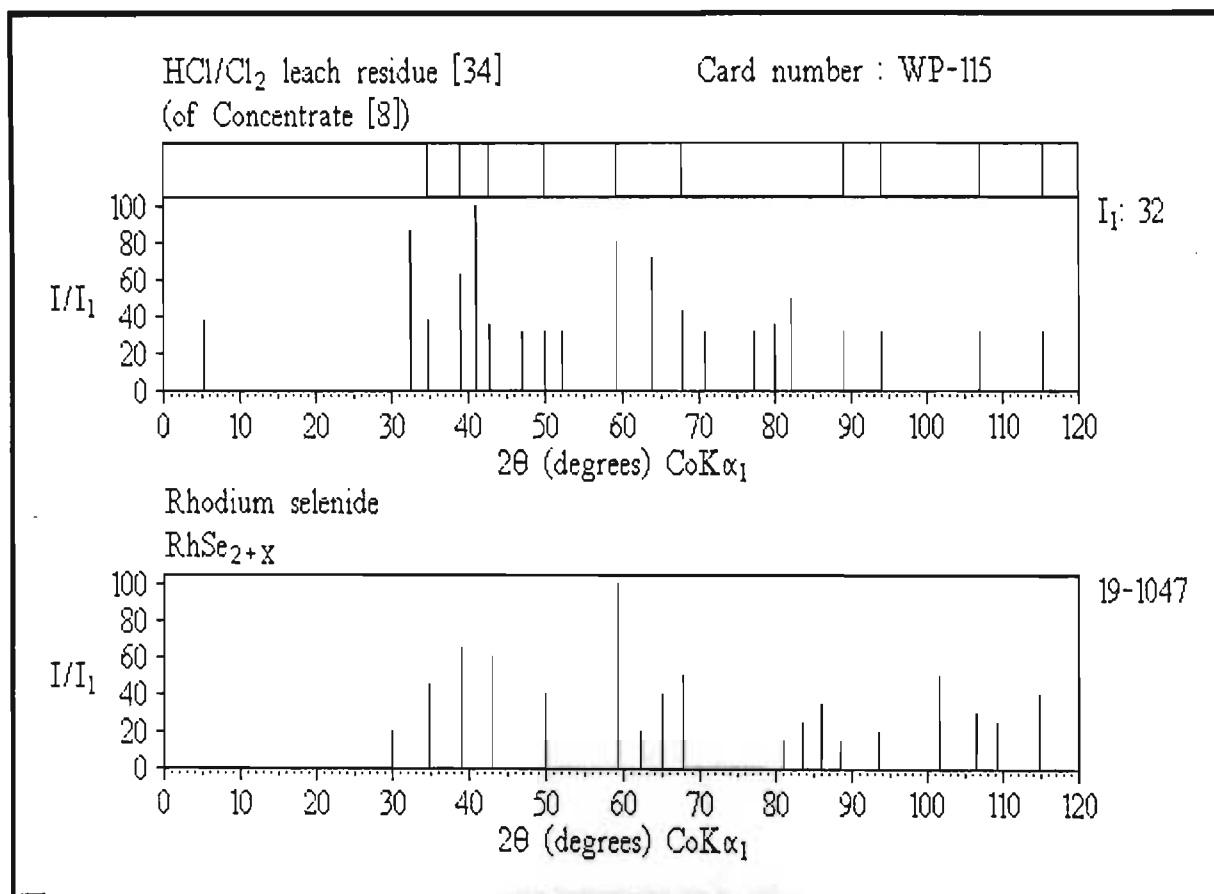

Figure 5.5.4-1(b)
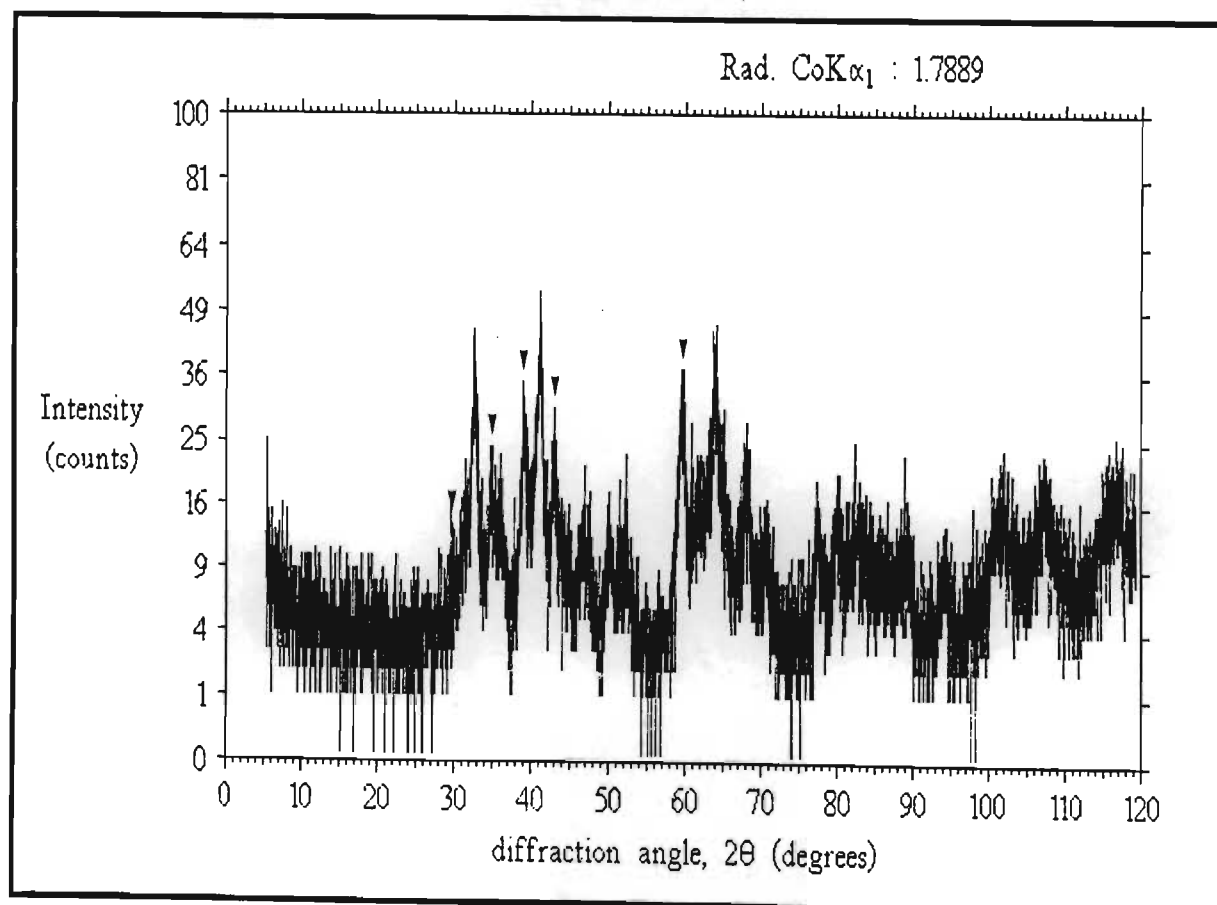
Figure 5.5.4-2(a)

Figure 5.5.4-2(b)

Table **5.5.4-4** compares the reference data for RhSe$_{2+X}$ with peaks observed for the residues of the two concentrates. Clearly RhSe$_{2+X}$ has remained unleached, and is thus responsible for low rhodium solubility, although other undetected phases (tellurides, sulphides, or mixed metal oxides *eg.* Ru$_{0.6}$Rh$_{0.4}$O$_2$ (§ 5.5.2)) are probably also involved. The oxide Rh$_2$O$_3$ was not detected in the samples, although traces might also be present.

Table 5.5.4-4   Comparison of RhSe$_{2+X}$ reference data with peaks observed for two minor concentrate leach residues

RhSe$_{2+X}$ Reference data [33]			HCl/Cl$_2$ residue [33] (WP-114) Observed data			HCl/Cl$_2$ residue [34] (WP-115) Observed data		
d(Å)	(I/I$_1$)	2θ	d(Å)	(I/I$_1$)	2θ	d(Å)	(I/I$_1$)	2θ
2.99	(45)	34.8	2.998	(64)	34.7	3.001	(48)	34.7
2.68	(65)	39.0	2.688	(80)	38.9	2.682	(78)	39.0
2.44	(60)	43.0	2.450	(64)	42.8	2.452	(45)	42.8
2.12	(40)	49.9	2.106	(64)	50.3	2.117	(40)	50.0
1.808	(100)	59.3	1.813	(100)	59.1	1.809	(100)	59.3
1.603	(50)	67.8	1.597	(100)	68.1	1.604	(52)	67.8
1.311	(35)	86.0	1.306	(64)	86.5	-	-	
1.281	(15)	88.6	1.277	(64)	88.9	1.278	(40)	88.9
1.227	(20)	93.6	1.219	(64)	94.4	1.223	(40)	94.0
1.156	(50)	101.4	1.160	(96)	100.9	-	-	
1.116	(30)	106.5	1.109	(68)	107.5	1.112	(40)	107.1
1.097	(25)	109.2	-	-		-	-	
1.062	(40)	114.8	-	-		1.060	(40)	115.1

Rhodium selenide has clearly been formed during the roasting of the selenium-rich precipitate cake obtained from the copper pressure leach solution, via the reaction :

$$Rh + (2+X)\,Se \longrightarrow RhSe_{2+X} \qquad (X \sim 0.01)$$
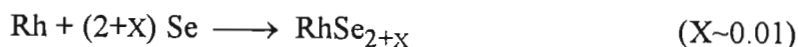
This is a sintering reaction [34] that is reported to take place at about 900°C [35]. The selenium roast is usually performed at about 700°C. Minor concentrates typically exhibit highly erratic rhodium solubility. This indicates that the selenium roast temperature is very near the critical temperature required for the formation of rhodium

selenide. The formation of this phase could probably be avoided by a slight lowering of the roast temperature and strict control ensuring no overheating.

Low rhodium solubility in normal concentrates is not simply explained. For some leaches, low rhodium solubility could be ascribed to the alloy phase platinum rhodium, $Rh_{0.57}Pt_{0.43}$. The observed data for this phase is compared to that of the reference alloy in **Table 5.5.4-5**. (It should be noted that this set of peaks can quite easily be mistaken for residual iridium (**Table 5.5.4-6**). The elemental analysis for this residue revealed high levels of platinum and rhodium thereby confirming the chosen assignment.)

Table 5.5.4-5   Comparison of $Rh_{0.57}Pt_{0.43}$ alloy reference data with peaks observed for a HCl/Cl$_2$ leach residue

$Rh_{0.57}Pt_{0.43}$ Reference data [36]			HCl/Cl$_2$ leach residue [7] (WP-011) Observed data		
d(Å)	(I/I$_1$)	2θ	d(Å)	(I/I$_1$)	2θ
2.227	(100)	47.4	2.227	(100)	47.4
1.927	(50)	55.3	1.924	(34)	55.4
1.362	(85)	82.1	1.360	(54)	82.3
1.162	(85)	100.7	1.161	(57)	100.7
1.112	(18)	107.1	1.111	(11)	107.2

Table 5.5.4-6   Comparison of $Rh_{0.57}Pt_{0.43}$ alloy reference data with Ir reference data

$Rh_{0.57}Pt_{0.43}$ Reference data [36]			Ir Reference data [37]		
d(Å)	(I/I$_1$)	2θ	d(Å)	(I/I$_1$)	2θ
2.227	(100)	47.4	2.2170	(100)	47.6
1.927	(50)	55.3	1.9197	(50)	55.5
1.362	(85)	82.1	1.3575	(40)	82.4
1.162	(85)	100.7	1.1574	(45)	101.2
1.112	(18)	107.1	1.1082	(15)	107.6

Figure 5.5.4-3 (a) and (b) shows this alloy as detected in an oxidative leach residue. The peaks occur at quite different spacings to those of platinum, and are generally quite broad. The insolubility of this alloy is shown by the fact that this phase had passed twice through the oxidative leach. This alloy is one of the few minerals of rhodium [38]. Not much is known about it except that virtually no other elements occur together with the alloy [38]. This phase was rarely observed in samples.

Another rhodium alloy detected in a selectively leached concentrate sample was iridium iron rhodium, **(Fe,Rh)$_{1.8}$Ir$_{0.2}$**. The observed XPD data gave a good fit with the reference data, which was not all that accurate, having been collected using three successive radiations (CuKα, CrKα, and FeKα) over the 2θ range [39] (**Table 5.5.4-7**).

Table 5.5.4-7   Comparison of (Fe,Rh)$_{1.8}$Ir$_{0.2}$ reference data with peaks observed for a leached pre-treated concentrate

| (Fe,Rh)$_{1.8}$Ir$_{0.2}$ Reference data [39] | | | Concentrate [1] (WP-013) Observed data | | |
d(Å)	(I/I$_1$)	2θ	d(Å)	(I/I$_1$)	2θ
2.98	(15)	34.9	2.984	(16)	34.9
2.115	(100)	50.0	2.116	(100)	50.0
1.720	(2)	62.7	1.729	(8)	62.3
1.493	(25)	73.6	1.498	(18)	73.3
1.34	(5)	83.8	1.341	(18)	83.7
1.22	(80)	94.3	1.225	(48)	93.8
1.06	(2)	115.1	1.061	(17)	114.9

This alloy is reported to contain two phases giving identical powder patterns. The first is iron-rich, white in colour, cubic, and has the formula Rh$_4$Fe$_5$Ir. The second is rhodium-rich, brown in colour, pseudo-cubic, and has the formula Rh$_5$Fe$_4$Ir [39]. The observed peaks for this phase were very sharp and quite distinct (**Figure 5.5.4-4(a) and (b)**). This phase is obviously a residual mineral. Tiny traces seemed to be present in the some oxidative leach residues of normal concentrates, although at these levels only
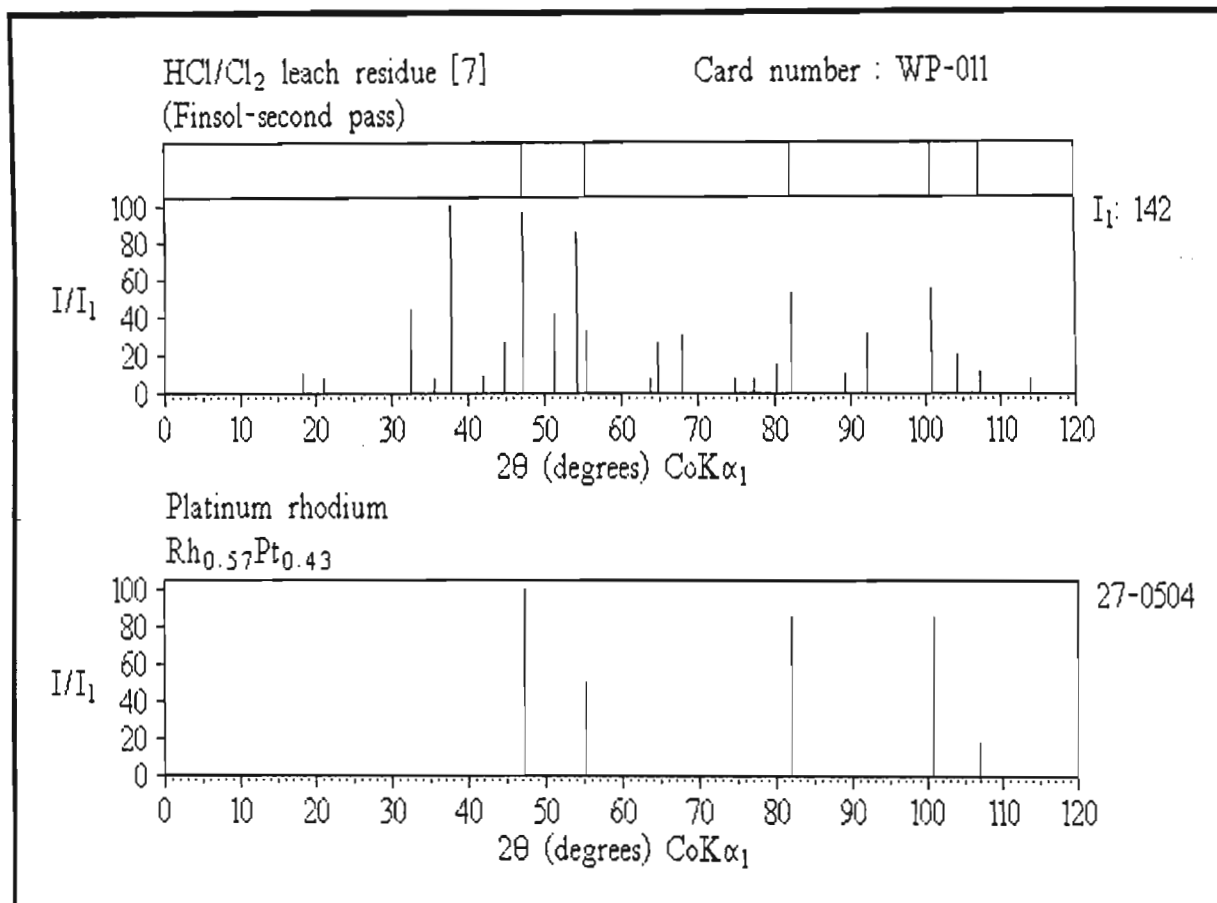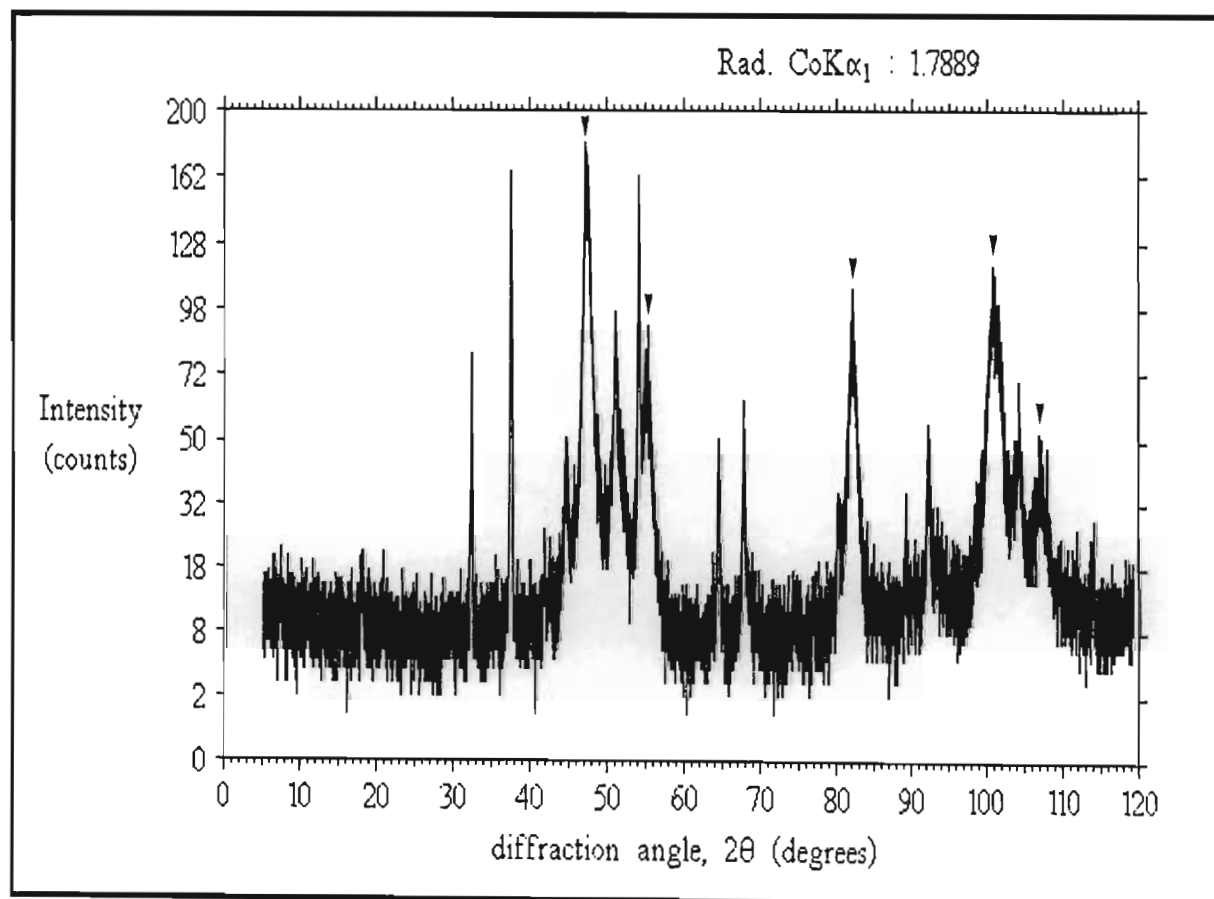
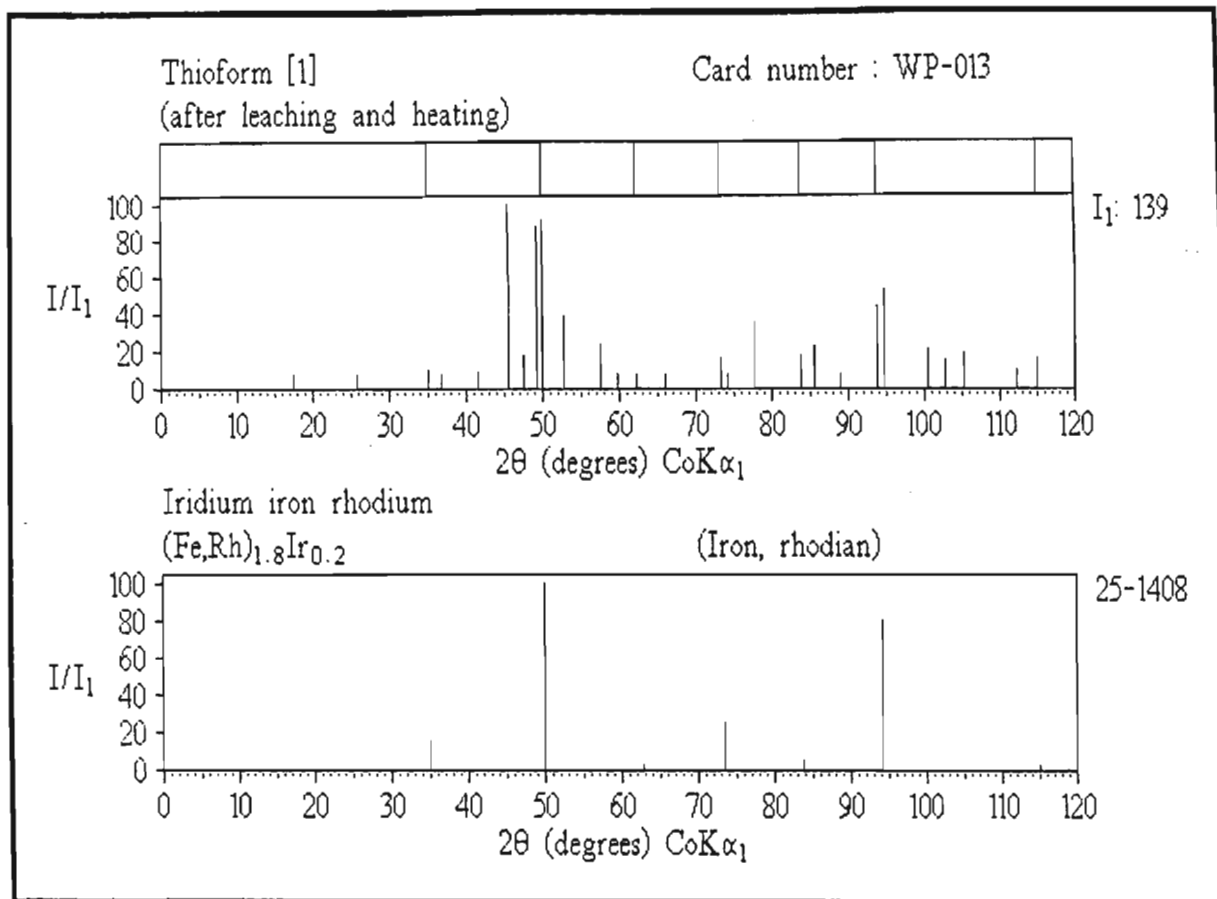**Figure 5.5.4-3(a)**

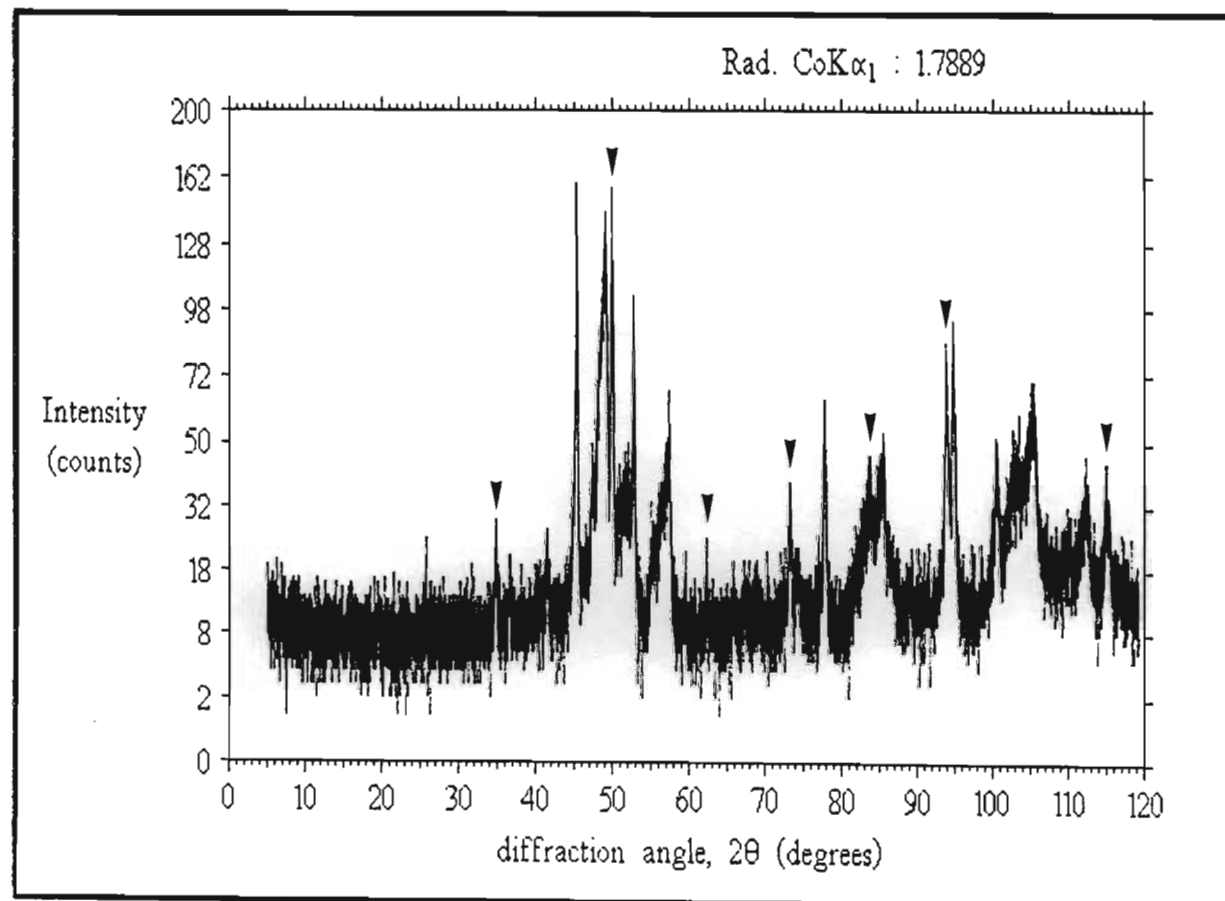**Figure 5.5.4-3(b)**

Figure 5.5.4-4(a)

Figure 5.5.4-4(b)

two lines are evident, which makes assignment difficult. It probably plays a minor role in rhodium and iridium insolubility.

Numerous low to medium intensity peaks appeared in almost every normal concentrate leach residue, that could not be fitted to any reference data with certainty. In one sample these peaks dominated all others and had intensities which corresponded well with those of ruthenium sulphide, RuS_2. The d-spacings where however greater, the peaks being systematically shifted from those expected (**Table 5.5.4-8**).

Table 5.5.4-8   Comparison of RuS_2 reference data with peaks observed for a HCl/Cl_2 leach residue

RuS_2 Reference data [40]			HCl/Cl_2 residue [30] (WP-111) Observed data			Deviation	
d(Å)	(I/I$_1$)	2θ	d(Å)	(I/I$_1$)	2θ	Δd(Å)	Δ2θ(°)
3.24	(75)	32.1	3.300	(54)	31.5	+ 0.060	- 0.6
2.805	(100)	37.2	2.861	(91)	36.4	+ 0.056	- 0.8
2.509	(20)	41.8	2.556	(40)	41.0	+ 0.047	- 0.8
2.290	(20)	46.0	2.326	(25)	45.2	+ 0.036	- 0.8
1.983	(60)	53.6	2.022	(70)	52.5	+ 0.039	- 1.1
1.691	(100)	63.9	1.721	(100)	62.6	+ 0.030	- 1.3
1.619	(20)	67.1	1.647	(14)	65.8	+ 0.028	- 1.3
1.556	(8)	70.2	1.590	(16)	68.4	+ 0.034	- 1.8
1.499	(10)	73.3	1.525	(16)	71.8	+ 0.026	- 1.5
1.287	(20)	88.1	1.311	(20)	86.1	+ 0.024	- 2.0
1.254	(20)	91.0	1.273	(19)	89.3	+ 0.019	- 1.7
1.145	(20)	102.7	1.164	(16)	100.4	+ 0.019	- 2.3
1.080	(35)	111.8	1.095	(25)	109.5	+ 0.015	- 2.3

Figure 5.5.4-5(a) and **(b)** show how well the intensities correspond to those of RuS_2. Note the peak shifts as indicated in the reduced spectra. Clearly this phase is not RuS_2, but closely related to it. Structurally, ruthenium sulphide is cubic [41].
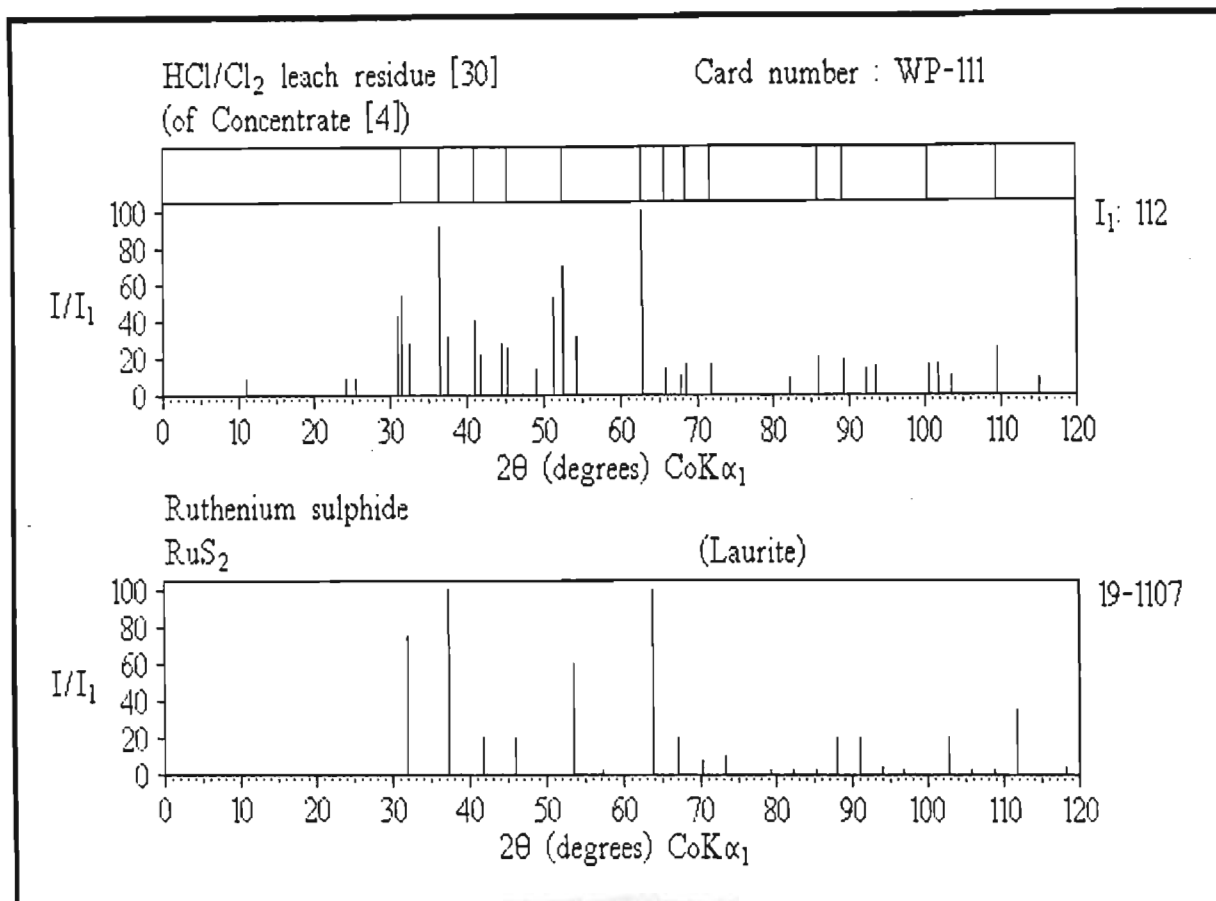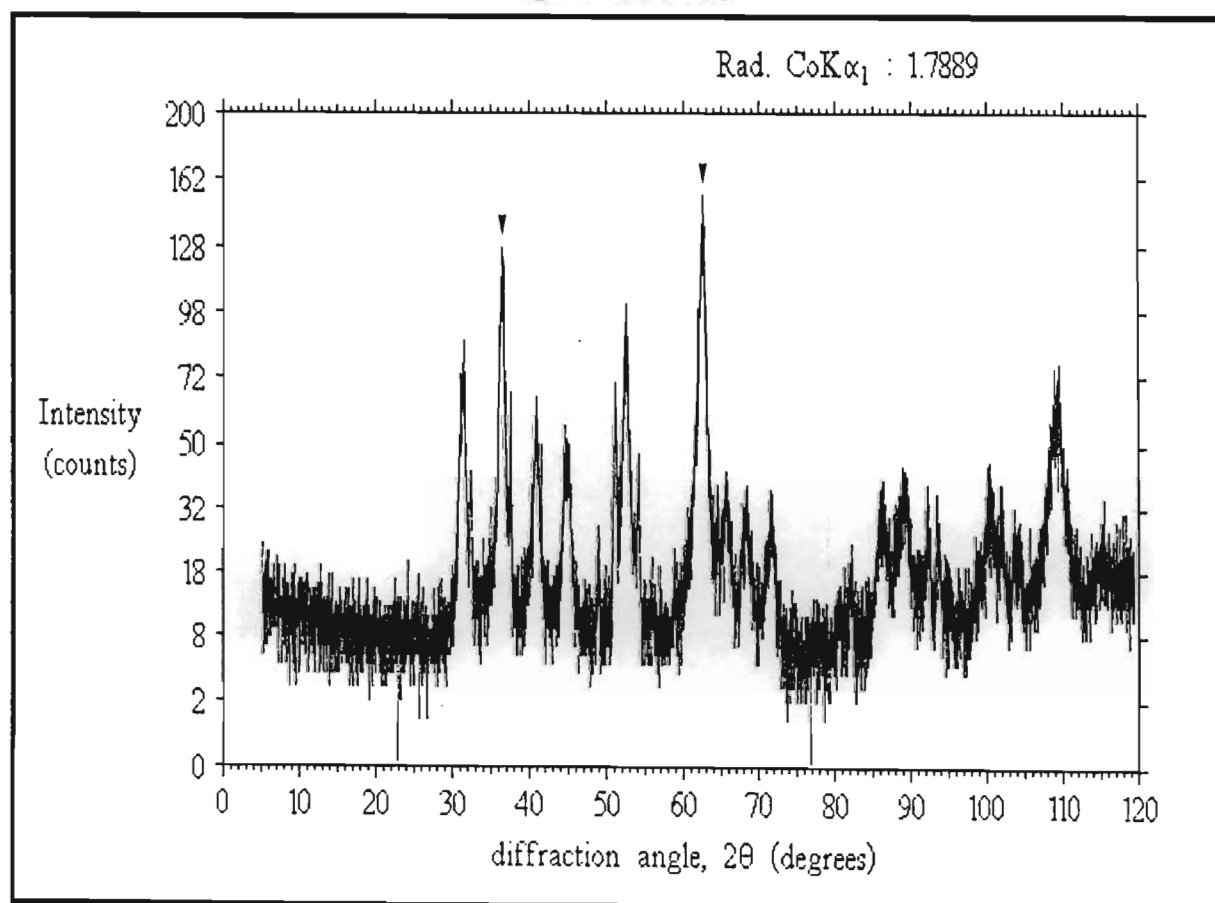
Figure 5.5.4-5(a)

Figure 5.5.4-5(b)

The unit cell dimension was calculated (using Cohen's least squares method - See **Appendix 1**) based on a cubic structure, and a unit cell dimension, a_0, of 5.6760Å obtained (Calculation data appears in **Table 5.5.4-9**.).

Table 5.5.4-9 **Calculation of unit cell dimension for the observed data given in Table 5.5.4-8 ($\lambda^2 = 3.2003$)**

d(Å)	2θ	θ	$\sin^2\theta$	(hkl)	$(h^2+k^2+l^2)$
3.300	31.46	15.73	0.0735	(111)	3
2.861	36.43	18.22	0.0977	(200)	4
2.556	40.96	20.48	0.1224	(210)	5
2.326	45.23	22.61	0.1479	(211)	6
2.022	52.52	26.26	0.1957	(220)	8
1.721	62.63	31.32	0.2701	(311)	11
1.647	65.78	32.89	0.2948	(222)	12
1.590	68.45	34.22	0.3163	(230)	13
1.525	71.81	35.91	0.3439	(321)	14
1.311	86.08	43.04	0.4658	(331)	19
1.273	89.26	44.63	0.4936	(420)	20
1.164	100.4	50.20	0.5902	(422)	24
1.095	109.5	54.76	0.6670	(333)	27

A = 0.024834	D = -0.000462	Unit cell dimension a_0 :	5.68 Å

Table 5.5.4-10 lists similar cubic compounds together with their a_0 values [42].

Table 5.5.4-10 **Cubic pgm chalcogenide minerals**

Formula	Mineral name	Structure	a_0(Å)	Card No.
$(Ru,Os,Ir)S_2$	laurite	cubic	5.61	19-1107
RuS_2	laurite	cubic	5.61	
$(Os,Rh,Ir)S_2$	erlichmanite	cubic	5.62	19-0882
$(Rh,Pt,Ru,Ir)AsS$	hollingworthite	cubic	5.77-5.80	
RhAsS	hollingworthite	cubic	5.78	
$(Ir,Ru,Rh,Pt)AsS$	irarsite	cubic	5.78	19-0591
IrAsS	irarsite	cubic	5.79	
$(Pt,Rh,Ru,Ir)AsS$	platarsite	cubic	5.79	29-0974
$Pt(As,S)_2$	platarsite	cubic	5.93	

Table 5.5.4-10 shows that based on the a_0 value, a compound with formula (pgm)AsS rather than (pgm)S_2 is indicated, where (pgm) represents some ratio of rhodium, platinum, ruthenium and iridium. A study of the mineral platarsite [43], found that as the platinum present in the pgm ratio increases, the measured a_0 value also increases. Given the low a_0 value measured (5.68Å), a compound of formula **(Ru,Rh,Ir,Pt)AsS** (with very low levels of platinum) is indicated by the observed data. **Figure 5.5.4-6** compares the reduced spectra of irarsite with that of the sample, showing that an iridium-rich compound also deviates from the observed data.

If the above assignment is correct, low rhodium solubility should be accompanied by low ruthenium solubility, and to a certain extent, low iridium solubility. **Table 5.5.4-11** compares the measured solubilities of these three pgms in the oxidative leach with XPD data for the phase assigned as (Ru,Rh,Ir,Pt)AsS. A clear correlation exists between the rhodium and ruthenium solubility of normal concentrates, extending in most cases to observed iridium solubility.

Table 5.5.4-11   Comparison of rhodium, ruthenium and iridium solubilities in the HCl/Cl$_2$ leach (for 8 concentrates)

	Solubility in the HCl/Cl$_2$ leach			Observed data		a_0
	Rh	**Ru**	**Ir**	**d(Å) (counts)**	**d(Å) (counts)**	**(Å)**
1	85.90	83.97	86.96	2.8793 (29)	1.7344 (21)	5.76
2	85.93	85.11	85.24	2.8606 (14)	1.7124 (13)	5.70
3	89.79	89.06	88.83	2.8741 (24)	- -	5.75
4	90.24	89.39	88.76	2.8330 (27)	1.7105 (36)	5.67
5	90.84	90.60	90.05	2.8362 (18)	1.7059 (18)	5.67
6	90.96	89.65	89.08	- -	1.7114 (10)	5.67
7	93.95	93.49	91.71	2.8732 (11)		5.75
8	98.06	97.91	95.75	- -	- -	-

The observed data in Table 5.5.4-11 relates to the two strongest peaks of the (Ru,Rh,Ir,Pt)AsS phase; these being a peak usually positioned at about 2.87Å
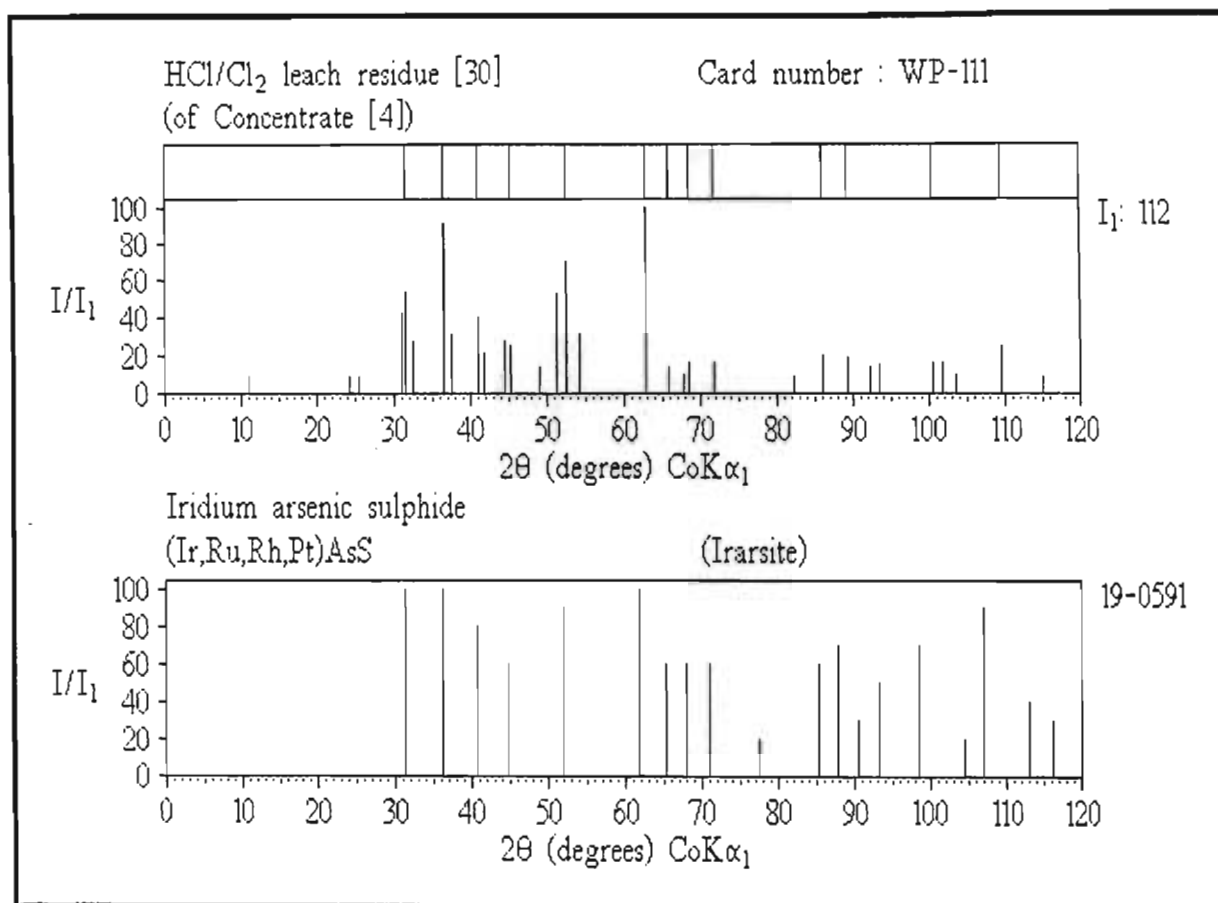
Figure 5.5.4-6

($2\theta = 36.3°$, (hkl) = **(200)**) and a peak positioned at about 1.71Å ($2\theta = 63.1°$, (hkl) = **(311)**). It should be noted that the d-spacings of these peaks are highly variable, reflecting variable unit cell dimensions (as shown by the roughly calculated a_0 values). Thus no definite Ru : Rh : Ir : Pt ratio seems to be indicated. No real relationship between the observed counts for this phase and solubility exists, except that when rhodium, ruthenium and iridium solubility is high, no peaks are observed.

5.5.5 LOW IRIDIUM SOLUBILITY

For minor concentrates low iridium solubility was ascribed to the formation of iridium oxide, **IrO_2**, that forms together with RuO_2 during the roast to volatilize selenium at the base metal refinery (§ 5.5.2). This also applies to normal concentrates if they have been overdried.

For normal concentrates dried correctly, low iridium solubility was shown to be closely related to a mixed chalcogenide, formulated as **(Ru,Rh,Ir,Pt)AsS**, where the platinum group metal ratio was variable, but low in platinum (§ 5.5.4). The iridium-containing alloy **$(Fe,Rh)_{1.2}Ir_{0.8}$** was also mentioned in § 5.5.4 as probably playing a minor role in iridium solubility.

One other iridium alloy was detected in a few samples. This was the alloy **(Os,Ir,Ru)** known mineralogically as iridosmine. **Table 5.5.5-1** compares the reference data for this compound with that observed for the oxidative leach residue of a normal concentrate (Note that the reference data is not all that accurate.).

Figure 5.5.5-1(a) and **(b)** shows the scan and reduced pattern of a sample containing this alloy. The peaks are usually of low intensity and sharp.

Table 5.5.5-1 Comparison of (Os,Ir,Ru) alloy reference data with peaks observed for a HCl/Cl$_2$ leach residue

(Os,Ir,Ru) Reference data [44]			HCl/Cl$_2$ residue [6] (WP-010) Observed data		
d(Å)	(I/I$_1$)	2θ	d(Å)	(I/I$_1$)	2θ
2.13	(100)	49.7	2.139	(100)	49.4
2.03	(50)	52.3	2.032	(67)	52.2
1.58	(50)	69.0	1.582	(67)	68.8
1.35	(60)	83.0	1.352	(53)	82.9
1.22	(100)	94.3	1.222	(100)	94.1
1.14	(40)	103.4	1.144	(67)	102.8
1.13	(10)	104.7	**1.134**	**(-)**	**104.2**
1.07	(70)	113.4	1.068	(53)	113.8

This is also a residual mineral phase. The analysis of the reference alloy (a natural sample from the Urals, Russia) gave a composition of 46.0% Os, 24.5% Ir, 18.3% Ru, 7.4% Pt and 2.6% Fe. Impurities were gold and copper [45]. The analysis of a South African sample gave an approximate formula of $Os_{0.69}Ir_{0.24}Ru_{0.05}Pt_{0.01}Fe_{0.01}$ [46]. As the levels of osmium in concentrates are very low, the effect of this alloy on iridium solubility will be almost negligible. The phase is nevertheless of interest as it shows in what form the small amounts of osmium are occurring.
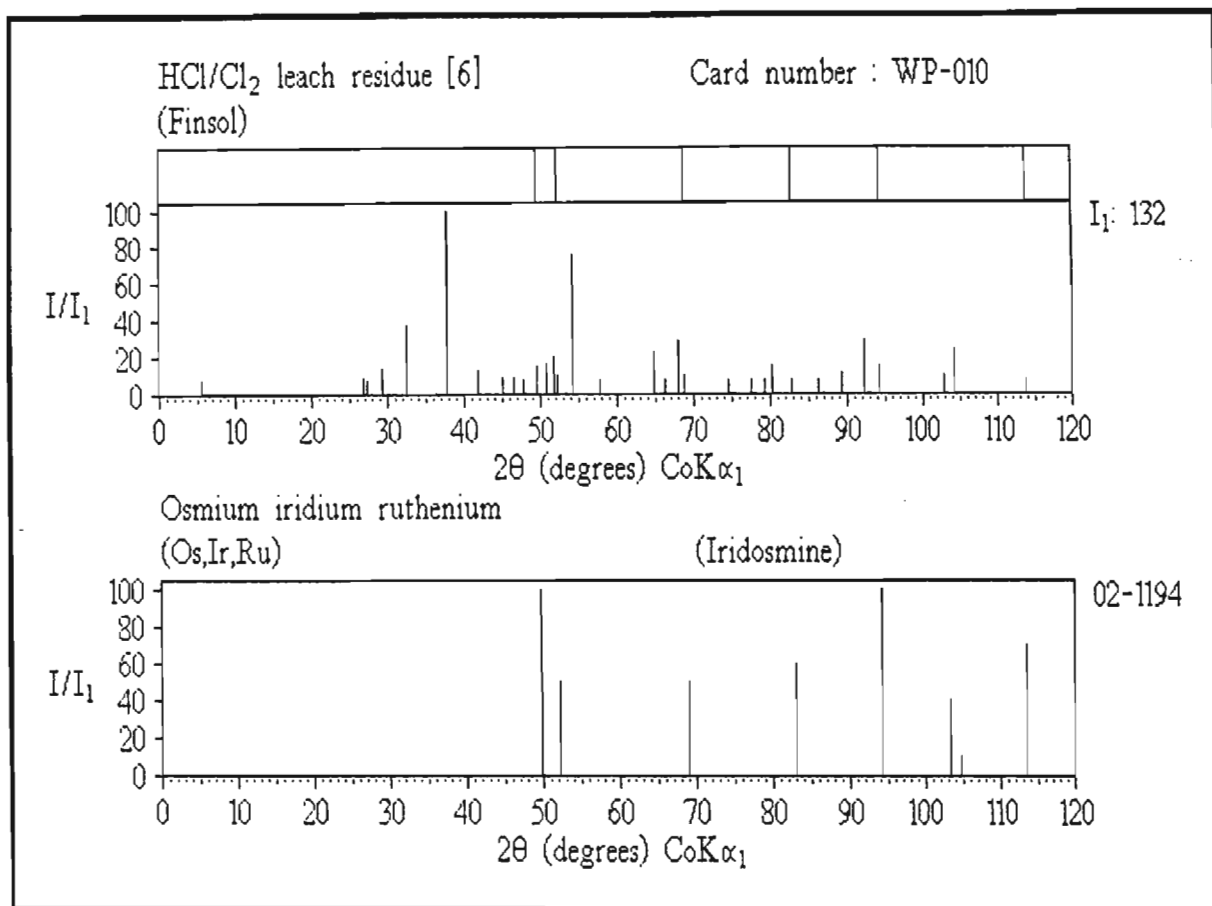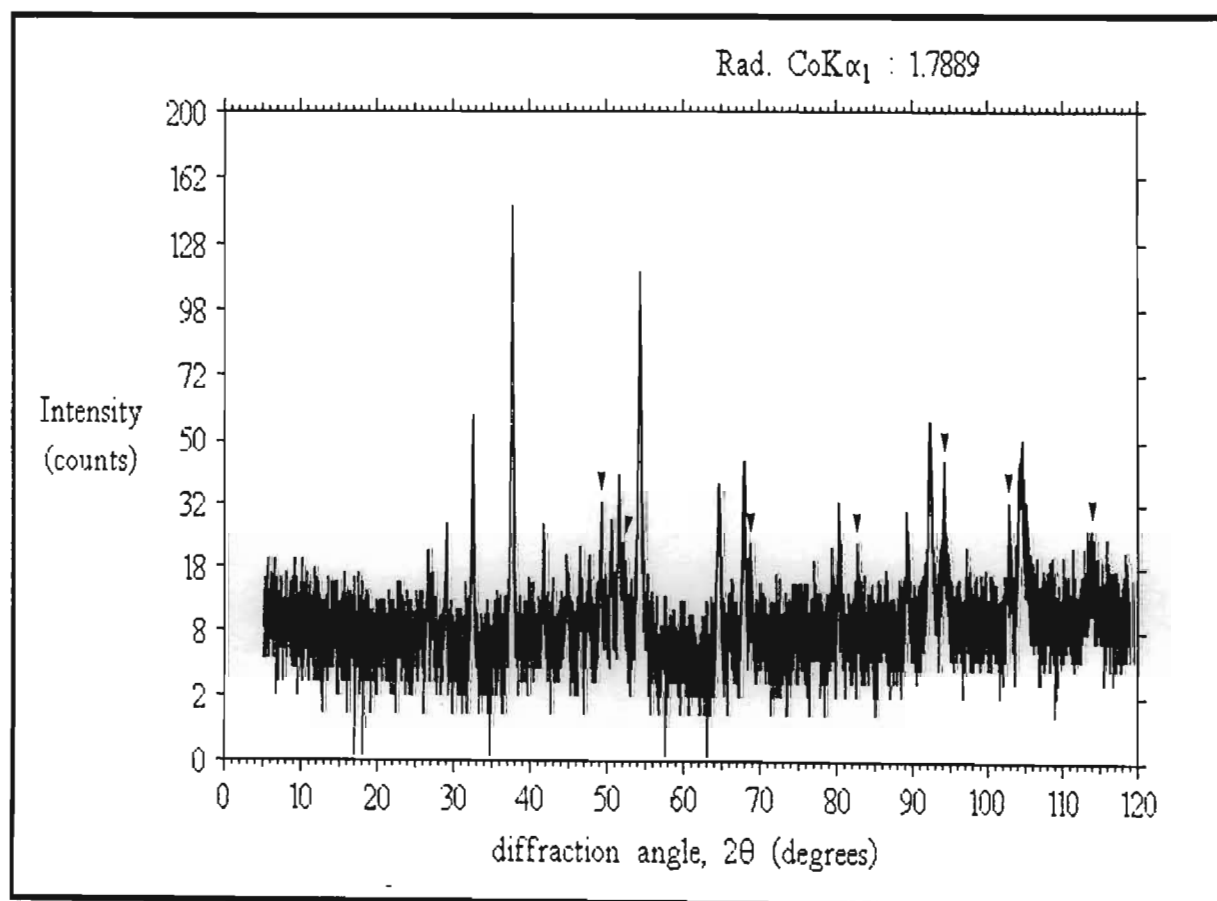
Figure 5.5.5-1(a)

Figure 5.5.5-1(b)

5.5.6 LOW PALLADIUM SOLUBILITY

Palladium solubility in the HCl/Cl$_2$ leach is the best of all platinum group metals (Table 5.5.1-1). For normal concentrates it rarely drops below 99%, and can be as high as 99.978%. The reason for small amounts of palladium in normal concentrates being insoluble is discussed in § 5.5.7. In some rare cases normal concentrates show quite bad palladium solubility. The XPD examination of the concentrate and the residue of one such case revealed that low palladium solubility was the result of insoluble palladium oxide, **PdO**. **Table 5.5.6-1** compares the reference data for this compound with that observed for a normal concentrate and its HCl/Cl$_2$ leach residue.

Table 5.5.6-1 Comparison of PdO reference data with peaks observed for a concentrate and HCl/Cl$_2$ leach residue

PdO Reference data [47]			Concentrate [1] (WP-095) Observed data			HCl/Cl$_2$ residue [26] (WP-107) Observed data		
d(Å)	(I/I$_1$)	2θ	d(Å)	(I/I$_1$)	2θ	d(Å)	(I/I$_1$)	2θ
2.644	(100)	39.5	2.636	(100)	39.7	2.624	(100)	39.9
2.153	(20)	49.1	2.156	(44)	49.0	2.148	(25)	49.2
1.674	(30)	64.6	**1.685**	**(-)**	**64.1**	**1.683**	**(-)**	**64.2**
1.536	(18)	71.2	1.536	(44)	71.2	1.543	(35)	70.9
1.319	(20)	85.4	1.315	(44)	85.7	1.316	(25)	85.7
1.1334	(6)	104.2	-	-	-	1.132	(25)	104.5
1.0806	(10)	111.7	-	-	-	1.079	(25)	111.9

Figure 5.5.6-1(a) and **(b)** shows palladium oxide as detected in the above residue. When palladium oxide is present, the strongest line occurring at about 2.64Å is generally the only one observed. This concentrate had been overdried at the base metal refinery. This was immediately evident as some ruthenium had been oxidized and a high crystallinity was noted. Some palladium had clearly been oxidized during drying.

Palladium oxide is insoluble in acids when anhydrous, but can be reduced to the metal on contact with hydrogen at room temperature [48].
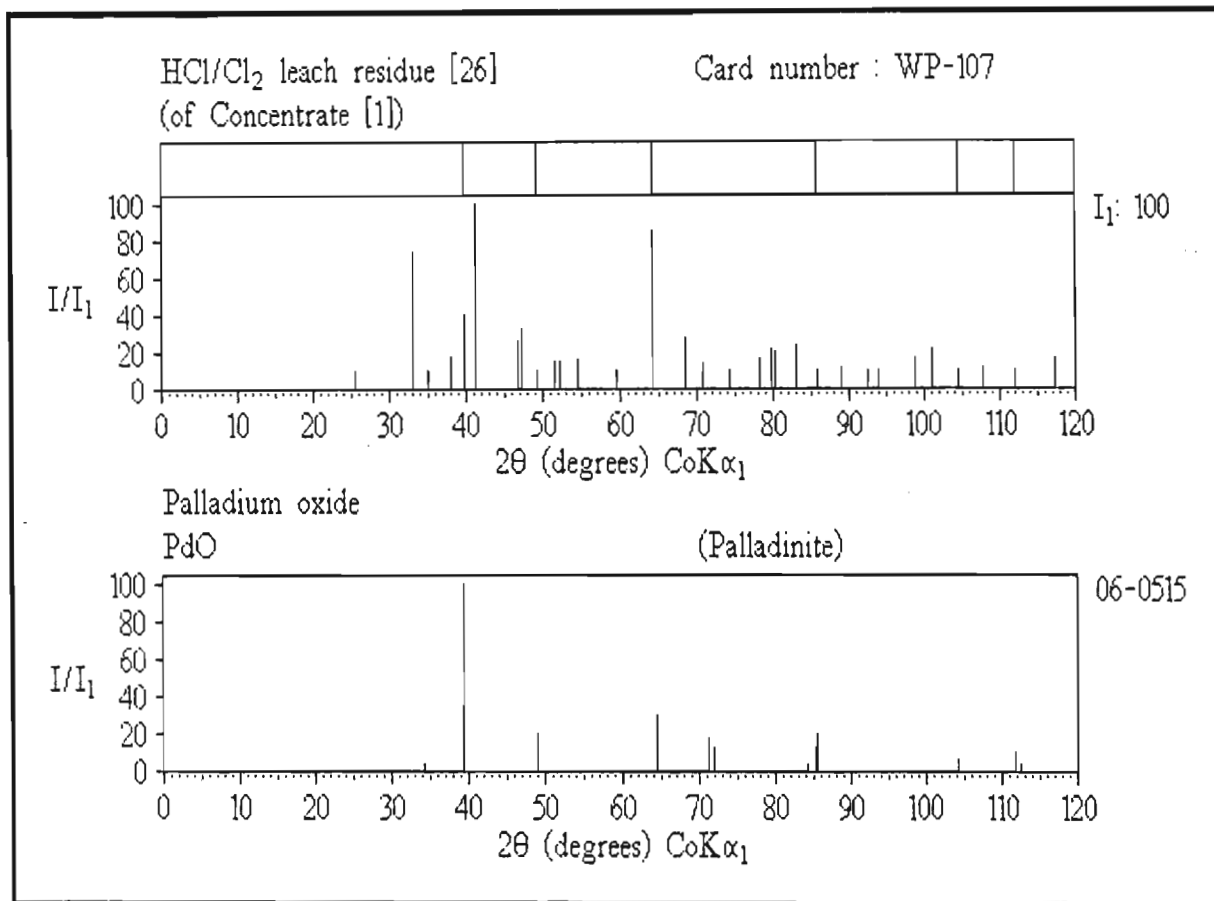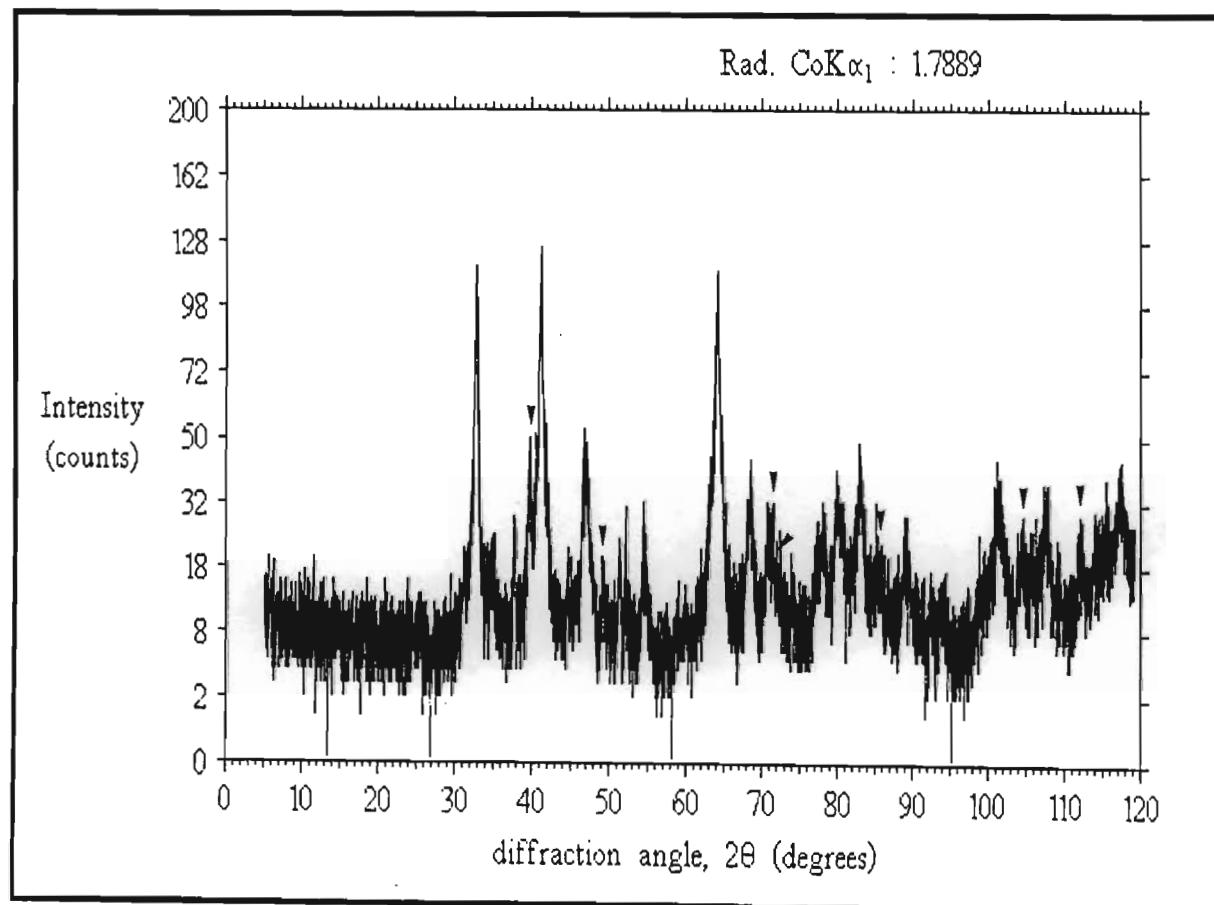
Figure 5.5.6-1(a)

Figure 5.5.6-1(b)

Determining the reasons for the low palladium solubility of minor concentrates is complicated by the fact that the two main phases present, $(Ru,Ir)O_2$ and $RhSe_{2+x}$, dominate the concentrate and residue spectra. Both PdO and PdSe could form, but PdO seems more probable, having been found in overdried normal concentrates.

5.5.7 LOW PLATINUM SOLUBILITY

Platinum solubility in the oxidative leach generally ranges from 95.6 to 99.9 % for normal concentrates. A typical consignment of such concentrate usually contains about 78kg of platinum, meaning that for every 0.1% drop in platinum solubility, 2.5 oz (troy) of platinum remain behind in the oxidative leach residue. In cases of severe insolubility the insoluble residue for a single consignment can contain over 100 oz (troy) of platinum that have to be processed by other methods. Normal concentrates and their HCl/Cl_2 leach residues were examined using XPD with the aim of explaining the lowering of platinum solubility. Results showed that in almost all cases only one platinum compound was responsible for solubility loss, this being the platinum sulphide **PtS**.

Table 5.5.7-1   Comparison of PtS reference data with peaks observed for two HCl/Cl_2 leach residues

PtS Reference data [49]			HCl/Cl_2 residue [4] [WP-004] Observed data			HCl/Cl_2 residue [26] [WP-116] Observed data		
d(Å)	(I/I_1)	2θ	d(Å)	(I/I_1)	2θ	d(Å)	(I/I_1)	2θ
3.02	(100)	34.5	3.025	(100)	34.4	3.020	(100)	34.5
2.452	(16)	42.8	2.461	(24)	42.6	2.452	(31)	42.8
1.910	(35)	55.8	1.916	(45)	55.6	1.914	(43)	55.7
1.754	(20)	61.3	1.761	(41)	61.0	1.759	(31)	61.1
1.733	(16)	62.1	1.736	(54)	62.0	1.734	(31)	62.1
1.505	(35)	72.9	1.508	(25)	72.7	1.505	(29)	72.9
1.296	(8)	87.3	-	-	-	1.299	(15)	87.0
1.233	(16)	93.0	1.239	(26)	92.4	1.237	(30)	92.7
1.226	(6)	93.7	1.226	(15)	93.7	1.227	(20)	93.6
1.152	(8)	101.9	1.152	(21)	101.9	-	-	-
1.137	(10)	103.8	1.137	(14)	103.8	1.135	(15)	104.1

Table 5.5.7-1 compares the data for this compound with data observed for peaks in two oxidative leach residues showing high levels of this sulphide.

Once the presence of this phase had been established, platinum solubility was compared to the intensity (as given in counts), and the relative intensity (I/I_1) of the **(002, 101)** PtS line. **Table 5.5.7-2** clearly shows that a relationship exists between the intensity of this peak and observed platinum solubility. As a general trend, it was also noted that the higher the sulphur content of the concentrate, the less platinum would be soluble.

Table 5.5.7-2   Comparison of Pt solubility with the intensity of the 3.02Å PtS line observed for a series of normal concentrates residues

Platinum Solubility (%)	HCl/Cl$_2$ residue 3.02Å (002, 101) PtS peak		Sulphur content of concentrate (%)
	counts	(I/I_1)	
95.58	67	(100)	11.3
98.11	37	(52)	10.3
98.12	24	(32)	9.3
98.83	21	(18)	11.1
99.41	10	(14)	8.6
99.89	0	(0)	8.5

Figures 5.5.7-1(a) and **(b)**   show PtS as detected in the oxidative leach residue of a normal concentrate showing low platinum solubility.

Figures 5.5.7-2, 3, 4, 5, 6 and **7** show the six residue scans corresponding to the data given in Table 5.5.7-2 (in the same order). In each case the **(002, 101)** PtS peak has been indicated.

This sulphide has a considerable inertness, being insoluble in all acids except nitric acid. It can however be decomposed by heating in air [50], via the reaction :

$$PtS + O_2 \longrightarrow Pt + SO_2$$

HCl/Cl$_2$ leach residue [4]   Card number : WP-004
(Finsol : Dried at 130°C)

I_1: 74

Platinum sulphide
PtS   (Cooperite)
18-0972

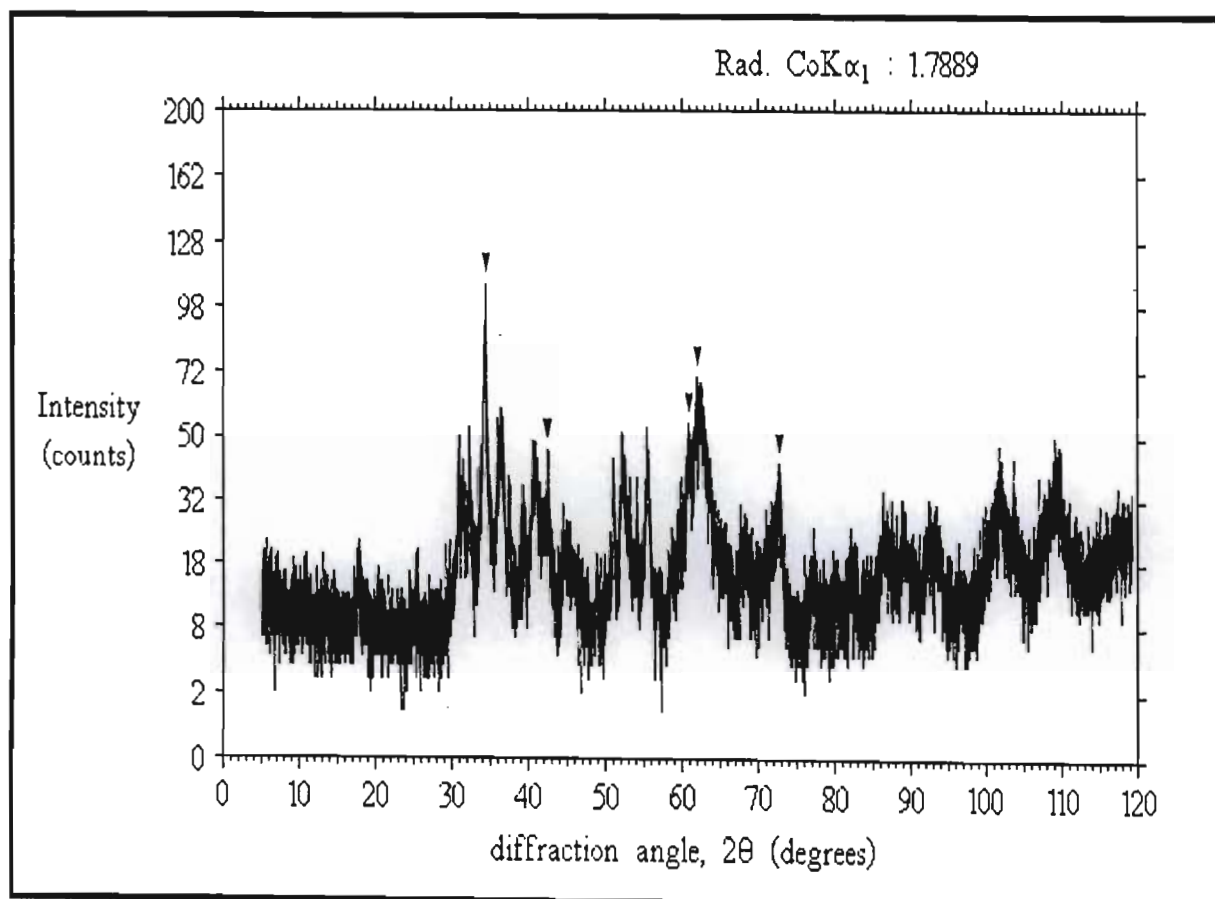**Figure 5.5.7-1(a)**

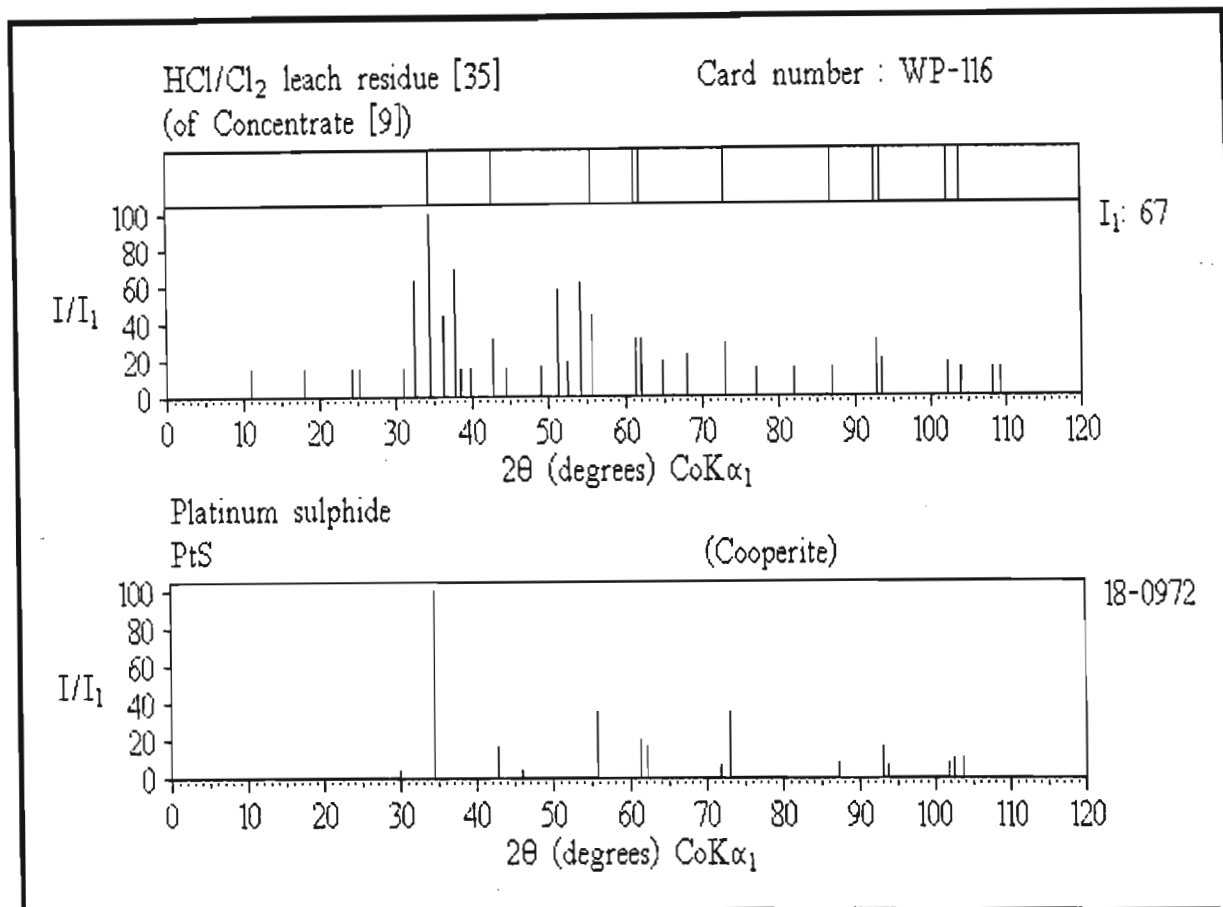Rad. CoKα_1 : 1.7889
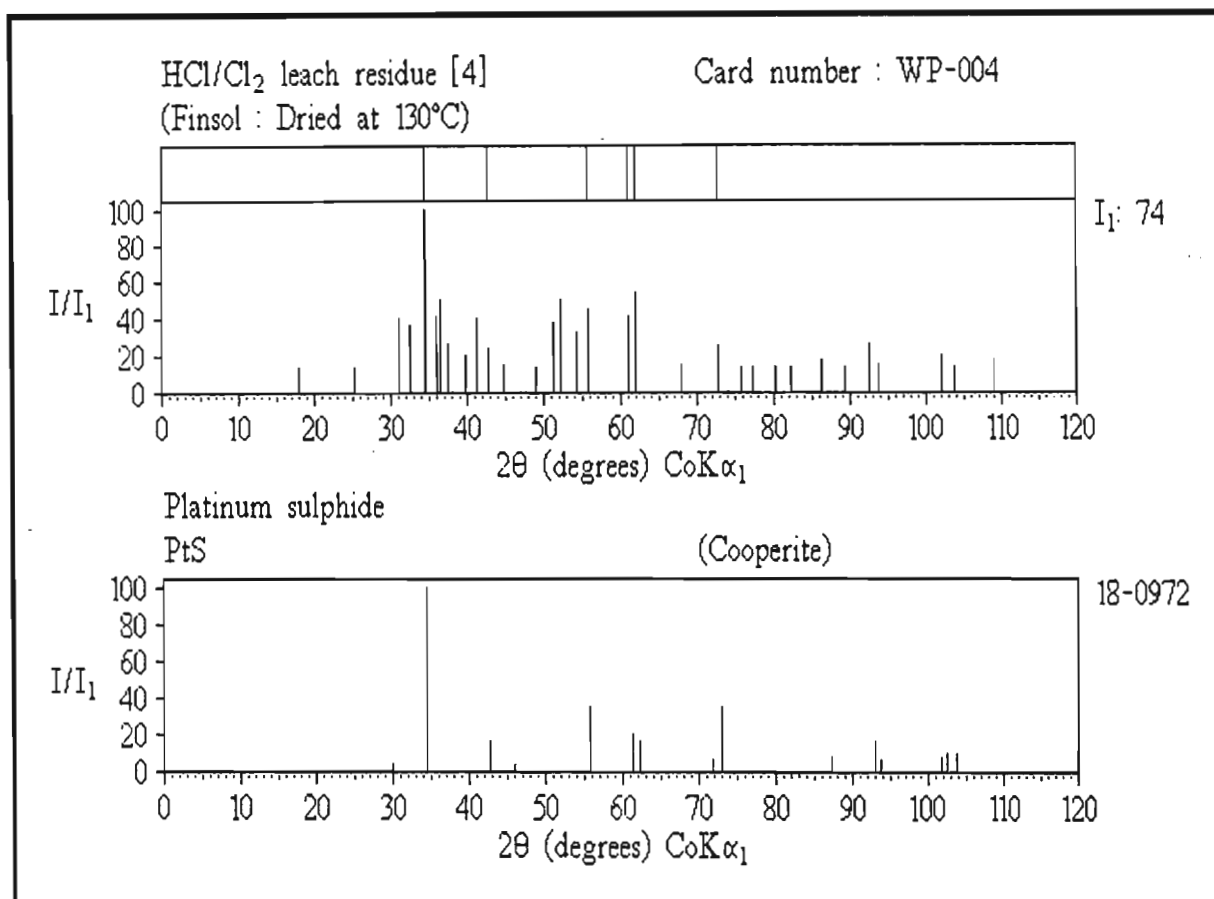
Figure 5.5.7-1(b)
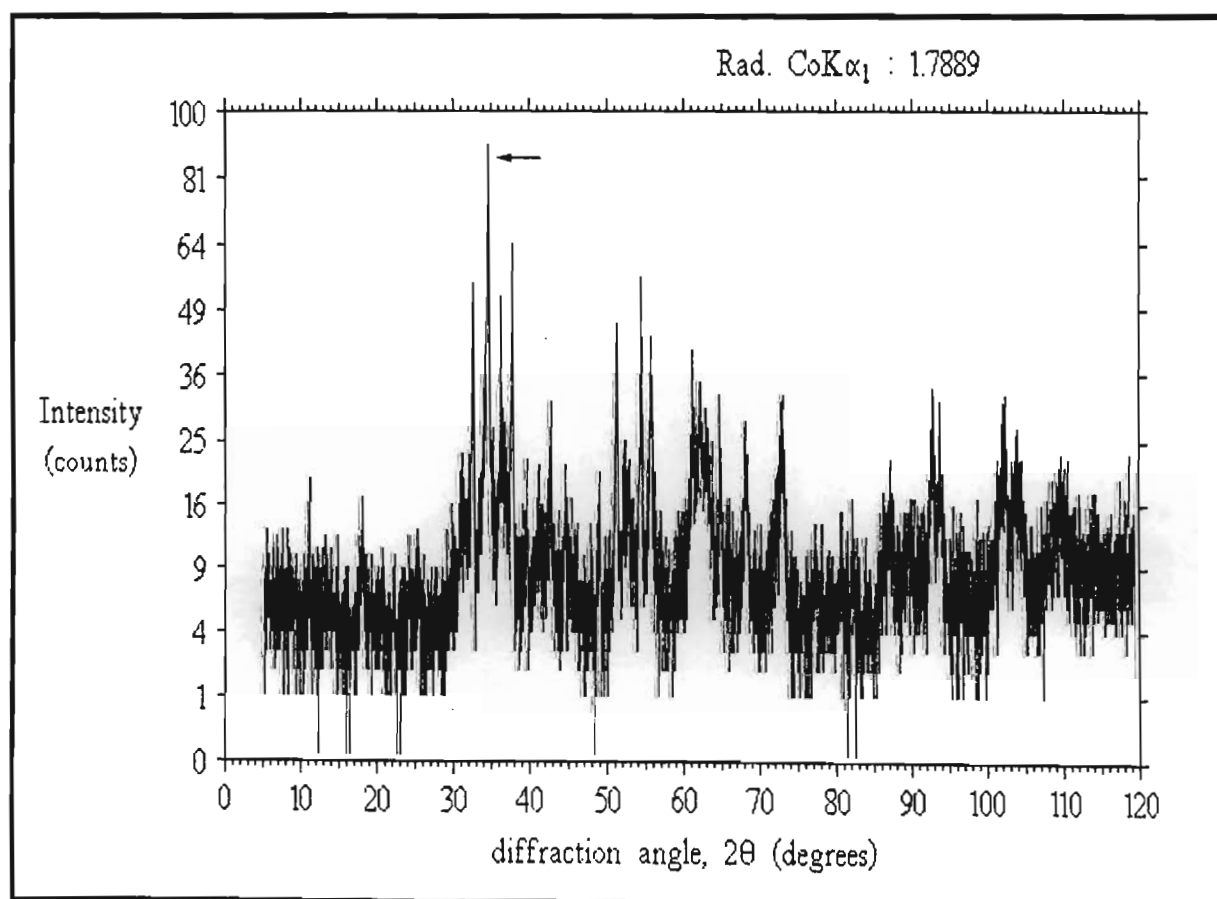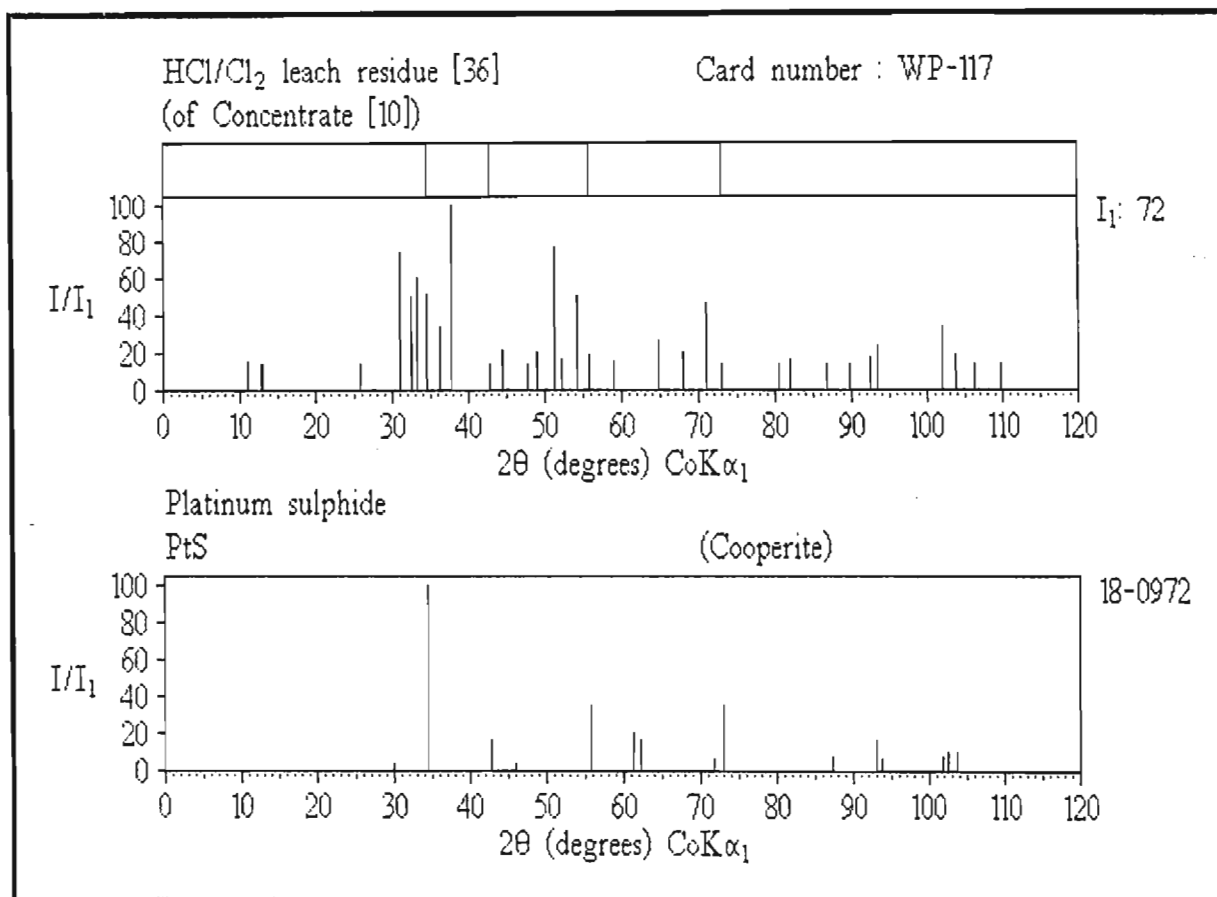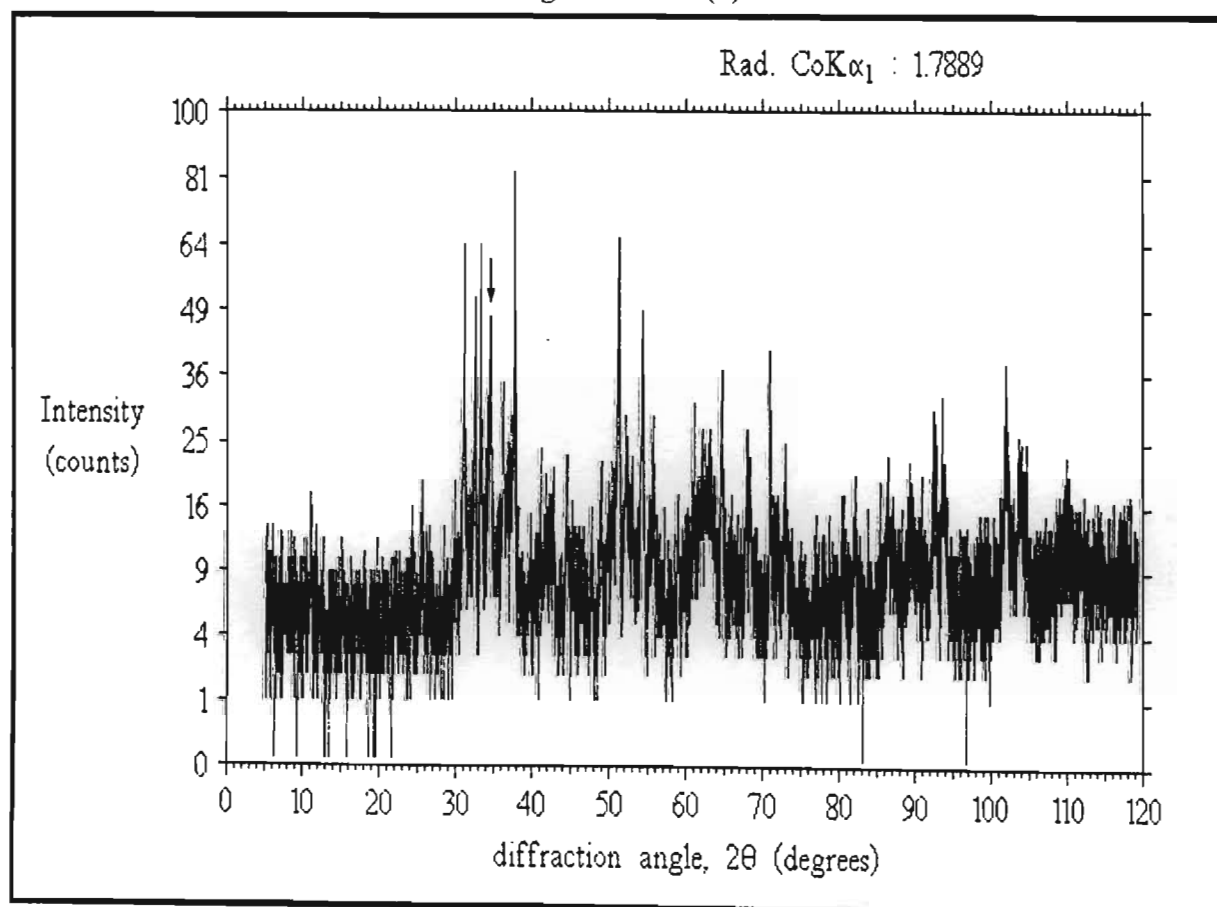
Figure 5.5.7-2(a)

Figure 5.5.7-2(b) Residue scan of a concentrate showing a Pt solubility of 95.58%

Figure 5.5.7-3(a)

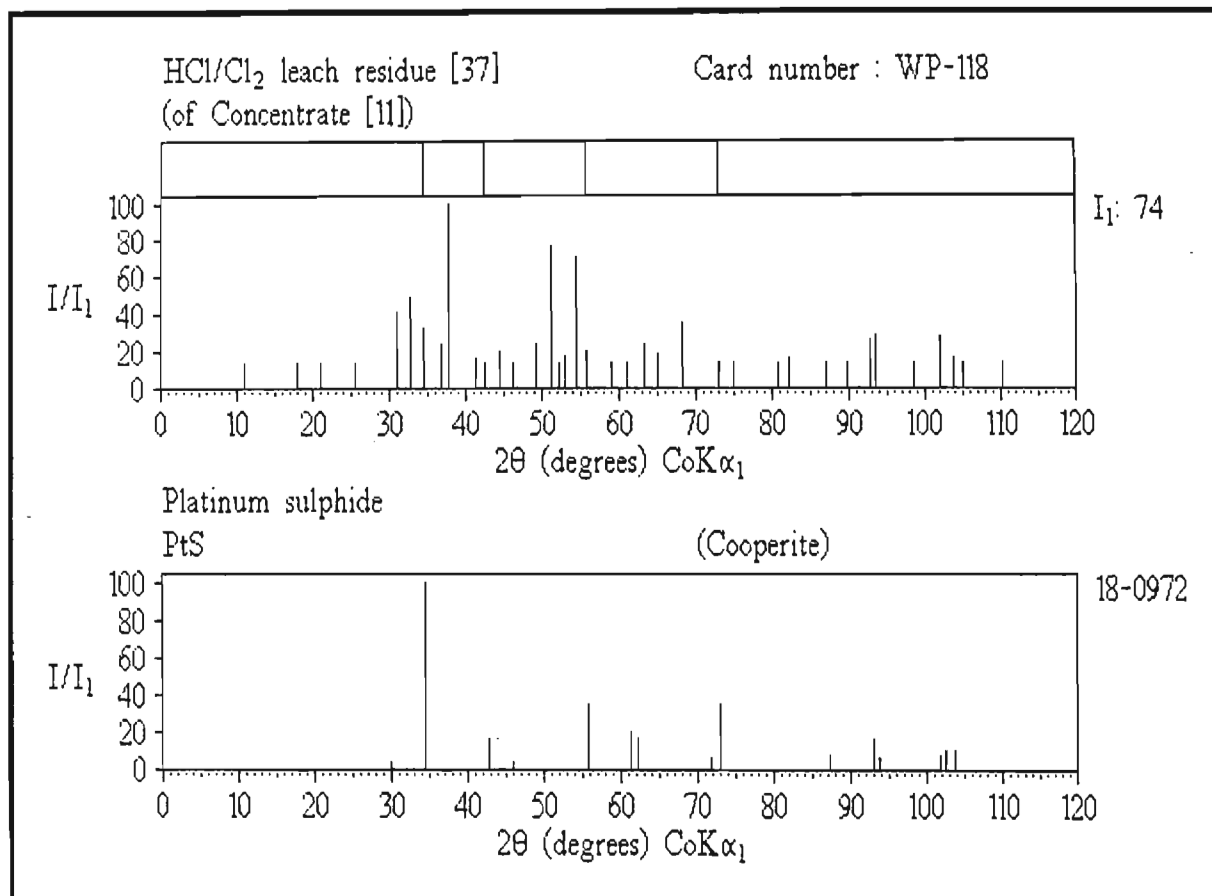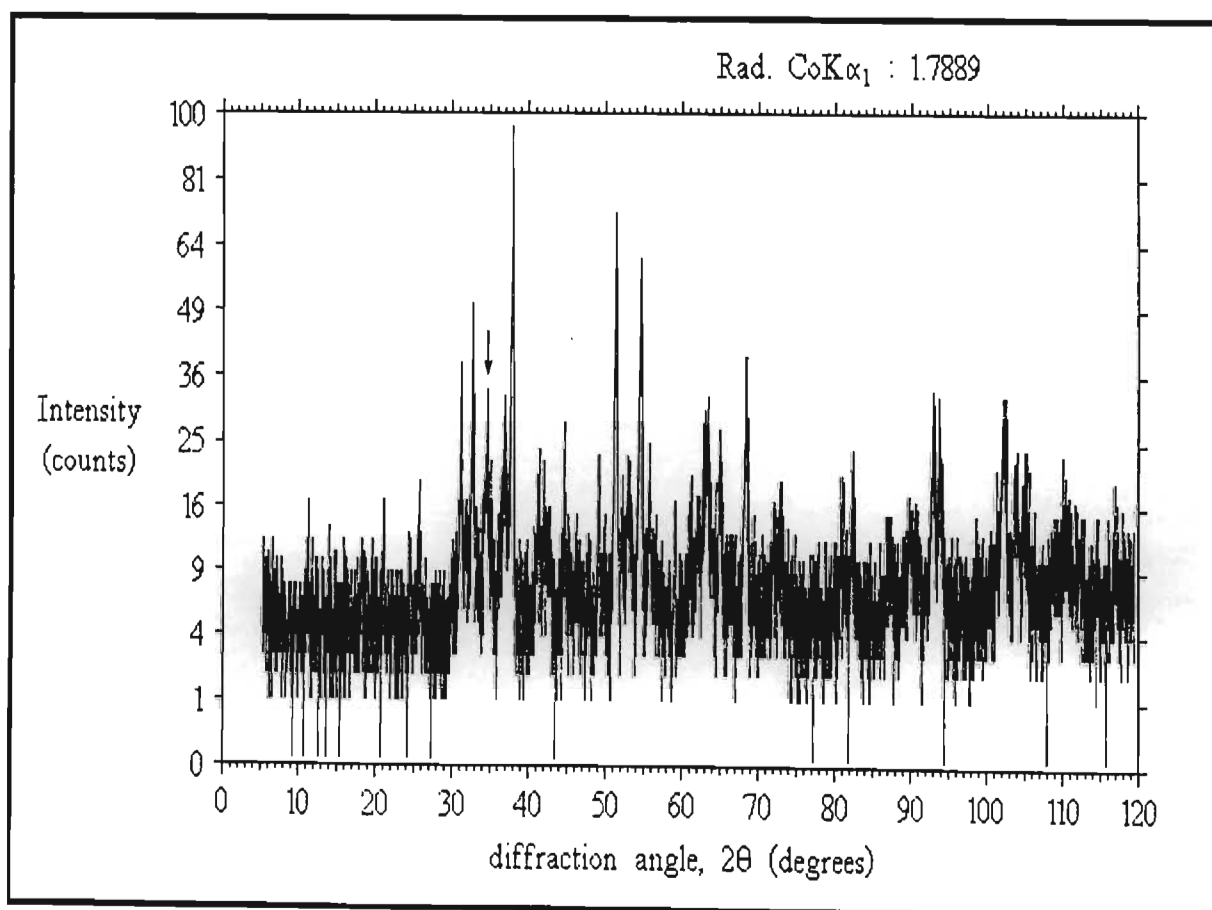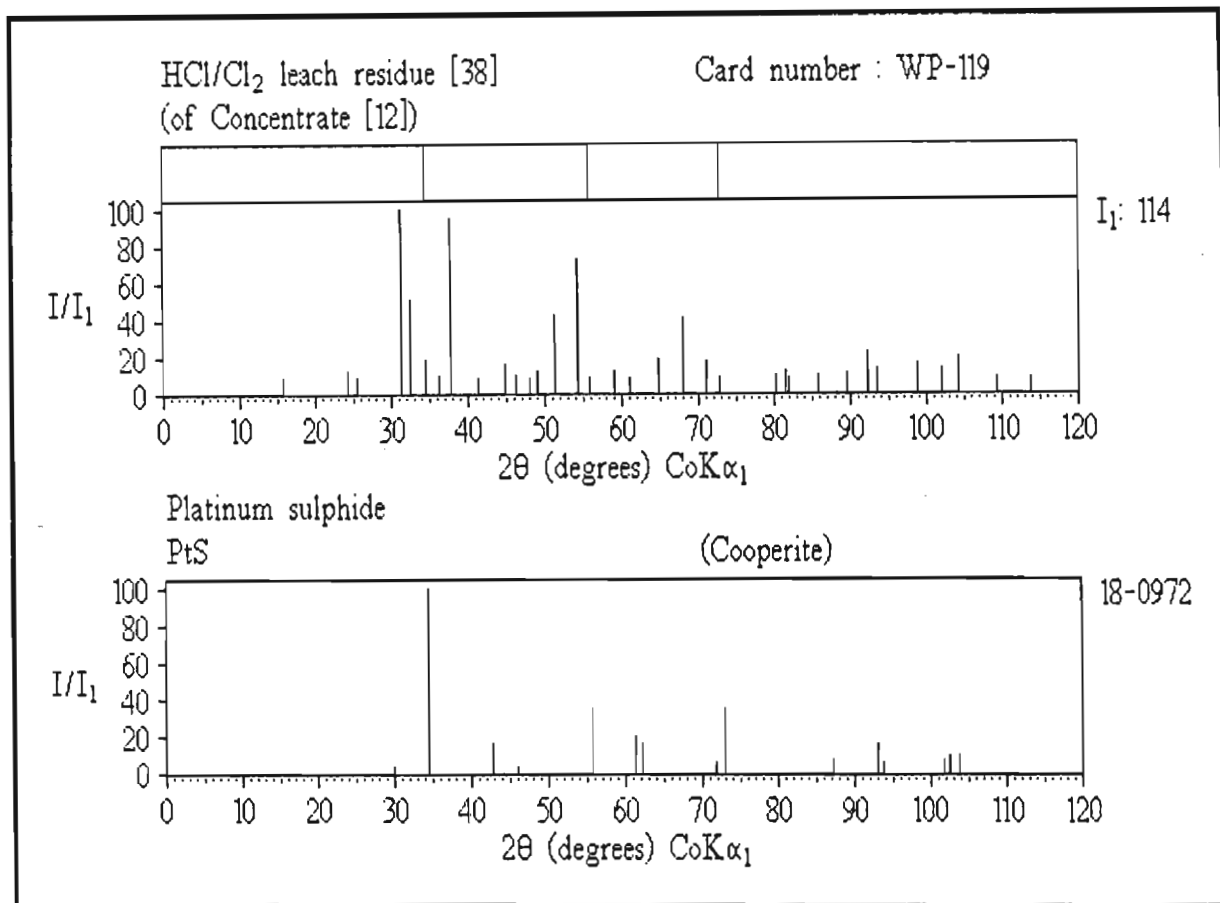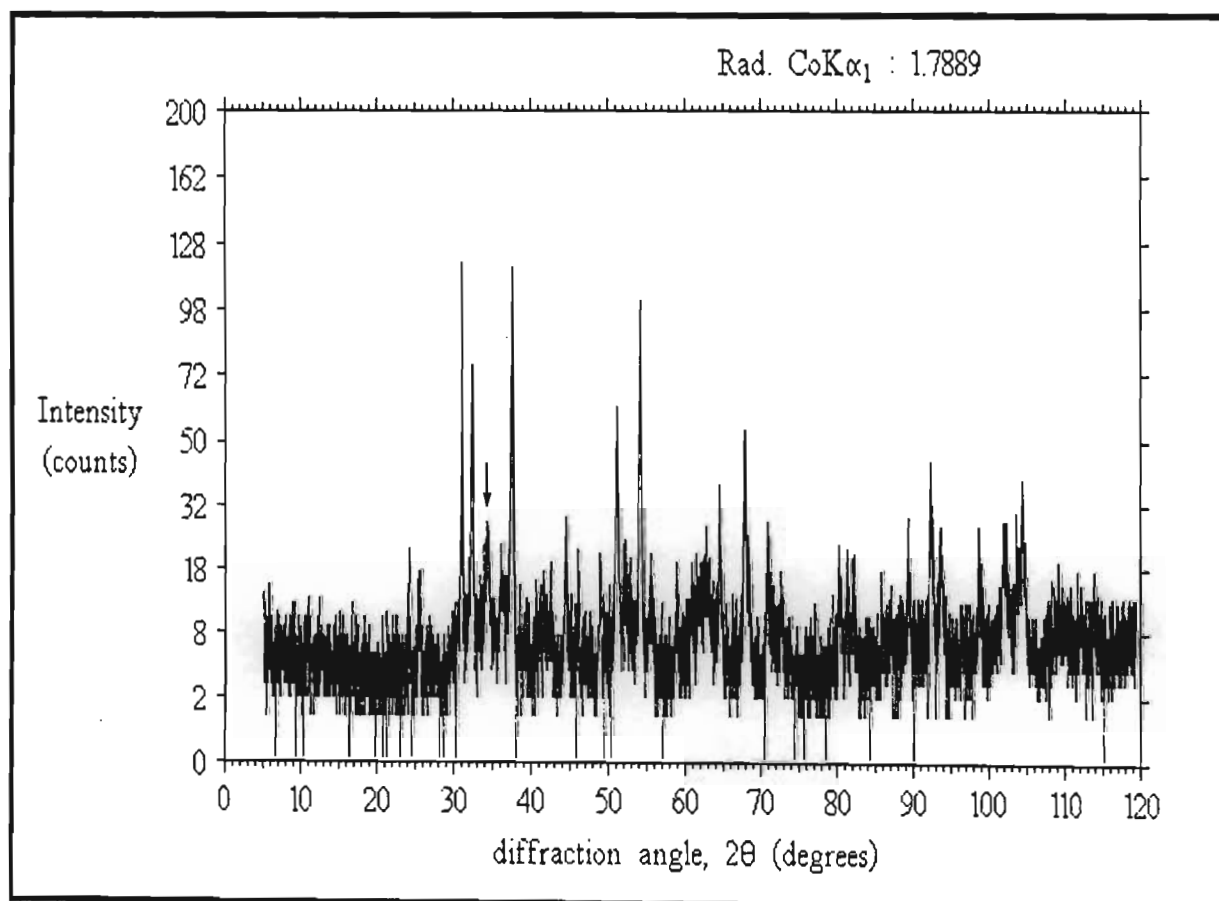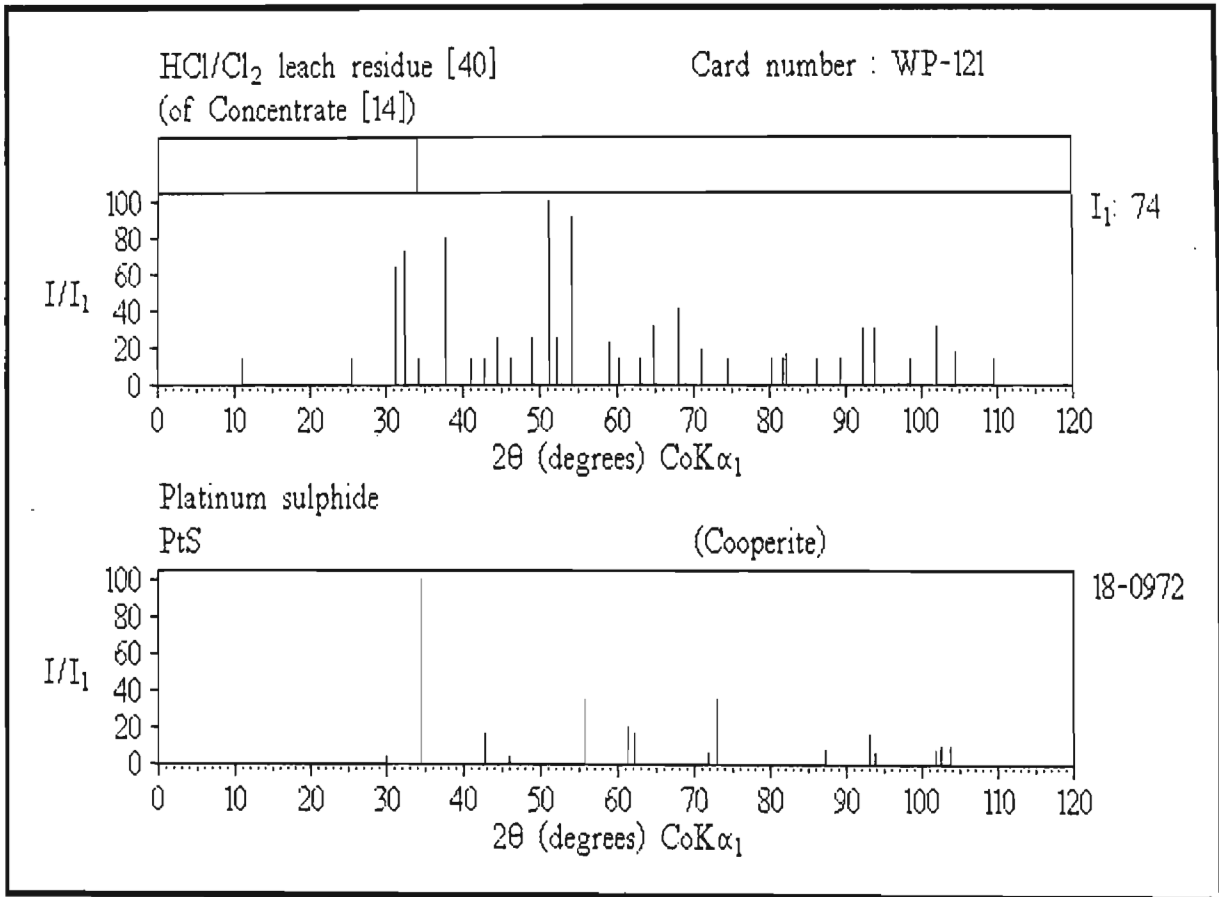**Figure 5.5.7-3(b)** Residue scan of a concentrate showing a Pt solubility of 98.11%

HCl/Cl$_2$ leach residue [37]   Card number : WP-118
(of Concentrate [11])

Platinum sulphide
PtS   (Cooperite)   18-0972

Figure 5.5.7-4(a)
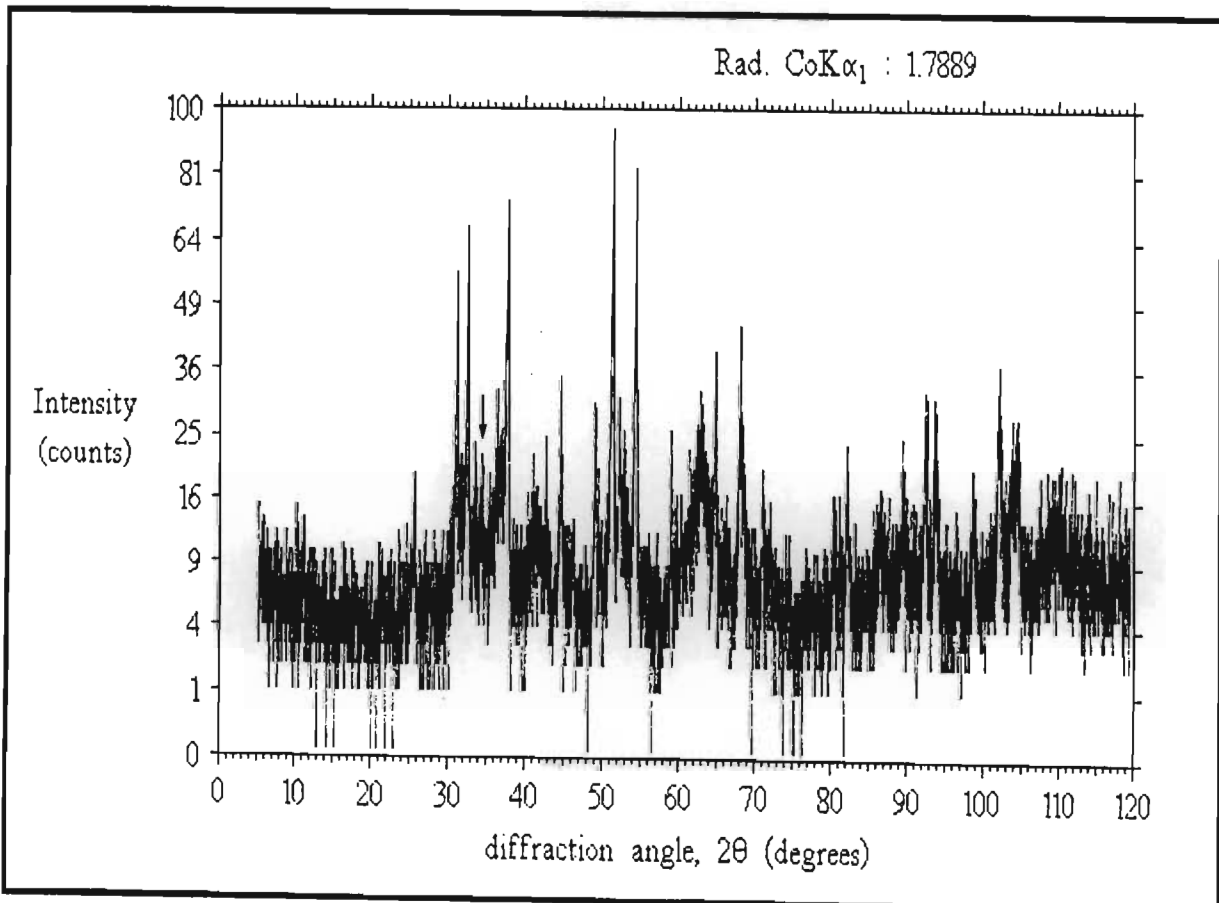
Rad. CoKα_1 : 1.7889

Figure 5.5.7-4(b) Residue scan of a concentrate showing a Pt solubility of 98.12%

Figure 5.5.7-5(a)

Figure 5.5.7-5(b) Residue scan of a concentrate showing a Pt solubility of 98.83%

Figure 5.5.7-6(a)

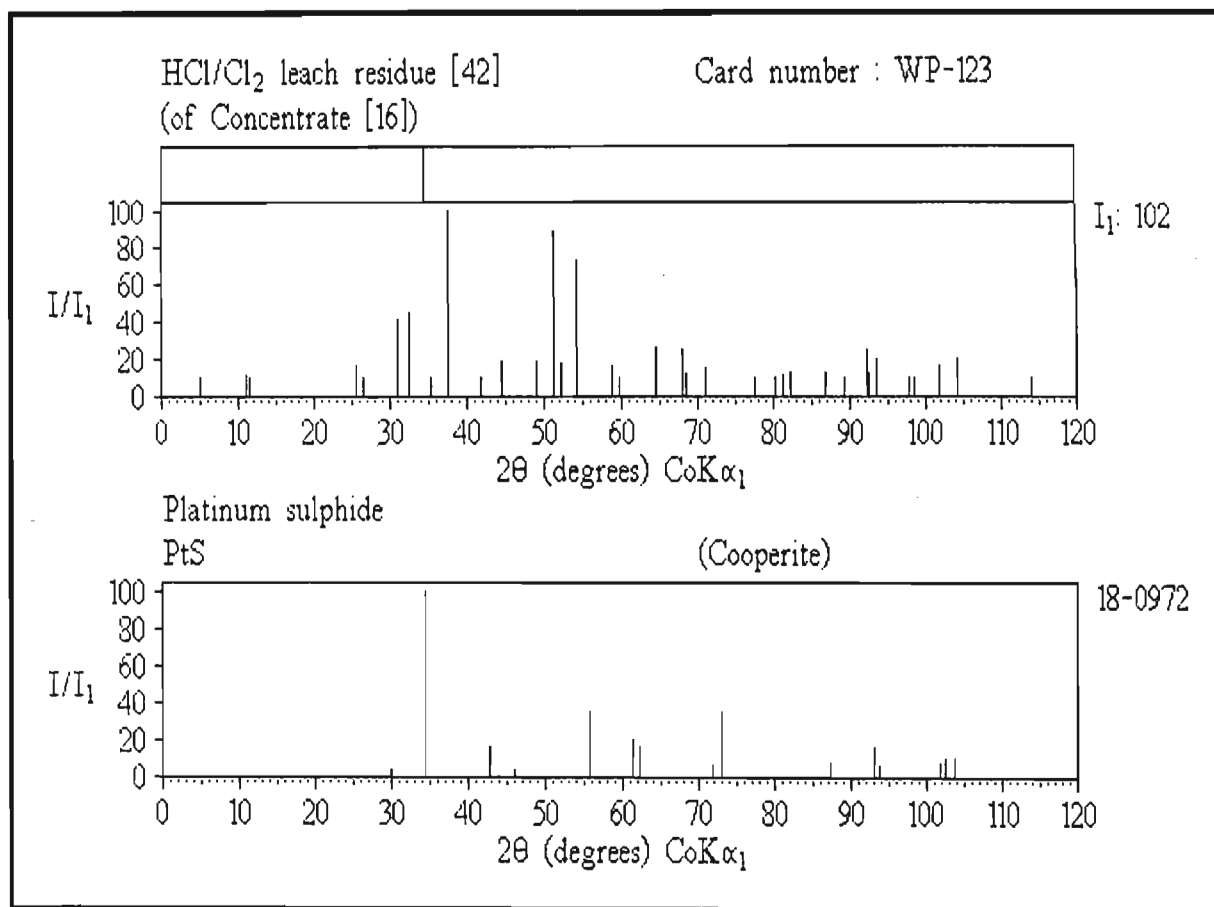**Figure 5.5.7-6(b)** Residue scan of a concentrate showing a Pt solubility of 99.41%
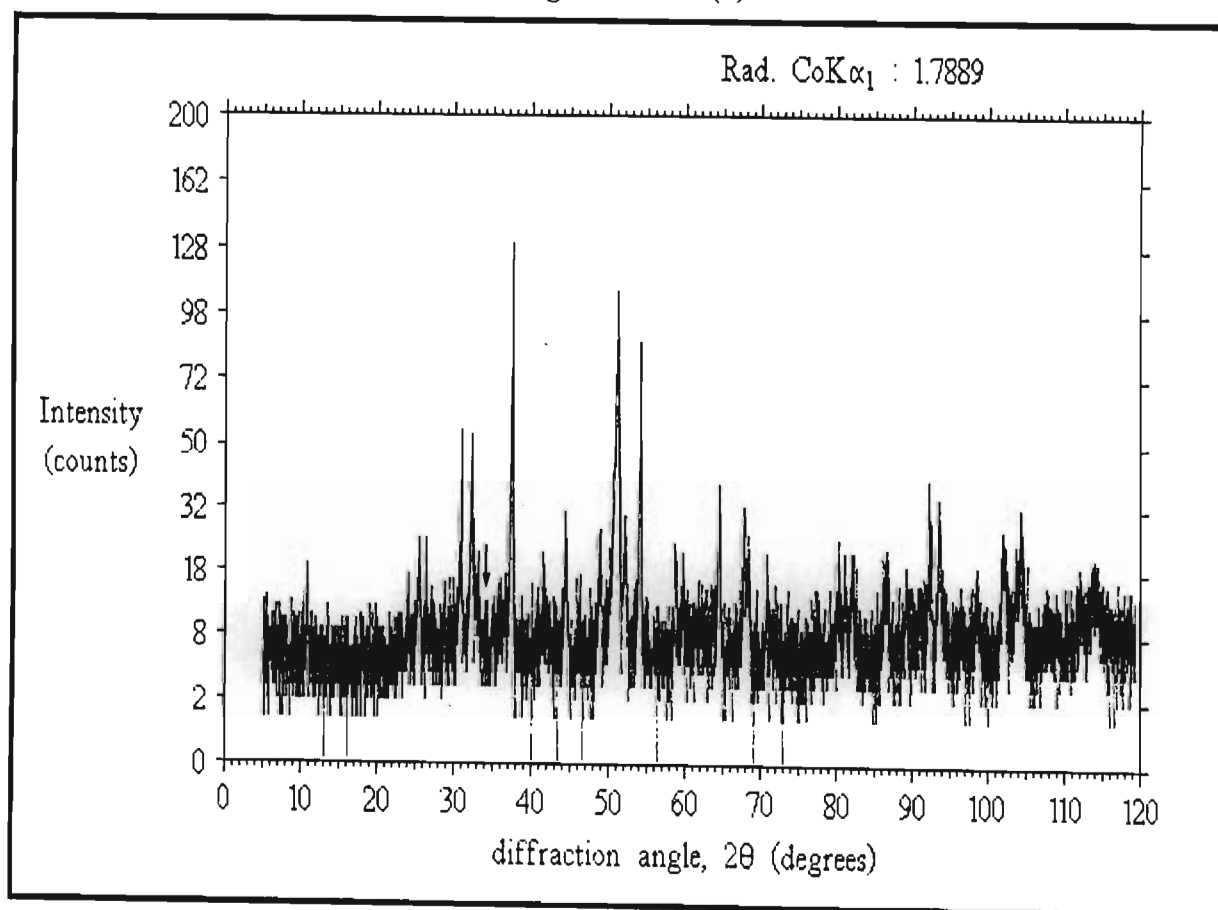
Figure 5.5.7-7(a)

Figure 5.5.7-7(b) Residue scan of a concentrate showing a Pt solubility of 99.89%

A sample showing a high PtS content was ignited at about 700°C, and the residue scanned. The intensity of the PtS (**002, 101**) line had been greatly reduced, and new lines corresponding closely to platinum had appeared (**Figure 5.5.7-8(a), (b)** and **(c)**). Pure platinum was not however indicated because a slight shift towards the d-spacings given by palladium was evident. In **Table 5.5.7-3** XPD data for reference platinum is compared to that obtained by the ignition of pure $(NH_4)_2[PtCl_6]$ and that obtained from the ignition of PtS. The last column gives the data for reference palladium for comparison. (See also **Figure 5.5.7-9(a)** and **(b)**.) The platinum residue thus had palladium present as an impurity, meaning the original sulphide is better formulated as **(Pt,Pd)S** (Pt>>Pd) rather than PtS.

Table 5.5.7-3 Comparison of XPD data for Pt obtained from the ignition of PtS and pure $(NH_4)_2[PtCl_6]$ with reference data for Pt and Pd

Pt Reference data [51]			Pt $(NH_4)_2[PtCl_6]$			Pt PtS			Pd Reference data [52]		
d(Å)	(I/I₁)	2θ	d(Å)	(I/I₁)	2θ	d(Å)	(I/I₁)	2θ	d(Å)	(I/I₁)	2θ
2.265	(100)	46.5	2.266	(100)	46.5	2.255	(100)	46.7	2.246	(100)	46.9
1.9616	(53)	54.3	1.965	(51)	54.2	1.956	(51)	54.4	1.945	(42)	54.8
1.3873	(31)	80.3	1.388	(45)	80.2	1.381	(35)	80.8	1.376	(25)	81.1
1.1826	(33)	98.3	1.1828	(62)	98.3	1.1763	(43)	99.0	1.1730	(24)	99.4
1.1325	(12)	104.3	1.1330	(22)	104.3	1.1248	(13)	105.4	1.1232	(8)	105.6

This platinum sulphide is one of the well known minerals of platinum (known mineralogically as cooperite). It commonly occurs in ore from all sectors of the UG-2 chromite layer [53], and accounts for about 40% of platinum group minerals in the Merensky Reef [54]. Microprobe analyses [55] have shown that some natural samples can contain 5.78% palladium; typical impurities were found to be nickel, lead and bismuth. Thus an ignition of the sulphide could produce a Pt-Pd residue (rather than a pure Pt residue), as was observed. The natural origin of this phase is also supported by the fact that PtS is stable in other sulphide phases [56]. In matte, PtS could remain in the
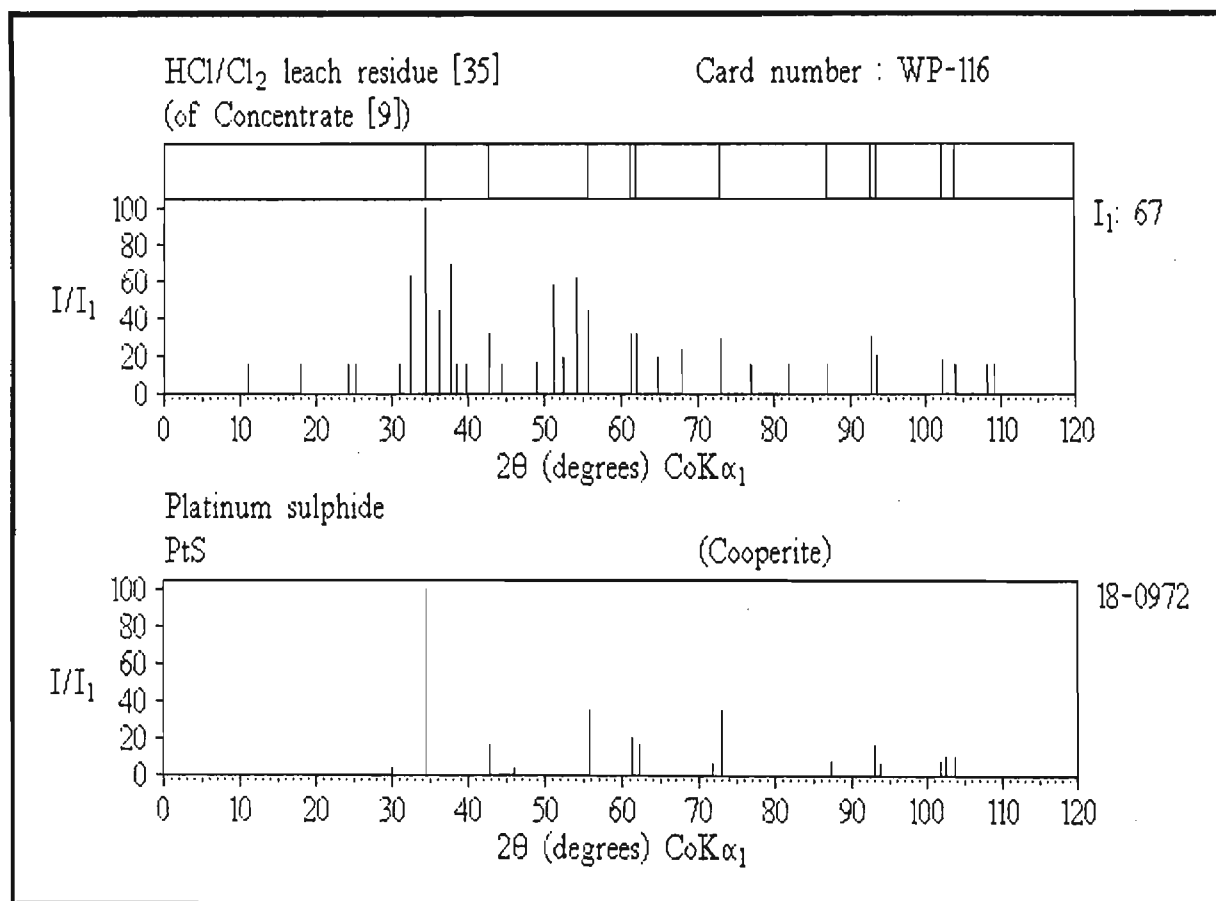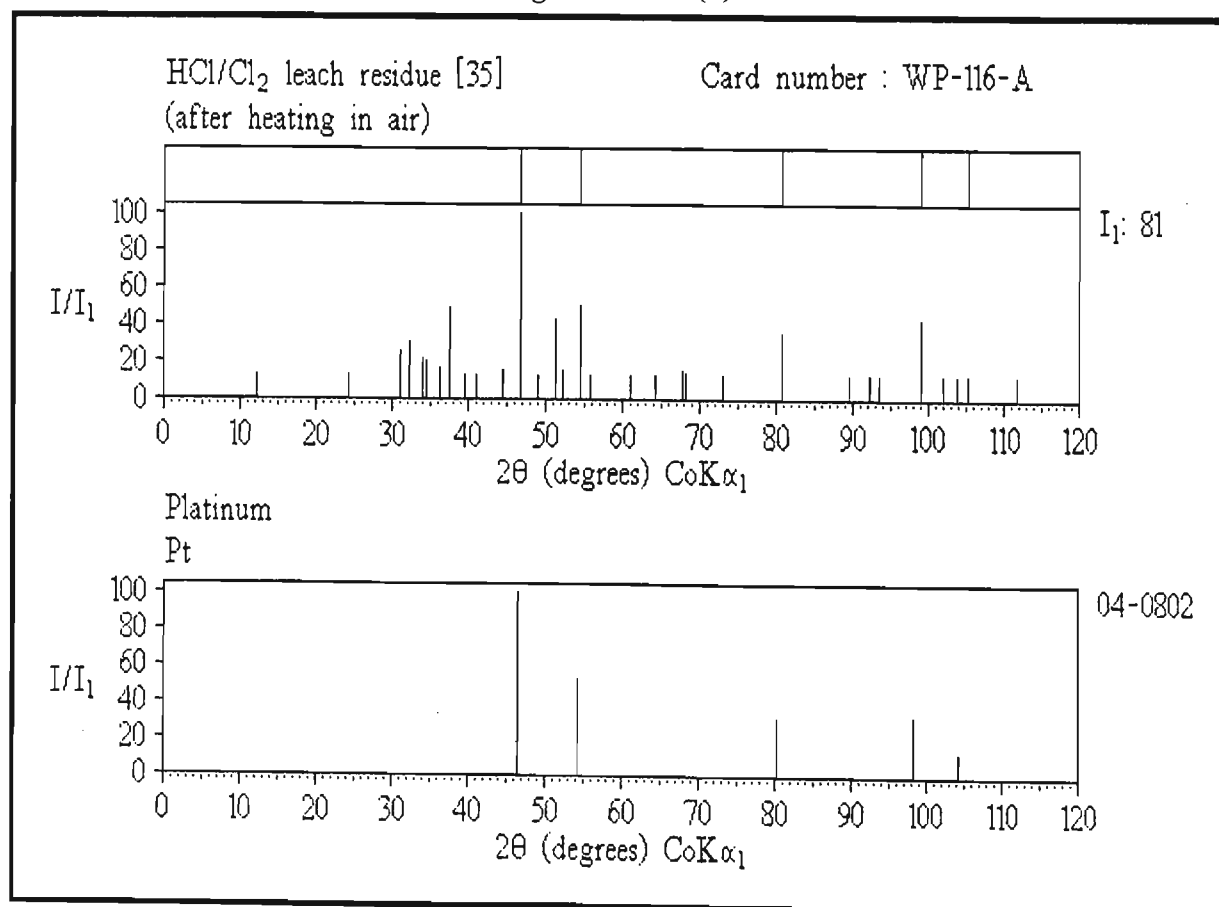
HCl/Cl$_2$ leach residue [35]   Card number : WP-116
(of Concentrate [9])

I$_1$: 67

I/I$_1$ (100 80 60 40 20 0)

2θ (degrees) CoKα$_1$

Platinum sulphide

PtS   (Cooperite)

18-0972

I/I$_1$ (100 80 60 40 20 0)

2θ (degrees) CoKα$_1$

Figure 5.5.7-8(a)

HCl/Cl$_2$ leach residue [35]   Card number : WP-116-A
(after heating in air)

I$_1$: 81

I/I$_1$ (100 80 60 40 20 0)

2θ (degrees) CoKα$_1$

Platinum

Pt

04-0802

I/I$_1$ (100 80 60 40 20 0)

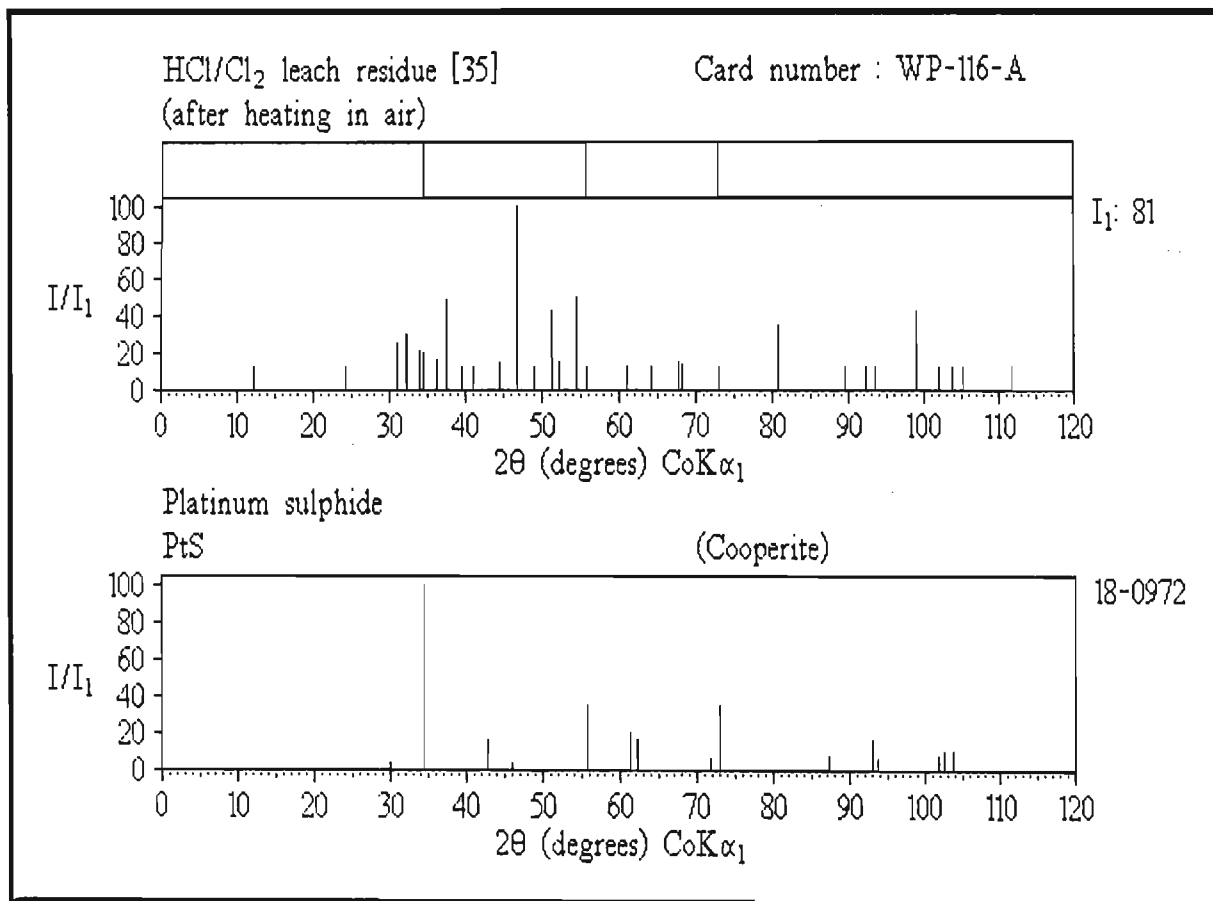2θ (degrees) CoKα$_1$

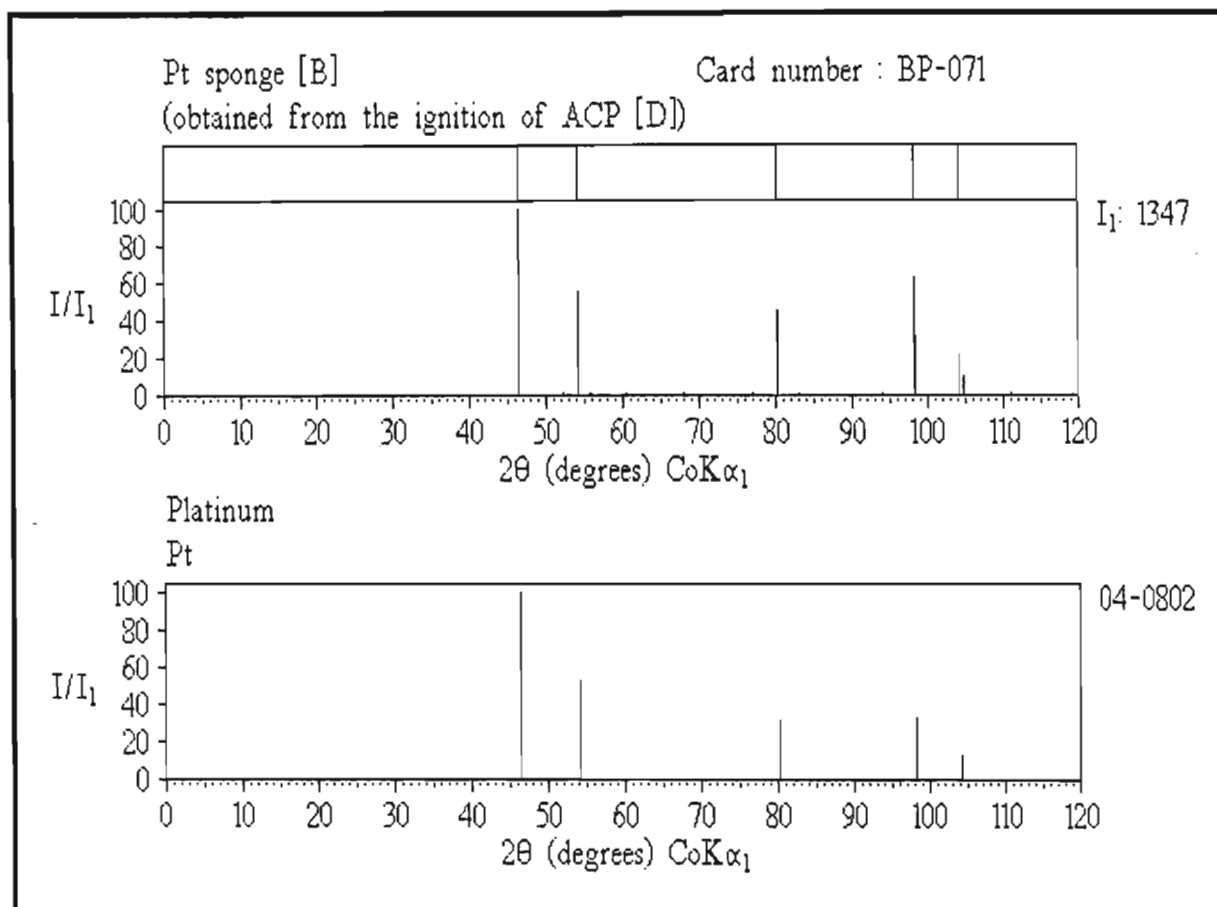**Figure 5.5.7-8(b)**

Figure 5.5.7-8(c)
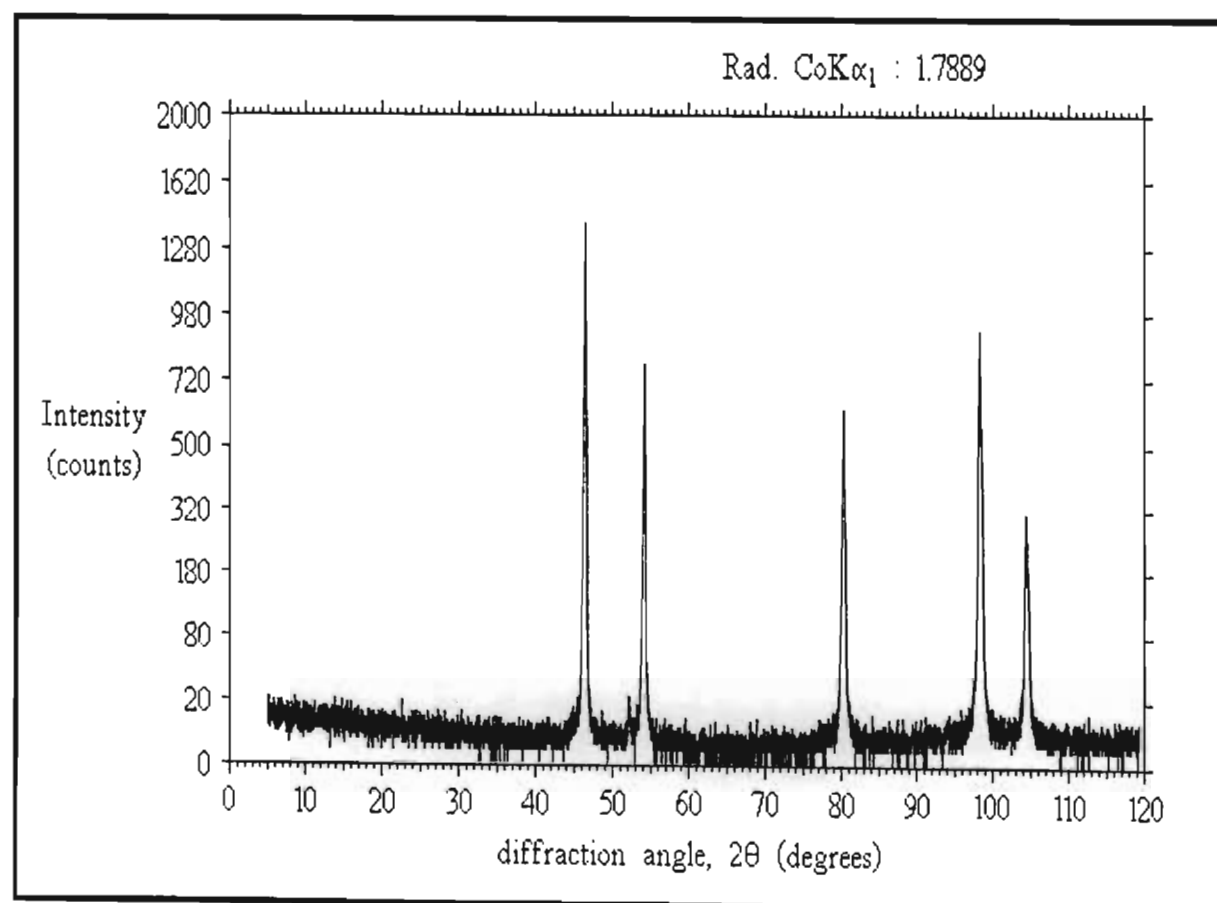
Figure 5.5.7-9(a)

Figure 5.5.7-9(b)   XPD scan for platinum sponge (pure)

nickel sulphide matrix after most of the other pgms have been taken up by the Ni-Cu alloy phase. This would explain why the formation of the Cu_3Pt alloy (§ 5.4.3) seems favoured in certain circumstances.

The small amounts of palladium present in this phase would also have an effect on palladium solubility. **Table 5.5.7-4** compares the solubilities of platinum and palladium for the series of samples examined above (Table 5.5.7-2), showing a clear relationship between the two.

Table 5.5.7-4 **Comparison of Pt solubility and Pd solubility with the the intensity of the 3.02Å PtS line observed for a series of normal concentrate residues**

Platinum Solubility (%)	HCl/Cl$_2$ residue 3.02Å (002, 101) PtS peak		Palladium Solubility (%)
	counts	(I/I$_1$)	
95.58	67	(100)	96.75
98.11	37	(52)	98.41
98.12	24	(32)	98.82
98.83	21	(18)	99.31
99.41	10	(14)	99.52
99.89	0	(0)	99.86

Another cause of low platinum solubility was found to be sintering. Overdrying normal concentrates causes sintering of the finely divided pgm second stage leach residue. Such concentrates dissolve much more slowly in the oxidative leach, due to a reduction in pgm surface area. It was observed that in cases where overdrying of the concentrate had taken place, sintered platinum, **Pt**, remained behind in the insoluble residue, while palladium, rhodium and iridium dissolved. **Table 5.5.7-5** gives XPD data for two oxidative leach residues in which sintered platinum of low solubility was observed (both concentrates had been overdried).

Table 5.5.7-5   Comparison of Pt reference data with data observed for residues showing residual sintered platinum

Pt Reference data [51]			Leach residue [1] (BP-027) Observed data			Leach residue [26] (WP-107) Observed data		
d(Å)	(I/I$_1$)	2θ	d(Å)	(I/I$_1$)	2θ	d(Å)	(I/I$_1$)	2θ
2.265	(100)	46.5	2.263	(100)	46.6	2.259	(100)	46.6
1.9616	(53)	54.3	1.960	(37)	54.3	1.957	(62)	54.4
1.3873	(31)	80.3	1.383	(45)	80.6	1.389	(77)	80.2
1.1826	(33)	98.3	1.182	(36)	98.3	1.178	(62)	98.8
1.1325	(12)	104.3	1.131	(13)	104.5	1.132	(38)	104.5

Figure 5.5.7-10 (a) and **(b)** shows sintered platinum as detected in residues.   Note the sharpness of the indicated peaks and the high crystallinity of the sample.

Figure 5.5.7-11 (a) and **(b)** shows another residue with smaller amounts of residual platinum.   Concentrate overdrying is immediately shown by the associated presence of ruthenium oxide (lower pattern), which was also present in leach residue [1].   As some residue samples showed ruthenium oxide and no sintered platinum, it would be reasonable to regard ruthenium oxidation as taking place slightly prior to platinum sintering.

Sintering was also found to be the primary cause of platinum insolubility in minor concentrates.
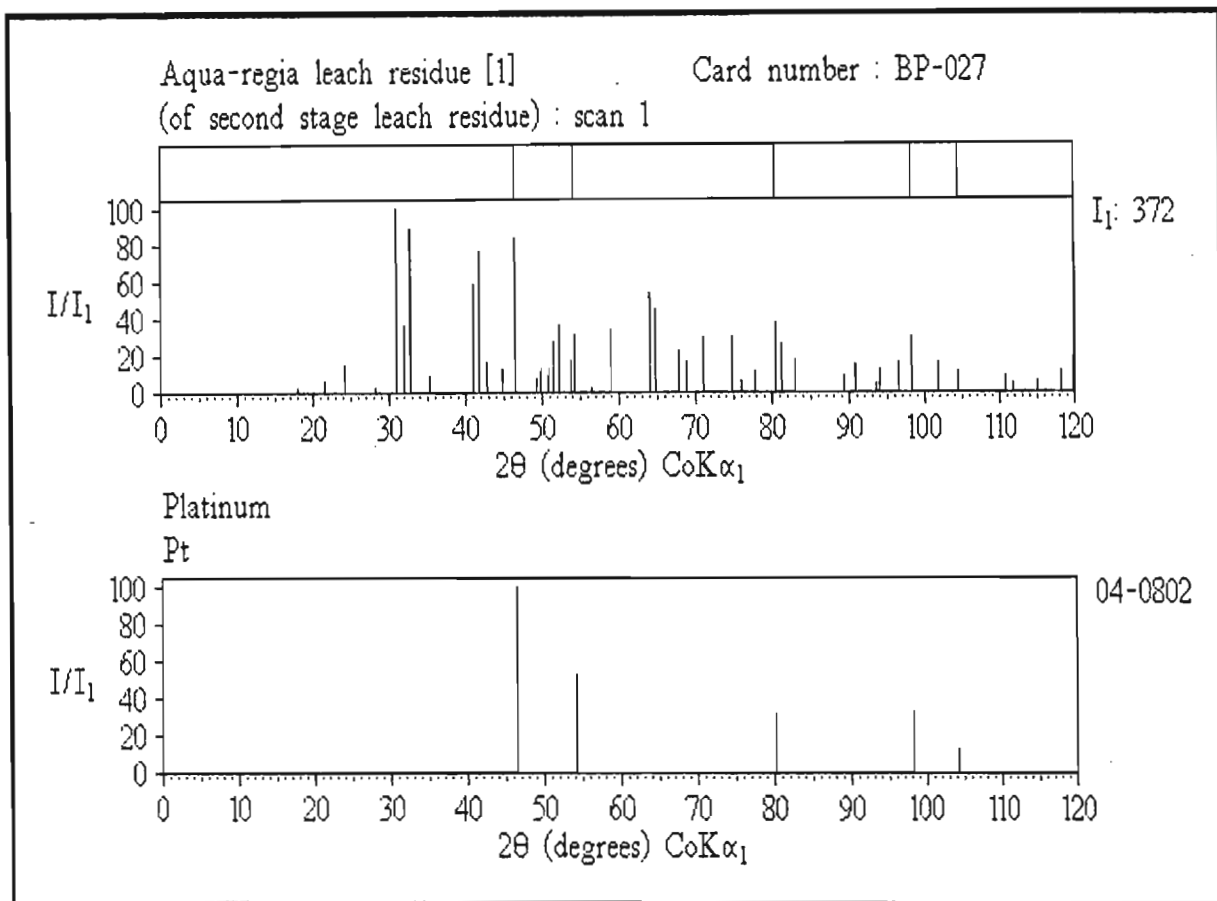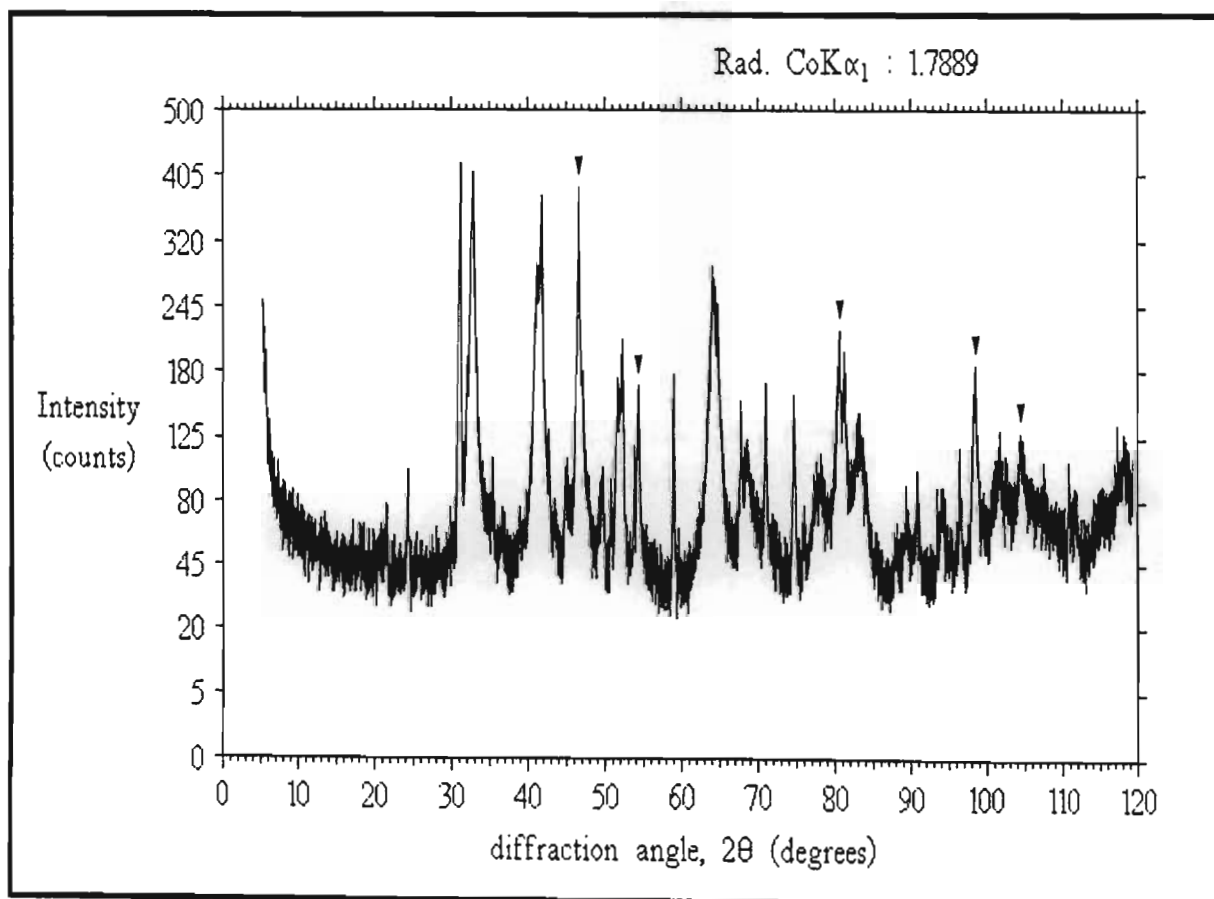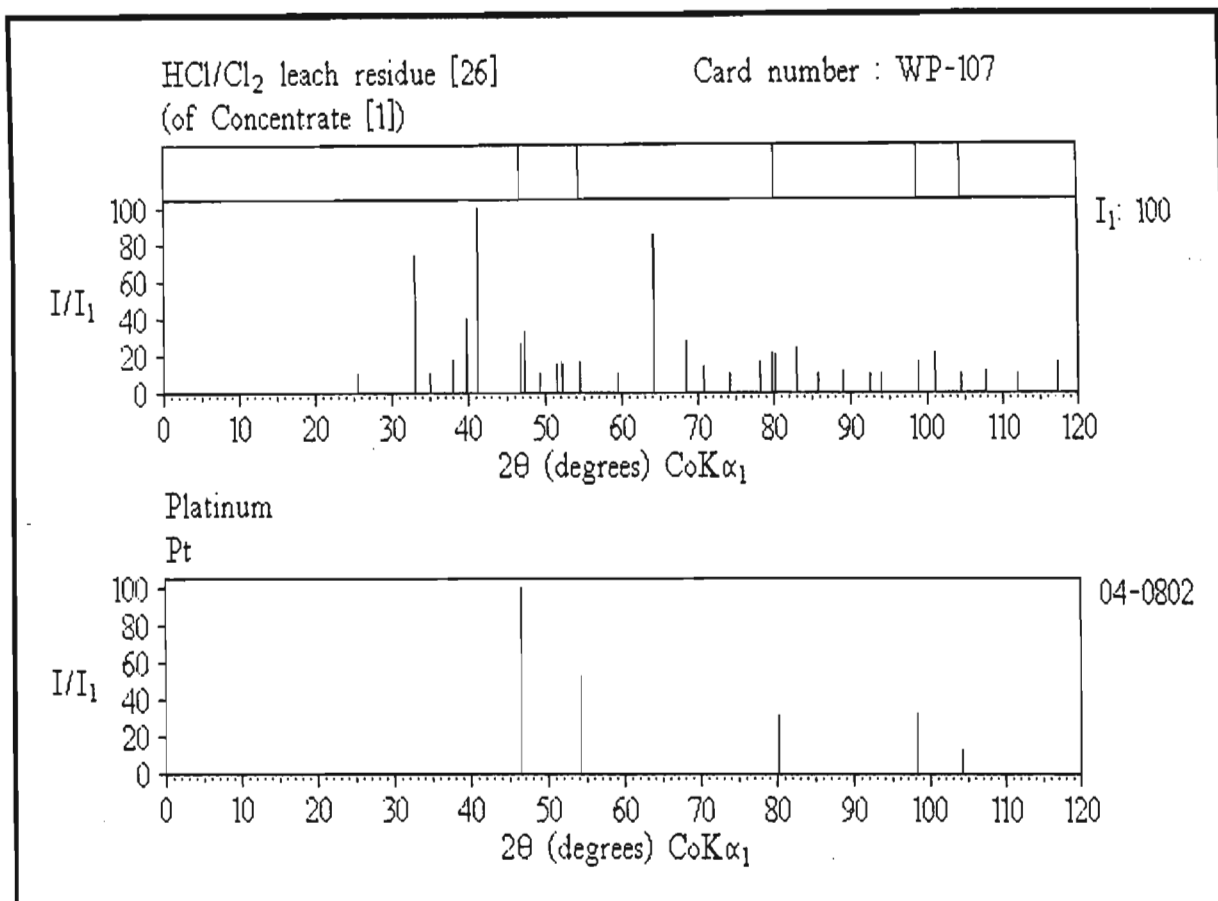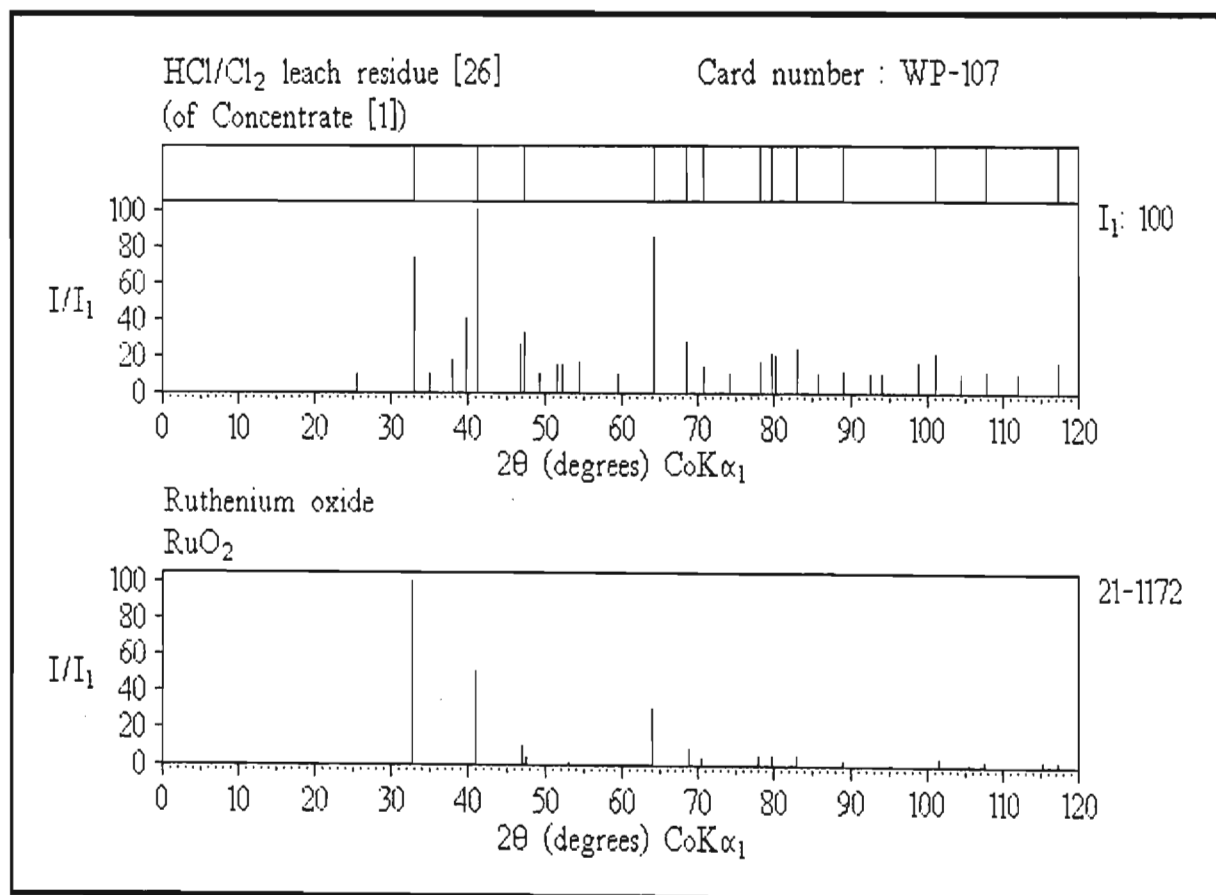
Figure 5.5.7-10(a)

Figure 5.5.7-10(b)

Figure 5.5.7-11(a)

Figure 5.5.7-11(b)

5.5.8 LOW SILVER SOLUBILITY

Silver generally accounts for less than 1% of minor concentrates and 1 - 2% of normal concentrates. The solubility of silver in the oxidative leach is usually not monitored. The silver content of leach residues usually ranges from 2 to 10 % and can be as high as 22%. XPD analysis of several residues revealed that most of the silver remains behind as silver chloride, **AgCl**. In hindsight, this was a rather obvious result, but had not been realized previously.

Table 5.5.8-1 compares the reference data for AgCl with that observed for two residues having high silver contents.

Table 5.5.8-1   Comparison of AgCl reference data with data observed for two HCl/Cl$_2$ leach residues

AgCl Reference data [57]			Leach residue [5] (WP-007) Observed data			Leach residue [22] (WP-056) Observed data		
d(Å)	(I/I$_1$)	2θ	d(Å)	(I/I$_1$)	2θ	d(Å)	(I/I$_1$)	2θ
3.203	(50)	32.4	3.178	(36)	32.7	3.186	(79)	32.6
2.774	(100)	37.6	2.758	(100)	37.8	2.763	(100)	37.8
1.962	(50)	54.2	1.954	(59)	54.5	1.957	(77)	54.4
1.673	(16)	64.6	1.669	(16)	64.8	1.670	(28)	64.8
1.602	(16)	67.9	1.599	(18)	68.0	1.600	(33)	68.0
1.387	(6)	80.3	1.386	(9)	80.4	1.385	(11)	80.4
1.273	(4)	89.3	1.272	(8)	89.4	1.271	(10)	89.5
1.241	(12)	92.2	1.240	(17)	92.4	1.240	(32)	92.3
1.1326	(8)	104.3	1.132	(15)	104.5	1.132	(22)	104.4
1.0680	(4)	113.8	1.067	(5)	114.0	1.067	(8)	113.9

In every case, d-spacings for silver chloride were observed to be smaller than those given by the reference data.

Figures 5.5.8-1(a) and **(b)**, and **5.5.8-2(a)** and **(b)** show the scans and reduced spectra for two silver-rich residues. Note the sharpness of the silver chloride lines (the
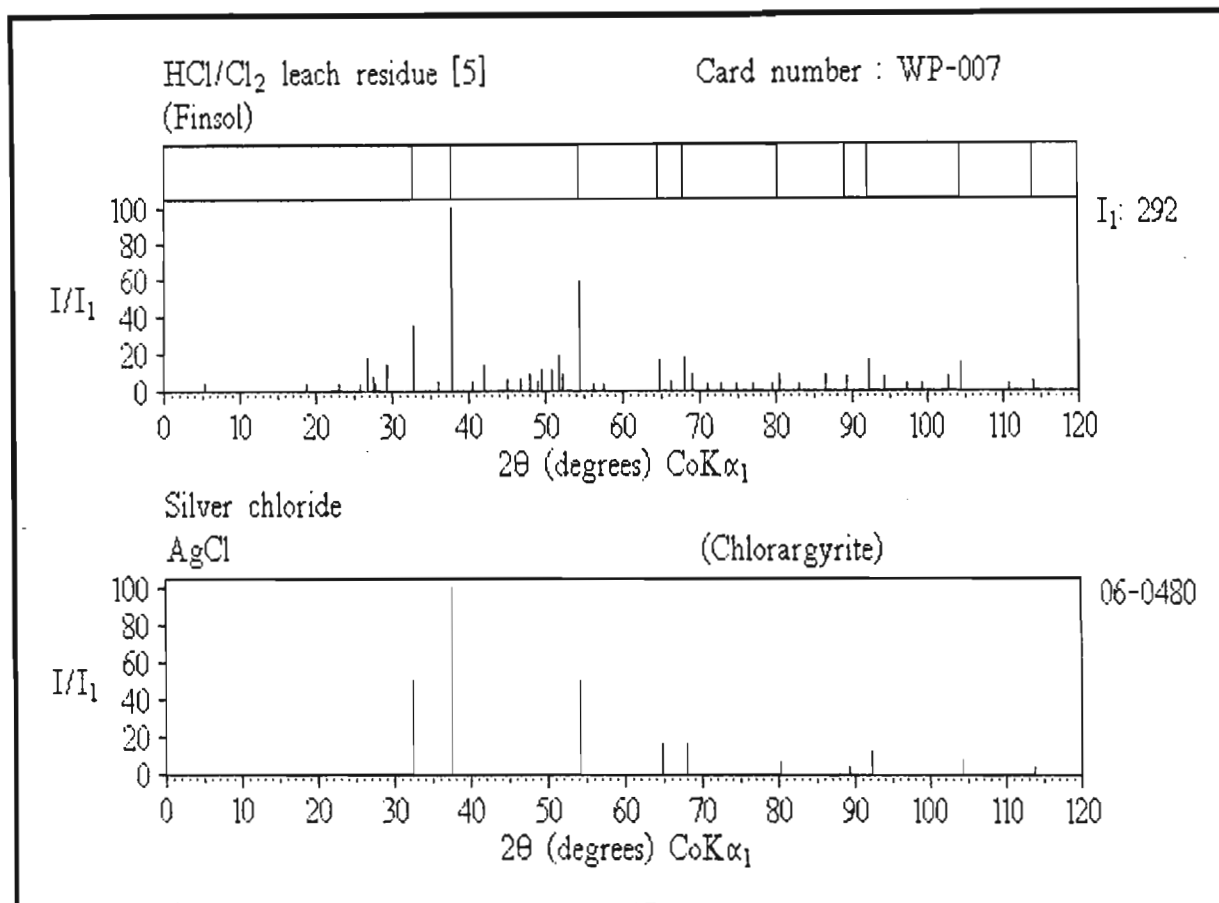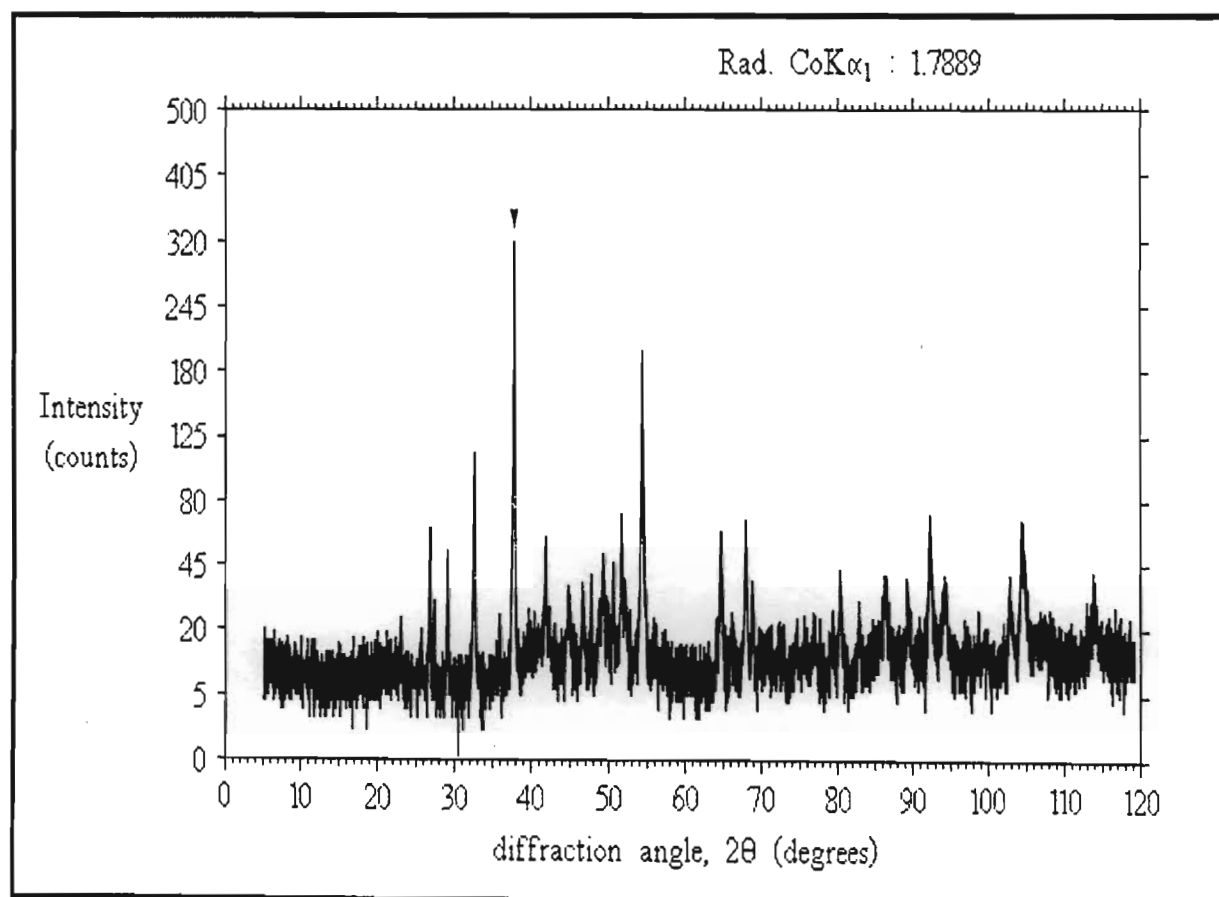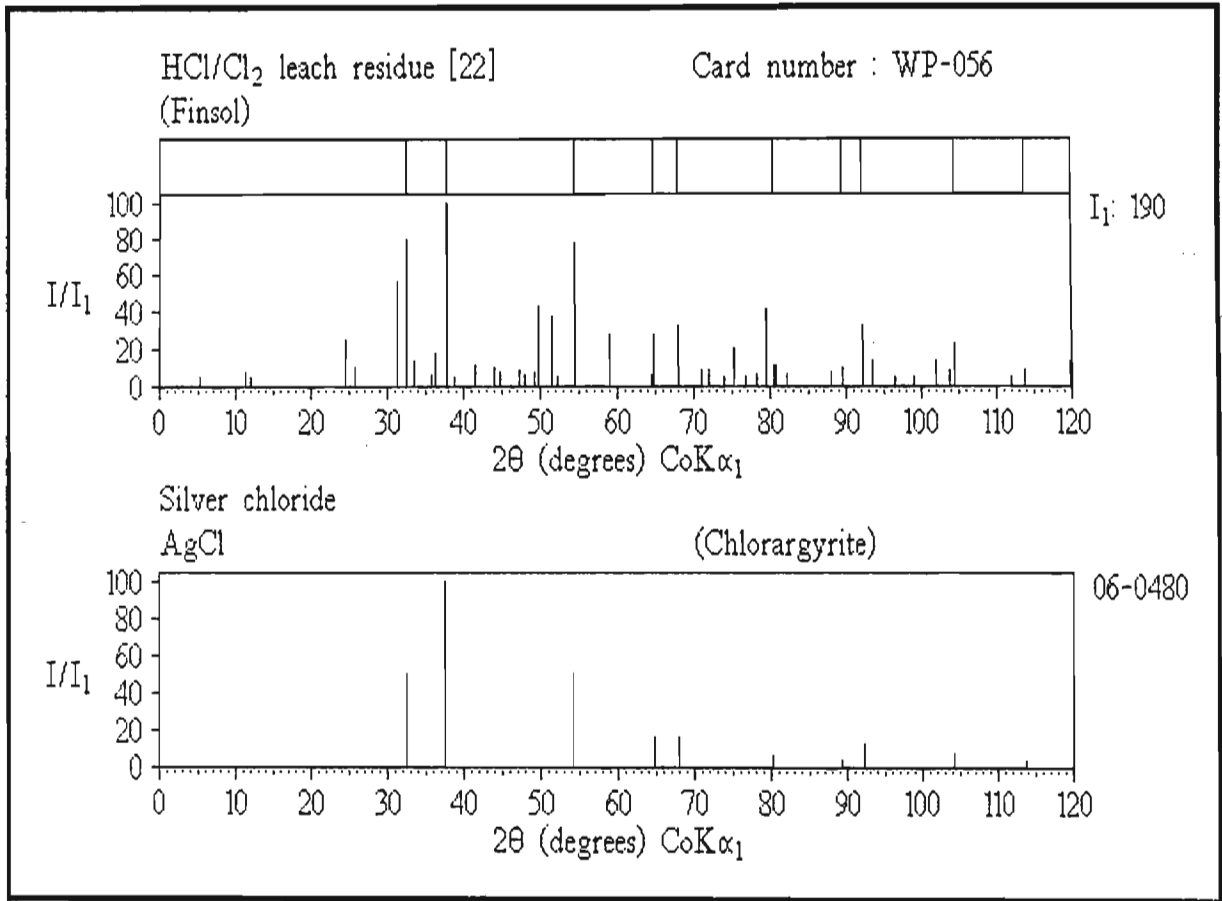
Figure 5.5.8-1(a)

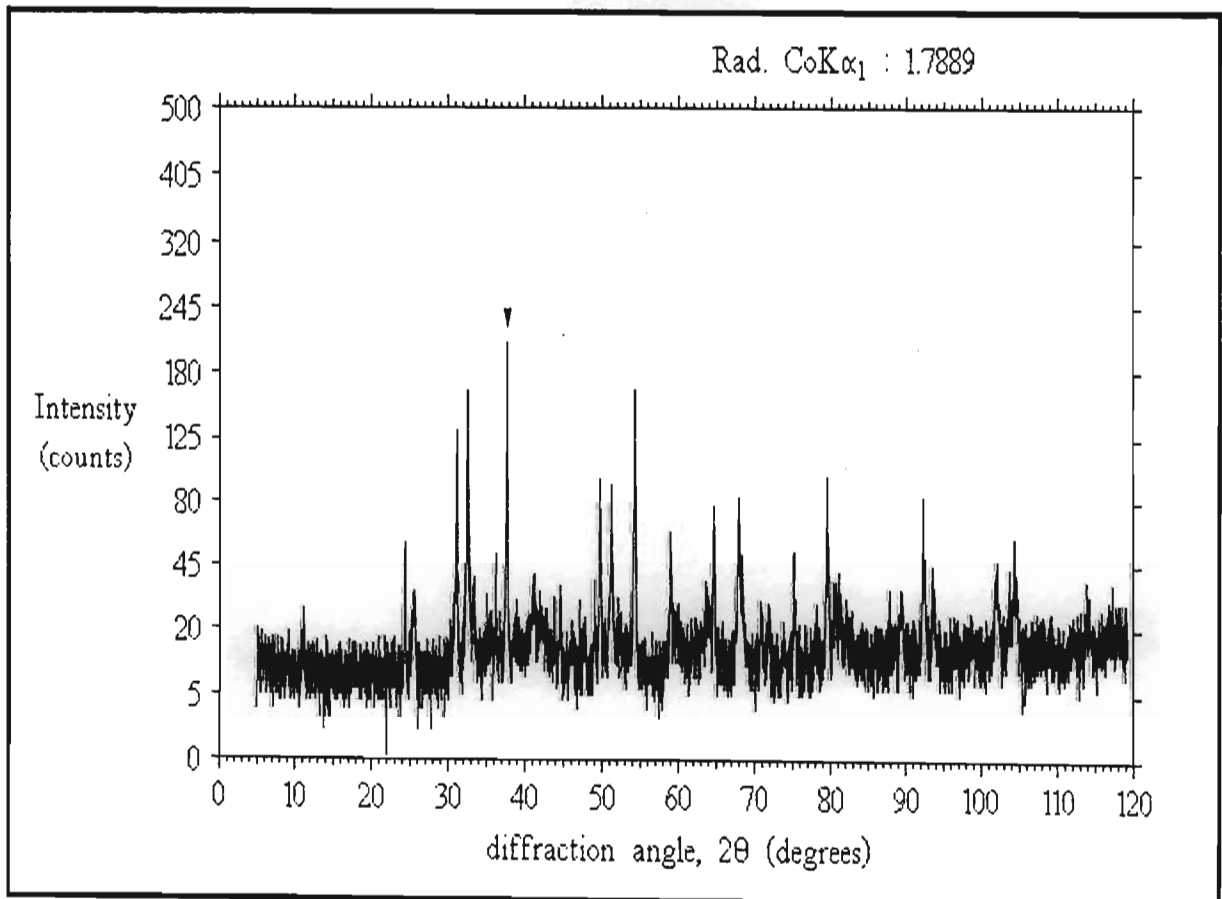**Figure 5.5.8-1(b)**

Figure 5.5.8-2(a)

Figure 5.5.8-2(b)

crystallinity of the silver chloride in leach residues was found to be substantially higher than that of silver chloride synthesised by normal laboratory methods).

Although silver chloride has a low solubility in water (1.4×10^{-4} g/100ml at 18°C) [58], the solubility in 6M hydrochloric acid is considerably higher due to formation of a soluble anionic complex via the reaction [59] :

$$AgCl + Cl^- \longrightarrow [AgCl_2]^-$$
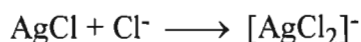
Thus substantial amounts of silver are also present in the hot oxidative leach solutions. Precipitation of the chloride usually occurs on dilution or pH adjustment of solutions.

Silver chloride is easily leached from residues using warm 4M aqueous ammonia, which results in the formation of a soluble ammine complex [60], via the reaction :

$$AgCl + 2\, NH_3 \cdot H_2O \longrightarrow [Ag(NH_3)_2]^+ + Cl^- + 2\, H_2O$$

Figure 5.5.8-3(a) and **(b)** show scans of an oxidative leach residue before and after total silver chloride removal.

It is well known that silver chloride slowly photodecomposes to silver metal. Unfortunately the main silver peak is overlapped by a strong Ru-Os alloy peak. A small amount of metallic silver seems to form as ammonia leach residues still show traces of silver to be present.

5.5.9 OTHER INSOLUBLES

XPD analysis showed that the bulk of many leach residues was silicon oxide, **SiO$_2$**. This was the usual alpha- form, known geologically as quartz. **Table 5.5.9-1** lists the SiO$_2$ reference peaks with those observed for a quartz-rich residue. **Figure 5.5.9-1(a)** and **(b)** shows the reduced spectrum and scan for this sample.
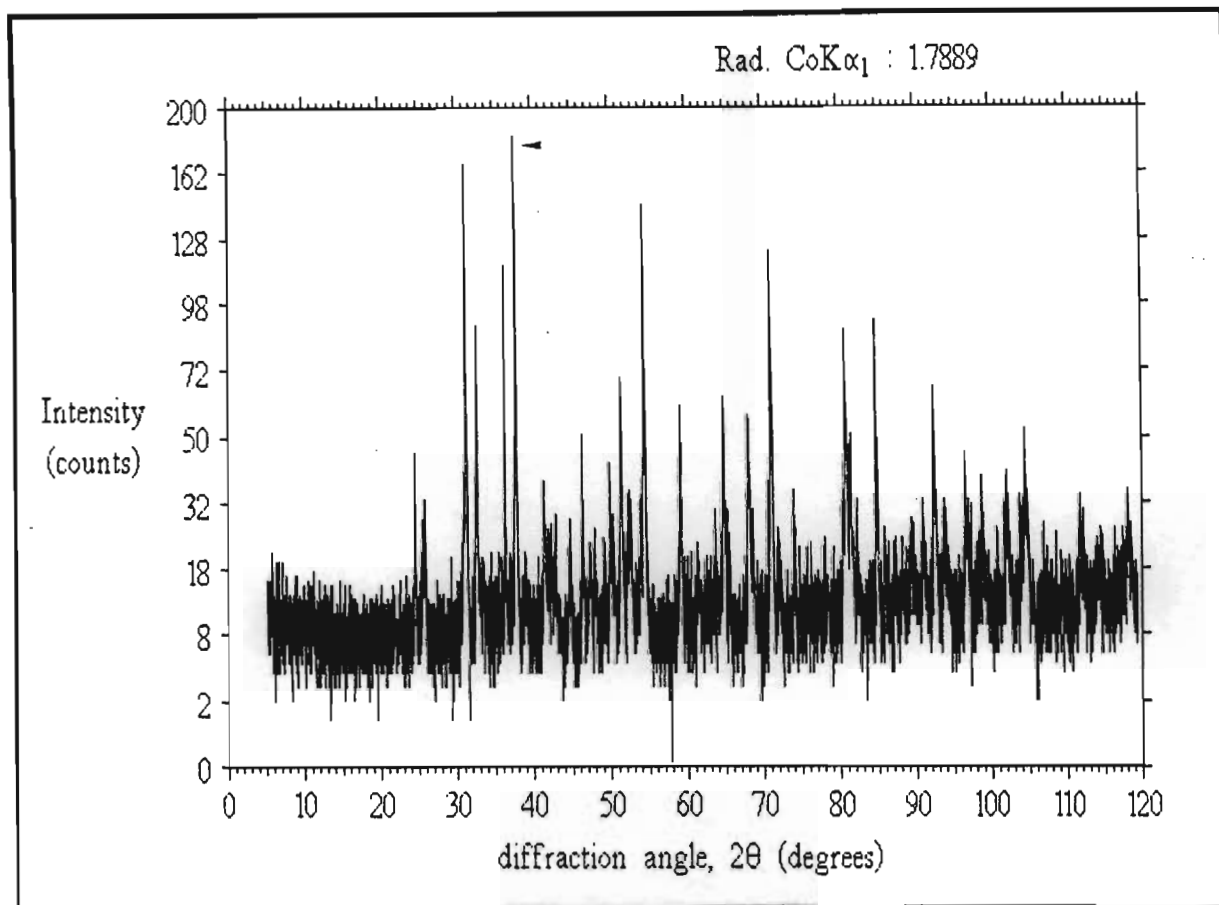
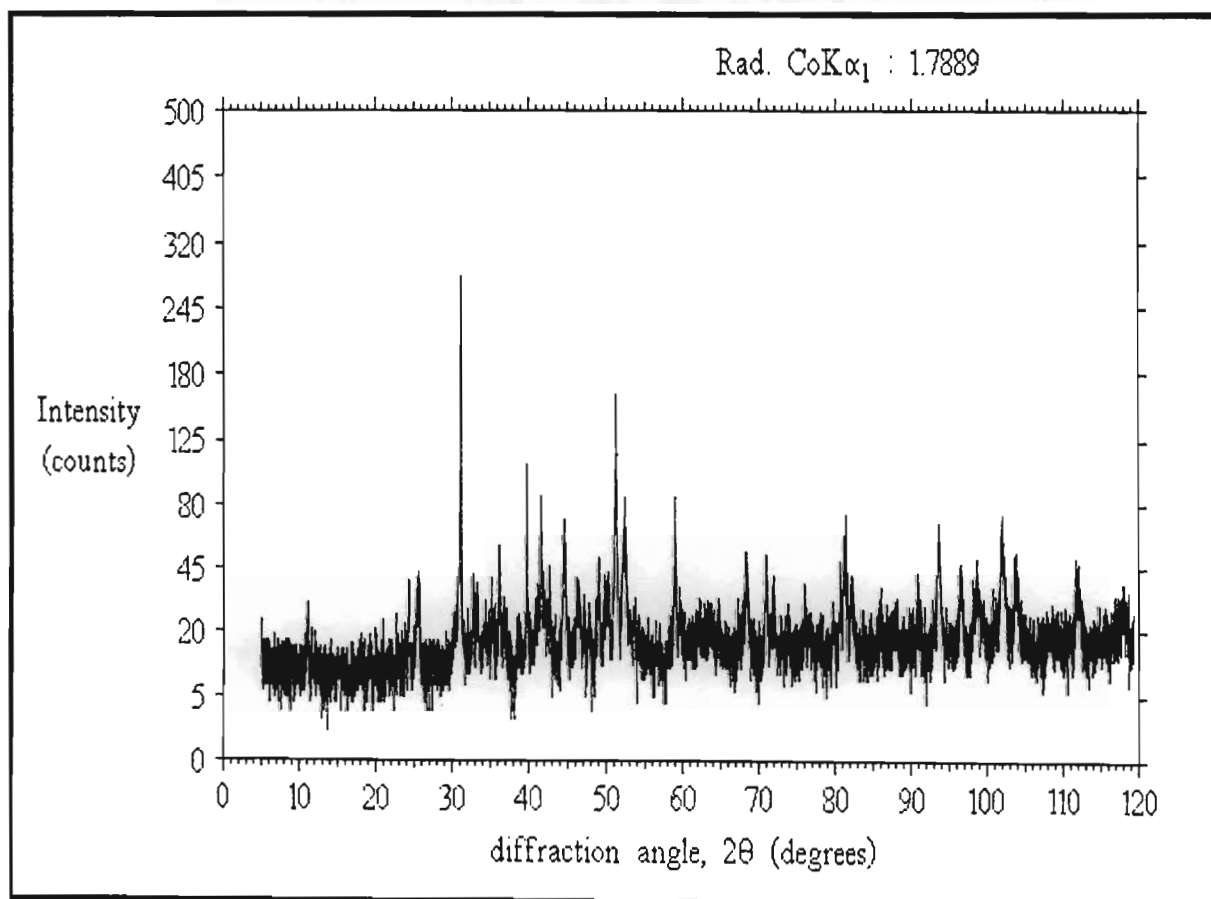**Figure 5.5.8-3(a)** XPD scan of a leach residue showing silver chloride peaks

Figure 5.5.8-3(b) XPD scan of the above residue after an ammonia leach

Table 5.5.9-1 Comparison of SiO$_2$ reference data with data observed for a HCl/Cl$_2$ leach residue

SiO$_2$ Reference data [61]			Leach residue [28] [WP-109] Observed data		
d(Å)	(I/I$_1$)	2θ	d(Å)	(I/I$_1$)	2θ
4.26	(35)	24.2	4.232	(10)	24.4
3.343	(100)	31.0	3.327	(100)	31.2
2.458	(12)	42.7	2.450	(12)	42.8
2.282	(12)	46.2	2.276	(9)	46.3
2.237	(6)	47.1	2.231	(7)	47.3
2.128	(9)	49.7	2.122	(9)	49.9
1.980	(6)	53.7	1.978	(4)	53.8
1.817	(17)	59.0	1.814	(26)	59.1
1.801	(1)	59.6	1.797	(7)	59.7
1.672	(7)	64.7	1.670	(4)	64.8
1.541	(15)	71.0	1.540	(14)	71.0
1.453	(3)	76.0	1.452	(5)	76.1
1.418	(1)	78.2	1.423	(4)	77.9
1.382	(7)	80.7	1.381	(10)	80.7
1.375	(11)	81.2	1.375	(16)	81.2
1.372	(9)	81.4	1.374	(19)	81.2
1.288	(3)	88.0	1.288	(4)	88.0
1.256	(4)	90.8	1.255	(6)	90.9
1.228	(2)	93.5	1.227	(19)	93.6
1.1997	(5)	96.4	1.199	(11)	96.5
1.1802	(4)	98.6	1.180	(10)	98.6
1.0816	(4)	111.6	1.081	(10)	111.6
1.0437	(2)	118.0	1.044	(6)	117.9

The quartz phase originates from residual ore matrix and from the silica flux added to remove the iron oxides from the matte (§ 4.2.2).   Microscopic examination of leach residues showed that quartz was present in two forms.   The first was granular and sand-like.   The second was globular (usually spherical), with tiny gas vesicles.   Some of these globules were various colours such as ruby red and amber yellow.

A second similar insoluble phase identified in residues was the magnesium iron silicate **(Mg,Fe)SiO$_3$**, known mineralogically as enstatite (ferroan) or bronzite.   This phase
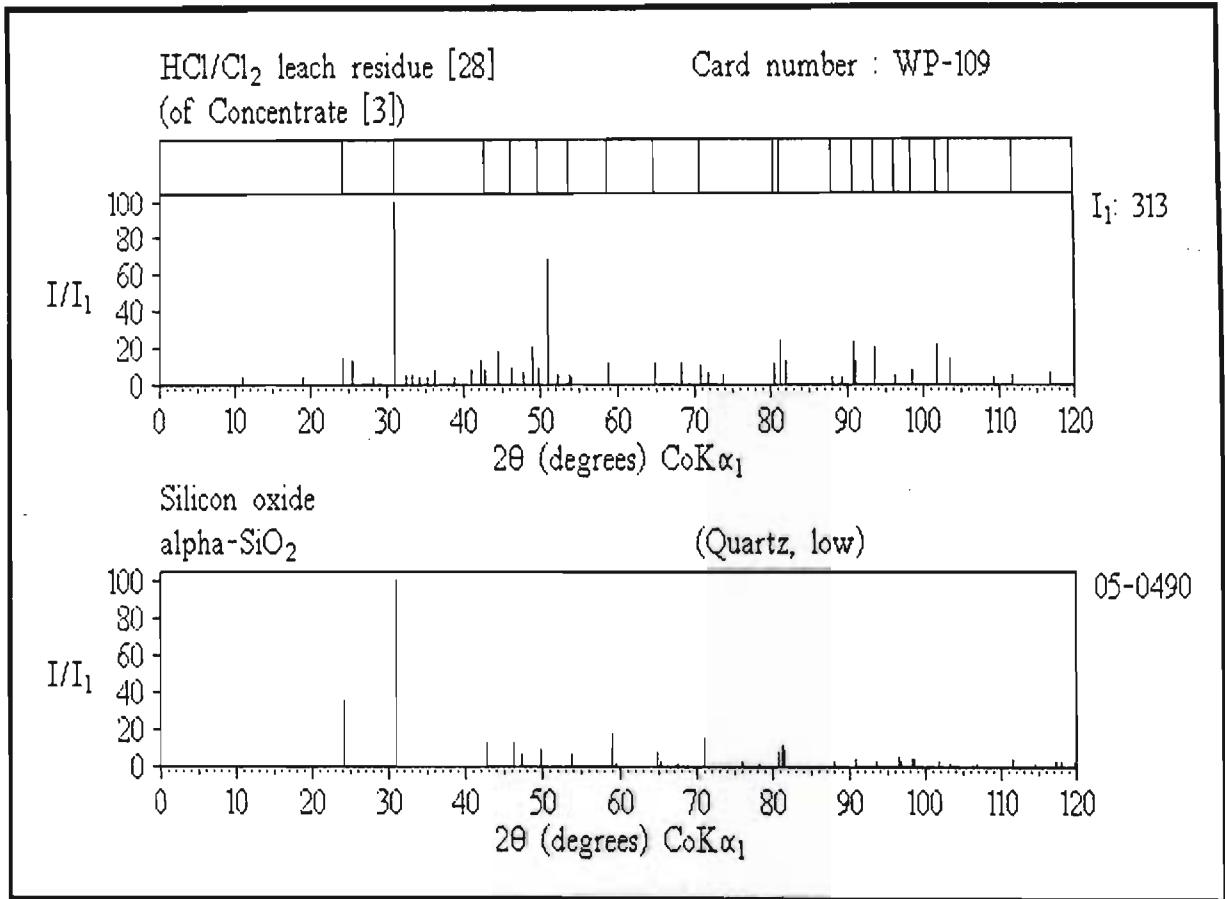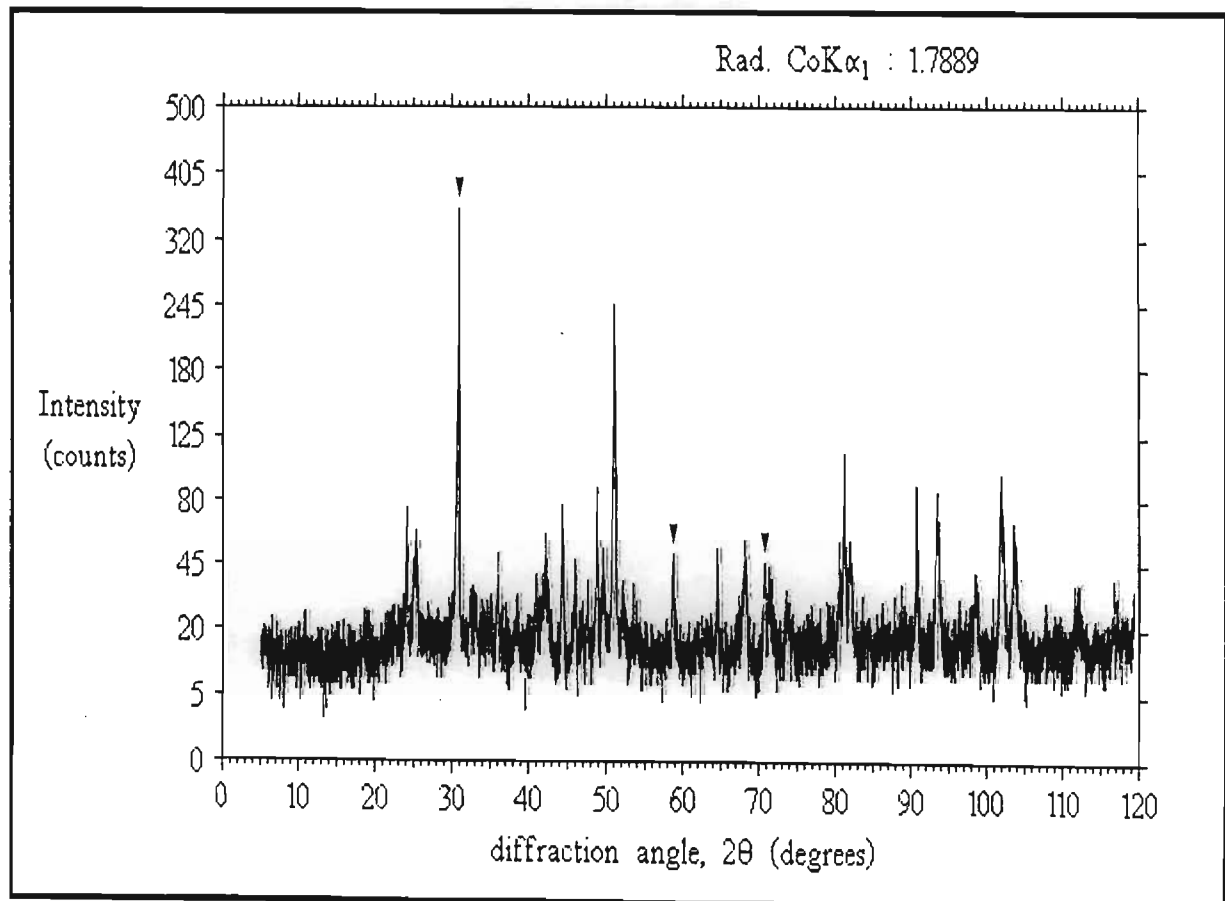
Figure 5.5.9-1(a)

Figure 5.5.9-1(b)

gives numerous sharp peaks, making identification difficult if other phases are present. The sample was thus separated into coarse and fine grains. Analysis of the coarse grains confirmed the assignment. **Table 5.5.9-2** compares the XPD reference data of this silicate with that observed for a residue sample (only peaks above 1.95Å have been listed).

Table 5.5.9-2   Comparison of (Mg,Fe)SiO$_3$ reference data with data observed for a separated HCl/Cl$_2$ leach residue

(Mg,Fe)SiO$_3$ Reference data [62]			Leach residue [12] (WP-046-A) Observed data		
d(Å)	(I/I$_1$)	2θ	d(Å)	(I/I$_1$)	2θ
4.01	(8)	25.8	4.054	(14)	25.5
3.30	(25)	31.5	**3.311**	**(-)**	**31.3**
3.15	(100)	33.0	3.158	(100)	32.9
2.934	(30)	35.5	2.931	(36)	35.5
2.865	(60)	36.4	**2.863**	**(-)**	**36.4**
2.819	(16)	37.0	2.814	(33)	37.1
2.698	(20)	38.7	2.700	(14)	38.7
2.528	(35)	41.4	2.530	(24)	41.4
2.489	(40)	42.1	2.484	(38)	42.2
2.463	(20)	42.6	2.458	(33)	42.7
2.351	(4)	44.7	2.352	(12)	44.7
2.237	(6)	47.1	2.246	(13)	46.9
2.108	(25)	50.2	2.116	(25)	50.0
2.091	(20)	50.7	2.094	(18)	50.6
1.979	(16)	53.7	1.972	(14)	53.9
1.954	(20)	54.5	1.954	(26)	54.5

Figure 5.5.9-2(a) and **(b)** shows the reduced spectra and scan for this sample. The reference compound analysed as 55.45% SiO$_2$, 34.48% MgO, 8.42% FeO and 2.03% Al$_2$O$_3$ (geological analysis) [62]. The identification of this phase was of interest as it explained the trace amounts of aluminium in samples. Although this silicate is of geological origin, it seems more probably to have been introduced by furnace bricks (these are predominately bronzite).
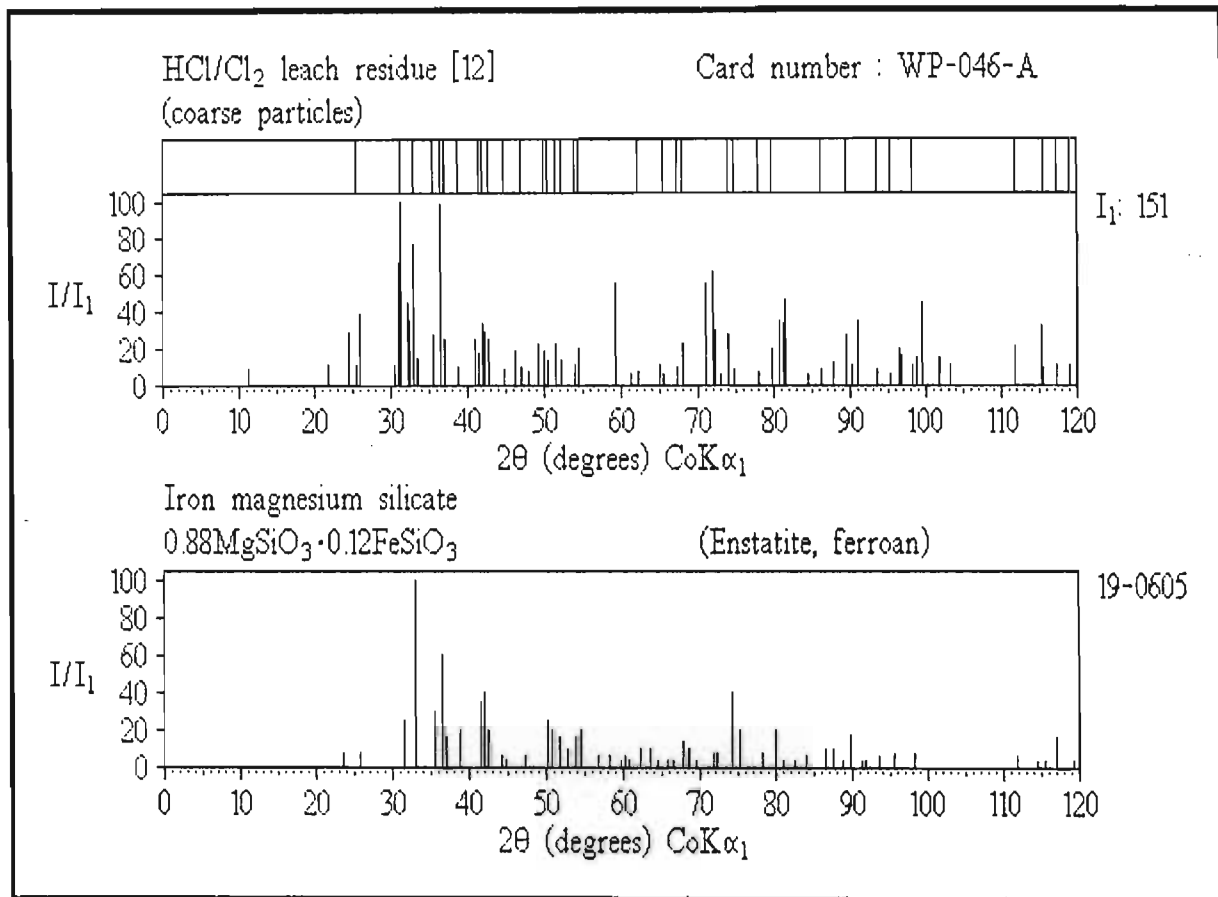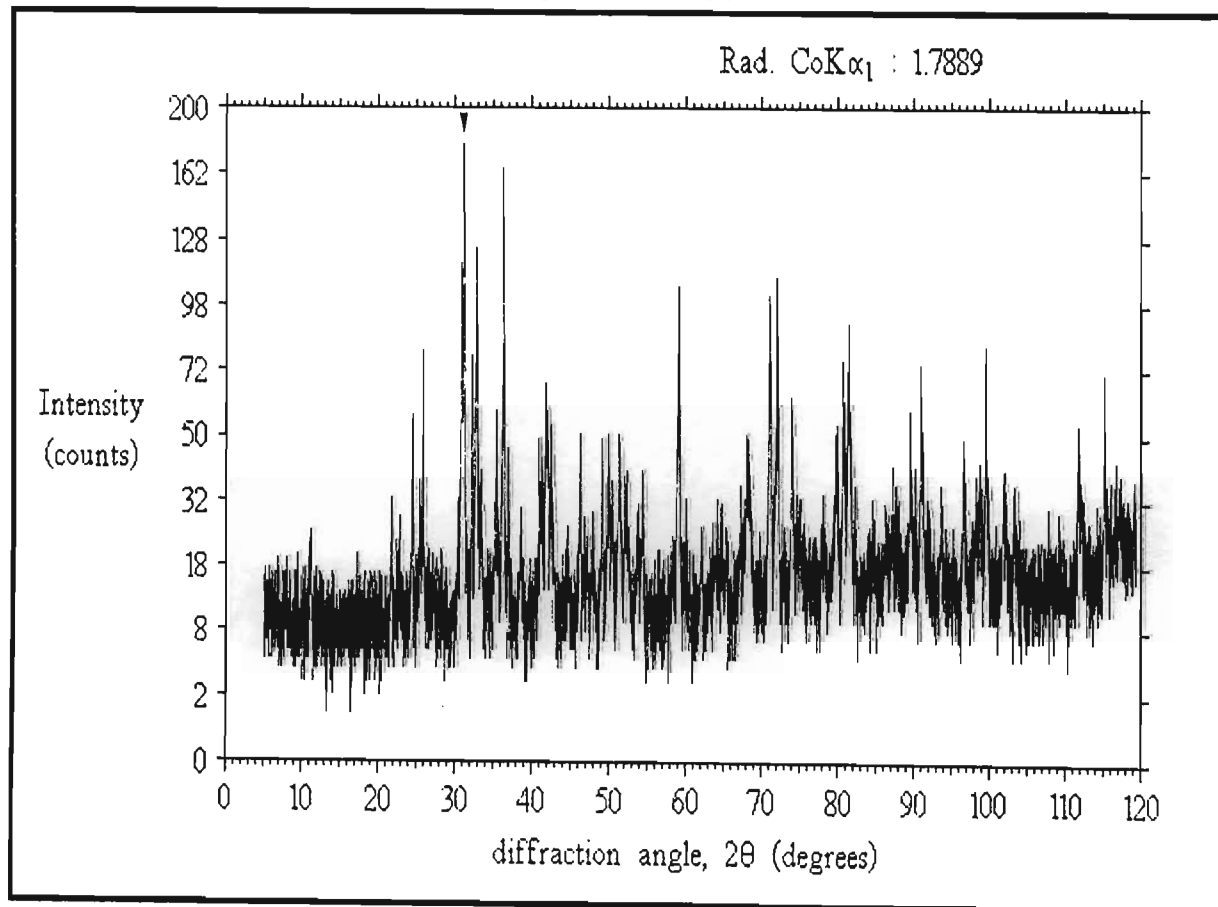
Figure 5.5.9-2(a)

Figure 5.5.9-2(b)

5.6 LEAD FUSION PROBLEMS

5.6.1 INTRODUCTION

Refinery operations generally produce numerous precipitates of impurities, dust and sweepings, insoluble residues, and dilute solutions, with non-negligible pgm content. The metal content of waste solutions are usually reduced with hydrogen produced by adding zinc or magnesium to the acidified solution. This produces impure 'metal black' precipitates. (An XPD scan and reduced spectra for such a precipitate is given in **Figure 5.6.1-1(a)** and **(b)**.) All these collected wastes and precipitates are dried and mixed with lead carbonate ($PbCO_3$, not $2PbCO_3 \cdot Pb(OH)_2$), and stongly heated in an arc furnace. The lead carbonate is decomposed and reduced to molten lead, which then acts as a collector of the pgms in a similar way to the nickel-copper alloy of matte. Other impurities form oxides and collect as a slag layer above the molten lead. After removal of the slag layer, the molten lead containing the pgms (as metals) is cast into ingots. These are dissolved in nitric acid which solubilizes the lead as soluble lead nitrate, leaving behind a very finely divided pgm-rich sludge relatively free from impurities, which can be oxidatively leached (HCl/Cl_2).

5.6.2 PGM AND LEAD INSOLUBILITY

Several of the problems being encountered with the lead fusion process were :

1) The weight of sludge produced in the process exceeded the mass of solid waste going into the process. Clearly the opposite should be true, as impurities are being removed.

2) Lead could not be completely leached out of the ingots, introducing large amounts of lead into the process.

3) The pgm content of the sludge was not completely soluble.

The third problem was the most serious. XPD analysis of leach residues indicated that lead had actually formed an alloy with palladium and to a certain extent platinum of general formula **Pb(Pd,Pt)₃**. It was this alloy which was proving insoluble. In **Table**
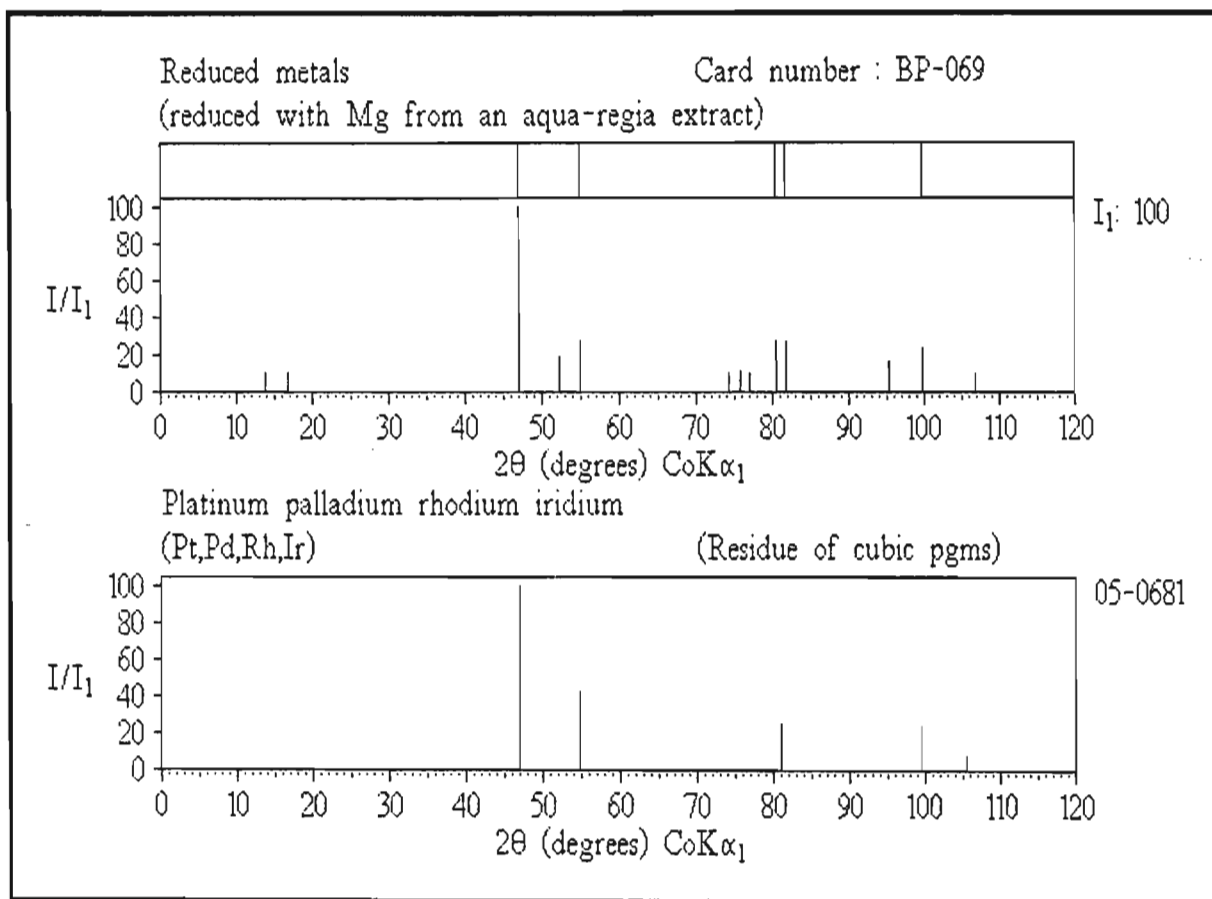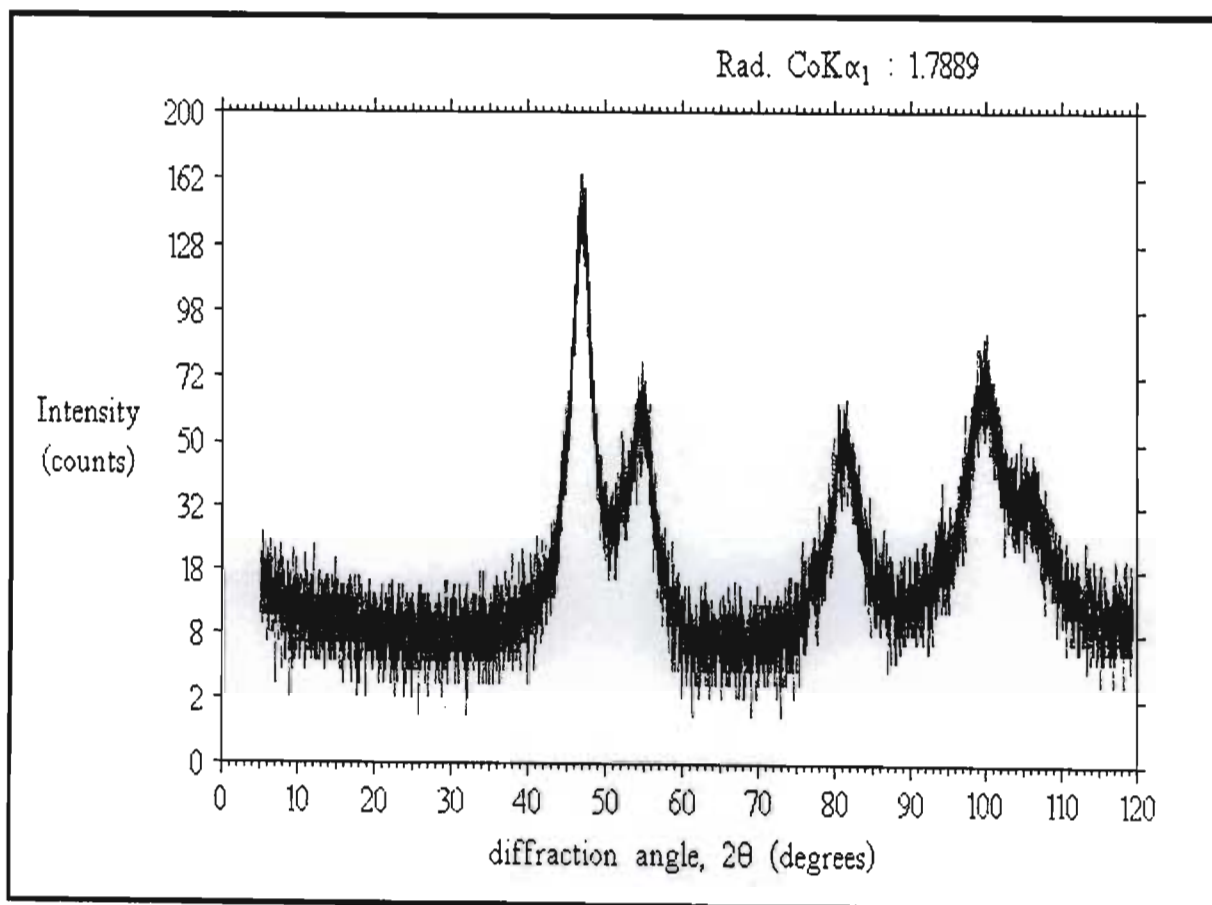
Figure 5.6.1-1(a)

Figure 5.6.1-1(b)

5.6.2-1 the reference data for the alloy $PbPd_3$ is compared to that observed in two leach residues. The scans and analyses for these residues are shown in **Figures 5.6.2-1(a)** and **(b)**, and **5.6.2-2(a)** and **(b)**.

Table 5.6.2-1   Comparison of $PbPd_3$ reference data with data observed for two sludge leach residues

$PbPd_3$ Reference data [63]			Leach residue [2] (WP-009) Observed data			Leach residue [1] (WP-006) Observed data		
d(Å)	(I/I_1)	2θ	d(Å)	(I/I_1)	2θ	d(Å)	(I/I_1)	2θ
2.32	(100)	45.4	2.328	(100)	45.2	2.329	(100)	45.2
2.01	(80)	52.8	2.017	(43)	52.7	2.019	(40)	52.6
1.80	(20)	59.6	-	-	-	1.804	(29)	59.4
1.644	(20)	65.9	1.638	(6)	66.2	-	-	-
1.423	(70)	77.9	1.429	(30)	77.5	1.433	(37)	77.3
1.342	(5)	83.6	1.338	(6)	83.9	-	-	-
1.215	(90)	94.8	1.221	(44)	94.2	1.223	(55)	94.0
1.163	(40)	100.5	1.168	(13)	99.9	1.170	(21)	99.7
1.077	(5)	112.3	1.074	(6)	112.8	1.072	(15)	113.0

This alloy also occurs naturally (as the mineral zvyagintsevite). In most cases small amounts of platinum are found together with palladium, *ie* $Pb(Pd,Pt)_3$ [64]. Even in 11M hydrochloric acid (at room temperature) this alloy was only mildly attacked.

The solution to the 'insoluble lead' problem was twofold. The XPD analysis of one nitric acid leach residue containing about 26% lead (should have been close to zero) showed that most of the residue was lead sulphate, $PbSO_4$. **Table 5.6.2-2** compares $PbSO_4$ reference data with that observed for a sample of nitric acid insolubles (only peaks above 1.95Å have been listed). The scan and reduced spectra for this sample are shown in **Figure 5.6.2-3(a)** and **(b)**.
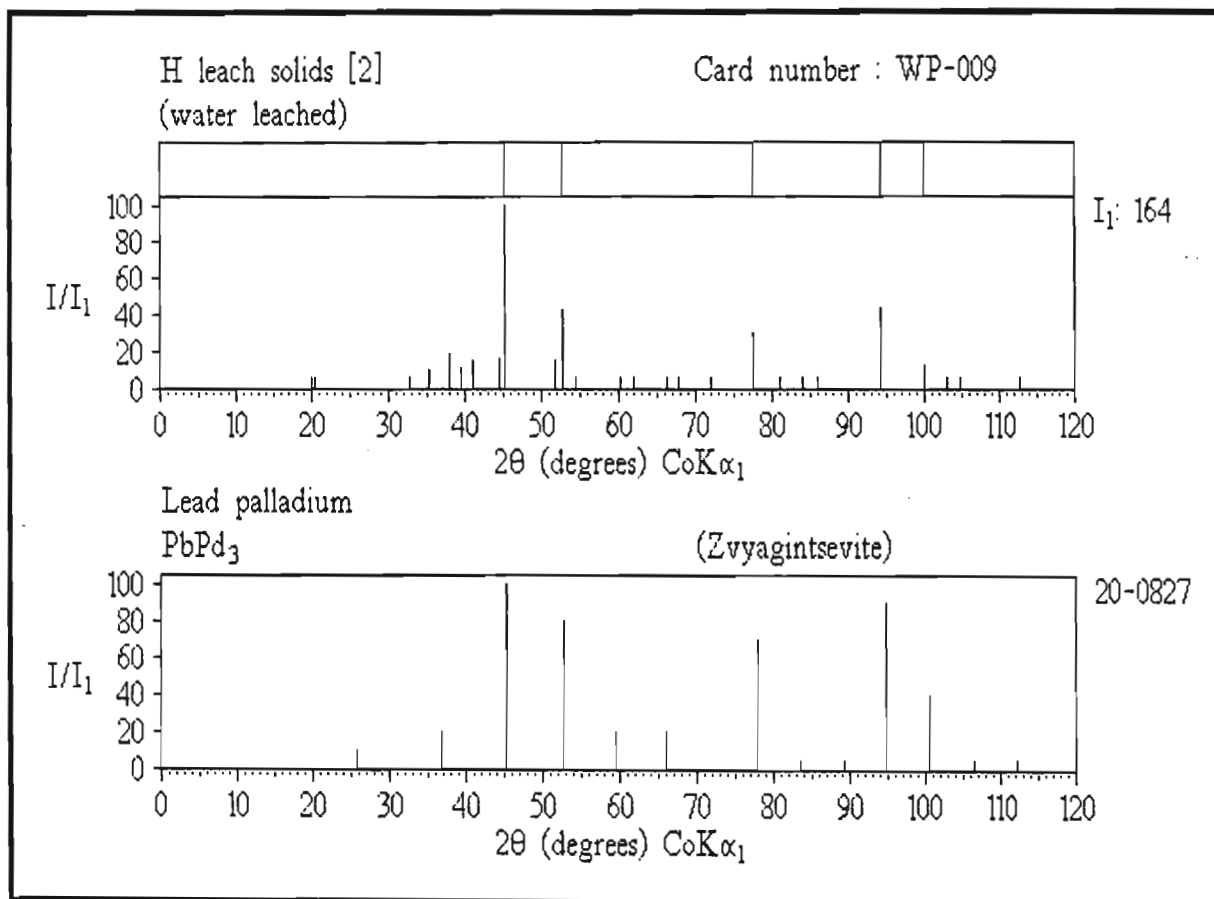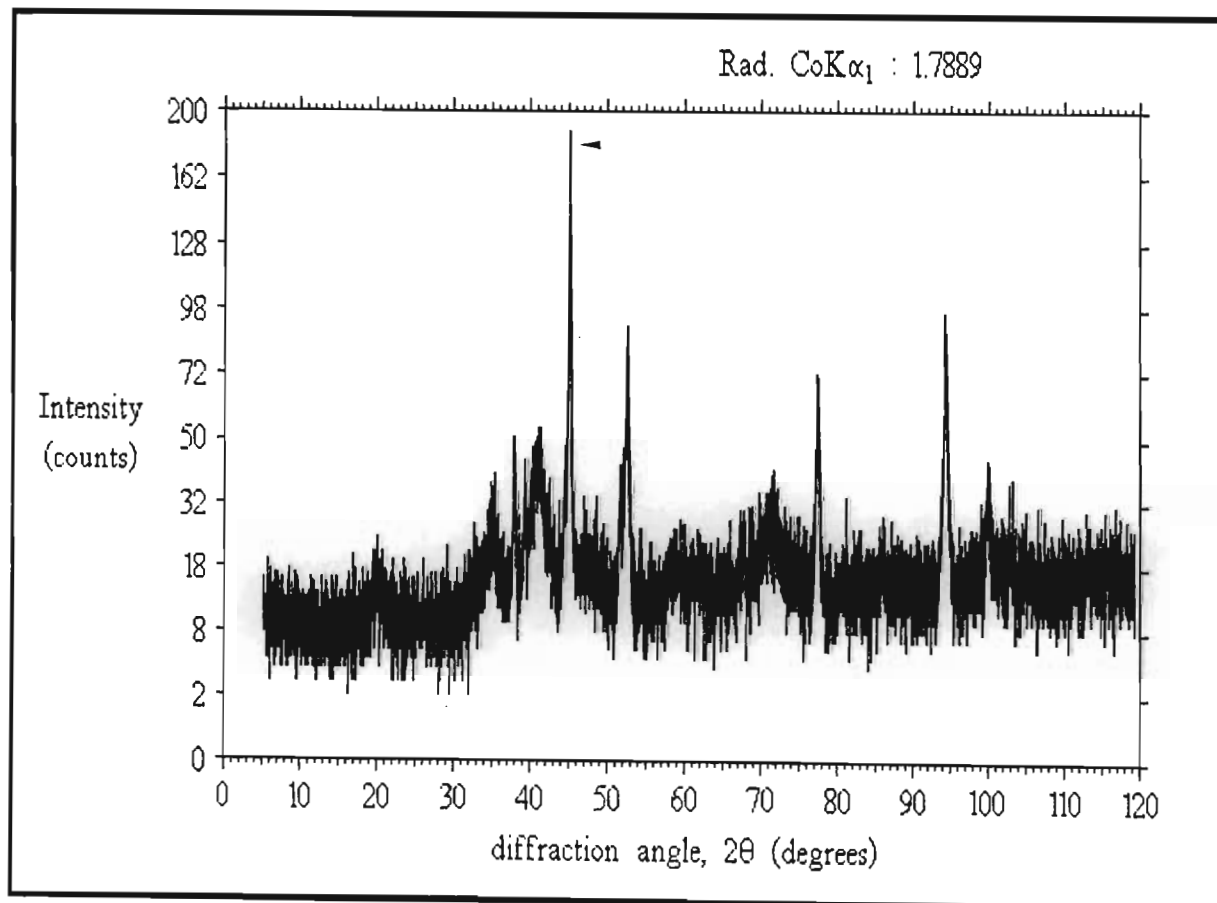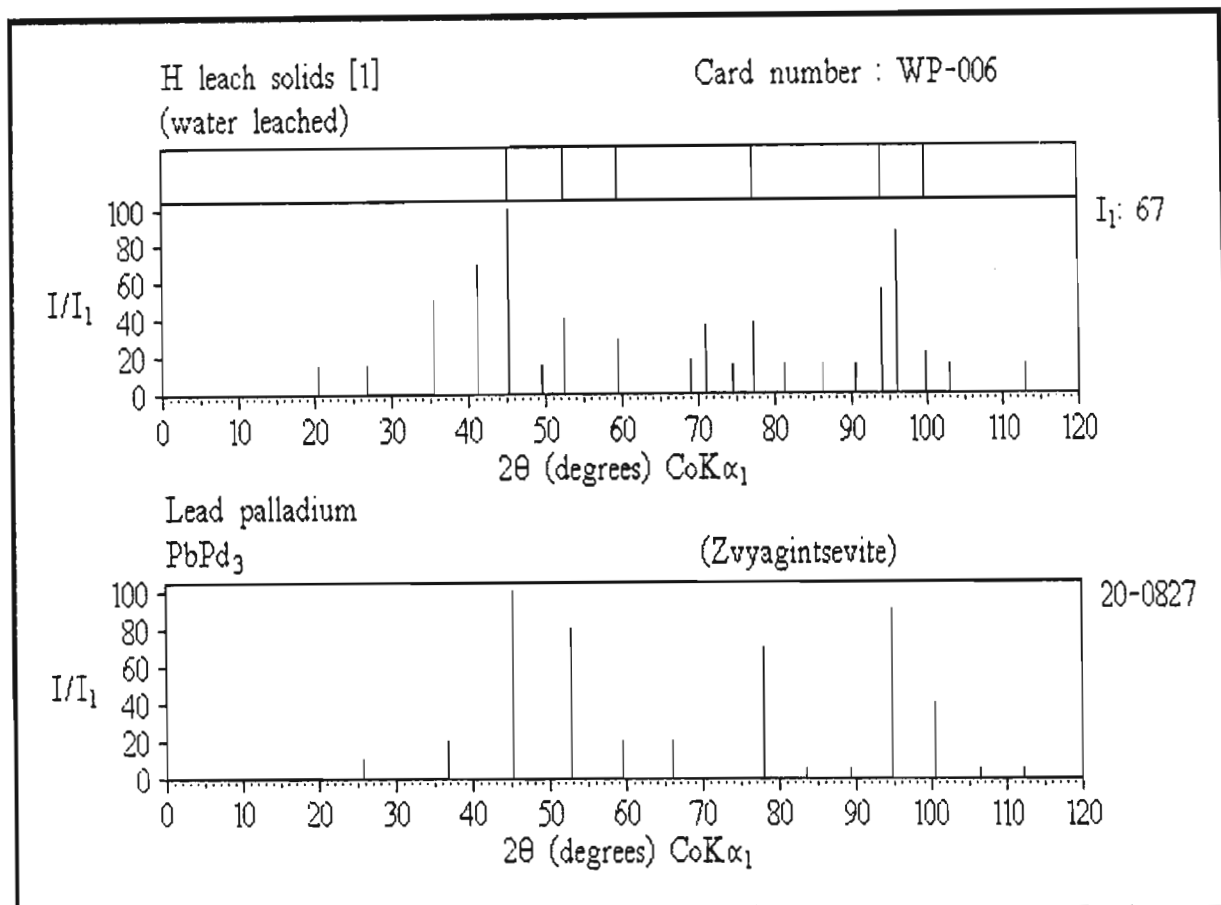
Figure 5.6.2-1(a)
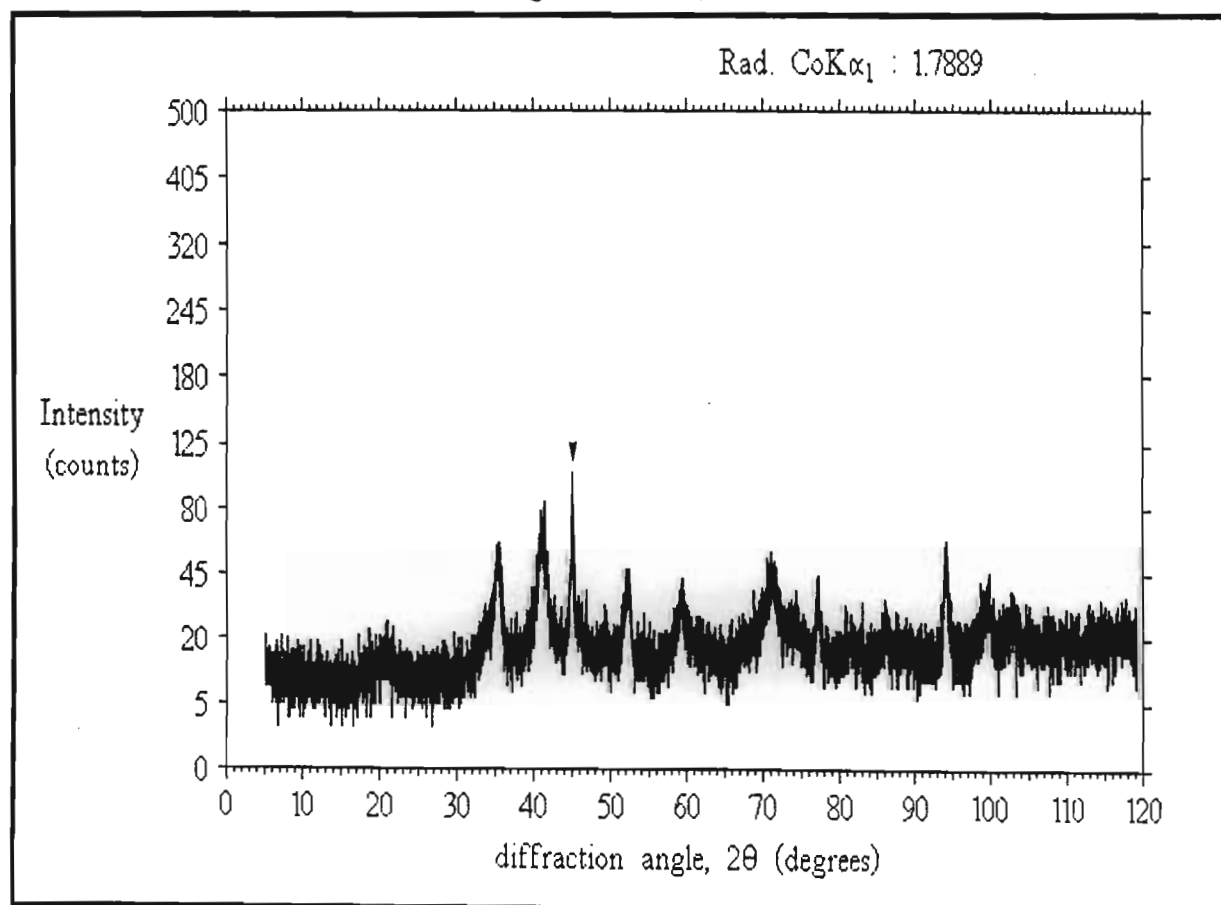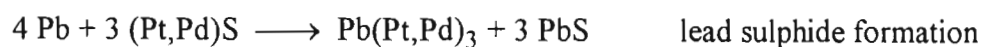

Figure 5.6.2-1(b)

Figure 5.6.2-2(a)

Figure 5.6.2-2(b)

Table 5.6.2-2   Comparison of PbSO$_4$ reference data with data observed for a nitric acid insoluble residue

PbSO$_4$ Reference data [65]			Nitric acid residue [2] (WP-008) Observed data		
d(Å)	(I/I$_1$)	2θ	d(Å)	(I/I$_1$)	2θ
4.26	(87)	24.2	4.252	(54)	24.3
3.813	(57)	27.1	3.801	(36)	27.2
3.622	(23)	28.6	3.610	(20)	28.7
3.479	(33)	29.8	3.470	(25)	29.9
3.333	(86)	31.1	3.324	(77)	31.2
3.220	(71)	32.3	3.212	(62)	32.3
3.001	(100)	34.7	3.000	(100)	34.7
2.773	(35)	37.6	2.760	(44)	37.8
2.699	(46)	38.7	2.694	(42)	38.8
2.618	(8)	40.0	2.612	(17)	40.0
2.406	(17)	43.6	2.406	(22)	43.6
2.276	(20)	46.3	2.271	(24)	46.4
2.193	(7)	48.1	2.192	(19)	48.2
2.164	(26)	48.8	2.163	(29)	48.9
2.067	(76)	51.3	2.066	(96)	51.3
2.031	(34)	52.3	2.033	(60)	52.2
1.973	(21)	53.9	1.971	(27)	54.0

Lead sulphate is almost totally insoluble in nitric acid (although it is soluble in sodium hydroxide) and not decomposed by furnace temperatures having a melting point of 1170°C [66]. This sulphate has two possible origins.

The first of these is based on reactions with sulphide phases. Here the reactions would be :

$$PbCO_3 \longrightarrow PbO + CO_2 \qquad \text{lead carbonate decomposition}$$

$$2\,PbO \longrightarrow Pb + O_2 \qquad \text{lead oxide reduction}$$

$$4\,Pb + 3\,(Pt,Pd)S \longrightarrow Pb(Pt,Pd)_3 + 3\,PbS \qquad \text{lead sulphide formation}$$

$$PbS + 2\,O_2 \longrightarrow PbSO_4 \qquad \text{lead sulphate formation}$$

Any residual sulphur or sulphides could lead to the formation of lead sulphide; the third reaction is just an example, based on one known source of sulphur.
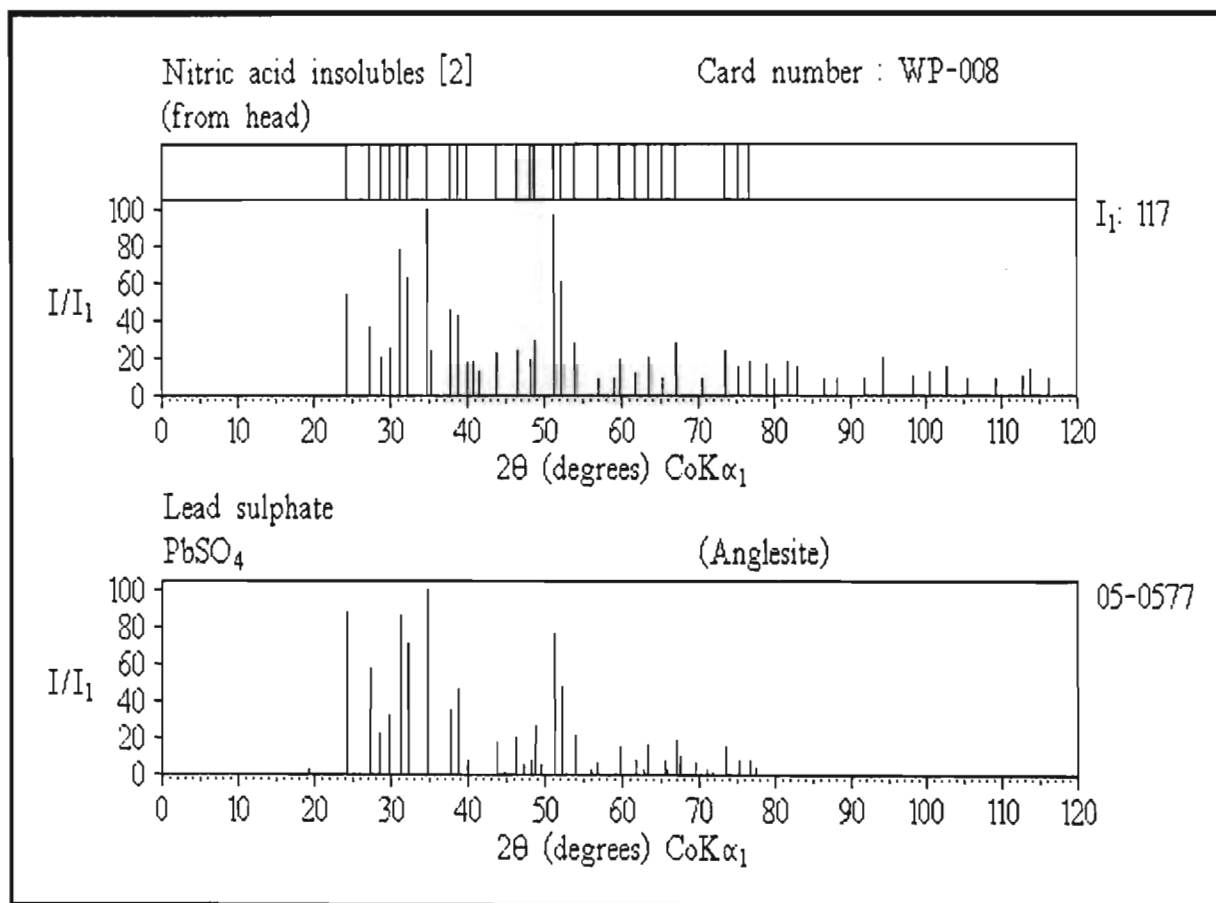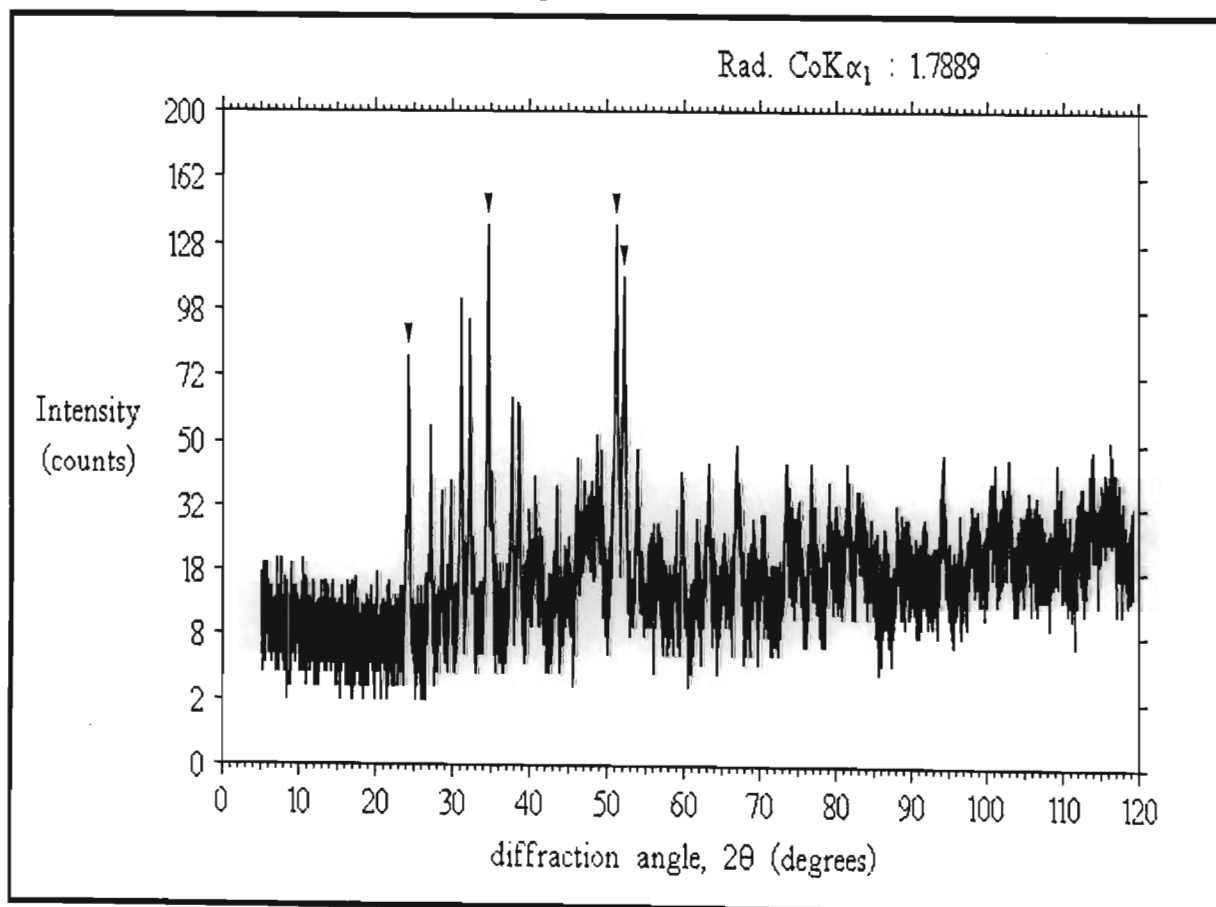
Figure 5.6.2-3(a)

Figure 5.6.2-3(b)

The second source of lead sulphate might simply be from the base metal refinery. Some concentrates can be over 3% lead. Evidence for this source came from a normal concentrate that had gone through a pre-treatment leach (3rd stage leach) to remove iron and nickel. This residue contained 5.6% lead and showed clear evidence of lead sulphate, although the sample was of low crystallinity (**Figure 5.6.2-4(a) and (b)**). Note the unleached pgm residue peaks. This is probably the most important source.

Although the above findings explained much of the problem, it was found that not only was lead alloying with pgms, it was also reacting with oxide dust (mainly ruthenium oxide). Another sample of insolubles from the nitric acid leach revealed the presence of the mixed metal oxide $Pb_2Ru_2O_{6.5}$. **Table 5.6.2-3** compares the reference data for this compound with data observed for a leach residue, before and after magnetic separation (to remove the iron oxide Fe_3O_4). Values in boldface indicate overlap with another phase, while those in italics indicate significant deviation from the reference values.

Table 5.6.2-3   Comparison of $Pb_2Ru_2O_{6.5}$ reference data with data observed for a nitric acid insoluble residue

| $Pb_2Ru_2O_{6.5}$ Reference data [67]			Residue [1] (WP-005) Observed data			Residue [1] (WP-005-B) † Observed data		
d(Å)	(I/I$_1$)	2θ	d(Å)	(I/I$_1$)	2θ	d(Å)	(I/I$_1$)	2θ
2.959	(100)	35.2	2.953	(100)	35.3	2.956	(100)	35.2
2.563	(35)	40.9	**2.551**	**(-)**	**41.1**	**2.558**	**(-)**	**40.9**
2.352	(9)	44.7	2.328	(11)	45.2	2.355	(18)	44.6
1.973	(5)	53.9	*1.952*	*(11)*	*54.6*	*1.959*	*(17)*	*54.3*
1.812	(50)	59.1	1.811	(54)	59.2	1.818	(50)	59.0
1.546	(55)	70.7	1.545	(44)	70.8	1.548	(46)	70.6
1.480	(12)	74.4	1.480	(27)	74.3	1.480	(24)	74.3
1.281	(7)	88.6	1.282	(14)	88.4	1.282	(13)	88.5
1.176	(19)	99.0	1.178	(35)	98.8	1.179	(34)	98.7
1.146	(17)	102.6	1.147	(23)	102.5	1.147	(26)	102.5
1.119	(1)	106.1	*1.112*	*(11)*	*107.1*	*1.112*	*(13)*	*107.1*
1.046	(15)	117.5	*1.049*	*(29)*	*117.0*	*1.050*	*(23)*	*116.9*

† The non-magnetic fraction of the residue
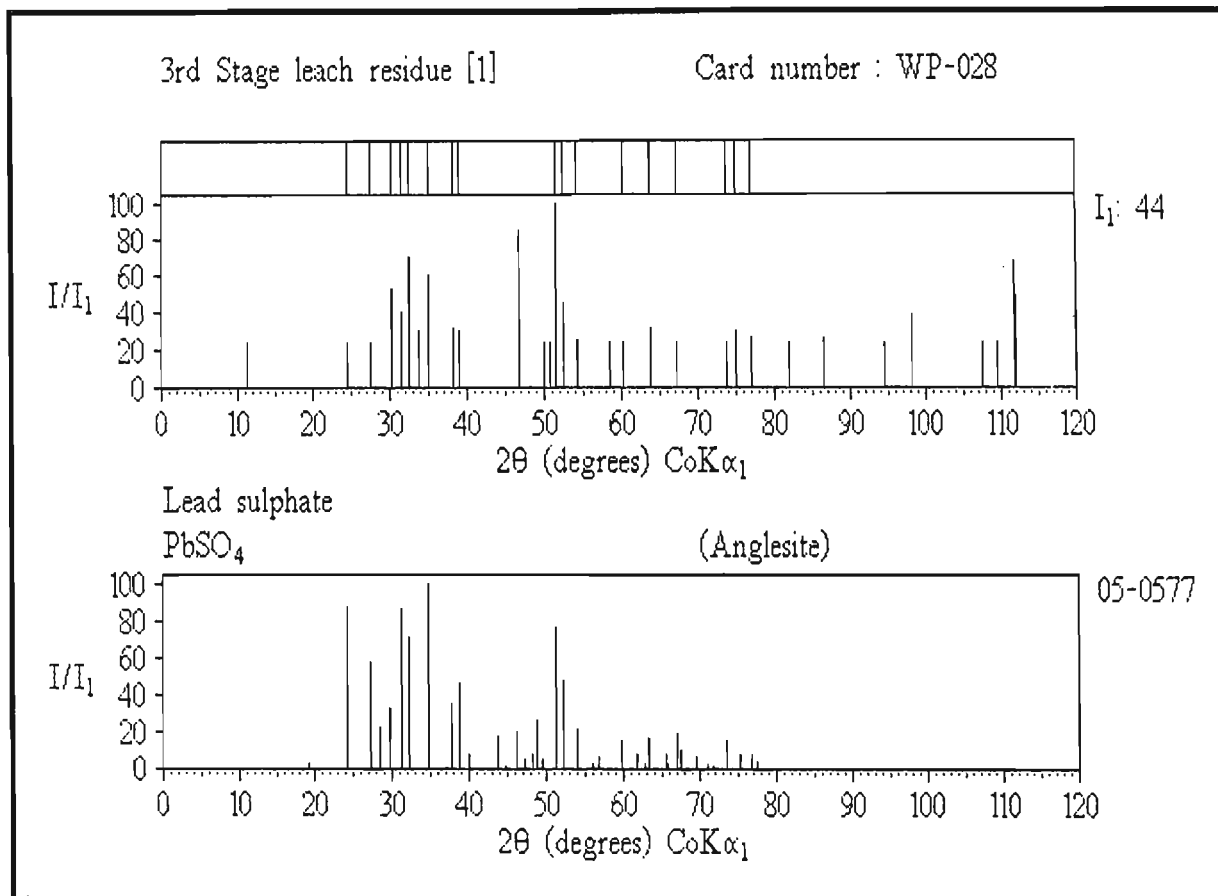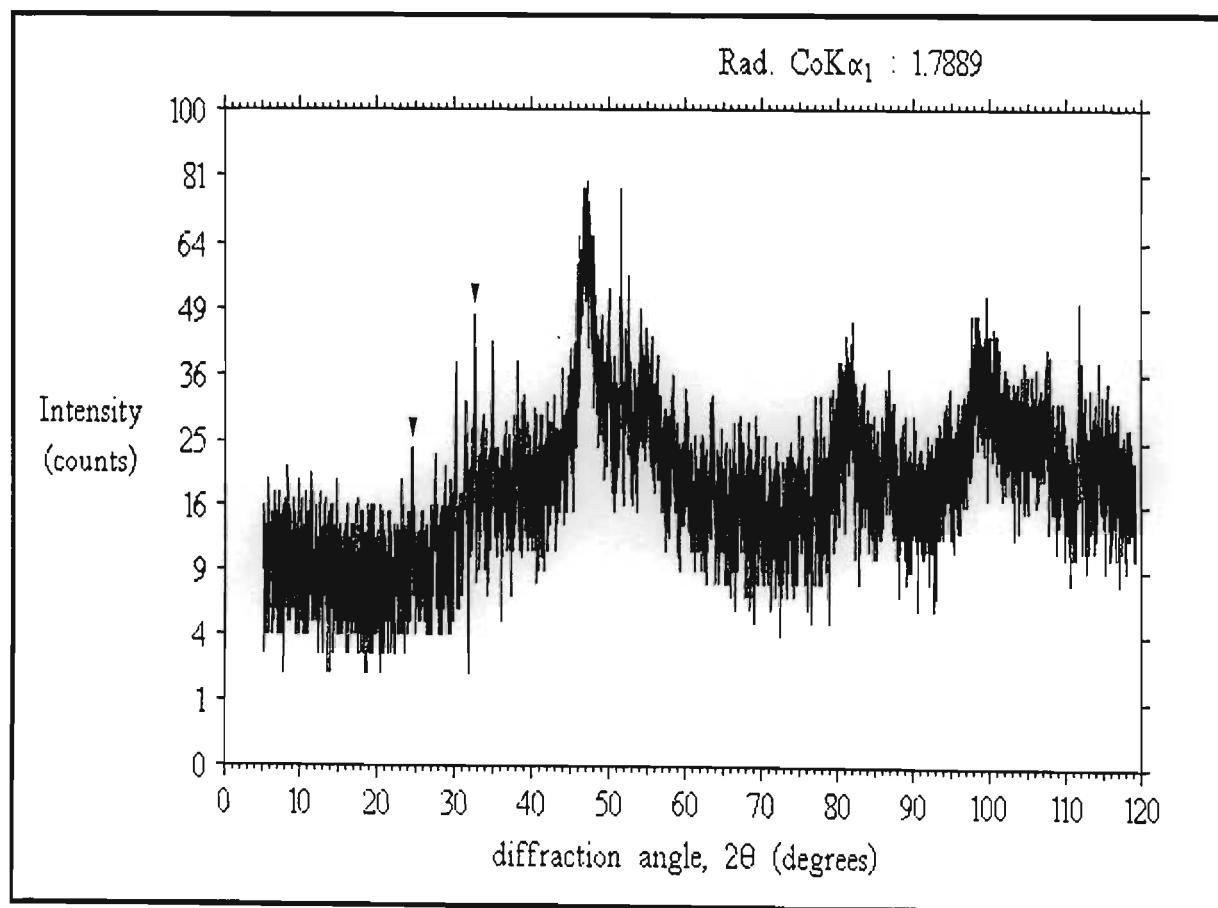
Figure 5.6.2-4(a)

Figure 5.6.2-4(b)

Deviations are due to the original preparation for the reference material producing a product of relatively low crystallinity. Some of the reference peaks were broad [68], while all those observed for the residue compound were relatively sharp.

Figures 5.6.2-5(a) and **(b)**, and **5.6.2-6(a)** and **(b)** show the scans and reduced spectra for the two residues of Table 5.6.2-3.

The discovery of this oxide was extraordinary as it has only been quite recently synthesised. It was the first example of an anion-deficient pyrochlore (the ideal formula should be $Pb_2Ru_2O_7$), and is capable of metallic conduction [68]. The oxidation states proposed in the given reference are : $(Pb^{2+})_2[Ru^{4+}Ru^{5+}](O^{2-})_{6.5}$.

The given laboratory synthesis [68] is to heat (850-900°C, in air) an intimately ground mixture of lead nitrate ($Pb(NO_3)_2$) and ruthenium oxide (RuO_2). At these temperatures lead nitrate decomposes into the basic monoxide (PbO) which then reacts with ruthenium oxide. The oxygen radical (O) was suggested as being important in the reaction. The simplified reactions are given below :

$$2\,Pb(NO_3)_2 \longrightarrow 2\,PbO + 4\,NO_2 + O_2$$
$$8\,PbO + 8\,RuO_2 + O_2 \longrightarrow 4\,Pb_2Ru_2O_{6.5}$$
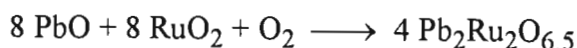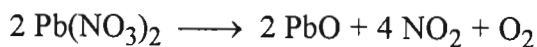
As lead monoxide is formed during the decomposition of lead carbonate to molten lead in the lead fusion process, the first reaction above would be replaced by :

$$PbCO_3 \longrightarrow PbO + CO_2$$
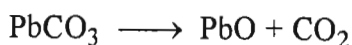
Unreacted ruthenium oxide (RuO_2) was found together with lead ruthenium oxide in the residue (PbO is soluble in nitric acid) (**Figure 5.6.2-7**). The reaction illustrates the mildly acidic nature of ruthenium oxide. The identification of this oxide explained why lead was not completely leachable, and the lead fusion mass balance problem. Attempts are being made to phase out the lead fusion process.

The iron oxide Fe_3O_4 was also found in nitric acid insoluble residues, as mentioned earlier (§ 5.4.1).
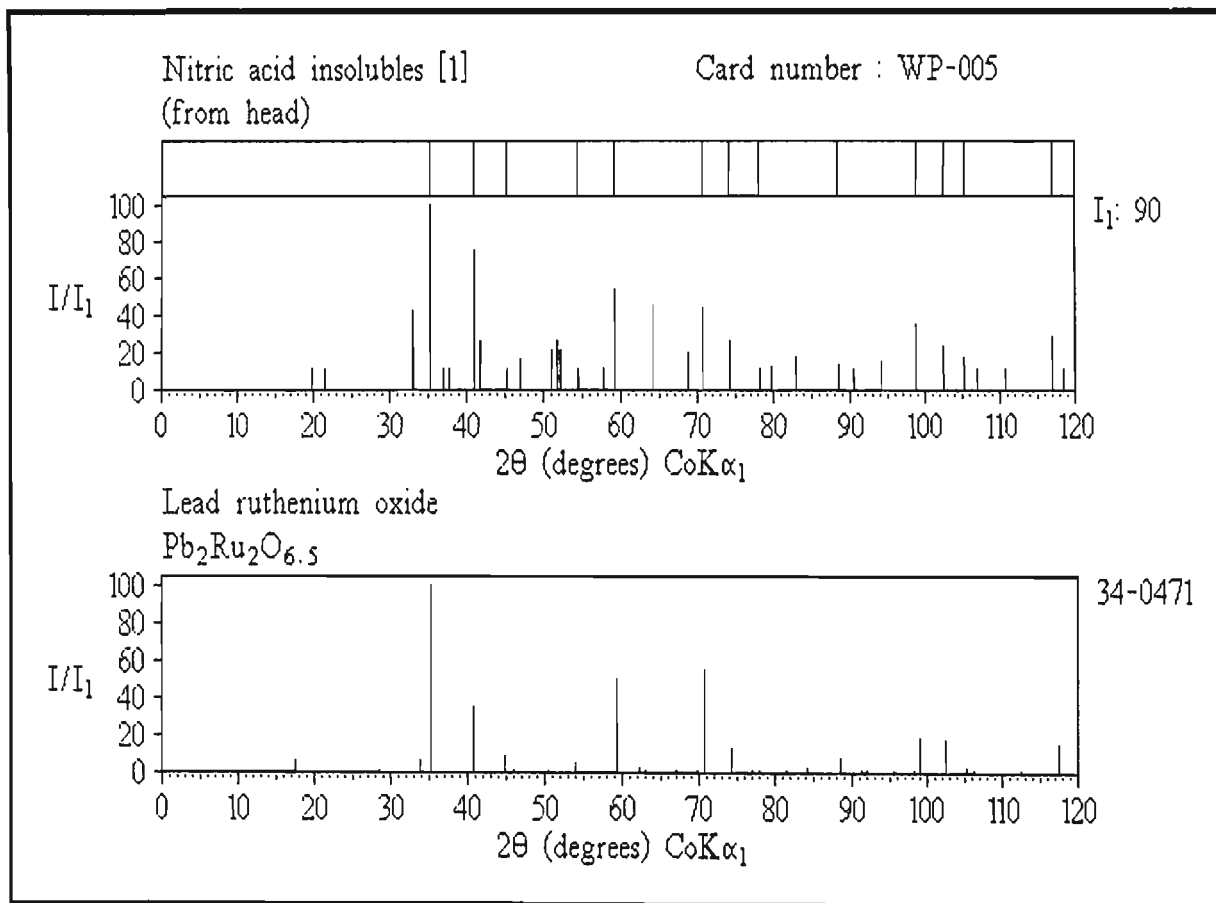
Figure 5.6.2-5(a)

Figure 5.6.2-5(b)

Nitric acid insolubles [1]
(non-magnetic fraction)

Card number : WP-005-B

I_1: 77

I/I_1

2θ (degrees) CoKα_1

Lead ruthenium oxide

Pb$_2$Ru$_2$O$_{6.5}$

34-0471

I/I_1

2θ (degrees) CoKα_1

Figure 5.6.2-6(a)

Rad. CoKα_1 : 1.7889

Intensity
(counts)

diffraction angle, 2θ (degrees)

Figure 5.6.2-6(b)

Nitric acid insolubles [1]   Card number : WP-005
(from head)

I_1: 90

I/I_1

2θ (degrees) CoKα_1

Ruthenium oxide
RuO$_2$

21-1172

I/I_1

2θ (degrees) CoKα_1
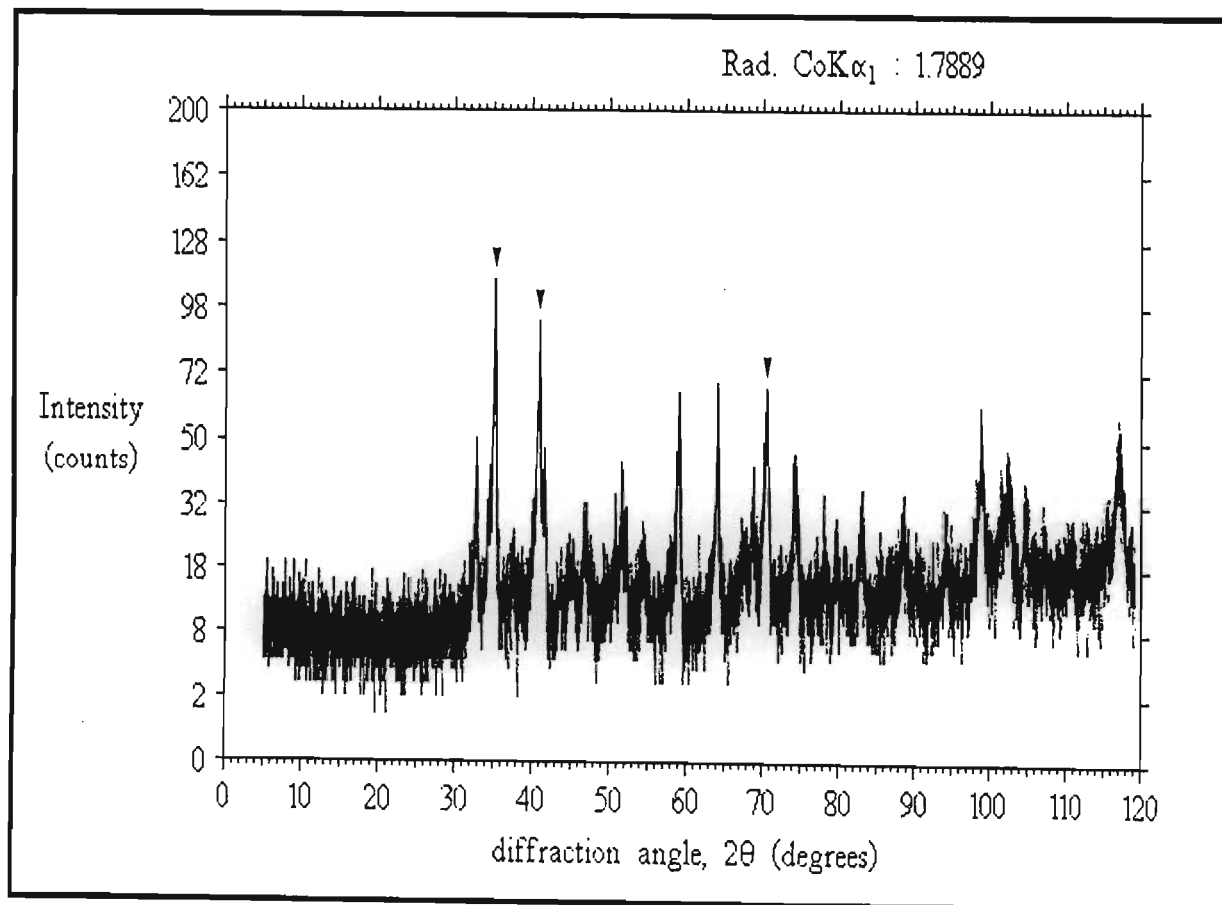
Figure 5.6.2-7

Most lead is precipitated from solutions by pH control. It can also precipitate automatically if chloride leach solutions are cooled as lead chloride, **PbCl$_2$** (which is only soluble in warm solutions). This was found to be occurring in several cases. **Table 5.6.2-4** compares lead chloride reference data with that typically observed in precipitate samples (only peaks above 1.95Å have been listed).
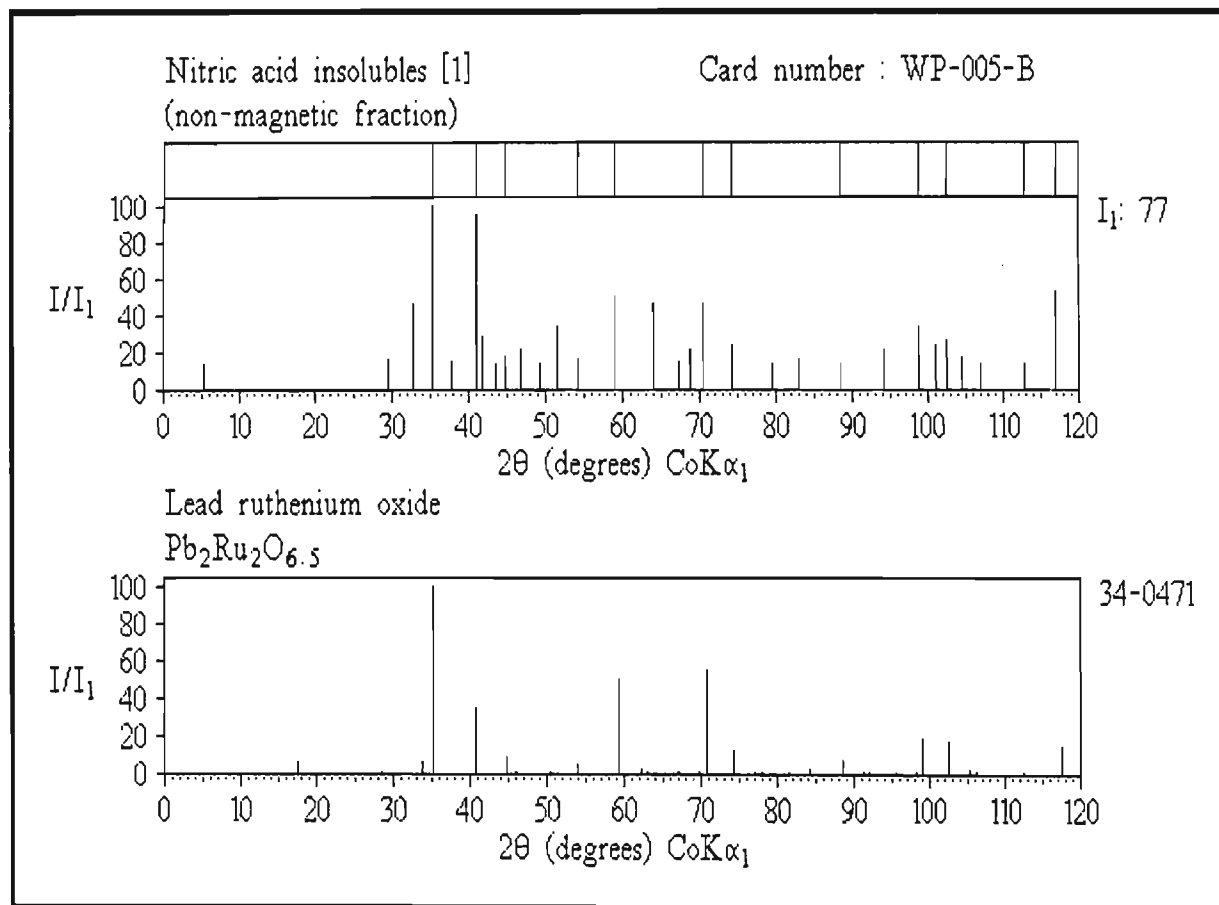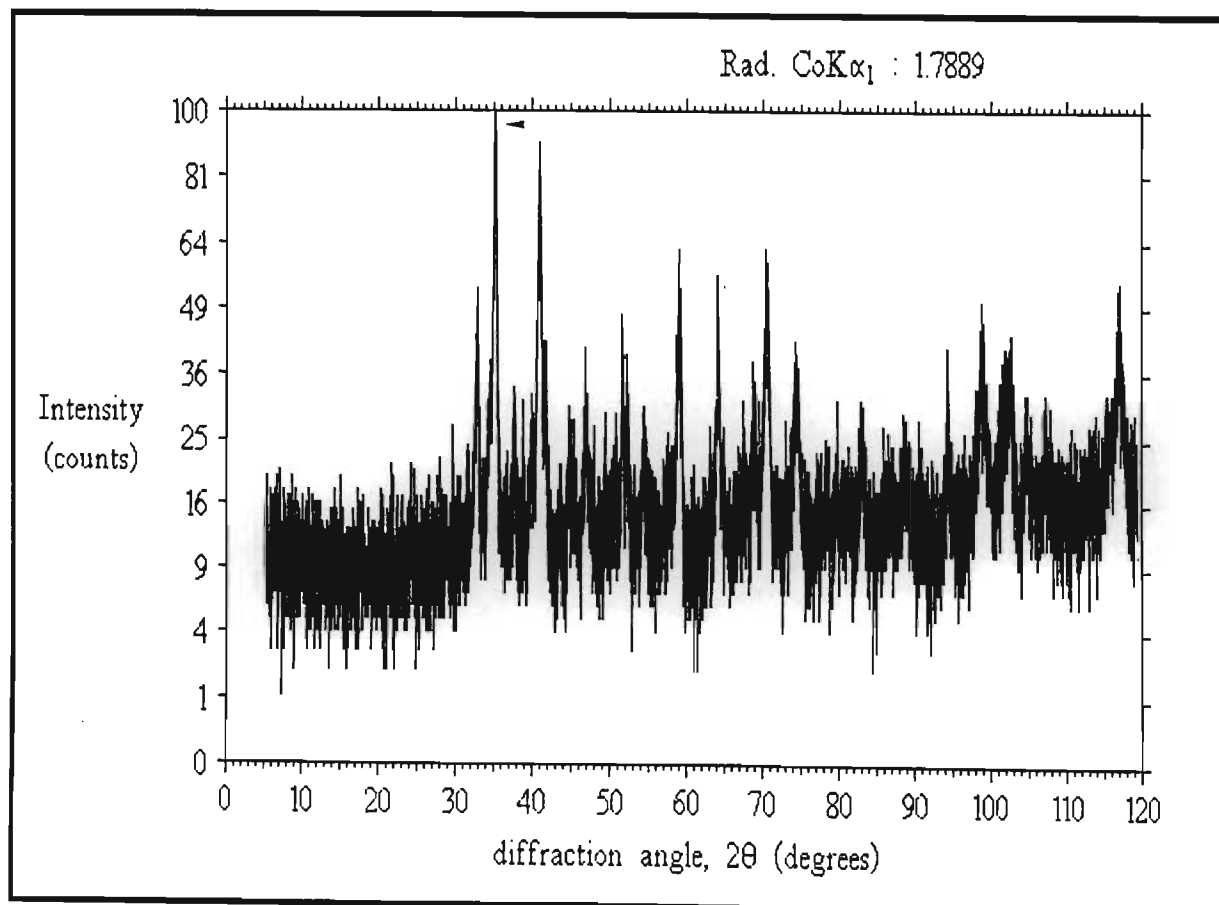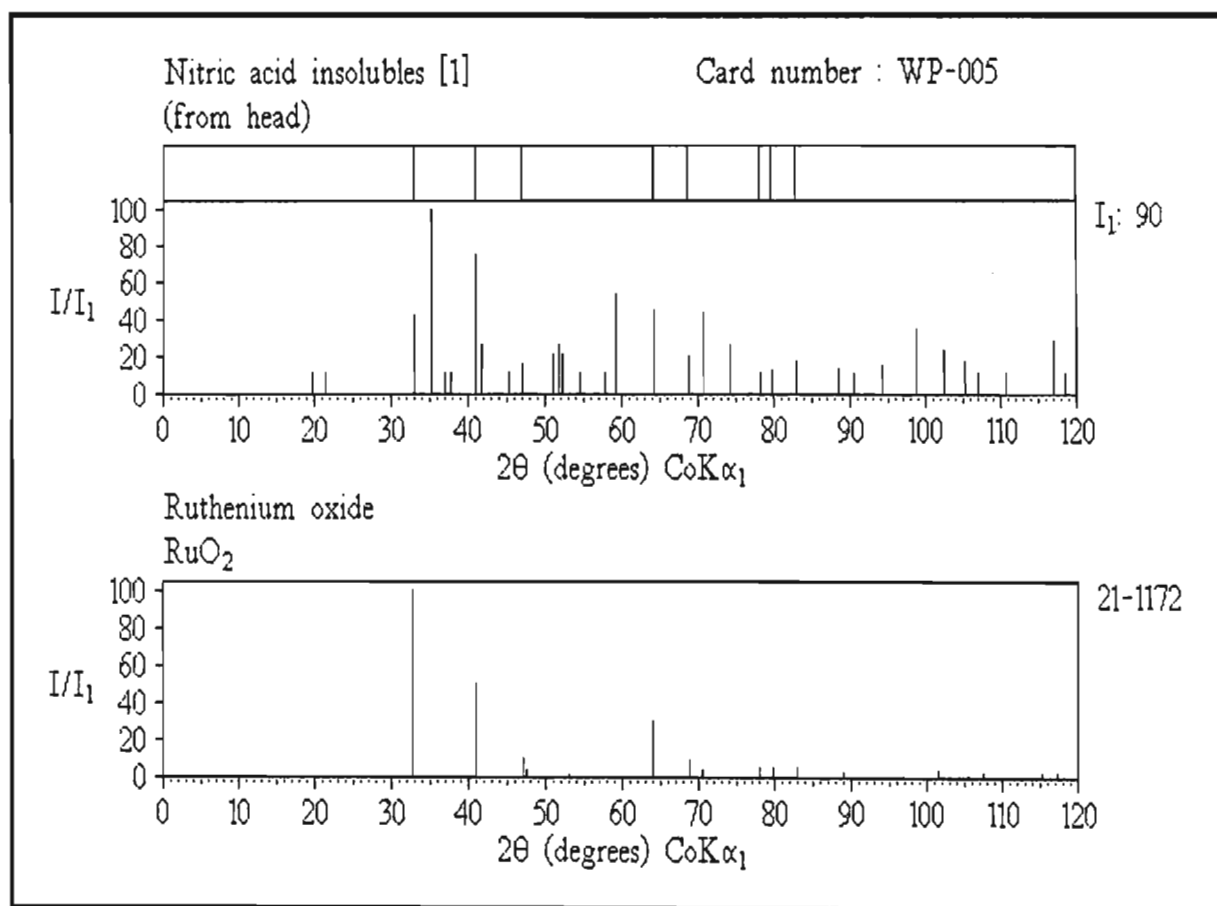
Figure 5.6.2-8 shows the reduced spectra of such a precipitate.

Table 5.6.2-4 Comparison of PbCl$_2$ reference data with data observed for a lead-rich precipitate

PbCl$_2$ Reference data [69]			Precipitate [1] (WP-019 : Sphone) Observed data		
d(Å)	(I/I$_1$)	2θ	d(Å)	(I/I$_1$)	2θ
4.523	(14)	22.8	4.501	(29)	22.9
4.057	(35)	25.5	4.051	(31)	25.5
3.890	(75)	26.6	3.887	(93)	26.6
3.810	(40)	27.2	3.797	(51)	27.2
3.579	(100)	28.9	3.567	(100)	29.0
2.776	(55)	37.6	2.771	(84)	37.7
2.510	(45)	41.8	2.506	(75)	41.8
2.261	(25)	46.6	2.260	(58)	46.6
2.214	(25)	47.7	2.215	(51)	47.6
2.152	(35)	49.1	2.147	(61)	49.2
2.096	(40)	50.5	2.094	(81)	50.6
1.959	(18)	54.3	1.956	(63)	54.4

5.7 GOLD PROBLEMS

5.7.1 GOLD-RICH PRECIPITATES

Species, like lead chloride, that precipitate automatically or erratically are highly undesirable as they have to be filtered out in places where a filtration line might be absent. This slows the whole process. One precipitate problem occurring in pgm refinery operations was the erratic deposition of precipitates that filtered with extreme difficulty. These were relatively rich in gold (5 - 6%). XPD analysis of these
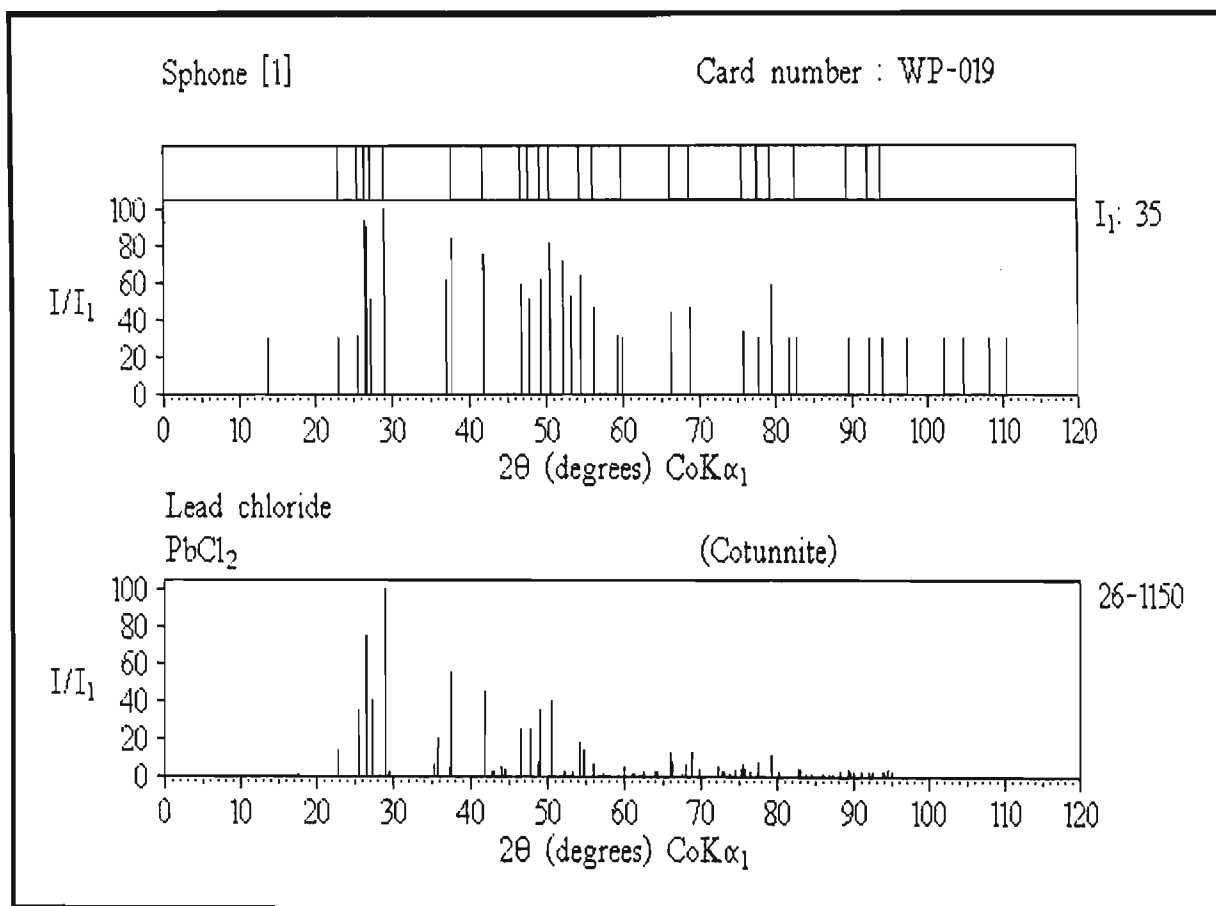
Figure 5.6.2-8

precipitates showed that the gold was present as particulate metallic gold, **Au**. **Table 5.7.1-1** compares the reference data for metallic gold with data observed for two such precipitates. The scans and reduced spectra are shown in **Figures 5.7.1-1(a)** and **(b)**, and **5.7.1-2(a)** and **(b)**.

Table 5.7.1-1   Comparison of Au reference data with data observed
for two gold-rich precipitates

Au Reference data [70]			Precipitate [1] (WP-018) Observed data			Precipitate [2] (WP-027-A) Observed data		
d(Å)	(I/I₁)	2θ	d(Å)	(I/I₁)	2θ	d(Å)	(I/I₁)	2θ
2.355	(100)	44.6	2.340	(100)	45.0	2.350	(100)	44.7
2.039	(52)	52.0	2.027	(60)	52.4	2.029	(55)	52.3
1.442	(32)	76.7	1.433	(32)	77.2	1.442	(32)	76.7
1.230	(36)	93.3	1.223	(47)	94.0	1.228	(33)	93.5
1.1774	(12)	98.9	1.174	(19)	99.3	1.177	(17)	98.9

The identification of particulate gold was important as it showed that the cyclone used to remove reduced gold was not working efficiently. An effective high-pressure filter press has since replaced the cyclone.

5.8 RESIDUE AND PRECIPITATE WASHING

The washing of residues and precipitates is a common pgm refinery operation. Incomplete washing is easily detected by XPD analysis. Evaporation of the wash solution, followed by analysis of the evaporate also reveals what salts are being removed by the wash. The pH adjustment of solutions was found to produce sodium chloride, **NaCl** [71], in many precipitates (**Figure 5.8-1**). The high crystallinity of this phase reduces the intensity of all other lines. It thus has to be removed from samples before a meaningful XPD analysis can be performed.

Fphone [5]   Card number : WP-018
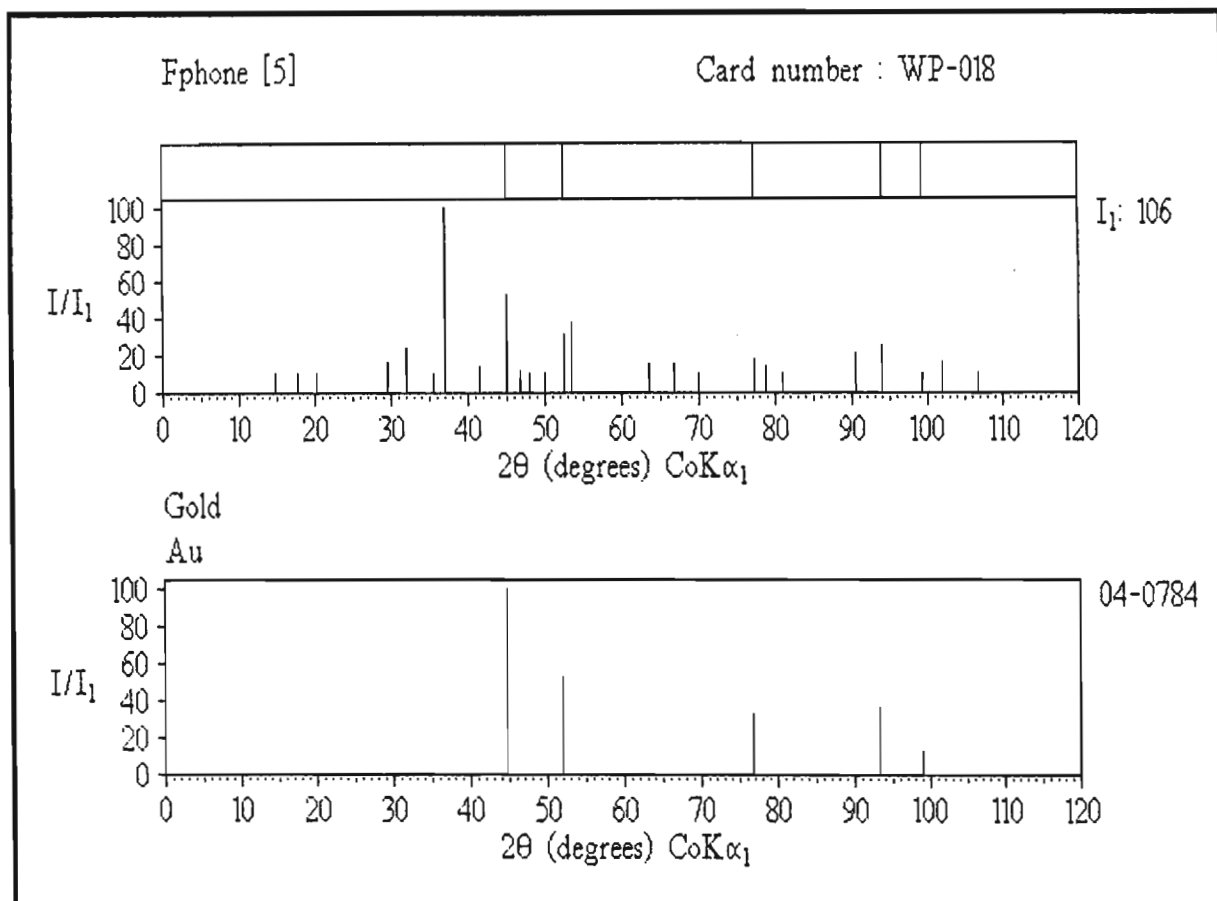
Figure 5.7.1-1(a)

Figure 5.7.1-1(b)

pH 1 Cake [1]
(after salt extraction)

Card number : WP-027-A

I$_1$: 61

I/I_1

2θ (degrees) CoKα$_1$

Gold
Au

04-0784

I/I_1

2θ (degrees) CoKα$_1$

Figure 5.7.1-2(a)

Rad. CoKα$_1$: 1.7889

Intensity
(counts)

diffraction angle, 2θ (degrees)
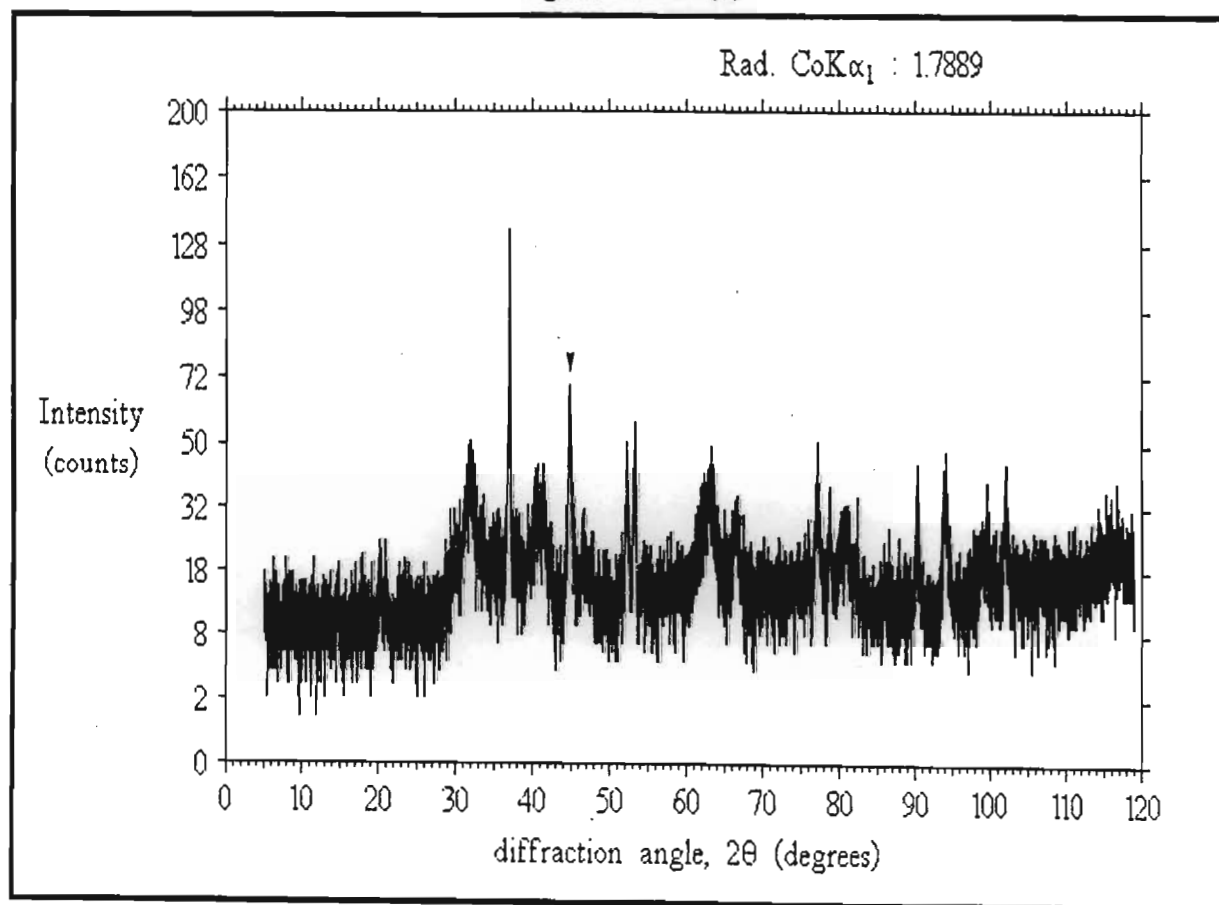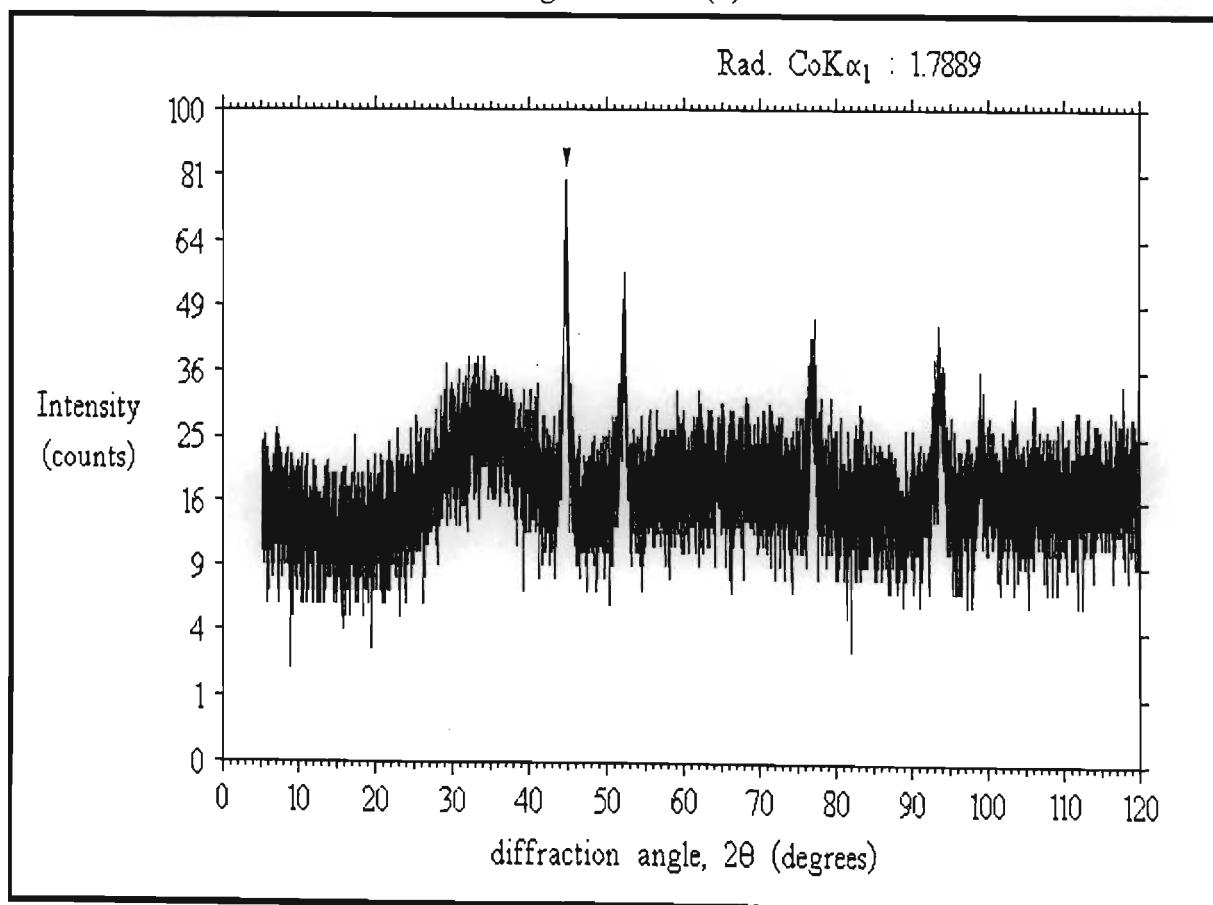
Figure 5.7.1-2(b)
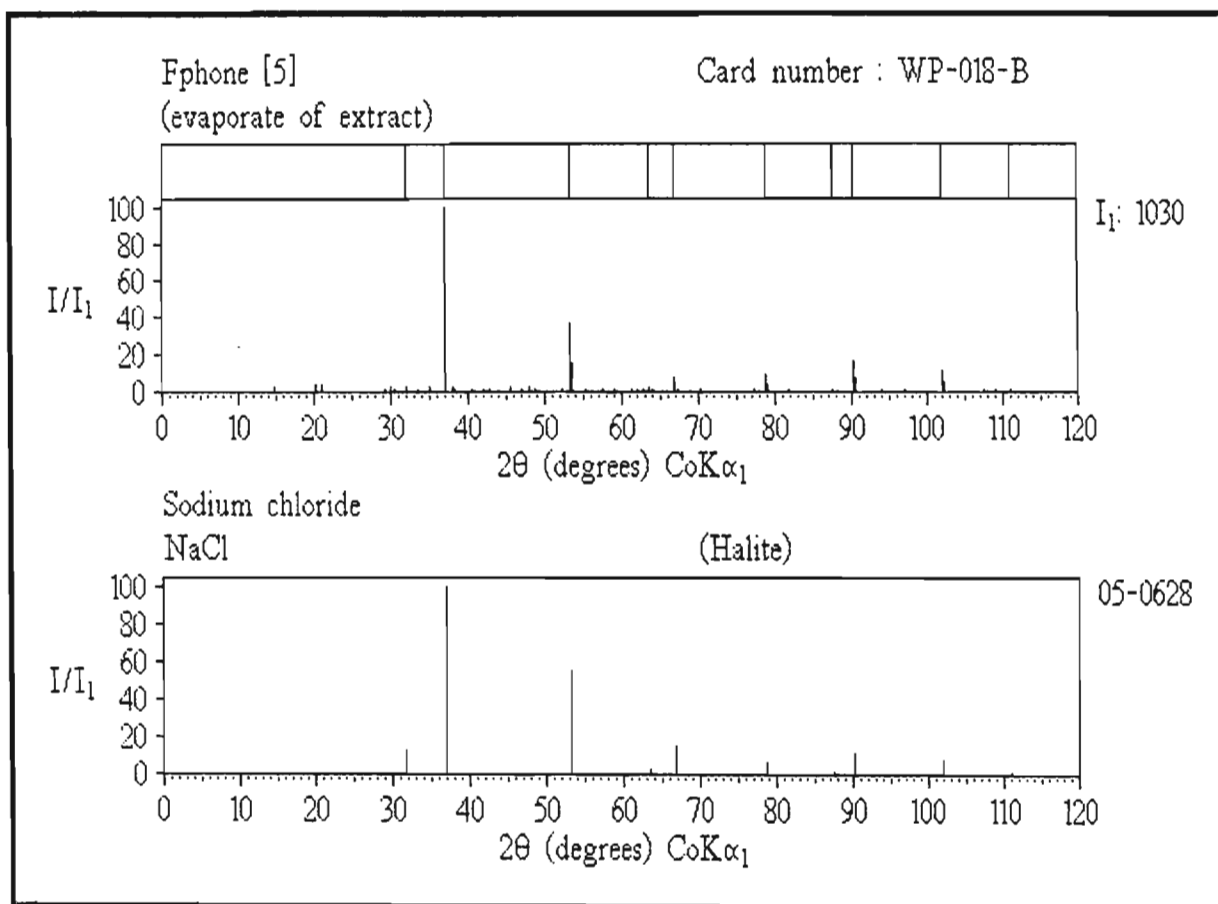
Figure 5.8-1(a)
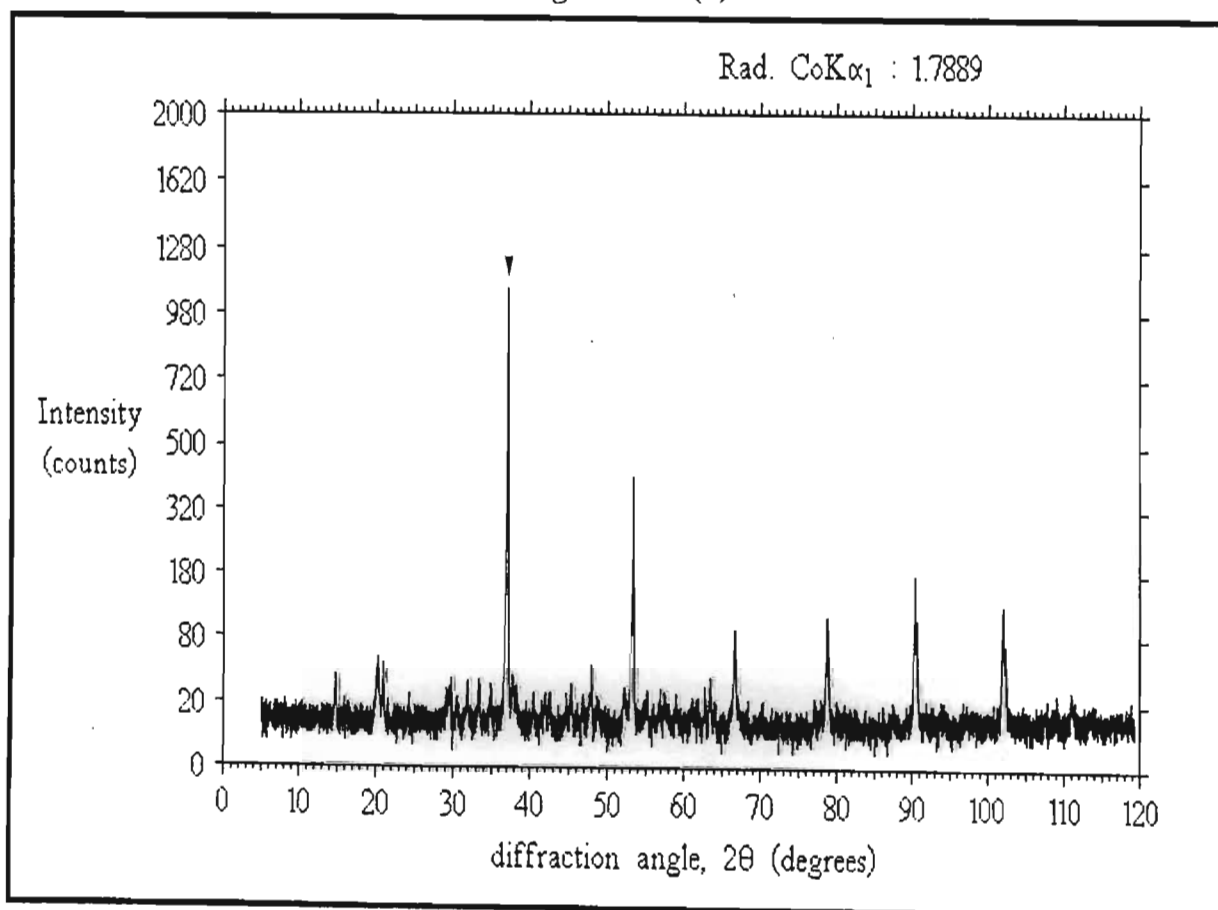
Figure 5.8-1(b)

Sometimes sodium carbonate is used to adjust pH. If this is not completely washed out of the residue, drying was found to result in the partially hydrated salt, $Na_2CO_3 \cdot H_2O$ [72] being present in residue cakes (**Figure 5.8-2**).

Another example of incomplete washing is shown in **Figure 5.8-3**. Here $(NH_4)_2[PtCl_6]$ provided by the refinery as the <u>pure</u> salt was found to contain relatively high levels of ammonium chloride, NH_4Cl [73]. The salt cannot be washed out with water as $(NH_4)_2[PtCl_6]$ is relatively soluble. Washing with cold 95% ethanol however removes this salt completely.

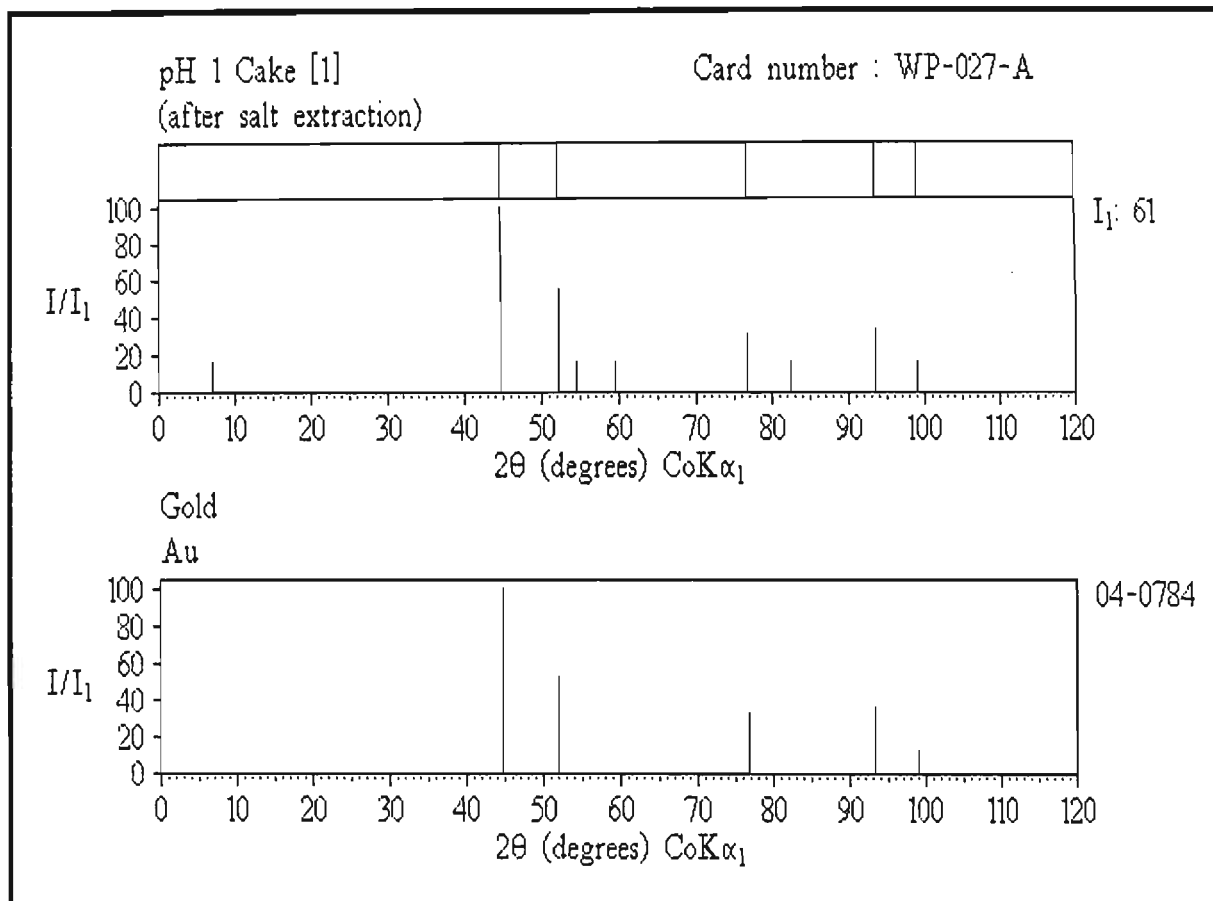Leaconc [4]   Card number : WP-072
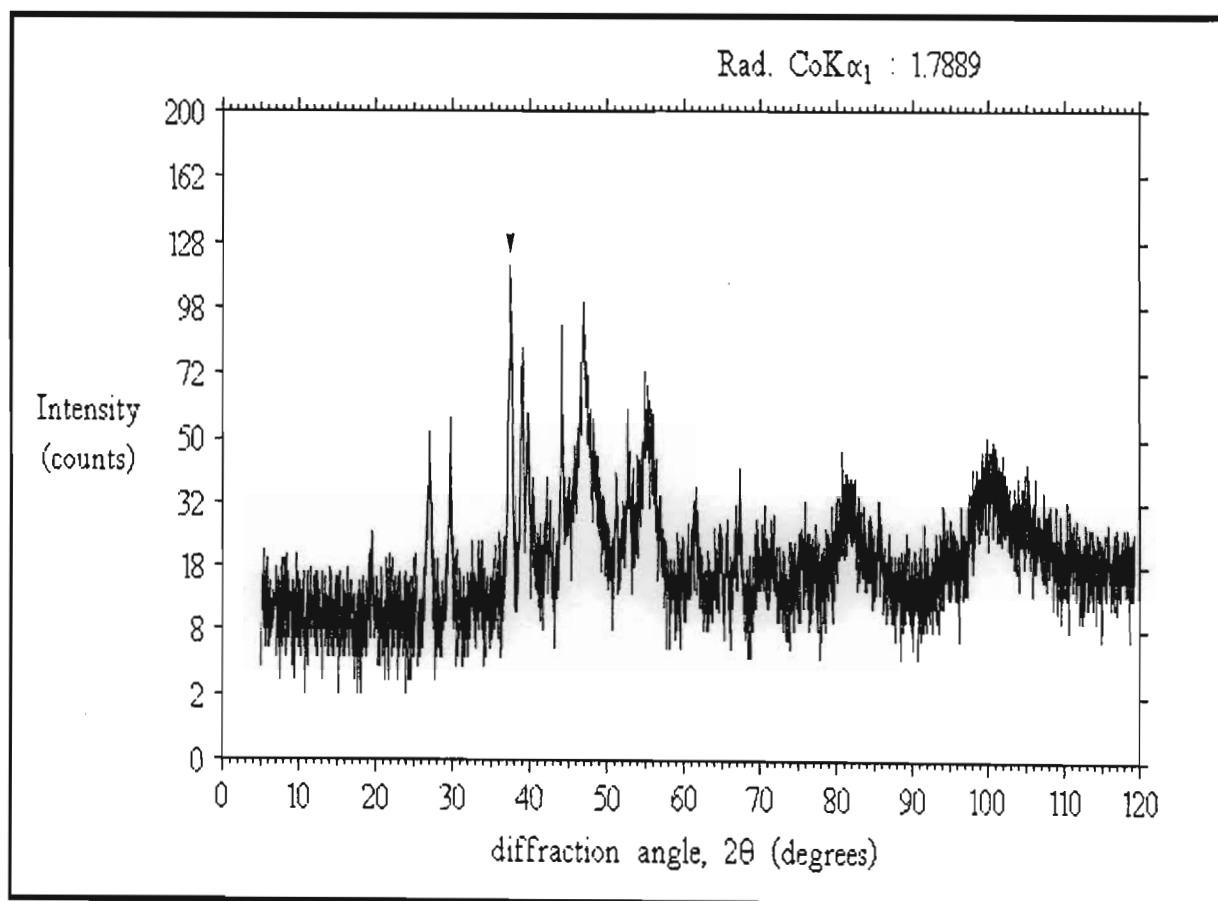
Figure 5.8-2(a)
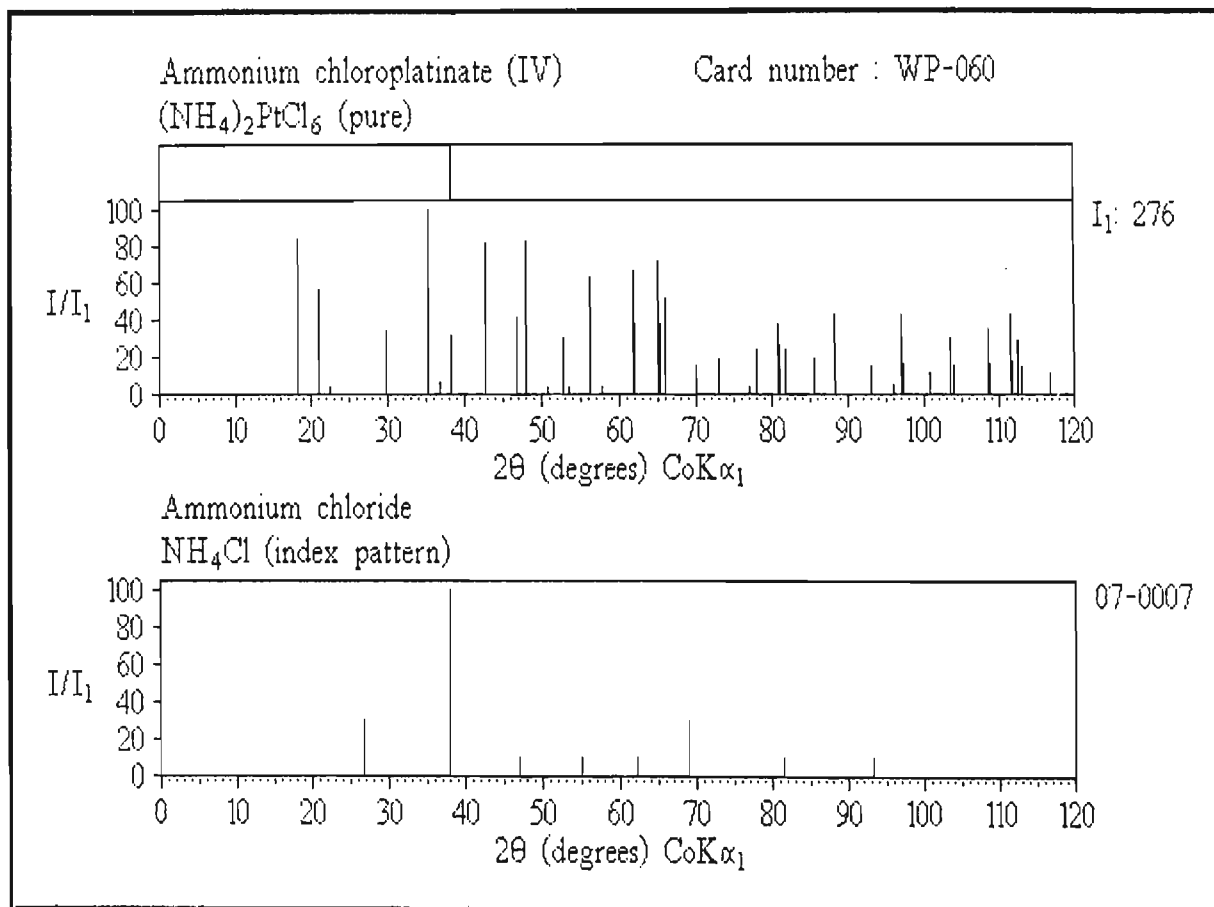
Figure 5.8-2(b)

Figure 5.8-3(a)

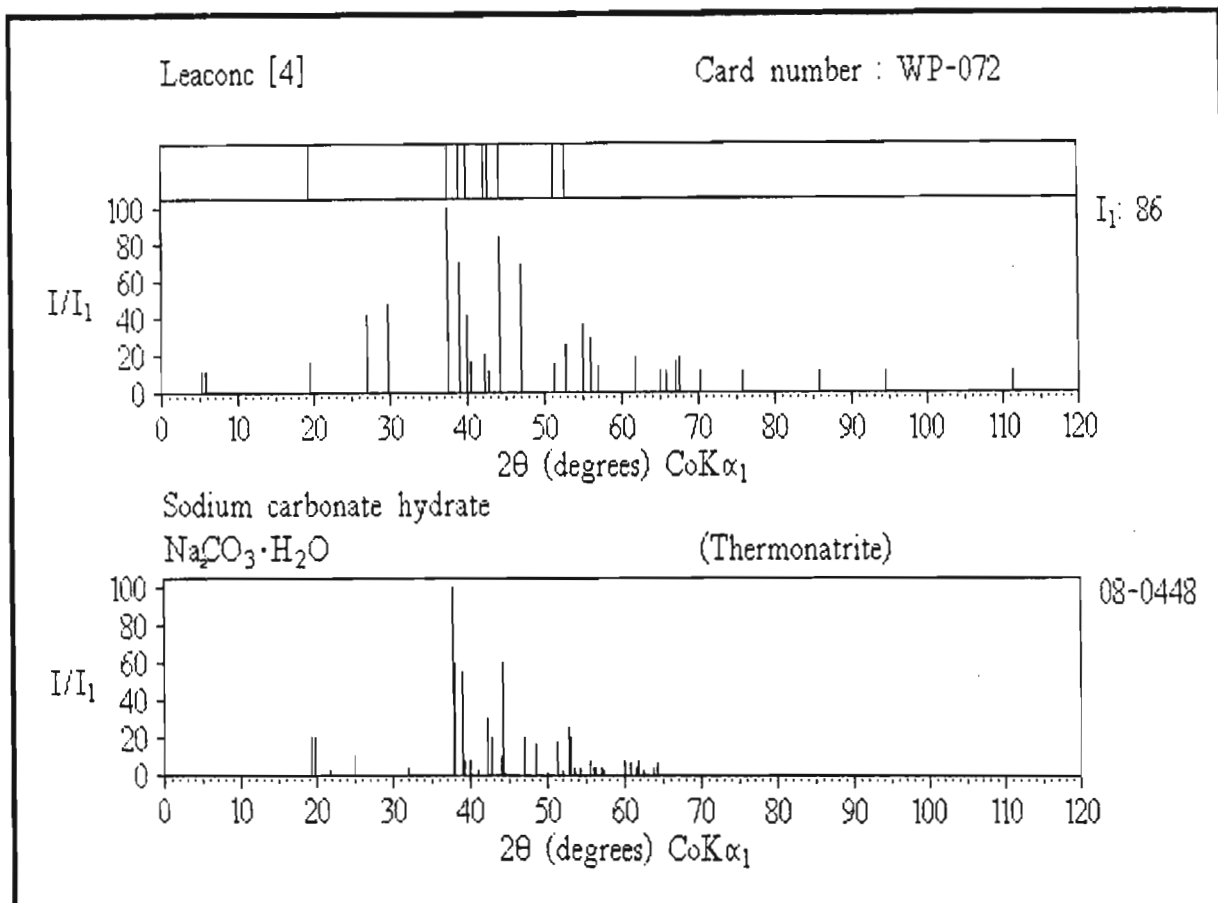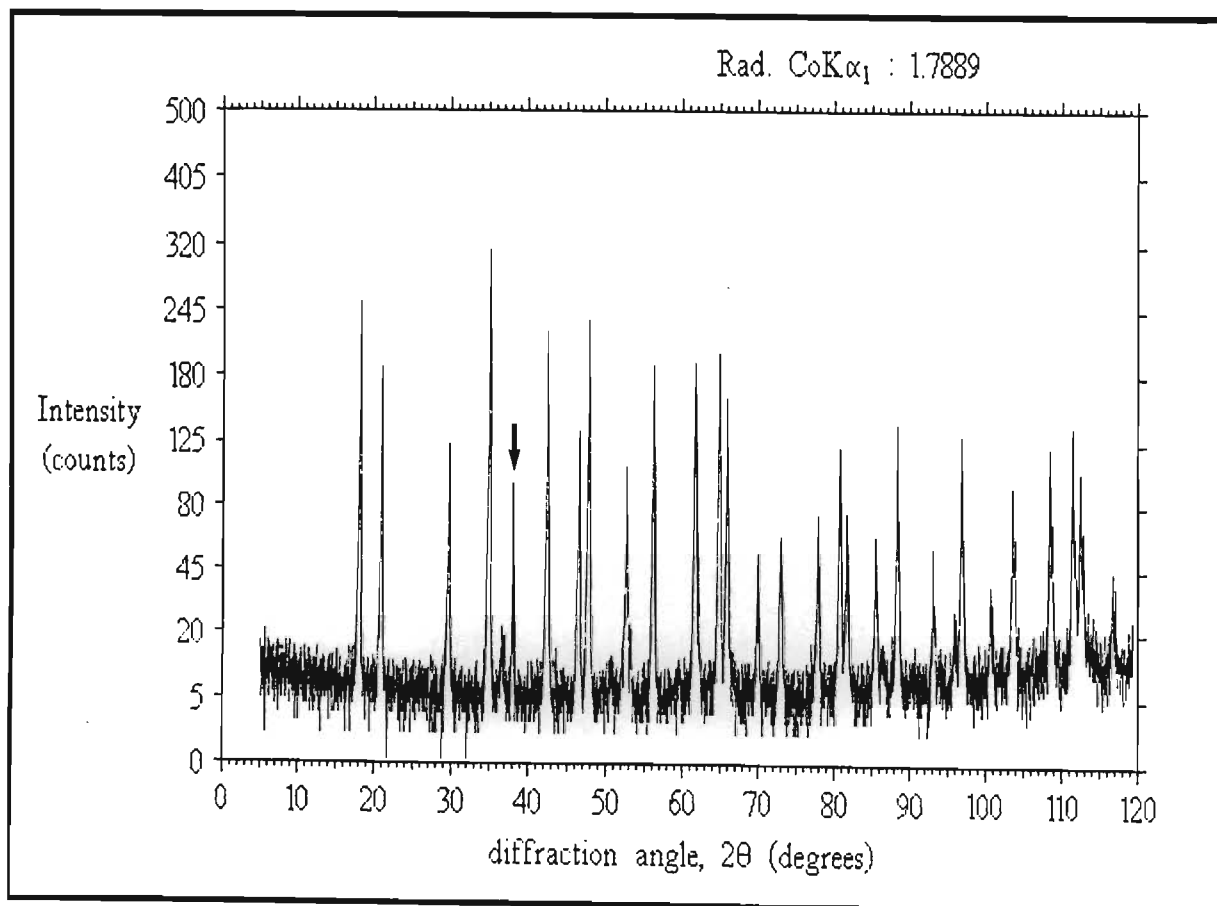Figure 5.8-3(b)

□□□
CHAPTER 6

CONCLUSIONS
□□□

The central aim of this project was to explain problems in platinum group metal extraction using x-ray powder diffraction analysis to identify species in matte, residue and precipitate samples. After the analysis of numerous process samples from both the base metal and platinum group metal refineries, a much clearer picture emerged of what was actually going on, what was dissolving, what was not dissolving, and what was precipitating. The results of this work are summarized below, and in the diagrams following.

6.1 CONVERTER MATTES

The main constituents of converter matte are **nickel sulphide** (Ni_3S_2), **copper sulphide** (Cu_2S), **nickel copper alloy** (Ni-Cu), **iron oxide** (Fe_3O_4) / **nickel iron oxide** ($NiFe_2O_4$) solid solution, **nickel oxide** (NiO), and trace amounts of **cobalt sulphide** (Co_3S_4).

Nickel iron oxide ($NiFe_2O_4$) occurs mainly as a grey crust in matte aeration cavities, together with **cobalt sulphide** (Co_3S_4).

XPD data can be used to detect **fast cooling**, determine the **alloy stoichiometry** and the **feasibility of magnetic separations**.

If iron oxide, nickel iron oxide and nickel oxide are absent, XPD data can be used to determine a **weight % estimate** of the Ni_3S_2, Cu_2S and Ni-Cu present in matte.

6.2 FIRST STAGE LEACH RESIDUES

The main constituents of first stage leach residue are **nickel sulphides** (Ni_3S_4 and NiS), **copper sulphide** ($Cu_{1.8}S$) and residual **nickel copper alloy** (Ni-Cu).

Leaching with potassium cyanide solution at 95°C removes almost all **copper sulphide** ($Cu_{1.8}S$) and almost all of the **nickel sulphide** Ni_3S_4.

Leaching with thiourea and hydrochloric acid removes almost all **copper sulphide** ($Cu_{1.8}S$), but none of the nickel sulphides nor any of the residual alloy.

6.3 BASE METALS IN NORMAL (OR MAJOR) CONCENTRATES

Copper occurs in normal concentrates as **copper sulphate** ($CuSO_4 \cdot 5H_2O$), **copper sulphide** (CuS), **copper platinum alloy** (Cu_3Pt) and **copper sulphate hydroxide hydrate** ($Cu_4SO_4(OH)_6 \cdot H_2O$).

The formation of **copper platinum alloy** (Cu_3Pt) would be favoured by the fast cooling of matte.

Copper sulphide (CuS) can be removed from concentrates (if present) by washing after the concentrate has been dried at 260°C in the presence of sulphuric acid.

Nickel occurs in normal concentrates as **nickel oxide** (NiO) and **nickel iron oxide** ($NiFe_2O_4$).

Iron is present in normal concentrates mainly as **nickel iron oxide** ($NiFe_2O_4$).

6.4 OTHER IMPURITIES IN NORMAL CONCENTRATES

Lead occurs in normal concentrates mainly as **lead sulphate** ($PbSO_4$).

Silicon occurs in normal concentrates mainly as **silicon oxide** (SiO_2), and in trace amounts as **magnesium iron aluminium silicate** $(Mg,Fe,Al)SiO_3$.

6.5 PGMS IN NORMAL CONENTRATES

Most of the **platinum, palladium, rhodium, iridium, ruthenium** and **osmium** content of pgm concentrates is contained as a fine residual metallic mud of low crystallinity.

The overdrying of normal concentrates at the base metal refinery produces **sintered platinum**, thereby reducing its solubility in the oxidative leach. (Small amounts of **palladium, iridium** and **rhodium** are also rendered insoluble by the sintering process.) Drying a normal concentrate in the presence of sulphuric acid produces a metallic pgm residue of **lower crystallinity** relative to a normal concentrate dried without sulphuric acid.

6.6 OXIDATIVE LEACHING OF NORMAL CONCENTRATES

Low **platinum** and **palladium** solubility in normal concentrates is the result of the mixed sulphide $(Pt,Pd)S$ (where $Pt>>Pd$). This seems to be a residual mineral phase.

$(Pt,Pd)S$ can be converted to metallic platinum and palladium of relatively low crystallinity by ignition in air.

Low **rhodium** and **ruthenium** (and **iridium**) solubility is due in most cases to a compound of the type $(Ru,Rh,Ir,Pt)AsS$. The composition of this compound is variable.

Low **rhodium** and **platinum** solubility in normal concentrates can be caused by the alloy $Rh_{0.57}Pt_{0.43}$, a residual mineral phase.

Low **rhodium** and **iridium** solubility in normal concentrates can be due to the alloy $(Fe,Rh)_{1.8}Ir_{0.2}$, a residual mineral phase.

Low **ruthenium** solubility is usually the result of insoluble highly crystalline ruthenium-osmium alloy $(\sim Ru_{16}Os)$.

Low **iridium** and **osmium** solubility can be due to the alloy iridosmine (Os,Ir,Ru).

Low **silver** solubility is due to insoluble silver chloride $(AgCl)$.

6.7 OXIDATIVE LEACHING OF OVERDRIED NORMAL CONCENTRATES

Low **platinum** solubility is due to sintered highly crystalline platinum (Pt)

Low **palladium** solubility is due to palladium oxide (PdO).

Low **ruthenium** solubility is due to ruthenium oxide (RuO_2).

Low **iridium** solubility is probably due to iridium oxide (IrO_2).

6.8 OXIDATIVE LEACHING OF MINOR CONCENTRATES

Low **platinum** solubility in minor concentrates is due to sintered platinum of high crystallinity formed during the high temperature roast to volatilize selenium.

Low **palladium** solubility in minor concentrates seems to be due to the formation of palladium oxide (PdO) (by analogy with overdried normal concentrates). This would be formed during roasting.

Low **rhodium** solubility is due to rhodium selenide ($RhSe_{2+x}$), formed by the reaction of precipitated rhodium with elemental selenium during roasting.

Low **ruthenium** (and **iridium**) solubility in minor concentrates is due to ruthenium oxide (RuO_2) (and iridium oxide - IrO_2) formed during roasting.

6.9 PRECIPITATES AND SALTS

Iron is precipitated by pH control from hot acidic solutions as **iron oxide hydroxide** (β-FeOOH).

Tellurium coprecipites well with iron oxide hydroxide.

Iron can be present in pre-treated concentrates as **sodium iron hydroxide sulphate hydrate** ($Na_2Fe(SO_4)_2(OH)\cdot3H_2O$).

After gold is reduced to **metallic gold**, highly efficient filtration is required to remove all particulate gold from solution or it can precipitate erraticaly during subsequent operations.

pH control using sodium hydroxide or sodium carbonate causes **sodium chloride** (NaCl) to be present in many precipitates.

Cooling chloride solutions can lead to the precipitaton of **lead chloride** ($PbCl_2$).

Dried precipitates can contain **sodium carbonate monohydrate** ($Na_2CO_3\cdot H_2O$).

Pure ammonium hexachloroplatinate (IV) can contain high amounts of **ammonium chloride** (NH_4Cl).

6.10 THE LEAD FUSION PROCESS

Fusing **metallic pgm waste** with lead can lead to the formation of a **lead-pgm alloy** of the type $Pb(Pd,Pt)_3$ of low solubility.

Ruthenium oxide reacts with lead oxide (formed during the decomposition of lead carbonate, $PbCO_3$) forming **lead ruthenium oxide** $Pb_2Ru_2O_{6.5}$ which does not dissolve in nitric acid.

Hydrated iron oxides (if present in waste precipitates) are converted to **iron oxide** (Fe_3O_4) in the lead fusion process, which does not dissolve in nitric acid.

Lead sulphate ($PbSO_4$) can be a major constituent of the nitric insoluble residue of lead ingots.

CONVERTER MATTE

Ni3S2	Cu2S	Ni-Cu
NiFe2O4	NiO	Fe3O4
	Co3S4	

FIRST STAGE LEACH RESIDUE

Ni3S4	NiS	Cu1.8S
	Ni-Cu	
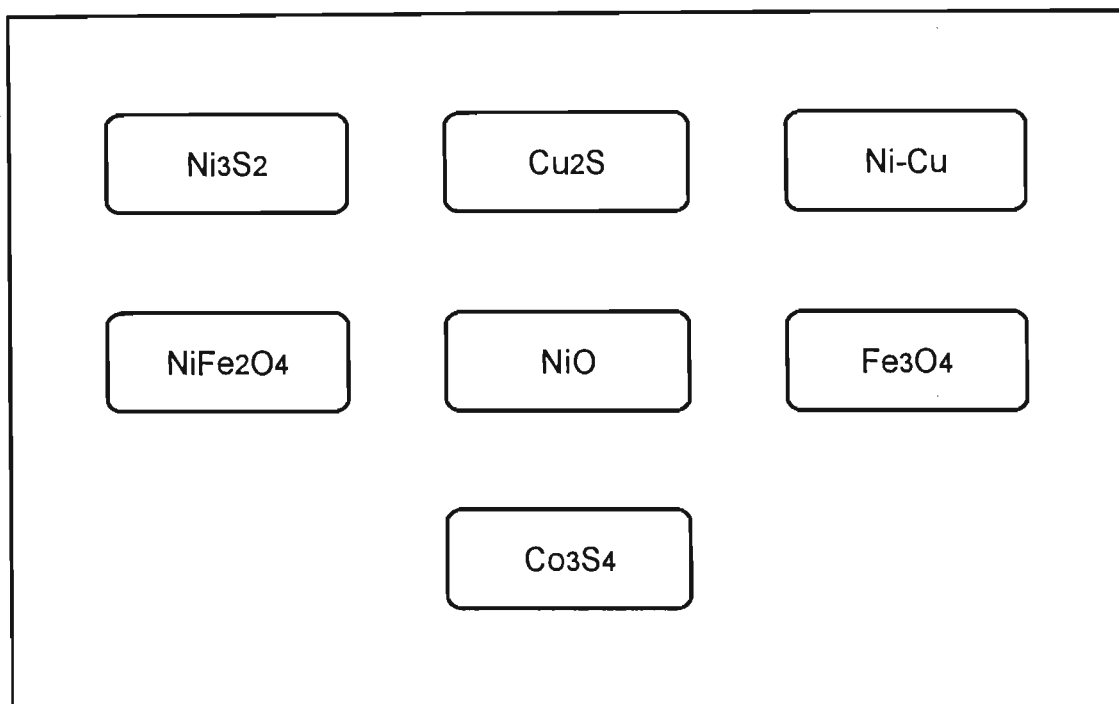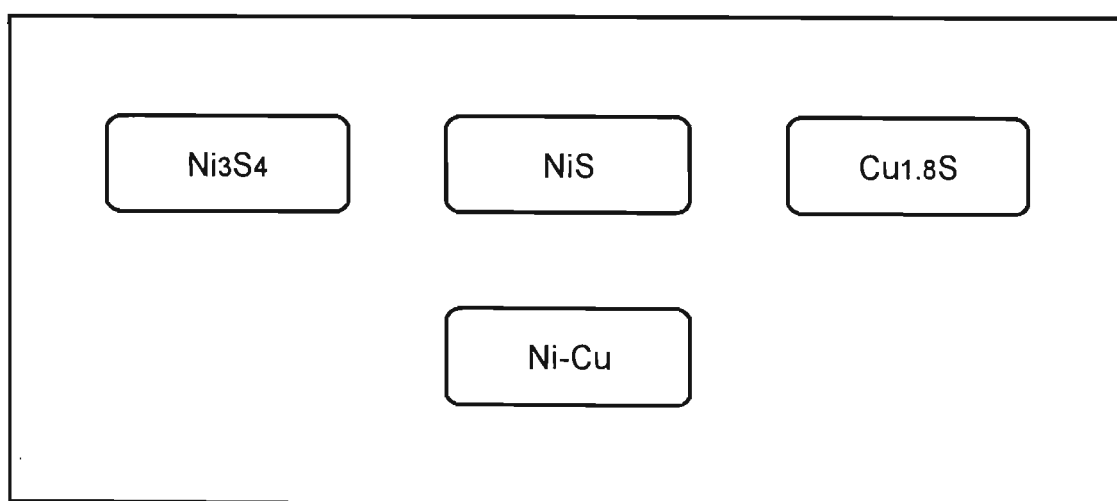
NORMAL CONCENTRATE

[Pt,Pd,Rh,Ir]	(Pt,Pd)S	[Ru,Os]
Cu_3Pt	$Ru_{16}Os$	
CuS	(Ru,Rh,Ir,Pt)AsS	
$CuSO_4 \cdot 5H_2O$	$(Fe,Rh)_{1.2}Ir_{0.8}$ (partially soluble)	
$Cu_4SO_4(OH)_6 \cdot H_2O$	$Rh_{0.57}Pt_{0.43}$	
NiO (partially soluble)	(Os,Ir,Ru)	Pt (SINTERED)
$NiFe_2O_4$ (partially soluble)	SiO_2	RuO_2 / IrO_2
$PbSO_4$	$(Mg,Fe,Al)SiO_3$	PdO

SOLUBLE	INSOLUBLE	INSOLUBLE (overdried)

MINOR CONCENTRATE

[Pt,Pd,Rh,Ir]

Pt
(SINTERED)

[Ru,Os]

RhSe2+x

RuO2 / IrO2

PdO (?)
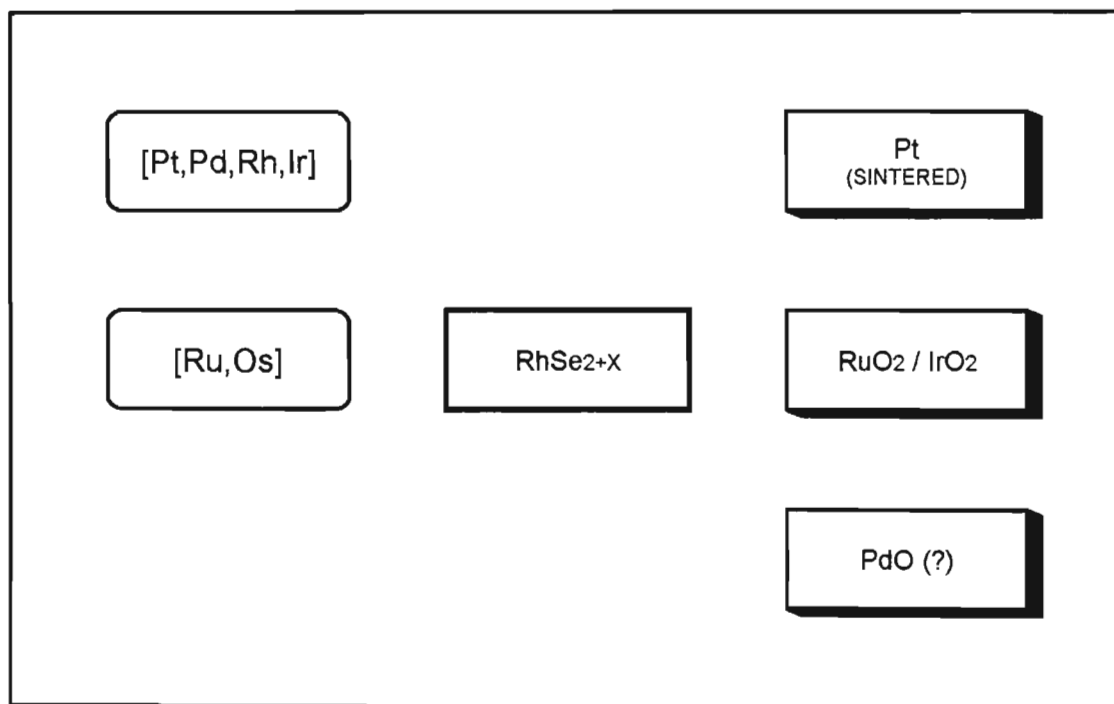
SOLUBLE

INSOLUBLE
(reacted)

INSOLUBLE
(overdried)

PRECIPITATES AND SALTS

β–FeOOH	$Na_2CO_3 \cdot H_2O$	NH_4Cl
$Na_2Fe(SO_4)_2(OH) \cdot 3H_2O$	NaCl	Au

LEAD FUSION PROCESS

```
  PbCO3  ────▶   PbO   ────▶    Pb

                  │              │
                  ▼              ▼

  FeOOH          RuO2          Pd,Pt

    │              │             │
    ▼              ▼             ▼

  Fe3O4        Pb2Ru2O6.5    Pb(Pd,Pt)3


                PbSO4
```
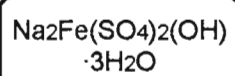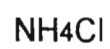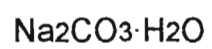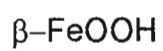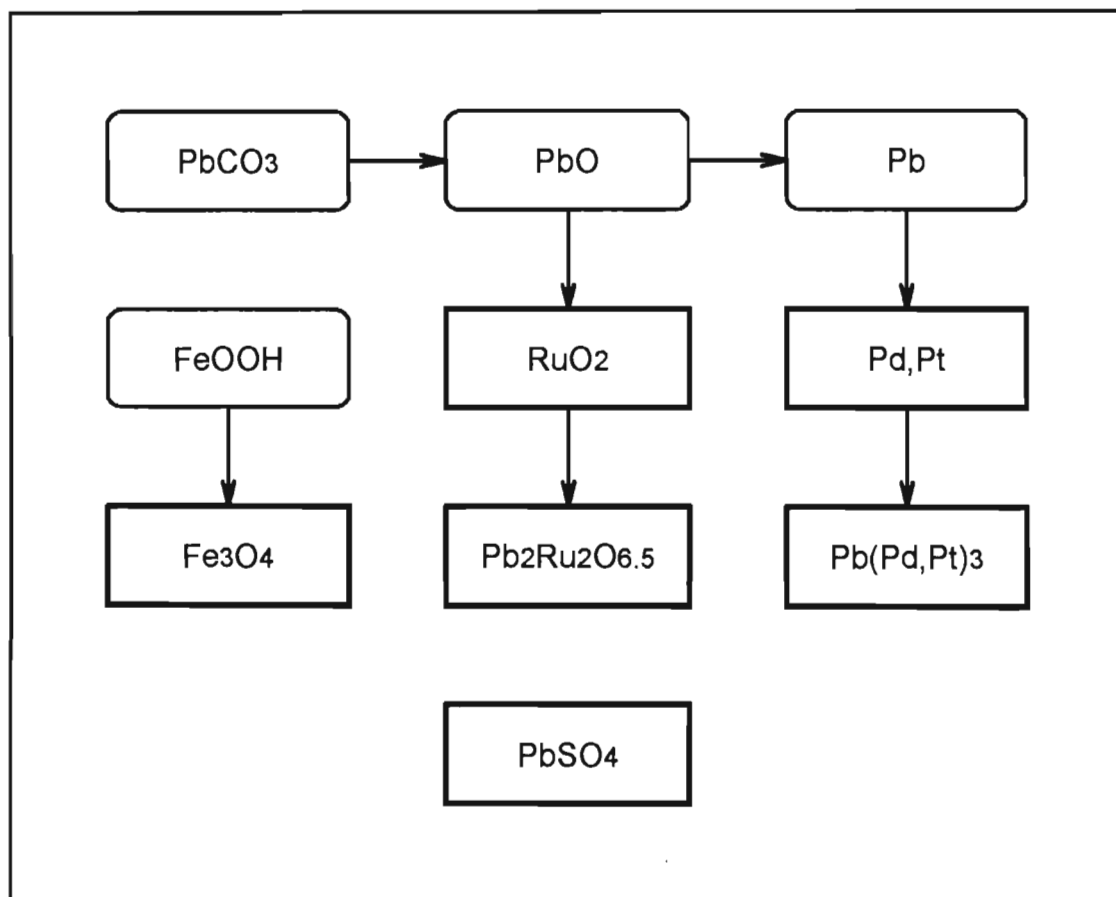
HNO3
SOLUBLE

HNO3
INSOLUBLE

REFERENCES AND NOTES

NOTE : All JCPDS Numbers apply to the following sources :

Joint Committee on Powder Diffraction Standards (JCPDS) -

International Centre for Diffraction Data (ICDD),

1601 Park Lane, Swarthmore, Pennsylvania 19081, USA (publishers)

(a) Powder Diffraction File, Sets 1-35

(b) Powder Diffraction File Search Manual, Inorganic, JCPDS-ICDD, 1990

(c) Metals and Alloys Search Manual, JCPDS-ICDD, 1978

(d) Selected Powder Diffration Data for Metals and Alloys, JCPDS-ICDD, 1978

(e) Inorganic Index, JCPDS, 1972

(f) Mineral Powder Diffraction File Data Book, JCPDS-ICDD, 1980

CHAPTER 1 INTRODUCTION

(1)   Hofirek, Z (1988), The chemistry of the nickel-copper matte leach process at Rustenburg Refiners (Rustenburg Refiners, Pty. Ltd.)

CHAPTER 2 X-RAY POWDER DIFFRACTION ANALYSIS

Bibliography

(1)   (a) Barrett, C & Massalski, T (1980), "Structure of the Metals", 3rd ed., Pergamon Press : U.K.   (Figure 2.2.2-1, p. 8)

(b) D`eye, W & Wait, E (1960), "X-Ray Powder Photography in Inorganic Chemistry", Butterworths : London

(c) Whiston, C (1987), "X-ray Methods", John Wiley & Sons : London

(d) Klug, H & Alexander, L (1970), "X-ray Diffraction Procedures for Polycrystalline and Amorphous Materials", John Wiley & Sons

(e) Stout, G & Jensen, L (1968), "X-ray Structure Determination - A Practical Guide", Macmillan

(f) Azaroff, L (1968), "Elements of x-ray crystallography", McGraw-Hill

(g) Guinier, A (1952), "X-ray Crystallographic Technology", Hilger and Watts Ltd. : London

(2)   See (1)(a)-(g).

(3)   See (1)(a)-(g).

(4)   Philips Operation Manual

(5)   Brindley, G and Brown, G, "Crystal Structures of Clay Minerals and their X-ray Identification", Chapter 7, p.425 (Publisher and date of publication unknown.)

(6)   See Note at beginning of References ((b)-(f))

CHAPTER 3 **PLATINUM GROUP METAL MINING IN SOUTH AFRICA**

Informational sources :

A. Newman, S (1973), Platinum, *Trans. Inst. Min. Metall., Section A*, 82, A52-68

B. Cabri, L (1981), " Platinum-Group Elements : Mineralogy, Geology, Recovery"
    The Canadian Institute of Mining and Metallurgy, CIM Special Volume 23,
    Canada, p. 201-205

C. McLaren, C et al. (1982), The platinum-group chemistry and mineralogy of the
    UG-2 chromite layer of the Bushveld complex, Economic Geology, 77,
    p. 1348-1366

D. McLaren, C, A mineralogical investigation of the platinum-group minerals in the
    UG-2 layer of the Bushveld complex with special reference to the recovery of the
    minerals from the ores.
    (Source : C McLaren, Dept. of Geology, Rand Afrikaans University,
    PO Box 524, Johannesburg, 2000)

CHAPTER 4 **THE BASE METAL REFINERY**

(1) Habashi, F (1986), "Principles of Extractive Metallurgy, Volume 3 :
     Pyrometallurgy", Gordon and Breach Science Publishers, UK
     Habashi, F (1994), "Conversion Reactions in Inorganic Chemistry"
     J. Chem. Ed., 71, 130

(2) Moore, J. (1981), "Chemical Metallurgy", Butterworths : London, p. 215-226
     & p. 232-236

(3) Gilchrist, J (1982), "Extraction Metallurgy", 2nd ed., Pergamon Press : Oxford,
     p.275-293

(4) Boldt, J (1967), "The Winning of Nickel", Longmans : Toronto, p. 227-288

(4a) Mellor, J (1936), "A Comprehensive Treatise on Inorganic and Theoretical
     Chemistry", Longmans : London, Volume XV, Chapter LXVIII (Nickel),
     p. 15-20

(5) Barplats Base Metal Refinery Process Outline, Barplats Refineries (Pty) Limited

(6) JCPDS Number : 08-0126
     Peacock (1946), *University of Toronto Studies, Geological Series.* 51, 59-69
     Structure : Westgren, A (1938), Die Kristallstruktur von Ni_3S_2,
     Z. Anorg. Chem. 239, 82-84

(7) JCPDS Number : 23-0961
     Cook, Jr., Thesis : The Cu-S Phase Diagram, Gould Labs, Cleveland, Ohio, USA
     Cook et al.(1970), *J. Appl. Phys.*, 41, 3058
     Structure : Evans, H (1971), Crystal structure of low chalcocite, *Nature*, London,
     232, 69-70

(8)   Ni : JCPDS Number : 04-0850

         Swanson & Tatge (1953), NBS Circular 539, $\underline{1}$, 13

         Cu : JCPDS Number : 04-0836

         Swanson & Tatge (1953), NBS Circular 539, $\underline{1}$, 15

(9)   JCPDS Number : 19-0629

         National Bureau of Standards (1967), Monograph 25, Sec. 5, 31

(9a)   JCPDS Number : 10-0325

         National Bureau of Standards (U.S.) (1960), Circular 539, $\underline{10}$, 44

(10)   JCPDS Number : 04-0835

         Swanson & Tatge (1953), NBS Circular 539, $\underline{1}$, 47

(11)   Putnam, A et al. (1973), "Metals Handbook", $\underline{8}$, "Metallography, Structures
         and Phase Diagrams", 8th ed., American Society for Metals

         Also Ref. (12), p. 294.

(12)   Vaughan, D & Craig, J (1978), "Mineral Chemistry of the Metal Sulphides",
         Cambridge University Press, p. 293

(13)   Ref. (6), (JCPDS card data)

(14)   Ref. (12), p. 60

(15)   Ref. (12), p. 60-61 & p. 161

(16)   Compare powder diffraction data of geological Ni_3S_2 (Ref. (6)) with synthetic
         Ni_3S_2 (JCPDS Number : 02-0772)

         Westgren (1938), *Z. anorg. allgem.Chem.*, $\underline{239}$, 82

(17)   Ref. (12), p. 290-291

(18)   Ref. (7), (JCPDS card data)

(19)   Kostov,I & Minceva-Stefanova, J (1982), "Sulphide Minerals-Crystal Chemistry,
         parageneses and systematics", E. Schweizerbart'sche Verlagsbuchhanlung :
         Stuttgart, p. 48

(20)   Ref. (19), p. 49

         Ref. (7), (Evans, H (1971))

(21)   Ref. (12), p. 384

(22)   See Ni-Cu phase diagram in Ref. (11).

(23)   West, E (1982), "Copper and it's Alloys", John Wiley & Sons, p. 119

(24)   Density range from JCPDS card data (See Ref. (8).).

(25)   See Ref. (9) and (9a).

(26)   Ref. (3), p. 315

(27)   Wells, A (1984), "Structural Inorganic Chemistry", 5th ed.,Oxford University
         Press : Oxford, p. 538

(28)   Ref. (3), p. 315

(29)   Ref. (10), (JCPDS card data)

(30) Ref. (11), p. 10

(31) Wood, E (1964), "Crystals and Light", van Nostrand, p.80

(32) Ref. (31), p. 81

(33) Wilcox, W (1969), *Separation Science*, 4, 95

(34) Brugman, C & Kerfoot, D (1986), Treatment of Nickel Copper Matte at Western Platinum by the Sherritt Acid Leach Process, 25th Annual Conference of Metallurgists, p. 2

(35) Ref. (34), p. 3

(36) Cahn, R (1965), "Physical Metallurgy", North Holland, p. 294-295

(37) Whiston, C & Prichard, F (1987), "X-ray Methods", John Wiley & Sons, p.133

(38) Ref. (37), p. 32

(39) Guinier, A (1952), "X-ray Crystallographic Technology", Hilger and Watts, p. 212

(40) Ref. (23), p. 119

(41) JCPDS Number : 08-0106
Gricaenko, Sludskaja & Ajdinjan (1953), *Zapiski Vses. Mineral. Obsh.*, 82, 42-52
Structure : Ref. (12), p. 49-51

(42) JCPDS Numbers given in Table 4.8-2. Cards can be found in :
Weissmann, S (Ed.) (1978), "Selected Powder Diffraction Data for Metals and Alloys", Data Book, 1st ed., International Centre for Diffraction Data : USA, Vol. I and II

(43) Morimoto, Koto & Shimazaki (1969), *Am. Mineral.*, 54, 1256-1268

(44) JCPDS Number : 23-0962
See Ref. (7) Cook, Jr. Thesis.

(45) JCPDS Number : 12-0041
National Bureau of Standards (U.S.) (1962), Monograph 25, Section 1, 37
Structure : Rajamani, V & Prewitt, C (1974), The crystal structure of millerite, *Can. Mineral.*, 12, 253-257

(46) Ref. (12), p. 51

(47) Known nickel-iron alloys are : NiFe
Known iron-platinum alloys are : PtFe (common), Pt_3Fe (rare)

(48) Ref. (34), p. 9

(49) Ref. (34), p. 10

(50) Hofirek, Z (1988), The chemistry of the nickel-copper matte leach process at Rustenburg Refiners (Rustenburg Refiners, Pty. Ltd.)

CHAPTER 5 THE PLATINUM GROUP METAL REFINERY

(1)   Various private communications
        Livingstone, S (1973), "The Chemistry of Ruthenium, Rhodium, Palladium,
        Osmium, Iridium and Platinum", Pergamon Texts in Inorganic Chemistry, 25,
        Pergamon Press, p. 1170-1173

(2)   JCPDS Number : 10-0325
        National Bureau of Standards (U.S.) (1960), Circular 539, 10, 44

(3)   JCPDS Number : 13-0157
        MacKay (1960), *Min. Mag.* 32, 545

(4)   See Ref. (3).

(4a)   For an excellent photo of β-FeOOH crystals see :
        Habashi, F (1986), "Principles of Extractive Metallurgy, Volume 3 :
        Pyrometallurgy", Gordon and Breach Science Publishers, UK, p. 277

(5)   Remy, H (1961), "Treatise on Inorganic Chemistry", Volume II, Elsevier
        Publishing Company, p.273

(6)   JCPDS Number : 17-0156
        Cesbron (1964), *Bull. Soc. franc. Mineral. Crist.* 87, 125-143

(7)   Mellor, J (1935), "A Comprehensive Treatise on Inorganic and Theoretical
        Chemistry", Longmans : London, Volume XIV, Chapter LXVI (Iron), p.45-46

(8)   See Ref. (7).

(9)   Wells, A (1984), "Structural Inorganic Chemistry", 5th ed.,Oxford University
        Press : Oxford, p. 599

(10)   Cabri, L (1981), " Platinum-Group Elements : Mineralogy, Geology, Recovery"
        The Canadian Institute of Mining and Metallurgy, CIM Special Volume 23,
        Canada, p. 91 & p. 144

(11)   JCPDS Number : 26-1139
        Cabri et al. (1973), *Can. Mineral.*, 12, 21-25

(12)   JCPDS Number : 04-0835
        Swanson and Tatge (1953), NBS Circular 539, 1, 47

(13)   JCPDS Number : 11-0646

(14)   JCPDS Number : 20-0364
        Mrose and Reichen (1967), *Am. Mineral.*, 52, 1582

(15)   Brugman, C & Kerfoot, D (1986), Treatment of Nickel Copper Matte at Western
        Platinum by the Sherritt Acid Leach Process, 25th Annual Conference of
        Metallurgists, p. 10

(16)   JCPDS Number : 06-0464
        NBS (1955), Circular 539, 4, 13-14

(17)   JCPDS Number : 35-1358

(18)   Ref. (9), p. 1297-1298

(19)   JCPDS Number : 07-0138

        Schubert et al. (1955), *Z. Metallkunde*, <u>46</u>, 692-715

(20)   JCPDS Number : 06-0663

        NBS (1955), Circular 539, <u>4</u>, 5

        Am. Mineral. (1976), <u>61</u>, 177

(21)   Ref. (10), p. 22

(22)   Livingstone, S (1973), "The Chemistry of Ruthenium, Rhodium, Palladium,
        Osmium, Iridium and Platinum", Pergamon Texts in Inorganic Chemistry, Vol 25,
        Pergamon Press, p. 1171 (Many other texts also give this information.)

(23)   Avtokratova, T (1969), "Analytical Chemistry of Ruthenium", Ann Arbor-
        Humphrey Science Publishers : London, p. 4

        Also Ref. (22), p. 1194.

(24)   Ref. (9), p. 541

(25)   Gutbier, A et al. (1916), *Z. anorg. Chem.*, <u>96</u>, 182

(26)   JCPDS Number : 21-1172

        Boman (1970), *Acta Chem. Scand.*, <u>24</u>, 116

(27)   JCPDS Number : 21-1315

        Roy and Muller (1967), *Bull. Am. Ceram. Soc.*, <u>46</u>, 881

(28)   JCPDS Number : 15-0870

        NBS (U.S.) (1965), Monograph 25, Section 4, 19

(29)   JCPDS Number : 23-1297

        Boman (1970), *Acta Chem. Scand.*, <u>24</u>, 123-128

(30)   Cotton, S & Hart, F (1984), "The Heavy Transition Elements", Macmillan Press :
        London, p. 83

(31)   JCPDS Number : 36-0242

(32)   Ref. (22), p. 1216

(33)   JCPDS Number : 19-1047

        Rummery and Heyding (1966), *Can. J. Chem.*, <u>44</u>

(34)   See Ref. (33).

        See also Hulliger (1964), *Nature*, <u>204</u>, 644.

(35)   See Ref. (33).

(36)   JCPDS Number : 27-0504

        Cabri, L et al. (1974), *Can. Mineral.*, <u>12</u>, 399-403

(37)   JCPDS Number : 06-0598

        NBS (1955), Circular 539, Vol. 4, 9-10

(38)   Ref. (10), p. 90

(39) JCPDS Number : 25-1408

      Snetsinger (1973), *Am. Mineral.*, 58, 189-194

      For radiation information see card and above reference.

(40) JCPDS Number : 19-1107

      Sutarno et. al. (1966), *Can. J. Chem.*, 44

(41) See Ref. (40).

(42) JCPDS Numbers given in Table 5.5.4-10

      Mineral species source : Ref. (10), p. 88-92

(43) Cabri, L et al. (1977), *Can. Mineral.*, 15, 385

      See also card information (JCPDS Number 29-0974).

(44) JCPDS Number : 02-1194

      Swjaginzeff and Brunowski (1932), *Z. Krist.*, 83, 188

(45) See Ref (44) and Ref. (10), p. 160.

(46) Ref. (10), p. 160

(47) JCPDS Number : 06-0515

      Swanson et al. (1955), NBS Circular 539, 4, 27

(48) Ref. (22), p.1279

(49) JCPDS Number : 18-0972

      Gronvold, et al. (1960), *Acta Chem. Scand.*, 14, 1879-1893

(50) Sidgwick, N (1962), "The Chemical Elements and their Compounds", Vol. II,
      Oxford University Press : Oxford, p.1581

(51) JCPDS Number : 04-0802

      Swanson and Tatge (1953), NBS Circular 539, 1, 31

(52) JCPDS Number : 05-0681

      Swanson and Tatge (1953), NBS Circular 539, 1, 21

(53) McLaren, C et al. (1982), The platinum-group chemistry and mineralogy of the
      UG-2 chromite layer of the Bushveld complex, Economic Geology, 77,
      p. 1348-1366

(54) See Ref. (53) and McLaren, C, A mineralogical investigation of the platinum-
      group minerals in the UG-2 layer of the Bushveld complex with special reference
      to the recovery of the minerals from the ores. (Source : C McLaren, Dept. of
      Geol., Rand Afrikaans University, PO Box 524, Johannesburg, 2000)

(55) Ref. (10), p. 166

(56) Ref. (10), p. 101

(57) JCPDS Number : 06-0480

      NBS (1955), Circular 539, 4, 44-45

(58) Vogel, A (1982), "Vogel's Textbook of Macro and Semimicro Qualitative
      Inorganic Analysis", 5th ed., Longman : U.K., p. 592

(59) See Ref. (60).

(60) Cotton, S & Hart, F (1984), "The Heavy Transition Elements", Macmillan Press : London, p. 140-141

(61) JCPDS Number : 05-0490
      Swanson and Fuyat (1954), NBS Circular 539, 3, 24

(62) JCPDS Number : 19-0605
      Howie (1963), *Mineralogy Society of America*, Special Paper No. 1

(63) JCPDS Number : 20-0827
      Cabri and Traill (1966), *Can. Mineral.*, 8, 541-550

(64) Cabri, L (1981), " Platinum-Group Elements : Mineralogy, Geology, Recovery" The Canadian Institute of Mining and Metallurgy, CIM Special Volume 23, Canada, p. 147

(65) JCPDS Number : 05-0577
      Swanson and Fuyat (1954), NBS Circular 539, 3, 67

(66) The Merck Index (1989), Merck : USA, 11th ed., 5302, p. 853

(67) JCPDS Number : 34-0471
      See also Ref. (68).

(68) Horowitz, H (1981), New oxide pyrochlores, *Mat. Res. Bul.*, 16, 489-496
      Horowitz, H, Longo, J & Haberman, J : U.S. Patent 4, 124,539

(69) JCPDS Number : 26-1150
      National Burea of Standards (1975), Monograph 25, Section 12, 23

(70) JCPDS Number : 04-0784
      Swanson and Tatge (1953), NBS Circular 539, 1, 33

(71) JCPDS Number : 05-0628
      Swanson and Fuyat (1953), NBS Circular 539, 2, 41

(72) JCPDS Number : 08-0448
      NBS (1959) Circular 539, 8, 54

(73) JCPDS Number : 07-0007

APPENDIX 1

COHEN'S LEAST-SQUARES METHOD

The Bragg equation for calculating the unit cell dimensions of a cubic cell in the absence of systematic errors is :

$$\sin^2\theta = A(h^2 + k^2 + l^2)$$

where $\theta = (2\theta / 2)$

h, k, l = Miller indices of the plane

$A = (\lambda^2 / 4a_0^2)$ $\qquad \lambda$: wavelength of x-ray radiation (Å) : *ie.* 1.78894Å

a_0 : edge length of the cubic unit cell (Å)

Cohen [1] has shown that if systemmatic errors, $(\Delta d / d)$, are present in the diffraction data, and these variations are assumed to be proportional to $\cos^2\theta$ for high angles, then the difference between the true and the observed $\sin^2\theta$ values ($\Delta \sin^2\theta$) will be equal to $D\sin^2 2\theta$, where D is known as the 'drift' constant.

The Bragg equation in the presence of systemmatic errors thus becomes :

$$\sin^2\theta = A(h^2 + k^2 + l^2) + D\sin^2 2\theta$$

If two or more reflections are obtained, A and D can be calculated, and hence an accurate value for a_0.

The best results are however obtained by combining all the high angle data and calculating A and D by the least-squares method. The equations used are :

$$A\Sigma\alpha_i^2 + D'\Sigma\alpha_i\delta_i = \Sigma\alpha_i\sin^2\theta_i$$
$$A\Sigma\alpha_i\delta_i + D'\Sigma\delta_i^2 = \Sigma\delta_i\sin^2\theta_i$$

where $\alpha = (h^2 + k^2 + l^2)$

$\delta = 10\sin^2 2\theta$

(a factor of 10 is introduced so that coefficients are of the same order of magnitude)

$D' = (D / 10)$

Thus :

$$A = \{ \ [(\Sigma\delta_i \sin^2\theta_i \ / \ \Sigma\delta_i{}^2) - (\Sigma\alpha_i \sin^2\theta_i \ / \ \Sigma\alpha_i\delta_i)] \ / \ [(\Sigma\alpha_i\delta_i \ / \ \Sigma\delta_i{}^2) - (\Sigma\alpha_i{}^2 \ / \ \Sigma\alpha_i\delta_i)] \ \}$$

from which an accurate value of a_0 can be calculated.

Using the Standard Powder Diffraction File data for copper one obtains an a_0 value of 3.6148Å using the above method on all listed peaks and 6 decimals throughout the calculation.   The value quoted is 3.6150Å.   The corresponding values for nickel are 3.5239Å (calculated), and 3.5238Å (quoted).

(1) Cohen M (1935), *Rev. Sci. Instr.*, <u>6</u>, p. 68

<u>See also :</u>   Barrett and Massalski (1980), "Structure of Metals", 3rd Rev Ed.,

Pergamon, UK, p. 146-147

APPENDIX 2

ISOLATION OF THE ALLOY PHASE

The isolation of the nickel-copper alloy phase from matte is difficult requiring the total dissolution of the binary sulphide matrix ($Ni_3S_2 + Cu_2S$). Samples of almost pure alloy can however be isolated much more easily from first stage leach residue. The original nickel sulphide component of the matrix (Ni_3S_2) is totally consumed in this leach. It cannot however be assumed that all the original copper sulphide has been consumed. In order to ensure that all the copper sulphides were consumed the following leach was performed :

20.0g of first stage leach residue were placed in a solution of 60.0g thiourea in 500ml 1M HCl. The suspension was rapidly stirrered for 40 minutes at room temperature using a glass rod. A magnetic stirrer was then introduced and stirring of the suspension continued. Magnetic alloy particles collected on the stirrer-bar as a silvery-black powder which was washed off into a crucible. After several collections the isolated alloy powder was washed in ethanol, followed by ether, and air dried.

An EDAX analysis showed the alloy to be 79 wt% nickel and 21 wt% copper. This agreed well with the value of 79.9 wt% nickel and 20.9 wt% copper calculated using XPD data collected from the original matte. The alloy present in first stage leach residue thus appeared to be identical with that present in the original matte.

Microscopic examination showed that not all the particles were well formed, although some well formed cubic and octahedral crystals were observed. The crystals were extremely small, this probably explaining the poor magnetic separation of this phase.

Two photographs of alloy crystals (cubic and octahedral), totally freed from the sulphide matrix, obtained using an electron microscope are shown in Figures A and B. The small size of the crystals should be noted.
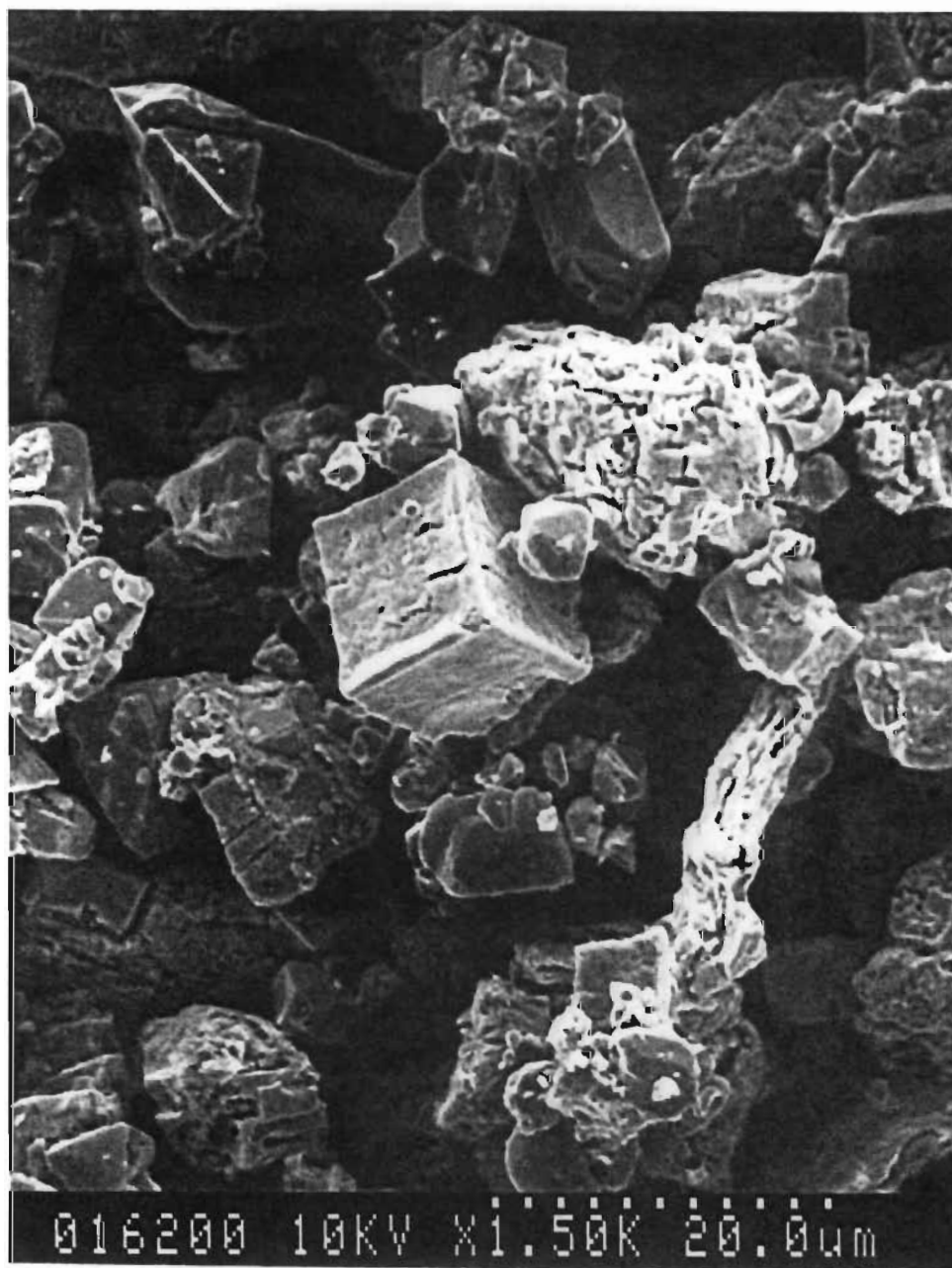
Figure A An isolated cubic Ni-Cu crystal

Figure B An isolated octahedral Ni-Cu crystal